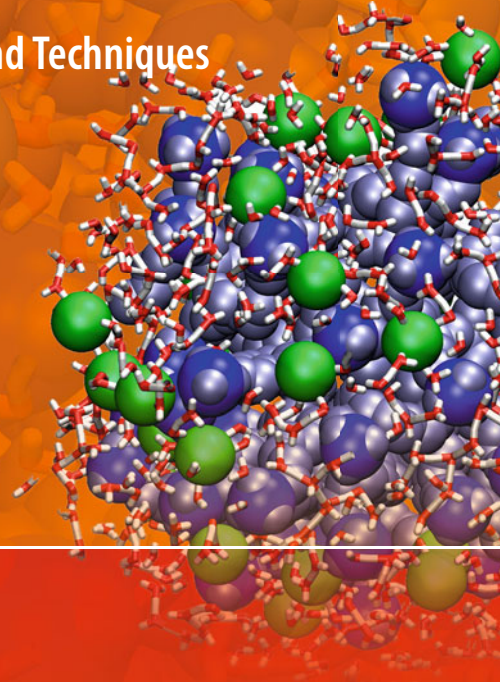


Neutron Scattering Applications and Techniques

Nikolay Kardjilov
Giulia Festa *Editors*



Neutron Methods for Archaeology and Cultural Heritage

EXTRAS ONLINE

 Springer

Neutron Scattering Applications and Techniques

Series editors

Ian S. Anderson, Oak Ridge National Laboratory, Oak Ridge, TN, USA

Alan J. Hurd, Los Alamos National Laboratory, Los Alamos, NM, USA

Robert L. McGreevy, ISIS, Didcot, UK

Neutron scattering techniques provide exceptional tools for studying the structure and dynamics of materials at the molecular level. New user facilities, instrumentation and software now provide the “non-expert” researcher with the opportunity of using neutron techniques to provide answers to challenging research questions in physics, biology, chemistry, engineering and medicine that cannot be answered by any other technique. In order to maximize this potential it is crucial to provide the research community with an up to date series of books which describe the fundamentals of the techniques as applied in a given field, and provide recent examples of applications to showcase the capabilities.

The Neutron Scattering Applications and Techniques book series is comprehensive, covering a broad range of research topics. Its goal is to provide scientists and engineers with reference books which highlight the unique capabilities of neutron techniques to elucidate critical questions in established and emergent areas of science. The books are suitable for graduate students, postdocs, and research professionals in the field, and serve as a reference to both experts and (scientific) newcomers wishing to learn about the subject.

Editorial Board

Masatoshi Arai, Japan Atomic Energy Agency

Shenda Baker, Harvey Mudd College

Collin Broholm, Johns Hopkins University

Patrick Gallagher, National Institute of Standards and Technology

Stephen Nagler, Oak Ridge National Laboratory

Roger Pynn, Indiana University

J. Michael Rowe, National Institute of Standards and Technology

Helmut Schober, Institut Laue-Langevin

Sunil Sinha, University of California

Ray Teller, Pacific Northwest National Laboratory

Jill Trehwella, University of Sydney

Christian Vettier, European Spallation Source

More information about this series at <http://www.springer.com/series/8141>

Nikolay Kardjilov · Giulia Festa
Editors

Neutron Methods for Archaeology and Cultural Heritage

 Springer

Editors

Nikolay Kardjilov
Institute of Applied Materials
Helmholtz Zentrum Berlin
Berlin
Germany

Giulia Festa
Department of Physics and Centre NAST
University of Rome Tor Vergata
Rome
Italy

ISSN 1868-0372

ISSN 1868-0380 (electronic)

Neutron Scattering Applications and Techniques

ISBN 978-3-319-33161-4

ISBN 978-3-319-33163-8 (eBook)

DOI 10.1007/978-3-319-33163-8

Library of Congress Control Number: 2016949631

© Springer International Publishing Switzerland 2017

This work is subject to copyright. All rights are reserved by the Publisher, whether the whole or part of the material is concerned, specifically the rights of translation, reprinting, reuse of illustrations, recitation, broadcasting, reproduction on microfilms or in any other physical way, and transmission or information storage and retrieval, electronic adaptation, computer software, or by similar or dissimilar methodology now known or hereafter developed.

The use of general descriptive names, registered names, trademarks, service marks, etc. in this publication does not imply, even in the absence of a specific statement, that such names are exempt from the relevant protective laws and regulations and therefore free for general use.

The publisher, the authors and the editors are safe to assume that the advice and information in this book are believed to be true and accurate at the date of publication. Neither the publisher nor the authors or the editors give a warranty, express or implied, with respect to the material contained herein or for any errors or omissions that may have been made.

Printed on acid-free paper

This Springer imprint is published by Springer Nature

The registered company is Springer International Publishing AG

The registered company address is: Gewerbestrasse 11, 6330 Cham, Switzerland

Preface

Our cultural heritage is the legacy that our society has inherited from the past, and is bestowed for the benefit of future generations. It gives us insight into where we came from and who we are. Its conservation is important not only from the cultural point of view, but also from a practical one. In this context, neutron-based characterization techniques play a fundamental role because neutrons are very penetrating and therefore ideal for the non-invasive investigation of artefacts, allowing both surface and bulk properties to be measured. The full suite of neutron techniques available for cultural heritage research is impressive and many essential results have been obtained using one or more of these tools to provide information that cannot be determined in any other way. Neutron methods allow the characterization of the composition and mechanical properties of ancient materials, helping to answer questions related to the dating, the manufacturing process or the state of degradation of artefacts. The results obtained from neutron investigations are in many cases essential for setting the proper restoration and conservation strategies or for performing the right classification of ancient samples. Nevertheless, the application of neutron beams for cultural heritage purposes is often considered as 'exotic' by the researchers and restorers in the field due to the limited availability of neutron sources which are usually large-scale research facilities with restricted access procedures and complex instrumentation.

The intent of this book is to provide an introduction to the wide range of neutron-based characterization techniques, and their impact in cultural heritage research, to the broad community of archaeologists, paleontologists, restorers and curators, historians and holders of private collections as well as material scientists and engineers dealing with the characterization of ancient materials. Answers to many practical questions will be given in conjunction with detailed examples describing some of the more fascinating highlights of applications of neutron techniques in recent investigations, in a form accessible to a large readership. Part I will be dedicated to stories describing discoveries brought about by the use of

neutron techniques in various applications. Part II will cover the experimental techniques in appropriate detail: basic principles, limitations and fields of application. The book encloses visual information in the form of videos related to the contents available in the e-book version of the volume.

Berlin, Germany
Rome, Italy
October 2016

Nikolay Kardjilov
Giulia Festa

Acknowledgments

We would like to thank all the authors and experts in the field of neutrons applied to cultural heritage for their valuable contributions, which made this book possible.

Berlin, Germany
Rome, Italy
October 2016

Nikolay Kardjilov
Giulia Festa

Contents

Part I Cultural Heritage and Neutrons

- 1 Probing Our Heritage with Neutrons—One Successful Story** 3
G. Festa, N. Kardjilov and C. Andreani
- 2 Bronze Sculptures and Lead Objects Tell Stories About Their
Creators: Investigation of Renaissance Sculptures and Ancient
Ingots by Means of Neutron Tomography** 19
E.H. Lehmann, R. van Lang, M. Estermann, S. Hartmann,
F. LoCelso, N. Kardjilov, P. Tisseyre and S. Tusa
- 3 Paintings Reveal Their Secrets: Neutron Autoradiography
Allows the Visualization of Hidden Layers** 41
A. Denker, C. Laurenze-Landsberg, K. Kleinert
and B. Schröder-Smeibidl
- 4 Neutrons Unveil Secrets of Musical Instruments** 53
G. Festa, D. Mannes and A. Scherillo
- 5 The Glory of Ancient Weapons and Armors: Neutron
Imaging and Diffraction Methods in Modern Archaeology** 67
F. Salvemini and F. Grazzi
- 6 Ceramics, Marbles and Stones in the Light of Neutrons:
Characterization by Various Neutron Methods** 89
Zsolt Kasztovszky, Veronika Szilágyi, Katalin T. Biró,
Judit Zöldföldi, M. Isabel Dias, António Valera, Emmanuel Abraham,
Maryelle Bessou, Fabrizio LoCelso and Valerio Benfante
- 7 Paleontology: Fossilized Ancestors Awaken by Neutron
Radiography** 141
Frikkie C. De Beer

Part II Neutron Experimental Methods

8	General Introduction to Neutron Physics and Instrumentation	175
	R. Pynn and I.S. Anderson	
9	Scattering Techniques: Small- and Wide-Angle Neutron Diffraction	183
	C.-K. Loong, A. Scherillo and G. Festa	
10	Neutron Activation Analysis (NAA)	209
	P. Bode	
11	Prompt Gamma Activation Analysis (PGAA)	221
	T. Belgya and Zs. Révay	
12	Neutron Resonance Analysis.	235
	H. Postma and P. Schillebeeckx	
13	Neutron Resonance Imaging.	285
	G. Gorini, E. Schooneveld, E. Perelli Cippo and D. Di Martino	
14	Prompt Gamma Activation Imaging (PGAI)	303
	Z. Kis, L. Szentmiklósi, R. Schulze and E. Abraham	
15	Neutron Activation Autoradiography.	321
	A. Denker, N. Kardjilov and B. Schröder-Smeibidl	
16	Neutron Imaging	329
	N. Kardjilov, E. Lehmann, M. Strobl, R. Woracek and I. Manke	

Part I
Cultural Heritage and Neutrons

Chapter 1

Probing Our Heritage with Neutrons— One Successful Story

G. Festa, N. Kardjilov and C. Andreani

Abstract Probing our heritage reminds us of a variety of issues in Heritage Science: from the correct determination of historical and cultural time-frame of artefacts, to their location and method of production, to the choice of best treatments and environmental conditions for their restoration. A large variety of chemical, physical and microstructural techniques are employed by Museums and art experts to characterize objects of cultural significance. Most of these methods are invasive and probes like X-rays and charged particles have limited penetration power. Neutrons penetrate thick layers, depending on their energy, without substantial attenuation, a quality which makes them ideal to study and visualize the interior (bulk) properties of materials in a totally non-destructive and non-invasive way. The high sensitivity to specific light elements (e.g. H) is an additional special property of the neutron probe. Neutron techniques are increasingly used for the quantitative, non-invasive analysis of many aspects of cultural heritage preservation in a broad sense: museum collections, artefacts, books, manuscripts, musical instruments, archaeological findings.

1.1 Historical Background

The experimental results were very difficult to explain on the hypothesis that the beryllium radiation was a quantum radiation, but followed immediately if it were supposed that the radiation consisted of particles of mass nearly equal to that of a proton and with no net charge, or neutron. (...) When such neutrons pass through matter they suffer occasionally close collisions with the atomic nuclei and so give rise to the recoil atoms which are observed.

G. Festa (✉) · C. Andreani
Department of Physics and Centre NAST, University of Rome Tor Vergata, Rome, Italy
e-mail: giulia.festa@uniroma2.it

N. Kardjilov
Helmholtz-Zentrum Berlin, Hahn-Meitner Platz 1, 14109 Berlin, Germany

C. Andreani
Museo Storico della Fisica e Centro Studi e Ricerche Enrico Fermi, 00184 Rome, Italy

The citation is from Chadwick's 1932 breakthrough article 'Existence of a Neutron' (Chadwick 1932) where he showed that the physical properties of radiation obtained by hitting a beryllium target with α -particles could be explained by invoking a neutral particle of one atomic mass unit: the neutron.

Already in 1920, Rutherford had postulated the existence of a new neutral and massive particle in the nucleus of atoms. Such assumption originated from the observation of a disparity between an element's number of protons, represented by the atomic number, and its atomic mass. Such disparity appears as a mass excess compared to the mass due to the already known proton particles. Rutherford called these uncharged particles *neutrons*. In 1931, Bothe and Becker found that if alpha particle radiation from polonium fell on beryllium, boron or lithium, a penetrating radiation was produced. In fact, when they hit a beryllium target with alpha particles presumably electrical neutral radiation that could penetrate 200 mm of lead was emitted. They assumed the neutral radiation to be high-energy gamma rays.

In the same year, several similar experiments were carried out in Europe. One experiment in particular caught Chadwick's attention: Joliot and Curie discovered that, when a beam of this yet unknown radiation hits a substance rich in protons (in their case paraffin), protons were emitted and easily detected by a Geiger counter. Joliot and Curie believed the radiation hitting the paraffin target must have been high-energy gamma photons. In 1932 Chadwick repeated their experiments with the goal of searching for a neutral, uncharged particle with about the same mass as a proton. He realized that the emitted radiation could not be gamma rays by measuring the emitted proton energy and discovering that to generate such an effect it should have been in the 50 MeV order of magnitude, therefore much larger than gamma ray energy (typically few MeV).

When a sheet of paraffin wax about 2 mm thick was interposed in the path of the radiation just in front of the counter, the number of deflections recorded by the oscillograph increased markedly. This increase was due to particles ejected from the paraffin wax so as to pass into the counter (Chadwick 1932).

Chadwick also tried different targets, including helium, nitrogen, and lithium, which helped him determine that the mass of the new particle was just slightly larger than the mass of the proton. In 1935 Chadwick won the Nobel Prize in Physics for the discovery of neutrons. Scientists soon realized that the newly discovered neutron, as an uncharged but massive particle, could be used to probe other nuclei. In 1934 Fermi (Nobel prize for Physics in 1938) obtained induced radioactivity in high atomic number elements by hitting them with neutrons. In 1938 Hahn (Nobel prize for Chemistry in 1945), Meitner and Strassmann discovered nuclear fission, the splitting of uranium nuclei into light elements, induced by neutron bombardment. The discovery of nuclear fission was the first step towards the development nuclear energy (Fig. 1.1).

After the discovery of the neutron, it became clear that the nucleus contains protons and neutrons. The nucleus is a compact body with dimension of about 10^{-15} m. The free neutron is unstable and cannot be stored. Therefore, it must be made free by certain nuclear reactions to be available for experiments.

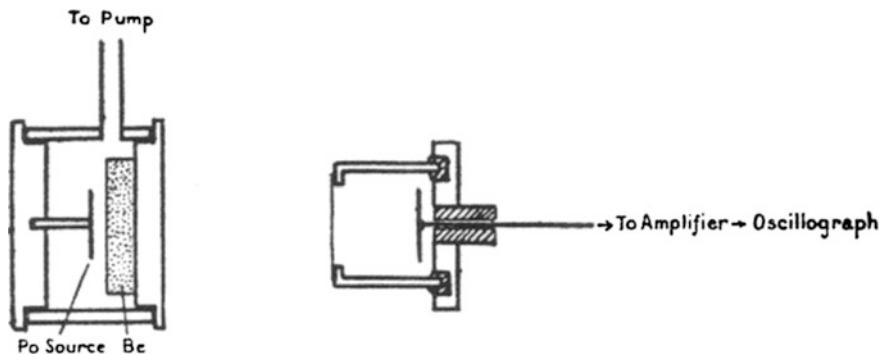


Fig. 1.1 Chadwick device

Research focused on ways to actually produce and use them in a series of different applications. Between the 1940s and the 1970s three kinds of methods were developed and applied for the production of neutrons: *radioactive decay* (for example in the spontaneous fission that occurs in very heavy chemical elements with atomic mass unit greater than 92), *nuclear reactions* (such as natural alpha and gamma bombardment of nuclides) and *induced nuclear fission* (as it occurs in nuclear reactors). Chicago Pile-1 (1942) was the first artificial nuclear reactor that went critical. It was built in the framework of the Manhattan Project, and carried out by the Metallurgical Laboratory at the University of Chicago under the supervision of Enrico Fermi. Chicago-Pile was made of a large amount of graphite and uranium, with control rods of cadmium, indium, and silver. Soon after, reactor technologies rapidly evolved becoming the most productive neutron sources and were used for power production and research as well as for military applications during World War II.

In the 1970s research started to focus on the spallation process, where neutrons are produced through disintegration of target nuclei (Carpenter 1986). Earlier research activity addressed to produce spallation facilities had been carried out between the years 1940s–1960s (Carpenter 1986). Lawrence’s proposed ‘cyclotron’ in 1940 was able to produce neutrons by hitting a beryllium target, paving the way to the use of accelerators for neutron production. The term ‘spallation’ was coined by Sullivan and Seaborg in 1959 (Harvey 1959). During the 1960s there was an increased interest for spallation neutron production as an alternative to other techniques (Tunncliffe et al. 1966). In 1974 the ZING-P neutron source prototype (developed by Jack Carpenter at Argonne National Laboratory) demonstrated the feasibility of a spallation neutron source (Carpenter 1986).

With the discovery of neutrons and the development of methods and technology in neutron production, the new research area of neutron science started to develop and neutron scattering and absorption (capture) rapidly became routine techniques for the non-invasive and non-destructive study of materials in the bulk.

Key research to establish the basic principles of neutron diffraction techniques was carried out in the 1940s by Wollan and Shull at Oak Ridge National Laboratory (formerly Clinton Laboratories USA) (Johnson and Schaffer 2008). In 1955 Brockhouse confirmed the quantum theory of solids through the first measurements of phonons using a prototype triple-axis neutron spectrometer. These were the seminal experiments for which, in 1994, Shull and Brookhouse were granted the Nobel Prize in Physics. The ‘special’ way neutrons interact with matter allows to ‘see’ where atoms are and how atoms move, making the neutron a unique probe for the studying the structure and dynamics of materials at the nanoscale.

1.2 Neutron Techniques

One can use nuclear reactions induced in a specimen by a particle beam (usually a neutron beam) to render certain constitutive elements of a material radioactive, permitting their analysis by identification of the radioactive decay products by detecting radiation emitted during such reactions or by measuring the portion of a neutron beam that traverses an object without any interaction.

1.2.1 *Activation Analysis*

The most common technique to create a nuclear reaction is the neutron activation, discovered in 1936 by Hevesy and Levi. They discovered that certain rare earth elements, contained in the irradiated samples, became radioactive as a consequence of neutron beam exposure (Zeisler et al. 2003). The neutron flux creates unstable nuclei in the specimen by the process of neutron capture. The resulting nuclear transition produce γ -ray emission, K-capture and other processes which then enables identification of the isotopic species present and of the elements. This phenomenon was then employed in Neutron Activation Analysis (NAA) for the identification of major, minor, trace and rare elements (Zeisler 2003).

The first experiment where NAA was applied to cultural heritage dated back to 1960 when Emeleus and Simpson published the first results of a study of a Roman pottery fragments analyzed through NAA and γ -ray spectrometry. The results of this experiment allowed them to distinguish between production factories (Emeleus & Simpson 1960). The experiment was carried out using the thermal neutron beam from the Bepo reactor in Harwell (UK). In the following decades, a series of research studies applying thermal neutrons to cultural heritage were carried out. NAA was applied to a large variety of samples such as fossil bones (Eisenbarth and

Hille 1977) where nitrogen and fluorine contents were measured relative to main constituents of the inorganic bone material (principally phosphorus and calcium). Measurements gave determination of the human remain dating in a non-destructive way. In 1987 Mommsen et al. studied ancient potteries from archaeological excavations through a new methodology where neutron-induced radiation in low energy region (10–135 keV) was measured with a high-resolution semiconductor detector. NAA is largely applied to the study of trace elements to determine provenance and manufacturing techniques. The principle of the NAA technique is presented in detail in Chap. 10.

1.2.2 Prompt Gamma Activation Analysis

Another technique that uses neutron absorption is Prompt Gamma Activation Analysis (PGAA) (Molnar 2004). This nuclear analytical technique utilizes the characteristic prompt γ -ray spectrum measured during the irradiation of the sample for the non-destructive determination of elemental and/or isotopic composition of samples.

PGAA technique is best suited for the investigations of materials containing light elements such as H, S, P and K.

A PGAA measurement campaign was carried out on so called ‘black boxes’ in 2008. The aim of this study, performed as ANCIENT CHARM European project activity, was to identify strengths and weaknesses of neutron techniques applied to the study of archaeological objects and to develop a best practice for a combined use of neutron analysis methods (such as Prompt Gamma Activation Analysis, Time of Flight Neutron Diffraction and neutron tomography) for different combinations of materials. For this purpose, 17 samples were used, known as *black boxes*, consisting of closed cubes containing geometrical arrangements of materials such as metals, minerals, ceramics, and organic matter. Result on a black box is shown in Fig. 1.2.

Nr.	Nominal comp.	PGAA results
1 + 2	Ag in talc	H, Si, Cl, Mn, Fe, Cu, Ag
3	Sand	H, B, Na, Al, Si, Cl, K, Ti, Mn, Fe, Cu
4	Iron grit	H, B, Al, Cl, Mn, Fe
5	Salt	Na, Al, Cl, Cu
6	Al sheet	–
7	Cu sheets	H, Na, Al, Si, Cl, Mn, Fe, Cu, Zn, Ag

The principle of the PGAA technique is presented in detail in Chap. 11. Examples of application of the PGAA method can be found in Chap. 6.

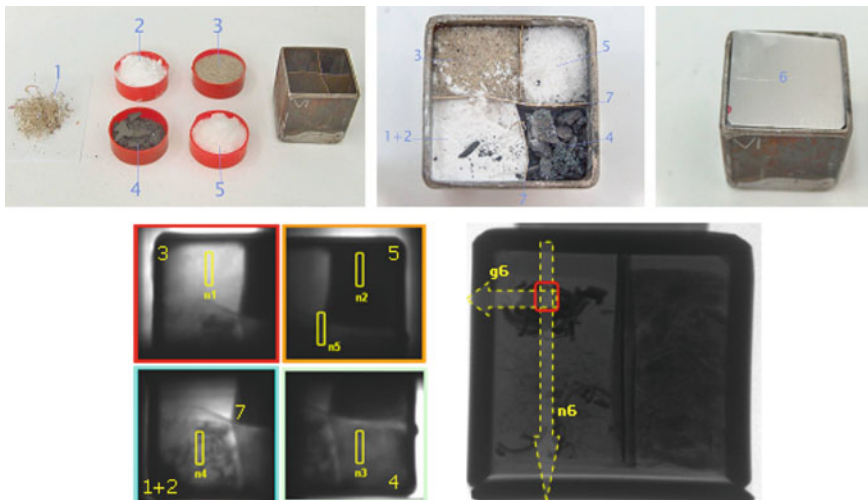


Fig. 1.2 *Iron box*: the black box internal feature—segments divided with two crossed sheets. With PGAA, the fiber-like material is identified as Ag chippings in regions (1 + 2). Predominantly Si was found in section 3 and Fe in section 4, whereas Na and Cl (in a molar ratio 1:1) in section 5. At the crossing point of the sheets the presence of Cu was confirmed

1.2.3 Neutron Resonance Analysis Methods

These methods are based on resonance absorption of neutrons with epithermal energies (Postma and Schillebeeckx 2005): absorption (capture and scattering) of neutrons by nuclei as a function of neutron energy shows sharp peaks (resonances) specific for elements (isotopes). The analysis of resonances allows the identification and quantification of elements and isotopes within an object in a non-destructive manner. This is the basis of Neutron Resonance Capture Analysis (NRCA), in which resonances are observed by detecting the prompt γ -radiation emitted directly after neutron capture as a function of the neutron energy. In NRCA, neutrons with energies corresponding to energy levels of the compound nucleus are captured preferentially. Resonances identify the nuclides present in the material whereas the areas under the resonance peaks provide information about their relative amount. They can be visualized in the neutron capture spectrum as a function of neutron energy. Another method based on neutron resonances, Neutron Resonance Transmission Analysis (NRTA), is the transmission of a neutron beam through a sample. Resonances are seen as dips in the transmission curve as function of neutron energy. A schematic representation of NRCA and NRTA measurements is shown in Fig. 1.3.

NRCA is particularly effective for samples composed of copper and its alloys because of the significant sensitivities for copper itself and for a range of elements such as Ag, As, Sb, Sn, and Zn (that are likely to be found in Cu alloys), and for Fe, which is also relevant for archaeological applications. It has to be stressed that activation in

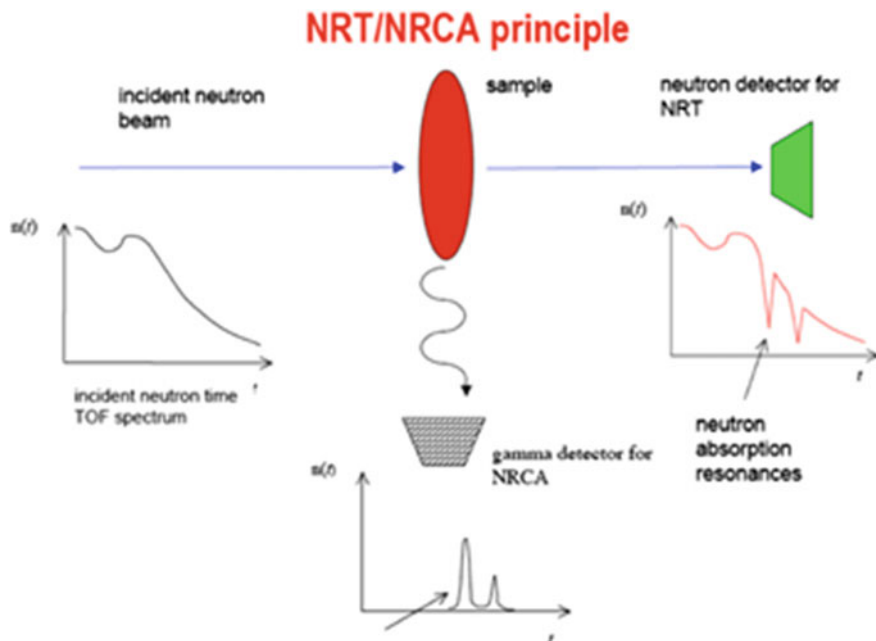


Fig. 1.3 Scheme of a set-up for Neutron Resonance Transmission Analysis (NRTA) and Neutron Resonance Capture Analysis (NRCA)

materials is mainly due to thermal neutrons, which can be removed from the beam with the aid of a Cd-filter. Hence activation is low after an NRCA run and normally negligible after a short waiting period. Thus artefacts can be returned to owners quickly. The principles of NRCA and NRTA are presented in detail in Chap. 12.

A technique beyond NRCA and NRTA is Neutron Resonance Transmission Imaging (NRTI). The potential of NRTI was studied at e.g. the J-PARC facility (Tremisn et al. 2014) and within the Ancient Charm project at the spallation neutron source ISIS of the Rutherford Appleton Laboratory (Gorini et al. 2007). It relies on the use of position sensitive neutron detectors. NRTI has been applied to produce 2D (Perelli et al. 2011) and 3D elemental contrast figures of archaeological samples (Festa et al. 2015) at ISIS.

1.2.4 Time Resolved Prompt Gamma Activation Analysis

Bi-parametric time-energy acquisition Prompt Gamma Activation Analysis (T-PGAA) is a technique that combines prompt gamma-ray analysis (PGA) and neutron resonance analysis (NRA). It was recently applied for the study of cultural heritage artefacts at ISIS (Festa et al. 2013a, b) and to study a meteorite sample at

J-PARC (Toh et al. 2014) facility. Time-resolved Prompt Gamma Activation Analysis consists in the measurement of gamma energy spectrum induced by radiative capture as a function of incident neutron Time of Flight (Festa et al. 2013a, b; Miceli et al. 2013, 2014).

T-PGAA enhances the capabilities of both the NRCA and PGAA techniques, providing a more general sensitivity for elements (Festa et al. 2013a, b, 2016; Toh et al. 2014) (Fig. 1.4).

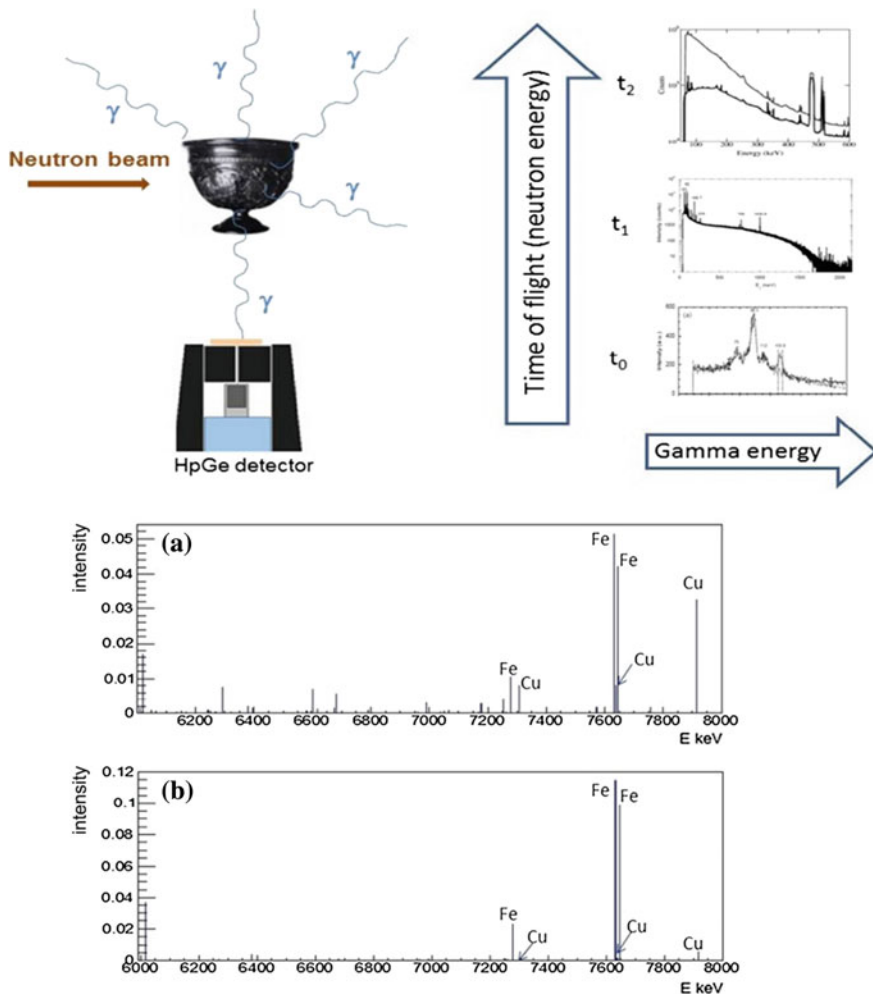


Fig. 1.4 Layout of the designed experiment recording gamma spectra at different neutron energy frames on the top. On the bottom, simulated gamma spectra are reported for (a) neutron resonance energy range from 200 to 900 eV (b) total neutron energy range from 0 to 1.2 keV

1.2.5 Neutron Diffraction

In 2001 first test measurements using a Time of Flight Neutron Diffraction on archaeological samples were performed on pottery fragments at the spallation source ISIS, (UK) (Kockelmann et al. 2001). Neutron Diffraction (ND) is based on elastic scattering of thermal neutrons by periodic, long-range ordered (crystalline) or non-periodic, short-range ordered (glass) arrangements of atoms. Nowadays ND is routinely used for the phase and structure analysis, texture analysis, microstructure analysis and residual stress analysis of artefacts with a minimum volume of $1 \times 1 \times 0.5$ mm. An important issue for curators is the assessment of the condition of material concerning production techniques. In this context through ND characterisation of an artefact one gains insight about the materials and technologies used by the craftsmen.

The principle of the ND technique is presented in detail in Chap. 9 and examples of ND studies can be found in Chap. 4.

1.2.6 Neutron Radiography and Tomography

Neutron radiography (NR) is a real space imaging method based on capture and scattering of thermal and cold neutrons (Domanus 1992). A neutron beam impinging onto any heterogeneous object is differently transmitted depending on thickness, density, chemical composition and total cross section of the material along the line of sight. Through NR one can obtain information on the internal view of materials with a spatial resolution down to 100 microns. By recording the transmitted beam it is possible to reconstruct the internal feature of the studied object. The attenuation of a neutron beam passing through objects provides contrast for different elements. Contrast is also achieved by variation of neutrons energies. Additional techniques are the Phase Contrast Radiography, based on neutron refraction (Lewis and Schutz 1937) and Neutron Tomography, providing 3D visual information about the internal structure of the sample (Kardjilov et al. 2004). Example for neutron tomographic investigation of Osiris bronze statue is shown in Fig. 1.5 (Agresti et al. 2015).

1.2.7 Developing of Neutron Techniques for Cultural Heritage Research in the Frame of the “Ancient Charm” Project

The Ancient Charm (“Analysis by Neutron resonant Capture Imaging and other Emerging Neutron Techniques: new Cultural Heritage and Archaeological Research Methods”) project was an international and interdisciplinary collaborative

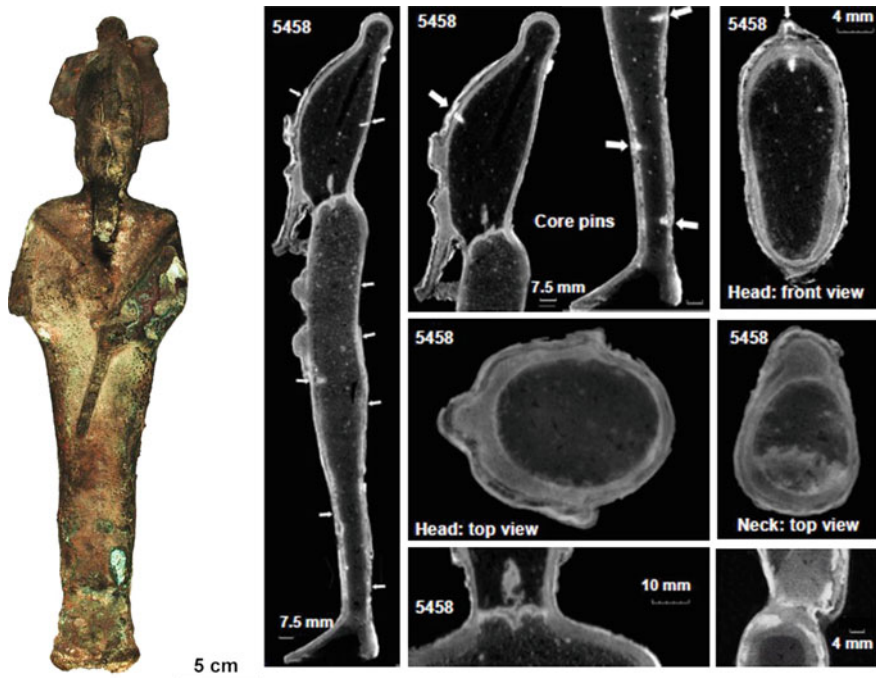


Fig. 1.5 Osiris bronze figure (*left*) was investigated by neutron tomography. The digital sections through the sample volume are shown on the right. The thickness of the bronze material as well as the position of the core pins reveal information about the casting ancient technology (Agresti et al. 2015—reproduced by permission of The Royal Society of Chemistry)

project, financed by the European Commission “New and Emerging Science and Technology” program. The idea of this project followed the exploitation and development of γ -detector for neutron spectroscopy with eV neutrons of the VESUVIO beamline at the ISIS spallation neutron source in 2006 (Gorini et al. 2007).

Within the Ancient Charm project new neutron-based analysis and imaging techniques and non-invasive methods for 3D tomographic imaging of the elemental and phase composition of cultural heritage objects were designed and realized. New techniques and methods were applied to the study of selected real archaeological objects and copies to test effectiveness of obtained reconstruction information (Gorini 2007). Results from this project can be found in Chaps. 13 and 14.

Today neutron techniques are routinely used to provide valuable and additional information to restores for the development of tailored procedures to prevent deterioration. They are employed to obtain a variety of information spanning from the elemental composition, the inner structure of materials and its morphology, the making techniques, the processing and provenance, the dating, the state of conservation and restoration and finally whether the materials is genuine or fake.

In the following Chaps. 4–7 some selected examples of application of most recent neutron analysis techniques are revised. The principle of the Neutron Radiography and Tomography techniques is presented in detail in Chap. 16.

1.3 Selected Highlights

Neutron methods have been used for investigation of prominent objects providing strong resonance in the scientific community and in the society. Some examples of selected research projects and important results are presented below.

- **Investigation of Napoleon's hairs**

Napoleon Bonaparte died on May 5th 1821 in exile on the island of Saint Helena maybe of arsenic poisoning. Instrumental Neutron Activation Analysis study was performed on several of Napoleon's hair, two samples cut the day after his death and two samples cut seven years earlier (1814) during his first exile on the island of Elba. Results show that all of the samples of Napoleon's hair have a high arsenic concentration. These results disfavor the arsenic poisoning theory (Lin et al. 2004). Details of this study are presented in Chap. 10.

- **NAA at the British Museum**

Neutron Activation Analysis was routinely used at the British Museum from 1978 to 2002 for provenance studies on ceramics and marble. Data obtained were compared with results coming from other laboratories and are the content of an extended database (Hughes 2007). Similar examples can be found in Chap. 6.

- **NRCA on bronze statuette**

Neutron Resonance Capture Analysis was carried out on bronze Etruscan statuettes from the National Museum of Antiquities (NMA) in Leiden (NL) to obtain their elemental compositions. Experiments shown different composition of the samples and could identify fakes (Postma et al. 2004). Examples of the application of this method are shown in Chap. 12.

- **Bronze statuettes at the Rijksmuseum.**

Renaissance bronze statuettes, collection preserved at Rijksmuseum of Amsterdam, were studied with the aim of obtaining fundamental information on manufacturing production techniques of these fine art objects. Sculptures were investigated through neutron tomography at the Paul-Scherrer Institut, Villigen, Switzerland. This method allowed studying the internal shape of the bronze sculptures and provided clues of different material compositions. The most interesting areas of the objects, identified through tomographies, were studied to obtain material compositions and crystalline structures using time-of-flight neutron diffraction on the ENGIN-X instrument at the ISIS facility (Rutherford Appleton Laboratory, UK) (van Langh et al. 2011). For more details, see Chaps. 2 and 4.

- **Painting autoradiography at the Berlin Gemäldegalerie**

Thanks to a more than two-decade-long collaboration between the Berlin Gemäldegalerie and the Helmholtz-Zentrum Berlin, a large number of paintings were examined by a consistent and systematic use of neutron-activation autoradiography (NAAR) and gamma-ray spectroscopy. The combination of both non-destructive methods provides insight into the pigments used, the brushwork, the state of preservation of the various layers of paint, and the many stages that went into creating the work. The NAAR method is used on regular base at the Painting Gallery in Berlin for taking a detailed look at a painter's creative process. Obtained information helps to gain insight into the artists and time periods of the paintings (Fischer et al. 1987). Examples of this method with detailed description are presented in Chaps. 3 and 15.

- **Ghiberti Heads**

The study of the gilded bronze artefacts, performed within the Ancient Charm project, was performed using integrated neutron techniques. The reliefs are part of the monumental Doors, *The Gates of Paradise* and *the North Gate*, located at the *Battistero di Firenze* by *Lorenzo Ghiberti*, a masterpiece of the Florentine Renaissance. The reliefs presented critical aspects regarding state of conservation and shows a re-melting whose extension and composition were unknown. The analysis of the Ghiberti Heads were performed using Prompt Gamma Activation Imaging (PGAI)—a technique which integrates the collection of structural information (neutron imaging) and elemental information (PGAA)—to reconstruct the elemental distribution of the elements with a few-mm resolution, Neutron Diffraction and Radiography to obtain valuable information on the manufacturing technique and state of conservation of the reliefs, and Neutron Resonance Transmission to map the gold layer distribution under the pollution deposits to assess the cleaning techniques used by the curators during the restoration process (Festa et al. 2009, 2011) (Fig. 1.6).

- **Metallic Ancient Flute**

The investigated sample was a small metallic duct flute from *Accademia Nazionale di Santa Cecilia* (Festa 2013b). It is a vertical metal whistle 'in D' with a standard conical bore slightly contracting towards the foot and six finger holes on the front (Fig. 1.7). The object was studied by means of integrated and simultaneous neutron-based techniques such as neutron diffraction, neutron radiative capture analysis and neutron radiography. The aim of the experiment was to characterize elemental and phase compositions of the material, at deriving information on the construction and restoration techniques, and on the role of chemical-physical material properties on the emitted sound.

Results of similar investigations can be found in Chap. 4.

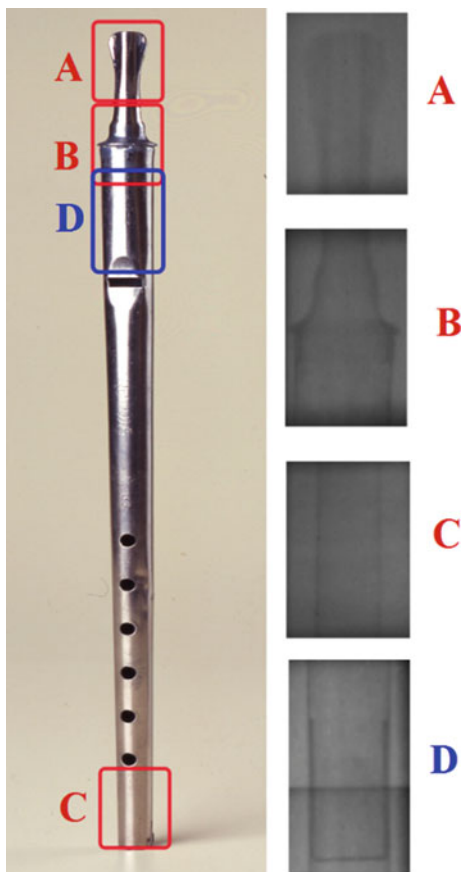
Fig. 1.6 Decorative element (Prophet Head) cleaned by a chemical solution and by laser



1.4 General Remarks

The successful application of neutron based investigation methods to study cultural heritage objects nowadays is a result of a long-term collaboration between the institutions taking care for the objects (museums, institutes and private collections) and the research infrastructures. In general it is not obvious that such collaboration could be possible and even successful. The aim of the restores and curators is to preserve the objects with as less as possible damage and impact through the time. Therefore any invasion related to research attempts is considered very carefully and as conservative as possible. From the other side the neutron researchers are claiming that the experiments with neutrons are non-destructive and non-invasive but this is not always sufficient to convince the cultural heritage specialists. Questions related to sample activation, change of the isotope balance and radiation damage are often neglected or wrongly interpreted. In addition the neutron sources are large-scale facilities and the investigated objects should be brought to the experimental installations. In this case important details like insurance issues, lack of safe storage places or acclimatized room are preventing the transportation of the samples to the research facilities. Nevertheless the unique properties of the neutrons providing results, which are impossible with other experimental methods, motivated the cultural heritage and the neutron researchers to collaborate. The active collaboration between researchers from the two sides made possible to solve all the problems and to establish protocols and good practices for investigation of cultural heritage objects. Nowadays neutron investigation methods are used on a regular base for samples from museum and private collections. There is also a trend to

Fig. 1.7 Photograph of the investigated whistle flute preserved at the *Accademia di Santa Cecilia* and neutron radiographies of selected regions (Festa 2013b)



present the results from the investigation as a media show beside to the exposed object in the museums. Example for this is the investigation of several bronze statues from the Rijksmuseum by neutron tomography of which the data are available in online media format. The neutron based methods are already recognized by the cultural heritage society as reliable and distinctive non-destructive research tools and many new collaborations and initiatives were started in the last few decades. They are supported on national and international levels by initiating scientific projects for popularization of the neutron research and for providing of easy access of the relevant objects to the neutron facilities. For example the “Ancient Charm” project was originated by the EU commission in which ten partners from six countries collaborated over four years on investigating cultural heritage objects.

The aim of the current book is to demonstrate the experience gained in the last decade of the successful application of neutron research methods in several cultural heritage fields and to help for further collaborations and joint research initiatives.

Acknowledgments The Ancient Charm work was partially supported within the CNR-STFC Agreement No. 06/2008 concerning collaboration in scientific research at the spallation neutron source ISIS, Chilton, Oxford, UK.

References

- Agresti J, Osticioli I, Guidotti MC, Capriotti G, Kardjilov N, Scherillo A, Siano S (2015) Combined neutron and laser techniques for technological and compositional investigations of hollow bronze figurines. *J Anal At Spectrom* 30:713–720
- Carpenter JM, Yelon WB (1986) ‘Neutron sources’ in ‘neutron scattering. In: Methods of experimental physics, vol 23. Academic press inc., London
- Chadwick J (1932) The existence of a neutron. *Proc Roy Soc A* 136:692–708
- Domanus JC (1992) Practical neutron radiography ‘a useful book describing the principle of neutron radiography technology’. Kluwer Academic Publ, The Netherlands
- Eisenbarth P, Hille P (1977) A nondestructive method for age determination of fossil bone. *J Radiolanalytical Chem* 40:203–211
- Emeleus VM, Simpson G (1960) Neutron activation analysis of ancient roman potsherds. *Nature* 185:196
- Festa G, Andreani C, De Pascale MP, Senesi R, Vitali G, Porcinai S, Giusti AM, Schulze R, Canella L, Kudejova P, Mühlbauer M, Schillinger B, Ancient Charm Collaboration (2009) A non destructive stratigraphic and radiographic neutron study of Lorenzo Ghiberti’s reliefs from Paradise and North doors of Florence Baptistery. *J Appl Phys* 106(4)
- Festa G, Senesi R, Alessandrini M, Andreani C, Vitali G, Porcinai S, Giusti AM, Materna T, Paradowska A (2011) Non destructive neutron diffraction measurements of cavities, inhomogeneities and residual strain in bronzes of Ghiberti’s relief from the Gates of Paradise. *J Appl Phys* 109:064908
- Festa G, Pietropaolo A, Andreani C, Grazzi F, Barzagli E, Scherillo A, Schooneveld E (2013a) Simultaneous and integrated neutron-based techniques for material analysis of a metallic ancient flute. *Measur Sci Technol* 24:095601
- Festa G, Miceli A, Senesi R, Andreani C, Perelli Cippo E, Gorini G, Cattaneo R (2013b) Bi-parametric time-energy acquisition prompt gamma activation analysis (T-PGAA) for cultural heritage studies. *J Phys Conf Ser* 470. ISBN 9788887237160
- Festa G, Perelli Cippo E, Di Martino D, Cattaneo R, Senesi R, Andreani C, Schooneveld E, Kockelmann W, Rhodes N, Kudejova P, Biro K, Duzs K, Hajnal Z, Gorini G (2015) Neutron resonance transmission imaging for 3D elemental mapping at the ISIS spallation neutron source. *J Anal At Spectrom* 30:745
- Festa G, Arcidiacono L, Pappalardo A, Minniti T, Cazzaniga C, Scherillo A, Andreani C, Senesi R (2016) Isotope mapping capabilities using time resolved prompt gamma emission from epithermal neutrons. In: International workshop on imaging. Varenna, Italy, 7–10 Sept 2015 (Journal of Instrumentation)
- Fischer C-O, Laurenze C, Leuther W, Slusallek K (1987) In: Barton JP, Farny G, Person J-L, Röttger H (eds) Neutron radiography. Springer, Netherlands, p 519
- Gorini G (2007) On behalf of the Ancient Charm collaboration (components of Ancient Charm Collaboration, members are listed at page 55 and 56 of this paper). *Il Nuovo Cimento C*, 30 (1):47–58. doi:10.1393/ncc/i2006-10035-9
- Gorini G, Ancient Charm Collaboration (2007) Ancient charm: a research project for neutron-based investigation of cultural heritage objects. *Nuovo Cimento* 30(1):47
- Harvey BG (1959) Spallation. In: Frisch OR (ed) Progress in nuclear physics, vol 7. Pergamon Press, pp 90–120
- Hughes MJ (2007) Neutron activation analysis at the British museum. *London Archaeometry* 49 (2):255–270

- Johnson L, Schaffer D (2008) Oak ridge national laboratory: the first fifty years. The University of Tennessee press, Knoxville
- Kardjilov N, Lehmann E, Steichele E, Vontobel P (2004) Phase-contrast radiography with a polychromatic neutron beam. *Nucl Instrum Methods Phys Res Sect A* 527–3(21):519–530
- Kockelmann W, Kirfel A, Hahnel E (2001) Non-destructive phase analysis of archaeological ceramics using TOF neutron diffraction. *J Archaeol Sci* 28(2):213–222
- Lewis GN, Schutz PW (1937) Neutron refraction. *Phys Rev* 51:1105 (Published 15 June 1937)
- Lin X, Alber D, Henkelman R (2004) Element Contents in Napoleon's Hair Cut Before and After His Death: Did Napoleon Die of Arsenic Poisoning? *Analytic and Bioanalytical Chemistry* 379:218
- Miceli A, Festa G, Senesi R, Gorini G, Andreani C (2013) *J Phys Conf Ser* 470:012001
- Miceli A, Festa G, Senesi R, Perelli Cippo E, Giacomelli L, Tardocchi M, Scherillo A, Schooneveld E, Frost C, Gorini G, Andreani C (2014) *J Anal At Spectrom* 29:1897–1903
- Molnar G (ed) (2004) Handbook of prompt gamma activation analysis with neutron beams. Springer. ISBN 978-1-4020-1304-1
- Mommsen H, Kreuser A, Weber J, Busch H (1987) Neutron activation analysis of ceramics in the X-Ray energy region. *Nucl Instrum Methods Phys Res A* 257:451–461
- Perelli Cippo E, Borella A, Gorini G, Kockelmann W, Moxon M, Postma H, Rhodes NJ., Schillebeeck P, Schoonenveld EM, Tardocchi M, Dusz K, Hajnal Z, Biro K, Porcinai S, Andreani C, Festa G (2011) Imaging of cultural heritage objects using neutron resonances, *J Anal At Spectrom* 26:992
- Postma H, Schillebeeckx P (2005) Non-destructive analysis of objects using neutron resonance capture. *J Radioanal Nucl Chem* 265:297–302
- Postma H, Schillebeeckx P, Halbertsma RB (2004) Neutron resonance capture analysis of some genuine and fake Etruscan copper alloy statuettes. *Archaeometry* 46:635–646
- Toh Y, Ebihara M, Kimura A, Nakamura S, Harada H, Hara KY, Koizumi M, Kitatani F, Furutaka K (2014) Synergistic effect of combining two nondestructive analytical methods for multielemental analysis. *Anal Chem* 86:12030–12036
- Tremis AS, Shinohara T, Kai T, Ooi M, Kamiyama T, Kiyonagi Y, Shiota Y, McPhate JB, Vallerga JV, Siegmund OHW, Feller WB (2014) Neutron resonance transmission spectroscopy with high spatial and energy resolution at the J-PARC pulsed neutron source. *Nucl Instrum Methods Phys Res A* 746:47–58
- Tunnicliffe P, Bartholomew G, Vogt EW (1966) AECL study for the intense neutron generator
- Van Langh R, James J, Burca G, Kockelmann W, Yan Zhang S, Lehmann E, Estermann M, Pappot A (2011) New insights into alloy compositions: studying renaissance bronze statuettes by combined neutron imaging and neutron diffraction techniques. *J Anal At Spectrom* 26: 949–958 (2011)
- Zeisler R, Vajda N, Lamaze G, Molnar GL (2003) Activation analysis. In: Vertes A, Nagy S, Klencsar Z (eds) *Chemical applications of nuclear reactions and radiations*. Kluwer Academic Publishers

Chapter 2

Bronze Sculptures and Lead Objects Tell Stories About Their Creators: Investigation of Renaissance Sculptures and Ancient Ingots by Means of Neutron Tomography

E.H. Lehmann, R. van Lang, M. Estermann, S. Hartmann,
F. LoCelso, N. Kardjilov, P. Tisseyre and S. Tusa

Abstract Renaissance bronze objects from the Rijksmuseum (Amsterdam) collection and lead ingots from ancient roman shipwrecks found near Sicily (Italy) were studied by means of neutron tomography. This was done with the aim to visualize and to measure the inner structures of the objects. In this way information about the manufacturing processes in the 16th century and the conservation status from the inside of the bronze sculptures was gained. Inscriptions found under the corrosion layer of the lead ingots gave hints about the trade routes in the past. Neutron imaging was proven perfect to transmit the relatively thick layers of Pb and Cu alloys while ceramic remains, soldering connections and corrosion effects become visible.

Electronic supplementary material The online version of this chapter (doi:[10.1007/978-3-319-33163-8_2](https://doi.org/10.1007/978-3-319-33163-8_2)) contains supplementary material, which is available to authorized users.

E.H. Lehmann · M. Estermann · S. Hartmann
Paul Scherrer Institut (PSI), 5232 Villigen, Switzerland

R. van Lang
Rijksmuseum, Amsterdam, The Netherlands

F. LoCelso
DiFC, University of Palermo, 90128 Palermo, Italy

N. Kardjilov (✉)
Helmholtz-Zentrum-Berlin, Hahn-Meitner-Platz 1, 14109 Berlin, Germany
e-mail: kardjilov@helmholtz-berlin.de

P. Tisseyre · S. Tusa
Soprintendenza del Mare della Regione Siciliana, Sicily, Italy

2.1 Introduction

The non-destructive investigation of metal objects in their full length of several centimeters is quite difficult task. The metals are strong absorbers of all kinds of ionizing radiations like X-rays, electrons and protons therefore the investigation methods using these rays are limited to surface applications. High-energy gamma rays can penetrate thick layers of metal but they are insensitive to organic inclusions and thin corrosion films. In opposite the low-energetic thermal neutrons penetrate easily centimeters of metal and are sensitive to hydrogenous substances. The non-destructive investigation of metallic cultural heritage objects like bronze or lead sculptures by neutron based methods provides very impressive results. Here we are presenting two imaging studies of metallic cultural heritage objects.

2.2 Used Experimental Methods

2.2.1 Neutron Tomography (NT)

The aim of the studies is the non-invasive analysis of the whole sample volume with the inherent spatial resolution of the tomography setup (Fig. 2.1). The contrast of the objects is given by the interaction probabilities of thermal neutrons for the material composition and the thickness of the material layer in beam direction. The cross-sections of the attenuation process are well known and tabulated (e.g. (Neutron attenuation)) and can be used for the quantitative data analysis.

The NT process is based on angular equidistant projections of the object when it is rotated around its vertical axis over the range of at least 180° (Banhart 2008; Schillinger et al. 2000). Since the neutron beam is not perfectly parallel but slightly conical it is preferred to sample over the full 360° . The number of projection defines the data quality (signal to noise) and the spatial resolution in the 3rd dimension.

After the data normalization (including open beam correction) and cleaning of “white spots” (caused by gamma events hitting the camera sensor) the projection data are ready for the reconstruction step. We used the common “filtered back-projection algorithm” which is based on the Fourier slice theorem, implemented in commercial software tools like “Octopus” (Octopus). In this manner, a stack of horizontal slices with the same pixel size of the projection data is produced which represents the whole voxel volume as the values of attenuation coefficients.

The reason why the X-ray tomography fails for bulky metallic samples is explained by the attenuation of the constituents of the objects. In Fig. 2.2 we compare the cross-section data, based on relevant libraries (Neutron attenuation, X-ray attenuation). The 100 keV X-rays compares to the spectral average of a medical X-ray tube with 180 keV high voltage. Although higher X-ray energies enable slightly higher transmission, beam hardening and scattering artifact are increased and disturb the image data quality. Therefore, it is justified to perform this kind of studies preferentially by means of NT, see Banhart et al (2010).

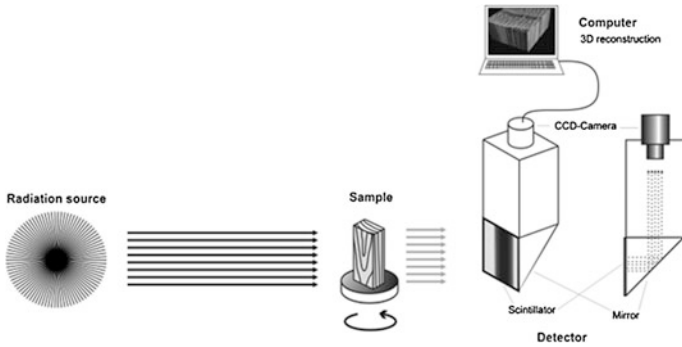


Fig. 2.1 Principle setup of the NT experiments, simplified with respect to dimensions and components, see more details in Kardjilov et al. (2011a) (courtesy D. Mannes, PSI)

More information related to the neutron radiography and tomography techniques can be found in Chap. 16 and in the following references Lehmann et al. (2005), Kardjilov et al. (2006), Lehmann et al. (2007), Kardjilov et al. (2008), Strobl et al. (2009), Lehmann et al. (2010), Kardjilov et al. (2011c).

2.3 Examples of Studies of Metal Objects by Neutrons

2.3.1 *Renaissance Bronze Objects from Rijksmuseum Amsterdam*¹

2.3.1.1 Description of the Investigated Artifacts

The artifacts which were investigated by neutron tomography are listed in Table 2.1 providing some basic information about the sculptures.

The composition of the bronze is not in all cases precisely known. The main constituents are Cu, Sn, Zn with traces of Pb.

2.3.1.2 Scientific Questions

During the long shutdown and restauration period of the Rijksmuseum Amsterdam (2003–2013) where no access by the public to the collections was possible the idea came up to perform dedicated studies of relevant bronze objects from the renaissance period in order to get information about inner compositions, manufacturing and restauration principles and about the casting processes in the 16th century.

¹Section written by E.H. Lehmann, R. van Lang, M. Estermann, S. Hartmann.

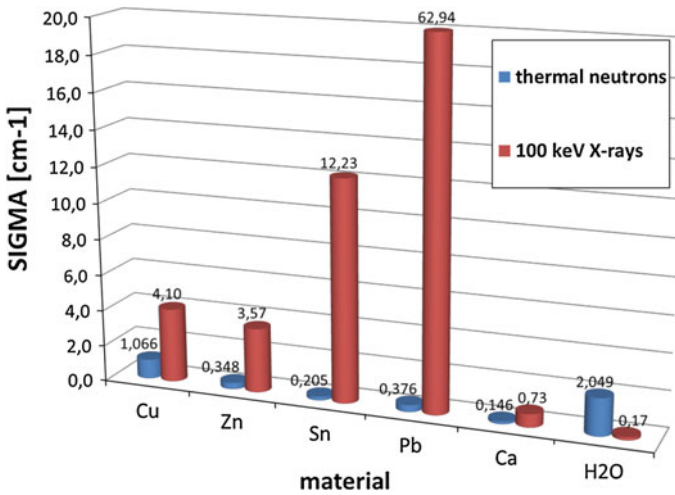


Fig. 2.2 Comparison of attenuation coefficients for the different compounds of bronze (water for comparison, symbolizing corrosion or wax, lacquer)

The two initiators of this campaign from that museum (R. van Lang, F. Scholten) were interested in non-destructive or even non-invasive investigations, partly driven by the idea of a concluding PhD thesis on that study by van Lang (2012). Their background is the restoration science and technology where the casting procedures and the finishing procedures in that time play an important role.

First radiography tests of objects by means of high-energy X-rays resulted in the conviction that the thick layers of alloys from copper, zinc, tin or even lead are hard to transmit due to the high attenuation of these materials. Therefore, it was considered better to use neutrons, in particular thermal neutrons for the transmission investigations. Since no neutron imaging facility is available and operational in the Netherlands, Belgium or Northern Germany the request for investigations was sent to PSI, where the techniques of neutron imaging are well established on an advanced level.

Thermal neutrons have the advantage of higher transmission through heavy metals than X-rays and enable even tomography studies for whole objects since the beam diameter is more than 30 cm. In NT, the three-dimensional material distribution is obtained where the dimensions, the composition, the structure, inner and outer surfaces and material failures can be extracted and analyzed. For this purpose, the object has to be rotated around its vertical axis while projects are taken from different viewing angles.

Here, we report about 14 successful investigations of objects from the Rijksmuseum's collection. About 500 years after their manufacturing it is now possible to get a virtual data volume of the samples which can be manipulated and analyzed with suitable software tools. Next to dedicated slices through the samples, extraction of different metal and ceramics structures, a full animated fly around and

Table 2.1 Information about the observed objects as far as they are available

Object	Artist	Life date	Production date	Place	Height (cm)	Inv. Nr.
Bust of a man	Severo Calzetta da Ravenna	1465/1475–1538	1458–1516	Padua or Ravenna	15.5	BK-NM-12080
Grotesque Animal	Arent van Bolten?	c. 1600			8.5	BK-1969-4
Grotesque Animal	Arent van Bolten	1573–1633	1620	Amsterdam or Zwolle	17	BK-16127
Hercules and Antaeus		1500		Padua	22.4	BK-1959-5
Mercury	Hendrick de Keyser	1565–1621	1611	Amsterdam	32.3	BK-1959-61
Nessus and Deianeira	Caspar Gras	1585–1674	1640–1650	Insbruck	33	BK-16508
Paris	Workshop Severo da Ravenna		1525	Ravenna or Pedua	26.5	BK-1959-4
Perfume burner	Desiderio da Firenze	1532–1545	1540	Veneto	40.5	BK-1957-3
She-Wolf with Romulus and Remus				Rome or Florence	11.5	BK-1958-39
Sol (The Sun)	Johan Gregor van der Schardt	1530–1581	1570–1581	Nuremberg	45.7	BK-1977-24
Striding Nobleman		1580–1600			35	BK-16083
Tiber	Tiziano Aspetti, called Mimio	1511/12–1552		Pesaro or Urbino	20 * 24 * 14	BK-1954-44
Venus holding an apple	Niccolo Roccatagliata	1560–1636	1600	Venice	14	BK-16942
Hercules Pomarius	Wilhelm van Tetrode	1525–1580	1562–1567		39.3	BK-1954-43

through the object can be delivered. Some animations are available in the e-book version of the volume as well as online through the links given to each figure.

2.3.1.3 Experimental Setup

For the investigation of the bronze sculptures the end position of the thermal neutron imaging station NEUTRA² at the Paul-Scherrer-Institute, Switzerland, was used, where a beam diameter of 35 cm circular and homogeneously illuminated was applied. The neutron spectrum can be approximated by a Maxwellian with a mean energy of 25 meV, corresponding to 1.8 Å. The collimation of the beam is characterized by an L/D-ratio of 550, corresponding to a divergence angle of 0.01°. The gamma content of the tangential beam is low and can be ignored since the detector is not much sensitive for this kind of radiation.

The detector is based on a CCD camera (ANDOR Icon-M, cooled to -50 °C for background and dark-current reduction. It observes the emitted light from a neutron sensitive scintillator screen (⁶LiF + ZnS, 0.2 mm thick) which is arranged perpendicular to the beam within a light-tight box. With the neutron intensity at the sample position of $5 \times 10^6 \text{ cm}^{-2} \text{ s}^{-1}$ the exposure time was on the order of 20 s per individual projection image.

At the time of the study, the pixel number of the CCD chip was 512 only, the resulting file was 2 Mbytes and the corresponding volume data set about 1 GByte. With the full field-of-view of 35 cm the pixel size was on the order of 0.35 mm. This relatively coarse scanning mode limits the spatial resolution (now 2048 pixels = 4 times higher resolution are common), but the major features of the objects can seriously be derived.

For the volume reconstruction step, next to the 365 projections, we took “open beam” and “dark field” images. The “open beams” were important to correct for the non-uniformity of the neutron beam, of the scintillator screen and of the CCD sensor. The “dark current” was taken to correct for the CCD off-set and other background features. In advance to the real volume reconstruction all obtained images have to be cleaned against “white spot” features, which occur if secondary radiation (mainly gammas) hit the CCD sensor. They cannot be avoided completely in neutron imaging experiments, but only reduced by some shielding and a clever arrangement of the detector with respect to the beam and the object. A perpendicular detector setup (Fig. 2.1) with a mirror between scintillator and camera has been proven to be the best solution.

²Neutron instruments are presented and described in Part II “Experimental methods”.

2.3.1.4 Results and Interpretation

Although the whole volumes of voxels are available for each object, the following data treatments were done to derive important information: outer views for comparison to photos, views of inner structures, including empty spaces, search for additional material regions next to the bulk structure, views into the often sealed inner volumes. Not in all cases important findings can be reported. However, the data material is also accessible for future more detailed studies, handed over to the museums experts. In this paper, we can show only a few images per object for the documentation of the work done.

General Observation Strategy

The three-dimensional data sets of the objects consist of values of the attenuation coefficients which are obtained by the inverse of the Beer-Lambert's law:




$$\Sigma = \ln\left(\frac{I_0}{I}\right)/d \quad (2.1)$$

Here, the intensities of the neutron beam in advance I_0 and behind the object I , with the sample thickness d are compared. Indeed the data set of the object is connected with the attenuation coefficient $\Sigma(x, y, z)$ or with the voxel index Σ_{ijk} , while the index numbers are given by the detector properties, e.g. the number of pixels of the sensor: between 512 and 2048.

Outside the object the attenuation values should be 0 (by definition). Inside the objects, different materials can be distinguished and separated if the differences in the attenuation coefficients are above the noise level. In the typical histogram of the Σ values we can see individual peaks which correspond to the different involved materials which can be separated by software means.




During our studies, we were able to separate and to visualize the following features: bulk metals, soldering and welding joins, repair work with other materials, resin or lacquer, ceramic remains from the casting process, inner structures for the stabilization during and after the casting process. These features will be discussed below individually for the different objects in detail.

Results from the tomography investigations of the objects listed in Table 2.1

Photo or preview	Homogeneity	Cross sections
<p>Men's head</p> 	 <p>■ hollow ■ different material</p>	


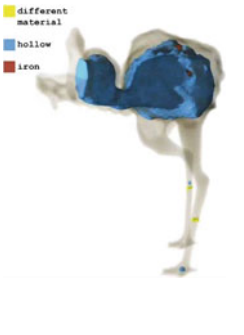
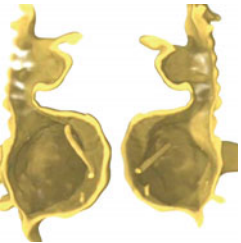
The inner volume of the object seen on the right photo is highlighted in the middle image (in blue), indicating the regions of the inner surface and some empty pores in the bulk. This is compared to the virtually sliced object on the right side. Obviously, on the heads peak some other (sealing?) material (in red) can be found closely connected with the filling channel remained in that region

Video: https://youtu.be/_mMSrHXzPb8

<p>Grotesque 1</p> 		
--	--	---

The transparent view (middle) and the virtual cut (right) verify casting mistakes/porosity (in blue) in the bulk of the sample and traces of wax/lacquer (in red) on the surface. No casting core is visible

Video: https://youtu.be/P7ejI_BT2Tw




<p>Grotesque 2</p> 	 <p>■ different material ■ hollow ■ iron</p>	
---	---	---

The empty space of this hollow casted sample is shown in the middle image (in blue), the inner surface and some stabilizing wires can be seen in the slices in the right figure. Some iron traces (in red) and different materials (in yellow) can be seen in the transparent structure in the middle image

Video: <https://youtu.be/F5gud6Mql7U>



(continued)

(continued)

Photo or preview	Homogeneity	Cross sections
<p><i>Hercules and Anteaus</i></p> 		

Whereas the lower figure is cast hollow (**in blue**), the “upper” body is filled with another material (**in red**), probably ceramics from the casting process; the tomography data show some outer damages of the lower figure, e.g. at the knee (middle image). The slices through the bodies (right image) show in detail the hollow areas, the remaining casting residuals and the non-homogeneities in the metal structure

Video: <https://youtu.be/WRPBFJnb5y8>




<p><i>Mercury</i></p> 		
--	--	---

These perspectives document well the empty areas (**in blue**) in the sculpture where the ceramic core was (partly) removed (middle image). In the bust region another material can be seen (**in yellow**) indicating some repair work or the filling point during casting, closed later. These cuts in the right image show the bronze material distribution inside the object. There is a clear separation line on half height of the body and numerous larger pores in the bulk. Some remaining core material is also visible

Video: <https://youtu.be/E9dEFWYcy98>




(continued)

(continued)

Photo or preview	Homogeneity	Cross sections
<p data-bbox="147 231 358 257"><i>Nessus and Deianeira</i></p> 		

The sculpture has large areas of emptiness (**in blue**), in particular within the riding person and the horse body. The cut demonstrates that the empty regions are stabilized by sticks and wires also made of metallic structures

Video: <https://youtu.be/xY4Z36QblUA>




<p data-bbox="147 702 201 728"><i>Paris</i></p> 		
--	--	--

Nearly the whole upper body is empty (**in blue**) whereas some different material (**in red**) can be found at the lower right leg. The hollow structure of the object is verified, the casted layer is solid and without voids or pores, some stabilizing cables can be seen near the shoulder. The legs are fully cast in metal, casting remains are mostly removed

Video: <https://youtu.be/YRdKmlOBEN8>

(continued)

(continued)

Photo or preview	Homogeneity	Cross sections
<p>Sol</p> 		




Half of the human body and that of the lion is emptied (**in blue**). In both parts of the sculpture the remaining casting core can be found with a different contrast compared to the metallic shape
 Video: <https://youtu.be/EwCXQ0ZLNVY>

<p>Striding Nobleman</p> 		
--	--	--

The object is mainly hollow (**in blue**), but the legs are separately added in a soldering process, the fixing point at the ground plate are made from a different material. These views demonstrate the components inserted to stabilize the structure of the object while the variable wall thickness can also be seen
 Video: https://youtu.be/rPM_kS8Zodg


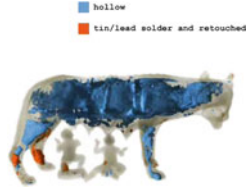

(continued)

(continued)

Photo or preview	Homogeneity	Cross sections
<p><i>Perfume</i></p> 		

While the man on top of the object is cast solid, the figures on the lower level are all empty (**in blue**). The structure through the metallic layers and all material distribution in the object can be derived from these slices

Video: <https://youtu.be/1PfsNfJd1fU>


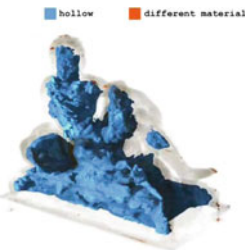

<p><i>She-wolf with Romulus and Remus</i></p> 		
---	---	--

The wolf's body is mainly hollow (**in blue**), some additional material can be seen in the legs (ceramic remains **in red**); the two kids are casted solid




Video: https://youtu.be/45LKr_E29BM

(continued)

(continued)

Photo or preview	Homogeneity	Cross sections
<p><i>Tiber</i></p> 		




The sculpture has a big hollow volume marked **in blue**
 Video: <https://youtu.be/mTc8XuHIBSY>

<p><i>Venus holding an apple</i></p> 		
---	--	---

This sculpture is more or less solid with only a few empty areas (**in blue**). Around the head and the arm some additional material (**in red**) can be found, probably from repair work. The regions with higher material porosity can be seen in these virtual slices in detail
 Video: <https://youtu.be/LfwtwC044iU>

(continued)

(continued)

Photo or preview	Homogeneity	Cross sections
<p data-bbox="145 225 332 254"><i>Hercules Pomarius</i></p> 		
<p data-bbox="145 717 1032 786">Nearly the whole body is empty (in blue), only in the legs and arms some remaining material (light gray) from casting can be found. The semitransparent view indicates the material distribution</p>		

2.3.1.5 Concluding Remarks Related to the Investigation of Bronze Objects

The presented data of the 14 objects from the collection of Rijksmuseum Amsterdam verified that a non-invasive investigation of even bulky bronze objects is possible by NT methods. In particular, thermal neutrons have much higher penetration ability than X-rays. For the current set of samples we did not register strong artifacts by the sample scattering like beam hardening in the X-ray case.

It was possible to distinguish between inner cavities, ceramic casting remains and the pores distribution in the bulk. In addition, some stabilization reinforcement parts inside the objects were identified. Measures of restauration become visible as areas with a different neutron contrast.

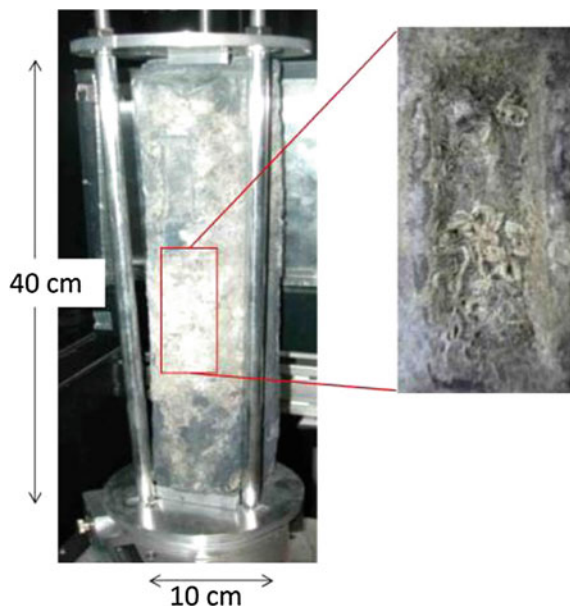


Fig. 2.3 Lead ingot from Siracusa in the experimental sample holder. The *zoomed region* refers to the *middle* cartouche (Triolo et al. 2014—Reproduced by permission of The Royal Society of Chemistry)

2.3.2 Shipwrecks Keep Invaluable Treasures³

2.3.2.1 Description of the Investigated Artifacts

Ancient roman lead ingots (3rd–1st century BC) were investigated by NT. The ingots are belonging to sunken roman ships in two different locations near Sicily's coast.

In the first location (Siracusa, Italy ca. I BC) 4 similar lead ingots were found under water. They have the same troncopyramidal shape, length of about 40 cm and same weight of ca. 33 kg (the maximum weight a slave could carry by the Roman law) as well as a rectangular mold mark on the top side. In Fig. 2.3 one of these ingots is shown in the specially developed holder which allows for rotation of the sample around its vertical axis.

The photography of the ingot in Fig. 2.3 shows that its surface is heavy damaged due to deposits of salts, algae and probably carbonaceous material, very likely coming from a fire occurred on the ship. The ingots are usually characterized by mold marks located in three regular indented rectangular areas (cartouches) where both characters and images are found. In this sample these areas of interest are

³Section written by F. LoCelso, N. Kardjilov, P. Tisseyre, S. Tusa.



Fig. 2.4 Picture of the whole lead ingot depicting its highly damaged state, concretions are clearly observable. It is also marked (*red square*) the area in one of the slanted sides where signs were found after the digital reconstruction (Triolo et al. 2014—Reproduced by permission of The Royal Society of Chemistry)

covered by deposit and in the middle section, one could see a hint of an image (zoomed region in Fig. 2.3).

Another kind of lead ingot was found in a second location in Capo Rasocolmo Messina (Italy) that could be probably date back to the 3rd century BC, as shown in Fig. 2.4. It has different shape in the cross section, different length and weight (length of 35 cm and weight of ~ 30 kg) compared to the one described in Fig. 2.3.

2.3.2.2 Scientific Questions

Lead was a basic material in the Roman age between 2nd century BC and the 1st century AC which was used in ship construction, both military and commercial, as well as in pipe systems for water and wastewater management. The Mediterranean Sea played an important role in the lead trading where the raw material was transported in form of ingots by commercial ships. Therefore the study of the ship wrecks on the sea ground and the characterization of rescued lead ingots are very important in showing us the net of ancient commercial trade routes.

The NT imaging technique is very suitable for the non-destructive investigation of corroded lead objects due to the high penetration power of the neutron radiation (lead is notoriously opaque to X-rays). The obtained digitalized volume can be processed by 3D volume rendering software which helps, for example, to remove digitally the corrosion layer and in this way to visualize the original surface of the sample. The final results of the epigraphic analysis will provide useful insights about the producer, the origin and the age of the finding.

2.3.2.3 Experimental Setup

The experiments were performed at the neutron imaging facility CONRAD⁴ at Helmholtz-Zentrum Berlin, Germany. The facility is situated at the end of a curved

⁴Neutron instruments are presented and described in Part II “Experimental methods”.

neutron guide facing the cold source of the BER-II research reactor (Kardjilov et al. 2011b). The neutron guide provides a cold neutron flux in the order of app. 2×10^8 n/cm² s directly at the end of the guide with a negligible background of γ -radiation and fast neutrons. A pinhole geometry with L/D of 170 (L = 500 cm, D = 3 cm) was used for achieving of better spatial resolution within a beam field of 10 cm \times 10 cm with a neutron flux of $\sim 10^7$ n/cm² s. The used detector system was based on a 16-bit CCD camera (Andor) with 2048 \times 2048 pixels. The images obtained from the LiZnS scintillator are projected via a mirror and a lens system onto the CCD chip (Kardjilov et al. 2011a).

For the tomographic measurements 300 radiographic projections at continuing rotation angles were taken over 360°. The exposure time per projection image was 10 s and the overall time for the tomographic measurement was about 1.5 h. Due to the limited field of view of 10 cm \times 10 cm the sample was measured only at 3 heights where the stamps were located. For samples without visible signs on the surface the whole sample length was scanned with vertical steps of 10 cm (4 tomographies in total). The data were reconstructed with a backprojection algorithm implemented in the software Octopus (Octopus). For visualization and 3D rendering the software VGStudioMax was used (Volume Graphics). After the illumination of the samples by the neutron beam the irradiated parts become radioactive. However after some decay time the samples were approved to be non-radioactive again. In our case the necessary decay time was about 3 days.

2.3.2.4 Results and Discussion

The NT reconstruction of the three cartouches of the lead ingot of Fig. 2.3 (see Fig. 2.5) shows, in the middle section, that the image found represents a dolphin. This fact is indeed consistent with the finding, in the two cartouches adjacent to the dolphin figure, of two different inscriptions in relief, as shown in Fig. 2.5 (top and bottom part). They read as MPLANILF, i.e. M(arcii) PLANI(i) L(ucii) F(ilii), and RVSSINI (Russini) respectively, accordingly to the tria nomina standard used mainly by Roman citizen (Domergue 1987). Indeed they were identified by a personal name, i.e. the praenomen (Marcius in its genitive form), followed by the family name, i.e. nomen (Planius in its genitive form) and then a third name, i.e. cognomen (Russini), which basically indicates a specific branch of the family. This epigraphic analysis refers therefore to the producer of the lead ingots and possibly also the mine owner in Carthago Nova in Spain (Trincherini et al. 2010; Tisseyre et al. 2008) which dates back to 1st century BC, when in fact the Planius family (either Marcius or Lucius, probably brothers and sons of Lucius, as the L(ucii) F(ilii) inscription suggests) was active in lead ingots trading. In fact the latter were found in ship wrecks in many locations along the coast of Italy and France.

Similar characteristics were found in the other three ingots which at naked eye also appear to have partially erased mold marks. The second lead ingot, as shown in Fig. 2.4 has not only different shape in the cross section compared to the one described in Fig. 2.3, but also different length and weight (length of 35 cm and

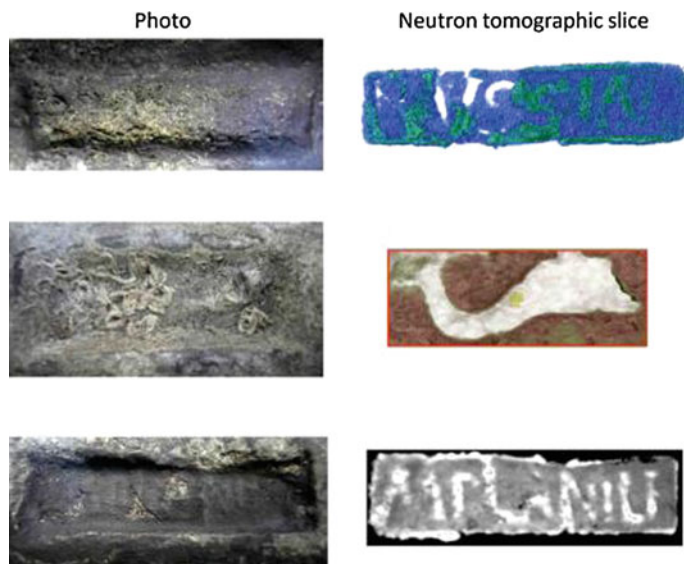


Fig. 2.5 Comparison between the three cartouches of lead ingot of Fig. 2.3; *on the left* the naked eye view, *on the right* the corresponding digitally reconstructed images (Triolo et al. 2014—Reproduced by permission of The Royal Society of Chemistry)

weight of ~ 30 kg). This ingot was a part of a load rescued in Capo Rasocolmo Messina (Italy) that could be probably date back to the 3rd century BC. It is possible to see that it has slanted sides and a rounded top while the base is still rectangular. The sample is heavily covered by calcareous concretions which in some parts include small spherical shaped stones (see the protrusion in the lower right part of Fig. 2.6b). There are two regions of interest, beneath the calcareous concretion in one of the slanted sides. It is possible to see, in the right part of Fig. 2.6a, a big X shaped sign running across the whole width of the ingot, while about 10 cm away, in the left part of the digital reconstruction, there is a group of characters which could lead to a possible identification of the maker.

The group of characters can be read as CP which can be probably traced back to one of the Cartagena's producers C(aius) P(ontileieni) which is contemporary to the Planius family. Indeed it has been found around 3rd century BC (Laubenheimer-Leenhardt 1973) that some of the Ingots produced by the Planius family have been stamped as well with Marcus Caius Pontilieni inscription. The big X shaped sign is probably a mark for the production or trade control. In Fig. 2.6b it is also shown in the vertical projection that the letters have been stamped; the depth of the stamp is 4.7 mm and it is triangularly shaped.

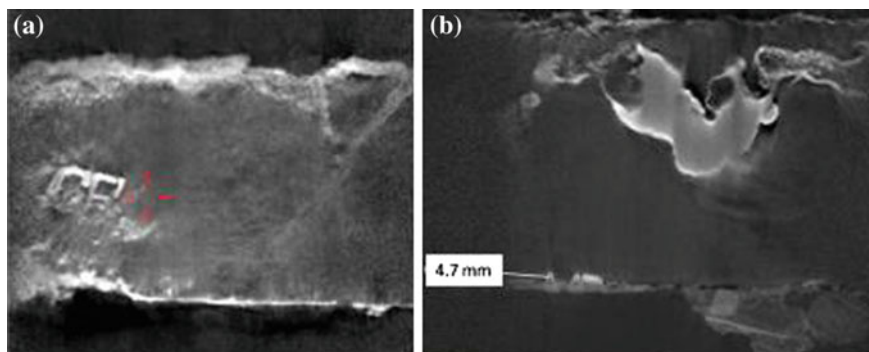


Fig. 2.6 **a** From the digital reconstruction a group of two letters as well as a big cross sign (not visible at naked eye) were found. The *red mark* on the image is showing the position of the cutting plane for the cross section shown in subsection **b**; **b** top view of the slanted side where the letters were found showing the shape and the depth of stamping marks (Triolo et al. 2014—Reproduced by permission of The Royal Society of Chemistry)

2.3.2.5 Concluding Remarks Related to the Study of Lead Objects

The results presented here give an insightful perspective on the possibilities offered by NT in the field of archeological investigations. The technique has been applied on severely damaged lead ingots rescued from underwater shipwrecks, and it has given final answers both on the provenance and the historical frame time in which the ingots were traded. It is very important to underline that this experimental technique allowed not only to examine rather bulky samples, but thanks to its selectivity to different elements it also made possible to digitally retrieve precious information in a non-destructive way.

Table 2.2 Conditions for activation of bronze compounds by bombardment with thermal neutrons

Material	Isotope	Content (%)	Capture CS [barn]	Resulting nuclide	Half life
Cu	Cu-63	69.17	4.506	Cu-64	12.7 h
	Cu-65	30.83	2.168	Cu-66	5.12 min
Zn	Zn-64	48.60	0.76	Zn-65	224.3 days
	Zn-68	18.80	1.073	Zn-69	13.76 h
	Zn-70	0.60	0.091	Zn-71	2.45 min
Sn	Sn-120	32.59	0.14	Sn-121	27.06 h
	Sn-122	4.63	0.18	Sn-123	129.3 days
	Sn-124	5.79	0.13	Sn-125	9.64 days
Pb	Pb-204	1.40	0.66	Pb-205	5.54 ms
	Pb-208	52.40	0.0005	Pb-209	3.25 h

2.4 Final Thoughts

There were some doubts about the activation of the bronze and lead samples during the neutron exposure. In Table 2.2 the capture cross-sections of the relevant isotopes in the observed materials and the half-lives of the exited nuclei can be found. The only relevant isotope is Cu-63 due to the relatively long half-live and a unneglectable capture cross-section.

Indeed, just after exposure there is some emission of secondary radiation due to the decay of activated nuclides. However, the involved material activity is short-living and the background level is reached after about 3 days at most. This is confirmed by the practical radiation measurements at real samples by experts. Materials like Co or Ag should be avoided to be studied since their half-lives are too long and the activation rate high. In the current study, there is no such material involved.

References

- Banhart J (ed) (2008) *Advanced tomographic methods in materials research and engineering*. Oxford University Press, Oxford, UK
- Banhart J, Borbely A, Dzieciol K, Garcia-Moreno F, Manke I, Kardjilov N, Kaysser-Pyzalla AR, Strobl M, Treimer W (2010) X-ray and neutron imaging—Complementary techniques for materials science and engineering. *Int J Mater Res* 101:1069–1079
- Domergue C (1987) Les lingots de plomb de l' épave romaine de Valle Ponti (Comacchio). *Epigraphica* 49:109–175
- Kardjilov N, Fiori F, Giunta G, Hilger A, Rustichelli F, Strobl M, Banhart J, Triolo R (2006) Neutron tomography for archaeological investigations. *J Neutron Res* 14:29–36
- Kardjilov N, Hilger A, Manke I, Benfante V, Lo Celso F, Triolo R, Ruffo I, Tusa S (2008) Neutron tomography in modern archaeology. *Notiziario Neutroni e Luce di Sincrotrone* 13:6–9
- Kardjilov N, Dawson M, Hilger A, Manke I, Strobl M, Penumadu D, Kim F, Garcia-Moreno F, Banhart J (2011a) A highly adaptive detector system for high-resolution neutron imaging. *Nucl Instrum Methods Phys Res, Sect A* 651:95–99
- Kardjilov N, Hilger A, Manke I, Strobl M, Dawson M, Williams S, Banhart J (2011b) Neutron tomography instrument CONRAD at HZB. *Nucl Instrum Methods Phys Res, Sect A* 651:47–52
- Kardjilov N, Manke I, Hilger A, Strobl M, Banhart J (2011c) Neutron imaging in materials science. *Mater Today* 14:248–256
- Laubenheimer-Leenhardt F (1973) *Recherches sur les lingots de cuivre et de plomb d'époque romaine dans les régions de Languedoc-Roussillon et de Provence-Corse*, Paris ed. de Boccard 1973
- Lehmann E, Hartmann S, Wyer P (2005) Neutron radiography as visualization and quantification method for conservation measures of wood firmness enhancement. *Nucl Instrum Methods Phys Res, Sect A* 542:87–94
- Lehmann E, Vontobel P, Frei G (2007) The non-destructive study of museums objects by means of neutrons imaging methods and results of investigations. *Nuovo Cimento Della Societa Italiana Di Fisica C (Geophys Space Phys)* 30:93–104
- Lehmann E, Hartmann S, Speidel MO (2010) Investigation of the content of ancient Tibetan metallic Buddha statues by means of neutron imaging methods. *Archaeometry* 52:416–428

- Mouchot D (1970) Pièces d'ancres, organeaux et ornements de plomb antiques découverts entre Antibes et Monaco. *Rivista di studi liguri* 36:307–318
- Neutron Attenuation. Available: <https://www.ncnr.nist.gov/instruments/bt1/neutron.html>
- Octopus. Available: <http://www.inct.be/en/software/octopus>. Accessed 12 Oct 2015
- Schillinger B, Lehmann E, Vontobel P (2000) 3D neutron computed tomography: requirements and applications. *Phys B* 276–278:59–62
- Strobl M, Mankie I, Kardjilov N, Hilger A, Dawson M, Banhart J (2009) Advances in neutron radiography and tomography. *J Phys D-Appl Phys* 42:243001
- Tisseyre P, Tusa S, Cairns WRL, Selvaggio Bottacin F, Barbante C, Ciriminna R, Pagliaro M (2008) *Oxford J Archaeol* 27:315–323
- Trincherini PR, Domergue C, Manteca I, Nesta A, Quarati P (2010). [arXiv:1002.3557](https://arxiv.org/abs/1002.3557)
- Triolo R, Lo Celso F, Tisseyre P, Kardjilov N, Wieder F, Hilger A, Mankie I (2014) Neutron tomography of ancient lead artefacts. *Anal Methods* 6:2390–2394
- Van Lang R (2012) Technical studies of Renaissance bronzes. Dissertation TU Delft. ISBN 978-90-71450-49-5
- Volume Graphics. Available: <http://www.volumegraphics.com/> (accessed)
- X-ray Attenuation. Available: <http://www.nist.gov/pml/data/xraycoef/>

Chapter 3

Paintings Reveal Their Secrets: Neutron Autoradiography Allows the Visualization of Hidden Layers

A. Denker, C. Laurenze-Landsberg, K. Kleinert
and B. Schröder-Smeibidl

Abstract The modern art history uses new methods for non-invasive investigation of valuable artifacts. Investigations of paintings by neutron beams benefit from the strong penetration power of neutron, the possibility for elemental analysis by using neutron activation analysis and the interaction of neutrons with light elements. Thus, neutron autoradiography allows the visualization of structures and layers beneath the top surface in a one to one scale.

3.1 Introduction

The visualization of hidden layers in paintings provides important information about conceptual changes of the picture's subject or valuable hints about the painting style of the artist. There are different methods for investigation of paintings but the only method which is sensitive to covered layers of pigments and materials containing light elements like phosphorus, potassium or sodium is the neutron activation autoradiography. The method is used by a few galleries worldwide for gaining additional information in clearing questions related to the painting authenticity or doubts in the declared authorship.

3.2 Used Experimental Methods

3.2.1 *Autoradiography*

Most museums apply analytical techniques based upon X-ray radiation. Whilst X-rays have a quite high penetration depth, X-ray transmission images only indicate

A. Denker (✉) · B. Schröder-Smeibidl
Helmholtz-Zentrum Berlin, Berlin, Germany
e-mail: denker@helmholtz-berlin.de

C. Laurenze-Landsberg · K. Kleinert
Gemäldegalerie Berlin, Berlin, Germany

dense matter or the distribution of heavy elements such as iron or lead, e.g. in the pigment lead white or mercury in the pigment vermilion. The analytical depth of X-ray fluorescence in paintings is in the order of 150 μm , and again, in large depths mainly heavy elements will be detected. Neutrons have no charge and therefore exhibit a huge penetration depth and they also interact with light elements and, thus, are a real complementary method.

The painting is placed at a small angle with respect to a collimated neutron beam. Thus a stripe of the painting is irradiated where the neutrons undergo nuclear interaction with the pigment layers. By moving the painting up and down a homogenous activation of large areas, e.g. in Berlin up to 120 cm by 120 cm, is possible. After stopping of the neutron irradiation 2D maps of the activated pigments from all layers are recorded on analog X-ray films, which have the advantage of being in a one to one scale, and alternately with X-ray imaging plates in digital format, which offer the advantage of image processing. The different decay times of the various activated elements permits to visualize a certain pigment by applying the films and the imaging plates at different times with various exposure times. Detailed description of the method can be found in Chap. 15.

3.2.2 *Gamma Spectroscopy*

Between the exposure of the films and the image plates, gamma spectra from specific colour areas (diameter 5 cm) in the painting are recorded. By analyzing the position and intensity of the energy peaks qualitative information about the chemical composition of the paint mixture and the approximate amount of the pigments can be obtained. In this way a position sensitive elemental analysis is possible. Detailed description of the method can be found in Chaps. 10 and 15.

3.3 Examples of Neutron Activation Autoradiographic Studies of Paintings

3.3.1 *Nicolas Poussin, “Armida Abducts the Sleeping Rinaldo”*

Nicolas Poussin (1594–1665) is one of the main representatives of pictorial classicism in the Baroque period. He was French, but spent most of his entire career in Rome but for two years as court painter to Louis XIII. The illustrations in his paintings address scenes from the bible and from classical antiquity. Already in 1625, the legend of the sorceress Armida and the crusader Rinaldo had inspired Poussin to a make a painting named ‘Armida and Rinaldo’, now owned by the Dulwich Picture Gallery in London, that has been identified as an original.

In contrast, the painting from the Berlin Picture Gallery “Armida abducts the sleeping Rinaldo” (Fig. 3.1) shows a different but similar scene, and was always considered by most art historians as a copy.

To clarify the controversial attribution a neutron autoradiography investigation was carried out at the Berlin Neutron Scattering Centre BENSCH.

The image of the X-ray transmission (Fig. 3.2) did not contribute to solve the problem: it primarily reveals the already visible distribution of white lead and vermilion, as well as the wooden stretcher with nails. Due to the size of the painting, the NAR was carried out in two separate irradiations. A combined image of the 1st autoradiograph composed of both irradiations is shown in Fig. 3.3. The different sets of X-ray films were processed digitally and assembled afterwards.

Already this first autoradiograph which shows the distribution of the short-lived isotope ^{56}Mn , contained in the brown pigment umber, revealed surprising pentimenti as conceptual changes: additional trees (which have been highlighted in Fig. 3.3) not present in the final, visible painting. These trees fit in the composition of the painting and contain the same pigments as the other structures. Obviously, these pentimenti are corrections made by the artist himself. A copyist would not have been aware of these changes.

Therefore, these pentimenti are strong and important hints that this painting can be attributed to the master himself, Nicolas Poussin.



Fig. 3.1 Nicolas Poussin, Replica, “Armida abducts the sleeping Rinaldo”, (c. 1637), $120 \times 150 \text{ cm}^2$, Gemäldegalerie, Staatliche Museen zu Berlin. Credits Staatliche Museen zu Berlin, Gemäldegalerie, Jörg P. Anders

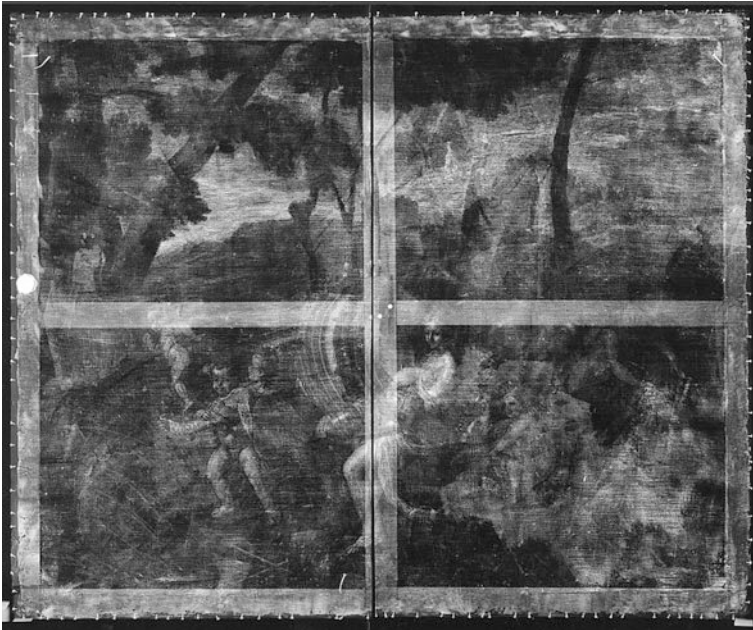


Fig. 3.2 Nicolas Poussin, ‘Armida abducts the sleeping Rinaldo’, X-ray transmission image, Christoph Schmidt, Gemäldegalerie, Staatliche Museen zu Berlin. *Credits* Staatliche Museen zu Berlin, Gemäldegalerie, Christoph Schmidt



Fig. 3.3 Nicolas Poussin, “Armida abducts the sleeping Rinaldo”, 1st neutron autoradiography, Assembly from 12 X-ray films: in order to investigate the whole picture, two separated irradiations were carried out and finally recomposed. *Credits* Helmholtz-Zentrum Berlin für Materialien und Energie

3.3.2 Tiziano Vecellio “The Girl with a Platter of Fruits”

Titian (1488/90–1576) was a court painter of the republic of Venice and present at the crowning ceremony of the emperor Karl V. in Bologna 1530. In Titian’s painting “Girl with a Platter of Fruits” (Fig. 3.4) a girl in a contemporary fashioned dress holds a silver platter with apples and lemons. This picture—formerly interpreted as a portrait of Titian’s daughter Lavinia—seems to be an allegory of fertility.

Already well known was the X-ray radiography shown in Fig. 3.5 which turned by 180° was interpreted as an official portrait of an old man, a representative like a Senator or Doge, standing upright.

Surprisingly, however, autoradiography reveals a sitting woman. Only her dress is shown which is painted with Realgar (As_2S_2) and Orpiment (As_2S_3). The 2nd autoradiograph, which demonstrates the distribution of arsenic, shows, if the painting is turned on top, a lady sitting on a chair: her arm and elbow, her skirt over the arm and around the leg of the chair (Fig. 3.6). The specific γ -spectroscopy of these areas showed ^{75}As ($T_{1/2} = 26.5$ h). Titian has employed the red pigment Realgar (As_2S_2) and the yellow colour Auripigment (As_2S_3) for the pleated dress. In addition it was observed a second outstanding and unexpected fact: the γ -radiation

Fig. 3.4 Tiziano Vecellio (“Titian”), “the girl with a platter of fruits” (c. 1555), Gemäldegalerie, Staatliche Museen zu Berlin. Credits Staatliche Museen zu Berlin, Gemäldegalerie, Jörg P. Anders



Fig. 3.5 Tiziano Vecellio (“Titian”), X-ray radiography, Gemäldegalerie, Staatliche Museen zu Berlin. *Credits* Staatliche Museen zu Berlin, Gemäldegalerie, Gerald Schulz



Fig. 3.6 2nd neutron autoradiography, composed of 12 imaging plates, exposure 1 d 7 h to 1 d 11 h after activation. *Credits* Helmholtz-Zentrum Berlin für Materialien und Energie

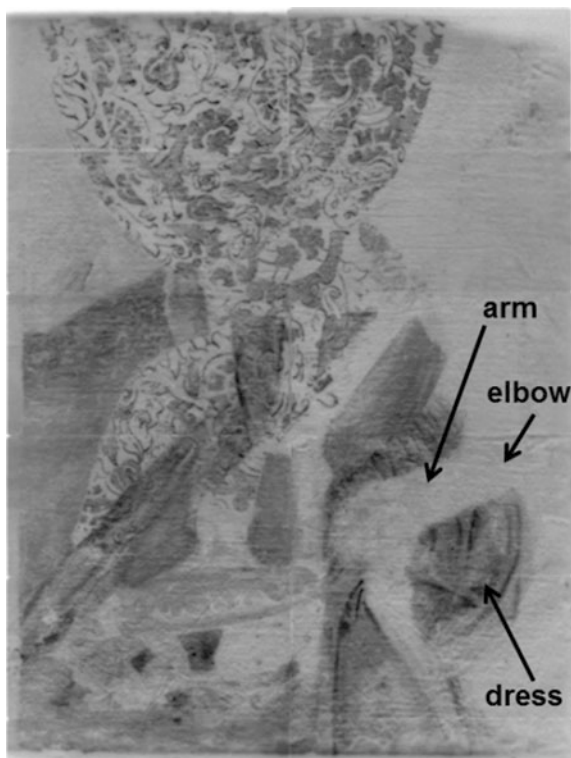


delivered the evidence of the two Sb isotopes: ^{122}Sb : $T_{1/2} = 2.7$ h, ^{124}Sb , $T_{1/2} = 60$ d. The exact microanalytic analysis shows that Titian might have employed the pigment Neapel Yellow ($\text{Pb}_2\text{Sb}_2\text{O}_6$). In the literature the name of this color and a description of the contents were at first mentioned in 1702. The discovery that Titian possibly has applied this colour already in 1555, 150 years earlier, was a little sensation.

The pigments of the visible brocade dress contain a lead-tin mixture, which cannot be activated by cold neutrons and therefore no darkening can be seen. But the precise pattern could be observed (Fig. 3.7). It was supposed that Titian had worked with templates. But the examination could exclude this assumption and confirm that it really was a pure freehand drawing (Fig. 3.8).

On the base of this NAAR-investigation this painting is published as earliest evidence and Titian is considered as first user of the pigment Naples-Yellow.

Fig. 3.7 2nd neutron autoradiography turned by 180° . *Credits* Helmholtz-Zentrum Berlin für Materialien und Energie



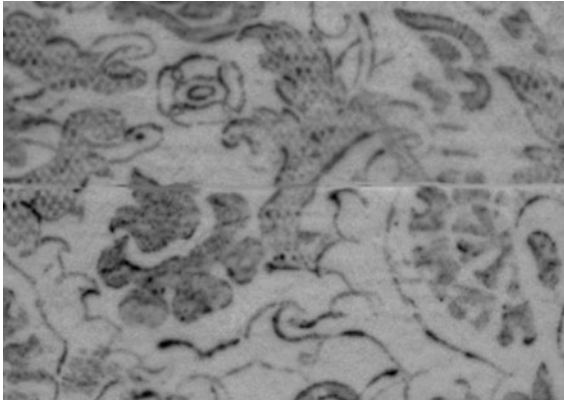


Fig. 3.8 2nd neutron autoradiography, zooming of the brocade dress: detail of the pattern. *Credits* Helmholtz-Zentrum Berlin für Materialien und Energie

3.3.3 Rembrandt: “The Money Changer” and “Jacob Wrestling with the Angel”

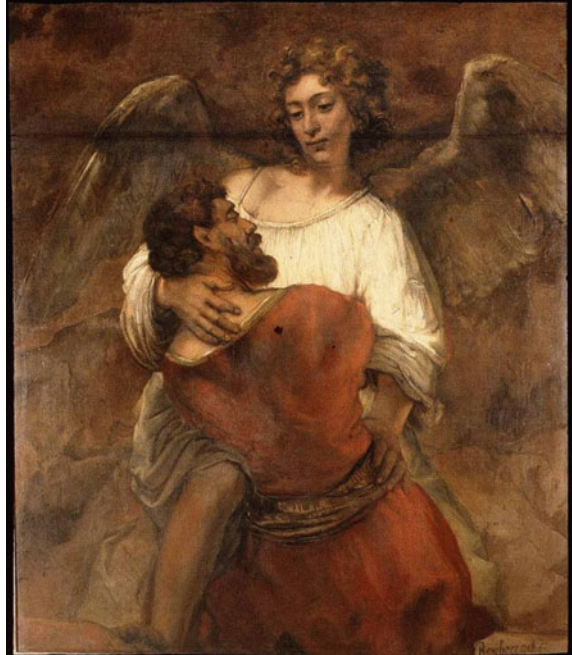
The painting *The Money Changer* is one of the earliest paintings by Rembrandt, dating from 1627 when Rembrandt was only 21 years old and still living in Leiden (Fig. 3.9). At a much later period, in 1660, *Jacob wrestling with the Angel* was created by him (Fig. 3.10).

The first autoradiograph of the early work, the *Parable of the Rich Man*, shows that the entire composition of the painting is laid down in a dark paint containing a high



Fig. 3.9 Rembrandt, “The Money Changer”, 1627, Gemäldegalerie, Staatliche Museen zu Berlin. *Credits* Staatliche Museen zu Berlin, Gemäldegalerie, Christoph Schmidt

Fig. 3.10 Rembrandt, “Jacob Wrestling with the Angel”, 1660, Gemäldegalerie, Staatliche Museen zu Berlin. Credits Staatliche Museen zu Berlin, Gemäldegalerie, Christoph Schmidt



amount of manganese. This form of layout of the composition is called dead-colouring and is described in texts of the 17th century as a first stage within a painting process. It is a more or less monochrome design defining the main forms, beneath the second layer, in which the actual colours were laid in. The dead-colouring technique was even stipulated by guild-regulations as an essential check for quality. With the first autoradiography of the *The Money Changer*, Fig. 3.11, it can be proven that Rembrandt still used the prescribed academic technique.

In contrast to the early painting, the last autoradiograph of *Jacob wrestling with the Angel* discloses a wonderful sketch. With loose and vital brushstrokes Rembrandt designed the contours of Jacob and the angel. During the sketching process he corrected the position of the angel's hand: In this way he created the intersecting diagonals of the two bodies which are embraced by the sweep of the angel's spread wings.

Perhaps not all lines can be attributed to a first sketch. Maybe some lines have served to reinforce contours at the end of the genesis of the painting. As autoradiographs show a summation of radiation from all layers the painting needs to be studied with the stereoscope for a more accurate evaluation. It may be possible that the depth of the reproduced paint layer can be located at edges or in open cracks of the painting, where the various paint layers become visible.

In the autoradiographs of this *Jacob wrestling with the Angel* (Figs. 3.12 and 3.13) the way of Rembrandt's build-up of a composition can be especially well witnessed. He first painted the background, leaving the space for the intended

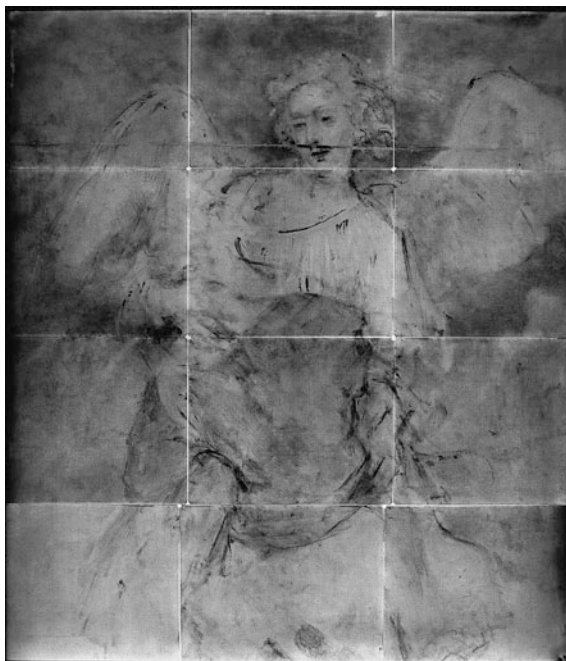


Fig. 3.11 “The Money Changer”, 1st neutron autoradiograph, showing the distribution of manganese. *Credits* Helmholtz-Zentrum Berlin für Materialien und Energie

Fig. 3.12 Jacob Wrestling with the Angel, 3rd neutron autoradiograph, showing the arsenic in smalt. *Credits* Helmholtz-Zentrum Berlin für Materialien und Energie



Fig. 3.13 Jacob Wrestling with the Angel, last neutron autoradiograph, showing the phosphorus in boneblack and mercury in vermilion for the lips. *Credits* Helmholtz-Zentrum Berlin für Materialien und Energie



foreground blank. The area left open for the wings is smaller than they were finally executed.

Both the third and the last film show the application of smalt and boneblack in the background, a color mixture, which is often found in paintings of the late Rembrandt.

3.4 Method Limitation and Peculiarities

With neutron autoradiographs different paint layers superimposed during the creation of the painting become visible. Quite often, the individual brushstroke of the artist is made apparent, as well as changes and corrections performed during the painting process. By investigating paintings that have been reliably authenticated, one can characterize the unique style or 'hand' of a particular artist.

One reason of the success of autoradiography applied to paintings by Rembrandt is that the distribution of the pigment boneblack is so excellently reproduced. Especially in his later works Rembrandt sketched the composition in boneblack.

The radioactivity decays with time and the most activated nuclides are very short-lived. The long schedule for the experiment of 6–8 weeks is due to the long exposure for the last film layer because at this time almost all the radioactivity has disappeared already. The residual radioactivity of the painting is measured and

documented after 2–3 months. At the end, the painting is returned to the museum going through a standard control procedure regulated by law and without any critical activity left. The technique is appropriately called a non-destructive method for two reasons: First, 4 in 10^{12} atoms become radioactive on average. Second, earlier experiments have shown that only doses of orders of magnitudes higher than applied today would be dangerous for paintings.

3.5 Conclusions

In the larger museums infrared reflectography and X-ray transmission are available and used routinely to investigate paintings. Mobile XRF-scanners are getting available. For NAR, it is compulsory to transfer the painting to a reactor. This method is more difficult and implies more risks with regard to the handling of the painting. Why is this method still an outstanding and very valuable tool?

The advantages of the use of neutrons in comparison to X-rays are evident. The neutrons have a high penetration depth and an activation cross section (n, β) depending on the isotope. Nuclides with various half-lives, thus various pigments, can be collected on separate films as a contrast variation. The result is completely different to what is observed by X-ray transmission. With the latter, pigments based on lead and iron are observed, and these elements cannot be activated by cold neutrons. XRF has limits on the detection of light elements like Phosphorous. Thus X-ray techniques and neutron autoradiography are in fact complementary methods.

Chapter 4

Neutrons Unveil Secrets of Musical Instruments

G. Festa, D. Mannes and A. Scherillo

Abstract Ancient musical instruments are complex objects constructed in the past with the aim of obtaining the best sound quality. Construction parameters change during time according to the aesthetics of the historical period and required sonic/musical features. Musical instruments are mostly made of wood, metals and hide. Neutron based methods such as diffraction, radiography and tomography can be used to study musical instruments providing a link between different disciplines including nuclear physics, metallurgy, cultural heritage and acoustics.

4.1 Introduction

Ancient musical instruments are not only relics of interest for cultural heritage, but also finely crafted objects with a specific feature: high quality sound emission. Neutron imaging and neutron characterization of materials can be employed to define the physical aspect of the musical instruments (i.e. internal shapes, constituent materials, crystal structure of the metal parts) in a non-destructive and non-invasive manner. Investigation of musical instruments provides details about their design and materials composition, helps understanding the original manufacturing process and aids the reconstruction of missing parts. Because of the complex and inhomogeneous nature of these objects (for example made of wood and metal), a combined use of neutron and X-ray beams is currently considered to be the best practice.

G. Festa (✉)

Department of Physics and Centre NAST, University of Rome Tor Vergata, Rome, Italy
e-mail: giulia.festa@uniroma2.it

G. Festa

Museo Storico della Fisica e Centro Studi e Ricerche Enrico Fermi, 00184 Rome, Italy

D. Mannes

Paul Scherrer Institute, Villigen, Switzerland

A. Scherillo

ISIS facility, STFC, Didcot, UK

In the following sections, some significant scientific case studies are presented and a brief introduction to the applied techniques is provided.

4.2 Used Experimental Methods

4.2.1 *Neutron Imaging (Radiography and Tomography—NR and NT)*

Computed Tomography (CT) is currently playing an increasingly important role in the field of Cultural Heritage diagnostics. In fact, it represents a powerful non-destructive investigation technique, capable of displaying the investigated volume in a three-dimensional way thanks to modern 3D rendering techniques (Lehmann et al. 2001a; Calzada et al. 2005). X-ray and neutron imaging are applied to the study of composite material samples containing wooden and metallic parts. X-ray imaging is a well-established non-invasive method for investigation of wooden objects; more recently neutron imaging was also used to study wooden materials (Lehmann et al. 2001b, 2005; Mannes PhD thesis; Mannes et al. 2009; Triolo et al. 2010). Sets of 2D neutron radiographies of the irradiated sample are recorded at different angles. The 3D matrix of the attenuation coefficients is then reconstructed from the radiographies by using mathematic algorithms. Internal features are visible through rendering software capable of digital cut, contrast variation and false colour associated to a specific attenuation coefficient range in the sample volume. Detailed description of the method can be found in Chap. 16.

4.2.2 *Neutron Diffraction (ND)*

ND is a powerful technique for investigating the crystal structure of samples. The diffraction process is described as the reflection of an incident beam by crystal planes (hkl). Neutrons can indeed be represented either as particles or as propagating waves due to the particle-wave dualism. The interference of neutron waves scattered from the periodic structure of atoms ordered in a crystal lattice is unique for each crystalline material (Squires 1978). Measurements provide diffraction patterns (Bragg peaks) used to identify phases and structures or to derive texture information. Peak positions and shapes are related to structural information at different scales and include *phase structure* describing compounds' content, *crystal structure* related to the atomic arrangement of each phase, *grain structure* representing size, shape and orientation of grains (texture), *micro-structure* describing structural deviation from an ideal crystal within a grain. A quantitative evaluation of structural properties requires analysis of data in terms of *peak position* related to changes in the lattice parameters, macro and micro strains; *peak widths* related to particle size and micro-strain broadening; and *intensities* related to the atom arrangements and grain orientations (Chateigner web). Detailed description of the method can be found in Chap. 9.

4.2.3 Neutron Resonance Capture Analysis (NRCA)

NRCA (Postma and Schillebeeckx 2005) is a nuclear technique for elemental and isotope analysis possible thanks to the peculiar interactions of epithermal neutrons ($E \approx 1\text{--}10^4$ eV) with materials. When a neutron beam hits a sample, there is a certain probability of neutron absorption by the component nuclei. For many nuclear species the absorption cross section in the epithermal energy range shows large peaks called resonances. When a neutron is absorbed by the nucleus, it passes to an excitation state. Its de-excitation to the ground state produces gamma photons in cascade with an energy spectrum characteristic of the isotope. Gammas are promptly emitted after absorption. NRCA is a Time-Of-Flight (TOF) technique: neutron flight-time is measured from the instant of neutron production until gamma detection thanks to the instantaneous gamma emission after absorption. Gamma-ray detectors, with good timing properties, are positioned near the sample and determine the end of a flight time measurement. The neutron TOF is directly related to neutron energy. NRCA spectra are directly related to the isotopes' sample content. For further reading about NRCA see Chap. 12.

4.3 Examples of Musical Instruments Neutron Studies

Some key examples of neutron techniques applied to the study of musical instruments are reported below.

4.3.1 The Savary Bassoon

Object of the study was a *Savary* bassoon part of the *Burri* collection, preserved in Bern. Jean-Nicolas Savary (1768–1853) was a famous French bassoonist and bassoon maker so formidable that, after his death, he was named as ‘*the Stradivari of the bassoon*’. The core of the instrument is made of wood with some metallic parts like keys and mechanisms inside the object (cf. Lehmann and Mannes 2012).

4.3.1.1 Measurement Set up

Neutron and X-ray tomography scans were performed at the NEUTRA¹ beamline located at the spallation neutron source SINQ, Paul Scherrer Institute, Switzerland. NEUTRA is an instrument for neutron radiography and tomography with thermal neutron beam. A 320 kV X-ray tube and related acquisition system can be inserted

¹Neutron instruments are presented and described in part II “Experimental methods”.

into the neutron beam-tube in order to perform X-ray imaging of the investigated samples in the same geometry as the neutron one. In this particular case, the field of view was chosen of $315 \text{ mm} \times 315 \text{ mm}$ and 2×2 binning resulting in a pixel size of ca. $300 \text{ }\mu\text{m}/\text{pixel}$. The camera used was an Andor L CCD-camera with 2048×2048 pixels resolution. For neutron detection a $100 \text{ }\mu\text{m}$ thick 6LiF:ZnS screen was used. Exposure time was 10 s and 625 projections were acquired over 360° . As the object was larger than the available field of view the tomography measurement had to be carried out in two runs at different heights and the resulting data sets had to be merged after reconstruction. The X-ray tomography differed from the neutron set-up in the scintillator, where a CAWO OG8 screen was used; the X-ray tube voltage used in the *Savary* bassoon experiment was 120 kV and exposure time was 2 s.

4.3.1.2 Results and Conclusions

Comparative results from neutron and X-ray tomographies are summarised in Fig. 4.1.

Figure 4.1 shows the complementarity of the radiation types. Neutrons easily penetrate the metallic parts of the instrument, while X-rays are blocked to a great extent by the metal. Hence, metal parts appear as very dark or black areas in the X-ray projection (i.e. the transmission image). For the hydrogen containing wooden parts of the instrument the opposite is shown. Here, the neutrons are strongly attenuated, while these regions are rather transparent for X-rays. This behaviour reflects in the reconstructed data sets. The wooden structure is clearly visible in the reconstructed X-ray-CT data as long as no metal is in the vicinity. As soon as metal is present its signal overshines that of the wood. In the presented example the X-ray energy was on the other hand not high enough to allow a detailed representation of the metallic mechanisms. By choosing a higher X-ray energy this problem might be overcome. As a drawback the contrast for the surrounding wood would drop even further, making it practically impossible to give a statement on the regions with organic material around the metal. In the reconstructed neutron data, these metal mechanisms are on the other hand clearly visible and even small details can be seen. As long as the wood visible in the reconstructed neutron CT slice is below a certain dimension the result is almost equivalent to the X-ray slice. Only when a certain size is exceeded and hence too few neutrons transmit the object for certain projection angles the result is not satisfying anymore. This can be seen in the slice where the inner surface of the groove on the wing cannot be determined with certainty anymore.

This study proves that in case of composite materials the two techniques (neutrons and X-ray tomography) are complementary. In fact only the combination of both methods provides a full overview of the sample, including its internal features, in a non-destructive and non-invasive manner by illuminating the blind spots of the other method respectively.

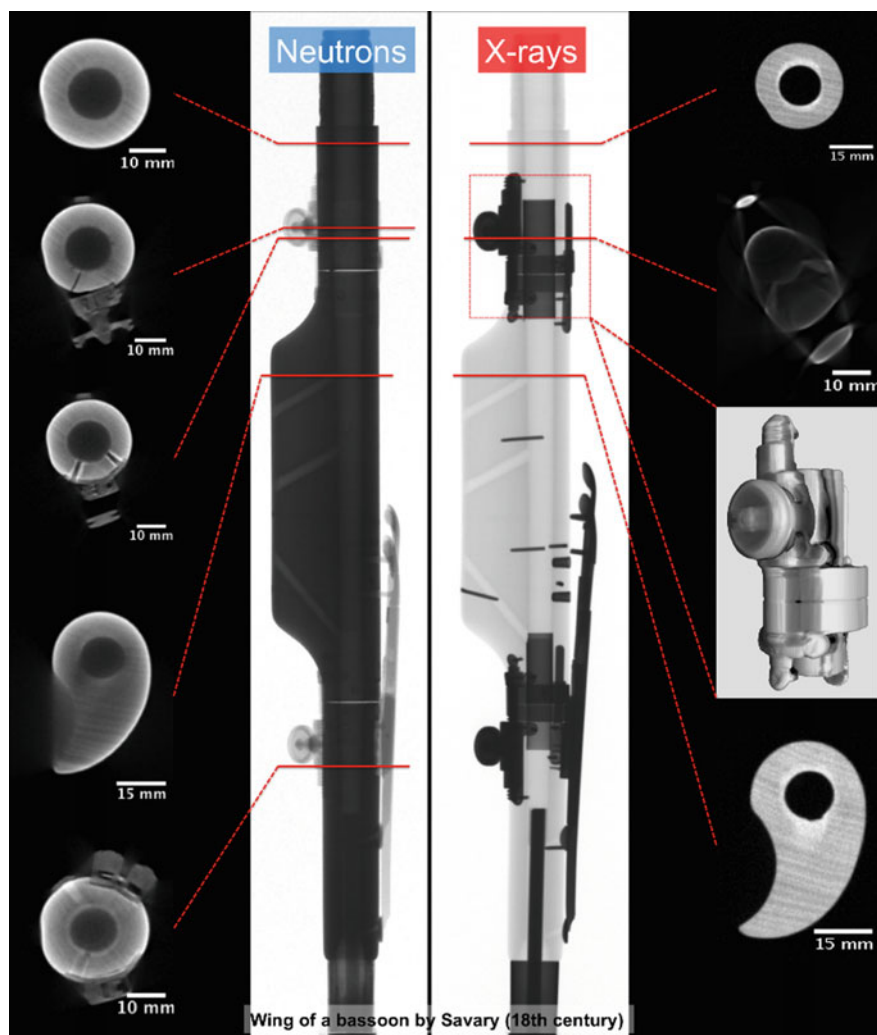


Fig. 4.1 Results of the neutron and X-ray investigation of the *Savary* bassoon; the centre (white background) shows projections with the respective radiation (left neutrons; right X-rays); in the periphery (black background) slices and 3D visualisation of the reconstructed CT-data are shown

4.3.2 Ancient Wind Instruments

4.3.2.1 Description of the Investigated Artefacts

The library of the ‘*Fondo Antico della Biblioteca del Sacro Convento*’ in Assisi—Italy, includes a small collection with of strong historical interest, recently discovered in the *Sacro Convento* (Festa et al. 2014; Sacro Convento Archive).



Fig. 4.2 Musical instruments collection of the *Fondo Antico della Biblioteca del Sacro Convento* ' in Assisi

They are seven wooden wind instruments dated between the second half of XVI century and the end of XVII century. The collection consists of a flute, a bass recorder a *dulciana* and four cornets. Recently discovered documents (Sacro Convento Archive) provided information about the provenance of the instruments and generated new interest about their construction technique and possible use (Fig. 4.2).

The samples are made of composite materials including wood, metals and leather. The four cornets of the collection (XVI century) are made of pear wood and leather attached with some kind of adhesive. The samples suffered alterations such as opening and closure of holes, addition of metal extensions and addition of metal insertions in some areas along the tubes. The bass recorder (XVII century) is made of maple wood in three parts and has a brass clef. It was modified by adding two wooden hand-worked pieces. The central piece (with holes) is made of box tree wood. The flute (XVII century) is made of three box tree wooden pieces with a brass clef. It is not clear if the instrument is complete or if a cap closure is missing. The *dulciana* (probably XVI century) is made of maple wood with brass insertions. An unidentified metal piece was present inside the tube before measurements and eventually removed during restoration.

4.3.2.2 Scientific Question

X-ray and neutron tomography/radiography were applied to the study of the collection with the following aim: to characterize the internal structure of the samples, the position of composite and added materials such as metals, wood fibre displays and deformations. These measurements provided information about construction methods and were used to guide the instruments' restoration processes. The musical

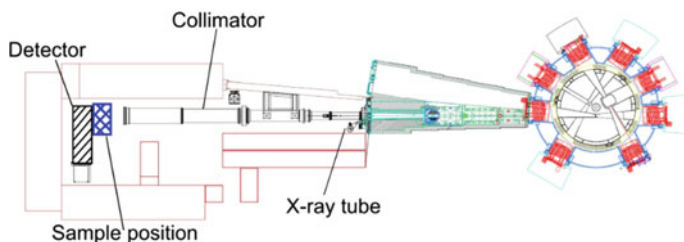


Fig. 4.3 NEUTRA beamline at SINQ, Paul Scherrer Institute, Switzerland

instruments were restored in Basel after neutron and X-ray measurements, and are now preserved in the Treasure Museum of the Assisi Basilica.

4.3.2.3 Measurement Set Up

The imaging measurements were carried out at NEUTRA² beamline, Fig. 4.3, at the spallation neutron source SINQ, Paul Scherrer Institute, Switzerland. For each radiography, acquisition time was of about 40 s for neutrons and 20 s for X-ray and the effective pixel size for both techniques was 100 μm . In both neutron and X-ray set-ups signals were detected by a scintillator-CCD camera system with field of view of 220×260 mm and 2160×2560 pixels. $^6\text{LiF:ZnS}$ scintillators with a thickness of 100 μm were used for neutrons while green-emitting converter foils (CAWOTM OG 8) were used for X-rays.

4.3.2.4 Results

Neutron and X-ray radiographies were performed on each instrument. Images were analysed to determine internal diameters and therefore to study wood deformation due to the time and morphological internal structure. The internal features of the bore-hole in wind instruments play a fundamental role in the identification of the construction methods while internal morphology is extremely useful in guiding the restoration process, attribution and state of conservation. X-ray and neutron radiographies of the musical instruments are shown in Fig. 4.4.

The borehole of wooden wind instruments has a fundamental role in the sound production and can be described, in first approximation, as a cylinder or cone. Small perturbations in the shape of an idealized instrument geometry are caused by

²Neutron instruments are presented and described in part II “Experimental methods”.

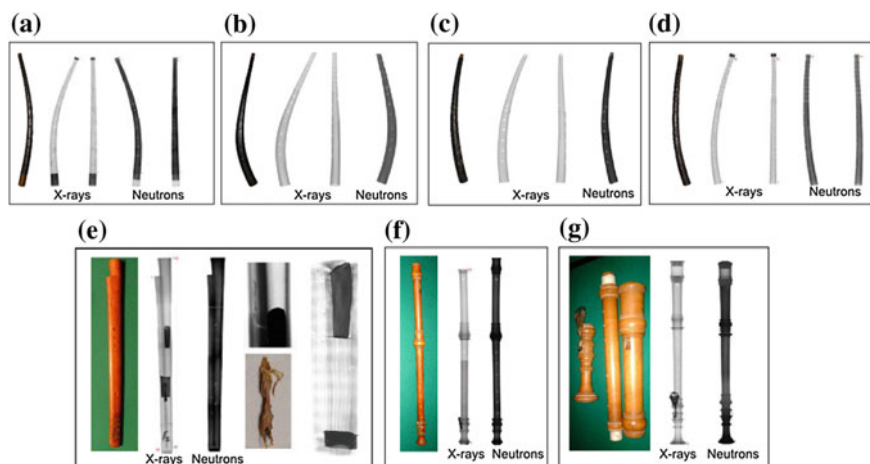


Fig. 4.4 Assisi musical instruments and radiographic images in frontal and lateral views. **a** Cornett, **b** cornett, **c** cornett, **d** cornett, **e** dulciana—a bat was discovered inside the bore hole—and neutron tomography, **f** transverse flute, **g** bass recorder

hand-made interventions. This divergence from the perfect geometry was used to adjust the instrument shape during the construction process; this method was used to properly align or displace instrument resonances and obtain the required sound (Posma and Schillebeeckx 2005).

Radiographies were used to measure diameters along the longitudinal directions for all instruments and evaluate the shape of the borehole and the divergence of the tube from the ideal circular geometry. Measurement points are spaced, for all instruments, by 6 mm and reported in Fig. 4.4. Cornets are made of two wooden halves bounded together with leather and show various degrees of deformations. Some present cavities, evidence of hand-made corrections performed during construction to adjust timbre and intonation of the musical instruments. The *dulciana* radiographies show the borehole of the instrument composed by two tubes in the same wood piece closed in the bottom part by a piece of wood. Two unexpected objects were discovered in the musical instrument: a conical metal artefact and a dried-out bat, subsequently extracted by the restorer.

Radiographies of the bass recorder and flute show boreholes with slight tapering and could therefore be attributed, in agreement to the historical sources, to the baroque period. Renaissance recorders have a nearly cylindrical borehole while instruments of the baroque period have a conically shaped borehole, two or more sections and decorative elements near the head and foot of the instrument (Fletcher and Rossin 2010).

4.3.2.5 Concluding Remarks Related to Investigations of Ancient Wind Instruments

A set of seven musical instruments, property of the ‘*Fondo Antico della Biblioteca del Sacro Convento*’ of Assisi were characterized by non-invasive neutron and X-ray imaging. The integrated X-ray and neutron results obtained on the internal structure of wooden and metal parts provided new conformational evidence about the objects. Internal diameter trends, studied using radiographies, provided information on construction techniques and borehole design, of key relevance for the characterisation of sound quality. The technique also provided useful information to guide the restoration process.

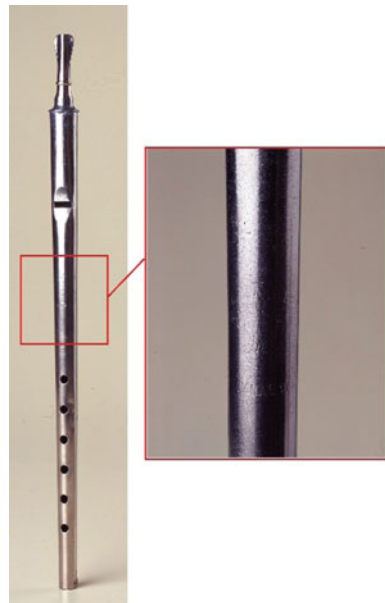
4.3.3 Material Analysis of a Metallic Ancient Flute

4.3.3.1 Description of the Investigated Artifact

The investigated sample is a small metallic duct flute from *Accademia Nazionale di Santa Cecilia* Festa et al. (2013). It is a vertical metal whistle ‘in D’ with a standard conical bore slightly contracting towards the foot and six finger holes on the front (Fig. 4.5)

The instrument body is made of a laminated sheet of metal, curved and soldered on the back, all along the pipe, while the mouthpiece is visibly made with another technique, probably with a mold. Little information is available about Charles

Fig. 4.5 Photograph of the investigated whistle flute preserved at the *Accademia di Santa Cecilia*



Mathieu, the instrument maker. His activity dates back at the end of the Nineteenth century when in Paris he was known for manufacturing mainly flutes, ocarinas and metal flageolet-type instruments. This flute became part of the *Accademia Nazionale di Santa Cecilia* collection before 1979 when it was found within the inventory list and in a picture, but little information about its provenance were given. Charles Mathieu also patented some other instruments, like the *Ocariflute* owned by the Miller Flute Collection at the Library of Congress of Washington (inventory number DCM 1003), which shows a mouthpiece quite similar to the sample. An anonymous vertical whistle (inventory n. DCM 0643), part of the same collection, is similar to the one investigated in the study. Another flute manufactured by Mathieu (inventory n. F.8) and almost identical to the one owned by the *Accademia Nazionale di Santa Cecilia* is present in the *Antonio Spada* private Italian collection.

The instrument seems to have been manufactured as a single piece. Sometime after 1992 the instrument was broken in two pieces, the top and the body, and was subsequently restored for preservation and exhibition purposes.

4.3.3.2 Scientific Case

The metallic whistle was studied by means of integrated and simultaneous neutron-based techniques: neutron diffraction, neutron resonance capture analysis and neutron radiography. The experimental investigation aimed at the characterization of elemental and phase compositions of material, at deriving information on the construction and restoration techniques, and on the role of chemical-physical material properties on the emitted sound. Since the irradiated area was the same during the simultaneous measurements, the irradiation time was kept at a minimum, with a drastic reduction of the decay time after irradiation.

4.3.3.3 Measurement Set Up

Neutron measurements were performed at ISIS spallation neutron source at INES³ facility. The beamline is characterized by a white pulsed neutron beam, moderated by water at about 295 K, placed at a distance $L_0 \approx 22.8$ m from the sample position. The maximum beam area at the sample position was 3.8×3.8 cm². The instrument started as a powder-diffractometer and was subsequently equipped with a camera for neutron radiography and a scintillator detector for Neutron Resonance Capture Analysis measurements. Neutron diffraction and NRCA spectra were collected simultaneously. For the latter YAP detectors have been used. See also Chap. 12.

³Neutron instruments are presented and described in part II “Experimental methods”.

4.3.3.4 Results

Diffraction spectra were analysed to obtain quantitative phase composition. In the top area of the flute the following phases were detected and the weight percentage of the detected phases were reported: Lead (Pb) (90.1 ± 0.3), Lead tetroxide (Pb_3O_4) (5.8 ± 0.3), Tin(II) sulphate (SnSO_4) (2.2 ± 0.1), zincite (ZnO) (1.89 ± 0.02). In the welding area the following phases were detected: lead (Pb) (77.1 ± 0.2), tin(II) sulphate (SnSO_4) (8.9 ± 0.2), Herzenbergite (SnS) (5.1 ± 0.1), zinc (Zn) (5.06 ± 0.03), palladium (Pd) (3.6 ± 0.1), lead tetroxide (Pb_3O_4) (0.3 ± 0.1). Finally in the bottom area the following elements were discovered zinc (Zn) (97.9 ± 0.2), palladium (Pd) (1.2 ± 0.1) and Herzenbergite (SnS) (0.9 ± 0.2). Diffraction patterns are summarised in Fig. 4.6.

Qualitative NRCA results are shown in Fig. 4.7. Spectra were collected for the three areas of the instrument and peaks were labelled and associated to the nucleus that produced the gamma line. The top area showed to be composed by lead (Pb) as major component, Zinc (Zn) as minor component and some trace elements such as Antimony (Sb), Arsenic (As), Bismuth (Bi) and Tin (Sn). The main components detected at the welded area were lead (Pb) zinc (Zn), copper (Cu) and nickel (Ni). Tin (Sn) was a minor component and antimony (Sb), arsenic (As), aismuth (Bi), palladium (Pd) and silver (Ag) were found as traces.

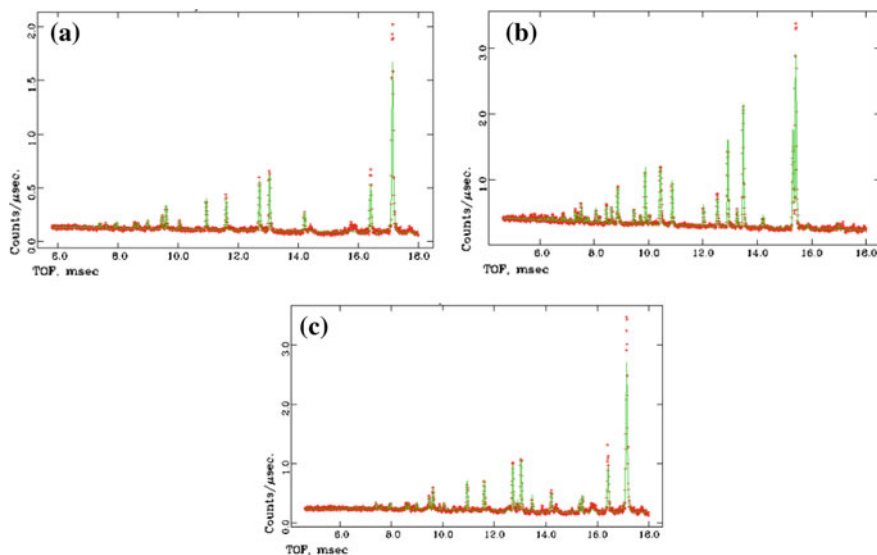


Fig. 4.6 Diffraction spectra of the whistle flute in different areas. **a** Top area, **b** welding area, **c** bottom area. Fits are reported in *green*

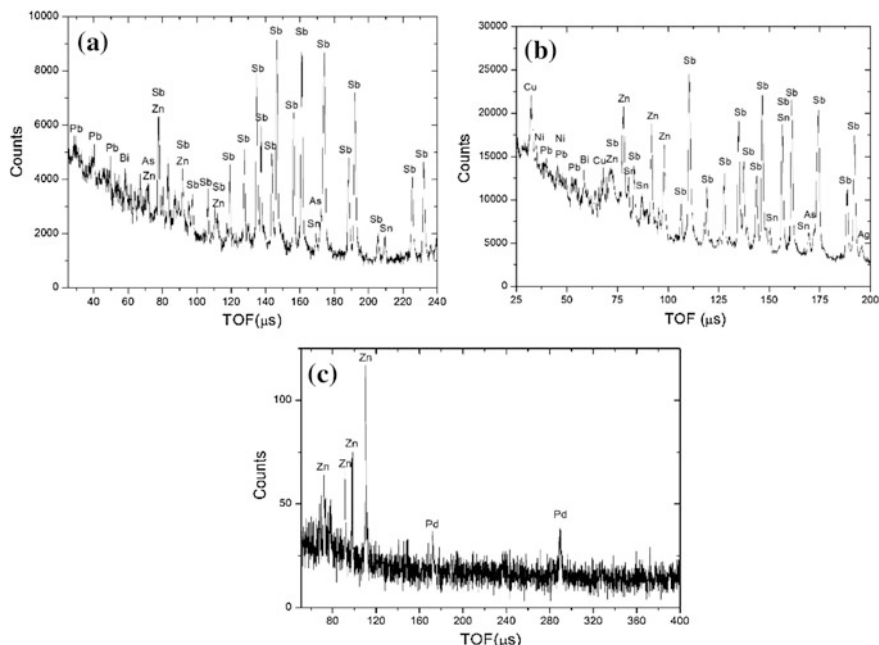


Fig. 4.7 Neutron resonance capture analysis results of the three sections of the whistle flute: **a** top area, **b** welding area, **c** bottom area. Detected peaks are labelled

4.3.3.5 Concluding Remarks Related to the Analysis of a Metallic Ancient Flute

Results provided elemental and phase compositions of the three areas of the musical instrument: the top (or embouchure), the body and the soldering which connects the two parts and is visible to the eye. The top of the whistle showed to be composed by lead with a low percentage of antimony generally used to strengthen the lead. The body was found to be composed by zinc covered with a palladium layer; a corrosion product named Herzenbergine was also discovered. The soldering was recognised as a Pb-Sn alloy. Near the soldering copper, nickel and silver were detected; they were attributed to a fipple plug shown by the radiography. Results from the neutron diffraction and neutron resonance capture analysis techniques provided compatible and complementary quantitative information.

4.4 Method Limitations and Peculiarities

The use of neutron techniques on precious museum objects implies taking extra precautionary measures to prevent possible damage of the samples or hindering their availability for a long period (e.g. because of a long-living residual radiation

activity). To this end, the samples should initially be characterized through preliminary fast test measurements or a preliminary Neutron Activation Analysis measurement in order to obtain an estimation of the elements inside the sample, concentration of trace and major elements (and their isotopes). These preliminary analyses are carried out with the aim of testing samples' activation rate and decay time as a function of their exposure time.

4.5 Conclusions

Neutron techniques have successfully been applied to the field of cultural heritage and in this case to the study of musical instruments. Musical instruments are generally non-homogeneous and composed by different materials such as wood, metals, leather and adhesives. These materials interact differently with neutron and X-ray beams. For this reason neutron analyses are able to complement, in many cases, X-ray investigations. Integrated information is obtained providing a complete overview of the investigated objects.

References

- Calzada E, Schillinger B, Grunauer F (2005) Construction and assembly of the neutron radiography and tomography facility ANTARES at FRM II. *Nucl Instrum Methods A* 542: 38–40
- Chateigner D, Combined analysis: structure-texture-microstructure phase-stresses determination by X-ray and neutron diffraction. <http://www.ensicaen.ismra.fr/~chateign/texture/combined.pdf>
- Festa G, Pietropaolo A, Andreani C, Grazzi F, Barzagli E, Scherillo A, Schooneveld E (2013) Simultaneous and integrated neutron-based techniques for material analysis of a metallic ancient flute. *Measure Sci Technol* 24:095601
- Festa G, Tardino G, Pontecorvo L, Mannes DC, Senesi R, Gorini G, Andreani C (2014) Neutrons and music: imaging investigation of ancient wind musical instruments. *Nucl Instrum Methods B* 336:63–69
- Fletcher NH, Rossing TD (2010) *The physics of musical instruments*. Springer, Heidelberg
- Lehmann EH, Vontobel P, Wiesel L (2001a) Properties of the radiography facility NEUTRA at SINQ and ITS potential for use as European Reference Facility. *Nondestr Test Eval* 16: 191–202
- Lehmann E, Vontobel P, Scherrer P, Niemz P (2001b) Application of neutron radiography as method in the analysis of wood. *Holz Roh-Werkst* 59(6):463–471
- Lehmann E, Hartmann S, Wyer P (2005) Neutron radiography as visualization and quantification method for conservation measures of wood firmness enhancement. *Nucl Instrum Methods A* 542:87–94
- Lehmann E, Mannes D (2012) Wood investigations by means of radiation transmission techniques. *J Cul Her* 13(3):S35–S43
- Mannes D, Non-destructive testing of wood by means of neutron imaging in comparison with similar methods. PhD thesis, ETH Zurich
- Mannes D, Josic L, Lehmann E, Niemz P (2009) Neutron attenuation coefficients for non-invasive quantification of wood properties. *Holzforschung* 63(4):472–478

Postma H, Schillebeeckx P (2005) *J Radioanal Nucl Chem* 265:297

Sacro Convento Archive, Register n. 154, Spese giornaliere del Sacro Convento 1703–07, c.34r

Squires GL (1978) *Introduction to the theory of thermal neutron scattering*. Cambridge University Press

Triolo R, Giambona G, Lo Celso F, Ruffo I, Kardjilov N, Hilger A, Manke I, Paulke A (2010) Combined application of X-ray and neutron imaging techniques to wood materials. *Conserv Sci Cult Herit* 10

Chapter 5

The Glory of Ancient Weapons and Armors: Neutron Imaging and Diffraction Methods in Modern Archaeology

F. Salvemini and F. Grazzi

Abstract Neutron-imaging techniques are emerging as an innovative and attractive investigative approach to characterise ancient artefacts without the need for sampling or invasive procedures. In this chapter, a selection of case studies developed in collaboration with several Research Groups and Museum Institutions will show case the potential of neutron imaging technique to investigate a particular class of Heritage materials: metals. Despite neutron technique can be widely applied to different artefacts, i.e. pottery, sculpture, paintings, we decided to focus on this class since the application of neutron imaging technique have disclosed a unique insight into the investigation of their composition and microstructure. Until recently, this task was mainly fulfilled basing on standard analytical techniques like, for example, metallography. Traditional analysis, however, though very accurate, is not always suitable for rare and unique objects of high scientific and economic value.

5.1 Introduction

Due to their high penetration power in metals, neutrons are well suited for investigation of ancient metal weapons and armors. Imaging methods allow for visualization of the inner volume of the object which helps to reconstruct its 3D structure and gain information about the assembly of different components. Neutrons can be considered as particles but also as propagating wave due to their particle-wave nature. The wavelengths of low-energetic (cold and thermal) neutrons are in the same range as the distances between the atoms and atom planes in the crystal lattice of metals. In this way monochromatic neutrons with a defined wavelength have a

F. Salvemini
Bragg Institute, ANSTO, Lucas High, Sydney, NSW, Australia

F. Grazzi (✉)
Consiglio Nazionale delle Ricerche, Istituto dei Sistemi Complessi,
50019 Sesto Fiorentino, FI, Italy
e-mail: francesco.grazzi@fi.isc.cnr.it

sense to different crystallographic phases of a certain material, e.g. steel, which helps to separate these phases even in 3D and to obtain hints about the manufacturing process at different weapons and armors.

5.2 Used Experimental Methods

5.2.1 *Neutron Imaging (Radiography and Tomography—NR and NT)*

Similarly to traditional X-ray methods, radiography results in a two-dimensional image of the sample studied while tomography provides three-dimensional information.

However, as the interaction with material differs from X-ray to neutron for the same element, neutron imaging can produce complementary data. Whereas X-rays are more suitable to investigate dense materials inside light ones, neutrons are able to detect light elements such as hydrogen, carbon, and nitrogen, embedded into metallic or ceramic objects. Moreover, neutrons, thanks to their high penetration power in dense matter, represent an almost unique method for the non-invasive characterization of the microstructure of massive metal objects.

In particular NT can provide useful information to characterize the structure, morphology and composition of artworks through a three-dimensional reconstruction of the sample under investigation. From these data it is possible to detect hidden features inside objects, to understand ancient manufacturing technology, to evaluate the conservation status and identify past restoration works, to characterize new conservation methods.

Detailed description of the NR and NT techniques is presented in Chap. 16.

5.3 Examples of Neutron Studies of Ancient Weapons and Armors

5.3.1 *Kabuto: Secret Technology Behind Beauty*

5.3.1.1 Description of the Investigated Artefact

Kabuto refers to the helmet of traditional samurai armour. Among the various components of the warrior equipment, it assumes, for obvious reasons, considerable importance. Here, the technological skill of the craftsman might reach the best results in joining lightness and effectiveness to defend the most important organ of the samurai's body: the head. In addition, being the most visible part of the warrior from a distance, the helmet assumed also the role of the distinctive sign of a leader

Fig. 5.1 The picture shows the *suji-bachi* helmet that is a multiple-plate type of hachi (Japanese helmet bowl) with raised ribs on every plate and connection rivets hidden into the internal structure



in battle. Thus, not only effectiveness, but also elegance and visibility became necessary qualities for the samurai's helmet, the kabuto.

The kabuto became an important part of the traditional Japanese armour during the feudal period, and was initially worn only by high-ranking warriors (Sakakibara 1963; Sinclare 2004). Their construction and design evolved through time in ways peculiar to different manufacturing schools and modified under the influence of foreign culture and new fighting techniques (Sinclare 2004).

Among the three main categories kabuto can be classified according to its structure, the most complex typology consists of a large number (varying between 8 and 128) of lamellar plates arranged in a circular fashion around the crown on top of the head (Sinclare 2004).

The kabuto shown in Fig. 5.1 is an example of this type. The helmet is a signed Saotome *bachi* made in the 1st half of the 17th Century by Saotome Ienari. He was the third craftsman of the Saotome dynasty, so the helmet is one of the oldest surviving of this type. The sample is made of 64 lamellar plates, finished with a visor decorated with two facing gold dragons. It is a typical *sujikabuto*, or “flange helmet bowl”, presenting ribs at the edge of each plate. The various components are joined by rivets invisible because the surface is lacquered on the inside and patinated on the outside. This helmet was kindly provided by a British private collector and was formerly part of the H. Russel Robinson Collection.

5.3.1.2 Scientific Question

These objects are quite rare and, when found in museums, are usually in an excellent state of conservation, being considered masterpieces representative of Japanese culture. For this reason, any detailed study of these artefacts must rely on non-invasive techniques and it was decided that NT should be employed. This

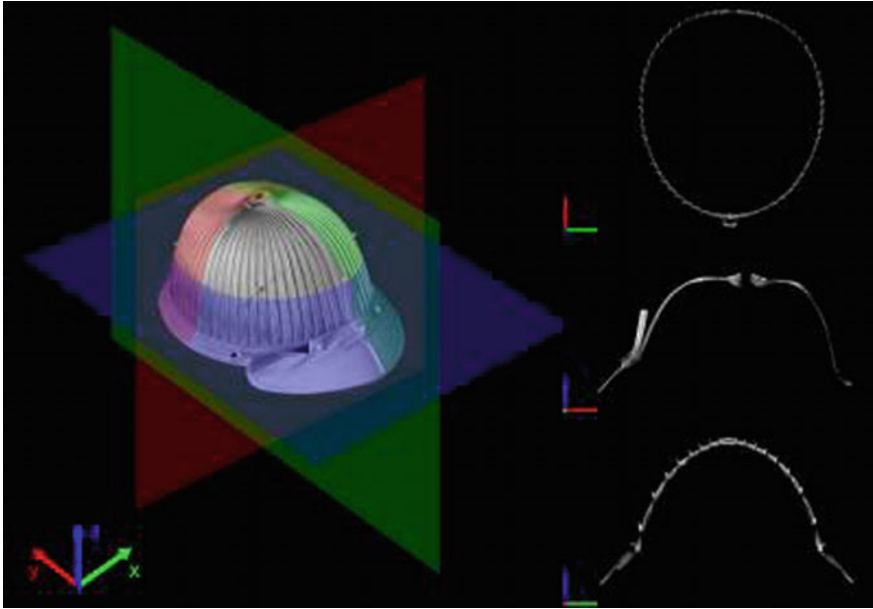


Fig. 5.2 On the left, perpendicular sections trough the helmet (*blue, green, and red* planes) and their orientation (*x, y, and z* axis) within the virtual 3D space. From *top to bottom* on the *right side*, axial, transversal, and normal views clearly show how the tomographic images were used to gain information on the kabuto inner structure. In the 3D reconstructed image, the *red square* marks the position of a hidden rivet. On the *right*, from *top to bottom*, the *red arrows* point its precise location in the axial, transversal and normal orthogonal views, respectively

investigation was conducted on NEUTRA¹ beamline at PSI (CH) (Lehmann et al. 2011).

5.3.1.3 Results

The tomographic reconstruction of the kabuto allowed us to acquire a wealth of information about the inner structure and assembly methods of this masterpiece, so that actual arrangement of the lamellar components in the kabuto was made visible (Fig. 5.2). The construction starts from the central plate, in the back of the helmet. The “S” shaped vertical plates overlap one another, leaving an empty space in the centre of the superimposed area. This arrangement was invented to absorb the energy of a blow and was probably evolved from a simpler structure and never reported in literature. The novelty is in the diagonal orientation of the rivets layout.

¹Neutron instruments are presented and described in part II “Experimental methods”.

This type of arrangement allows the helmet to be more resistant to blows. In fact, if the helmet is struck, every plate involved tends to transfer the impact to the next ones. This permits the differently curved parts to contribute to the absorption of the impact energy. Moreover, the external ribs located in the side end of the plates are facing towards the back of the helmet. Thanks to this arrangement, most of the impact energy is transferred to these ribs in case of a frontal or diagonal hit. The diagonal orientation of the rivets helps in keeping the structure stable under the blows offsetting their tendency to deform. It is amazing how a simple modification in the alignment of the boshi improves all the intrinsic advantages of the curved structure by adding stability and hence strength to the entire structure.

Moreover, all components contribute in holding together and stabilizing the two-layers structure. The rivets are arranged in six concentric rings running at different heights all around the helmet circumference joining adjacent plates that radiate vertically from a central opening at the top of the bowl. We also observed that the central plate located in the back of the kabuto is composed by a single metal sheet whose edges are completely covered by the two adjacent sectors. On the contrary, the frontal area was manufactured by superimposing a properly curved narrow metal sheet over a large 3-folded one that completes the round shape of the helmet, thus fixing and securing both sides of the hachi (helmet bowl) structure (Salvemini 2004).

5.3.2 *Katana: The Tradition of Japanese Masters*

5.3.2.1 Description of the Investigated Artefacts

It is since ancient times that Japanese swords are famous among all the others all over the world as the most effective in terms of hardness, resilience and, last but not least, aesthetic (Yumoto 1958; Kapp et al. 1998).

Their forging technique was almost unique; steel lumps, obtained from the furnace, were strongly pre-treated to obtain a homogenous and purified multilayered sheet. Distinctive carbon steels, characterized by different hardness, were shaped and specifically used for different parts of the blade components to optimize their mechanical feature (Yumoto 1958).

Since ancient time (Koto age, 10th–17th century) five different traditions developed distinctive construction techniques that evolved during the following historical periods (Nagayama 1997).

However, the actual techniques that were used by the early sword-smiths were never documented and the necessary information was orally transmitted from the master to his most skilled pupils. In spite of the large amount of studies, published on the subject, different manufacturing techniques are still not fully understood.

According to history, the different styles of Japanese sword-making are divided into four periods (Sato 1997; Nagayama 1997). Starting from the oldest one (Koto period; A.D. 987–1596), five traditions (Gokaden) evolved their own manufacturing

techniques; the smelting and smithing procedures, the forging, and the final treatments, were different and specific of the particular schools that each tradition started, in the frame of every peculiar tradition, in a specific province and then diffused in the rest of the country. These provinces were either related to centres of political power or simply were located in geographic areas rich in iron ore.

5.3.2.2 Scientific Question

Until recently, only expendable samples were investigated basing on standard analytical techniques which manly require sampling or are based on surface analysis. Nowadays, neutron diffraction (Grazzi et al. 2011a, b, c) and neutron imaging methods (Squires 1996; Sears 1992; Lehmann and Hartmann 2010; Josic et al. 2010) have been demonstrated to be the most suitable tools to qualitatively and quantitatively characterize composition and micro-structural properties of metal artifacts in a non-destructive way, mandatory for well conserved museum exhibits (Piaskowski and Hist 1993; Nagayama 1997).

5.3.2.3 Results

NT was performed on five fragments of ancient swords (Fig. 5.3), broken approximately at 10–20 cm from the tang and already analysed through time of flight neutron diffraction (Grazzi et al. 2011a, b, c). All swords are assigned to a specific tradition: four of them are attributed to the Koto Age forging traditions, and one is a more recent blade attributed to the Shinto period (A.D. 1596–1781). The attributions were made through the analysis of the signatures (certain attribution)

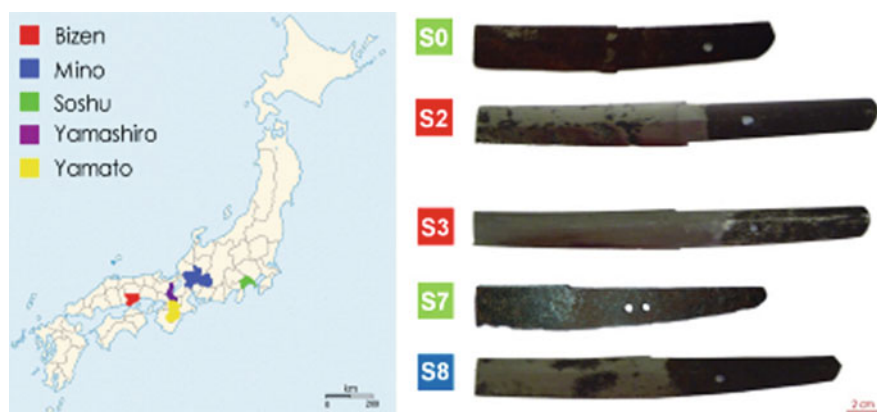
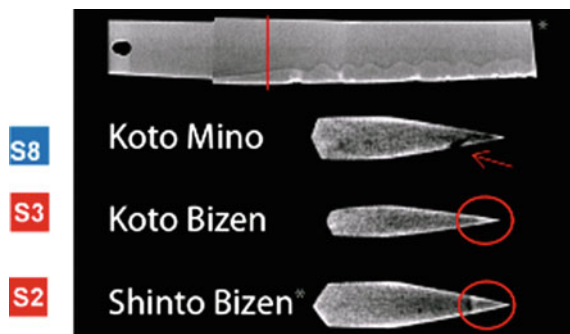


Fig. 5.3 Map of Japan (Honshu is the main island) showing the location of the provinces where the five Koto age sword-making traditions were originated (*left*) and a picture of the five blade fragments (*right*)

Fig. 5.4 Selected cross sections from the NT are reported for 3 samples: a crack is clearly visible along S8 (red arrow), while the martensitic structure is visible at the cutting edge of the swords S3 and S2 (red circles). The approximate location of the cross section is indicated by the red line in the upper 3D rendering model



and, in absence of signature, through the stylistic analysis by our museum experts (hypothetical attribution).

The overall study was carried on ICON² beamline at PSI (CH) (Kaestner et al. 2011) and full results were published at Salvemini et al. (2012); here a selection of the most important data is reported.

In particular, NT is able to provide morphological inner features, such as amount, distribution and shape of defects, porosity and slag inclusions, that are related to the manufacturing process (i.e. quenched microstructure along the edge, defects, slag inclusions, internal cracks). In addition, important information on the conservation status can be obtained from the determination of the mineralization phases and the corrosion products that can be easily mapped due to the high neutron attenuation cross-section for H-base compounds (Fig. 5.4).

Sample S2 is characterized by a homogeneous inner structure of the blade cross section. No trace of cracks or slags has been evidenced by the tomographic technique. Instead, we were able to detect a clear space pattern at the cutting edge where the crystalline structure of the steel changes from hard martensite to pearlite, giving rise to the hamon, clearly delimited in the Fig. 5.5a. The tomographic method also allowed mapping several rust spots that extend well below the sample surface (Fig. 5.5b).

Standard neutron tomographic technique can be further improved, to achieve materials discrimination, by a proper selection of the neutron energy. In fact, monochromatic neutron beams give the possibility of modifying the image contrast for different phases taking advantage of the abrupt change of the attenuation coefficients in the proximity of the so-called Bragg cut-off (Josic et al. 2010). This method is able to provide a map of the phase distribution phases. This information can be related to the use of different types of steel and can help to define the forging procedure of the samples.

²Neutron instruments are presented and described in part II “Experimental methods”.

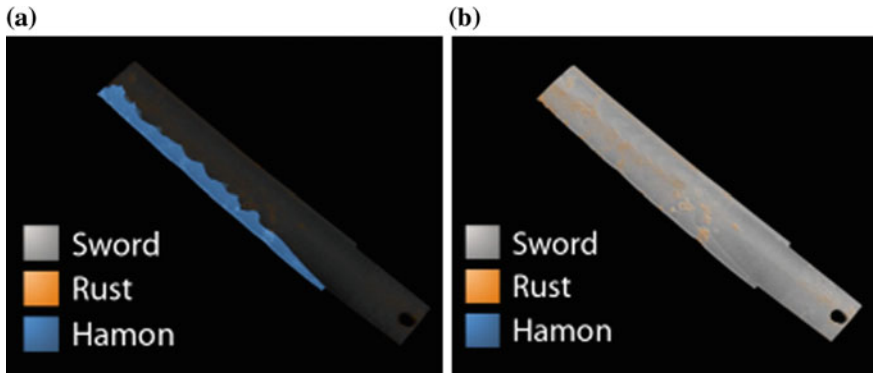
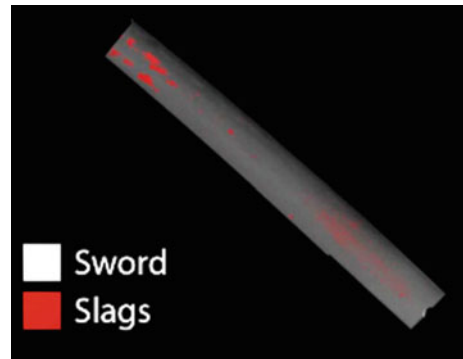


Fig. 5.5 **a** The 3D segmentation of blade S2 shows the progress of the martensitic microstructure, here reported in blue colour, outlining the hamon pattern along the cutting edge. **b** The 3D surface projection evidences the presence of rust spots (*orange* colours) diffusing below the surface of the fragment S2

Fig. 5.6 The white beam NT of the sample S3 has allowed mapping the distribution of the slag inclusions along the blade, here mapped indicated in *red*



Referring to Fig. 5.7, we observe that the inner volume of the fragment is characterized by different distributions of dark areas (cementite) and light areas (ferrite). Thus, the present method allows us identifying the typical structure of a Japanese sword, which is known to be composed of two distinct sections of different types of steel (Kapp et al. 1987). According to Kapp et al. (1987), Japanese medium- and full-size swords are composite structures made of a kawagane and shingane components. Kawagane (jacket steel) is the component forming the outer surface of the blade, including the sharp edge and the hamon. Shingane (core steel) is a slightly softer, low-carbon steel, which is embedded or wrapped into the high-carbon jacket steel along the entire length of the sword. Being more ductile than kawagane, it helps protecting the blade from cracking and breaking under stress. Still according to Kapp et al. (1987), Japanese smiths assemble the different pieces into a block, weld it together, and then draw out the steel bar into a sword. More complex structures might use four or more different pieces of steel for the

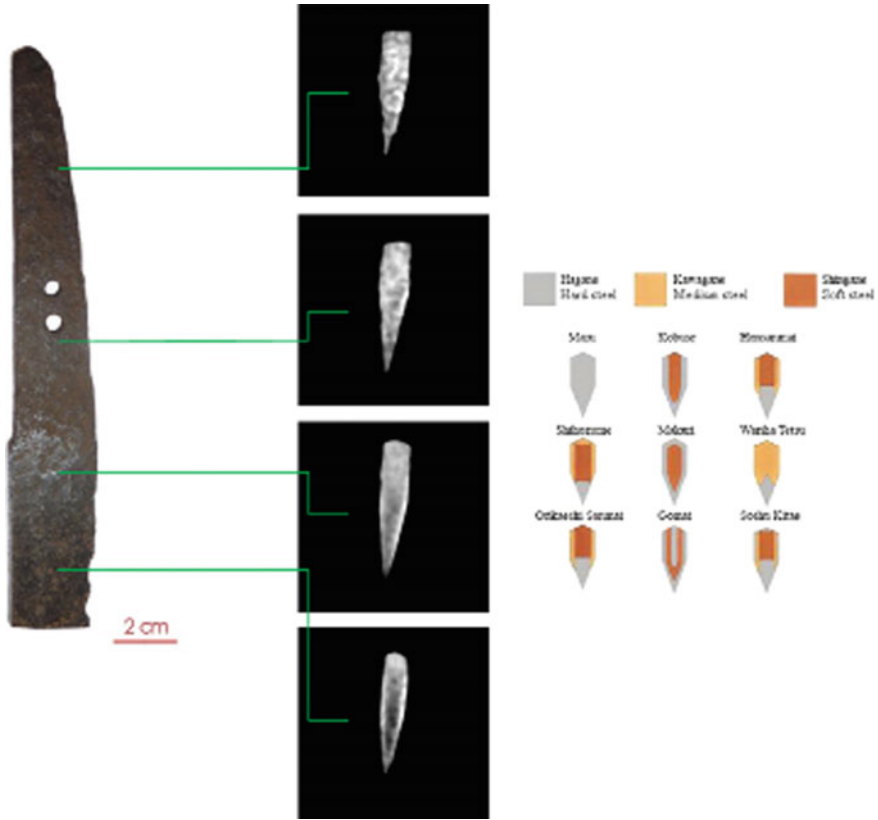


Fig. 5.7 Reconstructed slices at different height along the sword S7. Energy resolved tomography have been able to evidence light areas of ferrite and dark areas of cementite. On the *right*, we report some different sword configurations, using steels with different carbon contents, typical of Japanese swords (Kapp et al. 1987)

core, the edge, the side, and the back of the blade. This great variety of forging methods reflects the way the various schools developed, in isolation from each other, over the country. However, we should point out here that this interpretation of the inner structure is not unique and other determinations have been proposed following a metallographic analysis (Tawara 1953; Hoshi and Sasaki 2005; Notis 2000).

The tomographic slices, reported in Fig. 5.7, suggest that the S7 blade has been probably manufactured by assembling a “jacket” (side and back) of low-carbon steel (shingane) around a very hard steel (the so-called hagane) composing the “core” and the “edge” of the sword. Thus, the present structure appears to be inconsistent with the one suggested in Ref. 21. Nonetheless, it is still possible to identify the present configuration among the various possibilities given by Kapp et al. (1987) (cf. right picture in Fig. 5.7) and, consequently, the sword should be

assigned to one among the OrikaeshiSanmai, SoshuKitae, WarihaTetsu or Honsanmai configurations (Kapp et al. 1987).

5.3.3 *Koshirae: Decorative Motifs of a Social Status*

5.3.3.1 Description of the Investigated Artefacts

Japanese sword mountings are the various housings and associated fittings that hold the blade of a Japanese sword when it is being worn or stored. In particular koshirae refers to the ornate mountings of a Japanese sword.

The sword-fittings that are most admired today were considered to be adequate if practical function, and also aesthetic criteria, were fulfilled. These features were applied to their design or manufacture, thus leading to the evolution of more elaborate decorative techniques and the emergence of specialist sword-fitting makers (Sato 1997).

The commonest basic material for sword-mounts, especially among the earlier examples, is iron, usually of fine quality. The other metals employed, commonly known as soft metals, include silver, bronze, brass, copper, and the three special copper alloys which are peculiar of Japan (Sugimori 2004).

Several decorative methods were employed: surface pattern and finishing, piercing and openwork, relief-modelling and etching, inlay, overlay, and incrustation, engraving and chasing, to mention a few. Finally, the artefact was treated with special etching baths, whose result is to produce a rich palette of pigmentation for the different alloys. Although these colours are only skin-deep, they are practically permanent, as long as they are not subjected to scratching or rubbing with abrasives, which will rapidly destroy them and reveal the raw metal beneath.

5.3.3.2 Scientific Question

For the present study a set of two hand-guards of Japanese sword (tsuba) were investigated by means of NT on CONRAD2³ Beamline at HZB (DE) (Kardjilov et al. 2011). The study aimed to understand the manufacturing process used in the making of the artefacts.

5.3.3.3 Results

The first tsuba (Fig. 5.8a) is a slightly elliptical iron tsuba with a rounded rim. The tsuba is carved with a tendril design (sukashi technique), including facing dragons,

³Neutron instruments are presented and described in part II “Experimental methods”.

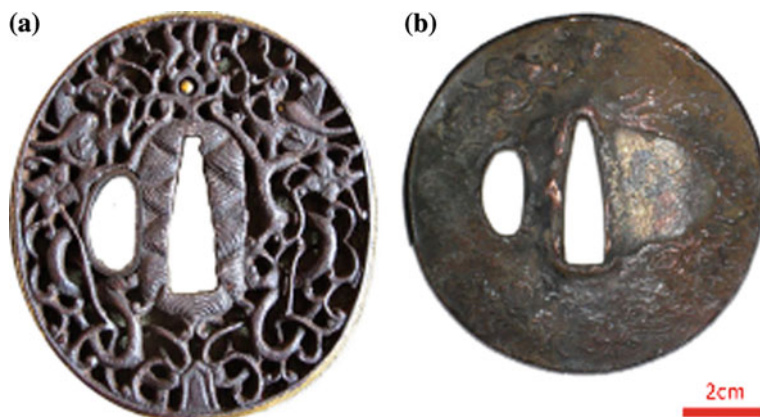


Fig. 5.8 a The iron tsuba, b the copper tsuba

a jewel, and stylized flowers. The rim is rounded and gilded and there are traces of gilding in other areas. It is not signed but can be dated to the first half of XVIII century, probably from Nagasaki (Hizen) area, in namban style. The Japanese word namban, translated as “southern barbarian”, was used by Japanese not only to indicate any foreigner who entered their country, but also to define a large number of artworks in which the decorations reflected a foreign influence in their appearance. The diameter of 8 cm leads us to presume that this hand-guard was created for a long sword (katana). It was equipped with a nakagohitsu, the central hole for fitting the tang of the blade, and a kozukahitsu, the left side hole for accommodating the handle of a small knife called kozuka.

The second Japanese hand-guard was made of copper and copper alloys (Fig. 5.8b) and is of sanmai type: this is composed by three layers with the central one made of a different alloy with respect to the others. The upper and lower layers are decorated through hammering. Decoration was typically made acting on the back of the layer and then fastening it to the central layer with adhesive or lacquer. A fukurin, i.e. soft metal, type rim was hammered around to hold the three layers together. The rim profile is rounded and not decorated. The decoration theme is made of waves and imaginary animals (dragons). The piece can be dated either to the end of Momoyama period or to the beginning of Edo period. It was probably made in the Kyoto area around the beginning of XVII century. A relief decoration is visible on the surface even though it is in poor conditions of conservation. Detachments are recognizable at the edge and on the decorated surface. As in the previous sample, there is a nakagohitsu and a kozukahitsu.

The analysis revealed a homogeneous body for the iron tsuba, probably filed starting from a single piece of iron (Fig. 5.9). As a matter of fact, starting from the Muromachi period, the sukashi technique evolved over time. The iron plate prepared as the ground metal was very uniformly forged and relatively soft in order to cut out the fine designs successfully but hard enough to avoid breakage during use.

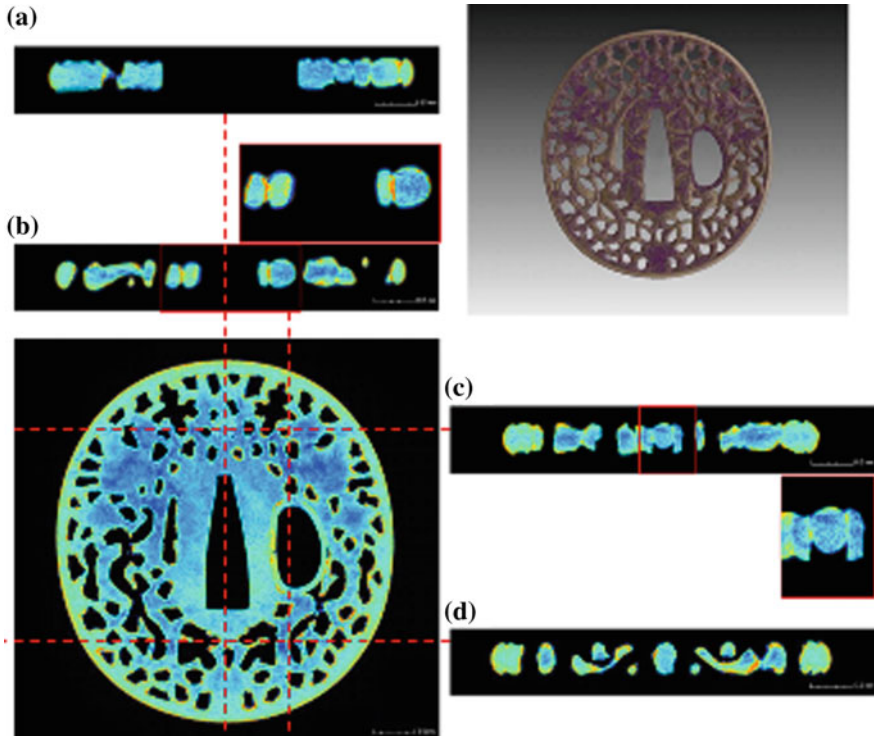


Fig. 5.9 On the *bottom left side* of the figure, a virtual cross section of the iron tsuba is reported in false colours (brighter areas relate to higher attenuation cross sections). The *red dotted lines* define the position of the orthogonal views shown alongside (**a**, **b**, **c** and **d**). The *red squares* map the area of interest inside the views and their respective enlargements. In the cross section **a**, the evidence of soldering are visible in *red-orange* tone at the edge of the ring. While images **c** and **d** allow observing the absence of such soldering and the *brighter spots* can be related to the patination or alteration of the surface. The view **d** gives an idea of the complicate arabesque-structure made by piercing a single metal disc. The *top right image* refers to a 3D rendering of the sample

Any void or significant irregularity in the iron body would have made the shaping of continuous decorative lines impossible. Extra effort in the preparation of the plate would have been necessary, as observed in inner volume of the samples which was free from any cracks, pores and inclusions (Sato 1997). Evidences of forge-welding were not identified in the design motifs involving plants and animals figures, apart from the gilded ring outlining the profile of the kozukahitsu. While the inner brighter areas are reconstruction artefacts, the ones detected on the surface were probably due to the application of a patina or to the early formation of products of alteration (Sugimori 2004).

Virtual cross sections taken at different heights of the copper tsuba revealed three layers of copper and copper alloys (Fig. 5.10). According to ancient metal working technique described in literature (Robinson 1970), the external sheets of metal were

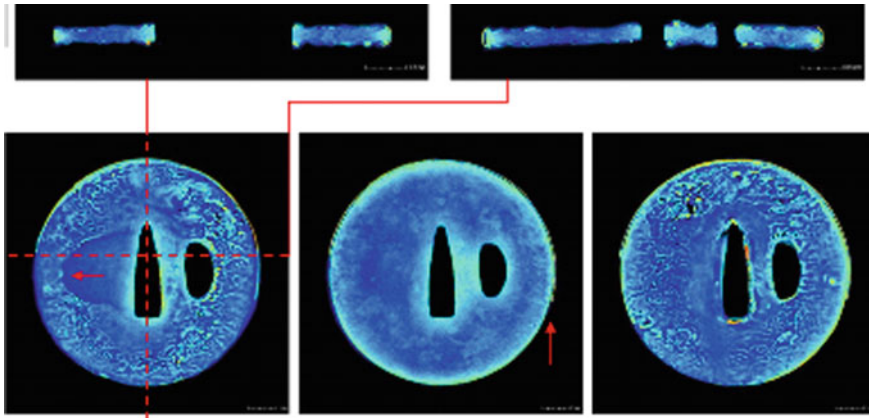


Fig. 5.10 The three *bottom* images refer to cross sections taken at different depths of the copper tsuba, starting from one side of the metal disk and progressively emerging on the other one. The layers closer to the surface (the first and the third radial cross sections) feature the decorative pattern and the lacking area (frontal cross sections), enhanced by the false colour visualization. Moreover, the remaining of a ring around the border of the tsuba is visible (*red arrow*, second image) The *red dotted lines* map the position for the orthogonal views, reported above, where the decorated layers joined to the bulk sheet and the enclosing ring can be observed

probably applied on the two sides of the inner core by heating and slightly hammering, while their rather soft surface was worked with a punch to give texture. All around the rim of the tsuba and the pierced hole, the composite structure was finally tightened by applying a thin ring appearing detached and lost in some areas (Salvemini et al. 2015).

5.3.4 The European Swords

5.3.4.1 Description of the Investigated Artefacts

The study of historical technologies allows revealing methodological process that leads to the conception, development, and evolution of a specific artefact, trying to establish the relationship existing among people that implemented it, as well as the socio-economical context that characterized the circumstances of its production.

By the year 1300, after nearly four thousand years of continuous development, the sword in Europe reached its apogee as an instrument of war. The evolution of the sword and the dagger throughout the Renaissance period presents a fascinating and complex picture. Long-cherished forms were retained side by side with forms

which changed from year to year, making exact chronologies sometimes difficult to establish.

In response to change in body armour, new military tactics or simply the dictates of fashion, many sword types flourished from the mid 15th century when the sword, and in particular the light and fast rapier, became an accepted part of soldier civilian dress and battlefield equipment.

The 17th century was a most important one in the evolution of the sword in Europe; from the 1600s the fashion for rapier and dagger play in fencing had considerably less popularity. A small version rapidly became the most commonly worn sword in Europe and in some countries continued its career until its decline during the 19th century (Coe et al. 2012).

Coeval documentation regarding the manufacturing and commerce of sword blades includes references revealing how blades were valued depending on their place of manufacture, with Toledo blades scoring on top, and the other ones priced down to three times less. The “old” Toledo masters (16th and 17th Century) made their best sword blades by means of forge-welding two strips of steel sandwiching a third strip of wrought iron, that formed the core. The composite block was forged and shaped into a blade. Finally the blade was heated and quenched only in the upper 80 % of its length, while the remaining 20 % was simply tempered. The purposefully composite assembly and the obtained microstructure found their explanation into the need of containing the cost related to the purchase of steel, the typology of rapier blades, the kind of fighting techniques adopted at that time, the need of avoiding fragile fractures, and the easy fitting of the mounting (Gener 2009).

5.3.4.2 Scientific Question

The present study was undertaken with the aim to determine differences in actual manufacturing technology among different European sword blades. To this aim, two rapier blade fragments from the 17th and 18th century have been investigated (Fig. 5.11).

5.3.4.3 Results

The first blade (labelled HE-4) is marked as being made in Solingen (actual Germany), while the second one (labelled HE-5), though subject to some debate, is marked as being made in Toledo (Fig. 5.11). We should point out that reasonable doubts could be raised about the second one’s origin and that this blade too is probably from Solingen.

The samples were not considered precious; therefore complete and half cross-sections were cut in different points of the longitudinal direction. Consequently, it was also possible to investigate the variations in construction and microstructure along the blade samples through standard metallography. The same

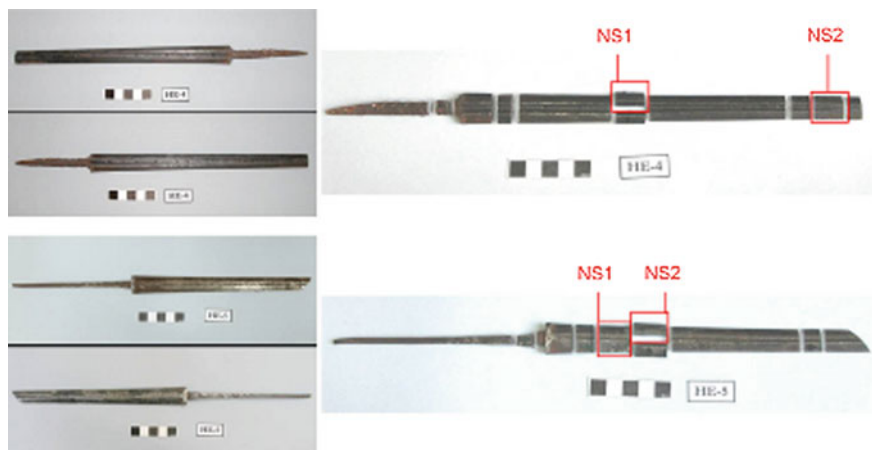


Fig. 5.11 On the *left*, the integer sword blades are shown on their both sides. On the *right* image, the *red frames* map the original position of the analyzed cross section

samples were analysed by means of neutron imaging to observe and to explore advantages and limits of the techniques, through validation based on previous metallographic investigation (Gener 2009).

The neutron imaging study was performed at the ICON⁴ beamline at the Paul Scherrer Institut (Giller et al. 2008).

Preliminarily, conventional NT was carried out to provide 3D information about the structure inside the sample. Then, in order to obtain information about the composition and material distribution, an energy-selective neutron imaging analysis was carried out too.

Conventional Tomography

In the fragment NS1 of Solingen blade HE4, the reconstructed volume of the two cross sections, evidences a very homogeneous body (Fig. 5.12, left side). As a matter of fact, the metallographic study of fragment HE4-3, the twin half of sample NS1 and longitudinally cut along the central channel, confirmed a very homogeneous microstructure. The inclusions appear elongated in the direction of the longitudinal axis of the blade, showing the direction in which the original metallic block was forged, and they are distributed in layers, which can be due either to the construction of the core using various fragments of steel welded together or to the consolidation processes that were part of the production of steel (Fig. 5.12a).

⁴Neutron instruments are presented and described in part II “Experimental methods”.

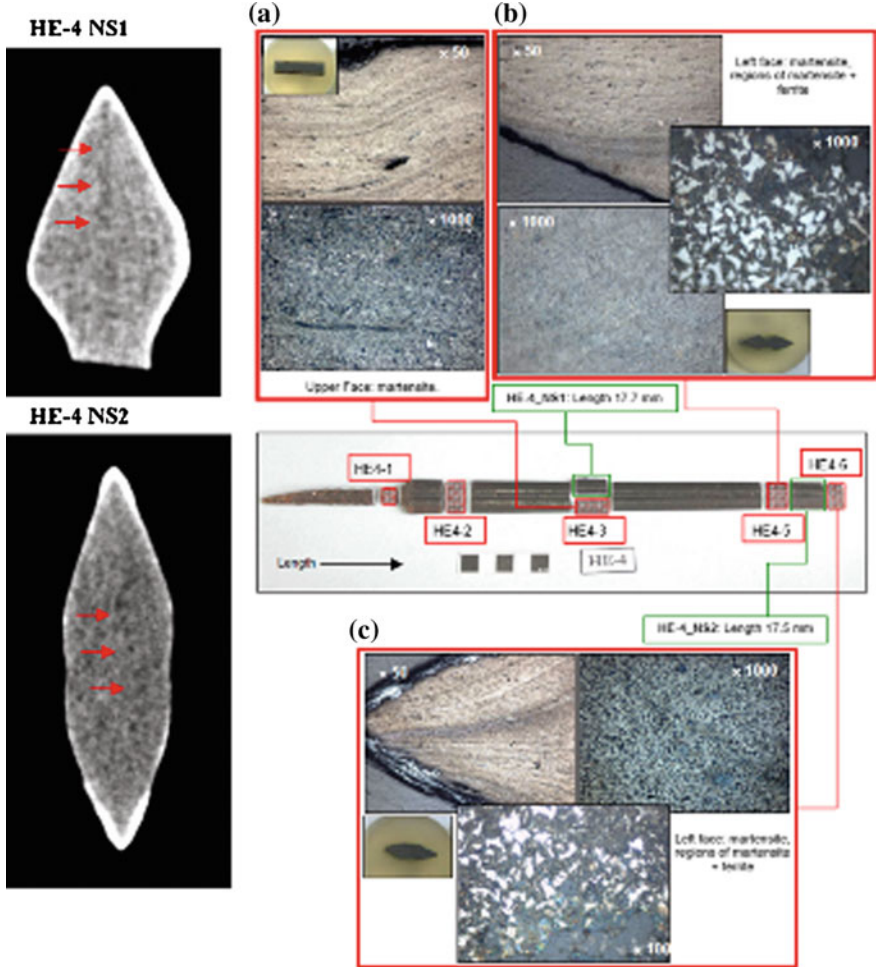


Fig. 5.12 On the *left* side, selected slices from the reconstructed volume of the HE-4 fragments are shown. In sample NS1, the *red arrows* point out the mark of a welding, while in sample NS2 the distribution of slag inclusions. On the *right* side, the central image maps the original location of the cut fragments; the cross sections analyzed by means of metallography are framed in *red*, and the samples analyzed through neutron imaging are reported in *green squares*. The metallographies are shown. The windows correspond to overviews of the samples **a** HE4-3 Detail of the area around a mark (**a** letter, hot-punched inside the central groove—or “fuller”—of the blade), showing the layered structure of the slag and how it conforms to the deformation of the mark ($\times 50$) with detail of the microstructure ($\times 1000$) **b** HE4-4 Detail of the edge, showing the weld ($\times 50$) with detail of the microstructure ($\times 1000$) **c** HE4-5 Detail of the edge, showing the weld ($\times 50$) with detail of the microstructure ($\times 1000$)

Moreover, along the two cutting edges, the presence of martensitic microstructure was revealed by the detection of a bright superficial area in neutron tomographies and confirmed by standard analysis where tempered martensite was observed (Fig. 5.12).

In the cross sections taken before and after the fragment NS2, the metallographic results were again coherent with neutron tomographic investigation (Fig. 5.12, left side). At this point we concluded that the blade is also composed of a single type of material, a heat-treated steel associated to tempered martensite microstructure (Fig. 5.12b, c).

The fragment NS1, pertaining to the sword blade HE-5, featured a composite construction instead, already visible in the white beam neutron tomographic reconstruction (Fig. 5.13, left side). These evidences have been confirmed by the metallographic investigation (Gener 2009).

The metallographied sample HE5-2, cut closer to the tang, respect to the fragment NS1, features the same construction. At this point, though, the external layer has been ground off at the edges of the blade, to the point of exposing the internal core in one of them. In this sample, the external strips feature ferrite, and the internal core shows a pearlite and ferrite microstructure corresponding to an approximate proportion of carbon around 0.5 %, with the pearlite also partially spheroidised (Fig. 5.13a) (Gener 2009).

Sample NS2 is also from a longitudinal cut done along the central channel. At the end of the sample closer to the tang, two wedges of iron are visible, marking the end of the iron wrapping, which only reaches this point. It can be observed and confirmed by the metallographic analysis conducted on the twin cross section HE5-3 (Fig. 5.13b).

Energy-Selective Imaging

In the second part of the experiment, energy selective neutron imaging analyses were performed.

Owing to the symmetry of the sample and the homogeneity in their inner structure, only radiographies were acquired (Fig. 5.14).

The radiography of the HE 4 cross sections confirmed the presence of a homogeneous body. In particular, sample NS2 (Fig. 5.14) evidenced a core that was probably made joining various bits of metal in order to have a piece of suitable steel big enough for the task (Gener 2009).

The presence of a dark region, outlining both fragments of the HE-4 sword blade can be related to the presence of martensitic structure, well detected and most extended with respect to the HE-5 samples. It is not to be excluded that this effect can also be relate the presence of corrosion products on the surface of the sample and slightly diffusing inside the body.

In the fragment HE5, a variation in contrast has been recognized, as evidenced in sample NS1 of Fig. 5.14. Crossing the 110 ferrite Bragg-edge (i.e. changing wavelength), the inversion of grey tones is visible and the obtained contrast

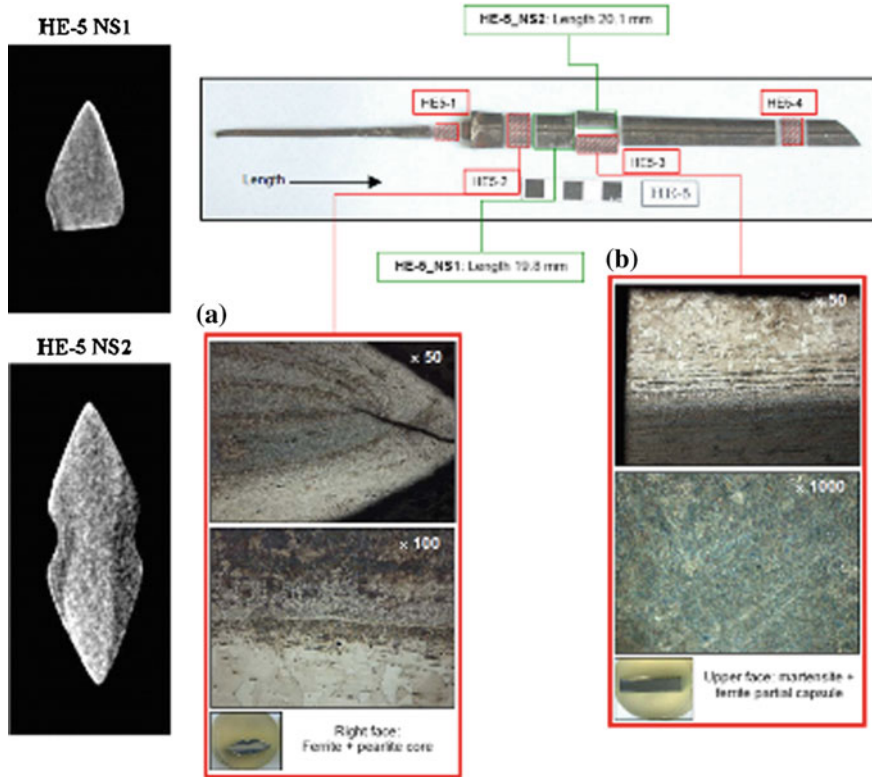


Fig. 5.13 The inner composite volume of the HE-5 fragments is visible from the tomographic slices. The stretching of the dynamic range allows to enhance the contrast and to discriminate between iron (*dark*) and steel (*light*). On the *right* side, the original location of the cut fragments is documented by the *upper* image; the cross sections analyzed by means of metallography are *framed in red*, and the samples analyzed through neutron imaging are reported in *green squares*. The respective metallographies are shown in the *bottom*. The windows correspond to overviews of the samples **a** HE-5-2 Detail of the edge area, showing the crack developed there ($\times 50$) with core microstructure, partially spheroidised pearlite ($\times 100$) **b** HE-5-3 Construction detail, showing the weld area between the iron external strip and the core ($\times 50$) and microstructure of the steel core, tempered martensite ($\times 1000$)

enhancement allowed discerning between iron and steel. On the contrary, fragment HE-5 NS2 did not evidence any variation in composition of the used steel.

Gray gradient in the image can be attributed to the shift in the incoming neutron wavelength distribution over the acquisition window. Due to the small field of view, the limited side of the analyzed sample and the required neutron energy resolution, the wavelength shift can be ignored (Peetermans et al. 2013).

Small blurring in the contour (i.e. sample HE-5 NS2) are caused by misalignment in the positioning of the sample respect to the neutron beam axis.

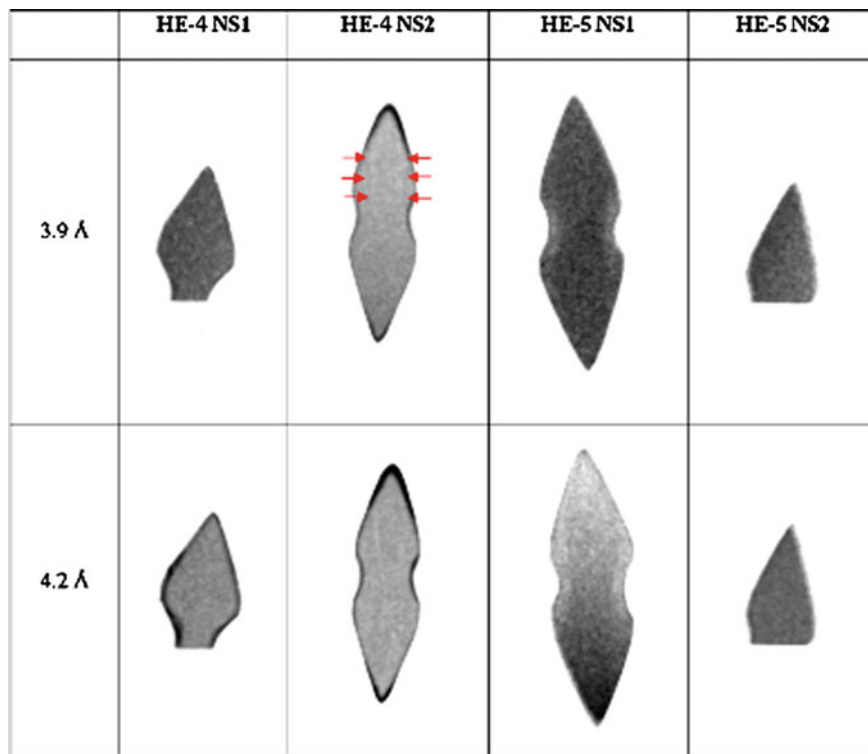


Fig. 5.14 Monochromatic neutron radiographies taken at 3.9 and 4.2 Å are reported for each fragment that was labelled at the *top* of each image. In the case of sample HE-4 NS2, the *red arrows* indicate the weld of pieces of metal

However, the result obtained from the energy-selective imaging study, gave coherent data with respect to the metallographic analysis. We want to stress that the composite structure of European Renaissance blade, described in historical documents and detected through standard destructive analysis, was recognized using a non-destructive method. Thanks to the energy-selective radiography, the volume of samples was qualitatively and quantitatively characterized, allowing detecting the forge-welding strips of wrought iron sandwiching a third strip of steel that formed the core (Salvemini 2014).

5.4 Conclusion

The case studies presented in this chapter clearly demonstrated the potential of neutron imaging techniques for the characterization of metal artefacts of historical, archaeological and cultural interest.

In particular, neutron tomographic methods allowed identifying structural components and morphological features that can be related to the manufacturing process, the life cycle, and the state of conservation of artefacts. For instance:

- the presence, location, direction and arrangement of structural components can be determined;
- inclusions and porosity can be mapped, localized and quantified;
- phase of different composition and microstructure can be evidenced;
- presence of possible welding, soldering or binding materials can be clarified;
- patination of the surface can be verified;
- defects and corrosion products can be identified for assessing the conservation status.

From the archaeometallurgical standpoint, this information can be extremely useful to establish interesting relationships and cross-matching among technologies developed by different material cultures. Especially considering arms and armours, NT can reveal their composite assembling that evolved over time in order to obtain specifically desired technical and mechanical performance as well as aesthetical design.

On the big picture, these studies could reveal a sympathetic overview of the lost traditional manufacturing procedures, mainly transmitted orally to the present, and often recovered by contemporary craftsman on a personal level, referring to partial information reported in written documents not always fully reliable.

A new interesting possibility has been disclosed by neutron imaging methods and further work will be needed to gain a more thorough understanding of the ancient manufacturing methods.

The present analysis could not have been carried out using traditional (invasive) analytical methods, which cannot be applied to such ancient and rare artefacts where a non-invasive, non-destructive experimental approach is mandatory.

In our study, neutron imaging allowed revealing unexpected features with respect to the current literature report and some of the obtained results were reported in the international literature for the first time.

Despite neutron-imaging techniques, in a combination with other method, especially neutron diffraction, provide an attractive approach, it is very rarely applied to help conservation and diagnostic of museum objects. By presenting the obtained positive results, we hope this work will ideally encourage further study and application of neutron techniques to different types of objects or a more in-depth look at their application to metal artefacts, whose current problems, or open questions, cannot be solved with the current, often invasive, commonly used techniques (Salvemini 2014).

References

- Coe MD, Connolly P, Harding A, Harris V, LaRocca DJ, North A, Richardson T, Spring C, Wilkinson F (2012) Swords and hilt weapons. Prion Book Limited
- Gener M (2009) Metallographic study of some 17th and 18th c, European sword (rapier) blades. In: 2nd International Conference Archaeometallurgy in Europe 2007. Selected papers. Associazione Italiana di Metallurgia, pp 282–293. ISBN 88-85298-71-0
- Giller L, Filges U, Kühne G, Wohlmuther M, Zanini L (2008) Validation of Monte-Carlo simulations with measurements at the ICON beam-line at SINQ. Nucl Instrum Methods Phys Res A 586:59–63
- Grazzi F, Bartoli L, Civita F, Franci R, Paradowska A, Scherillo A, Zoppi M (2011a) From Koto age to modern times: Quantitative characterization of Japanese swords with time of flight neutron diffraction. J Anal At Spectrom 26:1030
- Grazzi F, Civita F, Williams A, Scherillo A, Barzagli E, Bartoli L, Edge D, Zoppi M (2011b) Ancient and historic steel in Japan, India and Europe, a non-invasive comparative study using thermal neutron diffraction. Anal Bioanal Chem 400:1493
- Grazzi F, Bartoli L, Barzagli E, Civita F, Paradowska A, Scherillo A, Zoppi M (2011c) Microstructural characterization of two Koto age Japanese swords. La Metallurgia Italiana 5:13
- Hoshi H, Sasaki M (2005) Tetsu-to-hagane 91:103–107
- Josic L, Steuwer A, Lehmann EH (2010) Energy selective neutron radiography in material research. Appl Phys A 99:515
- Kaestner AP, Hartmann S, Kuhne G, Frei G, Grunzweig C, Josic L, Schmid F, Lehmann EH (2011) The ICON beamline A facility for cold neutron imaging at SINQ. Nucl Instrum Methods Phys Res Sect A 659:387
- Kapp L, Kapp H, Yoshihara Y (1987) The craft of the Japanese sword, Kodansha International
- Kapp L et al (1998) The craft of the Japanese sword. Kodansha International
- Kardjilov N, Dawson M, Hilger A, Manke I, Strobl M, Penumadu D, Kim FH, Garcia-Moreno F, Banhart J (2011) A highly adaptive detector system for high resolution neutron imaging. Nucl Instrum Methods Phys Res A 651(1):95–99
- Lehmann E, Hartmann S (2010) Investigation of the content of ancient Tibetan metallic Buddha statues by means of neutron imaging methods. Archaeometry 52(3):416–428
- Lehmann EH, Kaestner A, Josic L, Hartmann S, Mannes D (2011) Imaging with cold neutrons. Nucl Instrum Methods Phys Res Sect A 651(1):161–165
- Nagayama K (1997) The Connoisseurs book of Japanese swords. Kodansha International
- Notis MR (2000) The history of the metallographic study of the Japanese sword. Mater Charact 45:253–258 (and references within)
- Peetermans S, Grazzi F, Salvemini F, Lehmann E (2013) Spectral characterization of a velocity selector type monochromator for energy-selective neutron imaging. Phys Procedia 43:121–127
- Piaskowski J, Hist J (1993) Met Soc 27:110
- Robinson BW (1970) The arts of the Japanese sword. R. MacLehose and Company
- Sakakibara K (1963) 1800 The manufacture of armour and helmets in 16th century Japan: (chūkokatchūseisakuben). In: Robinson, Russel H (ed, rev) Hogitarō Inada, 1912 (trans: Wakameda T, revised by Koop AJ). The Holland Press, London
- Salvemini F (2014) Development of innovative methodologies for non-invasive characterization of metal artefacts of archaeological, historical, and industrial interest, through neutron diffraction and neutron imaging techniques. Ph.D. thesis in DOTTORATO DI RICERCA IN Scienza per la Conservazione dei Beni Culturali, supervisors M Zoppi and F Grazzi
- Salvemini F, Grazzi F, Peetermans S, Civita F, Franci R, Hartmann S, Lehmann E, Zoppi M (2012) Quantitative characterization of Japanese ancient swords through energy-resolved neutron imaging. J Anal At Spectrom 27:1347–1354
- Salvemini F, Grazzi F, Kardjilov N, Manke I, Civita F, Zoppi M (2015) Neutron computed laminography on ancient metal artefacts. Anal Methods 7:271–278
- Sato K (1997) The Japanese sword: a comprehensive guide. Kodansha International

Sears VF (1992) Neutron News 3:29

Sinclair C (2004) Samurai: the weapons and spirit of the Japanese warrior. The Lyons Press, Guilford

Squires GL (1996) Introduction to the theory of Thermal Neutron Scattering. Dover Publication Inc. New York

Sugimori E (2004) Japanese patinas, Brynmorgen Press

Tawara K (1953) Nippon-to no Kogataki Kenkyu (Scientific study of Japanese swords). Tokyo

Yumoto JM (1958) The Samurai sword. A handbook. Tuttle, Tokyo

Chapter 6

Ceramics, Marbles and Stones in the Light of Neutrons: Characterization by Various Neutron Methods

Zsolt Kasztovszky, Veronika Szilágyi, Katalin T. Biró, Judit Zöldföldi, M. Isabel Dias, António Valera, Emmanuel Abraham, Maryelle Bessou, Fabrizio LoCelso and Valerio Benfante

Abstract In this chapter we give a brief overview of neutron based analytical investigations applied to study archaeological ceramics, and different types of stones. Since the vast majority of archaeological objects are made of ceramics and various stones—all are of geological origin—, one of the key objectives of these studies to determine the origin of raw material. This research is called provenance

Zs. Kasztovszky (✉) · V. Szilágyi
Centre for Energy Research, Hungarian Academy of Sciences,
H-1121 Konkoly-Thege str. 29-33, Budapest, Hungary
e-mail: kasztovszky.zsolt@energia.mta.hu

V. Szilágyi
e-mail: szilagyi.veronika@energia.mta.hu

K.T. Biró
Hungarian National Museum, H-1088 Múzeum krt. 14-16, Budapest, Hungary
e-mail: tbk@hnm.hu

J. Zöldföldi
Institute of Materials Science, University of Stuttgart, Stuttgart, Germany
e-mail: Judit.Zoeldfoeldi@mpa.uni-stuttgart.de

M. Isabel Dias
Centro de Ciências e Tecnologias Nucleares. Campus Tecnológico e Nuclear,
Instituto Superior Técnico, Estrada Nacional 10, ao km 139,7,
2695-066 Bobadela LRS, Portugal
e-mail: isadias@ctn.tecnico.ulisboa.pt

A. Valera
Era Arqueologia, Núcleo de Investigação Arqueológica – NIA, Cç. de Santa Catarina,
9C, 1495-705 Cruz Quebrada – Dafundo, Portugal
e-mail: antoniovalera@era-arqueologia.pt

A. Valera
Interdisciplinary Center for Archaeology and Evolution of Human Behavior
(ICArHEB), Universidade do Algarve, Campo de Gambelas, Faro, Portugal

E. Abraham
University of Bordeaux, LOMA, CNRS UMR, 5798 Talence, France
e-mail: emmanuel.abraham@u-bordeaux.fr

research, and a wide range of neutron based methods are applicable in it. Following a very basic, user-oriented description of the methods, we introduce examples from our everyday practice. The examples are about provenance of prehistoric stone tools, about the sources of 4th–3rd c. B.C. millennium limestone idols found in the South of Portugal, as well as about the characterization of 15th–16th c. A.D. Inka pottery. A very unique application of combined neutron techniques was aimed to determine the inner content of an Eighteenth Dynasty Egyptian sealed vessel. In addition, investigations of samples from different epochs and characterization of marbles are presented.

6.1 Introduction

Combination of different neutron investigation methods helps to obtain detailed picture about the properties of ancient materials like marbles, ceramics and stones. Neutron activation techniques allow for detection of the chemical composition of the materials with high precision. Neutron diffraction provides information about the crystallographic structure, textures and different phases in the materials. Imaging methods show the morphology of the materials like macro porosity, inclusions and mineral distributions. The quality of marbles can be characterized by Small Angle Neutron Scattering which provides a measure about the homogeneity and the fine granular structure of the material. The arrangement of results from the different investigations and the analysis of multi-dimensional data volumes is quite demanding task requiring broad expertise and collaboration of researchers from different fields. In this chapter, examples of such multidisciplinary investigations on ancient materials are presented.

6.2 Used Experimental Methods

6.2.1 *Instrumental Neutron Activation Analysis (INAA)*

Historically, this was the first of the activation analytical methods, in which a few mg of the sample is irradiated in a reactor core and the induced radioactivity is measured post-irradiation. It is a destructive elemental analytical method, mostly applicable to determine the trace elements in various materials (stones, ceramics,

M. Bessou
University of Bordeaux, PACEA, CNRS UMR, 5199 Pessac, France
e-mail: maryelle.bessou@u-bordeaux.fr

F. LoCelso · V. Benfante
DiFC, University of Palermo, 90128 Palermo, Italy

metals, etc.). It is rather sensitive down to ppb or ppt level. Fingerprint-like trace element patterns (e.g. rare-earth patterns) help to identify the geographical origin of certain raw materials (called provenance analysis); it requires a 1–100 mg sample from the objects. The principle of the method is present in detail in Chap. 10.

6.2.2 Prompt Gamma Activation Analysis (PGAA)

A particular kind of Neutron Activation Analysis; the irradiation is performed at a guided external neutron beam, and the prompt- and delayed gamma photons are measured simultaneously with the irradiation. It is absolutely non-destructive, large objects can be irradiated (external beam), and in practice, no long-lived induced activity is produced. It is applicable mostly to quantify almost all the major and minor components (H, Na, K, Mg, Al, Si, Ti, Mn, Fe and Cl) and some trace elements (B is an important one, occasionally also Cr, Sc, V, Nd, Sm and Gd). PGAA is quite applicable in provenance studies of various stone objects and ceramics, too. PGAA and Instrumental Neutron Activation Analysis (INAA) are good complementary methods which allow for detection of almost every chemical element. Most of the following examples discuss PGAA measurements at Budapest Neutron Centre (BNC) and at Heinz Maier-Leibnitz Zentrum (MLZ), Garching, Germany. For detailed information related to the PGAA experimental method, please see Chap. 11.

6.2.3 Neutron Imaging (Radiography and Tomography—NR and NT)

The neutron imaging methods are rarely used to investigate homogeneous objects, like stone tools or bulky ceramics, but it can be useful to visualize the inner content of a closed vessel, or to investigate manufacturing (e.g. joins) of a ceramic vessel. One example of an Egyptian jar is discussed as an example. The NR&NT experimental methods are described in detail in Chap. 16.

6.2.4 Prompt Gamma Activation Imaging (PGAI)

PGAI is a combination of the neutron imaging methods with the elemental analysis, i.e. an extension of bulk PGAA towards the 3D elemental mapping. It is less important when investigating a homogeneous object, but is necessary to study the special distribution of various elements within inhomogeneous objects. The most important factors are the sensitivity, which is determined by nuclear constants similarly to PGAA and the spatial resolution, which is determined by the width of the neutron beam. The example of the Egyptian jar is illustrative here also. For more information about the PGAI technique, please see Chap. 14.

6.2.5 *Time-of-Flight Neutron Diffraction (TOF-ND)*

TOF-ND is used for exploring crystallographic phases, and other atomic-scale structural features. It can be used to identify various minerals in rocks or ceramics. From the literature, we know there was an attempt to investigate archaeological ceramics with TOF-ND. The ND method is presented in detail in Chap. 9.

6.2.6 *Small Angle Neutron Scattering (SANS)*

SANS is a technique for studying nanometer scale structural features in various materials. The information obtained is characteristic for the whole irradiated volume of the sample. Practically, the measured piece is free from outer-shape, physical, chemical or structural changes; there is no need of sampling. SANS makes possible the determination of void sizes in porous media, observation of typical grain sizes, anisotropy in the precipitate orientation in minerals or metals, as well as the investigation of particle agglomeration in ceramic bodies and evolution of pores during different types of processing. Detailed information about the principle of the SANS method can be found in Chap. 9.

6.3 Examples of Neutron Studies on Ceramics, Stones and Marbles

6.3.1 *Provenance Studies on Prehistoric Stone Objects*¹

Lithic artefacts are among the first documented evidence of human tool use. They occur from the earliest Palaeolithic times up to modern hunter-gatherer communities of the recent past. In Hungary, the first stone implements are connected with the Vértesszőlős Lower Palaeolithic site (400,000 B.C.) and they are in use all through prehistoric times, including the Neolithic Period and also into the age of metals. On Fig. 6.1 we show a simplified chronological chart for the interior parts of the Carpathian Basin (after Biró and Regenye 1995; Visy et al. 2003).

In the Palaeolithic period, chipped stone objects were produced, e.g. blades, scrapers, projectile points; while in the Neolithic period, apart from the traditional chipped stone implements, nicely elaborated polished stone tools appeared as well. Prehistoric people were absolutely aware of the requirements for producing optimal

¹Section written by Zsolt Kasztovszky and Katalin T. Biró.

Period	Age	Transdanubian cultures	To the East of the Danube (Alföld and North-Hungarian Mts.)	Time scale (thousand years)
Historical periods		Pannonia (Roman Empire)	Barbaricum	2
Prehistoric period	Iron Age	Celts Halstatt culture Urnrave culture	Scythians Prescythian culture	3
	Bronze Age	Mouldgrave culture Incrusted ware culture	Gáva culture Füzesabony culture Nyírség culture	4
	Copper Age	Baden culture Balaton-Lásinja culture	Baden culture Bodrogkeresztúr c. Tiszapolgár culture	5
	Neolithic = New Stone Age	Lengyel culture Linearband pottery culture Starčevo culture	Tisza culture Linearband pottery culture	6
Mesolithic period		?	Körös culture Jászszág group	8
			Gravettian culture	10
Palaeolithic period	Upper Pal.	Gravettian culture	Gravettian culture	18
	Middle Pal.	Jankovichian culture	Szeletian culture	30
	Lower Pal.	Mousterian culture Buda industry (= Vértesszőlős)	Aurignacian culture Mousterian culture	50
				500

Fig. 6.1 Simplified chronological chart for the interior parts of the Carpathian Basin (after Biró and Regénye 1995; Visy et al. 2003). The time scale indicates thousand years before present (B.P.)

stone tools and the localities of occurrence for good quality raw materials. The locations and quality of different rocks, such as obsidian, flint, radiolarite, silex, porphyry and metamorphic rocks (greenschist, blueschist, serpentinite, nephrite, etc.) are primarily determined by geological factors. These factors are embedded as signals in the raw materials proper. In other words, their geochemical composition is very often ‘fingerprint-like’, i.e., characteristic for the provenance of the raw material used for lithic artefacts.

One of the key questions for archaeometry is to find the provenance (place of origin, the geological source) of the archaeological objects found in controlled and documented context on the archaeological sites. If we are able to identify and quantitatively measure characteristic features (isotopic, elemental or mineralogical composition of the artefacts), we might have a chance to provide data about the geographical distribution of different raw materials, as transported by prehistoric people by means of regional supply systems or occasionally long distance trade networks.

Obsidian is a homogeneous type of natural (volcanic) glass. It has perfect conchoidal fracture, is easy to work on with simple percussion techniques, yielding very sharp cutting edges. Though it is as brittle as any glass, obsidian is hard enough for regular use. Because of its attractive appearance and advantageous mechanical qualities, it was a popular raw material during prehistory. The formation of obsidian requires the co-existence of specific geological conditions. It is formed when the fluid volcanic melt meets seawater or ice and quickly solidifies. This process is known as quenching. However, not every volcanic glass is regarded as obsidian; it requires rhyolitic lava with a very high SiO₂ content and a low amount of volatiles, especially water.

Because of the very specific geological conditions of obsidian formation, the major obsidian sources are quite well known. One can find obsidian all over the world along young volcanic insular arches, in New Zealand, the Andes or in Japan. In Europe and the Near East, the most important sources can be found in the Mediterranean region (Sardinia, Lipari, Melos and Anatolia). Most of the obsidian sources are geologically very young since glass is typically not stable under normal surface conditions. The Central European obsidian sources are relatively old, formed in the Tertiary period. The sources are mainly located in the Tokaj-Eperjes Mountains, at the border of today's Hungary and Slovakia. Further obsidian occurrences are known from Transcarpathian Ukraine in the environs of Huszt around Rokosovo. The Central European obsidian sources are generally referred to, in archaeometrical technical literature, as 'Carpathian' obsidian, though this term is incorrect from a geographical or geological aspect.

Fortunately, the geochemical (elemental) compositions of various obsidians are very characteristic for the conditions of the formation, and hence for the place of geological origin. The first research on archaeological obsidian with the support of geological methods was started as early as in the 1860s in Hungary, in the pioneering works of Rómer (1867) and Szabó (1867), respectively. From the late 1960s, modern analytical methods have been gradually introduced to determine the geochemical properties of obsidians of different origin. Besides more or less simple spectroscopic methods such as Optical Emission Spectroscopy (OES) (Cann and Renfrew 1964), the methods of Instrumental Neutron Activation Analysis (INAA) (Oddone et al. 1999), X-ray Fluorescence Spectroscopy (XRF) (Tykot 1997) and also ion-beam analytical (PIXE, PIGE) methods (Bourdonnec et al. 2005) have been applied to quantify the amount of characteristic major-, minor- and trace elements. Although many of the above mentioned methods proved to be successful in determination of fingerprint-like trace elements, like Rb, Sr, Nb, Y, Zr and Ba, almost all of them require sampling of the archaeological objects, which is impermissible in many cases.

According to our present knowledge (Biró 2014), there exist three main types of Carpathian obsidian. The oldest (15–16 million years) black or transparent greyish Carpathian 1 (C1) is the best quality, it appears around Viničky, Mala Bara, Kašov and Cejkov in Slovakia. The younger (10–12 million years) non-transparent black or grey, very rarely reddish-brown Carpathian 2 (C2) comprises two subgroups, C2E from Mád–Erdőbénye–Olaszliszka and C2T from Tolcsva–Erdőbénye–Abaujszántó. They are from the Southern slopes of the Tokaj Mountains in Hungary. Finally, a third one, the Carpathian 3 (C3) has been discovered around Rokosovo, close to the western border of Ukraine. The best quality C1 has been transported for hundreds of kilometres, C2 has been circulated in long distance trade, while C3 being of lower quality has served only as local raw material—as was proved with the help of analytical results.

In the beginning of 2000s, the Hungarian National Museum launched a co-operation with the Budapest PGAA laboratory at the Centre for Energy Research (former Institute of Isotopes), Hungarian Academy of Sciences. We aimed to investigate whether the geochemical components measurable with PGAA (namely

the major elements of H, Na, Al, Si, K, Ti, Mn, Fe and the trace elements of B, Cl, Nd, Sm, Gd) are suitable to separate obsidian from other similarly appearing material like black opalites and other siliceous rocks, and if we would be able to differentiate between raw materials from various geological locations.

Already after the first set of measurements, it turned out that PGAA can easily discriminate between obsidian and other silicates (e.g. slags or silex). Also, it seemed to give a chance to identify various outcrops according to the compositions of obsidians from there (Kasztovszky et al. 2008). We have continued with systematic study of obsidian reference objects available in the comparative raw material collection (Lithotheca) of the Hungarian National Museum, as well as in the Prehistoric and Palaeolithic Collections of the Museum. Besides the existing reference materials in the Lithotheca collection, we have obtained comparative material by means of further fieldworks and also by scientific exchanges with several countries. Up to now, after more than 10 years, we have analysed around 180 archaeological artefacts and 160 geological reference samples. In our work, we focused on the research of the Carpathian region. Therefore, thanks to the international co-operations with many archaeologists and geologists, we have analysed archaeological objects from Hungary, Romania, Serbia, Croatia, Bosnia-Herzegovina and even from Poland. Geological references represent the most important Central European and Mediterranean sources, such as Tokaj Mts., Sardinia, Lipari, Melos, Antiparos, Pantelleria, Palmarola, Yali, Armenia and Anatolia.

As is known from the literature (Oddone et al. 1999; Tykot 1997), Instrumental Neutron Activation Analysis (INAA), X-ray Fluorescence Analysis (XRF) or Inductively Coupled Plasma Mass Spectrometry (ICP-MS) are quite sensitive and suitable to identify a series of trace elements in obsidians. Compared to the above methods, PGAA can detect fewer trace elements but it has some significant advantages. Since neutrons can go deep into the sample's material, the obtained compositional data are characteristic for the 'bulk' and are not affected much by surface contamination or weathering. Furthermore, it is not necessary to take a sample from a larger archaeological object, the whole object can be placed in the external neutron beam and a selected region can be investigated. Because of the relatively low beam intensity (10^7 – 10^9 cm⁻² s⁻¹), the induced radioactivity is negligible and quickly decays. No damage of the objects has been ever observed.

Based on our PGAA measurements, we have found that boron (B) and chlorine (Cl) seem to be the elements that can most effectively discriminate between obsidians of different origin. For instance, boron concentrations are usually around some tens of ppm, but in case of Lipari obsidians, it can reach the order of 200 ppm, and at the same time, with high chlorine content. Besides B and Cl, iron (Fe), titanium (Ti) and alkaline elements (Na and K) were found also to be characteristic (Fig. 6.2). Usually, we construct bivariate or trivariate diagrams, or we apply statistical methods (Principal Component Analysis or Factor Analysis) to reveal similarities or differences between the samples (Kasztovszky et al. 2008).

So far, we have found the most definitive results with PGAA, when we have done provenance study of archaeological obsidians from Croatia, Serbia and

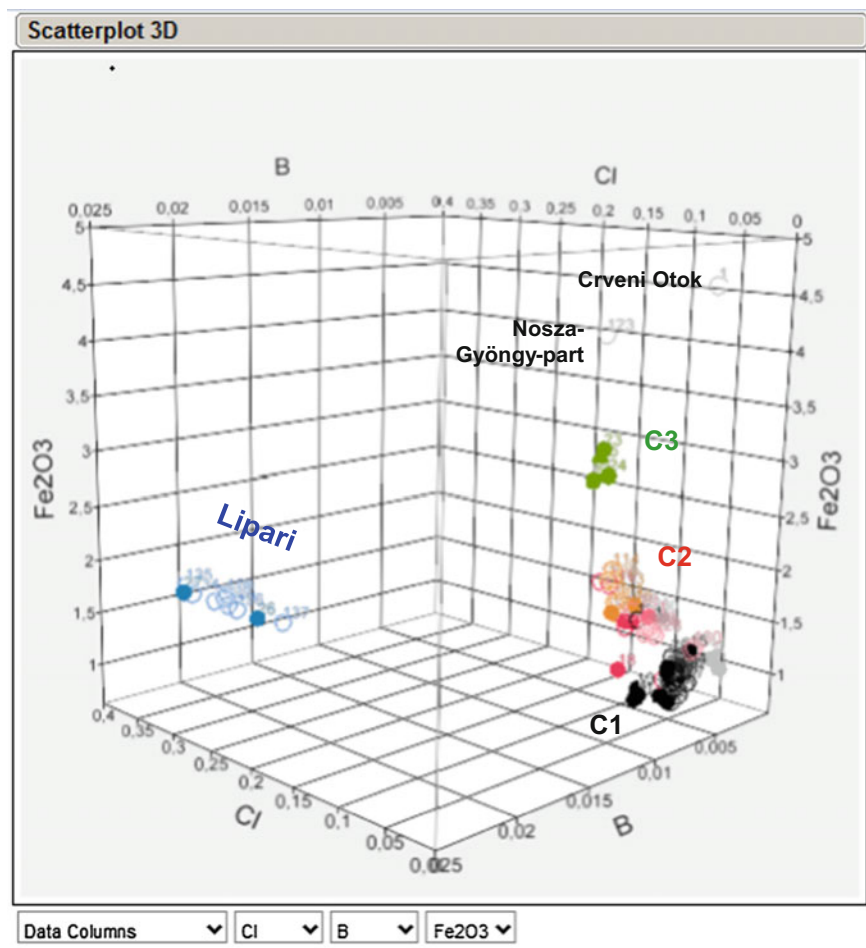


Fig. 6.2 Discrimination of archaeological and geological obsidians according to their elemental compositions measured with PGAA

Bosnia-Herzegovina (Kasztovszky et al. 2012). We have proved that there are two distinct types of archaeological pieces found in this territory. The ones from the Dalmatian shore turned out to be Lipari type, whereas the others found on the continental part proved to be Carpathian 1 (C1) type. In the case of the Dalmatian obsidian, other Mediterranean sources, such as Sardinia or Melos could be excluded with high confidence (Fig. 6.3). In another study, we have identified the furthest occurrence of Carpathian 1 type obsidian in Upper Palaeolithic and Neolithic settlements found near Morsko, Rudna Wielka, Kowalewko and Cichmiana, Central Poland (Kabaciński et al. 2015)

Similarly to obsidian, we have also successfully applied PGAA to determine the provenance of Szeletian felsitic porphyry tools (Markó et al. 2003). Szeletian

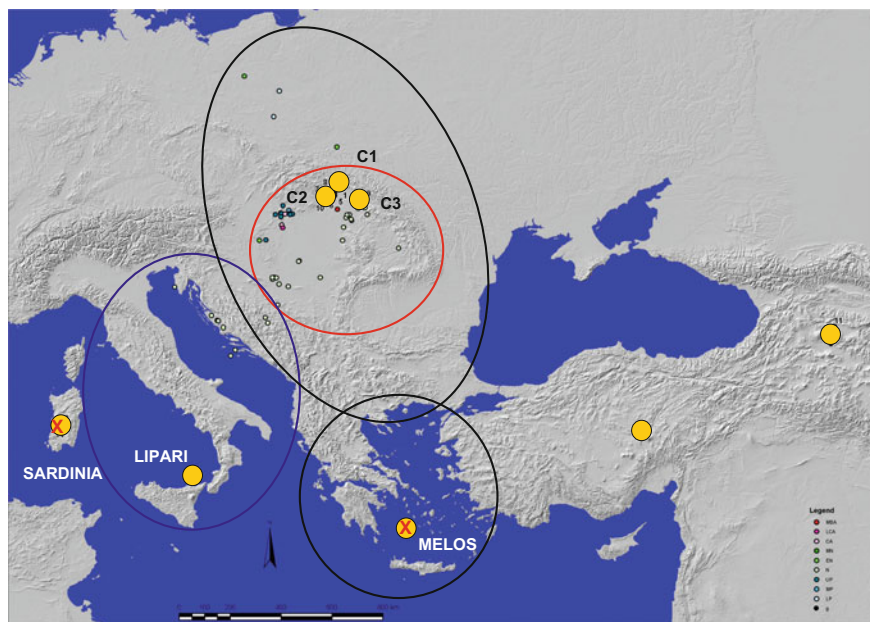


Fig. 6.3 Supposed raw material sources of archaeological obsidians found in the Central European (Carpathian) and Adriatic regions

felsitic porphyry was another popular prehistoric raw material; the name refers to the Szeleta cave in North-East Hungary where this specific raw material was first identified in archaeological context (Vértes and Tóth 1963). The first instrumental characterisation of this material was performed in the early 1960-ies (Vértes and Tóth 1963) by X-ray diffraction. In our studies (Markó et al. 2003), artefacts, macroscopically identified as Szeletian felsitic porphyry, turned out to be either Szeletian felsitic porphyry proper with relatively lower amount (75.3–82.4 wt%) of SiO_2 , while for some siliceous rocks with similar appearance but different origin, the SiO_2 content was found to be between 95.5 and 98.5 wt%, which is characteristic for hornstone, radiolarite or for limnic quartzite (Fig. 6.4). Besides the silica content, concentrations of Na_2O , K_2O and TiO_2 were found to be discriminative factors. Partly on the basis of the analytical results, the intensive use of felsitic porphyry is well established in the Cserhát Mts. The on-site processing of the raw material in the Vanyarc type Middle Palaeolithic industry is documented at the distance of 100–125 km from the source area in the Bükk Mts.

Equally successful provenance research was performed on Neolithic polished stone objects made of greenschist-metabasite varieties (high-pressure metamorphite, nephrite, serpentinite, greenschist and blueschist). The aim of the study was again to map and characterise prehistoric resources, taking into consideration contemporary geographical and socio-economic relations in the Central European

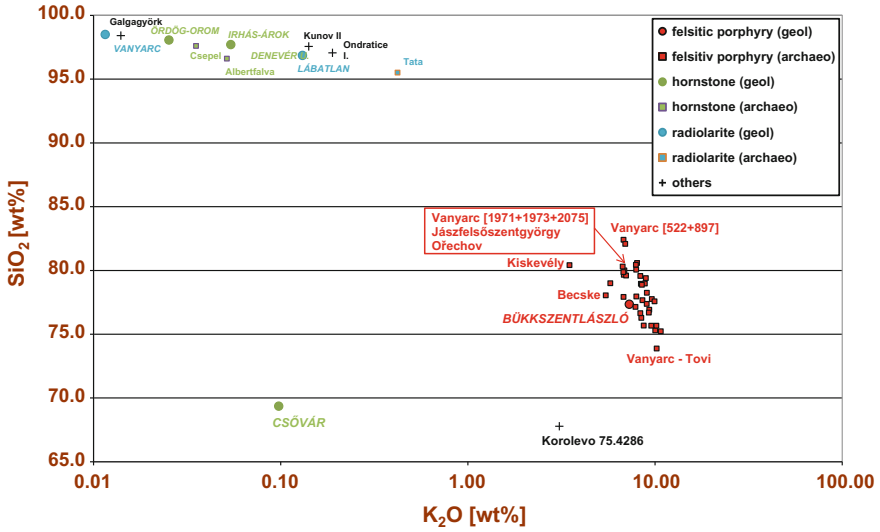


Fig. 6.4 Differentiation between Szeletian felsitic porphyry and silex samples, based on their Si- and K-contents

region, as well as “long distance” raw material sources known to play important role in the European prehistoric exchange network (Szakmány et al. 2011).

When we attempt to perform a provenance study of high silica-content siliceous raw materials, we will experience less success. Silex is a general term for very high silica-content (95–98 wt% SiO₂) sedimentary rocks, such as flint, radiolarite, chert, jasper or limnoquartzite. Unfortunately, because of the exceptionally high SiO₂ content, the possibility to detect other elements suitable for characterisation is very difficult for methodological reasons. It seems that we might have a chance to distinguish between silex types, but the identification of individual sources may require complementary (but not necessarily non-destructive) methods (Biró and Kasztovszky 2009).

6.3.2 *Lapis Lazuli—A Geological Gift*²

Archaeological finds, like beads, gems, seals and small decorative objects made of lapis lazuli are widely distributed in the ancient East and some date back as early as the second half of the fourth millennium B.C. in Central Asia. Also the blue pigment “ultramarine”, used by the Grand Old Masters was nothing else but pulverised lapis lazuli. This paper provides a summary of multi-elemental characterization and

²Section written by Judit Zöldföldi and Zsolt Kasztovszky.

provenance analysis of lapis lazuli based on non-destructive Prompt Gamma Activation Analyses. The data show elemental distinctions between the well-known lapis lazuli sources, like Afghanistan, Russia, Chile and Ural Mountains. In the last few years, Prompt Gamma Activation Analysis, a non-destructive analytical technique has been applied in order to determine the place of origin of lapis lazuli. PGAA is one of the few non-destructive methods, which is applicable in bulk elemental analysis of valuable archaeological objects, like beads and cylinder seals. Some first successes in distinguishing lapis lazuli raw materials from different sources (Afghanistan, Lake Baikal, Ural, Canada and Chile) were already published (Zöldföldi and Kasztovszky 2003, 2009).

6.3.2.1 Lapis Lazuli as Archaeological Goods

Lapis lazuli, this opaque, deep blue gemstone looks back at a long history. Some of the most ancient lapis lazuli finds in Northern Mesopotamia are artefacts from Gavra XIII dated ca. 3500 B.C., and in Southern Mesopotamia—those from the Uruk II period (Derakhshani 1998). Among the most interesting Sumerian objects from precious minerals and gold in the Ur necropolis (26th c. B.C.) are the so called “Standard of Ur”, with a mosaic inlay of small lapis lazuli and shell pieces, as well as goldbearing bull heads with lapis lazuli beard or standing goat figures with horns and decoration from lapis lazuli. Among some of the other objects in the British Museum in London can be noted rectangular and cylindrical seals, as well as a sceptre with triangular lapis lazuli inlay (Woolley 1934). Among the numerous poems from the period of the first civilizations in Mesopotamia, there exist an epic tale of Enmerkar and the Lord of Aratta (III mill. B.C.). It tells the story about the exchange of corn for lapis lazuli, gold and silver from the mountainous country Aratta needed for the building of palaces (Kramer 1952). Many researchers have been trying to trace the country Aratta, from where or through which the precious lapis lazuli and noble metals have been found or traded (Derakhshani 1998). According to some ideas, the country Aratta has to be located to the south or southeast of the Caspian Sea (Herrmann 1968), and according to others this country coincides in its location with the mountainous Badakhshan, because in the poem one can find expressions as “lapis lazuli in pieces”, “they gather for her (goddess Innana) lapis lazuli from the deposits” or “lapis lazuli from the mountains” (Sarianidi 1971). Another hypothesis relates the Shahr-I-Sokhta site to the mythical country Aratta. Lapis lazuli has been included in epic poems of the Sumerians, which have also influenced later Babylonian or Hittitic versions of the myths: the Epic of Gilgamesh, the visit of the goddess Innana (she decorated herself with lapis lazuli jewellery) in the underground world; the myth for the origin of the mattock “with a forehead of lapis lazuli” and a lot of others (Kostov 2004).

From at least 4000 B.C. lapis lazuli was being traded. Royalty felt safer for the journey if they could placate the gods with gifts of sacred lapis lazuli; it was a kind of insurance. Never has lapis lazuli been quite as highly valued as it was intermittently over some two thousand years by the people of Sumer. Occupants of four

and a half thousand year old graves were determined to do all they could to placate the gods who ease the passage to the underworld (Searight 2010). Lapis lazuli, or za-gin of the Sumerians of the late third millennium B.C. Ur, was the great treasure (Moorey 1994), synonymous in literature with gleaming splendour, the attribute of gods and heroes. Thousands of lapis lazuli beads and objects have been found in graves excavated around huge temple complexes, as for instance at the greatest of Sumerian cities, Uruk, Ur and Mari or in the excavation of Qatna. The evocative name is a compound of “lapis”, the Latin word for stone, and the Arabian word “azul”, denoting the colour blue. It was one of the first stones ever to be used and worn for jewellery. Excavations in the antique cultural centres all around the Mediterranean provided archaeologists with finds which were left in tombs to accompany the deceased into the hereafter. Again and again this jewellery and objects crafted from lapis lazuli is the clear indication that thousands of years ago the people in Mesopotamia, Egypt, Persia, Greece and Rome cherished deep blue lapis lazuli. Especially in the oriental countries, it was considered as a gemstone with magical powers.

6.3.2.2 Mineralogy and Geology of Lapis Lazuli

Lapis lazuli is an opaque semi-precious stone consisting mainly of a blue mineral, lazurite, an alumo-silicate of the complex feldspathoid sodalite group, and can be described as an isomorphic combination of haüyn and sodalite (Webster 1975). The chemical formula for lazurite is $(\text{Na,Ca})_4(\text{AlSiO}_4)_3(\text{SO}_4\text{Cl})$, but with considerable variation in the amounts of SO_4 , S and Cl (Hurlbut 1954). Additionally, pyrite and calcite together with relatively small amounts of accessory minerals are present in the stone lapis lazuli. The colour of lapis lazuli can vary from intense marine blue to violet blue, but lighter blue and green varieties also occur, depending on the shifting chemical composition. The finest and bluest lapis lazuli comes from just such pressures in the Hindu Kush mountain (Badakhshan) backbone of Afghanistan, but there are relatively few other occurrences of lapis lazuli worldwide: the Pamir Mountains in Tadjikistan, the Lake Baikal source in Siberia, Burma, Baffin Island in Canada, Edwards in N.Y. State (USA), the Green River Formation of Wyoming-Colorado-Utah, California (USA), Chile, Angola in Africa, Atlas Mountains in North Africa, Latium in Italy and the Ural Mountains in Russia. The sources of lapis lazuli are described by Rosen (1988) and Zöldföldi and Kasztovszky (2003) and are shown in Fig. 6.5.

Despite a number of studies, related to mineralogy and metamorphic conditions (Blaise and Cesbron 1966; Faryad 1999; Grew 1988), the origin of lapis lazuli and related mineralization remains unclear. Lapis lazuli is usually found in metamorphic limestone or dolomite, and typically in zones affected by contact metamorphism (occurrence type 1). The basic chemical framework, thus, stems from igneous sources, as in other sodalite group minerals, but characterizing elements, such as calcium (Ca) and sulfur (S) lazurite have been picked up from the limestone/marble/dolomite surroundings. Lapis lazuli also characteristically contains calcite and pyrite

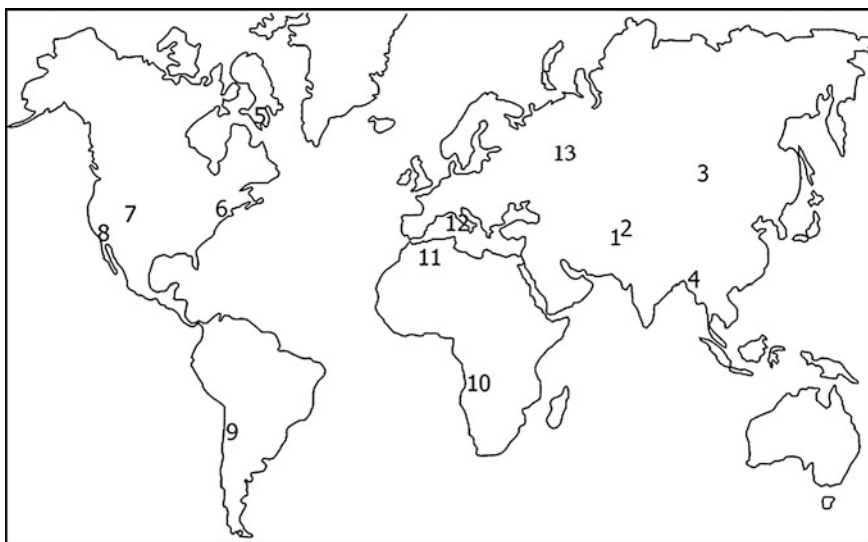


Fig. 6.5 Lapis lazuli occurrences of the world. 1 Badakhshan, 2 Pamir, 3 Lake Bajkal, 4 Burma and Pakistan, 5 Baffin Island 6 Edwards, USA, 7 Wyoming-Colorado-Utah, USA, 8 California, USA, 9 Chile, 10 Angola, 11 Atlas Mountain, 12 Latium, Italy, 13 Ural

emanating from the limestone type host rock in addition to a number of minerals, which have igneous origins. According to Yurgenson and Sukharev (1984), the lapis lazuli deposits resulted from interaction between granite related hydrothermal fluids (Na-metasomatism) and marbles with high amounts of pyrite (occurrence type 2). A metamorphic origin for lapis lazuli deposits and whiteschists from primary evaporates and mudstone (occurrence type 3) was proposed by Kulke (1976), Hogarth and Griffin (1978) and Schreyer and Abraham (1976). The rather specific type of combination between a restricted range of igneous or evaporite rocks and carbonate (metamorphic) sediments, accounts for the rare occurrence of lapis lazuli.

Until recent years, it was supposed that the first lapis lazuli finds found at 4th millennia sites in Mesopotamia, Iran and the Indus came from the famous Badakhshan mines (Afghanistan). However, there is evidence as early as ca. 2700 B.C. for use of lapis lazuli from Lake Baikal and this source cannot be excluded simply because of its long distance from Mesopotamia (Buchanan 1966). Moreover, there is evidence that lapis lazuli from 3rd millennium Shahr-I-Sokhta originates from the Pamir Mountains in Tadjikistan, the Chagai Hills in Pakistan and from Badakhshan in Afghanistan, thus destroying the generally accepted hypothesis of only one supply source (Casanova 1992; Delmas and Casanova 1990).

Until recent times, it was not possible to differentiate between the lapis lazuli from Afghanistan and other sources by any mineralogical and chemical examination. Herrmann reports that different scientific tests failed to distinguish Afghan from Baikal lapis lazuli (Herrmann 1968). There used to be few scientific methods

available, including mineralogical investigation, trace elements analyses by X-ray fluorescence and optical spectroscopy (Herrmann 1968), as well as atomic absorption spectroscopy (Chakrabarti 1978; Faryad 2002; Herrmann 1968; Hogarth and Griffin 1978; Casanova 1992). There are differences in the percentages of MgO and K₂O in lapis from Afghanistan, Russia, Italy, the Pamirs, Baikal and Burma (Hogarth and Griffin 1978). Unfortunately, all the above investigations are definitely destructive. As lapis lazuli is a very rare and precious archaeological material, in most cases they are not allowed to undergo destructive analytical investigations. Lo Giudice et al. (2009) and his co-workers described differences in the cathodoluminescence and ionoluminescence behaviour of different lapis lazuli raw materials. Re et al. (2011) reported about the micro-PIXE characterization of lapis lazuli. They turn their attention to single phases and investigations of the surface instead of the whole rock; in particular on two main minerals, the lazurite and diopside.

6.3.2.3 Experimental Setup

From 2002, we have tried to explore how effectively we can apply the bulk elemental composition—measured by PGAA at the Budapest Neutron Centre—to determine the provenance of lapis lazuli. Bulk samples (whole rocks) have been irradiated by a horizontal cold neutron beam at the Budapest Research Reactor. The thermal equivalent intensity of the beam was $10^8 \text{ cm}^{-2} \text{ s}^{-1}$. The upgraded PGAA facility is described by (Szentmiklósi et al. 2010). The acquisition time was chosen between 2200 s and 50,600 s, in order to detect as many trace elements as possible. The prompt-gamma spectra were detected by a calibrated Compton-suppressed HPGe detector, the spectra were evaluated using the Hypermet-PC program (Molnár et al. 2002; Révay et al. 2005). The basis of the quantitative analysis was the standardisation using k_0 -method, a kind of comparator method, which was earlier used in INAA, and later adopted in PGAA (Molnár et al. 1998; Révay 2009). The applied PGAA spectroscopic data libraries were developed at the Institute of Isotopes (Révay et al. 2001a, b). The effect of the spectroscopic background originating from the surrounding material, was taken into account, based on accurate background measurement.

Reliability of the PGAA method was checked several times on geological standard reference materials. With PGAA, we were able to quantify all the major components and some trace elements in whole rock samples. Concentrations of detectable chemical elements are calculated in wt% or in ppm. As a convention in geochemistry, major components are given in oxide forms, calculated according to the oxidation numbers. The accuracy of the chemical analysis is mainly determined by the peak areas as they used in the efficiency calculation, in determination of partial cross-sections, as well as in analysis of unknown samples (Révay 2006). As a result, for major components, the typical relative uncertainties of concentrations are between 1 and 3 %. Since lapis lazuli is an inhomogeneous rock, the variation of composition within one piece of rock was tested on various cuts of the same rock.

Because of the relatively low intensity of neutron beam, the induced radioactivity is practically negligible and decays quickly. The biggest advantage of PGAA is the applicability to investigate whole archaeological objects or pieces of rocks without any sampling or destruction of the objects. Since neutrons can penetrate many centimetres deep into the sample material, one can obtain an average composition of a few cm^3 sample volume.

In comparison to the methods of contemporary researchers—Lo Giudice et al. (2009) and his co-workers who described differences in the cathodoluminescence and ionoluminescence behaviour of different lapis lazuli raw materials and Re et al. (2011) who reported about the micro-PIXE characterisation of lapis lazuli—we turn our attention to the non-destructive investigation of the chemical composition of the whole rock and not only the surface, which partially undergoes significant weathering due to time. For this purpose, in the last decade, Prompt Gamma Activation Analysis (PGAA) has been applied in order to determine the origin of lapis lazuli. PGAA is one of the few non-destructive methods which is applicable in bulk elemental analysis of valuable archaeological objects, like beads and cylinder seals. Some early successes were achieved in distinguishing lapis lazuli raw materials from different occurrences (Afghanistan, Pakistan, Tadjikistan, Lake Baikal, Ural, Canada and Chile).

6.3.2.4 Results and Discussion Related to Investigation of Lapis Lazuli

With PGAA we were able to detect the major components H, Na, Ca, Al, Si, S, Cl, K, and the accessory elements Mg, Fe and Mn. In addition, the trace elements of B, Sc, V, Cr, Co, Sm and Gd were also identified.

The geological history and mineral compositions described above imply the presence of fluid phases with high concentrations of CO_2 , halogens and S during metamorphism of the rocks. S and halogens (e.g., Cl, B) are incorporated in the following minerals: Cl and B in scapolite, sodalite, biotite, amphibole and apatite; S in haüyne, lazurite, scapolite, pyrite and pyrrhotite and F in apatite, biotite, amphibole, titanite and clinohumite. With the exception of accessory pyrrhotite, pentlandite and some scapolites, S-bearing minerals originated during retrogression and metasomatism.

Based on this geological and mineralogical knowledge, we have chosen the elements S, B and Cl to distinguish the lapis lazuli samples from different occurrences. Unfortunately, the detection of F is impossible with the PGAA method, because of the very low neutron capture cross section of fluorine.

With the help of PGAA all the major (Si, Al, Ti, Fe, Mn, Mg, Ca, Na, K, S, H, occasionally P, C) and some accessory elements (Cl, B, Sm, Gd, in some cases Nd, V, Co, Sc) of lapis lazuli were possible to quantify. As an average chemical characteristic of bulk lapis lazuli samples, the less variable major element concentrations are the following: 40–45 wt% SiO_2 , 9–11 wt% Al_2O_3 , 0.02–0.05 wt% MnO, 10–13 wt% MgO, 14–21 wt% CaO, 4–6 wt% Na_2O , 0.4–2.0 wt% K_2O and 0.6–1.2 wt% H_2O . Although, the calcium content showed larger variation, it cannot

be considered as a characterizing element of certain rock sources, since it is directly correlates with the calcite content. Applying discrimination calculations with concentrations and concentration ratios, the PGAA analyses proved that based on the bulk chemical composition, the lapis lazuli from Chile and Ural can be clearly distinguished from each other and from the Afghan and Baikal sources. However, the raw material' compositions of Afghanistan and the Baikal region significantly overlap (Fig. 6.6). We have found the most important discriminative elements to be Cl, S, Fe and B. Especially, Cl, B and S are basic variable components of lazurite, the major blue mineral phase. From this data, these elements are assumed to behave sensitively in different (contact metamorphic or Na-metasomatic) conditions of the petrogenesis. However, iron and sulphur are the major constituents of one of the important impurities of the lapis lazuli, the pyrite (FeS_2). To eliminate the chemical effect of pyrite, normalization by $\text{SO}_3/\text{Fe}_2\text{O}_3$ ratios was applied for the bulk chemical data (Fig. 6.7). The Chilean lapis source is characterized with the highest

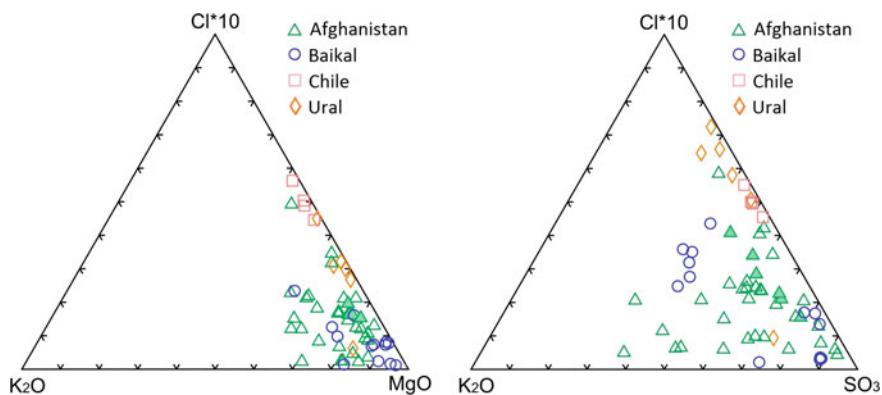
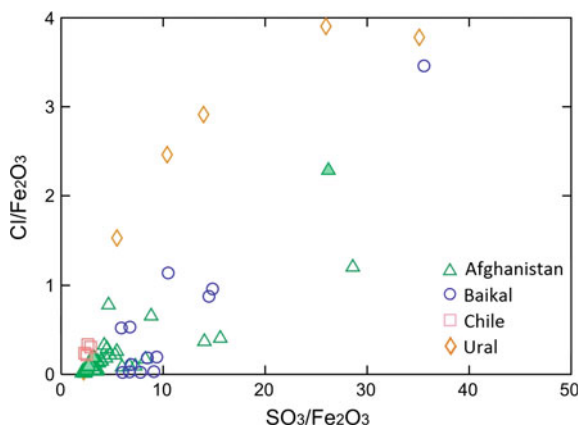


Fig. 6.6 Ternary plots showing the variable major element concentrations

Fig. 6.7 Sulphur and chlorine contents of lapis lazuli samples, normalized by iron content



chlorine, iron and sulphur content. The lapis lazuli of the Ural source has medium chlorine concentrations, while the Fe, S and also the B content is much lower than that of the Chilean. The lapis lazuli samples from the Afghanistan localities show the widest scattering in their chemical composition.

The most significant chemical characteristics of these samples are the highest boron content and the medium Fe, S, and Cl concentrations. As a methodological aspect, one sample from Afghanistan and another from Baikal Lake was selected for the investigation of their heterogeneity. For this reason, two pieces of lapis lazuli blocks (Afghanistan and Lake Baikal) have been cut into 4 slabs and measured separately (Fig. 6.8). Figure 6.9 shows that the element ratios of Cl/SiO₂ and B/SiO₂ are not affected by the sample heterogeneity, and allow the distinguishing between the different occurrences, with minor overlaps.

In its present state, a preliminary database of chemical composition of lapis lazuli raw materials from the main known sources is appropriate to distinguish between the most relevant quarries.

In addition to the above mentioned calculations, Principal Component Analysis—a multivariate statistical method—has been carried out to seek patterns of differential distribution of the samples within the compositional space. This would

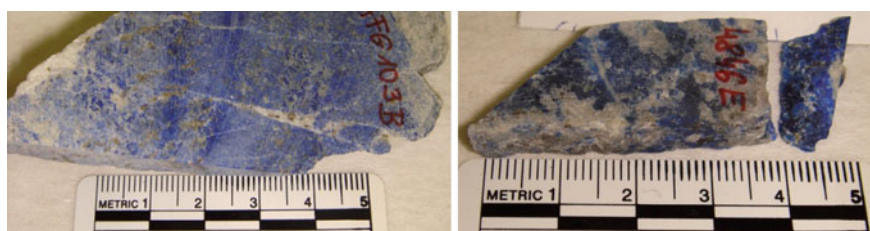


Fig. 6.8 Slabs of the lapis lazuli samples from Afghanistan and Lake Baikal

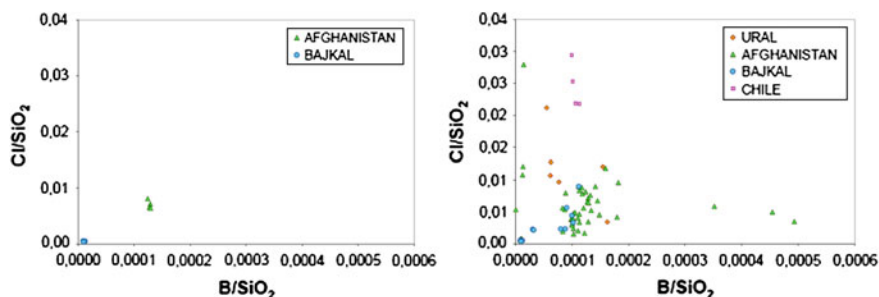


Fig. 6.9 Cl/SiO₂ and B/SiO₂ ratios; *left* measurements of the same block but in different slabs; *right* discrimination diagram of the raw materials stems from well-known lapis lazuli occurrences

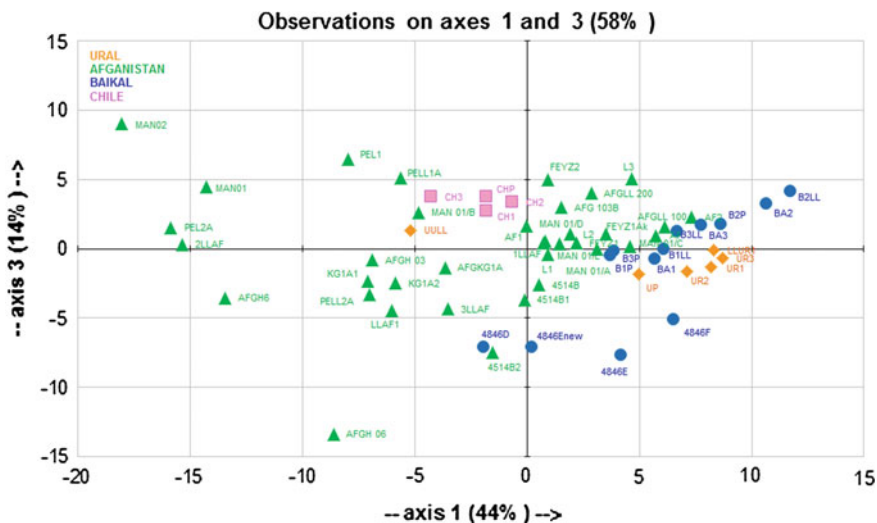


Fig. 6.10 Principal Component Analysis (PCA) analyses, including all the analytical data of lapis lazuli raw material

allow us to see the data dispersion when the correlation among the elements was part of the data analysis. As the components are linear combination of all the original composition data, PCA can reveal some significant differences/similarities between the objects—even in the absence of rigorously defined groups. Figure 6.10 shows the 1st and 3rd Principal Components, calculated from all the analytical data of lapis lazuli raw material that allows obtaining different clusters on the basis of the provenance of natural lapis lazuli deposits. This approach, tested on a large number of samples, shows that a significant discrimination of lapis lazuli coming from different natural deposits is possible based on the bulk chemistry, although some overlaps occur. This knowledge could be of great relevance in the identification of the provenance of lapis lazuli in archaeology and works of art and in the discrimination between their natural or synthetic origin.

6.3.2.5 Concluding Remarks

Lapis lazuli is a very rare and precious archaeological material, which in most cases is not allowed to undergo destructive analytical investigations.

PGAA is one of the few non-destructive and methods which is applicable in elemental analysis of these valuable archaeological objects. With the help of PGAA we were able to measure all the major and accessory components of lapis lazuli. Cl/SiO_2 and B/SiO_2 are not affected by the sample heterogeneity, and allow the distinguishing between the different sources, with minor overlaps.

6.3.3 Stone Travellers. Contribution of Non-invasive Nuclear Techniques to Determine Culture Identity, Mobility and Interaction in the Recent Prehistory of South Portugal³

6.3.3.1 How to Understand the Perdigões Interaction Network

Studies of provenance are a valuable tool for archaeological research, especially when dealing with the socio-economic and cultural impact of trade routes.

The Perdigões site is one of the largest known Portuguese Chalcolithic ditched enclosures, occupied during the late 4th–3rd millennium B.C. (Valera et al. 2014a) in the Reguengos de Monsaraz region, in the South of Portugal.

This circular shaped site spreads over an area of about 20 ha, and presents twelve roughly concentric ditches (Márquez et al. 2011). Several interdisciplinary teams have been working at this site. Work developed so far suggests the existence of a very complex range of activities, namely burial ground areas (Lago et al. 1998; Valera et al. 2000, 2008, 2014b). The burial remains are diversified and mainly consist of pottery, lithic artefacts, stone (marble, limestone and others) and bone and ivory idols, pecten shells, ivory combs, adornment artefacts, etc. (Valera 2008, 2012a, b).

Pottery artefacts include all the typical morphologies of the Late Neolithic and Chalcolithic of the South West of the Iberian Peninsula and there are differences between the style, production technology and provenance of funerary and domestic pottery (Dias et al. 2005).

At the Perdigões ditched enclosures several funerary contexts have been excavated dating from the Chalcolithic (3rd Millennium B.C.). In the eastern side there is a tholoi tomb necropolis and in the centre some funerary pits with the deposition of cremated human remains. Excavations reveal that the funerary practices in these two areas of the enclosure present different ritual procedures, not just in terms of architecture and body manipulation, but also in terms of what kind of votive materials were use (they differ in category and typology).

One of the item types found in the necropolis is stone idols, but with different typologies and raw material, apparently mostly made of marble or limestone, suggesting different origins for these artefacts, since both rocks do not occur locally, but regionally. Some questions remain to be answered, like their compositional nature and their provenance.

Stone idols in Chalcolithic were found in several archaeological sites from Estremadura and Southern Portugal. But, so far, no archaeometric approach has been made to these materials. This compositional study will be the first one to be performed, especially aiming to contribute to provenance issues, by means of

³Section written by M. Isabel Dias and António Valera.

compositional studies of both artefacts and potential raw materials, and to the characterization of the diverse funerary contexts, by answering questions such as:

- (1) Is it possible to differentiate raw materials used in the stone idols of the two types of funerary contexts—tholoi tomb necropolis and funerary pits? It is important to extend the evidence that these two areas of the enclosure have diverse funerary practices, with evidences of different ritual procedures, architecture, body manipulation and votive materials.
- (2) Provenance/circulation issues: do these stone idols point to different provenances, with diversified raw materials (local? regional? unknown?) like the more differentiated provenances already found for ceramic from funerary contexts as opposed to non-funerary pottery (Dias et al. 2005)?

So, one of the main goals of this work was to determine if diverse raw material resources were used by studying the composition of a set of stone idols and ritual stone vessels, together with geological samples (marbles and limestones), trying to evaluate the degree of compositional homogeneity between idols, as well as possible areas of origin, all contributing to understanding the interaction network in which Perdigões was involved. Another important goal of the study was to determine whether Prompt Gamma Activation Analyses could be successfully used to trace the source(s) of those Chalcolithic artefacts made of carbonate rich raw materials.

Scientific data on the provenance of the ornamental stone material of individual monuments and archaeological objects, like sculpture, are becoming increasingly available. For the Iberian Peninsula, many studies have dealt with the distribution and (archaeological, petrographic and geochemical) characterisation of the ornamental stones especially for Roman chronologies, considering the main Roman exploitation centres (white and coloured marbles), such as the white marbles of Estremoz, Almadén de la Plata, Macael and Sierra de Mijas, and the coloured stones of Antequera, Sintra, Broccatello, Buixcaró, Santa Tecla and Espejon (i.e. Lapuente 1995; Lapuente and Turi 1995; Morbidelli et al. 2007; Domínguez Bella 2009; Origlia et al. 2011; Beltrán et al. 2012; Mañas Romero 2012; Taelman et al. 2013; Taelman 2014).

A large problem in sourcing carbonate rich artefacts is that macroscopically they may look similar, even if they come from different sources. From a mineralogical point of view, they are almost pure CaCO_3 with a very heterogeneous mixture of impurities. As already noticed for sourcing microcrystalline quartz artefacts (Crandell 2012), also in this case of carbonate artefacts, especially those deriving from the metamorphic evolution of previous carbonates (marbles), the stone materials are often rather similar to each other in many respects (i.e. mineralogical, physical–structural and chemical), and their sources are thus difficult to identify. Due to the fact that impurities are generally heterogeneous in this kind of geological source, a significant overlap with other sources may occur.

Among the most common impurities, such as silica, alumina, iron and manganese oxides, carbonates, carbonaceous materials, the alkalis occur usually in very small

amounts in limestones and marbles. Impurities present in the limestone during recrystallization affect the mineral/chemical composition of the marble that forms, thus the difficulty in source differencing of this kind of materials.

Another important issue related to the analysis of these artefacts is the fact that the objects involved are often unique in nature. To achieve the main goals, and regarding the rareness and importance of these stone artefacts only non-invasive analysis is possible. Analysing objects of historic and archaeological nature such as the stone idols should be non-destructive, i.e., respecting the physical integrity of the material object, but must be sensitive, so that provenance analysis can be done by means of not only major elements but also trace-element fingerprints, and multi-elemental, so that in a single measurement, information on many elements is obtained simultaneously. Also, to better obtain provenance correspondence between artefacts and potential raw materials, the same methodological approach should be performed on both.

Prompt Gamma Activation Analysis is one of the new techniques available to deal with this problem. Its basis is the radioactive capture of neutrons, or the (n,γ) reaction. During this nuclear reaction, an atomic nucleus captures a thermal or sub-thermal neutron, and emits a number of gamma photons promptly (Révay and Belgya 2004). Because of the low intensity of external neutron beams, PGAA can be considered non-destructive, and is applicable to objects that must be preserved intact and do not require sample preparation, being positioned directly in the neutron beam. Indeed, in most cases no significant long-lived radioisotopes are produced during the analysis. After some days of cooling, the analysed artefacts are in perfect condition to be returned to museums, collectors, and researchers. Nevertheless it is important to emphasize that PGAA, due to the high penetrability of the neutron will give the composition of the bulk material (not possible to evaluate composition of the body separately from the surface of the objects). This nuclear analytical technique for non-destructive quantitative determination of elemental compositions has been successfully applied to characterize archaeological objects made of various rocks (Kasztovszky et al. 2008). In the case study of this work the PGAA facility used was the Budapest Research Reactor, which has become a leading laboratory for applications of PGAA in archaeometry (Szilágyi et al. 2012; Kasztovszky et al. 2004).

6.3.3.2 Stone Idols and Ritual Stone Vessels Versus Geological Materials

Limestones in Portugal occur mainly near the shore, to the north of Lisbon and in the Algarve region, in the south. The main mining district of ornamental limestones is the Maciço Calcário Estremenho (MCE), located 150 km north of Lisbon. It is a limestone massif from the Mesozoic carbonated rocks tectonically elevated. Most of the MCE limestones are fine to coarse-grained calciclastic sparitic rocks. The region of Pêro Pinheiro, just North of Lisbon, is also one of the most traditional production centres of ornamental stones of Portugal. Quarrying has signs that it has been

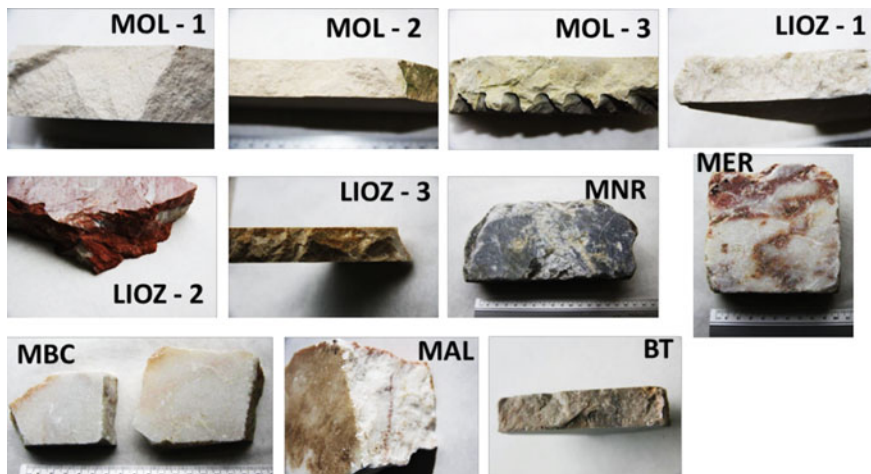


Fig. 6.11 Photos of the samples described in Table 6.1

started in Roman times. In the Algarve region ornamental stones are extracted near the localities of Escarpão (municipality of Albufeira), Mesquita (municipality of S. Brás de Alportel) and Santo Estevão (municipality of Tavira).



Fig. 6.12 Stone artifacts from Perdigões archaeological site; Inventory (UE) Ref. Lab

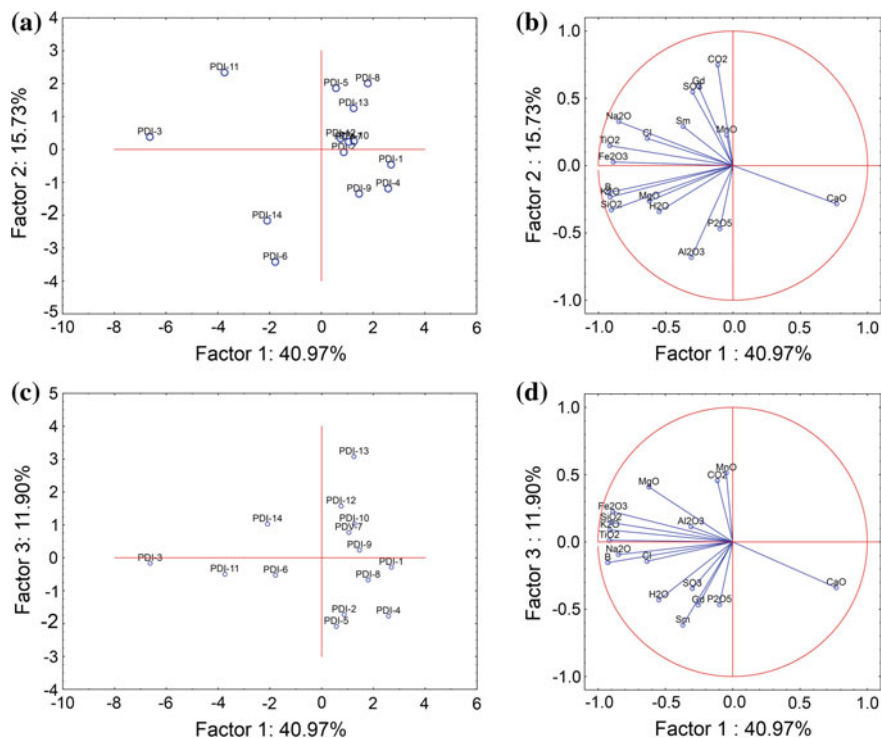


Fig. 6.13 Projection of the cases (a) and of the chemical elements (b) as variables, on the factor-plane 1 \times 2, for artefacts; Projection of the cases (c) and of the chemical elements (d) as variables, on the factor-plane 1 \times 3, for artefacts

Marbles occur mainly in the Alentejo region, where the Anticlinal de Estremoz is the main production centre. The earliest evidence for exploitation of this resource in this region dates back to the year of 370 B.C. (Martins and Lopes 2011). They present a large spectrum of colours, from white to dark grey, but the most common are the light-cream coloured with streaks of different tonalities (Figs. 6.11 and 6.12).

Based on archaeological and geological considerations, in the investigations for possible geological sources of stone idol artefacts found at Perdigões, the sources were separated into three categories: (a) nearby sources (~ 40 km distance—area known as the “marble triangle” Estremoz—Borba—Vila Viçosa, in Alentejo’s northeast, between Sousel and Alandroal, contains Portugal’s most important ornamental rock deposit.), (b) moderate distance areas (~ 130 km—limestone from Tavira—Tavira Breccia) and (c) remote areas (160–200 km—Limestones from Pêro Pinheiro—Lioz and from the Maciço Calcário Estremenho—Moleanos) (Table 6.1; Fig. 6.13).

Seven limestone samples (Moleanos limestone: MOL-1, MOL-2, MOL-3; Lioz limestone: LIOZ-1, LIOZ-2, LIOZ-3; Tavira breccia BT) and four marble samples (MNR, MAL, MBC, MER) were analyzed. Regarding artifact samples, thirteen stone idols and one votive vase were analyzed (Fig. 6.12).

For both artifacts and geological materials, the same methodological approach was used, so by using the same variables better comparisons and provenances ascriptions of provenance are achieved.

Prompt Gamma Activation Analysis of a total of 14 artefacts and 11 geological samples has been performed at the PGAA instrument of the Budapest Research Reactor. The PGAA instrument operates on a $7.6 \times 10^7 \text{ cm}^{-2} \text{ s}^{-1}$ intensity guided horizontal cold neutron beam. The samples have been irradiated with a beam collimated to 24 mm^2 or 44 mm^2 . The prompt- and delayed gamma photons emitted after neutron capture were detected with an HPGe detector in Compton-suppression mode. The typical acquisition time varied between 2300 and 8300 s, in order to collect statistically significant counts. The collected spectra have been evaluated with the Hypermet PC software; the element identification and calculation of concentrations are based on BNC PGAA library.

Table 6.1 Geological materials

Sample reference	Sample description	Note
MOL-1	Limestone “Moleanos”	Moleanos—Aljubarrota, Alcobaça (board of the Natural Park of Serra D’Aires and Candeeiros). Leiria. Central Portugal (~ 100 km North Lisbon)
MOL-2	Limestone “Moleanos”	Pé da Pedreira—Alcanede (Natural Park of Serra D’Aires and Candeeiros), Santarém, Portugal.
MOL-3	Limestone “Moleanos”	Ataija, Aljubarrota, Alcobaça. Leiria
LIOZ-1	Limestone “Lioz”	Pero Pinheiro, Sintra.
LIOZ-2	Limestone “Lioz”	Fervença, Terrugem, Sintra
LIOZ-3	Limestone Lioz—Lioz de Montemor	Montemor, Sta Maria de Loures, Loures, Lisboa
MNR	Marble “Negro Ruivina”	Lagar, Vila Viçosa Santos, Bencatel, Vila Viçosa, Évora
MER	Marble “Estremoz Rosado”	Estremoz (Santa Maria) Évora, Primavera, Bencatel, Santos, Vila Viçosa
MBC	Marble “Borba” “Estremoz” corrente	Évora, Estremoz/Borba/Vila Viçosa
MAL	Marble Alandroal	Alandroal
BT	Limestones—Brecha “Tavira”	Julião, Sta Catarina do Bispo, Tavira, Faro, S. Brás de Alportel

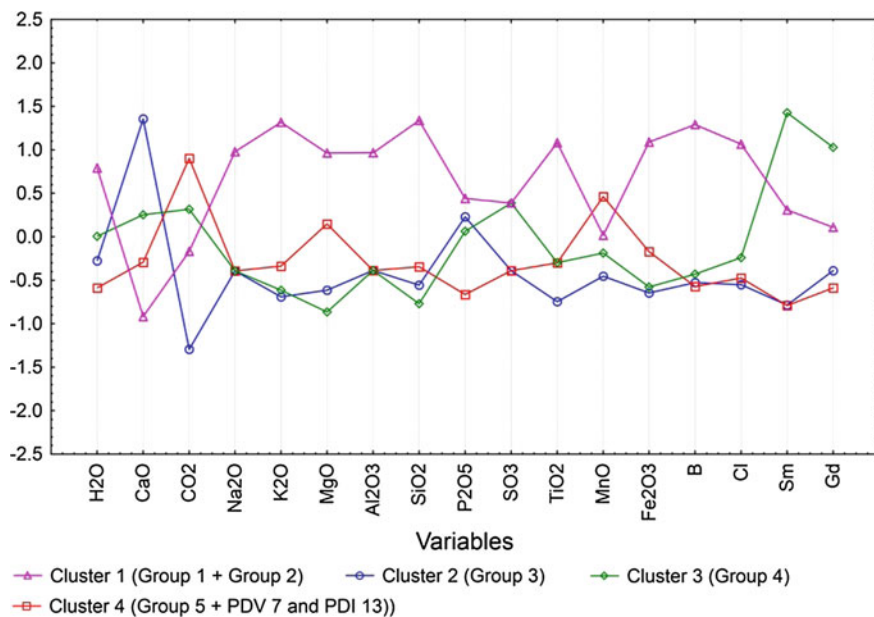


Fig. 6.14 Plot of means for each cluster by using the k-means clustering method on chemical contents as variables and artefacts as cases

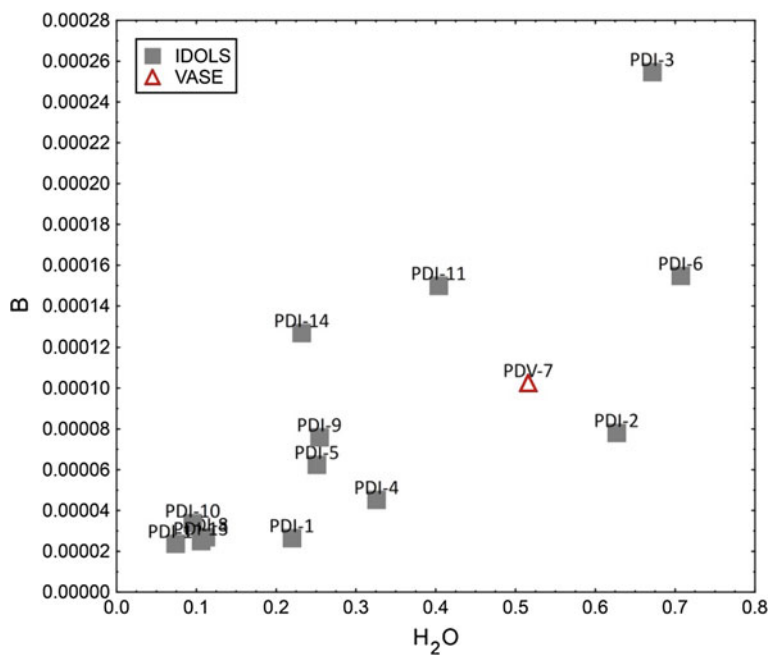


Fig. 6.15 Scatterplot of B against H_2O of Perdigões stone artefacts

6.3.3.3 Tracing Stone Artefacts at Perdigões Site

The first non-destructive analytical approach using PGAA for studying the limestone and marble artefacts from Perdigões, together with potential raw materials, provided chemical data that can be used to differentiate, from a compositional point of view, both artefacts and geological sources.

For the statistical interpretation of the PGAA data, only the oxides/elements which were above the quantification limit in most of the samples were used i.e. CaO, CO₂, LOI (H₂O), SiO₂, Fe₂O₃^t, MnO, K₂O, MgO, TiO₂, B, Cl, Sm and Gd.

The materials used to make the idol stone artefacts at Perdigões do not vary widely in the visual characteristics, as well as in their typology. The most commonly used materials appear to be limestones and/or marbles.

CaO and MgO are the most important elemental oxides in carbonates. In calcitic marble CaO is usually in the order 50–54 wt% while MgO is <15 wt%. Dolomitic or magnesian type marble has CaO values in the range of 28–31 % and MgO values in the range of 15–21 wt% (Goldschmidth et al. 1955).

In the studied samples CaO is the prevailing major component, ranging from 50 to 57 wt% in artefact samples, and between ~51 and ~56 wt% in the geological samples. All analysed samples have a relatively low MgO concentration (<2 wt%). The MgO content in the marble samples range from 0.4 to 0.61 wt%, in the limestones ranges from 0.26 to 1.6 wt%, and in the stone idols from 0.21 to 0.80 wt%. In Lioz-2 limestone no Mg was detected, and in 4 idols (PDI 1, 2, 4 and 8) and in the vase (PDV 7) also no Mg was detected.

The distribution of Ca/Mg and its reciprocal Mg/Ca ratio in limestones were utilized by Todd (1966) as a parameter for chemical classification (Table 6.2). The studied geological samples are all included in calcitic type marble and pure limestone, but the breccia Tavira sample (BT) is a limestone more enriched in Mg. Regarding the artefact samples, they are all pure limestones/calcitic marbles.

Mg/Ca ratios in raw geological samples vary from 0.029 to 0.009 %, and in artefacts from 0.01 to 0.007 %. In order to establish the paleo-environment of deposition Marschner (1968) pointed out that the Ca/Mg ratio is indicative of stability condition during the formation of carbonate rocks and any decrease in Ca/Mg ratio is related to corresponding increase in salinity. The high value of Ca/Mg ratio indicates comparatively less evaporation of sea water during the time of limestone deposition. From the results we may infer that Lioz limestones have in general lower Mg/Ca ratios (Table 6.2).

Table 6.2 Chemical classification of Shella limestone^a

Descriptive term	Standard ratio Ca/Mg	Reciprocal ratio Mg/Ca
Pure limestone	100.00–39.00	0.00–0.03
Magnesian limestone	39.00–12.30	0.03–0.08
Dolomitic limestone	12.30–1.41	0.08–0.71

^aTodd (1966)

Silica in carbonate rocks is contributed mainly from silicate minerals. The SiO₂ content in the marble samples range from 0.64 to 3.7 %, in the limestones ranges from 0.27 to 2 %, and in the stone idols from 0.09 to 2.9 %.

The alkali elements such as Na and K may be indicative of salinity levels (Na and K concentration in marbles tend to decrease with increase in salinity). Sodium was below detection limit in almost all the samples (only in two idol samples it was detected). Potassium was not detected in most of the geological materials, only in the Lioz Limestones and Ruivina and Alandroal marbles, ranging from 0.031 to 0.101 %; in the idol samples potassium was detected in half of the samples, ranging from 0.010 to 0.138 %. The smaller but appreciable concentration of manganese in carbonates is probably also attributable to similarity in ionic size with ion Ca²⁺. In marble samples manganese ranges from 0.0059 to 0.023 %, in limestones from 0.0074 to 0.0100 %, and in stone artefacts from 0.0035 to 0.0233 %. The low content of Mn in the studied samples may be attributed to the substitution of Mn by Ca.

The other oxide contents are generally low. Alumina was detected in a few samples, indicative of the absence of alumina-silicates, most of them the geological ones, ranging from 0.25 to 1.5 %. Iron oxide (Fe₂O₃ total in %) was detected in most of the samples, with a maximum of less than 0.39 %. In the marble samples iron ranges from 0.069 to 0.17 %, in the limestones from 0.068 to 0.19 % and in the stone artefacts from 0.05 to 0.39 %. Titanium oxides were also detected in most of the samples, in general with low values, ranging in the geological samples from 0.0066 to 0.025 % and in the stone artefacts from 0.0024 to 0.044 %. Phosphorous and sulphur were detected in very few samples, the first only in the idols (ranging from 0.016 to 1.9 %), and the second in a few idols and limestones with a maximum of less than 0.16 %.

We can infer loss on ignition (LOI) by the content of volatiles (CO₂, H₂O) present in the samples. In general, the sums of the two values are high, indicating high volatile content and by implication high carbonate content.

Regarding trace elements, immobile trace elements such as the Rare Earth Elements (REE) are usually important for provenance determination. With PGAA we have determined Sm and Gd. Gadolinium was detected only in two geological samples, and in a few stone artefacts, varying from 0.061 to 0.445 µg/g. Samarium contents in marbles ranges from 0.089 to 0.349 µg/g, in limestones from 0.041 to 0.380 µg/g, and in the stone artefacts from 0.038 to 0.446 µg/g. No Sm was detected in two idols and in the vase.

Boron contents of limestones are generally low, and are only elevated when the clay or organic contents are high, largely incorporated in illite, being used as a paleo-salinity indicator and marine environment. In the limestones studied in this work B contents were observed from 0.337 to 3.170 µg/g, and in the marble samples lower contents were detected, from 0.315 to 1.572 µg/g. In the artefacts B content also has a varied range, from 0.238 to 2.540 µg/g.

Chlorine was not detected in one marble sample and the other two have similar Cl contents (0.0023 to 0.0029 %). In two Lioz limestones Cl was not also detected, varying in the others from 0.0016 to 0.0079 %. Regarding artefacts, Cl was not detected in three, and in the others varies from 0.0011 to 0.0153 %.

It is important to emphasize that PGAA results correspond to the bulk sample, and idols have not been cleaned from surface deposits, which appears on some of them in considerable amounts, and is particularly enriched in crushed bones and soil. A special care was taken in order to evaluate whether the analysed chemical contents might have been affected due to bone contamination, and not specifically to the nature of the geological source, but no correlation was directly established between the analysed artefacts, and the chemical contents that are usually present in bones, and are also used for paleo nutrition research (Allmäe et al. 2012).

A statistical approach was performed for the fourteen stone idols analysed, as well as for the geological materials, taking into consideration chemical elements as variables. The analysis of obtained results for the stone idols, particularly the statistical results obtained by PCA and clustering methods applied on the chemical contents (Figs. 6.13 and 6.14), clearly detach the following groups: Group 1—PDI 3 and PDI 11; Group 2—PDI 6 and PDI 14; Group 3—PDI 1, PDI 4, PDI 9; Group 4—PDI 2, PDI 5, PDI 8; Group 5—PDI 10, PDI 12. Idol sample PDI 13 is not similar to any of the others. The vase sample analysed (PDV 7) has also a different chemical behaviour.

It is important to emphasize that the 2 samples from Group 1 were gathered in the cluster analysis mainly due to lower CaO contents and, because they are the only ones where Na was detected. Concerning the other elements significant differences were observed questioning the possibility of a same source, particularly PDI 3 has higher amounts of Ti and Fe, and PDI 11 more Cl. Moreover, none of the raw materials studied have a significant correlation with either of these two artefact samples. Group 2 is the only one where aluminium was detected, and also no correlation was established with the analysed geological materials. Group 3 differs from the others due to higher amount of calcium and lower of CO₂. Group 4 has the higher samarium and gadolinium contents. The group 5 has the higher potassium amounts, and high contents of magnesium. The sample PDI 13 has higher iron and manganese contents, and lower samarium contents. The vase analysed (PDV 7) has high content of H₂O, and low contents of titanium and Samarium, and has high boron content (Fig. 6.15).

Among geological samples, those from the nearby sources in the same “marble triangle” have chemical heterogeneities that make geochemical fingerprinting within them very challenging, as well as establishing correlations with artefacts. However, some correlations were possible to establish. For Groups 3, 4 and 5 artefacts the most likely source includes samples from the “marble triangle” Estremoz—Borba—Vila Viçosa, disregarding the Ruivina marble, which is the only one detachable from the others due especially to higher Si and lower Ca contents. The medium distance area sample—Tavira Breccia, like the latter, doesn't present any chemical affinity with the analysed artefacts. The remote area geological samples (MCE limestones—Moleanos, and Pêro Pinheiro—Lioz), don't seem to be a source for the artefacts, and LIOZ 2 is diverse from the others limestones. On the other hand, the vase PDV 7 is the only sample that has chemical similarity with a limestone sample, particularly the Moleanos 2 sample from MCE.

Among artefact samples no special correlation was established between the defined groups, and the respective archaeological contexts. Only samples PDI 10

and PDI 12 (Group 5) belong to the same context (pit 40), the other groups have artefacts from both “environment 1” and “pit 40” contexts. Unfortunately only one sample (PDV 7) was analysed from Sepulchral 1 context, and is also the only one pointing to a more remote source area.

6.3.3.4 The Achievements: Nearby and Long Distance Stone Procurement

Interpretations of the data may be used for general assessments of provenance, and PGAA became useful in distinguishing the various analysed artefacts revealing their diverse compositions, as well as being able to aid in the pointing to possible sources. A larger number of analyses may give more accurate results, especially for the geological materials. It is important to discuss the results obtained in a critical approach, taking into consideration that a more detailed geological survey and sampling are scheduled to be performed in the near future. Complementary analytical methods, including non-destructive ones are also planned to perform on both artefacts and geological material. Indeed, a larger number of geological samples may increase the accuracy of the predictions as well as make the indicated probability of provenance more realistic.

The stone artefacts at Perdigões show signs of both nearby and long distance procurement, as well as some of unknown attribution, as was already found for the ceramic materials (Dias et al. 2005). Among the stone materials, more than half (57 %) appear to have come from nearby, in particular from the marble triangle Estremoz-Borba-Vila Viçosa. Only one artefact definitely points to a long distance material source (in particular MCE limestones). The rest are from unknown sources.

Based on these results it would seem that imported foreign materials were used in parallel with regionally available materials. It is also interesting to notice that the object that points to the Lisbon peninsula limestones is of a different typological category (it is a vase) and was found in the tholoi tomb 1, which represents a different funerary procedure from that of the stone idols. So, different raw material provenances seem to be associated with different contexts and rituals, deepening the contrasts that we can see between these funerary features in Perdigões.

Besides provenance, one of the objectives of the study was to determine whether Prompt Gamma Activation Analyses (PGAA) could be successfully used to distinguish between marble/limestone samples originating from different known geological sources, as well as for matching artefacts to sources. It is important to emphasize that since the number of trace elements that can be measured by PGAA is restricted, also conclusions are limited, especially when dealing with such heterogeneous geological sources. Some of the present results might seem inconclusive; however, interpretations of the data may be used for general assessments of provenance.

6.3.4 *Distinguishing Style and Provenance of Ceramic Vessels*⁴

6.3.4.1 Summary of the Investigation

12 pottery fragments from the Inka Period (A.D. 1450–1532) Paria Basin, Bolivia were investigated by PGAA. One white sherd seemed to be foreign due to its different stylistic features (e.g. decorative motifs, paste). Based on their chemical composition it was possible to prove that 11 pots were manufactured from local raw material, while the white ceramic was non-local. In addition to its different style, the white pottery was formed from a raw material unknown in 30 km diameter circle around the archaeological site.

6.3.4.2 Standardized Inka Pottery: Imperial Ones and Resembling Others

This paper presents partial results of a comprehensive study, the Paria Archaeological Project (PAP 2004–2006), which—besides other topics—reconstructed the pottery handicraft of the Late Prehispanic Paria Basin of the Bolivian Altiplano (Condarco Castellón and Gyarmati 2012). As a result of the systematic surface survey carried out on a 95.5 km² area part of the Paria Basin in 2004 by the PAP, 113 sites ranging from the Formative Period (B.C. 1000–A.D. 600) until the Colonial Period (A.D. 1535–1825) were located. The most important and extended archaeological site of the basin is Paria, an Inka provincial administrative center (Gyarmati and Condarco Castellón 2014).

Pottery handicraft in the Inka Empire had a very characteristic pattern. As a part of the handicraft system, ceramic manufacturing was highly standardized. Hence, Inka Imperial pottery can be easily recognized through the whole Empire. Based on the archaeological record, it can be assumed that the Inka Imperial pottery manufacturing (1) was connected to certain workshops or (2) was assigned to strict conventions/regulations concerning the shape (categories were established by Meyers 1975, 1998; Matos n.d.), surface colour and treatment, and decorative motifs and their quality of the vessel. In this way, these items of the material culture could also express the strength and omnipotent aspect of the Empire (Fig. 6.16).

The majority of the Inka Period ceramic assemblage of the Paria Basin and the provincial center created during the Inka Period (A.D. 1450–1532) consisted of household pottery (various types of mostly undecorated or simple pattern painted pots, pitchers, and bowls used for storing liquids and raw foodstuffs, or for preparing food and beverages), and serving and storing vessels (jars, bowls, plates). According to their style, Inka Imperial, Inka imitation, mixed, local, and another

⁴Section written by Veronika Szilágyi.

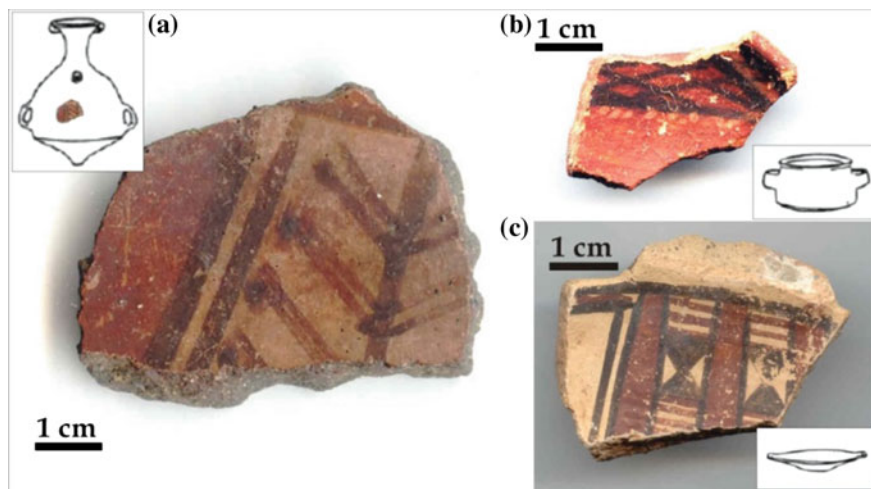


Fig. 6.16 Pottery fragments typical for the Inka Period assemblage of the Paria Basin. **a** No. PA/4, aribalo, Inka Imperial style; **b** No. BA/1, bowl, local style; **c** No. PA/5, plate, 'white pottery type'

style could be distinguished in the ceramic assemblage of the Paria Basin. The stylistic differentiation is based on a comprehensive macroscopic observation of form, quality and decoration. Inka Imperial style comprises vessels representing the best quality wares, and shapes and decorations are typical for the Inka culture. The Inka imitation style ceramics copy the Inka Imperial style vessels, but those are more poorly made and the decorations are less carefully executed. The mixed style blends the characteristics of the Inka and the Late Intermediate Period (in the following it is called Pre-Inka, A.D. 1100–1400). The local style is a ceramic type which survived from the Pre-Inka Period into Inka Period. The fifth stylistic group is represented by vessels which cannot be assigned either to the Inka or to the Pre-Inka pottery style. This group continues another Pre-Inka tradition that is foreign to the Paria Basin. It is typical for all the above mentioned five stylistic categories that the pots are red, orange, brown, grey or black on their surface, while they are entirely red or show sandwich structure in their profile.

'White pottery type' at Paria was made in the Inka Imperial style, decorated with motifs familiar from Cuzco polychrome pottery. This group incorporates bowls and plates of white, greyish white, or pinkish white body and sometimes of white slip. In terms of their shape, the whitish plates do not differ from the most common plate types made in the Inka Imperial style. Decorative elements are foreign to the altiplano (e.g. painted ulupica (*Capsicum cardenasii*) peppers, handle of a plate fragment modelled in the shape of a jaguar head).

Thus, we have to consider this 'white pottery type' as a member of the Inka Imperial style ceramic tradition but with a special manufacturing technology resulting in the white paste. It is an important question whether this technological

Table 6.3 Archaeological information and chemical data on the investigated Inka pottery fragments, and sedimentological information (gr. means granulometry) and chemical data on the comparative geological sample

Sample	BA/1	PA/1	PA/4	PA/6	P/12.13	P/12.17	P/12.20	P/34.143	P/53.79	P/63.7	P/92.4	PA/5	SED-01	SED-02	SED-03
Sample type	Pottery	Pottery	Pottery	Pottery	Pottery	Pottery	Pottery	Pottery	Pottery	Pottery	Pottery	Pottery	Sediment	Sediment	Sediment
Arch era	Inka	Inka	Inka	Inka	Inka-Col.	Inka-Col.	Inka-Col.	Inka	Inka	Inka	Pre-Inka	Inka			
Style/source	Local	Inka Imp.	Inka Imp.	Inka Imp.	Inka Imp.	Inka Imp.	Inka Imp.	Inka Immit.	Inka Immit.	Inka Immit.	Local	'White'	River bed	Terrace	Terrace
Functional/gr.	Bowl	plate	Aribalo	Aribalo	Bowl	Plate	Plate	Bowl	Plate	Plate	Plate	Plate	Fine sand	Fine sand	Fine sand
<i>Major elements (wt%)</i>															
SiO ₂	58.00	64.00	62.00	62.12	63.48	63.00	64.00	65.36	61.09	59.25	55.66	59.00	77.00	75.00	88.00
TiO ₂	0.97	0.94	0.64	0.74	0.76	0.62	0.85	0.69	0.79	0.76	0.88	1.23	0.53	0.60	0.34
Al ₂ O ₃	21.00	19.00	19.40	18.76	18.79	18.70	18.80	18.85	20.82	22.52	21.74	29.80	10.20	10.60	4.70
Fe ₂ O ₃	7.10	6.70	4.80	4.99	5.37	5.10	6.70	5.46	7.04	7.20	6.40	2.50	4.20	4.20	2.78
MnO	0.19	0.114	0.064	0.06	0.12	0.084	0.081	0.04	0.10	0.10	0.06	0.03	0.067	0.065	0.32
MgO	2.50	2.00	2.20	1.67	2.28	2.00	1.90	1.88	2.07	2.12	2.39	0.70	0.80	1.40	0.31
CaO	2.60	0.38	1.90	2.19	2.90	1.40	1.00	0.98	1.16	1.12	2.74	0.34	0.91	0.95	0.30
Na ₂ O	1.86	1.01	2.13	2.30	1.40	2.51	1.29	1.11	0.88	0.85	2.00	0.83	1.49	1.33	0.44
K ₂ O	4.50	4.70	4.80	5.31	4.02	5.20	4.00	4.69	4.68	4.77	3.76	4.10	2.41	2.52	1.13
H ₂ O	1.07	1.28	2.145	1.74	0.79	1.40	0.81	0.82	1.27	1.22	4.23	1.49	2.42	2.97	1.72
Sum	99.79	100.12	100.08	99.88	99.91	100.01	99.43	99.88	99.90	99.91	99.86	100.02	100.03	99.64	100.04
<i>Trace elements (ppm)</i>															
Ni	52	59	55	76	49	36	53	43	41	36	67	80	35	38	18
Sm	5.7	9.7	5.8	6.5	5.6	5.8	5.9	5.1	5.7	5.4	7.0	8.9	3.7	4.1	2.1
B	94	91	109	118	149	143	117	205	136	130	104	125	61	93	74
Cl	154	60	350	400	78	430	600	295	86	94	582	32	69	400	95
Gd	6.4	9.0	6.0	6.0	6.0	5.0	6.8	5.1	6.4	6.2	6.4	10.6	4.2	4.9	2.8

trick is based on (1) the usage of a special raw material or (2) the introducing of a special firing technique. Comparison of the chemical composition of the ‘white pottery type’ with the classical Inka Imperial style vessel fragments can give answer to this problem.

The 12 pottery fragments investigated were found in the systematic surface survey of the PAP at different archaeological localities of the Paria Basin and from Inka Period context. According to the functional classification, these sherds belonged to plates-bowls or aribalos (narrow-necked jars similar to Roman amphorae) (see Table 6.3). One sample (No. PA/5) represents the ‘white pottery type’ described above, while other 11 sherds show stylistic features typical for the Inka Imperial, Inka imitation or the local style.

In addition to the archaeological samples, three comparative geological samples as potential raw materials were also subjected to PGAA. These samples were collected from the alluvial sediments of the Paria Basin.

In order to get a larger data set, comparative chemical data from an earlier investigation (Szilágyi et al. 2012) in the framework of the PAP was also utilized, as it is shown in Fig. 6.17. Those chemical concentrations were measured on archaeological and comparative geological materials by XRF and INAA.

6.3.4.3 Investigation of Pottery by PGAA: Is that a Good Choice?

PGAA seemed to be an effective analytical method for the chemical investigation of ceramics because of its non-destructive feature. Compared to other bulk chemical methods, it is possible to get the average composition without time-consuming

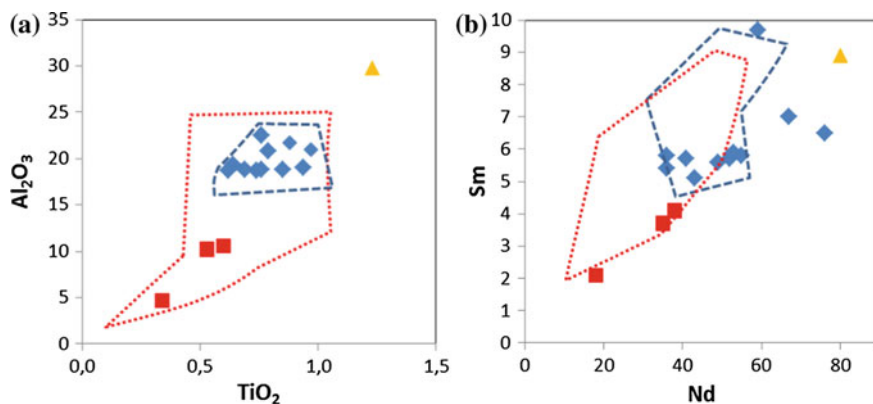


Fig. 6.17 Discriminating bivariate diagrams for **a** major-minor (TiO_2 vs. Al_2O_3) and **b** trace elements (**b**, Nd vs. Sm) (plotted concentrations are in wt% and $\mu\text{g/g}$). Inka ceramics measured by PGAA; ■ raw materials measured by PGAA; ▲ ‘white pottery type’ measured by PGAA; — — — Inka ceramics measured by other methods (Szilágyi et al. 2012); ····· raw materials measured by other methods (Szilágyi et al. 2012)

preparation of homogenized powder or fused bead. However, it is important to make sure that the irradiated volume of the sample does not contain any large-sized inhomogeneity (e.g. gravel-sized mineral/rock inclusion, thick decorative pigment layer, weathered layer, crack filled with secondary/post-burial phase). Since the neutron beam entirely penetrates the relatively thin and relatively light material of ceramics, it is not possible to separately measure the ceramic body (paste) and the surface layers (e.g. pigments, slips, glazes). Hence, it is important to know exactly which part of the pottery fragment was irradiated during the measurement. It will fundamentally determine the interpretation of the gained concentration data.

For example, the 12 pot sherds investigated here are 5 to 15 mm thick, and have <1 mm slip and/or <0.5 mm pigment layer on their surface. It is known that the pigments used are earth pigments and the slips are refined clayey suspensions. Hence, their composition is very similar to the ceramic body composed of clay minerals and other silicates. In addition, their quantity is almost negligible compared to the ceramic body. The applied collimations of the neutron beam were 10 mm², 24 mm², 1 cm × 1 cm and 1.41 cm × 1.41 cm. That means about 0.135 to 8.1 g (assuming a 2.7 g/cm³ average density for ceramics) of the irradiated volume per sample. This mass is a representative amount to get information about the bulk chemical composition of the ceramic samples.

Another parameter to decide about is the optimal acquisition time per sample which was 3000–5000 s (live time) in the case of the 12 sherds investigated. Optimal time means long enough to get statistically reliable information (counts) in the spectrum, and as short as possible to save time. It is also conditioned by the counting rate which can be practically modified by collimation.

As an advantage, the range of elements measurable with PGAA (in this study—major: Si, Al, Fe, Mg, Ca, Na, K, H; minor: Ti, Mn; trace: Nd, Sm, Gd, B, Cl) can be more or less compared to other analytical methods (especially XRF) applied to another sample set of the Paria pottery assemblage (Szilágyi et al. 2012). Since the aim of the archaeometric study was to determine the provenance, the observed chemical elements were the geochemically immobile (partly incompatible) major, minor and trace elements. The oxides of the following major (SiO₂, Al₂O₃, partly Fe₂O₃) and minor elements (TiO₂, MgO), and trace elements (Nd, Sm and Gd) were considered. Immobile elements behave relatively constantly during the pottery manufacturing process (washing of the clay, tempering or mixing, firing) and the burial (leaching out or precipitation in soil solutions). Hence, these elements can show the initial/original chemical concentrations of the raw material even in the final product (i.e. pottery). As an experiment for ceramic archaeometric studies, other immobile trace elements (e.g. V, Cr, Co and Sc) would also be useful to be measured. Although, their detection is possible by PGAA, the quantification is possible only with large uncertainty. Another group of trace elements (e.g. other REEs, Th, U, Hf, Ta, As, Sb and Cs) cannot be successfully measured by PGAA but the data set can be easily completed with the help of INAA which is a conventional complementary method in trace element measurements.

6.3.4.4 From Chemical Data to Archaeological Interpretation

The 12 pot sherds investigated (belonging to Inka Imperial, Inka imitation and local styles) show a major element composition similar to an average argillaceous sedimentary rock (claystone, shale, siltstone). For comparison, see the PAAS (Post Archaean Australian Shale) which is a preferred standard material in geochemistry for fine-grained siliciclastic sediments (Nance and Taylor 1976; Taylor and McLennan 1985; McLennan 1989, 2001). The major element distribution for these sherds can be characterized with a moderate silica/alumina ratio (between 2.5 and 3.5), relatively high concentrations of specific cations in the silicate phases ($1.67 < \text{MgO} < 2.50$ wt%, $0.34 < \text{CaO} < 2.90$ wt%, $0.85 < \text{Na}_2\text{O} < 2.51$ wt%), while TiO_2 (between 0.62 and 0.94 wt%) and Fe_2O_3 (between 4.80 and 7.20 wt%) show lower concentrations compared to the average argillaceous sediments. Concerning the trace element distribution, Inka ceramics have relatively high concentrations of rare earth elements (REEs) ($36 < \text{Nd} < 76$ $\mu\text{g/g}$, $5.1 < \text{Sm} < 9.7$ $\mu\text{g/g}$, $5.0 < \text{Gd} < 9.0$ $\mu\text{g/g}$).

The major and trace element distribution of sample No. PA/5 (i.e. the representative of the ‘white pottery type’) is basically different from that of the other samples. The low silica/alumina ratio (1.98), the high TiO_2 (1.23 wt%) and average rare earth element content ($\text{Nd} = 80$ $\mu\text{g/g}$, $\text{Sm} = 8.9$ $\mu\text{g/g}$, $\text{Gd} = 10.6$ $\mu\text{g/g}$), and the low Fe_2O_3 (2.50 wt%), MgO (0.70 wt%) and CaO (0.34 wt%) content of the sample underlines a peculiar chemical character. This element distribution pattern quite differs from the average argillaceous sedimentary composition (i.e. PAAS). This supports the idea of a different geological origin of the ‘white pottery type’. The enrichment of the TiO_2 , Al_2O_3 and REEs can possibly indicate rather a metamorphic origin of the raw material (e.g. mica schist).

The three comparative fine-grained sand samples have much higher silica/alumina ratios (between 7.1 and 18.7) which reflect more sandy sediments than that of the raw material of the investigated ceramics. This characteristic affects the whole chemical element distribution of the samples, i.e. parallel with the higher SiO_2 concentration all other elements (especially TiO_2 , Al_2O_3 , MgO , K_2O , REEs) have lower concentrations than in the ceramic samples.

Figure 6.17 shows bivariate correlation diagrams of major (Fig. 6.17a, TiO_2 vs. Al_2O_3) and trace (Fig. 6.17b, Nd vs. Sm) elements of both the samples measured by PGAA and the data set published elsewhere (Szilágyi et al. 2012). Chemical data of Inka Imperial, Inka imitation and local style ceramics fit very well into the cluster outlined by the earlier data, although REEs show higher scattering by PGAA than by other methods. The three comparative fine-grained sand samples plot at the edge of the cluster outlined by the earlier data. It can be the result of the coarser grain size of the sand samples measured by PGAA, while the earlier work investigated clayey-silty sediments, too. Although, the three fine-grained sand samples could not act as real raw materials of the ceramics, it is clear that the cluster of the raw materials overlap with the cluster of the ceramics. In addition, the potential raw

material samples of the Paria Basin much rather similar to the Inka Imperial, Inka imitation and local style ceramics than to the ‘white pottery type’ which on both diagrams plots to the right upper corner.

Based on the chemical data of the investigated 12 pottery and the three sand samples, it can be assumed that the Inka Imperial, Inka imitation and local style ceramics of the Paria Basin and the provincial centre derived from local raw materials. The one representative of the ‘white pottery type’ seems to be foreign to the local sources of the Paria Basin regarding its chemical composition. Even if the comparison with the raw materials is extended to a data set collected from a 30 km circle around the archaeological site (Szilágyi et al. 2012), the above statement is correct.

6.3.4.5 Concluding Remarks

12 pottery fragments from the Inka Period Paria Basin, Bolivia were investigated by PGAA. One white sherd, though considered as member of the Inka Imperial style ceramic tradition, seemed to be manufactured with a special technology resulting in the white paste. Based on the chemical composition it was proved that one specialty of the technology was the usage of a special raw material (and not the application of a special firing technique). In addition, it was possible to establish that 11 pots were manufactured from local raw material, while the ‘white pottery type’ was non-local. Apart from its different style, the white pottery was formed from a raw material unknown in 30 km diameter circle around the archaeological site.

The statements of this study are established on the measurement of a single ‘white pottery type’ fragment. Even so, assuming that the same raw material was used for all the white coloured fragments (the pinkish hue can no doubt be attributed to the firing), vessels made in the Inka Imperial style but with white paste can be regarded as genuine imports. Moreover, almost 100 % of the ceramic assemblage of the Paria Basin and the provincial center created during the Inka Period had been manufactured locally, including the vessels previously considered as import wares from Cuzco (Gyarmati and Condarco Castellón 2014). ‘White pottery type’ as high prestige import wares, principally occur among the plates made in the Inka Imperial style used for consuming food.

The 176 analyzed sherds (Szilágyi et al. 2012; Szilágyi 2010; Gyarmati and Condarco Castellón 2014) included no more than nine bowl and plate fragments fired to a white or pink color made from a raw material not typical to the region. Although it was not possible to perform comparative analyses, the paste, decoration, and surface treatment of these vessels suggested that they had presumably been produced in the Milliraya state ceramic workshop (see Alconini 2013). Tschopik (1946) labelled this ware as Taraco Polychrome based on its primary distribution.

Fig. 6.18 Photo of the Eighteenth Dynasty (15th c. B.C.) Egyptian sealed pottery (Property of the Museum of Aquitaine in Bordeaux, France)



6.3.5 *Looking Inside a Closed Egyptian Vessel*⁵

A sealed pottery vessel originated from the Eighteenth Dynasty Egypt (15th c. B.C.) has been investigated using terahertz (THz) radiation, X-rays and neutrons. The vessel—among over 300 other objects found in pharaohs' graves—was bought by Dr. Jean Ernest Godard during his 1861 Egyptian mission. The object now belongs to the collection of the Museum of Aquitaine in Bordeaux, France (Saragoza 2008). A photo of the object can be seen on Fig. 6.18. A computed tomography with THz electromagnetic waves aimed to reveal its content non-destructively. Furthermore, owing to their higher spatial resolution and contrast, X-rays and neutrons were used to study its fabrication and conservation more precisely, together with the nature of its contents (Abraham et al. 2014). With neutron tomography, we were able to determine the method used to seal the jar, as well as the finer structure of the inner content. The investigations aimed to produce images with the help of neutrons—the methods have been discussed in Sect. 4.4. Applying a collimated beam of cold neutrons, elemental compositions of selected parts of the object were possible to determine. When

⁵Section written by Emmanuel Abraham, Maryelle Bessou, Zsolt Kasztovszky.

comparing the results of elemental analysis obtained from the void and full parts of the vessel, we can estimate the nature of the inner content, which was assumed to consist of dried germinated seeds (Abraham et al. 2014).

The neutron-based investigations of the Egyptian pottery have been performed at the NIPS-NORMA station of the Budapest Neutron Centre. On the basis of neutron radiography and tomography images taken at NIPS-NORMA, representative parts of the object have been chosen to determine their elemental composition. This method, which can save significant beamtime compared to the elemental mapping of the entire object, is called NR/NT-driven Prompt Gamma Activation Imaging (PGAI) (Kis et al. 2015). A cold neutron beam with a $2.7 \times 10^7 \text{ cm}^{-2} \text{ s}^{-1}$ thermal equivalent flux has been collimated to $10 \times 10 \text{ mm}^2$ area; the composition of selected parts have been analysed and semi-quantitative elemental compositions of each part were obtained. The acquisition time for each selected region of the PGAI measurement was set to 60,000 s. As neutrons travel through the whole body of the jar, they irradiate the wall of the jar, some void part, as well as the unknown inner content—in a chord-like volume.

Because of the special geometric arrangement of the different materials to be analysed, it was decided to irradiate the inner content together with the jar wall, as well as an irradiation of a part without filling material, which was performed separately (see Fig. 6.19). It would have needed a special measurement arrangement to analyse only the inner content from one single measurement. Unfortunately, collimating both the beam and the solid angle of the gamma detection would have significantly increased the acquisition time. Comparing the result of the two PGAA measurements, one can estimate the element composition for the inner content of the jar. Furthermore, the composition of the closure plug has also been determined similarly.

The elemental compositions of three different parts, determined by PGAI are given in Table 6.4. On Fig. 6.19, we indicate the parts where elemental analysis has been done marked with red boxes. The investigated parts are the following: (i) ‘Full’: irradiation of the inner content and surrounding wall; (ii) ‘Void’: irradiation of a void part of the bottle without the filling material (e.g. practically only the wall material); (iii) ‘Plug’: irradiation of the closed neck region and surrounding walls. Since the geometry of the investigated sample is indefinite, and the efficiency and self-absorption corrections are uncertain, absolute concentrations of the identified chemical elements were not possible to obtain from the measured data. Instead, one can consider the results in Table 6.5, as a semi-quantitative identification of significant chemical elements. One can see that characteristic elements for ceramics (Na, Mg, Al, Si, K, Ca, Ti, Mn and Fe) are roughly in the same amounts in both ‘Full’ and ‘Void’ measurements, confirming the correctness of this approach. On the other hand, some elements characteristic of some organic material (H, C, N, S and Cl) show an excess in case of the ‘Full’ measurement, compared to the ‘Void’ one. Furthermore, the composition of the plug shows an excess of H, C, N, S and Cl too, which supports the organic nature of the string-like closure material.

As a result, we can finally conclude that the content could consist of germinated seeds (or any other dried organic material) such as barley which was a staple cereal

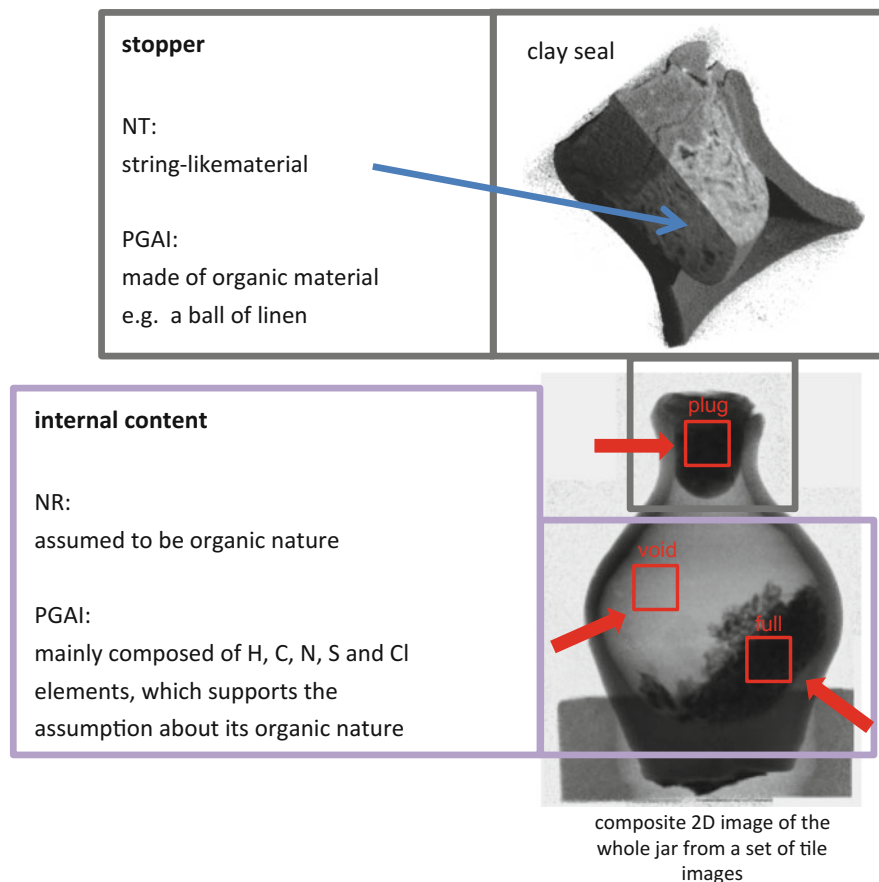


Fig. 6.19 Visualisation of inner parts of the sealed pottery by Neutron Tomography (NT) and by Neutron Radiography (NR); determination of composition by Prompt Gamma Activation Imaging (PGAI) at the Budapest Neutron Centre

Table 6.4 Composition of different parts of the sealed Egyptian pottery, measured by PGAI at the Budapest Neutron Centre

Full			Void			Plug		
El	wt%	Rel. Unc. %	El	wt%	Rel. Unc. %	El	wt%	Rel. Unc. %
H	1.3	8	H	0.4	11	H	1.4	6
B	0.0015	8	B	0.0016	11	B	0.0012	6
C	8.0	11	C	<D.L.		C	16.1	8
N	0.85	10	N	<D.L.		N	0.18	23
O	60.0	5	O	61.0	7	O	52.6	6
Na	0.89	8	Na	1.24	11	Na	0.95	7
Mg	1.3	9	Mg	1.6	14	Mg	1.2	8

(continued)

Table 6.4 (continued)

Full			Void			Plug		
Al	5.4	8	Al	6.3	11	Al	4.5	7
Si	14.4	8	Si	19.5	11	Si	13.2	6
S	0.046	23	S	< <i>D.L.</i>		S	0.14	8
Cl	0.058	8	Cl	0.033	11	Cl	0.18	6
K	0.93	8	K	1.05	11	K	0.66	6
Ca	2.2	9	Ca	2.3	11	Ca	4.5	7
Sc	0.0011	8	Sc	0.0006	17	Sc	0.0007	7
Ti	0.61	8	Ti	0.82	11	Ti	0.56	7
V	0.0082	15	V	0.016	13	V	0.012	10
Cr	0.039	24	Cr	0.042	16	Cr	0.017	10
Mn	0.071	8	Mn	0.098	11	Mn	0.065	7
Fe	4.0	8	Fe	5.6	11	Fe	3.6	7
Nd	0.0024	15	Nd	0.0032	14	Nd	0.0024	11
Sm	0.00042	8	Sm	0.00056	11	Sm	0.00034	7
Gd	0.00032	10	Gd	0.00046	13	Gd	0.00028	9

<*D.L.* means “less than the Detection Limit”

of Ancient Egypt. We also concluded with high confidence that the internal plug could be made of a ball of linen. Further investigation should consist in characterizing the molecular composition of these materials using a portable THz spectrometer in order to avoid the transportation of the fragile object and the use of a huge and costly instrument such as a research reactor.

6.3.6 *Small and Ultra Small Angle Neutron Scattering Investigation of Marbles*⁶

6.3.6.1 Description of the Investigated Artifacts

Investigations by means of SANS and USANS on marbles try to reveal a relationship between the mesoscopic structural evidences and the genetic conditions of the samples, known as the metamorphic process. This process consists on a iso-chemical evolution, depending on various parameters such as temperature and pressure, of a protolith, usually a a sedimentary carbonate with a highly variable calcitic–dolomitic composition, or a previous marble. It is characterized by the destruction of the originating minerals (mostly calcite—dolomite) followed by a further crystallization process. The metamorphic process proceeds through the progressive building up of structural units of increasing size: starting from

⁶Section written by Fabrizio LoCelso and Valerio Benfante.

elementary cells (nanometers, intermediate aggregates (micrometers), to the final crystals (millimeters) (D'amico et al. 1987). Here we show a selected group of white marbles, coming from several quarries in Northern Italy (Carrara, Elba, Musso, Campiglia) that have, despite their similar chemical composition, a different metamorphic history. The mesoscopic features will highlight their metamorphic evolution (the most important parameter is the temperature at which the process has taken place) within a rather confined geographical area, i.e. the Mediterranean basin, a region well known from the geological point of view.

6.3.6.2 Scientific Question

The use of SANS and USANS for fingerprinting white marbles originates from the fact that this material has been widely used, through the centuries, as a common building stone in monuments, statues and other objects of archaeological or cultural heritage interest. Numerous well known quarries are spread in the Mediterranean basin between Northern Italy and Greece, so it is clear that not only artistic and technological reasons move the archeologist but also the provenance and commercial routes that can testify social contacts between different cultures. It has always been quite a challenge to identify the origin of white marbles (they look very similar at plain sight) and usually petrographic and isotopic analytical investigations have been used for fingerprinting purposes. These two techniques have surely well characterized the microscopic and macroscopic size domain while the scattering techniques will try to bridge the gap between the two, giving structural information on the mesoscopic regime. Indeed the combination of Small Angle Neutron Scattering (SANS) and Ultra Small Angle Neutron Scattering (USANS) allows indeed to obtain a way to interpret a possible link between the structure at mesoscopic level and the process that originates the marble, the metamorphic process. To this respect the thermal genetic characterization of the samples is a very important issue, since the temperature basically is the most important parameter in the history of a marble formation. In general, the maximum temperature involved in a metamorphic event can be calculated by using different mineralogical and geochemical geothermometers. For example trace minerals (silicates, etc.) acting as thermal markers, the solid solution of magnesite in the calcite lattice (Mg substituting for Ca), of iron sulphide into sphalerite (Fe substituting for Zn), which are in turn dependent on the crystallization temperature, the fluid inclusions which remain trapped in a number of crystals, and any eventual floating minerals, the isotopic fractionations concerning different mineral pairs (and nuclides): carbonate—carbonate (oxygen and carbon), carbonate—silicate or carbonate—oxide (oxygen). The petrographic investigation in the absence of the latter geothermometric information, can give an estimated metamorphic temperature by means of a simple observation (microscope with transmitted polarized light) of the marble in thin section (grain size, kind of aggregation, etc.).

6.3.6.3 Results

Geological materials are in general complex multiphase systems. However marbles, when investigated by means of neutron scattering, even if they are strictly multiphase they can be treated as a two phase system, as most of the scattering originates from the contrast between the inorganic components and the voids.

From the scattering theory we know that when a beam of neutrons radiation illuminates a volume V in which scattering centers (i.e. atoms and/or their aggregates) are distributed in real space (r) according to a distribution law $\rho(r)$, scattering events take place and a scattered beam will be generated, whose coherent elastic differential scattering cross-section (often simply called scattering intensity) is related to the structure (distribution law $\rho(r)$), to the composition of the sample and to the scattering variable q ($q = 4\pi\sin\theta/\lambda$, where 2θ is the scattering angle and λ is the wavelength of the incident radiation). The form of this relationship depends on the degree of complexity of the structure present in the sample.

The scattering from geological systems has been described in terms of fractal structures (mass and/or surface fractals) and fractal exponents (Wong et al. 1986; Lucido et al. 1989, 1991). The possibility of extending the range of the scattering variable with the combined USANS and SANS techniques indeed allow a spatial resolution range of structural determination which can possibly reach about 30 nm in almost ideal conditions (Agamalian et al. 1997). The interpretation of scattering data from marbles, i.e. rocks originated from the building up of primary particles undergoing a continuous series of interaction processes mainly controlled by the metamorphic degree, depending mainly from the temperature (D'amico et al. 1987; Gorgoni et al. 2002) has been done with a rather simple model for describing fractal systems; a hierarchical structure model that takes into account the existence of a network of fractal aggregates of size R formed by monodispersed solid primary particles of radius r (Emmerling et al. 1994; Schmidt 1991).

The scattering intensity is therefore expressed as follows:

$$I(q) \propto P(q, r, D_s)S(q, r, D, R)$$

where

$$P(q, r, D_s) = (1 + (\sqrt{2}/3) q^2 r^2)^{0.5(D_s-6)}$$

and

$$S(q, r, D, R) = 1 + (D\Gamma(D-1)/qr^D)(1 + 1/qR^2) \sin[(D-1) \arctan(qR)]$$

$P(q, r, D_s)$ being the form factor referring to the single primary particle and $S(q, r, D, R)$ the structure factor that reflects the degree of order of primary particles along the aggregates (of size R). D_s is related to the dimensionality of the interfacial region of the primary particles, and its value must be between 2 and 3 ($D_s = 2$ is for smooth

particles following the Porod law $I \propto q^{-4}$). D is the power law exponent of the fractal aggregates.

Figure 6.20 (right column) shows schematically such a model (symbols are experimental data, the black solid line is the fit of the model to experimental data). At very low q the intensity is high and with tendency to level off; in other words, neutrons are probing length scales at which the system does no longer show any inhomogeneities and therefore it cannot be resolved. For larger values of q ($q > 1/R$) the scattering intensity drops because clusters of particles of radius R are being resolved; indeed it follows a power law characterized by the exponent D which is related to the fractal dimension or the branching of the aggregate. Going towards even larger q values it is possible to evaluate the radius r of the primary particles as well as D_s .

Based on the information available in the literature (Di Pisa et al. 1985; Cortecchi et al. 1994; Pertusanti et al. 1993; Leoni and Tamponi 1991; Diella et al. 1992; Siletto et al. 1990), thermal ranges, related to the metamorphic process for the various samples were derived and reported in Table 6.5.

The results of the chemical analyses indicate that all samples are mainly calcitic, with only a minor, although variable, magnesian (i.e. dolomitic) component. Such evidence is important in order to exclude any significant mesostructural effects to be eventually related to a highly variable crystal chemistry (i.e. variable calcitic–dolomitic composition). The thin section photographs reported in Fig. 6.20 (left columns), all taken at the same magnification for comparative evaluation, show the macroscopic structure of the samples. Their fabric is rather homogeneously granoblastic (i.e. homeoblastic) in almost all cases. Only sample A from Musso has a preferential orientation (i.e. lineation) of the tiny calcite grains forming the matrix in which a number of rather dispersed, larger crystals are included. Samples B and C from Carrara show a more markedly homogeneous fabric and very regular crystal boundaries, giving an overall polygonal to mosaic configuration. This is due to metamorphic equilibrium reached over very long time at the metamorphic temperature (Gorgoni et al. 2002). Generally speaking, the rough temperature–grain size correlation indicated above is confirmed by these pictures, with the exception of sample E. In fact, its high thermal range (500–600 °C, Table 6.5) is not consistent with the average grain size (0.25 mm), which is apparently indicative of a medium to medium-low metamorphic degree.

Parameters derived from the fits are reported in Table 6.5. It appears clearly that the radius r of the primary structural units increases homogeneously as a function of the thermal history of the samples, thus confirming the general control of the temperature on the dimension of the structural units. However, in the case of the scattering data, the correlation is perfectly shown by all the marbles analyzed, including sample E, meaning that the temperature–size relationship is better defined at the mesoscopic level compared to the macroscopic one. With the exception of sample A, the dimensionality of the interfacial region of the primary particles (D_s) roughly increases in the same direction, passing from 2 (very smooth surfaces) for the low and medium-low metamorphic degrees to around 2.3 for the higher grades. This would seem to indicate that the surface of these primary particles becomes

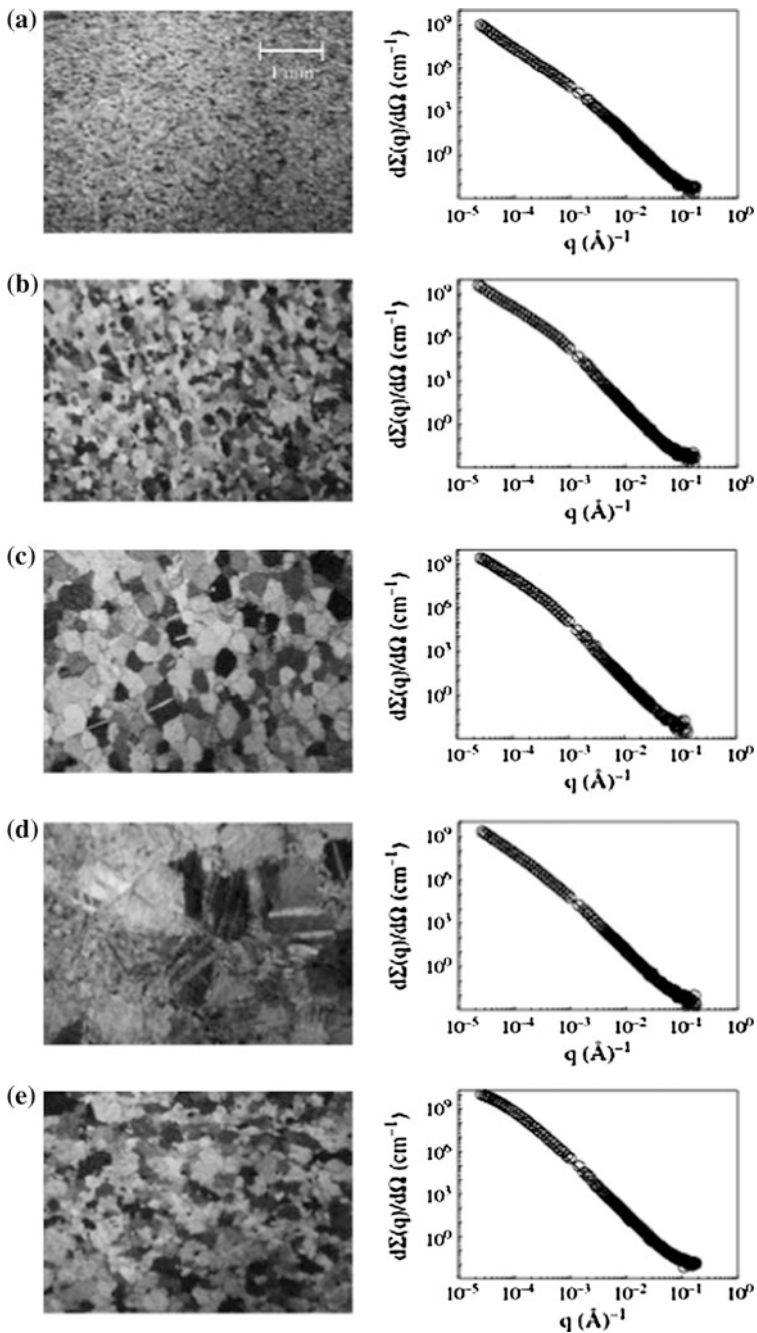


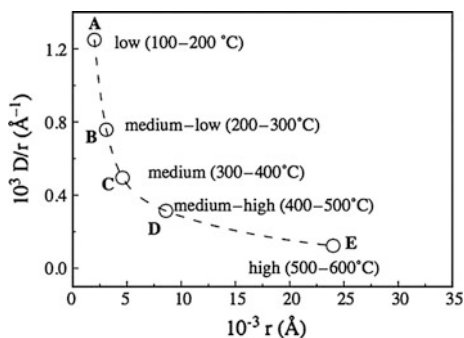
Fig. 6.20 Thin section photographs showing comparatively, at the same magnification, the macrostructural characteristics (i.e. fabric) of the marble samples (polarized light and crossed Nicols). Alongside are the corresponding measured neutron scattering cross sections

Table 6.5 The samples considered and analytical results from the fit for 5 different samples

Sample	Average grain size (mm)	Metamorphic degree (thermal ranges in °C)	D	r (Å)	$10^3 D/r$ (Å ⁻¹)	D _s
(A) Musso	0.05	Low (100–200)	2.50	2	1.225	2.45
(B) Carrara I	0.1	Medium-Low (200–300)	2.35	3.1	0.758	2
(C) Carrara II	0.35	Medium (300–400)	2.28	4.6	0.495	2
(D) Elba	1.5	Medium-High (400–500)	2.70	8.6	0.314	2.33
(E) Campliglia M.	0.25	High (500–600)	2.95	24	0.013	2.25

rougher with the increasing crystallization temperature. In such a context, it is interesting to notice that samples B and C from Carrara are the ones characterized by the smoothest possible surfaces of the structural units at both the meso- and macro-scale. The anomalously high D_s value for sample A could be explained by considering, in addition to the temperature, the effect of other parameters and features on the smoothness of the surface of the mesostructural units: (i) the amount (and kind) of fluids and the related control on the rheology of the system; (ii) the importance of time (at a given temperature) for the attainment of equilibrium or disequilibrium conditions, similarly to what is found at the macroscale level; and (iii) the possibility of a metamorphic evolution is more complex than usual, as already indicated. The situation for sample A from Musso is rather peculiar. On one hand, the prevailing matrix formed by very fine calcite crystals (Fig. 6.20a) is indicative of low crystallization temperatures (100–200 °C, Table 6.5). This anomalous feature has to be related to a rather complex evolutionary history, as indicated above, with special reference to the occurrence of those “retrograde phenomena” involving one or more further dynamometamorphic (low temperature) re-elaboration(s) of a previous higher grade marble, a process not unusual in the Alps, including this central-southern section (Diella et al. 1992; Siletto et al. 1990). Such an evolutionary complexity is probably responsible for a sort of memory

Fig. 6.21 D/r versus r plot for the five samples investigated, with indication of the corresponding metamorphic degree



effect. The relatively straightforward examination of the data already points out to a correlation between the fit parameters of the scattering data and the metamorphic conditions. As discussed above, the anomalies found hamper the use of simple correlation graphs, also on account of the limited (although representative) number of samples considered.

However, the binary correlation becomes much more significant when preceded by further processing of the data, i.e. by a normalization procedure. In particular, the D/r versus r correlation graph shown in Fig. 6.21 clearly indicates a hyperbolic trend, which can be easily explained considering the effect that the different metamorphic conditions have on the general mesostructural characteristics of the marbles analyzed.

6.3.6.4 Concluding Remarks Related to Marble Characterisation

A hierarchical structural model was used to analyze combined USANS—SANS patterns of white marble samples in order to relate their genesis with the features observed in the scattering experiments. By properly processing the fit parameters, we have been able to connect the characteristic parameters of the mesoscopic structure to the metamorphic evolution. In particular, the dimension r of the building units shows better correlation with the crystallization temperature than determined for the whole crystals at a macroscopic level. A similar but somewhat poorer correlation is found from aggregation (fractal dimension, D) and the surface characteristics (dimensionality of the interfacial region, D_s) of these intermediate clusters.

6.4 Final Thoughts

In the above examples, we have shown how neutron analytical methods can contribute to the research of tangible Cultural Heritage. In particular, a large number of specific questions regarding the provenance of objects can be answered with the help of analytical information (i.e. elemental- or isotopic composition, structure).

Obviously, during the investigations, any kinds of damage—neither visible nor invisible—are not allowed in case of valuable objects. Although a few methods, for instance the Instrumental Neutron Activation Analysis requires sampling of the objects, the rest apply external beam of neutrons, therefore large objects can be studied without sampling.

Furthermore, thanks to the low energy and relatively low intensity (10^7 – 10^9 cm^{-2} s^{-1}) of guided neutron beams, neutrons are perfect tools to study valuable and irretrievable objects of Cultural Heritage. Following the irradiation, no damage of the objects can be observed, and the induced radioactivity decays within a few days. The most common questions addressed the objects' provenance, i.e. the origin of its raw material, or the workshop or technique of its production. Sometimes, it is important to know whether the object is an original or a counterfeit. In fortunate instances many of these questions can be answered using non-destructive analytical methods.

Another advantage of using neutrons that neutron beam can penetrate into the sample, so as to supply analytical information from deeper regions of the objects. This feature is particularly advantageous if one intends to study the bulk composition of corroded metals, painted pottery or rocks with a layer of weathering. Certainly, the most comprehensive result can be obtained, when complementary ‘surface’ and ‘bulk’ methods are used simultaneously. Typical ‘surface’ methods that are applied in archaeometry: X-ray Fluorescence Analysis (XRF) and Proton Induced X-ray Emission (PIXE) analysis.

Finally, when a Cultural Heritage expert scheme a series of analytical investigations, he or she has to consider the availability and the cost/benefit ratios of various methods. Obviously, neutron based methods are usually realized on the basis of large scale facilities, such as research reactors or so called spallation sources (i.e. neutron sources maintained by collisions of accelerated protons on a heavy metal target). Both facilities are quite rare, only a few tens are available in the World. They are operated by a large number highly skilled staff. In addition, the operation of such facilities requires numerous safety issues. It follows that such methods are far not cheap, if one counts all the accessory costs of analysis. In principle, it is possible to operate mobile neutron analytical equipment, which uses radioactive neutron sources, but its efficiency is much lower than that of the large facilities. Many times, users of the Cultural Heritage research prefer to apply the easily available ‘non-neutron based’ methods, but sometimes the application of neutrons cannot be bypassed when valuable information is requested.

Acknowledgments The neutron-based experiments have been performed at the Budapest Neutron Centre, Hungary and at the FRMII, Germany. Most of the above mentioned research projects (the study of prehistoric stone objects, lapis lazuli, stone idols, the Egyptian vessel) have been performed using the financial support by the Transnational Access to Research Infrastructures activity in the 7th Framework Programme of the EU (CHARISMA Grant Agreement n. 228330).

The provenance study of prehistoric stone objects was also supported by the OTKA Hungarian Scientific Research Fund (Grant K 100385).

The archaeological project was carried out with the permission of the Dirección Nacional de Arqueología, Bolivia, and was financially supported by the OTKA Hungarian Scientific Research Fund (Grant T 047048), the Curtiss T. and Mary G. Brennan Foundation and the Heinz Foundation.

The colleagues from the Centre for Energy Research are thankful to Jesse L. Weil for the careful proofreading.

References

- Abraham E, Bessou M, Ziégélé A, Hervé M-C, Szentmiklósi L, Kasztovszky Zs, Kis Z, Menu M (2014) Terahertz, X-ray and neutron computed tomography of an eighteenth dynasty Egyptian sealed pottery. *Appl Phys A* 117:963
- Agamalian MM, Wignall GD, Triolo R (1997) Optimization of a Bonse-Hart ultra-small-angle neutron scattering facility by elimination of the rocking-curve wings. *J Appl Crystallogr* 30:345
- Alconini S (2013) Chungara—*Revista de Antropología Chilena* 45:2

- Allm e R, Limbo-Simovart J, Heapost L, Verš E (2012) The content of chemical elements in archaeological human bones as a source of nutrition research. *Pap Anthropol* XXI:27
- Beltr n J, Loza Azuaga ML, Ontiveros Ortega E, Rodr guez Guti rrez O, Taylor R (2012) The quarrying and use of Marmora in Baetica. An archaeometry-based research project. *Italica* 1:220
- Bir  K (2014) Carpathian obsidians: state of art. In: *Lithic raw material exploitation and circulation in Pr history. A comparative perspective in diverse palaeoenvironments*, ERAUL, vol 138, p 47
- Bir  KT, Kasztovszky Zs (2009) In: Moreau JF, Auger R, Chabot J, Herzog A (eds) *Proceedings of the 36th international symposium on archaeometry. Cahiers d'arch ologie du CELAT*, n. 25, S rie arch om trie n. 7, p 143
- Bir  KT, Regenye J (1995) <http://www.ace.hu/szentgal/>
- Blaise J, Cesbron F (1966) Donn es min raliques et p trographiques sur le gisement de lapis-lazuli de Sare Sang. *Bull Soc Fr Min r Cristallogr* 89:333
- Bourdonnec F-X, Delerue S, Dubernet S, Moretto P, Calligaro T, Dran J-C, Poupeau G (2005) PIXE characterization of western mediterranean and anatolian obsidians and Neolithic provenance studies. *Nucl Instr Meth B* 240:595
- Buchanan B (1966) *Catalogue of ancient near eastern seals in the ashmolean museum I, cylinder seals*
- Cann JR, Renfrew C (1964) The characterization of obsidian and its application to the mediterranean region. *Proc Prehist Soc* 30:111
- Casanova M (1992) The sources of lapis lazuli found in Iran. In: Jarrige C (ed) *South Asian archaeology 1989*, p 49
- Chakrabarti DK (1978) Human origins studies in India: position, problems and prospects. *Man Environ* 1–2:51
- Condarco Castell n C, Gyarmati J (2012) *An Reun Anu Etnol* 23
- Cortecci G, Leone G, Pochini A (1994) Stable isotope composition and geothermometry of metamorphic rocks from the Apuane Alps, northern Tuscany, Italy. *Miner Petrogr Acta* 37:51
- Crandell O (2012) Evaluation of PGAA data for provenance of lithic artifacts. *Studia UBB Geologia* 57(1):3
- D'amico C, Innocenti F, Sassi FP (1987) *Magmatismo e metamorfismo*, Utet, Torino
- Delmas AB, Casanova M (1990) The lapis lazuli sources in the ancient east. In: Taddei M (ed) *South Asian archaeology 1987*. Rome, p 493
- Derakhshani J (1998) Die Arier in den n h stlichen Quellen des 3. und 2. Jahrtausends v. Chr. *Grundz ge der Vor- und Fr hgeschichte Irans*
- Di Pisa A, Franceschelli M, Leoni L, Meccheri M (1985) Regional variation of the metamorphic temperatures across the Tuscan id I unit and its implications on the Alpine metamorphism (Apuan Alps, Northern Tuscany). *Neues Jb Mineral* 151:197
- Dias MI, Prud ncio MI, Valera AC, Lago M, Gouveia MA (2005) *Geoarch Bioarch Stud* 3:161
- Diella V, Spalla MJ, Tunesi A (1992) Contrasted thermo-mechanical evolutions in the Southalpine metamorphic basement of the Orobic Alps (Central Alps, Italy). *J Metam Geol* 10:203
- Dom nguez Bella S (2009) Huellas de cantera romana de m rmol en Almad n de la Plata (Sevilla), un patrimonio a conservar. In: Nogales T, Beltr n J (eds) *Marmora Hispana: explotaci n y uso de los materiales p treos en la Hispania Romana*, Roma, p 377
- Emmerling A, Petricevic R, Wang P, Scheller H, Beck A, Fricke J (1994) Relationship between optical transparency and nanostructural features of silica aerogels. *J Non-Cryst Solids* 185:240
- Faryad S (1999) Metamorphic evolution of the Precambrian South Badakhshan block, based on mineral reactions in metapelites and metabasites associated with whiteschists from Sare Sang (Western Hindu Kush, Afghanistan). *Precambrian Res* 98(3–4):223
- Faryad SW (2002) *J Petrol* 43(4):725
- Gebhard R, Wagner FE, Albert P, Hess H, Revay Z, Kudejova P, Kleszcz K, Wagner U (in preparation) *J Radioanal Nucl Chem*
- Goldschmidt JR, Graff L, Joensu OI (1955) The occurrence of magnesian calcites in nature. *Geochim Cosmochim Acta* 1:212

- Gorgoni C, Lazzarini L, Pallante P, Turi B (2002) In: Herrmann JJ, Herz N, Newman R (eds) *Interdisciplinary studies on ancient stone. Archetype*, London, p 115
- Grew ES (1988) Nerupine at the Sar-e-Sang, Afghanistan, whiteschist locality: implications for tourmaline-kornerupine distribution in metamorphic rocks. *KorAm Mineral* 73:345
- Gyarmati J, Condarco Castellón C (2014) Paria la Viexa. Pre-hispanic settlement patterns in the Paria Basin, Bolivia, and its Inka Provincial Center. *Museum of Ethnography, Budapest*
- Herrmann G (1968) Lapis lazuli: the early phases of its trade. *Iraq* 30:21
- Hogarth DD, Griffin WL (1978) Lapis Lazuli from Baffin Island, a Precambrian meta-evaporite. *Lithos* 11:37–60
- Hurlbut CS (1954) *Dana's manual of mineralogy*, 17th edn. John Wiley & Sons Inc, New York
- Kabaciński J, Sobkowiak-Tabaka I, Kasztovszky Zs, Pietrzak S, Langer JJ, Biró KT, Maróti B (2015) Transcarpathian influences in the Early Neolithic Poland. A case study of Kowalewko and Rudna Wielka Sites. *Acta Arch Carp* 50:5–32
- Kasztovszky Zs, Antczak MM, Antczak A, Millan B, Bermúdez J, Sajo-Bohus L (2004) Provenance study of Amerindian pottery figurines with prompt gamma activation analysis. *Nukleonika* 49(3):107
- Kasztovszky Zs, Biró KT, Markó A, Dobosi V (2008) Cold neutron prompt gamma activation analysis—a non-destructive method for characterization of high silica content chipped stone tools and raw materials. *Archaeometry* 50(1):12
- Kasztovszky Zs, Biró KT, Szilágyi V, Maróti B, Težak-Gregl T, Burić M, Hágó A, Astalos C, Nagy-Korodi I, Berecki S, Hajnal A, Rác B (2012) Abstracts of the 39th international symposium on archaeometry, Leuven, Belgium, 05.28–06.01
- Kis Z, Szentmiklósi L, Belgya T (2015) NIPS–NORMA station—a combined facility for neutron-based nondestructive element analysis and imaging at the Budapest Neutron centre. *Nucl Instr Meth A* 779:116
- Kostov R (2004) Roots of Bulgarian civilization. In: *Academic interdisciplinary conference. Bul-Koreni*, Sofia, p 77
- Kramer SN (1952) *Enmerkar and the Lord of Aratta: a Sumerian epic tale of Iraq and Iran*. University Museum, University of Pennsylvania
- Kulke HG (1976) Die Lapislazuli-Lagerstätte Sare Sang (Badakhshan). *Afghanistan J* 3(2):43
- Lago M, Duarte C, Valera AC, Albergaria J, Almeida F, Carvalho A (1998) Povoado dos perdigos (Reguengos de Monsaraz): dados preliminares dos trabalhos arqueológicos realizados em 1997. *Rev Port Arqueol Lisboa* 1(1):45
- Lapuente P (1995) Mineralogical, petrographical and geochemical characterization of white marbles from Hispania. In: Maniatis Y, Herz N, Basiakos Y (eds) *The study of marble and other stones used in antiquity*, vol 151. London
- Lapuente P, Turi B (1995) Marbles from Portugal: petrographic and isotopic characterization. *Sci Technol Cult Herit* 4(2):33–42
- Leoni L, Tamponi M (1991) *J Mineral Geochem* 4:145
- Lo Giudice A, Re A, Calusi S, Massi M, Olivero P, Pratesi G, Albonico M, Conz E (2009) Multitechnique characterization of lapis lazuli for provenance study. *Anal Bioanal Chem* 395:2211
- Lucido G, Caponetti E, Triolo R (1989) Uso dei frattali in petrologia: esperimenti di scattering di neutroni ai bassi angoli su rocce magmatiche. *Miner Petrogr Acta* 32:185
- Lucido G, Caponetti E, Triolo R (1991) Fractality as a working tool for petrology: small-angle neutron scattering experiments to detect critical behaviour of magma. *Geol Carpath* 42:85
- Mañas Romero I (2012) Marmora de las canteras de Estremoz, Alconera y Sintra: su uso y difusión. In: García-Entero V (eds) *El marmor en Hispania: explotación, uso y difusión en época romana*, Madrid, p 331
- Markó A, Biró KT, Kasztovszky Zs (2003) Szeletian felsitic porphyry: non-destructive analysis of a classical Palaeolithic raw material. *Acta Arch Acad Scient Hung* 54:297
- Marschner H (1968) Ca-Mg-distribution in carbonates from the Lower Keuper in NW-Germany. In: *Recent developments in carbonate sedimentology in Central Europe*. Springer, Heidelberg, pp 128–135

- Márquez JE, Valera AC, Becker H, Jiménez V, Suárez J (2011) El complejo arqueológico dos Perdighões (Reguengos de Monsaraz, Portugal). *Prospecciones Geofísicas—Campaña 2008–09*, Trabajos de Prehistoria, Madrid
- Martins R, Lopes L (2011) Mármore de Portugal. *Rochas Equip* 100:32
- Matos M, *Los Incas Arte y Símbolos* (Banco de Crédito del Perú, Lima), p 109
- McLennan SM (1989) In: Lipin BR, McKay G A (eds) *Geochemistry and mineralogy of rare earth elements*. *Reviews in Mineralogy*, vol. 21, p 169
- McLennan SM (2001) Relationships between the trace element composition of sedimentary rocks and upper continental crust. *Geochem Geophys Geosyst* 2, 2000GC000109
- Meyers A (1975) Algunas problemas en la Clasificación del estilo incaico, Puma-punku, vol 8
- Meyers A (1998) *Los Incas en el Ecuador análisis de los restos materiales*. Quito, Abia-Yala
- Molnár GL, Révay Z, Paul RL, Lindstrom RM (1998) Prompt-gamma activation analysis using the k_0 approach. *J Radioanal Nucl Chem* 234:21
- Molnár GL, Révay Z, Belgya T (2002) Wide energy range efficiency calibration method for Ge detectors. *Nucl Instr Meth A* 489:140
- Moorey PRS (1994) *Ancient mesopotamian materials and industries: the archaeological evidence*. Clarendon Press, Oxford
- Morbidelli P, Tucci P, Imperatori C, Polvorinos A, Preite Martinez M, Azzaro E, Hernandez MJ (2007) Roman quarries of the Iberian peninsula, *Eur J Mineral* 19(1):125
- Nance WB, Taylor SR (1976) Rare-earth element patterns and crustal evolution. *Geochim Cosmochim Acta* 40:1539–1551
- Oddone M, Márton P, Bigazzi G, Biró KT (1999) Chemical characterisations of Carpathian obsidian sources by instrumental and epithermal neutron activation analysis. *J Radioanal Nucl Chem* 240(1):147
- Origlia F, Gliozzo E, Meccheri M, Spangenberg JE, Turbanti Memmi I, Papi E (2011) Mineralogical, petrographic and geochemical characterisation of white and coloured Iberian marbles in the context of the provenancing of some artefacts from Thamusida (Kenitra, Morocco). *Eur J Mineral* 23:857
- Pertusanti PC, Raggi G, Ricci CA, Duranti S, Palmeri R (1993) Evoluzione post-collisionale dell'Elba centro-orientale. *Mem Soc Geol Ital* 49:297
- Re A, Giudice AL, Angelici D, Calusi S, Giuntini L, Massi M, Pratesi G (2011) Lapis lazuli provenance study by means of micro-PIXE. *Nucl Instr Meth B* 269:2373–2377. doi:[10.1016/j.nimb.2011.02.070](https://doi.org/10.1016/j.nimb.2011.02.070)
- Révay Z (2006) Calculation of uncertainties in prompt gamma activation analysis. *Nucl Instrum Meth A* 564:688
- Révay Z (2009) Determining elemental composition using prompt gamma activation analysis. *Anal Chem* 81:6851
- Révay Z, Belgya T (2004) Principles of PGAA method. In: Molnár GL (ed) *Handbook of Prompt Gamma Activation, Analysis with Neutron Beams*. Kluwer Academic Publishers, Dordrecht, Boston, New York, pp 1–30
- Révay Z, Belgya T, Ember PP, Molnár GL (2001a) Recent developments in hypermet-PC. *J Radioanal Nucl Chem* 248:401
- Révay Z, Molnár GL, Belgya T, Kasztovszky Z, Firestone RB (2001b) A new γ -ray spectrum catalog and library for PGAA. *J Radioanal Nucl Chem* 248:395
- Révay Z, Belgya T, Molnár GL (2005) New prompt k_0 and partial cross section values measured in the cold neutron beam of Budapest research reactor. *J Radioanal Nucl Chem* 265:261
- Rómer F (1867) Első obsidian-Eszközök Magyarországon (in Hungarian) [First obsidian implements in Hungary]. *Arch Közl* 7:161
- Rosen LV (1988) Lapis lazuli in geological and in ancient written sources. Partille, Sweden
- Saragoza F (2008) *Revue archéologique de Bordeaux*, Tome IC, p 131 (French)
- Sarianidi VI (1971) *Archaeology Magazine* 12
- Schmidt PW (1991) Small-angle scattering studies of disordered, porous and fractal systems. *J Appl Crystallogr* 24:414

- Schreyer W, Abraham K (1976) Three-stage metamorphic history of a whiteschist from Sar e Sang, Afghanistan, as part of a former evaporite deposit. *Contrib Mineral Petrol* 59:111
- Searight S (2010) Lapis lazuli. In: Pursuit of a celestial stone. East and West Publishing Ltd., London
- Siletto GB, Spalla MJ, Tunesi A, Nardo M, Soldo L (1990) Structural analysis in the Lario Basement (Central Southern Alps, Italy). *Mem Soc Geol Ital* 45:93
- Szabó J (1867) A Tokaj-Hegyalja obsidiánjai (in Hungarian) [Obsidians of the Tokaj Mts]. *A Magyarhoni Földtani Társulat Munkálatai (Pest)* 3:147–172
- Szákány Gy, Kasztovszky Zs, Szilágyi V, Starnini E, Friedel O, Biró KT (2011) Discrimination of prehistoric polished stone tools from Hungary with non-destructive chemical Prompt gamma activation analyses (PGAA). *Eur J Mineral* 23:883
- Szentmiklósi L, Belgya T, Révay Z, Kis Z (2010) *J Radioanal Nucl Chem* 286:501
- Szilágyi V (2010) History of the Hungarian applied arts after 1945. Ph.D. thesis. Eötvös Loránd University of Budapest, Hungary
- Szilágyi V, Gyarmati J, Tóth M, Taubald H, Balla M, Kasztovszky Zs, Szákány Gy (2012) Petro-mineralogy and geochemistry as tools of provenance analysis on archaeological pottery: study of Inka period ceramics from Paria, Bolivia. *J South American Earth Sci* 36:1
- Taelman D (2014) Contribution to the use of marble in Central-Lusitania in Roman times: The stone architectural decoration of Ammaia (São Salvador da Aramenha, Portugal), *Archivo Espanol de Arqueologia*, pp 175–194
- Taelman D, Elburg M, Smet I, De Paep P, Luís L, Vanhaecke F, Vermeulen F (2013) *J Arch Sci* 40(5):2227
- Taylor SR, McLennan SM (1985) The continental crust: its composition and evolution. Blackwell Scientific Publications LTD, Oxford
- Todd TW (1966) Petrogenetic classification of carbonate rocks. *J Sediment Petrol* 36(2):317
- Tschopik MH (1946) Papers of the peabody museum of American archaeology and Ethnology 27(3)
- Tykot RH (1997) Characterization of the Monte Arci (Sardinia) obsidian sources. *J Archaeol Sci* 24:467
- Valera AC (2008) Cosmologia e recintos de fossos da Pré-História Recente: resultados da prospeção geofísica em Xancrea (Cuba, Beja). *Apontamentos de Arqueologia e Património*, 7, Lisboa, *Era Arqueologia*, 8, Lisboa
- Valera AC (2012a) In: Gibson A (ed) Mind the gap: Neolithic and Chalcolithic enclosures of South Portugal. Enclosing the Neolithic. Recent studies in Britain and Europe, BAR, p 165
- Valera AC (2012b) In Gibaja JF, Carvalho AF, Chambom P (eds) Funerary practices from the mesolithic to the chalcolithic of the Northwest Mediterranean, *British Archaeological Reports*, p 103
- Valera AC, Lago M, Duarte C, Evangelista LS (2000) Ambientes funerários no complexo arqueológico dos Perdigões: uma análise preliminar no contexto das práticas funerárias calcólicas no Alentejo, *Era Arqueologia*, vol 2, Lisboa, *Era/Colibri*, p 84
- Valera AC, Silva AM, Márquez Romero JEM (2014a) The temporality of Perdigões enclosures: absolute chronology of the structures and social practices, *SPAL* 23:11
- Valera AC, Silva AM, Cunha C, Evangelista LS (2014b) In: Valera AC (ed) Recent prehistoric enclosures and funerary practices, vol 2676. BAR International Series, Oxford, pp 37–57
- Vértes L, Tóth L (1963) Der Gebrauch des Glasigen quartzporphyrs im Paläolithikum des Bükk-Gebirges. *Acta Arch Hung* 15:3
- Visy et al (eds) (2003) Hungarian archaeology at the turn of the Millennium, Nemzeti Kulturális Örökség Minisztériuma, Budapest
- Webster M (1975) Gems, their sources, description and identification, London
- Wong PZ, Howard J, Lin JS (1986) Surface roughening and the fractal nature of rocks. *Phys Rev Lett* 57:637

- Woolley CL (1934) *Ur excavations 2: the royal cemetery*, Oxford
- Yurgenson GA, Sukharev BP (1984) Localization conditions and mineral zoning of lazurite-containing bodies of Badakhshan. *Zap Vses Min Obsch* 113:498–505
- Zöldföldi J, Kasztovszky Zs (2003) In: Hahn O, Goedicke C, Fuchs R, Horn I (eds) *Proceedings of the international conference on archäometrie und Denkmalpflege*. Universität Berlin, Berlin, p 194
- Zöldföldi J, Kasztovszky Zs (2009) In: Maniatis Y (eds) *ASMOSIA VII. Proceedings of the 7th international conference of association for the study of marble and other stones in antiquity*. École française d'Athènes, Athenes, p 677

Chapter 7

Paleontology: Fossilized Ancestors Awaken by Neutron Radiography

Frikkie C. De Beer

Abstract Fossils and fossil bearing materials are in principle irreplaceable and are globally a scarce commodity. Countries with natural fossil collections and known fossil sites, which are only a few, thus do take special care of their “heritage” and fossil findings and in the process enhances the role of non-destructive testing and related examination procedures on these findings. This chapter summarizes the documented research utilizing neutron radiography & tomography and the penetrating power of neutrons in a combined effort with other non-destructive analytic techniques to find answers from the “past”. In the quest to “solve the past”, the role of neutron radiography as a modern, unique, non-invasive and non-destructive analytic technique, is being described through several full length article case studies to assist to answer modern paleontology questions.

7.1 Introduction

The palaeosciences is a unique combination of all the scientific disciplines that tell us the story of life on Earth, including the story of humankind (SA Strategy 2011). Palaeosciences denotes thus to the fields of palaeontology, palaeo-anthropology, archaeology, and related disciplines. It is a complex saga, where the many layers of knowledge and understanding of what were in the past and how it proceed and plays a role in history and modern existence, are increasingly being revealed through research and discovery.

“Fossils” as being described within this chapter, refers to the remains of animal, plant or hominid remnants typically imbedded in a kind of matrix such as sedimentary rocks that preserved it over thousands to millions of years. Fossils are generally rare as the landscape/area must have the right conditions to stimulate fossilization. It has been assessed that for every animal that dies, its chances of

F.C. De Beer (✉)

Radiation Science Department, South African Nuclear Energy Corporation, (Necsa),
Pretoria, South Africa

e-mail: frikkie.debeer@necsa.co.za

becoming fossilized in this way are to be less than one in a million (Maropeng 2015a).

Fossils are formed when minerals such as calcium carbonate, over time, envelope and/or replace bones and other organic matter. The covering hardens and casts them into the rock matrix, called breccia, which remains untouched and thus unchanged for millions of years. Breccia is a conglomerate rock consisting of cave infill that forms when material—bones, rocks, and vegetation falls into the cave. Mineralization of the bones and organic materials is also possible, making them as hard as rock once the sediment contains the ideal mineral constituents.

Some evidence of neutron radiography being applied in the study of bones or remnants of dinosaurs was found in the open literature and thus does also form part of the discussion within this chapter. Fossils usually represent the hard parts, such as bones or shells of animals and leaves, seeds, or woody parts of plants. Fossils occur on every continent and on the ocean floor. Through the scientific study of fossils and their stratigraphy, it is somehow possible to recreate ancient communities of living organisms and to suggest the evolution of species (Fossil and Fossilization 2015).

Unsurprisingly, the fossils become uncovered again after millions of years through either human activities (limestone mining or dedicated cave exploration) or natural occurrences (erosion, earthquakes). The history of the past then becomes unlocked through scientists (Palaeo-scientists and palaeo-anthropologists) who actively study cave formations and -morphologies, landscape morphologies that support palaeo related findings and others to reveal a window to our past.

In the process to find the truths about the existence of life through the palaeosciences, various modern scientific analytical methods are applied to reveal the contents of these breccia materials which are in a form of blocks of limestone with imbedded possible fossil materials (See Fig. 7.1).



Fig. 7.1 The fossilised tooth of a sabre-toothed cat embedded in breccia. *Photo* Tara Turkington (Maropeng 2015b)

As the fossil materials are imbedded into the breccia matrix, it was actually impossible to perform a study of the physical structure and the morphological nature of the fossil. Time consuming and long pain staking mechanical- and/or chemical preparation processes are applied, both with their own advantages and disadvantages in order to reveal the fossil materials in the best original form possible for further study.

7.2 Preparation of Fossils for Scientific Evaluation

Once the fossil blocks are recovered from their location which is again thoroughly documented, careful planning to expose the fossil material is made as each sedimentary block has its own morphology and material composition. Normally mechanical—(see Fig. 7.2) and/or acid preparation (see Fig. 7.3) is being performed to reveal the fossil materials depending on the nature of the breccia materials. It is normally unknown to the palaeoscientist or preparator of the blocks if any “one in a kind” fossil materials could possibly be “hidden” within the breccia blocks. Thus, the process to expose the target of study e.g. the fossils from the breccia material in both preparation mechanisms takes thus painstaking long. On average for a breccia block of 25 kg the average preparation time applying mechanical preparation is up to 1–2 years and a couple of months using the a weak chemical acid process. In many cases the fossil materials are only partially revealed once the surrounding breccia materials were removed and important information regarding e.g. dental- and cochlea morphologies or even brain cavity volume



Fig. 7.2 Mechanical preparation—preparator at work fossils are prepared in a laboratory using small, pointed chisels and light-weight hammers. Fine cleaning of important fossils is done under a microscope with dental picks and air scribes (Maropeng 2015c)



Fig. 7.3 DITSONG National Heritage Museum: chemical preparation laboratory with fossils imbedded in acetic acid within plastic buckets—operational as from 2012 (Gommery and Potze 2013)

can-not be determined—even when the total fossil has been recovered from the breccia materials.

Once most breccia materials are removed, morphological analyses and other speciation assumptions of the fossil materials can be performed through visual inspection (the normal scientific practice as from early 1900) also taking in consideration the location of the finding, the sedimentology as well as stratigraphic information of the surrounding rocks.

Due to the disadvantages of both preparation processes where either smaller bone losses occur or long term effects of acid could have a detrimental effect on the recovered fossil, the modern era of computational palaeontology, started in the late 20th century, where computers and associated technologies begin to play a more prominent and highly exiting role saving time and costs in not only in revealing the fossilized materials inside the breccia materials but also non-invasively accurately visualize the inner morphology structure of prepared fossils (Ashraf 2011).

7.3 Radiation Based Non-invasive Analytical Techniques

From about 2000, with the introduction of highly sophisticated electronic analytical techniques, palaeo-scientists gave preference to radiation based non-invasive and non-destructive techniques to recover hidden information of fossilized materials even when the fossils are still imbedded within the breccia blocks. These techniques

do not harm or destroy the fossil materials evidence or information which, in many cases, are imbedded in/on a single recovered/found breccia fossil sample. Modern radiation based analytical techniques, such as 3D tomography using X-rays or neutrons became available to be used to investigate either the untreated breccia materials or the recovered fossils after treatment. These non-invasive techniques became, as from about 2005 state-of-the-art analytical investigation tools to researchers from the palaeosciences. Hidden information such as fossil position and location within the breccia block to assist to speed up the recovery process becomes a state of the art activity. Morphological data of the fossil materials became possible and thus adds value to the investigation process even before they are recovered from the breccia blocks. The relative availability of e.g. neutron tomography as unique analytic technique makes it possible for researchers worldwide to access, through beam time submitted proposals, these highly sophisticated instruments. These are well established facilities and are being described and discussed elsewhere in this book.

For many years the unique nature of X-ray penetrating radiation, found at many X-ray tomography (XCT) facilities around the globe, was the favorite amongst researchers due to the relative very high resolution, up to a few microns, that is being achieved. Although the focus of this chapter is on the application of the relative unknown application of neutron radiography/tomography within the palaeo-sciences, only reference to XCT is made for the comparison of and enhancement of the complementary benefit of neutron radiography/tomography. The nature of neutron radiography/tomography within this unique application and specifically the contrast obtained between fossil- and the breccia materials are being generalized and first order theoretically described however neutron radiography principles and techniques are been described in detail in Chap. 16.

No formal studies were conducted in breccia materials where the only focus is to compare X-ray- and neutron radiography with respect to the contrast that can be obtained between the breccia and fossilized materials. The problem is the vast different composition of breccia materials to predict what the contrast could be reached with either one of the techniques. However, a generalized approach is taken in the following paragraphs by assuming hydroxyapatite as the most abundant fossilized materials present in the calcified rock and the composition of the breccia materials originate from Bolts Farm and from the Taung child as listed in Table 7.1.

From the table and the respectable composition and densities of these materials, the relative linear attenuation coefficients for X-ray and neutrons are compiled through 1st-order calculations as being listed in Table 7.2.

Penetration capabilities of breccia materials by X-rays and neutrons are predicted and listed in Table 7.3. Penetration of radiation through the breccia is needed for any success in radiography. As an unwritten rule, 10 % transmission or radiation in all angles through the breccia sample is preferred for tomography to be successful without major artifacts being created in the virtual volume reconstructed data set.

In a first order assumption about breccia materials it is taken to be pure CaCO_3 mineral. It is evident from Table 7.3 that neutron penetration through breccia material is about 100 % better than with X-rays. However, we can generalize and

Table 7.1 General % elemental composition of hydroxyapatite and the breccia materials^a

Hydroxyapatite % in composition	Ca ₅ (PO ₄) ₃ (OH)												
	SiO ₂	Al ₂ O ₃	Fe ₂ O ₃	FeO	MnO	MgO	CaO	Na ₂ O	K ₂ O	TiO ₂	P ₂ O ₅	Cr ₂ O ₃	NiO
% Range: Breccia materials ^b	11.9–47.1	1.1–4.5	0.1–0.3	0.4–2.4	0.1–0.7	0.3–1.3	16.6–82.3	0–0.1	0.2–0.6	0.1–0.3	0.5–3.9	0.01–0.036	0–0.04

^a Average percentages used in further calculations^b J.F. Thackeray for 13 × breccia samples from Taung; J.F. Thackeray, Dominique Gommery and Sandrine Prat and Stephany Potze and Lazarus Kgasi for 7 × breccia samples from Bolts Farm

Table 7.2 First order calculated linear attenuation coefficients of breccia (theoretical CaCO₃) and hydroxyapatite by X-rays and neutrons

Sample		Radiography technique using	
Description	Density (g/cm ³)	X-ray (cm ⁻¹) (^a 5 g/cc)	Thermal Neutrons at 0.05 eV (cm ⁻¹)
Hydroxyapatite	3.156 ^a	0.95 @ 200 kV 1.10 @ 160 kV 1.49 @ 100 kV	0.48
Breccia materials calcite (CaCO ₃)	5.0 ^a Calc: 2.71	1.43 @ 200 kV 1.63 @ 160 kV 2.18 @ 100 kV	0.34 max for pure CaCO ₃

^aTheoretical density**Table 7.3** Thickness of breccia for 10 % transmission of X-ray- and neutron radiation (Theoretical)

Sample	Radiography technique using:	
	X-ray (120 kV) (cm)	Thermal neutrons at 0.05 eV (cm)
Breccia materials	2.95 10–20 cm @ 225 kV	6.77

through assumptions, a difference and comparison in the investigations of fossil containing breccia materials using X-ray- and neutron tomography is being obtained.

7.4 Fossil Locations/Areas

Although many fossils and fossil bearing rock exists in many places around the globe and many books were published describing fossils about their existence many years ago—making assumptions based on visual inspection of some findings—this chapter only describes the application of neutron radiography and -tomography in the non-destructive investigation of fossils and fossil bearing rock. In general, more hominids fossil materials are found in Africa while most a higher abundance of dinosaur's fossils are found in the America's. More reading can be found at (Franco 2011, List of fossil sites, List of human evolution fossil and Dinofossils locations 2015).

7.5 X-Ray Tomography

It will be unfair not to mention as well the possibilities and complementary nature of micro-focus X-ray tomography (XCT) to neutron tomography as an application in the palaeo-sciences.

Braga et al. investigated in breccia free pre-prepared fossil samples the cochlear morphological features associated with hearing capacities across 22 living and 5 fossil catarrhine species. The goal was to look at reliable indicators of auditory capacities by investigate the phylogenetic signal of cochlear features, which is also taxonomically useful among apes' main lineages (Braga et al. 2013). The study provides evidence to improve classifications of fossil hominid species into true monophyletic groups in that evidence was found that body mass-dependent and non-homoplasious changes of cochlear elongation in apes contributes mainly but not only to their evolutionary history (Fig. 7.4).

Because this chapter focusses on the application of neutron tomography in this field, other XCT application in this field are only referenced for further reading (Braga et al. 2010; Sutton 2008; de Beer et al. 2008).

To illustrate why neutron radiography/tomography should be considered as complementary technique to X-ray tomography within the Palaeosciences, the results of X-ray acquisition of the breccia block embedding the specimen STS 1039 from Sterkfontein, South Africa, has been compared with neutron tomography results as shown in Fig. 7.5. While the enamel tissue is slightly better discriminated from the dentine material on X-rays sections, the distinction between bone/matrix (1) and between dental tissues/matrix (2) is definitely more accurate in neutron-based images and allows a virtual reconstruction of the specimen (Beaudet et al. 2015).

The following sections of this chapter discuss the development and showcase with some case studies the role of neutron radiography in the Palaeosciences.

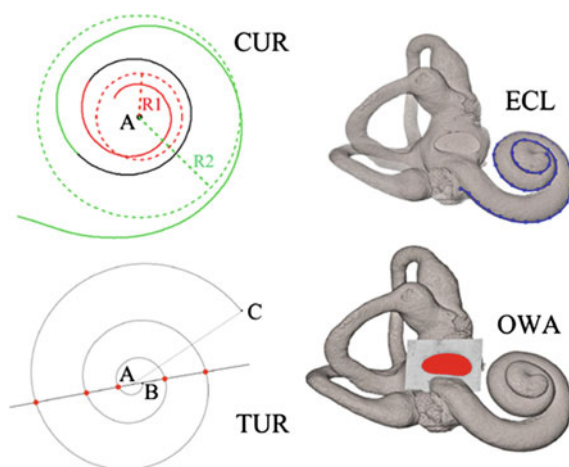


Fig. 7.4 Illustrations of the five cochlear features expressed as continuous variables. The external cochlear length (ECL, in mm), number of turns (TUR, expressed as the sum of full circle rotations and the angle between lines “AB”—center to apex—and “AC”—center to base), and relative length (RECL = ECL/TUR, in mm), the curvature gradient (CUR, expressed as a dimensionless ratio between the radii of the larger first—noted “R2”—and the smaller last spiral turns—noted “R1”), and the oval window area (OWA in mm²). *Courtesy* Braga et al. (2015)

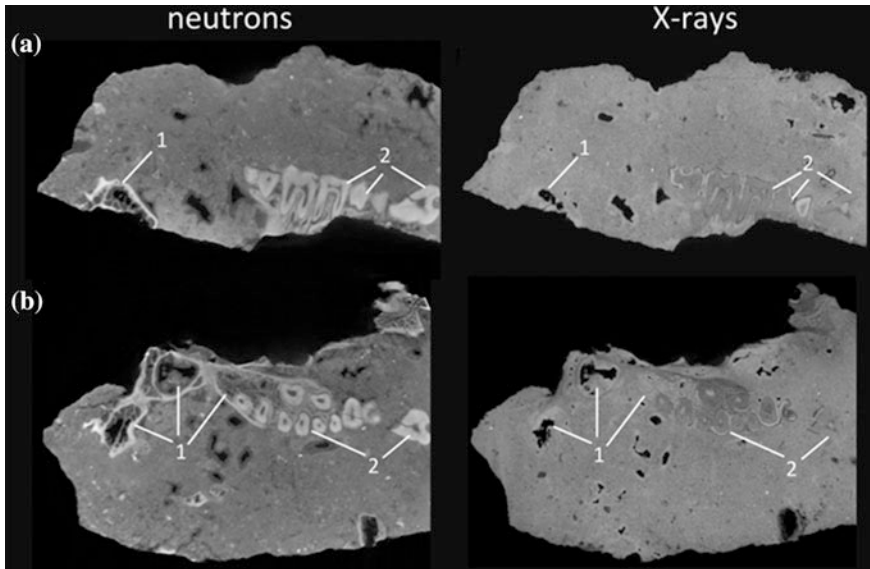


Fig. 7.5 Comparison of sagittal (a) and traverse (b) sections of the breccia block embedding STS 1039 obtained by neutron-based and X-rays acquisitions performed at a similar resolution. While traditional X-rays microtomography fails to fully discriminate bone from matrix (1) and dental tissues from matrix (2), the neutron-based microtomography successfully separates the biological and mineral materials

7.6 Film Based Neutron Radiography and Fossils—Early Days

The power of neutron radiography also in the field of fossil evaluations was realized by Berger et al. as early as in 1962 (Berger 1962).

With the very first known published article of this kind in 1997, Le Roux et al. focused on the use of neutron radiography, as non-destructive technique, to facilitate the identification of structures in the STS 5 fossil specimen found at the Cradle of Human Kind, Sterkfontein, South Africa.

The aim was to facilitate the identification of structures in the fossil specimen, as indicated in Fig. 7.6, and to investigate methods used to obtain planar neutron radiographs and evidence of damage (cracks and breaks) at the time of discovery or preparation of the specimen (Le Roux et al. 1997). The H-rich clue lines in between the fractured parts of the cranium could easily be identified. This study reports the results of groundbreaking research in South Africa utilizing the neutron radiography facility at the SAFARI-I nuclear research reactor at Pelindaba. The focus of the study was on fossils from Sterkfontein, including cranial bone of the celebrated ‘Mrs Ples’ (STS 5), representing *Australopithecus africanus*.

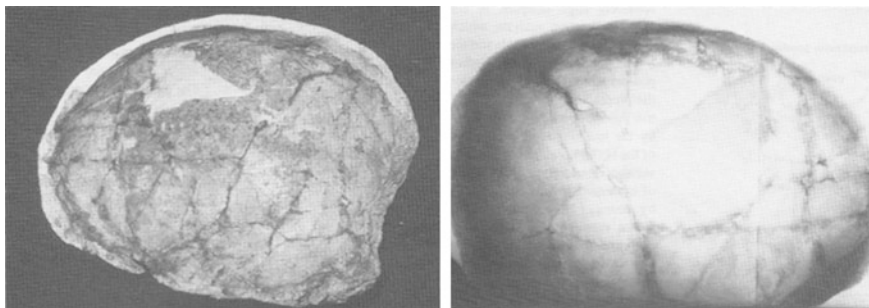


Fig. 7.6 *Left* Photo of the top of the cranium of STS 5 (Mrs Ples). *Right* Subsequent film based neutron transmission radiograph

7.7 Digital Radiography: Neutron Radiography Experience

With the introduction of digital neutron radiography/tomography, the value added by neutron radiography (NRad) related research to the palaeosciences increased dramatically. It took many years before the connection between the palaeoscience-the NRad communities was made and the value added by NRad could be practically experienced by the palaeoscience community. The selected examples in this section of the chapter are from full length research publications trying to capture the capabilities, advantages and possibilities of neutron radiography/tomography within the palaeosciences as from the first known publication to the latest in Dec 2015.

7.8 Examples of Neutron Studies of Paleontological Samples

7.8.1 *Sauropod Vertebrae*

7.8.1.1 Scientific Question

The main goal for this investigation was the comparison of neutron tomography (NT) as a research tool in the investigation of fossilized sauropod vertebrae and the comparison with corresponded CT images. Comparisons between X-ray tomographic and neutron tomographic scans were made to identify: (i) if NT is an appropriate method for the investigation of diagenetically altered bone fragments; (ii) the benefits and limits of NT analysis of vertebrate remains; (iii) advantages and differences between CT and NT images; and (iv) how differential preservation and preparation of the specimens affects both techniques (Schwarz et al. 2005).

7.8.1.2 Materials and Methods

The Neutron Transmission Radiography Station (NEUTRA¹ <http://neutra.web.psi.ch/>) of the Paul-Scherrer-Institute (PSI) in Villigen/Switzerland has been available since 1997 also for the nondestructive testing of fossilized materials.

The Saurier-Museum Aathal/Switzerland provided remains of diplodocid sauropods from the Late Jurassic (Kimmeridgian) Morrison Formation of Wyoming for the NT and CT analyses. The sample investigated consisted of five cervical vertebrae and one cervical rib each belonging to juvenile individuals. One caudal vertebra was scanned both with CT and NT to compare with a vertebra without internal cavities. In order to preserve the fossils, internal cavities, openings and foramina are filled with siliciclastic mud characterized by calcareous cement (Ayer 2000). The bones are partially badly fractured and most fractures and cracks were filled with quick drying cyano-acrylate resin and missing parts of the vertebrae have been remodeled with polyester cast resin (Fig. 7.7).

Samples were scanned with a neutron flux of about 3.6×10^6 [n/cm²/s], collimation ratio (L/D) of 550 and rotated over 180° while up to 300 transmission projections were taken. A relative large neutron path length of 12 cm through the specimen was achieved.



Fig. 7.7 Photo of the fourth cervical vertebra (No. H25-2) of an undetermined diplodocid sauropod with broken parts of vertebral body and diapophysis modelled in polyester cast resin in left lateral view—*red bars* indicate axial cross-sections displayed in Fig. 7.8. *Courtesy* Schwarz et al. (2005)

¹Neutron instruments are presented and described in part II “Experimental methods”.

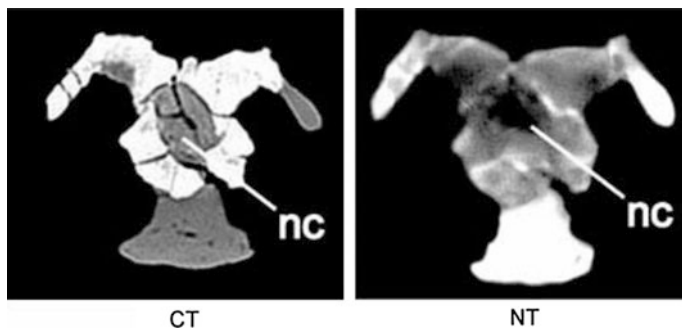


Fig. 7.8 Axial section in the cranial third of the vertebra: both in the CT image (*left*) and the NT image (*right*), the polyester cast resin can be distinguished from bone, but only in the NT image the resin has a different colour than the matrix; *nc* neural canal (Schwarz et al. 2005)

7.8.1.3 Results

Neutrons are sensitive to detect small differences in the concentration of some light materials such as hydrogen. This study demonstrates through 3-D visualization and characterization of internal structures of vertebrate remains this unique ability of neutrons (Schwarz et al. 2005). The quality of the 3D neutron tomograms of the sauropod vertebrae was unfortunately decreased due to several aspects such as the density of the fossil bones, the within openings of the bones that was filled with high amount of marly sediment matrix as well as glue inserted into the multiple fractures of the specimens. Unfortunately NT results are strongly influenced by the resins used for preservation and preparation of these fossilized objects. However, the advantage of neutron tomography lies in the fact that the distribution of glue within the fossil remains can be evaluated at a spatial resolution achieved at PSI of 0.1–0.27 mm. The complementary nature of XCT and NT data supported knowledge generation about the internal structure of sauropod vertebrae (Fig. 7.8).

This study confirms that NT would be an adequate or even better 3D analytical technique than XCT:

- when objects contain metal inclusions;
- when the distribution of sediment in unprepared fossil bones in their internal cavities needs to be investigated, and
- when the authenticity of fossils in a forensic or historical context needs to be investigated. E.g. the nature of historical preparation of museum fossilized specimens (e.g., identifying the resin materials used to glue individual parts— See the white marks in Fig. 7.8 on NT slice).

7.8.2 Dinosaur Eggs

7.8.2.1 Scientific Question

Investigation of the capabilities of NT to reveal the concealed information of a partially opened dinosaur egg.

7.8.2.2 Materials and Methods

A 9 cm diameter dinosaur egg (Fig. 7.9) was found at the Aptian–Albian Algui Ulaan Tsav site, Mongolia. In 2008 egg specimen NSM60104403-20554450, with a few visually detected embryonic bones, was denoted by the Public Procurement Service of South Korea to the National Science Museum of Korea. Over time the egg was diagenetically altered into a hollow calcite geode. The embryonic bones partially condensed on the egg surface and below within a thin layer. The egg is also eroded away on the one section revealing a hollow egg that reveals the calcite geode. The surface of the remaining eggshell present does not show any fractures suggesting that minimum compression had occurred after the egg was buried. The neutron tomography study was performed at the Neutron Radiography Facility of HANARO, KAERI, Korea which allows for a spatial resolution of 0.228 mm. For the reconstructed egg when scanned through 180° and a total of 600 sequential images (Grellet-Tinner et al. 2011).

7.8.2.3 Results

The anterior surface of the 18.8 mm long humerus, the most diagnostic bone among those visible on surface (Fig. 7.9) is partly exposed. It is found with neutron

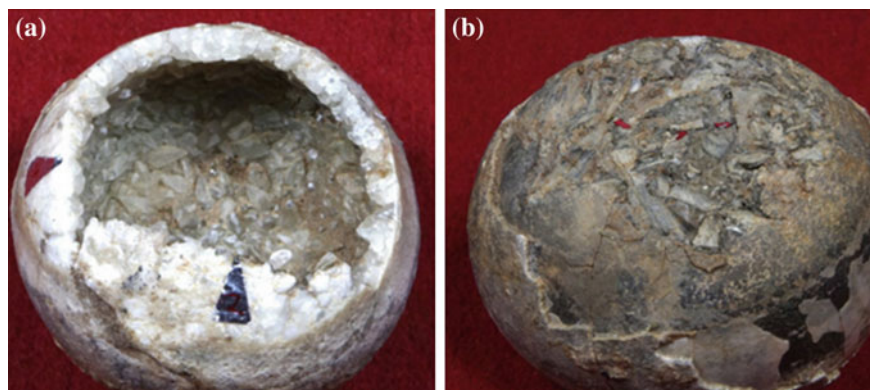


Fig. 7.9 Photo of egg with **a** calcite crystals and **b** embryo skeleton surfaces, *Courtesy Grellet-Tinner et al. (2011)*

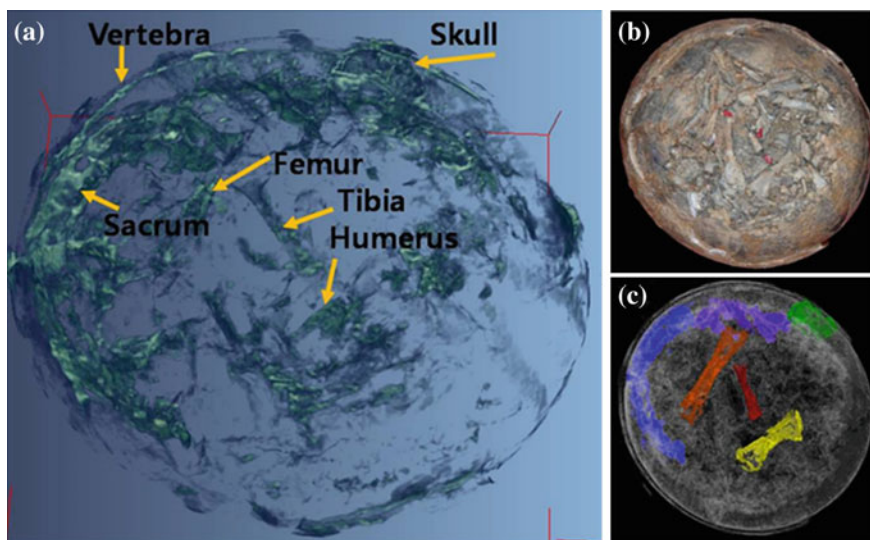


Fig. 7.10 Neutron image on dinosaur embryo, **a** skull, sacrum, limbs and vertebra preserved in the layer identified by neutron tomography (X-Z view), **b** embryonic skeleton settled down at the unopened pole of the egg (*red arrows* on limbs), **c** pseudo coloring Skull, sacrum, limbs and vertebra preserved in the layer identified by neutron tomography (X-Z view). *Courtesy Grellet-Tinner et al. (2011)*

imaging (Fig. 7.10), that the humerus becomes totally visible and extends diagonally into the calcitic matrix.

The femur, a 29.17 mm long bone in posterior view is also noticeable, which, similar to the humerus, is partially encased in the thin calcitic matrix. Although the proximal section of the femoral head is absent, the application of NT revealed the full extent of the bone also within the calcitic matrix (Grellet-Tinner et al. 2011).

7.8.2.4 Concluding Remarks Related to the Study

The aim was to complement X-CT with NT to fully expose and identify the various bones partially imbedded into the calcite structure. Additionally, NT could provide successfully accurate dimensional measurements of the Humerus, Femus and Tibia of the embryo. Fossil embryos are difficult to study due to their small size and fragility—an advantage for and only feasible using NT. Unique and specific taphonomic and diagenetic processes should work together for their preservation thus making fossil embryos not common in the fossil record. NT as non-destructive analytical technique could successfully be utilized in this study where it was difficult to categorize this fossil embryo, adding valuable information to the current knowledge of fossil embryos but also in general to fossil research.

7.8.3 *Ichthyosaurus in Iron Block*

7.8.3.1 Materials and Methods

More than 100 million years old saurian fossils, and specially ichthyosaurus, which is a relatively large fossil, was studied due to its structure and specific finds. The fossil, embedded into the stone slab and partially hidden in the rock (Fig. 7.11) could not be totally cleaned out from the breccia material (Liang et al. 2008).

Only the head section of this fossil could be successfully scanned at the Neutron Transmission Radiography Station (NEUTRA (cf. footnote 1) <http://neutra.web.psi.ch/>) of the Paul-Scherrer-Institute (PSI) in Villigen/Switzerland.

7.8.3.2 Results

The penetration capability of neutrons and the ability to differentiate between different materials although with similar densities, allowed for the head of the ichthyosaurus fossil to be easily distinguished from the stone. Within Fig. 7.12, a zoomed in view of the photograph of the head section under investigation and imbedded into the stone, is shown. The neutron transmission radiograph of the eye area, which is being magnified due to the high spatial resolution achieved at the NR station at PSI is shown in the center while a full 3D reconstructed neutron tomogram of the head of the fossil, with relative detailed information preserved, is shown on the right (Liang et al. 2008).

7.8.3.3 Concluding Remarks Related to the Study

Fossils has no organic materials present within but its structures deliver quite a high contrast compared to the surrounding and embedding breccia materials when subjected to neutron radiography/tomography investigations. The study shows that NR permits non-destructive evaluation of large fossil materials. Morphological information is easily be extracted in a non-invasive manner through high quality segmentation of the skeleton from the rock matrix that give insight into the development of the fossil through a study of its brain cavity and other distinct features.



Fig. 7.11 A 1.4 m long ichthyosaurus fossil imbedded into the rock matrix

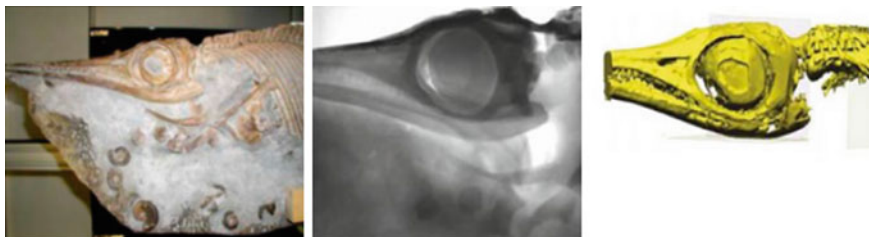


Fig. 7.12 *Left* Photo of the head section; *Middle* Transmission neutron radiograph; *Right* 3D printed model based on neutron tomography data of the head section. *Courtesy* Liang et al. (2008)

7.8.4 *Spondarthritis in the Jurassic*

7.8.4.1 Scientific Question

The South African Karoo, a semi desert area, is known for numerous findings of fossil materials and especially those from the Lower Triassic (~245 million years old) period. The study focused on the vertebral series that belonged to a carnivorous archosaurian reptile and reports some evidence of spondarthritis, a form of arthritis found in pre-Cenozoic vertebrates especially regarding reptiles which is not yet well documented.

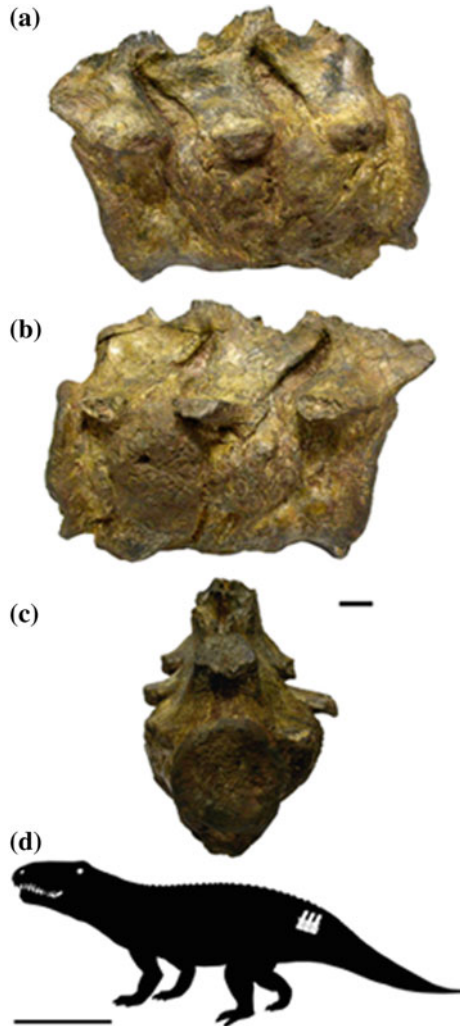
7.8.4.2 Materials and Methods

South Africa and some neighboring countries contain the “Karoo Basin”, an area that has produced an unmatched wealth of past life. The area provided a detailed record of fossil vertebrates that highlight the Permo-Triassic biotic crisis. One such record is the vertebral re-mains of a carnivorous reptile from the Lower Triassic, that shows macroscopic signs of severe bone pathology.

Three articulated anterior caudal vertebrae of a large, basal archosaurian reptile (Fig. 7.13), specimen BP-1-5796, collected at Driefontein District, Free State Province, South Africa and stored at the Bernard Price Institute for Palaeontological Research, Johannesburg was scanned. The nearly complete specimen comprises out of three nearly complete, fused vertebral bodies and partial zygapophyses (Fig. 7.13) with a total length of 116 mm and with no signs of taphonomical alteration. Evaluating the size of these vertebrae, it is assumed that they could originate from a large and probably old individual (Cisneros et al. 2010).

Neutron tomography was performed at the SANRAD facility at the SAFARI-1 nuclear research reactor and operated by the South African Nuclear Energy Corporation (Necsa) in Pretoria. A total of 180 neutron radiography projections in 180 angular degrees were made with a resultant spatial resolution of 100 micron. Good neutron penetration through the specimen were achieved that eliminated ring and beam hardening artifacts in the 3D virtual tomograms of the specimen.

Fig. 7.13 External views of vertebrae BP-1-5796. **a** Left lateral view. **b** Right lateral view. **c** Posterior view. **d** Schematic drawing of a basal archosaurian reptile, showing the likely placement of the vertebral series within the caudal region of the column. *Scale bars* represent 10 mm for **(a, b)**, and 1 m for **(d)**. *Courtesy Cisneros et al. (2010)*



7.8.4.3 Results

The neutron tomography (Fig. 7.14) revealed no traces of fracture or trauma in the vertebral series. Through the tomography we observed that the intervertebral disc spaces (both annulus fibrosus and nucleus pulposus) are totally ossified, producing the complete ankylosis of the vertebrae (Fig. 7.14f, g). In this way, it is not possible to distinguish the limits of each vertebral element. No evidence of zygapophyseal ankylosis, however, was found through the tomography (Fig. 7.14e, h), thus, confirming what was recognized by the external exam of the specimen. Neutron images also showed that in the innermost layer of the vertebral bodies the trabecular bone forms trabecular bridges that follow a regular pattern across the ankylosed

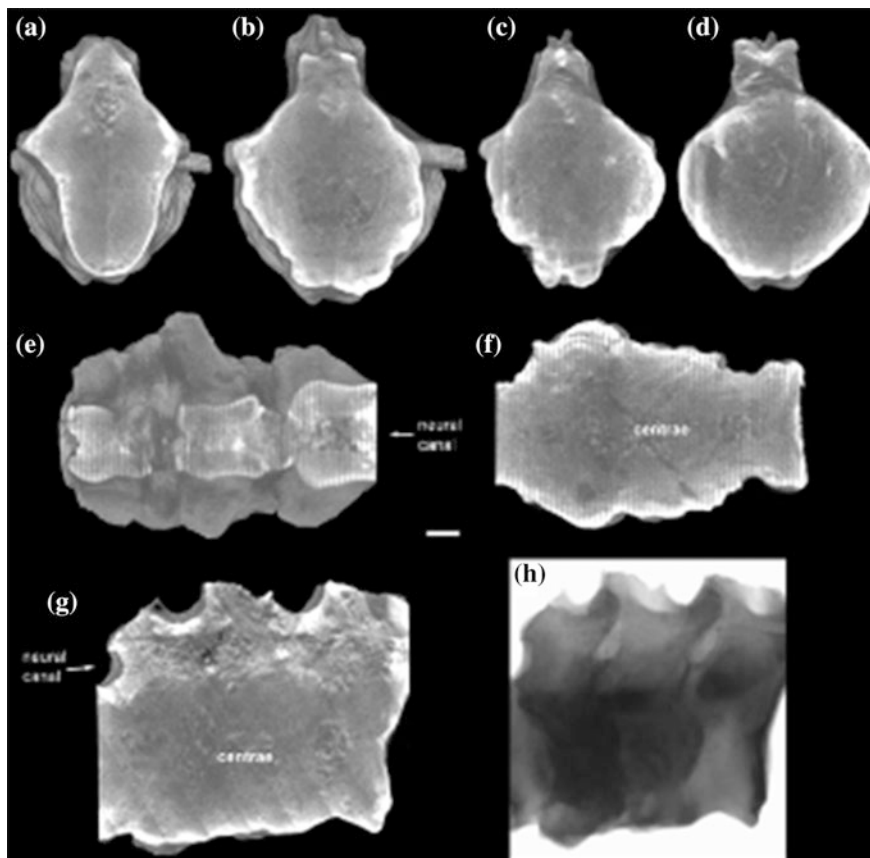


Fig. 7.14 Neutron tomographies of vertebrae BP-1-5796. **a** First (anterior to posterior direction) preserved vertebrae. **b** Second vertebrae. **c**, **d** Third vertebrae. **a–c** Transversal slices, in anterior view, at level of anterior border of the transverse process. **d** Transversal slice, in anterior view, at level of maximum thickness of inflammation. **e**, **f** Coronal slices of the vertebral series in dorsal view, **e** at level of the neural canal, **f** at level of the centrae, anterior to the left. **g** Sagittal slice of the vertebral series in right view. **h** Raw neutron image in right lateral view. Scale bar represents 10 mm. *Courtesy Cisneros et al. (2010)*

areas (Fig. 7.14g). The absence of an irregular pattern of trabecular bone allows discarding the hypothesis of an infectious process or tumor (Cisneros et al. 2010).

7.8.4.4 Concluding Remarks Related to the Study

A severe pathology was recognized in both macroscopic examination and neutron tomography data that revealed features that are diagnostic of the condition, spondyloarthritis which comprises a diverse group of related inflammatory arthritides. This

finding represents the earliest example of this pathology in the fossil record. It is postulated that spondylarthritis was probable the indirect cause of the death of the animal.

Neutron tomography confirmed the macroscopic collected data, revealing the ossification of the entire intervertebral disc space which supports the diagnosis of spondylarthritis.

7.8.5 *Breccia of Sterkfontein*

7.8.5.1 Scientific Question

Sterkfontein, a Plio-Pleistocene karstic complex site in the Gauteng Province, South Africa, is located within the well-known and so-called “Cradle-of-Humankind”. Within this region, numerous australopithecine remains, as well as evidence of early Homo were discovered including more cercopithecoid remains than any other fossiliferous site in South Africa. The aim of the study includes the successful virtual extraction through micro neutron tomography of a cercopithecoid partial cranium (STS 1039) which is still embedded within breccia material.

7.8.5.2 Materials and Methods

A sedimentary breccia block prior to preparation towards revealing possible concealed imbedded fossil materials, and has an uncertain taxonomic attribution, was the focus of the study (Fig. 7.15). The block of breccia is permanently stored at the Ditsong National Museum of Natural History, Pretoria, South Africa that contains the partial cranium STS 1039 (c. $13.5 \times 7 \times 3$ cm). To reveal the presence of any

Fig. 7.15 Photograph of a block of breccia materials with cercopithecoid partial cranium (STS 1039) imbedded into the rock matrix (Beaudet et al. 2015)



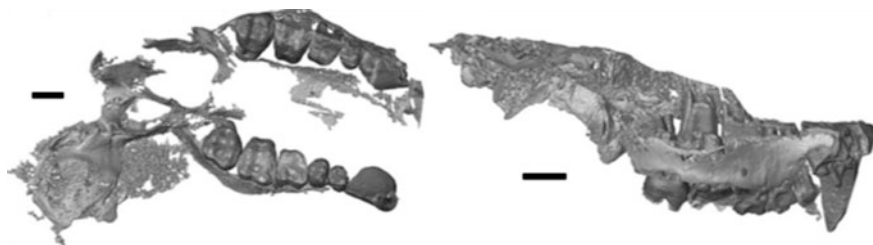


Fig. 7.16 The 3D neutron tomography reconstruction of the virtually extracted maxilla is shown in occlusal (*left*) and right lateral (*right*) views. Scale bars 1 cm. Courtesy Beaudet et al. (2015)

possible diagnostic element preserved in the hardened sediment, microfocus X-ray tomography, as preliminary investigation (Fig. 7.5), was applied at the MIXRAD facility at Necca, South Africa (Beaudet et al. 2015).

The specimen has been detailed by micro neutron CT at the ANTARES (cf. footnote 1) Imaging facility of the Heinz Maier-Leibnitz Center (FRM II) of Technische Universität München, Germany. Scanning parameters include a collimation ratio of L/D 550 (ratio between sample-detector distance and collimator aperture), a neutron intensity of 6.43×10^7 n/cm²s and a final voxel spatial resolution of 75.0 μ m.

7.8.5.3 Results

XCT partially failed due to the extremely low contrast between the breccia and bony/tooth elements as no reliable information of taxonomic value could be obtained. However, micro neutron tomography (μ -nCT), which results are depicted in Figs. 7.16 and 7.17, clearly reveals that the specimen preserves several bony structures. Morphological information of the maxillary bones, the pterygoid bones and part of the left temporal bone, including the mastoid process and the external acoustic meatus, up to the level of the canine jugum (Fig. 7.17b) could be obtained.

Through the utilization of μ -nCT, more detailed information of the concealed fossil materials became available. Apart from the relatively complete right and left upper post canine dentition, the crown of the left maxillary canine and a small root fragment of the right canine could be revealed. Due to the occlusal wear of both third molars as well as the completely developed roots, fossil STS 1039 is postulated to represent an adult, more likely a young adult individual.

From Fig. 7.17a, b it can be seen that the third and fourth premolar, as well as the first molar crowns have lost most of their enamel. Additionally, it is observed that the roots of the left post-canine teeth are perfectly preserved while some of the right raw, are broken.

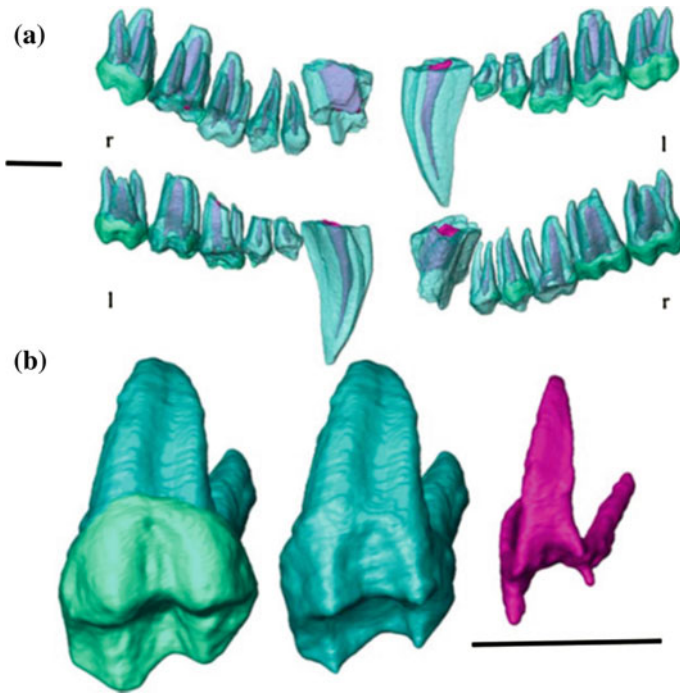


Fig. 7.17 **a** The virtually extracted right (r) and left (l) tooth rows of STS 1039 rendered in semi-transparency in buccal (*upper*) and lingual view (*lower*). **b** 3D rendering of the upper RM3 showing the outer enamel and dentine (*left*), the enameldentine junction (*centre*), and the pulp cavity (*right*) in occlusolingual view. *Scale bars* 1 cm. *Courtesy* Beaudet et al. (2015)

Neutron micro CT also allows for cartography of the enamel thickness distribution across the overall M3 crowns in STS 1039 and clearly reveals relatively thin enamel across the entire crown (Beaudet et al. 2015).

7.8.5.4 Conclusion Remarks Related to the Study

The ability of μ -nCT to provide an accurate picture of all the elements contained in the breccia block makes it a valuable probe for palaeontologists to use in similar situations of concealed fossilized materials. It reveals data previously impossible to access (e.g., bone morphology, enamel thickness across the crown, EDJ shape, etc.) using XCT.

The use of micro neutron tomography (μ -nCT) to inspect the STS 1039 breccia block embedding the partial monkey cranium from Sterkfontein was successful. This study, providing the excellent neutron tomography results on micron scale, is the first to be documented to virtually disclose and 3D render the content of breccia with enclosed primate remains from the South African hominin-bearing cave sites.

7.8.6 *Therapsids*

7.8.6.1 Scientific Question

During the Late Permian and Early Triassic, the therapsids were the dominant tetrapods. Therapsids, pelycosaurs and mammals belong to the same clade, Synapsids, a clade which possess one temporal fenestra in the skull, includes therapsids, pelycosaurs and mammals. Therapsids were formerly also known as “mammal-like reptiles” due to their ancestry to mammals therapsids, are up to hippopotamus-sized animals and are thus of special interest for evolutionary biologists and palaeontologists. Therapsid fossils are rare and thus very valuable and the use of destructive methods to investigate the internal anatomy of therapsid skulls, that include hidden cavities which are almost completely enclosed by bony walls, is usually not considered e.g. the morphology of the inner ear labyrinth, surrounded by bones of the neurocranium, is not known. Knowledge about the internal features of the skulls of Therapsids originate from a few broken fossils or well preserved natural casts of cranial cavities, which were exposed by breakage or weathering. However, a number of questions regarding the early evolution of mammals can be answered through the study of therapsids. These include the origins of the mammalian brain, hearing and masticatory apparatus, respiration, endothermy, apparatus and locomotion (Laaß and Schillinger 2015).

7.8.6.2 Materials and Methods

“Red Beds”, an iron-rich sediment, usually fills up the relatively large and massive skulls of therapsid fossil findings. That is why non-invasive technologies which include X-rays for investigation of the internal cranial anatomy of therapsids are rarely used.

This investigation of fossil therapsid skulls focuses on neutron tomography as non-destructive analytical technique to overcome the problems mentioned earlier in the analysis of therapsids fossil findings. Due to the relative high spatial resolution obtained in the neutron tomography (NCT) data sets, NCT supported the reconstruction of the hearing apparatus. The measurements were performed at the ANTARES (cf. footnote 1) facility for Neutron Imaging at the FRM II reactor of Technische Universität München. See Fig. 7.18, the NT result obtained at ANTARES.

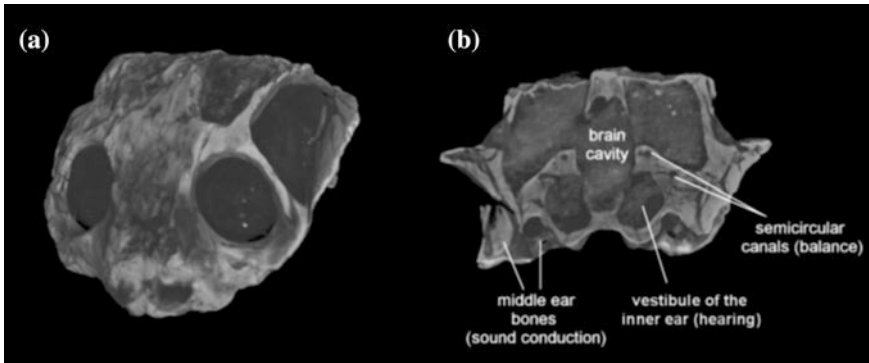


Fig. 7.18 Volume model of the skull of the anomodont *Cistecephalus* (BSPG 1932 I 56) from the Late Permian of South Africa. **a** Frontolateral view. **b** Virtual section through the otic region showing the casts of the inner ears and the sound conducting bones. *Courtesy* Laaß and Schillinger (2015)

7.8.6.3 Results

NCT was applied in order to obtain morphological data of the hearing apparatus of therapsids and specially the middle and inner ear as well as the volumes of bones and important cavities within the skull as depicted in Fig. 7.19, that support the hearing capabilities of therapsids.

Indirectly, the length of the cochlea cavity of the inner ear acts as the auditory sensory organ which is roughly correlated with the length of the basilar papilla. In general, the longer the basilar papilla, the wider is usually the hearing range of frequencies. It was found that therapsids such as cynodonts and therocephalians, which were usually ground-dwelling animals, have often long horizontally oriented stapes that points to the supposed eardrum at the lateral side of the mandible. This supports the hypothesis that it might be an indication that these species were adapted to hear airborne sound as well as that the reflected lamina served as a sound receiver. Therefore, the suggestion is that this animal heard substrate sound by bone-conduction due to the downward sloping stapes combined with a relatively large footplate of the small anomodont *Cistecephalus* from the Late Permian of South Africa (Figs. 7.18 and 7.19).

7.8.6.4 Concluding Remarks Related to the Study

Neutron tomography is an excellent analytical and non-destructive probe for investigations of the auditory region of the precious and scarce therapsids fossil findings. The advantage to apply cold neutron radiation that penetrates iron-rich materials such as fossils in the range between ca. 5 to 15 cm, produces good contrast between fossil bones and matrix.

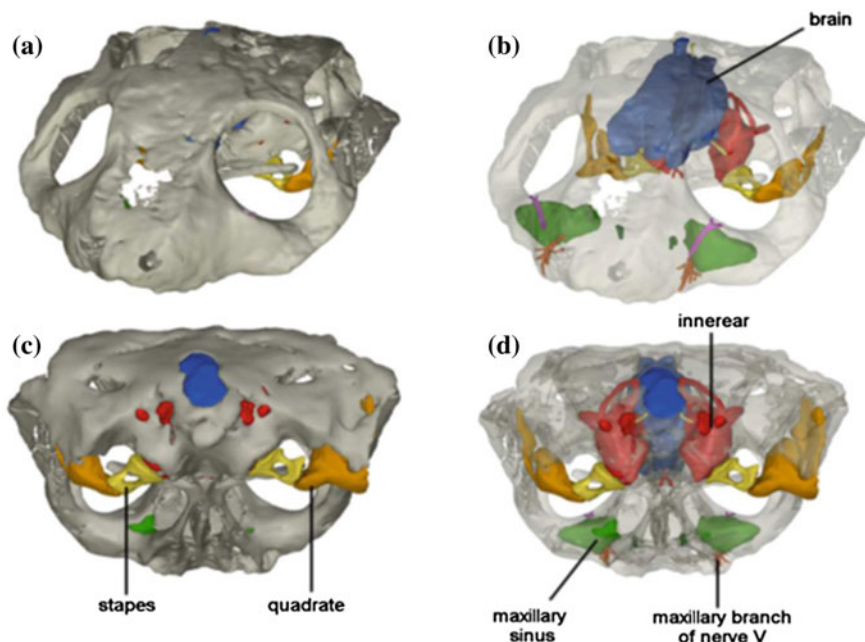


Fig. 7.19 Virtual 3D model of the *Cistecephalus* specimen in Fig. 7.18. **a** Frontolateral view. **b** Frontolateral view with transparent bones showing several internal structures of interest such as the brain, the maxillary sinuses, the trigeminal nerves as well as the auditory apparatus, which is marked by different colors. *Courtesy* Laaß and Schillinger (2015)

The 3D-NRad created models provided important and previous inaccessible information of auditory middle and inner ear parameters and capabilities of extinct animals, their behavior and lifestyle.

Hydrogen-containing minerals in fossil bones such as Hydroxyl-Apatite might be the reason why neutron radiation creates a good contrast between fossil bones and iron rich matrixes.

7.8.7 Prehistoric Stone Slabs

7.8.7.1 Scientific Question

Several ironstone slabs, originated from the late Earlier Stone Age, exhibit some markings such as clear incisions/surface modifications on their surfaces that might be anthropogenic and have thus a high probability to be significant to understand human symbolic behaviour. One of these ‘incised’ ironstone slabs have a series of visible parallel incised lines which indicate that the surface modifications were inconsistent with natural processes and point to intentional modification by hominins.



Fig. 7.20 *Left* Slab external #23 from the slopes above Wonderwerk cave. A photograph of the surface of the slab: no lines are visible on this surface. *Right* Slab BB147 from Excavation 6. A photograph showing a grid of lines visible on the surface. *Courtesy* Jacobson et al. (2013)

It was thus necessary to determine whether the incisions represent intentional actions or were they formed through natural modifications, given the amorphous and unclear nature of these surface incisions.

7.8.7.2 Materials and Methods

Several ironstone slabs were found at the back of Wonderwerk Cave, Northern Cape Province, South Africa, that represent a late Earlier Stone Age period. Two ironstone slabs were selected to be analysed using Neutron tomography due to grid-like patterns of deep lines on one aspect as visual inspection of the fissures in the rock have suggests the probability that these lines are only the surface expression of internal fissures. (See Fig. 7.20) On the other hand, the grid pattern on the surface of the slabs could also suggest to be the result of hominin action. The samples are branded as External sample #23 ($9.9 \times 6.8 \times 2.4$ cm), External sample #22 and Slab BB147 ($10.6 \times 7.2 \times 4.2$ cm).

Neutron- and X-ray radiography was carried out at the South African Neutron Radiography (SANRAD) facility, being hosted by The South African Nuclear Energy Corporation (Necsa). A spatial resolution of 100 μ m was achieved by rotation taking 375 projections within 360° in a field of view (FOV) of 10×10 cm (Jacobson et al. 2013).

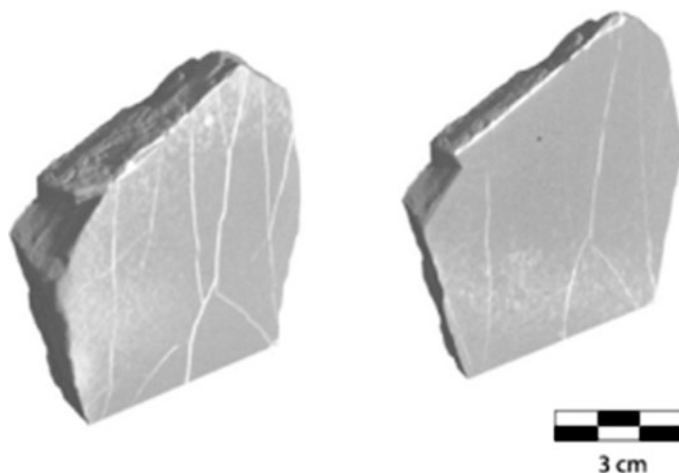


Fig. 7.21 *Left* A slice of #23 at a depth of ~ 5 mm, showing a dense network of fissures visible as white lines. *Right* A slice at a depth of ~ 10 mm, showing a decrease in the number of fissure lines with depth from the surface. *Courtesy* Jacobson et al. (2013)

7.8.7.3 Results

The linear attenuation coefficients of neutrons for the sample matrix (0.19 cm^{-1}) and Fe-stone-rich area (0.73 cm^{-1}) are relative low and thus allow easy penetration of neutrons through relatively thick samples. Neutron tomography (NT) results clearly identify fissures, both in cases where lines are visible on the surface and in cases where there is no surface expression of internal fissures. NT results of one archaeological case found lines on the surface of a slab that are not associated with internal fissures (Jacobson et al. 2013).

Sample #23 as depicted in Fig. 7.21, has no lines visible on the surface while NT showed multiple, irregular internal fissures. Virtual cutaways into the NT data of the sample show that the cracks propagate from the midplane of the slab out towards the surface (Fig. 7.21c, d).

Visual inspection of Slab BB147 (Fig. 7.22) shows a very clear pattern of deep lines regularity layout on the surface. Neutron tomography raised the possibility that the cracks could be filled with water but after the sample was dried in an oven for 2 days at $50 \text{ }^\circ\text{C}$, the white lines (indicate higher neutron attenuation) were still present. NT clearly shows that the lines (cracks) on the surface of this slab extends through the entire slab. This is shown in Fig. 7.22c of slices taken along the plain of the face of the slab. A graphic summary of the continuation of the lines through the body of the slab is shown in Fig. 7.22b in three dimensions. It is concluded that NT results proof that the lines on the surface of this sample are the result of internal fissures within the ironstone and not the result of hominin intervention (Jacobson et al. 2013).

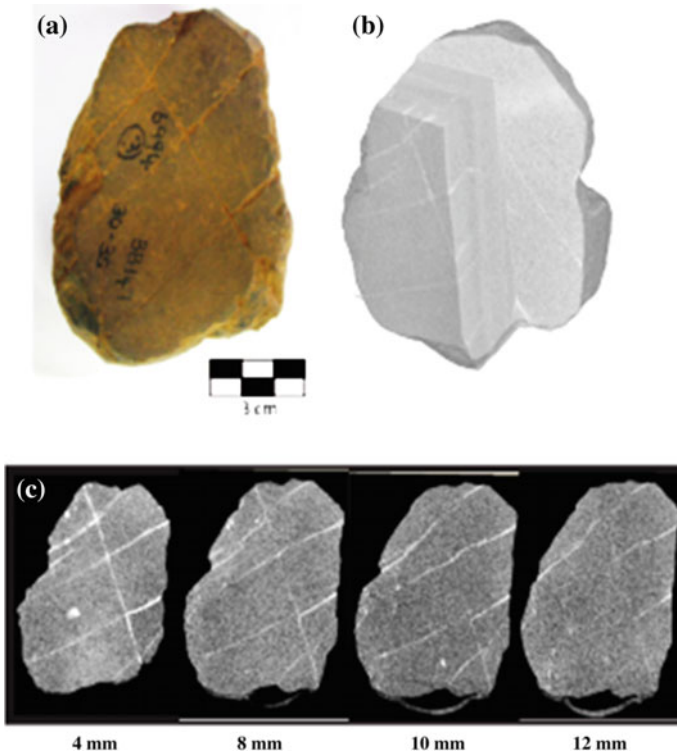


Fig. 7.22 Slab BB147 from excavation 6. **a** A photograph showing a grid of lines visible on the surface. **b** A cutaway midway through the slab, showing that the lines continue as fissures (visible as *white lines*) through the slab. **c** Slices at 4, 8, 10 and 12 mm from the surface, showing the persistence of the grid pattern through the slab. *Courtesy* Jacobson et al. (2013)

7.8.7.4 Concluding Remarks Related to the Study

NT offers an innovative and appropriate method for a study of this kind. Given that NT provides non-destructively high-resolution 3D results of so-called impermeable materials, NT proved here to be an effective tool to penetrate high density iron samples and distinguish surface incisions from lines that are the expression of internal fissures in the rock.

The capability of NT to create a 3D virtual reconstruction of the internal structure of dense material has further potential applications for Palaeolithic archaeology such as the possibility of examining controversial examples of modified stones. One such sample is the Tan-Tan or Berekhat Ram figurines, to determine whether the lines seen on the surface are truly the expression of internal fissures. The same method also holds promise for detecting microfractures in stone tools due to extensive usage where this kind of data could complement understandings of use-wear analysis which is limited to surface features.

7.9 Constraints of NRad in Palaeoscience Applications

National agencies controlling the movement and activities of countries regarding fossilized materials such as SAHRA (South Africa), have restrictions in the movement of fossils from South Africa to analytical facilities abroad. As neutron tomography facilities is not readily available through-out the world, such restrictions place a burden on the movements and thus the research that can be conducted. When the fossilized materials are obtainable, beam time at NRad facilities are not always available and can hinder research as palaeosciences have to compete with other research proposals to obtain access at high profiled and quality NRad research facilities.

As with any analytical technique there is a limitation in the thickness of breccia materials that can be penetrated by neutrons. This makes it impossible to obtain research data in 3D of relative large samples which might contain a number of fossilised materials and the subsequent cutting of these breccia blocks could have a damaging effect on possible fossils imbedded in the large block.

Activation of samples (Sutton 2008) is always a possibility when high-intensity neutron bombardment that induce hazardous levels of radioactivity in some geological materials. Researchers thus have to be careful when samples contain levels of cobalt or europium; samples may thus need to be interred for months or years after NT study. Dealing with precious museum objects implies taking extra precautionary measures preventing possible damage to the samples. To this aim, the samples could initially be characterized through a preliminary Neutron Activation Analysis test measurement. This analysis is used to evaluate the concentration of trace and major elements (and their isotopes) in the sample with the aim of testing its activation rate and decay time as a function of the exposure time. In order to limit the activation level induced by the presence of critical elements and to avoid a decay time longer than a few hours, the samples were investigated for a limited neutron exposure time.

7.10 Future Prospects

The power of fast neutron radiography (MeV) was described by Berger (1962) as early as in 1962 where the absorption differences of materials are much reduced for fast neutrons while better radiographic discrimination is possible utilizing its resonance neutron region. This is now possible as new facilities with a fast neutron radiography capability such as NECTAR and SANRAD became available (Henke et al. 2007; Bücherl et al. 2011; de Beer et al. 2015).

Neutron Radiography is integrated into the Development and Activities of the South African Palaeo-Scientific Community through association of a Fossil

preparation Laboratory located at Necsa. This proves to be a major step forward in the utilization also of Neutron Radiography as an analytical probe by the palaeoscience (Necsa annual report 2013/2014) community. The use of neutron beam facilities to support heritage studies is gaining momentum among the South African research community and decision to establish a Fossil Preparation Laboratory on the Necsa site to assist the heritage research community in making even more efficient use of its beam line research facilities. This will enhance Necsa's potential contribution to knowledge generation within the scope of the newly established South African Department of Science and Technology Centre of Excellence in Palaeosciences.

The South African Nuclear Energy Corporation (Necsa) is situated within the Pelindaba complex at the North East corner of the "Cradle of Humankind". It is on the same dolomitic band that houses the fossil deposits and would have been included within the Cradle were it not a nuclear facility. Geologically it is part of the Cradle and spatially it is right next to the Cradle. The Radiation Science (RS) Department of Necsa, which is part of its R&D Division, has recently designated heritage and heritage materials studies as one of the core focus areas of its activities in its support of the National System of Innovation and Necsa's mandate to promote research in radiation sciences. Necsa provide thus access to its scientific expertise and facilities for the Cultural heritage communities to exploit its potential and capabilities. In this regard, Necsa provides capacity to exploit neutron- and micro-focus X-ray tomography scanning services (non-diagnostic) to many researchers in a variety of scientific research fields—also to the palaeosciences and archaeological sciences.

The complementary nature of neutron and X-ray tomography allows for a full understanding on a non-destructive basis of the internal information of e.g. fossil bearing rock, through the creation of detailed 3D virtual images of fossil material—critical to the scientist in evaluating also internal features of fossils e.g. morphology of the cochlea. It is foreseen that palaeontologists and palaeoarcheologists will increasingly utilise these radiation based analytical techniques to investigate critical internal detail of valuable fossilized specimens in a non-invasive manner without damage to the specimens as more international state-of-the-art neutron CT facilities are being commissioned.

7.11 Conclusions

Neutron Radiography/Tomography has, in a complementary manner with X-ray tomography, a significant role to play in answering the question of questions for mankind—the ascertainment of the place which Man occupies in nature and of his relations to the universe of things (Henke et al. 2007). Neutron Radiography being practiced at various highly sophisticated facilities worldwide, plays also an important but also proven significant role to advancing our understanding of various aspects of the story of life on Earth; it can reveal of how plant and animal life

developed, how humans evolved and thus play a part to reveal the history of mankind (SA Strategy 2011).

The Neutron radiography technique is advantageous by being non-destructive in revealing internal details, and is being applied to study specific morphological features (e.g. trabecular details) inside fossilized specimens that is not possible using classical methods.

Breccia blocks are prioritized for preparation by surface examination and preparing of a standard 2 kg block of breccia can take up to 6 months. However, neutron radiography and tomography allows the internal details of breccia blocks to be easily visualised and can reveal the contents of a given block and thus fast-track preparation of promising fossil containing blocks. Application of neutron radiography has already stimulated new directions of re-search avenues in paleontology and the future promises further exciting results and insights.

References

- Abel RL, Laurini CR, Richter M (2012) A palaeobiologist's guide to 'virtual' micro-CT preparation. *Palaeontologia Electronica* 15, <http://palaeo-electronica.org/content/pdfs/284.pdf>
- Ashraf MTE (2011) Computational paleontology (Google eBook). Springer Science & Business Media, 04 Mar 2011
- Beaudet A, Braga J, de Beer FC, Schillinger B, Steininger C, Vodopivec V, Zanolli C (2015) Neutron microtomography-based virtual extraction and analysis of a cercopithecoid partial cranium (STS 1039) embedded in a breccia fragment from sterkfontein member 4 (South Africa). *Am J Phys Anthropol* (Submitted for publication)
- Berger H (1962) Neutron radiography: a 1962 progress report. In: Symposium on physics and nondestructive testing, San Antonio, Texas, pp 1–37
- Braga J, Loubes J-M, Descouens D, Dumoncel J, Thackeray JF, Kahn J-L et al (2010) Disproportionate cochlear length in genus homo shows a high phylogenetic signal during apes' hearing evolution. *PLoS One* 10:e0127780. doi:[10.1371/journal.pone.0127780](https://doi.org/10.1371/journal.pone.0127780)
- Braga J, Loubes J-M, Descouens D, Dumoncel J, Thackeray JF, Kahn J-L, et al (2015) Disproportionate cochlear length in genus homo shows a high phylogenetic signal during apes' hearing evolution. *PLoS ONE* 10(6):e0127780. doi:[10.1371/journal.pone.0127780](https://doi.org/10.1371/journal.pone.0127780)
- Braga J, Thackeray JF, Dumoncel J, Descouens D, Bruxelles L, Loubes J-M, Kahn J-L, Stambanoni M, Bam L, Hoffman J, de Beer F, Spoor F (2013) A new partial temporal bone of a juvenile hominin from the site of Kromdraai B (South Africa). *J Hum Evol* 65. doi:[10.1016/j.jhevol.2013.07.013](https://doi.org/10.1016/j.jhevol.2013.07.013)
- Buecherl T, von Gostomski L, Breitzkreutz H, Wagner F (2011) NECTAR—A fission neutron radiography and tomography facility. *Nucl Instr Phys Res A* 651:86–89. doi:[10.1016/j.nima.2011.01.058](https://doi.org/10.1016/j.nima.2011.01.058)
- Cisneros JC, Gomes Cabral U, de Beer F, Damiani R, Costa Fortier D (2010) Spondylarthritis in the Triassic. *PLoS One* 5:e13425. doi:[10.1371/journal.pone.0013425](https://doi.org/10.1371/journal.pone.0013425)
- Dinofossils Locations (2015) <http://www.enchantedlearning.com/subjects/dinosaurs/dinofossils/locations/>. Accessed 1 Nov 2015
- de Beer FC, Prevec R, Cisneros J, Abdala F (2008) Hidden structure of fossils revealed by neutron and X-ray tomography. In: Arif M, Downing RG (eds) Proceedings of the 8th world conference on neutron radiography (WCNR-8) held at NIST, Gaithersburg, USA, Sept 2006, Neutron radiography 8, Destech Publications, Lancaster, pp 452–461

- de Beer FC, Radebe MJ, Schillinger B, Nshimirimana R, Ramushu MA, Modise T (2015) Upgrading the neutron radiography facility in South Africa (SANRAD): Concrete shielding design characteristics, *Phys Proc* 69, 115–123 (2015). doi:[10.1016/j.phpro.2015.07.017](https://doi.org/10.1016/j.phpro.2015.07.017)
- Franco M (2011) Our top 10 stops on a fossil road trip. Available at: <http://adventure.howstuffworks.com/destinations/road-trips/10-stops-for-a-fossil-road-trip.htm>
- Fossil and Fossilization (2015) <http://www.scienceclarified.com/Ex-Ga/Fossil-and-Fossilization.html>. Accessed 1 Nov 2015
- Gommery D, Potze S (2013) SAHARA report: Bolt's farm-greensleeves (2010–2013), permit renewal (2013–2016). In: S negas F, Kgasi L (eds) Hope research unit. Plio-Pleistocene Section, Ditsong National Museum of Natural History, Pretoria, South Africa, 17 July 2013. http://www.sahra.org.za/sahris/sites/default/files/additionaldocs/SAHRA%20Report%20BF-Greensleeves%2017.06.2013_0.pdf
- Grellet-Tinner G, Sim CM, Kim DH, Trimby P, Higa A, An SL, Oh HS, Kim TJ, Kardjilov N (2011) Description of the first lithostrotian titanosaur embryo in ovo with neutron characterization and implications for lithostrotian Aptian migration and dispersion. *Gondwana Res* 20:621–629
- Henke W, Tattersall I, Hardt T (2007) *Handbook of paleoanthropology*, vol 1. Springer Science & Business Media. ISBN 3540324747, 9783540324744
- Jacobson L, de Beer FC, Nshimirimana R, Horwitz LK, Chazan M (2013) Neutron tomographic assessment of incisions on prehistoric stone slabs: a case study from Wonderwerk Cave, South Africa. doi:[10.1111/j.1475-4754.2012.00670.x](https://doi.org/10.1111/j.1475-4754.2012.00670.x)
- Laaß M, Schillinger B (2015) Reconstructing the auditory apparatus of therapsids by means of neutron tomography. *Phys Proc* 69:628–635. doi:[10.1016/j.phpro.2015.07.089](https://doi.org/10.1016/j.phpro.2015.07.089)
- Le Roux SD, de Beer FC, Thackeray JF (1997) Neutron radiography of cranial bone of Sts 5 from Sterkfontein, South Africa. *S Afr J Sci* 93:176
- List of human evolution fossils, https://en.wikipedia.org/wiki/List_of_human_evolution_fossils
- List of fossil sites, https://en.wikipedia.org/wiki/List_of_fossil_sites
- Liang L, Rinaldi R, Schober H (2008) *Neutron applications in earth, energy and environmental sciences*, (Google eBook). Springer Science & Business Media, 11 Dec 2008, p 338 <https://books.google.co.za/books?isbn=0387094164>
- Maropeng (2015a) http://www.maropeng.co.za/content/page/what_are_fossils. Visited on 10 June 2015
- Maropeng (2015b) http://www.maropeng.co.za/news/entry/bolts_farm_the_kingdom_of_the_big_cats. Visited on 15 June 2015
- Maropeng (2015c) http://www.maropeng.co.za/content/page/the_science_of_studying_fossils. Visited on 10 July 2015
- Necsa annual report 2013/2014: <http://www.necsa.co.za/Portals/1/Documents/Necsa/Necsa%20Annual%20Report%202014.pdf>. Accessed 1 May 2015
- PSI, http://www.psi.ch/industry/MediaBoard/neutron_imaging_e_07.pdf
- SA Strategy (2011) The South African strategy for the palaeosciences. Incorporating palaeontology, palaeo-anthropology and archaeology. Government Gazette, 20 Sept 2011, General notice 657 of 2011, No. 34624 http://www.gov.za/sites/www.gov.za/files/PALEO_STRATEGY_DST_Final_.pdf
- Schwarz D, Vontobel PL, Eberhard H, Meyer CA, Bongartz G (2005) Neutron tomography of internal structures of vertebrate remains: a comparison with X-ray computed tomography, *Paleontol Electronica* 8, www.uv.es/pe/2005_2/neutron/neutron.pdf
- Sutton MD (2008) Tomographic techniques for the study of exceptionally preserved fossils. *Proc Roy Soc B Biol Sci* 275(1643):1587–1593. doi:[10.1098/rspb.2008.0263](https://doi.org/10.1098/rspb.2008.0263). PMC2394564. PMID18426749

Part II
Neutron Experimental Methods

Chapter 8

General Introduction to Neutron Physics and Instrumentation

R. Pynn and I.S. Anderson

Abstract This chapter provides a simple overview of the properties, production, and interactions of neutron beams as they may be applied for the study of cultural heritage and related artifacts. The content is deliberately brief and provides background information for the subsequent chapters. Excellent introductions to Neutron Scattering Theory and the Instrumentation can be found on the website of this book series (Liang et al. in *Neutron applications in earth, energy and environmental sciences, neutron scattering applications and techniques*. Springer, 2009).

8.1 Introduction

The neutron is a spin- $\frac{1}{2}$ particle, electrically neutral but with a magnetic moment. However, it has no electric dipole moment or at least not a detectable one to a very low limit. Therefore, neutrons only interact with materials through the short-range nuclear forces and by magnetic interactions. Free neutrons are unstable and decay to protons (β -decay) with a half life of 882 s. Hence the only abundant source of neutrons is the atomic nucleus which contains both protons and neutrons. The mass of the neutron is slightly larger than that of the proton. In lighter nuclei the number of neutrons and protons are roughly equal whereas in heavy nuclei the number of neutrons is considerably larger than the number of protons. Consequently heavy nuclei are excellent candidates for neutron sources.

Neutrons can be freed from nuclei using various nuclear reactions (see section below and Chap. 1). Typically these reactions yield neutrons with energies higher than typically used for neutron scattering experiments (\sim meV) and so they have to be slowed down, or moderated, to suitable energy ranges. Hence neutron sources can provide neutron beams with a range of energies depending on the type of

R. Pynn
Indiana University, Bloomington, USA

I.S. Anderson (✉)
ORNL, Oak Ridge, USA
e-mail: andersonian@ornl.gov

reaction used to liberate the neutrons and associated moderators. The distribution of neutrons in energy, and time, has a direct bearing on the type of characterization that can be carried out and the design of experiment.

8.2 Properties of Neutron Radiation

Neutrons are generally categorized according to their means of production and their energies. The term *slow neutrons* is generally used to include all those having energies that are currently used in neutron characterization of materials or that may be used in the foreseen future, $E < 1000$ eV. Neutrons with energies above 1000 eV are typically referred to as *fast neutrons*. A summary of neutron properties is provided in Table 8.1.

Neutrons have no charge, and their electric dipole moment is either zero or too small to measure which helps them to penetrate matter far better than charged particles.

As a consequence, neutrons can penetrate thick layers of most materials without being scattered or absorbed. The attenuation, or decrease in intensity, of a beam of neutrons by aluminum, for example, is about 1 % per millimeter compared with 99 % per millimeter or more, depending on the energy, for X-rays. Figure 8.1 illustrates just how easily neutrons penetrate various materials compared with X-rays or electrons.

The high penetration power of neutrons allows for investigation of large samples of several hundred cubic centimeters even when the sample is placed in a metal container (such as would be required for a liquid or powder sample, for example, or if the sample had to be maintained at low temperature or high pressure). On the other hand neutrons are only weakly scattered once they do penetrate.

The combination of weak interactions and low fluxes makes neutron scattering a signal-limited technique, which is practiced only because it provides information about the structure of materials that cannot be obtained in simpler, less expensive ways. One important characteristic of cold neutrons that can be deduced from Table 8.1 is that their wavelengths and energies are simultaneously similar to interatomic distances and typical vibration energies. Hence they are very sensitive probes of both the structure and dynamics of materials at the atomic scale. Moreover neutron energies can be easily tailored by using moderators at the source.

8.3 Neutron Sources

Today, neutron beam research into cultural heritage is typically carried out at large scale facilities, either nuclear reactors or powerful accelerator-based neutron sources. However, certain experiments such as low-resolution/low-flux imaging can also be carried out with small radioactive or small-accelerator-based sources, which

Table 8.1 Neutron properties

Fundamental properties						
Mass	$m_n = 1.674927351 \times 10^{-27}$ kg = 1.0086474 amu					
Magnetic moment $\mu_N =$ nuclear magneton	$\mu_N = -1.9130427 \mu_N = -0.96623647 \times 10^{-26}$ J/T = $-6.0307740 \times 10^{-9}$ meV/gauss					
Larmor frequency	$\omega_L = \gamma_n \vec{B} $					
Gyromagnetic ratio	$\gamma_n = 2\mu_N/\hbar = 1.83247179 \times 10^4$ radians/s/gauss					
Numerical conversions of neutron attributes [units]						
E [meV]	k^2 [\AA^{-2}]	$1/k^2$ [\AA^{-2}]	v^2 [m^2/s^2]	v [Thz]	T [K]	B [gauss]
E	$\hbar^2 k^2 / 2m_n = 2.072$ 125 k^2	$\hbar^2 / 2m_n = 81.804$ meV \AA^2	$m_n = 1.0454 \times 10^{-5}$ meV (s/m) ²	$h = 4.1357 \times 10^{-12}$ meV s	$k_B = 0.086173$ meV/K	$ \mu_n = 6.0308 \times 10^{-9}$ meV/gauss
	$\hbar^2 k^2 / 2m_n = 2.0721$ meV \AA^2	$\hbar^2 / 2m_n = 81.804$ meV \AA^2	$m_n = 1.0454 \times 10^{-5}$ meV (s/m) ²	$h = 4.1357 \times 10^{-12}$ meV s	$k_B = 0.086173$ meV/K	$ \mu_n = 6.0308 \times 10^{-9}$ meV/gauss
λ [\AA] = $h/m_n v = 3956.0340/v_n$, $v =$ neutron speed [m/s]						
Neutron categories according to energy distribution						
Slow neutrons: $E < 1000$ eV	Fast neutrons: $E > 1000$ eV					
Thermal neutrons: $E \sim 0.025$ eV	Epithermal neutrons: 0.025 eV $< E < \sim 1000$ eV					
Cold neutrons: $E < 0.005$ eV	Very cold neutrons: ~ 8 $\mu\text{eV} < E < 800$ μeV					
	Ultracold neutrons: $E < 8$ μeV					

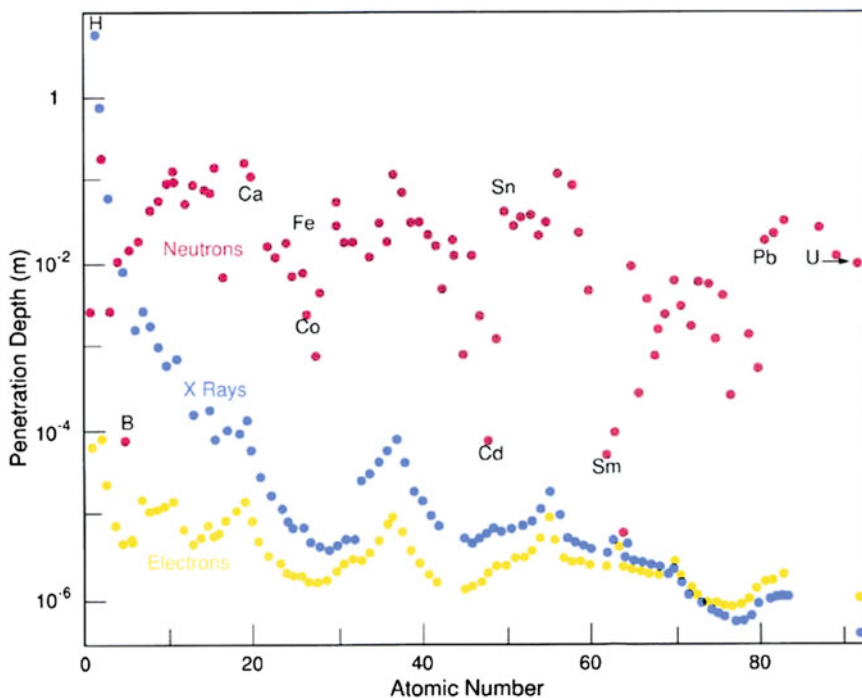


Fig. 8.1 The plot shows how deeply a beam of electrons, X-rays, or thermal neutrons penetrates a particular element in its solid or liquid form before the beam's intensity has been reduced by a factor $1/e$, that is about 37 % of its original intensity. The neutron data are for neutrons having a wavelength of 0.14 nm

can be fixed or portable. This is particularly useful for the investigation of artifacts that cannot be transported to a large scale facility.

Nuclear reactors use the fission process to produce neutrons. Abundant numbers of neutrons are obtained by fission of the heaviest nuclei (e.g. ^{235}U) when they absorb neutrons. In this process several neutrons with energies of a few MeV become free, enabling the possibility of controlled chain reaction. An important requirement is that the energy of these fission neutrons must be reduced in order to keep the reaction going. Therefore current reactors contain materials of light nuclei (e.g. water), the moderator, which lowers the neutron energy by multiple scattering processes. As a consequence the reactor contains a cloud of neutrons with a thermal (Maxwellian) energy distribution with mean energy of about 0.024 eV, determined by the temperature of the moderator, and a tail of high-energy neutrons up to several MeV. In order to shift the Maxwellian distribution to higher or lower energies, hot or cold moderators (respectively) can be installed close to the core of the reactor and within the thermal moderator. Cold moderators of liquid hydrogen producing high fluxes of neutrons with energies of a few meV are particularly common.

Most of the current reactor sources for scattering applications were built in the 1960s and 1970s and were primarily designed for materials testing for the nuclear industry, providing medium flux. Reactors coming into operation more recently include JRR3 at the Japan Atomic Energy Agency (1990), HANARO at the Korea Atomic Energy Research Institute (1997), FRM-II in Munich, Germany (2004), OPAL at the Australian Nuclear Science and Technology Organization (2006), and the China Advanced Research Reactor (CARR) in Beijing, China (2010).

Neutrons can also be produced by the spallation process, in which high-energy protons strike a solid target, usually a heavy metal. The pulsed nature of most accelerator-based neutron sources can offer a significant advantage in experiments using the time-of-flight (TOF) method, in which the speed of the neutron is measured by timing its flight from the source to the detector. All accelerator driven sources require associated moderators, surrounding the target to slow down the neutrons to useable energies. Typically moderators for neutron scattering applications contain hydrogen, either liquid (cryogenic), in water or in a solid hydrocarbon form, since it presents enough degrees of freedom to slow down neutrons to the meV regime. The temperature of the moderator defines the energy spectrum available. Furthermore, moderators can be used to tailor the resulting neutron pulse time to suit the requirements of the experiment.

Pulsed proton-driven neutron sources recently completed include the Spallation Neutron Source (SNS) in the United States, the Japanese Spallation Neutron Source (JSNS) of the Japan Proton Accelerator Research Complex (J-PARC) project in Japan (2008), and the second target station at the ISIS facility in the UK (2009). Two other large facilities are under construction: the China Spallation Neutron Source (CSNS) in China and the European Spallation Source (ESS) in Sweden.

A detailed list of neutron facilities worldwide can be found at: <http://neutronsources.org/>

8.4 Neutron Interactions

Neutrons interact with matter principally via nuclear rather than electrical forces, and nuclear forces are very short ranged. Hence, as far as the neutron is concerned, solid matter is not very dense and interaction probabilities are low.

Neutrons do however possess a magnetic moment and so can experience a force of magnetic origin when moving in a field. A good example is the field produced by unpaired electrons in matter. Magnetic moments in solids can therefore give rise to magnetic scattering of neutrons much the same as the nuclear interactions and X-ray atomic electron interactions. The magnetic interaction, unlike the nuclear interaction is not isotropic, it is dipolar and depends on the relative orientations of neutron moment, and hence its spin, and the scattering moment. Neutron scattering is therefore sensitive to the spatial distribution of both the direction and magnitude of

magnetization in a material. Magnetic forces can also be used effectively to steer neutron beams even though the forces are, in general, weak.

8.4.1 Neutron-Nucleus Interactions

There are numerous types of neutron-nuclear interactions as portrayed in Fig. 8.2.

- Nuclear elastic reaction. The nucleus is left in the same internal quantum state after interaction as before, but may gain or lose laboratory kinetic energy while the neutron respectively loses or gains kinetic energy. Neutron-nuclear elastic scattering is the main basis of neutron scattering measurements, in which the cross sections are usually independent of neutron energy (see Chap. 9). Cross sections in many cases depend on the relative orientation of nuclear spin and neutron spin: usually, samples or neutron beams are not spin-polarized, and cross sections are then the average over relative spin orientations. There is some confusion in the nomenclature here that beginners should be aware of. Neutron scattering can be elastic or inelastic depending on whether the neutron changes energy on the scattering process or not; both cases are still nuclear elastic reactions.
- Nuclear inelastic reactions. The nucleus absorbs energy from the neutron and is left in a different internal quantum state after the interaction than before. The struck nucleus decays by photon (gamma-ray) emission, and the neutron emerges with lower energy than before colliding.

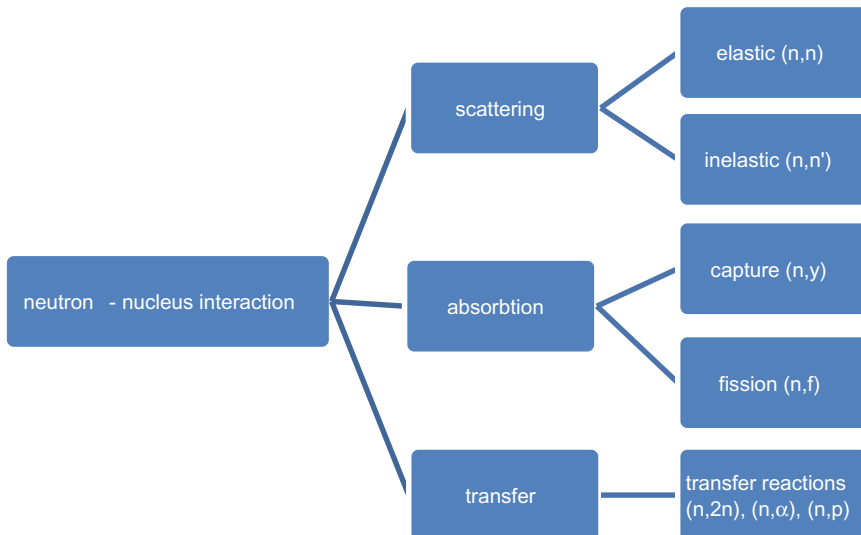


Fig. 8.2 Neutron-nucleus interactions

- *Absorption*. The neutron disappears into the nucleus, forming a compound nucleus that is in an excited state, one mass unit heavier than the original, which decays by emitting lighter particles or electrons. Usually the formation of a compound nucleus is promptly accompanied by emission of gamma rays. In many instances, a massive charged particle emerges from the reaction, and the products carry substantial kinetic energy. The residual nucleus may have a long lifetime (this is neutron activation) and beta decay may be followed by emission of characteristic gamma rays. This interaction is the basis of the Prompt Gamma Activation Analysis (PGAA) and the associated Prompt Gamma Activation Imaging (PGAI) techniques described in Chaps. 10–14. The absorption cross sections for some isotopes are spin-dependent, that is, depend on the relative orientation of the nucleus and the neutron spin.
- *Fission*. The neutron disappears into the nucleus momentarily leaving it in a highly excited state from which the nucleus (must be a heavy nucleus, $Z > 80$) splits into two roughly equal fragments and a few light particles, almost always neutrons. Fission fragments carry about 180 MeV of energy, which appears as ionization and heat in the surroundings.
- *Capture*. The neutron disappears into the nucleus regardless of what happens afterwards (therefore, capture includes absorption and fission). Capture cross sections for low energy neutrons are usually proportional to the neutron wavelength.
- *Transfer*. The neutron collides directly with the nucleus and emits nucleons.

8.5 Instrumentation

Neutron sources, reactor or accelerator driven, provide beams of neutrons in a wide energy range depending on the temperature of the moderator. For a typical measurement the emitted beam from the source has to be tailored in direction, divergence, energy and sometimes polarization before impinging on the sample to be characterized. After interaction the scattered or transmitted beam has to be detected again as function of direction, divergence, energy and polarization. Sometimes it will be a secondary emitted particle that is detected following neutron capture. There are a variety of methods that can be used to direct and select neutrons and hence a diverse range of instrumentation exists often highly optimized for neutron source and the type of experiment to be carried out.

An excellent overview of neutron instrumentation can be found in the document entitled “Neutron Scattering Instrumentation” available on the web site of this book series (Liang et al. 2009).

8.6 Conclusion

Neutron beam techniques provide exceptional tools for the study of materials related to cultural heritage. The penetrating power of neutrons makes them ideal for looking inside artefacts and determining bulk properties. A wide range of instrumentation is available at user facilities across the world and in some cases portable sources can be used for local investigations.

References

Liang L et al (eds) (2009) Neutron applications in earth, energy and environmental sciences, neutron scattering applications and techniques. Springer. doi:[10.1007/978-0-387-09416-8_2](https://doi.org/10.1007/978-0-387-09416-8_2). The first two chapters of the initial book in this series are available for free download. <http://www.springer.com/series/8141>

Chapter 9

Scattering Techniques: Small- and Wide-Angle Neutron Diffraction

C.-K. Loong, A. Scherillo and G. Festa

Abstract Neutron scattering techniques are widely used for materials characterization and may be used to study meso-, micro- and nano-structures of objects of cultural heritage interest. This chapter presents the theoretical framework and introductory instrumentation of neutron diffraction techniques together with some practical examples.

9.1 Introduction

Neutron scattering is a versatile method for structural investigations at atomic/molecular level of materials and may benefit cultural heritage applications, generating information of interest to restorers, architects, curators as well as the general public. The artefacts are generally made of polycrystalline materials such as metals, alloys, ceramics, stone, etc. by ancient technologies. Neutron scattering, in particular elastic scattering, provides information about chemical composition, crystal structures, strain maps and micro-pore size distribution over local regions or the entire object nondestructively. For example, crystallographic analysis by neutron diffraction allows quantitatively determination of atomic composition specific to the crystal structures and phase contents such as the effect due to incorporation of Sn into the copper fcc lattice in bronze artefacts. As anticipated, real objects do not conform to the ideal crystal structure. Therefore, detailed examination of the diffraction profile, phase composition, residual strains and other imperfections can reveal valuable telltale evidence of manufacture processing, utilization, wear and tear, degradation, etc. At a length scale beyond interatomic distances, small-angle neutron scattering can determine the sizes (from tenths to thousands of nanometers)

C.-K. Loong (✉) · G. Festa
Department of Physics and Centre NAST, University of Rome Tor Vergata, Rome, Italy
e-mail: ckloong@gmail.com

A. Scherillo
ISIS Spallation Neutron Source, Oxfordshire, UK

and shapes of inhomogeneous features such as pores, aggregates, and textures in organic and inorganic matters such as bones, stones, ancient tools and weapons, etc.

In this chapter, we focus on small-to-wide-angle diffraction techniques, first providing the background and theoretical framework for the various methodologies (Squires 1978; Dörner 1999; Carpenter and Loong 2015) and time-of-flight neutron diffraction (Kockelmann 2001). The following sections present key aspects of instrumentation and illustrative examples of cultural-heritage applications.

9.2 Background

If our desire is to characterize the static structure of a bulk substance at the atomic/molecular length scale, i.e., of the order of $0.1\text{--}10^5$ nm, the available experimental probes are limited to electrons, photons, protons and neutrons. Adding the criteria of nondestructive and noninvasive investigation, which is crucial to studying objects related to cultural heritage, we have to restrict the energies of these probes to below the threshold energy of chemical-bond dissociation. Next, suppose we want to examine the texture introduced in a metal by forge welding, such as the anisotropic orientation of crystalline grains across the blade of a sword, we need to resolve the crystal structure, often of multiple phases, within an interior gauge volume that is sufficiently small to discern the variation of local mechanical properties yet large enough to encompass a statistical distribution of grains. Although the technique of neutron diffraction and radiography arrived after the electron, x-ray, and proton counterparts, its versatility proves to be very prominent across a broad spectrum of materials characterization. In the following sections, we first introduce the basic theory and methodology of neutron diffraction with an accent on cultural heritage research. The methodology of neutron-diffraction studies of the interplay between the structures of crystalline, disordered and composite materials and functionalities relevant to cultural heritage are discussed, followed by a brief conclusion of the present and future progress of the field.

9.3 Theoretical Framework

We use the convention of describing a quantity of the incident and scattered neutron by subscript 0 and 1, respectively. Now consider that the scattered neutrons, after interaction with a sample—the *scatterer*, are collected by a detector whose window subtends a solid angle $d\Omega$, the *double differential cross section* in terms of the *coherent* and *incoherent scattering functions* denoted by $S_{coh}(\vec{Q}, E)$ and $S_{inc}(\vec{Q}, E)$, respectively is

$$\frac{d^2\sigma}{d\Omega dE} = \frac{1}{N} \frac{k_1}{4\pi k_0} \left[\sigma_{coh} S_{coh}(\vec{\mathbf{Q}}, E) + \sigma_{inc} S_{inc}(\vec{\mathbf{Q}}, E) \right], \quad (9.1)$$

where $\hbar\vec{\mathbf{Q}}$ is the neutron momentum transfer, $\vec{\mathbf{Q}} = \vec{\mathbf{k}}_0 - \vec{\mathbf{k}}_1$ with $\vec{\mathbf{k}}_0$ and $\vec{\mathbf{k}}_1$ the incoming and outgoing neutron wave vectors, E is the neutron energy transfer ($E = E_0 - E_1$), N is the number of scattering units whose coherent and incoherent scattering cross sections are $\sigma_{coh} = 4\pi(b_{coh})^2$ and $\sigma_{inc} = 4\pi(b_{inc})^2$, respectively, b_{coh} and b_{inc} are the corresponding coherent and incoherent *scattering lengths*.

Owing to the fact that neutrons interact with the atomic nuclei, which are the fundamental constituent of all scatterers, the scattered wavefunction of the neutrons comprises the coherent and incoherent parts. Coherent scattering represents a mean scattering that is common to all the scattering units and incoherent scattering represents the deviation from the mean. Therefore, coherent scattering carries information about the spatial-temporal correlation of the scattering units—the collective static and dynamic structure of the scatterer because of inference of the corresponding outgoing wavefunctions. Incoherent scattering, which corresponds to the interference of an outgoing wavefunction with itself, only contains information about a single scattering unit. There are several origins of incoherent scattering: In neutron-nucleus scattering if the deviation arises from the dependence of the nuclear-spin operator, it is the *spin-incoherency*. If the deviation arises from the differing isotopes against the mean scattering of a natural element, it is the *isotopic incoherence*. If the deviation arises from inhomogeneity against the scattering of a mean composition of the scatterer, it is the *compositional incoherence*. Incoherent scattering amounts to diffuse, scattering-angle-independent background superimposed on the coherent-scattering signals. Purposeful variation of isotope fractions, *isotope substitution*, is one of the advantageous features of neutron scattering techniques. This is useful to emphasize or de-emphasize scattering in sample materials from selected sample components, especially fruitful in small-angle neutron scattering and H/D substitution (assuming unchanged chemical properties which may not be true). In functional components of neutron scattering experiments such as sample containers and beam windows, judicious isotope substitution can eliminate coherent scattering effects that complicate measurements.

In general, the energy dependence of the coherent and incoherent scattering functions arises from the time evolution of the scattering units (the dynamics) which is represented by the corresponding *intermediate scattering functions*, $I(\vec{\mathbf{Q}}, t)$ and $I_s(\vec{\mathbf{Q}}, t)$:

$$S_{coh}(\vec{\mathbf{Q}}, E) = \frac{1}{2\pi\hbar} \int_{-\infty}^{\infty} dt \exp(-iEt/\hbar) I(\vec{\mathbf{Q}}, t), \quad (9.2)$$

and

$$S_{inc}(\vec{\mathbf{Q}}, E) = \frac{1}{2\pi\hbar} \int_{-\infty}^{\infty} dt \exp(-iEt/\hbar) I_s(\vec{\mathbf{Q}}, t). \quad (9.3)$$

The *Elastic scattering*, ($k_0 = k_1$, $E = 0$), concerns only the time-independent, average structure of the sample in equilibrium, which is denoted by

$$\begin{aligned} \left(\frac{d\sigma}{d\Omega}\right)_{coh}^{el} &= (b_{coh})^2 I(\vec{\mathbf{Q}}, \infty) \\ &= (b_{coh})^2 S_{coh}(\vec{\mathbf{Q}}), \end{aligned} \quad (9.4)$$

and

$$\begin{aligned} \left(\frac{d\sigma}{d\Omega}\right)_{inc}^{el} &= (b_{inc})^2 I_s(\vec{\mathbf{Q}}, \infty). \\ &= (b_{inc})^2 S_{inc}(\vec{\mathbf{Q}}). \end{aligned} \quad (9.5)$$

In (9.5) $S_{coh}(\vec{\mathbf{Q}})$ is the *elastic (coherent) structure factor* and $S_{inc}(\vec{\mathbf{Q}})$ is the *elastic incoherent structure factor*. The elastic structure factors are normally much larger ($\sim 10^2$ – 10^3) than their inelastic counterparts.

The objective of diffraction studies is to determine the time-independent, average structure of the sample in an environment characterized by temperature, applied pressure and electromagnetic fields, etc. usually in thermodynamic equilibrium. However, in practice, most *diffractometers* collect data with detectors fixed along a $\vec{\mathbf{k}}_1$ direction without discrimination either the incident or the scattered energy. The data obtained in this way are almost always *total scattering*, which is not the same as elastic scattering, because $|\vec{\mathbf{k}}_1|$ varies along a fixed detector angle so that the condition of $k_1 = k_0$ is not satisfied. Physically, the total scattering measures an average of instantaneous snapshots of the time-dependent structure whereas the true elastic scattering measures the averaged structure at equilibrium. But the difference is sufficiently small that the practice, *static approximation*, is deemed acceptable as long as the occurred energy transfers (the inelasticity) are small compared to the incident energy.

In the following we describe the formulation of the elastic coherent and incoherent elastic structure factors for various systems and comment on the applications for cultural heritage studies. We assume the intermediate scattering functions of (9.2) and (9.3) admit solely density-density correlations of non-magnetic atoms and/or molecules (or collectively called particles in large structures, see discussion of small-angle scattering below) thereby rendering only the chemical structures. This is chiefly the case for cultural heritage studies. On the other hand, inclusion of density-density correlations of the magnetization—the magnetic structure—can be

formulated in a similar (but more complex) fashion. Experimentally, ignoring magnetic scattering implies little need for using polarized neutrons.

9.3.1 Crystalline Materials

For a perfect crystal containing N_c unit cells each having a volume, v_0 , (9.4) becomes

$$\left(\frac{d\sigma}{d\Omega}\right)_{coh}^{el} = N_c \frac{(2\pi)^3}{v_0} \sum_{\vec{\tau}} \delta(\vec{Q} - \vec{\tau}) \left| F_{hkl}(\vec{Q}) \right|^2, \quad (9.6)$$

where

$$F_{hkl}(\vec{Q}) = \sum_d b_{coh}^d \exp(-W_d) \exp(i\vec{Q} \cdot \vec{d}) \quad (9.7)$$

is the *crystallographic unit-cell structure factor*. The equilibrium position vector of atom d in the unit cell is denoted by \vec{d} , and the index of the sum cover the atoms of the basis in the unit cell, not to be confused with the lattice spacing d . Therefore, diffraction from a perfect crystal yields nonzero (singular) intensities only at the *reciprocal vectors*, $\vec{\tau}$, characterized by the hkl reflections. Here,

$$\vec{\tau} = h\vec{a}_1^* + k\vec{a}_2^* + l\vec{a}_3^*, \quad (9.8)$$

where \vec{a}_1^* , \vec{a}_2^* , \vec{a}_3^* are the primitive vectors of a reciprocal unit cell, corresponds to the direct-lattice counterpart,

$$\vec{R}_\kappa = \kappa_1\vec{a}_1 + \kappa_2\vec{a}_2 + \kappa_3\vec{a}_3, \quad (9.9)$$

where \vec{a}_1 , \vec{a}_2 , \vec{a}_3 are the primitive vectors of the unit cell and $(\kappa_1, \kappa_2, \kappa_3)$ is a set of integers. The condition of

$$\vec{Q} \cdot \vec{R}_l = 2n\pi \quad (n = \text{an integer}) \quad \text{for all } \vec{R}_l \quad (9.10)$$

is called the *Bragg condition*, or the *Laue condition*, which was discovered by William Lawrence (the younger) Bragg in conjunction with Max von Laue's pioneering measurement on x-ray diffraction. It can be shown that $W \propto Q^2$ in the *Debye-Waller factor*, $\exp(-W_d)$, that thermal motion of atoms suppresses the intensities, especially for the high- Q reflections. The deduced intensity reappears as *thermal diffuse scattering* (or phonons) in the inelastic region.

In a diffraction experiment on crystalline materials we typically measure the intensities $\propto \left| F_{hkl}(\vec{Q}) \right|^2$ but not completely the complex quantity

$$F_{hkl}(\vec{\mathbf{Q}}) = |F_{hkl}| \exp(i\alpha_{hkl}) \quad (9.11)$$

which includes a *phase* α_{hkl} . We recall that it is the phases of the scattered waves from individual scattering centers that permit an interference effect from which we can derive structural information about the centers' distribution. Without the phase, we cannot find the basis function of the crystal by an inverse Fourier transformation of the measured intensity. This deficiency is termed the *phase problem*. On the other hand, if we take the inverse Fourier transform of the elastic intensity, namely,

$$A \int I^e(\vec{\mathbf{Q}}) \exp(i\vec{\mathbf{Q}} \cdot \vec{\mathbf{r}}) d^3\vec{\mathbf{Q}} = P(\vec{\mathbf{r}}), \quad (9.12)$$

we obtain, up to a normalization constant A , the *Patterson function*, $P(\vec{\mathbf{r}})$. This facilitates a means to generate a *Patterson map* in the direct space using only the observed diffracted intensity. However, because of the lack of phase information, a Patterson map is not truly the basic function. For example, a peak position of $P(\vec{\mathbf{r}})$ does not represent the atomic density at $\vec{\mathbf{r}}$ but rather the density difference between two atoms separated by $|\vec{\mathbf{r}}|$.

Identification of the multiple crystal phases in composite specimens is one of the primary interests in culture heritage research, which are suitable for powder diffraction studies. The *Rietveld method* (Rietveld 1969) is a well known methodology for the refinement of powder diffraction profiles by goodness-of-fit tests. It was first applied by Hugo Rietveld in 1969 for the analysis of x-ray data. Since then, the use of the Rietveld method for neutron powder diffraction has been made easy by computer programs that incorporate the pertinent factors as parameterized functions and provide simultaneous profile refinement for both x-rays and neutrons, and sometimes EXFAS and other data. To a lesser extent, structural imperfections with respect to a powder, such as the average grain size and preferred orientation of crystallites, can be assessed qualitatively by fitting corresponding empirical functions to the data.

On the experimental side, the *Laue method* employs a polychromatic neutron beam incident on the sample; this means that, the direction of $\vec{\mathbf{k}}_0$ is fixed but the magnitudes $k_0 \equiv k = 2\pi/\lambda$ are distributed in a continuum. It becomes very powerful by applying the time-of-flight (TOF) technique on pulsed-source diffractometers because all the scattering events are uniquely accounted for by recording data in 4 dimensions, i.e., the detected location (x, y, z) at an area detector, and the flight time, t . The intensity captured by a detector width of $\Delta\theta$ for the entire *Debye-Scherrer cone* of the hkl reflections from a powder is

$$I_{Laue}^p = N_c \frac{\phi(\lambda)}{4} \frac{\lambda^4}{\sin^2 \theta} j \frac{|F_{hkl}(\vec{\tau})|^2}{v_0} \cos \theta \Delta\theta, \quad (9.13)$$

where $\phi(\lambda)$ is the wavelength (λ)-dependent incident neutron flux, θ is the *Bragg angle*, (2θ is the scattering angle for diffraction), and the multiplicity j is the number of equivalent hkl reflections.

Alternatively, for diffraction experiments at a steady-state source, a monochromatic beam of mean wavelength λ_0 with a width $\Delta\lambda_0$ is usually prepared. The intensity from a powder sample is

$$I_{\lambda_0}^p = N_c \phi(\lambda_0) \Delta\lambda_0 \frac{\lambda_0^3}{4 \sin \theta} j \frac{|F_{hkl}(\vec{\tau})|^2}{v_0}. \quad (9.14)$$

The above derivation stems from the application of the Born approximation and the Fermi pseudopotential. This approach, under the *kinematical approximation*, is to consider solely the single-scattering event of an incident beam of neutrons diffracted collectively by an assembly of atoms characterized by crystalline atomic planes, either in a perfect single crystal or an ideal powder, resulting in a coherently scattered beam captured by a detector. It does not take into account that neutron waves attenuate as they pass through a sample. For example, some neutrons may consecutively be diffracted by multiple atomic planes, or some may be absorbed selectively by some of the atoms as they traverse the sample, resulting in attenuated secondary beams. The real reflectivity of a thin domain in the crystal and of the mosaic structure of the domains give rise to *primary extinction* and *secondary extinction*, respectively, which influences the apparent spreads (and intensities) of the diffracted and transmitted beam. Rigorous treatment of extinction, multiple-scattering, absorption and other multi-beam effects are dealt with by the *dynamic theory of scattering*, a topic important to neutron optics and interferometry, which is beyond the scope of this discussion.

9.3.2 Disordered Materials

The structures of disordered materials, e.g., glasses and liquids, are characterized by statistical functions in the context of short-range order (SRO), intermediate-range order (IRO), and extended-range order (ERO). We note that the nature of orientation randomness in these materials reduces scattering data to a one-dimensional display even though the SRO, IRO, and ERO are not isotropic. Although the intensity profiles of disordered materials in general are much broader than Bragg reflections of crystalline solids, we still aim at the resolution of interatomic distances. Diffraction at large \vec{Q} , hence measurements at relatively high scattering angles and short wavelengths—a condition well suited for pulsed source diffractometers, are essential to achieve the required spatial resolution.

For simplicity we first consider a monatomic system displaying randomly distributed disorder. The elastic structure factor is:

$$S_{coh}(Q) = 1 + 4\pi\rho_0 \int_0^{\infty} r^2 [g(r) - 1] \frac{\sin Qr}{Qr} dr, \quad (9.15)$$

where ρ_0 is the mean number density of the specimen. $g(r)$ is the static pair-distribution function, which, in a classical picture, gives the number density at a point \vec{r} relative to an arbitrarily chosen particle. From (9.15) the measured $S_{coh}(Q)$ from a diffraction experiment can be used to evaluate the integral:

$$\int_0^{\infty} Q[S_{coh}(Q) - 1] \sin(Qr) dQ = 2\pi^2 r \rho_0 [g(r) - 1]. \quad (9.16)$$

The quantity $[S_{coh}(Q) - 1]$ on the left-hand side is the structure factor with the self-term removed. Therefore, the experiment senses the interference between distinct atomic pairs. Then multiplying this interference function with Q and taking the Fourier transform, we obtain the structural information in terms of $\sim r\rho_0[g(r) - 1]$, the *reduced pair-distribution function*.

The *total distribution function* (TDF) is

$$T(r) \equiv 4\pi r \rho_0 g(r). \quad (9.17)$$

The peak positions in $T(r)$ correspond to the mean distances between atomic pairs. If severe overlap of the peaks does not occur, aided by high spatial-resolution measurements at large Q values, $T(r)$ provides a basis to identify the average bond lengths between near neighbors.

The radial distribution function (RDF), which is the number of atoms lying in a distance interval of $(r, r + dr)$ from an atom at the origin, is

$$N(r) \equiv 4\pi r^2 \rho_0 g(r) \quad (9.18)$$

Thus the integrated area under a peak in the RDF is a measure of the coordination number of the atoms. If overlapping of peaks is substantial, fitting of the peak profile as the sum of contributions from multiple pairs is necessary. Obviously, $T(r)$ and $N(r)$ oscillate around the lines, $4\pi r \rho_0$ and $4\pi r^2 \rho_0$, respectively.

The above analysis can be extended to treat a multicomponent system, say, containing C components in which the j th component has N_j identical atoms with coherent scattering length b_j , hence $c_i = N_i/N$, and the total coherent scattering cross section per atom is $4\pi \sum_i (c_i b_i)^2 \equiv 4\pi \bar{b}^2$. For example, (9.5) is still valid provided that the $g(r)$ for a multicomponent system is defined as

$$g(r) = \frac{\sum_{\alpha,\beta} c_{\alpha} b_{\alpha} c_{\beta} b_{\beta} g_{\alpha\beta}(r)}{\bar{b}^2}, \quad (9.19)$$

where $g_{\alpha\beta}(r)$ is the *partial radial distribution functions* (PRDF) defined as the number of atoms of component β at a distance r from a given atom of the α component, i.e.,

$$g_{\alpha\beta}(r) \equiv \frac{dn_{\alpha\beta}(r)}{4\pi r^2 \rho_{\alpha} dr}, \quad (9.20)$$

where

$$\rho_{\alpha} = \frac{N_{\alpha}}{V} = \frac{Nc_{\alpha}}{V}. \quad (9.21)$$

and V is the volume of the sample.

Experimentally, it will require, in principle, at least $C \times (C + 1)$ sets of independent datasets to solve all the partial distribution functions. This may be done, at least in part, for some chemical-element constituents, using variant samples obtained by isotopic substitution. This technique is practical only for relatively simple systems for which isotopes of the elements are available and affordable; however, it has proved to be valuable in a number of cases.

9.3.3 *Between the Crystalline and Glassy Ends: Diffuse Scattering*

Practical materials seldom form perfect crystals or glasses (and liquids) according to purely disordered structural models. This is particularly relevant to culture heritage studies as the underlying structural imperfections of an object often reveal interesting technical and/or functional aspects related the history of preparation and utilization of materials. Neutron diffraction studies of these structural properties fall into the category of *diffuse scattering*. Normally, an average structure, based either on a crystalline or amorphous model, is defined and hence its structure factor. The observed data are then compared against the calculated intensity of the average structure, through which an interpretation of deviation from the average, often termed the defects or microstructures, is obtained.

One kind of microstructures of particular pertinence to cultural heritage studies is called *texture*, which is the preferred orientation of the crystalline grains in materials. For example, the texture in an artifact may unveil the history of processing and/or utilization of the object. Here, the average structure is a crystalline powder composed of randomly oriented grains. The *pole figure method* involves the analysis of the crystal orientation distribution function through diffraction

measurements as two-dimensional projection on the specimen reference frame (or vice versa, the distribution of the specimen parameters such as normal, rolling and transverse directions of a rectangular sheet on the crystal reference frame).

A variety of local structures and defects, including thermal motion of atoms (phonons), chemical disorders in alloys, strain distribution over a moderate distance from defect centers in a crystal, etc. can be studied by diffuse scattering. The *Patterson-function* and the *pair distribution function (PDF) methods* are well-known approaches of data analysis.

9.3.4 *Small-Angle Neutron Scattering (SANS) and Ultra-Small-Angle Neutron Scattering (USANS)*

The previous sections describe diffraction over a wide range of scattering angles by monochromatic neutrons at steady-state sources and diffraction at relatively high scattering angles using a wide range of neutron wavelengths, λ , (by TOF technique), which concern mainly structures at interatomic distances, no matter whether the samples exhibit overall long-range ordered or disordered structures. Now we consider materials that contain ‘particles’, each of which is made up of hundreds or more of atoms, such as the clusters (or pores) in an alloy, colloids in an emulsion, macromolecules in a solution, and magnetic domains in a ferromagnet. Here, the primary interests are the composition, dimensions and shapes (hence the average molecular weight), the surface roughness of the particles, and the nature of particle dispersion or aggregation in the host matrix. Interatomic distances are no longer the concern. Although the particles may not be isotropic or homogeneous, they usually are distributed randomly over all orientations. Therefore, with a few exceptions, the pair distribution as a function of the radial distance, r , i.e., a 1-D function, suffices. Because of the larger length scale ($d \sim 10\text{--}100$ nm), scattering falls into the range of very small wave vectors, Q , following the argument of $Q = \frac{2\pi}{d} = 2 \sin \theta / \lambda$ (where 2θ is the scattering angle). Thus usable data range on the low- Q side depends on the attainable good signal-to-noise ratio at the smallest value Q_{\min} through judicious control of the incident-beam collimation and the detector resolution near the forward direction. Conventional SANS instruments may reach a Q_{\min} of $\sim 10^{-4} \text{ nm}^{-1}$. Further extension to lower Q_{\min} values of the order of $\sim 2 \times 10^{-6} \text{ nm}^{-1}$ is possible by specially designed USANS instruments.

The intensity of SANS from the particles against the background matrix of scattering-length density (SLD) ρ_{bkgd} for centrosymmetric systems is

$$I(Q) = \Phi V \Delta \rho^2 [P(Q)]^2 S(Q). \quad (9.22)$$

Otherwise,

$$I(Q) = \Phi V \Delta\rho^2 \frac{|\langle P(Q) \rangle|^2}{\langle |P(Q)|^2 \rangle} S(Q). \tag{9.23}$$

Here, Φ is the neutron flux and $\Delta\rho$ is the scattering contrast factor characterized by the difference between the SLD of the particle and that of the background matrix,

$$\Delta\rho \equiv \langle \rho(r) \rangle - \rho_{bkgd}. \tag{9.24}$$

In (9.22) and (9.23) $P(Q)$ is the *particle form factor* which is equal to the Fourier transform of the particle’s SLD in the direct space. In a dilute system, particle-particle interaction can be ignored, hence $S(Q) = 1$, then the SANS experiment provides a means to determine the size and shape of the particle through fitting the data with hypothetical form factors. The analytical expressions of several simple homogeneous objects are given in Table 9.1.

Particles of identical size and shape occur only in idealized monodisperse system. Polydispersity, i.e., systems containing particles of different sizes and shapes, may be accounted for by incorporation of a size distribution function into the data fitting. One of the effects of polydispersity is smearing of the data by superimposing different particle form factors with respect to the one parameterized with a mean size and shape.

The radius of gyration, R_g for a particle of density $\rho(\vec{r})$ and volume V is related to the second moment in the expression:

Table 9.1 The particle form factors of a few simple homogeneous objects

Objects	$P(Q)$
Sphere of radius R	$\frac{3}{QR} J_1(QR) = \frac{3}{(QR)^3} [\sin(QR) - QR \cos(QR)]$
Cylinder of radius R , length L , oriented such that the cylindrical axis makes an angle ϑ with \vec{Q}	$\left[\frac{\sin(Q\mu L/2)}{Q\mu L/2} \right] \left[\frac{2J_1(Q\sqrt{1-\mu^2}R)}{Q\sqrt{1-\mu^2}R} \right],$ <p>where</p> $\mu \equiv \cos \vartheta, \text{ and } J_1(z) = \frac{1}{i\pi} \int_0^\pi d\phi \exp(iz \cos \phi) \cos \phi$
Homogeneous parallelepiped of dimension $a \times b \times c$	$\frac{1}{V} \int_V \rho(x, y, z) \exp(i\vec{Q} \cdot \vec{r}) dx dy dz = s(Q_x, a) s(Q_y, b) s(Q_z, c),$ <p>where</p> $s(Q_x, a) = \frac{1}{a} \int_{-a/2}^{a/2} \exp(iQ_x x) dx = \frac{2}{Q_x a} \sin(Q_x a/2)$

$$R_g^2 = \frac{1}{\langle \rho(\vec{r}) \rangle} \int_V \rho(\vec{r}) r^2 d\vec{r}. \quad (9.25)$$

By examining the intensity at small Q , the interval—obviously limited by Q_{\min} referred to as the Guinier region, we obtain a scheme to estimate R_g for dilute systems:

$$I(Q) \approx I(0) \exp \left[-\frac{(QR_g)^2}{3} \right], \quad (9.26)$$

or,

$$\frac{c}{I(Q)} \approx \frac{1}{I(0)} \left[1 + \frac{(QR_g)^2}{3} \right]. \quad (9.27)$$

Equations (9.26) and (9.27) are called the Guinier approximation and the Zimm approximation, respectively. The values of R_g obtained from these two approximations differ for large QR_g .

From (9.22) the SANS intensity from a dilute system (setting $S(Q) = 1$) can be expressed as the *Debye equation*:

$$I(Q) = \int_V \int_V \rho_u \rho_v \frac{\sin(Qr_{uv})}{Qr_{uv}} dudv, \quad (9.28)$$

where $r_{uv} = |\vec{u} - \vec{v}|$. Debye and Burche also defined an autocorrelation function, $\gamma(r)$, which is related to the *radial Patterson function* as

$$\gamma(r) = \frac{1}{4\pi} P(r), \quad (9.29)$$

so that

$$I(Q) = v \int_0^\infty \gamma(r) \frac{\sin(Qr)}{Qr} 4\pi r^2 dr, \quad (9.30)$$

where v is the volume of the particle. This implies that $\gamma(r)$ can be calculated from experimental data by the inverse Fourier transform

$$\gamma(r) = \frac{1}{2\pi^2\nu} \int_0^\infty Q^2 I(Q) \frac{\sin(Qr)}{Qr} dQ. \quad (9.31)$$

At $Q = 0$ all the scattered waves are in phase, so that $I(0)$ equals the square of the total scattering density, which must be invariant for any canonical ensembles. Therefore, $\gamma(0)$ is also invariant. From (9.31) we obtain the *Porod invariance*:

$$\int_0^\infty Q^2 I(Q) dQ = 2\pi^2 \int_V [\Delta\rho(r)]^2 dr. \quad (9.32)$$

Although $I(0)$ is not exactly measurable, it can be estimated by careful extrapolation of the observed intensity to $Q = 0$. Firstly, the quantity $\gamma(r)/\gamma(0)$ is a characteristic function which depends only on the shape of the particle. It represents the probability of finding a point within a particle at distance r from the origin. Secondly, for uniform particles, the first derivative evaluated at $r = 0$ is proportional to the surface area, S , multiplied with the density, ρ_0 , of the particles:

$$\gamma'(0) = -\frac{(\Delta\rho)^2 S}{4}. \quad (9.33)$$

Thirdly, the second derivative of $\gamma(r)$ is proportional to the chord-length distribution, $C(\ell)$, such that $C(\ell)d\ell$ prescribes the probability of finding a line connecting two surface points (a chord) that has a length between ℓ and $\ell + d\ell$. Lastly, the asymptotic behavior of the intensity is related to the nature of the particle surfaces through

$$I(Q) \underset{Q \rightarrow \infty}{=} -\frac{8\pi}{Q^4} \gamma'(0). \quad (9.34)$$

From (9.33) to (9.34) an intensity profile in the high- Q region (often called the *Porod limit*) showing a slope of -4 in a log-log plot of I versus Q would imply continuous variation of the particle density, hence high smoothness of the particle surfaces. The surface area, or specific surface, may be obtained experimentally from a plot of I versus Q^4 .

The situation of polymeric molecules in aggregates or gels precipitated from semi dilute and concentrated solutions is more complex. The particle-particle interactions, which play a critical role in the microstructure, have to be assessed by modeling or through other means and the expected intensity according to (9.22) or (9.23) is to be compared with the SANS data through goodness-of-fit methods.

9.4 Instrumentation

We introduce the instrumentation of a generic neutron diffractometer by a schematic drawing of Fig. 9.1a. A neutron source emits either a steady-state beam or periodic bursts of neutrons, which are incident on a sample. Neutron-matter interactions cause the neutrons to be scattered to all directions in the laboratory frame coordinate system. A diffractometer is to record the neutrons each of which is elastically scattered once by the sample into detectors located at well-defined positions. This in general requires the use of insertion devices in both the incident and scattered beams to select only the elastic-scattering events. These devices may be crystal monochromators, choppers, filters, or other energy-selectors and/or collimators, guides, polarizers, flipping coils, or other beam-defining instruments. If

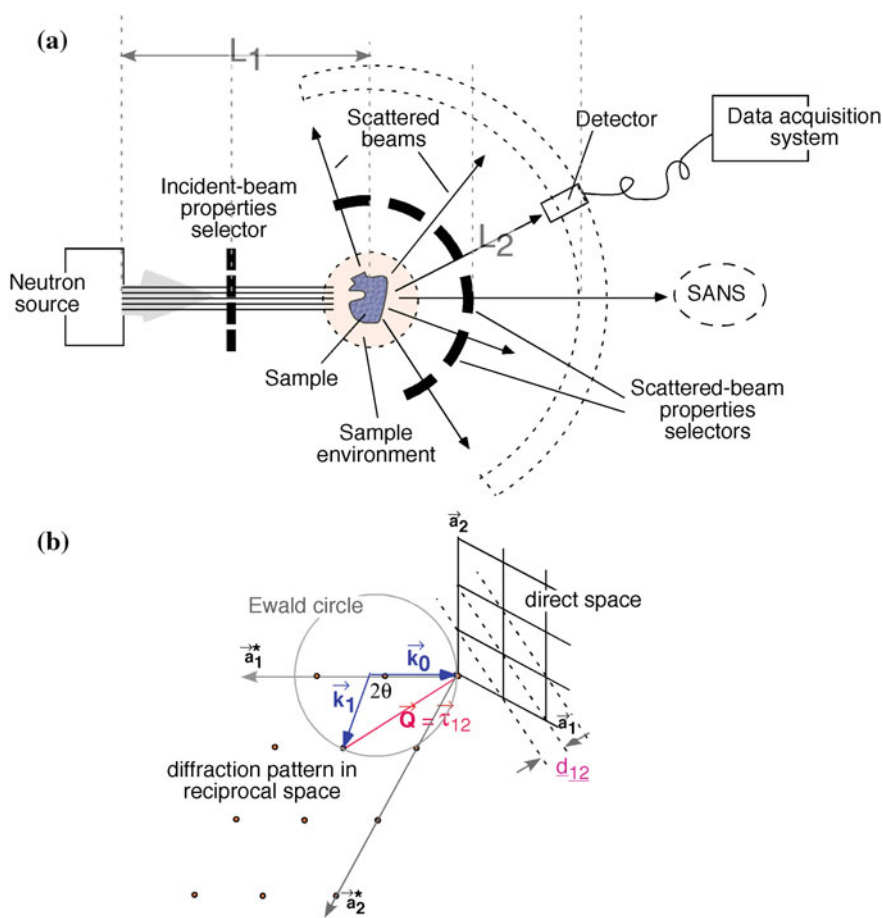


Fig. 9.1 **a** A schematic layout of a generic neutron diffractometer. **b** An example of 2D representation of a crystallographic plane in the direct space and the occurrence of a Bragg reflection in the reciprocal space

energy-selecting devices associated with either the incident or the scattered beam are omitted, the diffractometer approximates elastic scattering by total scattering measurement, as discussed in Sect. 9.3. If a monochromator is employed to select the incident neutrons, the entire sample-detector assembly will be rotated by the monochromator scattering angle, ϕ_s , (also called the *kick-off angle*) relative to the direct beam from the source (not shown in Fig. 9.1a). The relative uncertainty in Q (hence the spatial resolution of desired structure under study) is usually expressed as

$$\left(\frac{\delta Q}{Q}\right)^2 = \left[\cot\left(\frac{\phi_s}{2}\right)\delta\left(\frac{\phi_s}{2}\right)\right]^2 + \left(\frac{\delta\lambda}{\lambda}\right)^2, \quad (9.35)$$

where λ is the neutron wavelength. Therefore, large kick-off angles (also true for the diffraction angles) and long wavelength are favorable as long as they provide the desired Q . For pulsed-source TOF diffractometry, narrow source pulses and/or using fast choppers in conjunction with long flight paths (using neutron guides to preserve fluxes over long distances) are desirable. The resolution of a powder diffractometer in terms of $\frac{\Delta d}{d}$ where d denotes the d -spacing of crystal lattice planes (hkl) is

$$\left(\frac{\delta d}{d}\right)^2 = \left[\left(\frac{\delta t}{t}\right)^2 + \left[\cot\left(\frac{\phi_s}{2}\right)\delta\left(\frac{\phi_s}{2}\right)\right]^2 + \left(\frac{\Delta L}{L}\right)^2\right], \quad (9.36)$$

where t is the neutron flight time and L is the total flight distance (see Fig. 9.1a). A long primary (source-to-sample) flight distance, L_1 , is the major factor in achieving high resolution. The secondary (sample-to-detector) flight path L_2 , is determined mainly by matching the uncertainties of L_2 and the detector pixel size. It amounts to typically 1–3 m. Equations (9.35) and (9.36) have not taken into account the uncertainty of the scattered neutrons over a single detector.

There exist a number of computer programs, based on either analytical schemes or numerical simulations, to aid detailed design of diffractometers.

For further details regarding powder and single-crystal diffractometers, small-angle and ultra-small-angle diffractometers, we refer readers to consult Chap. 5 of (Carpenter and Loong 2015).

9.4.1 Instrumental Factors Relevant to Cultural Heritage Studies

Over the length scale of interatomic distances a major interest in cultural heritage studies is the chemical composition and crystal structure of the artifacts. Since samples are chiefly polycrystalline substances, a powder diffractometer is well suited for most studies. However, most artifacts are far from being a perfect

powder, e.g., exhibiting preferred crystallographic orientation of the grains, so for texture studies an orientor that enables the setup of specific sample orientations with respect to the neutron beams is useful. For this purpose a single-crystal diffractometer may come in handy by virtue of its built-in sample goniometer and high-definition of gauge volume.

From (9.10) the projection of a direct lattice vector $\vec{\mathbf{R}}$ on $\vec{\mathbf{Q}}$ corresponds to an atomic plane spacing d , therefore

$$d = \frac{2\pi}{Q} \quad (9.37)$$

From Fig. 9.1b the diffraction triangle, $\vec{\mathbf{Q}} = \vec{\mathbf{k}}_0 - \vec{\mathbf{k}}_1$, and $|\vec{\mathbf{k}}_0| = |\vec{\mathbf{k}}_1| = \frac{2\pi}{\lambda}$ lead to $\frac{Q}{2\pi} = \frac{2\sin\theta}{\lambda}$. Combining this with (9.37) we obtain the familiar Bragg law:

$$\lambda = 2d \sin \theta \quad (9.38)$$

The TOF technique makes use of the de Broglie equation

$$\lambda = \left(\frac{h}{m_n} \right) \frac{1}{v}, \quad (9.39)$$

where m_n , λ and v are the neutron mass, wavelength and speed, respectively, and h is the Plank constant. As the inverse neutron speed is the ratio of the measured flight time, t , over a known distance, $L = L_1 + L_2$, we obtain the expression of d -spacing for TOF measurements:

$$d = 1,978,015 \frac{t}{(L_1 + L_2) \sin \theta}, \quad (9.40)$$

where d , t , and L are in the unit of Å, s, and m, respectively. Equation (9.40) shows that a (pulsed-source) TOF powder diffractometer can, in principle, measure the entire diffraction pattern with a single detector located at scattering angle 2θ .

We note that a crystal lattice has infinite lattice d -spacings with decreasing values. While increasing the flight path of L_1 improves the d resolution, a very long flight path will limit the usable bandwidth of neutron wavelengths because, for a given period of the pulsed source, the fastest neutrons will eventually catch up with the slowest neutrons of the same burst over a long enough flight path. Using a frame-removal chopper to lengthen the period may mitigate such problem. In any case, the delta function in (9.6) holds true only for an idealized powder. Real materials always have physical reasons for intrinsic peak broadening, e.g., by the mosaic-block sizes, which would impose a limit of resolving power. For crystal structure characterization related to cultural heritage specimens high resolution usually is not a critical requirement.

9.5 Cultural Heritage Applications

In the following section typical applications of neutron scattering techniques to the study of cultural heritage objects are presented.

9.5.1 *Quantitative Multiphase Analysis of Polycrystalline Materials*

The quantitative phase analysis is mainly based on three principles: each phase exhibits a unique set of Bragg diffraction peaks; the intensity of each peak of a particular phase is proportional to the phase weight-fraction; the measured diffraction pattern is the simple sum of all single-phase patterns. The first step in quantitative phase analysis is to identify the phases present in the sample. For such identification the Bragg peak positions of experimental diffraction patterns are compared with the peak-sets of known compounds, usually obtained through databases such as PDF (PDF 2000), ICSD (ICSD 2004) and CRYSTMET (CRYSTMET 2002). The structure information (such as lattice parameters, space group, atom position) of identified phases obtained from these databases are generally stored in the CIF ('Crystallographic Information File') file format, the standard data exchange file format used in crystallography (Hall et al. 1991). The second step is to fit the experimental diffraction patterns with those of known compounds obtaining quantitative multi-phase analysis through the Rietveld method. The core of the procedure is to make a least-square fitting of the calculated pattern and provides values of the phase composition and the adjustment of the structure parameters. Micro-structural characterization and preferred orientation parameters through refinement of peak broadening are also available. The multi-phase Rietveld refinement can be performed with software such as GSAS (Larson and Von Dreele 2000; Toby 2001) MAUD (Ferretti and Lutterotti 1994) or FULLPROF (Rodriguez 1993).

Figure 9.2 shows an example of Rietveld refinement through the GSAS software. The basis and the lattice constants, denoted by \vec{d} and $\vec{a}_1, \vec{a}_2, \vec{a}_3$, can be determined to high precision, typically $\sim 0.1\%$, from refinement of the structure factor in (9.7), see the matching of the fitted line and the data points in Fig. 9.2.

First experiments of quantitative multiphase analysis applied to objects of cultural heritage interest such as ceramics and bronzes were reported in the following references (Kockelmann and Kirfel 2001; Siano et al. 2002; Kockelmann et al. 2004; Rinaldi et al. 2002).

First experiments of quantitative multiphase analysis applied to objects of cultural heritage interest such as ceramics and bronzes were reported in the following references (Kockelmann and Kirfel 2001; Siano et al. 2002; Kockelmann et al. 2004; Rinaldi et al. 2002).

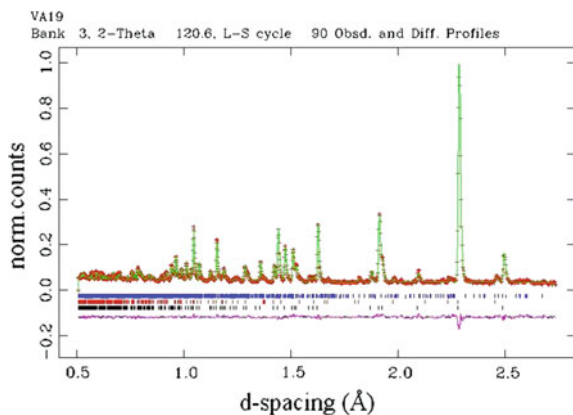
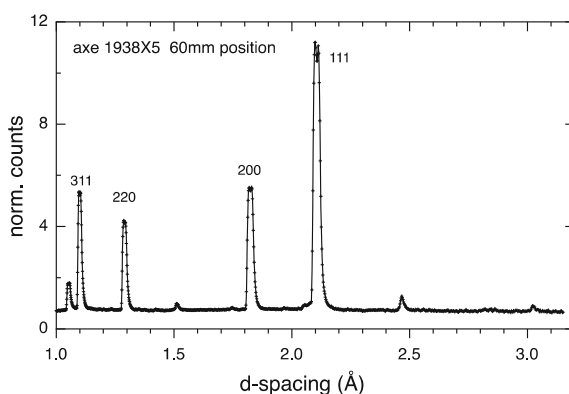


Fig. 9.2 A diffraction spectrum showing normalized number of counts as a function of d -spacing from a marble sample through GSAS software. Data are reported in *red*, best fit of data is shown (*green line*), the peak position of the different components, and residue is reported in *violet*. Components of the sample calculated through the Rietveld method with GSAS software: calcite (*blue*), quartz (*red*) and muscovite/illite (*black*)

Fig. 9.3 Part of the diffraction spectrum of a Geistingen axis (inv. number 1938/X5 from Groningen Institute of Archaeology)



TOF-neutron diffraction was applied frequently together with other techniques such as neutron methods sensible to elements such as in reference. Two axes of the Geistingen type were studied through TOF-diffraction and Neutron Resonance Capture Analysis (see Chaps. 10–12) providing information about the compositional, structural and phase properties. Geistingen axes are from copper with considerable amounts of arsenic, antimony and nickel, small amounts of silver and cobalt, and varying amounts of tin. The diffraction pattern is typical for α -phase copper, however with their diffraction lines split indicating that there are basically two copper α -phases with slightly different lattice parameters. See Fig. 9.3. According to Vegard (1921) the lattice parameter changes due to elements

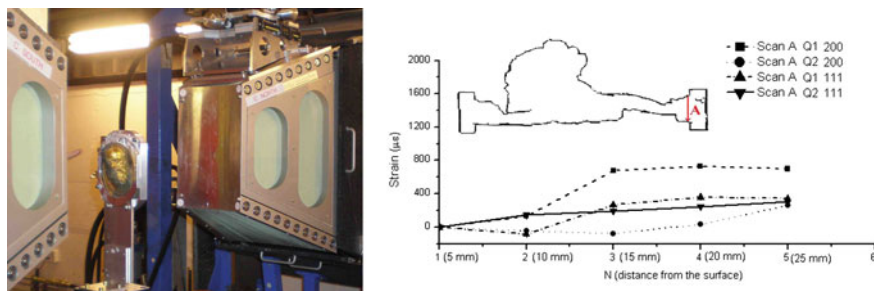


Fig. 9.4 *Left* A photo showing the bronze relief mounted on the sample position. Diffraction from a well-collimated neutron beam into the detector allows detection of strain distribution in the bulk with spatial resolution of ~ 1 mm. *Right* A left-to-right strain scan across the primary-fusion region to the re-melting region (Festa et al. 2011)

dissolved into the copper. Basically following (Siano et al. 2003) the lattice parameter a_{alloy} is given by:

$$a_{\text{alloy}} = a_{\text{Cu}} + \sum_Z V_Z^{\text{at}} X_Z^{\text{at}} \quad (9.41)$$

in which V_Z^{at} are correction factors for the lattice parameter for element Z with atomic fraction X_Z^{at} . It is argued that one of the copper α -phases observed in the Geistingen axe, inv. number 1938/X4 from the Groningen Institute of Archaeology, is enriched in high melting elements (Ni, Co, Ag), while the other phase is enriched in the low-melting elements (Sb, As, Sn) as described in a simple solidification model.

9.5.2 Analysis Residual Strains in Crystalline Composites

The recorded diffraction pattern is strictly related to the crystal lattices and the distance between atomic planes (the inter-planar spacing) within the material.

Generally, depending on the preparation method, processing, and utilization, stains may have developed and reside among the crystalline grains in a composite. When a material is strained, some compressions or elongations are produced within the crystal lattice, which change the inter-planar spacing of the hkl lattice planes. This induced change in d -spacing will cause a shift in the diffraction pattern. By precise measurement of this shift, the change in the inter-planar spacing can be evaluated and thus the strain within the material deduced. The overall strain has to be naturalized by the compensating compressed and tensile components. An analysis of the distribution of residual strains in an artifact contributes valuable insights into the history of technology and way of life of ancient users.

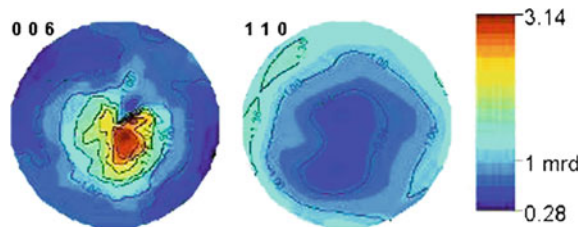
An example of neutron strain measurements applied to a gilded bronze relief is illustrated in Fig. 9.4 (Festa et al. 2011). The bronze relief belongs to the East Monumental Door located at the *Battistero di Firenze*, manufactured by *Lorenzo Ghiberti* and named by *Michelangelo* as ‘The Gates of Paradise’. The analysis was carried out by neutron diffraction at ENGIN-X (Santisteban et al. 2006a, b).

Some other valuable examples were reported in references (Siano et al. 2006; Santisteban et al. 2006a, b).

9.5.3 Texture Analysis

Texture is the preferred orientation of crystallites and is an intrinsic characteristic of materials such as metals, ceramics, rocks. This characteristic influences physical properties of the samples and is related with geological phenomena in the rocks-formation or with the working methods of metals and ceramics. Different mechanisms can produce or modify texture and many methods have been used to determine preferred orientation depending on the type of sample. Diffraction techniques can be used to measure such properties of materials. Neutron Diffraction offers some advantages compared to other techniques in the case of bulk samples namely the fact that there is no need to section the object under examination. Firstly, in order to determine the orientation of a given lattice plane hkl of a single crystallite, the detector is set to the proper Bragg angle (θ) of the diffraction peak of interest. Then the sample is rotated in a goniometer until the lattice plane hkl reaches the reflection condition. In a polycrystalline material, the intensity recorded at a certain sample orientation is proportional to the volume fraction of crystallites with their planes in the reflection geometry (Wenk and Molli 2003; Wenk and Van Houtte 2004). In a pulsed neutron source detector panels are present and cover large angular areas thus recording simultaneously diffraction spectra from crystals in different orientations. As mentioned in Sect. 9.2.3, texture information is displayed by means of pole-figures in which a specified crystallographic axis (or *pole*) from each of a representative number of crystallites is plotted in a stereographic projection, along with directions relevant to the material’s processing history (such as the rolling direction and transverse direction or the fiber axis). Therefore, a pole figure is a two-dimensional projection of the 3-dimensional function representing

Fig. 9.5 Pole figures representing texture images of a marble composed by only calcite



the continuous density distribution of orientations. Such pole figure represents the probability of finding a pole to a lattice plane (hkl) in a certain sample direction.

Figure 9.5 shows a neutron-diffraction study of the texture, i.e., preferred orientation of the crystalline grains, in marbles, which is caused by geographical processes during the formation. Marble is one of the most favorite stones used for monuments, statues and other objects of archaeological interest and is typically composed either of calcite, dolomite or a combination of the two. Diffraction aims at distinguishing different marble types on the basis of mineral phase compositions and crystallographic textures.

Pole figures maps of the marble crystal grains orientations correlated with geographic and mineralogical data can be used as a fingerprint to identify their physical origins, types and production locations. An example of marble pole-figure is shown in Fig. 9.5. The (006) and (110) pole-figures represent the c -axis and a -axis distribution, respectively. The marble sample exhibits a strong pole density maximum in the (006) pole figure, a texture typical of natural calcites that have suffered ‘pure shear’ or ‘simple shear’ deformations (Wenk and Molli 2003; Wenk and Van Houtte 2004). Pure shear occurs when the geological forces press the mineral in only one direction while ‘simple shear’ is a combined compression and viscous translation.

Some other valuable examples are reported in references (Kockelmann et al. 2006; Arletti Cartechini et al. 2008; Yanxia et al. 2004).

9.5.4 Small Angle Neutron Scattering for Cultural Heritage

In Small Angle Neutron Scattering experiment the radiation is elastically scattered by a sample and the resulting scattering pattern is analyzed to provide information

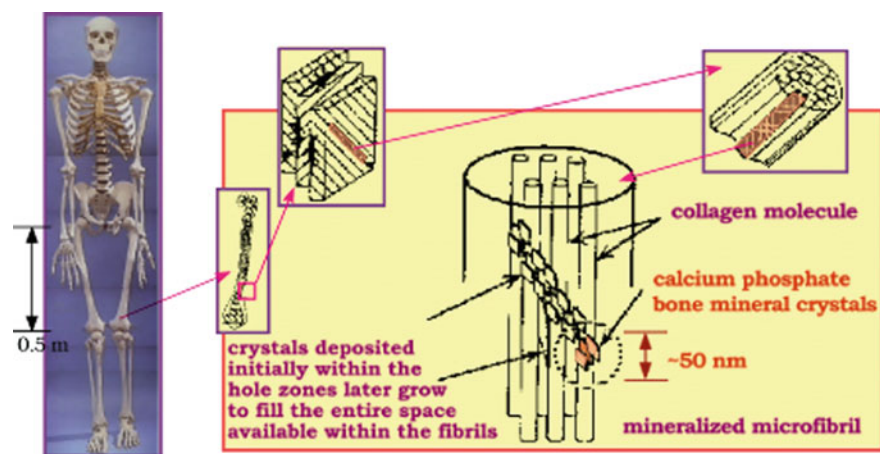


Fig. 9.6 A schematic drawing showing the hierarchy of the bone structure. Of special interest is the organization of the calcium phosphate apatite monocrystals in the hole zones of the fibrilis

about the size, shape, surface characteristics of the aggregates of minerals and orientation of some component of the sample. SANS was successfully applied to the study of pottery showing results about the study of their firing technology.

One example is the study of the bone apatite crystals by wide-angle and small-angle diffraction.

Bone is a nanocomposite containing principally collagen and mineral apatite. Figure 9.6 shows the hierarchical structure of bone progressively from macroscopic to nanometer scale: cancellous and cortical bone, osteons, lamellae, collagen fibres, and apatite crystals. It is generally believed that bone apatite crystals differ from hydroxyapatite, $\text{Ca}_{10}(\text{PO}_4)_6(\text{OH})_2$ or HAp, (of hexagonal structure with space group symmetry $P6_3/m$) in deficiency of calcium and OH ions due to ion substitution by CO_3 and HPO_4 groups. In bone the apatite crystals cluster in the hole-zone where the arrays of aligned collagen molecules meet end to end, and orient with the crystallographic c -axis roughly parallel to the long axes of the collagen molecules (see Fig. 9.6).

However, when a chronic force is applied to a bone during the life of a human or animal, the apatite crystals in the region may systematically develop certain preferred orientation to withstand the stress. G.E. Bacon and his team carried out a series of neutron-diffraction studies of human and animal bones (Bacon et al. 1984). Figure 9.7 shows a pole-figure analysis of the apatite crystals of a human calcaneus, a bone joining the talus and the lower foot. By monitoring the intensity of the (0002) reflection as a function of the sample orientation repeatedly over different spots, the preferred orientation of the apatite crystals with respect to the talus and the front foot directions was mapped. This is represented in Fig. 9.7 by two maxima presumably corresponding to the stress exerted by the lower foot and the joint with the talus.

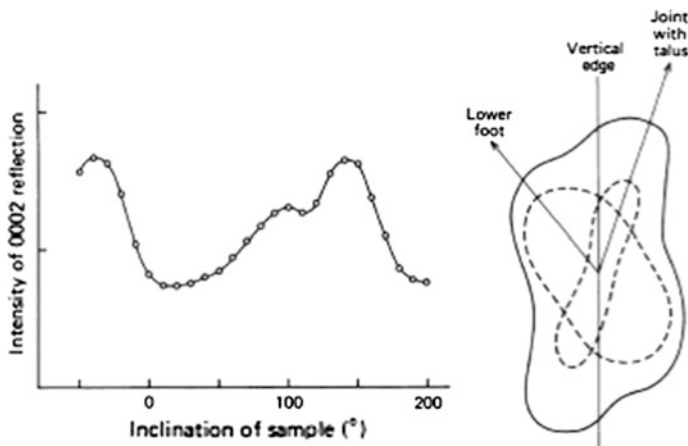
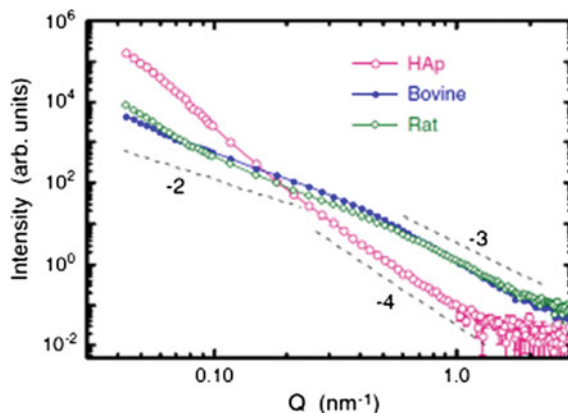


Fig. 9.7 The recorded intensities of the (0002) reflection as a function of the inclination angle, showing two maxima pointed to the lower foot direction ($\sim 100^\circ$) and to the joint with talus ($\sim 150^\circ$). (Bacon et al. 1984)

Fig. 9.8 The SANS profiles of a synthetic HAp and two bone apatite powders at room temperature. The *dashed lines* are power-law behavior for comparison with different regions of the observed profiles (Loong et al. 2004)



At a larger scale (~ 50 nm), the morphology, such as the size and the density, of the bone apatite crystals, which is important to the growth and healthiness of the bone, can be studied by SANS. Figure 9.8 shows the SANS profiles of the bone apatite crystals of bovine and rat (obtained by a plasma-ashing technique for the removal of organic components) as well as a synthetic HAp powder. Clearly, the bone crystals show a markedly different profile than that of the HAp powder. The nearly single-power-law behavior in the HAp profile is typical of crystalline powder made up with particles with smooth surfaces (Porod slope of -4). Both the bovine and rat bone apatite crystals, on the other hand, show a power-law slope approximately -2 at $Q < 0.45 \text{ nm}^{-1}$ is consistent with the platelet-like morphology of the bone crystallites (see Fig. 9.6). Moreover, a power-law slope of about -3 in the high- Q region suggests a high degree of roughness, possibly due to the presence of defects and/or adsorbed ions/molecules on the surfaces of the bone apatite crystals. The SANS of all three powders do not level off at the lowest observed Q around 0.03 nm^{-1} , indicating the existence of large (>200 nm) agglomeration of particles. A USANS investigation may reveal further details of such microstructure.

9.6 Facilities

Diffractometers including small-angle diffractometers are the most basic and widely used neutron instruments. The table below lists the main facilities which have been used in Cultural Heritage applications.

Facility	Country	Scattering-instrumentation available
ISIS	United Kingdom	INES, ENGIN-X, GEM, SANS2D
ILL	France	D1B, VIVALDI, LADI-III
BNC	Hungary	TOF, SANS
FRMII-MLZ	Germany	STRESS-SPEC

(continued)

(continued)

Facility	Country	Scattering-instrumentation available
HZB J-PARC/MLF	Germany Japan	E9, V4NOVA, TAKUMI, iMATERIA
PSI	Switzerland	SANS I and II
JCNS	Germany	KWS-1 and -2
SNS	United States	POWGEN
OPAL	Australia	WOMBAT
HFIR	United States	IMAGINE

9.7 Conclusions

Small-to-wide-angle neutron diffraction is a versatile method for nondestructive characterization of the structures of a great variety of bulk materials. The techniques and instrumentation applied to diffraction studies of single crystals, crystalline powders, and amorphous materials are well developed at steady-state and pulsed neutron sources. SANS and USANS are specialized diffractometers for investigations of microscopic- to mesoscopic structures. The field of cultural heritage can readily take advantage of the neutron-diffraction methodology to examine crystalline and non-crystalline structures as well as inhomogeneities in artifacts and archeological samples over a length scale of 0.1 to ~ 1000 nm. The results may shed light into the historic, cultural, and technological development of ancient societies.

References

- Arletti Cartechini L, Rinaldi R, Giovannini S, Kockelmann W, Cardarelli A (2008) Texture analysis of bronze age axes by neutron diffraction. *Appl Phys A* 90:9–14
- Bacon GE, Bacon PJ, Griffiths RK (1984) A neutron diffraction study of the bones of the foot. *J Amat* 139(2):265
- Carpenter JM, Loong C-K (2015) *Elements of slow-neutron scattering*. Cambridge University Press, Cambridge
- CRYSTMET (2002) STFC chemical database service
- Dorner B (1999) Basic concepts. Lecture Notes on neutron scattering. Introductory course to ECNS'99, KFKI-1999-04/E(REPORT)
- Ferrari M, Lutterotti L (1994) Method for the simultaneous determination of anisotropic residual stresses and texture by X-ray diffraction. *J Appl Phys* 76(11):7246–7255
- Festa G, Senesi R, Alessandrini M, Andreani C, Vitali G, Porcinai S, Giusti AM, Materna T, Paradowska A (2011) Non destructive neutron diffraction measurements of cavities, inhomogeneities and residual strain in bronzes of Ghiberti's relief from the Gates of Paradise. *J Appl Phys*, vol 109(6)

- Hall SR, Allen FH, Brown ID (1991) The crystallographic information file (cif): a new standard archive file for crystallography. *Acta Crystallogr A* 47:655–685
- ICSD (2004) Inorganic crystal structure database. Germany National Institute of Standard and Technology, USA
- Kockelmann W, Kirfel A (2001) Non-destructive phase analysis of archaeological ceramics using TOF neutron diffraction. *J Archaeol Sci* 28:213–222
- Kockelmann W, Siano S, Schreiner MR (2004) Time-of-flight neutron diffraction (TOF-ND) for characterising archaeological artefacts. *STUDIO E CONSERVAZIONE DI MANUFATTI ARCHEOLOGICI*. Nardini Editore, Firenze
- Kockelmann W, Siano S, Bartoli L, Visser D, Hallebeek P, Traum R, Linke R, Schreiner M, Kirfel A (2006) Applications of TOF neutron diffraction in archaeometry. *Appl Phys A* 00:1–8
- Larson AC, Von Dreele RB (2000) General structure analysis system (GSAS). Los Alamos National Laboratory report LAUR 86-748
- Loong C-K, Thiyagarajan P, Kolesnikov AI (2004) Neutron-scattering characterization of nanostructured materials relevant to biotechnology, *Nanotechnology* 15:S664
- PDF (2000) Power diffraction file. International centre for diffraction data
- Rietveld HM (1969) A profile refinement method for nuclear and magnetic structures. *J Appl Crystallogr* 2(2):65–71
- Rinaldi R, Artioli G, Kockelmann W, Kirfel A, Siano S (2002) The contribution of the neutron scattering of cultural heritage. *NOTIZIARIO NEUTRONI E LUCE DI SINCROTRONE*, vol 7 (2) (Giugno)
- Rodriguez-Carvajal J (1993) *J Phys B* 192:55
- Santisteban JR, Daymond MR, James JA, Edwards L (2006a) ENGIN-X: a third-generation neutron strain scanner. *J Appl Crystallogr* 39:812–825
- Santisteban J, Siano S, Daymond M (2006b) neutron strain scanning of archaeological bronzes. *Mater Sci Forum* 01:524–525
- Siano S, Kockelmann W, Bafle U, Celli M, Iozzo M, Miccio M, Mose O, Pini R, Salimbeni R, Zoppi M (2002) Quantitative multiphase analysis of archaeological bronzes by neutron diffraction. *Appl Phys A* 74[Suppl.]:S1139–S1142
- Siano S, Bartoli L, Zoppi M, Kockelmann W, Daymond M, Dann JA, Garagnani MG, Miccio M (2003) Microstructural bronze characterisation by time-of-flight neutron diffraction. *Proc Archaeometallurgy Eur* 2:319–329
- Siano S, Bartoli L, Santisteban JR, Kockelmann W, Daymond MR, Miccio M, De Marinis G (2006) Non-destructive investigation of bronzes artefacts from the marches national museum of archaeology using neutron diffraction. *Archaeometry* 48(1):77–96
- Squires GL (1978) Introduction to the theory of thermal neutron scattering. Cambridge University Press
- Toby BH (2001) EXPGUI, a graphical user interface for GSAS. *J Appl Cryst* 34:210–213
- Vegard L (1921) *Zeitschrift für Physik* 5:17–26
- Wenk HR, Molli G (2003) Texture and microstructure. *J Struct Geol*, vol 25
- Wenk HR, Van Houtte P (2004) Texture and anisotropy. *Rep Prog Phys* 67:1367–1428
- Xie Y, Lutterotti L, Wenk HR, Kovacs F (2004) Texture analysis of ancient coins with TOF neutron diffraction. *J Mater Sci* 39:3329–3337

Chapter 10

Neutron Activation Analysis (NAA)

P. Bode

Abstract Neutron activation analysis (NAA) is an isotope specific analytical technique for the qualitative and quantitative measurement of chemical elements. The method is based upon the conversion of stable atomic nuclei into radioactive nuclei by irradiation with neutrons and the subsequent detection of the radiation emitted during the decay of these radioactive nuclei. All of the stable elements have properties suitable for production of radioactive isotopes albeit at strongly different reaction rates. Each radionuclide is uniquely characterized by its decay constant—the probability for the nuclear decay in unit time- and the type and energy of the emitted radiation. Amongst the several types of radiation that can be emitted, gamma-radiation offers the best characteristics for the selective and simultaneous detection of radionuclides and thus of elements.

10.1 History

The discovery of the artificial radioactivity by Irene Curie and Frederic Joliot in 1934 motivated many physicists and chemists to perform experiments where stable nuclides convert into radioactive after irradiation with alpha particles, protons and the recent discovered neutron (1932). In (1936) George de Hevesy and Hilde Levi used for first time nuclear reactions after irradiation with neutrons for elemental analysis. They worked at that time in the by Niels Bohr headed Institute for Theoretical Physics at the University of Copenhagen. The idea of George de Hevesy was very simple: he used the correlation between the stable initial nuclides

P. Bode (✉)

Faculty of Applied Sciences, Department for Radiation Science and Technology,
Reactor Institute Delft, Delft University of Technology, Mekelweg 15,
2629JB Delft, The Netherlands
e-mail: p.bode@tudelft.nl; info@nuqam.com; peter.bode@ymail.com

P. Bode

NUQAM Consultancy, 3284LK Zuid-Beijerland, The Netherlands

and the produced amount of radioactive nuclides in order to obtain qualitative and quantitative analysis of the chemical elements which belong to the initial products.

The available neutron fluxes were small at that time and the identification of the obtained radionuclides was possible due to their different half-life times only. In spite of this the first example showed successful analysis of 1 % Dysprosium in Yttrium sample after bombardment with neutrons.

After World War II nuclear reactors with neutron flux densities in order of magnitude of $10^{12} \text{ cm}^{-2} \text{ s}^{-1}$ became available which allowed for achieving a detection limit for certain elements below 1 μg . This opened new research fields in solid state physics where the properties of the materials as a function of their impurity were investigated.

The development of the methodological procedures and high resolution gamma-spectrometry detectors enable nowadays to analyze simultaneously up to 50–60 elements in a single sample.

10.2 Theory

The activation of samples will result in a mixture of activities, which can be analysed for individual contributions by two approaches:

- i. The resulting radioactive sample is decomposed, and through chemical separations it is divided into fractions with a few elements each: Destructive or Radiochemical Neutron Activation Analysis.
- ii. The resulting radioactive sample is kept intact, and the elements are determined by taking advantage of the differences in decay rates via measurements at different decay intervals utilizing equipment with a high energy resolution: Non-destructive or Instrumental Neutron Activation Analysis (INAA, Greenberg et al. 2011).

10.2.1 Activation

The activation with neutrons is, upon preparation of the test portion, the first stage in an INAA procedure. Each atomic nucleus can capture a neutron during irradiation, resulting in a nuclear reaction in which often the nuclear mass changes; immediately (typically 10^{-14} s) after the capture ('promptly') excess energy in the form of photons and/or particles will be emitted. If the newly formed nucleus is unstable, it starts already during the activation decaying to a stable state by the emission of radiation through one or more of the following processes: α -decay, β -decay, electron capture, β^+ -decay, or internal transition decay. In most cases γ - and X-radiation will be emitted too, Fig. 10.1.

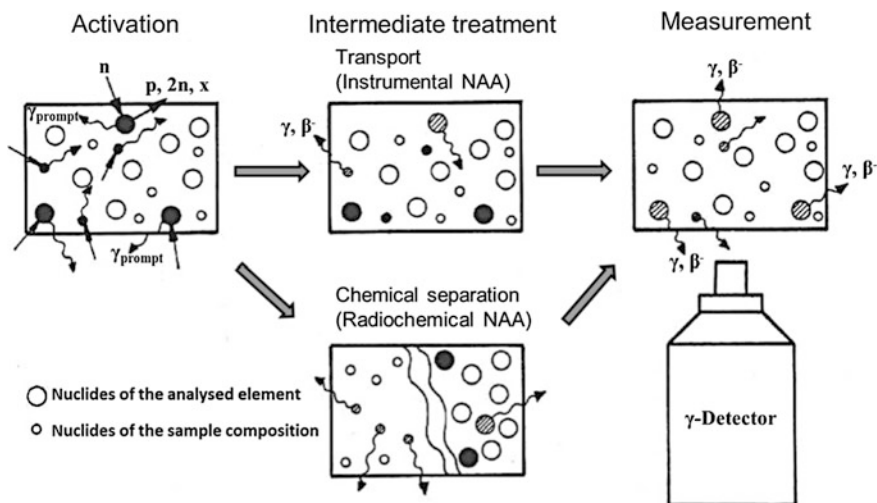


Fig. 10.1 NAA principle: the neutron activation produce short-lived isotopes which emit gamma radiation with specific energies detected by a gamma-detector

Neutrons are produced in:

- Isotopic neutron sources, like $^{226}\text{Ra}(\text{Be})$, $^{124}\text{Sb}(\text{Be})$, $^{241}\text{Am}(\text{Be})$, ^{252}Cf .
- Particle accelerators or neutron generators. The most common types are based on the acceleration of deuterium ions towards a target containing either deuterium or tritium, resulting in the reactions $^2\text{H}(^2\text{H},n)^3\text{He}$ and $^3\text{H}(^2\text{H},n)^4\text{He}$, respectively.
- Nuclear research reactors. These are the strongest sources of neutrons. The neutron output of research reactors is often quoted as neutron flux in an irradiation facility and varies, depending on reactor design and reactor power, between 10^{11} and $10^{14} \text{ cm}^{-2} \text{ s}^{-1}$.

In the majority of INAA procedures reactor neutrons are used for the activation. Materials can be activated in any physical state, viz. solid, liquid or gaseous. There is no fundamental necessity to convert solid material into a solution prior to activation; INAA is essentially considered to be a non-destructive method although under certain conditions some material damage may occur due to thermal heating, radiolysis and radiation tracks by e.g., fission fragments and α -radiation emitting nuclei.

10.2.2 Decay

Radioactive decay is a statistically random process; the probability that a given nucleus will decay in a certain time interval depends only of the time of observation. It is not possible to predict when a given nucleus will decay, but the decay

characteristics can be described by the physical laws of radioactive decay whereas documented decay schemes provide the details of the decay of radionuclides, such as, e.g., half-lives involved, types of radiation emitted and relative intensities.

10.2.3 Measurement

In NAA, nearly exclusively the (energy of the) gamma-radiation is measured because of the penetrating power of this type of radiation, and the selectivity that can be obtained from the distinct energies of the photons. The gamma-spectrum is analyzed to identify the radionuclides and their amounts of induced activity in order to derive the target elements from which they have been produced. The masses of the elements are derived from the net peak areas by comparison with the induced activity of the same neutron activation produced radionuclides from known amounts of the element of interest in the calibrator.

The combination of energy of emitted radiation, relative intensities if photons of different energies are emitted and the half-life of the radionuclide is unique for each radionuclide, and forms the basis of the qualitative information in NAA.

10.3 Experimental Procedures

10.3.1 Practical Execution of NAA

In the practice, a NAA procedure consists of the simultaneous irradiation of test portions of the unknown sample and a known amount of a comparator of the same element—serving as a calibrator—, and the sequential measurements of the activities. An INAA procedure has the following steps:

- Preparation (e.g., drying) and weighing of test portions of sample and calibrator; no need for dissolution.
- Encapsulation of the test portions in e.g., plastic foil, plastic capsules or quartz ampoules.
- Activation via simultaneous irradiation of test portions and calibrators with neutrons.
- No chemical separations, material remains intact.
- Sequential measurements of the activities in each test portion and calibrator by gamma-ray spectrometry after one or more decay periods. Thus, complementary information on various elements can be obtained.
- Interpretation of the gamma-ray spectra towards elements and their masses.

The turnaround time (time between initiation of analysis and reporting) is largely element and matrix dependent, as the signal of the radionuclide of interest has to be

measured in the presence and intensity of the signals of the radionuclides produced of the other elements in the sample. It may be necessary to wait hours to weeks after the irradiation to attain the optimal measurement conditions by decaying the interfering activity. Results on elements that can be measured via short-half-life radionuclides (such as Al, Mg, Ti, V, Cl, Mn, Se, Ca, S) can be available within minutes to hours since the measurement follows immediately the irradiation. In other cases, the turnaround time may vary from 1 week to 3 weeks.

10.3.2 Analytical Characteristics

The analytical characteristics of INAA are:

- Non-destructive analysis. The test-portion does not have to be converted into a solution, thus dissolution losses do not exist.
- Bulk analysis. The penetrating power of neutrons and gamma-radiation allows for analysis of the bulk masses of test portions up to several kilograms in size.
- The method is based upon processes in the atomic nucleus. The chemical form and physical state of the elements do not influence the activation and decay process.
- The method can be applied in a self-validating manner. A unique combination exists of the gamma-ray energies, their intensity ratios and the half-lives of the radionuclides, which provides opportunities for consistency checking.
- Many adjustable experimental parameters, sometimes over several orders of magnitude, allow for optimizing the experimental design and identifying potential problems.
- Elements such as C, H, N, O and Si, often found as major components of many matrices, do not activate well and contribute little or no gamma-ray activity.
- The method is suitable for measurement of masses in the order range of 10^{-6} – 10^{-9} g and less, depending on the element to be measured.

10.4 Areas of Application

The element of interest and sample matrix should have specific chemical properties, physical forms and physical characteristics for analysis by NAA. The activation rates, half-lives and energies of the gamma-ray emission of the radionuclides are decisive factors for selecting NAA. The very low Z elements (like H, He, B, Be, C, N, O) are not suitable for measurement by (thermal neutron) NAA, as are a few other elements like Tl, Pb and Bi.

Sample matrices of high density that contain significant fractions of high atomic number elements (both affecting gamma-ray self-attenuation) are not good candidates for NAA measurements. Similarly, matrices that have extremely high neutron

absorbing properties are difficult to measure accurately due to neutron self-attenuation. Significant mass fractions of B, Li and U are undesirable because their neutron capture results in the emission of charged-particle radiation, which may cause excessive thermal heating during the irradiation.

Examples of measurements where the analytical characteristics of neutron activation analysis are employed at full advantage include:

- Solid materials that are difficult to bring completely into a solution, such as soils, rocks, minerals, air particulate matter, new composite materials, and materials with C, H, N, O as major elements like biological material and plastics
- Solid materials that are easy to contaminate during preparation of the test portion if digestion would be needed for a different analytical technique. Examples are ultrapure materials, ultra-small amounts and biological tissues and fluids
- Solid materials that are unique and should keep their integrity, such as materials from forensic studies and archaeological, cultural and art objects
- Solid materials of which the bulk composition must be determined and for which surface, or near-surface techniques such as X-ray fluorescence spectrometry and some solid-state spectrometric techniques are inadequate.

Such samples can be found within the following selected group of disciplines:

- Archaeology—amber, bone, ceramics, coins, glasses, jewelry, metal artifacts and sculptures, paintings, pigments, pottery, soils and clays, stone artifacts.
- Biomedicine—animal and human tissues, blood and blood components, bone, drugs and medicines, gallstones, hair, implant corrosion, kidney and—stones, medical plants and herbs, milk, nails, placenta, snake venom, teeth, dental enamel and—fillings, urine and—stones.
- Environmental science and related fields— aerosols, atmospheric particulates, fossil fuels and their ashes, animals, birds, insects, fish, aquatic and marine biota, seaweed, algae, lichens, mosses, plants, trees, household and municipal waste, soils, sediments, sewage sludge.
- Forensics—bomb debris, bullet lead, explosives, glass fragments, paint, hair, gunshot residue swabs, shotgun pellets.
- Geology and geochemistry— asbestos, bore hole samples, bulk coals and coal products, coal and oil shale components, crude oils, cosmo-chemical samples, coral, diamonds, exploration and biogeochemistry, meteorites, ocean nodules, rocks, sediments, soils, glacial till, ores and separated minerals.
- Industrial products—alloys, catalysts, ceramics, refractory materials, coatings, electronic materials, fertilizers, fissile and other safeguard materials, graphite, high purity and high-tech materials, integrated circuit packing materials, oil products, pharmaceutical products, plastics, semiconductors, pure silicon and silicon processing.
- Nutrition—composite diets, foods, honey, seeds, spices, vegetables, milk and milk formulae, yeast.

10.5 Examples

The measurement by INAA of elements in wood as an indicator of metal-organic wood preservatives illustrates the unique capabilities of the technique. Such an assessment cannot be done using XRF since results would only indicate the contents at the surface, not what has penetrated. Other techniques such as AAS or ICP, requiring dissolution of the wood, are not reliable, because the chemical may form insoluble species in the wood; even if the chemical is soluble, it is still necessary to dissolve the whole piece of wood to be able to measure it. Second, they are too labour intensive and costly. A measurement by INAA can be done on a bulk sample of $20 \times 20 \times 4 \text{ mm}^3$ without any sample preparation preceding the neutron irradiation.

The use of potentially environmental hazardous elements like Cd in plastics is restricted by law in several countries. The recycling industry has to assess the Cd mass fraction of 'input' raw materials consisting of pieces of plastic of approximately $0.5 \times 0.5 \text{ cm}^2$, usually of different colours and composition (Fig. 10.2).

- For conventional analysis such as by XRF, AAS or ICP, the pieces should be either dissolved, or reduced further in size and a thoroughly homogenized. The alternative is analysis by INAA where easily samples of several grams to kilograms can be analysed without the need to homogenization. Plastics contain mainly of the elements H, C, O and N, which upon neutron irradiation do not produce interfering activity. As such, the material become 'transparent' for the radiation emitted by the radionuclides produced in the bulk sample from the other elements in the material.

One of the famous examples of application of NAA for cultural heritage research is the investigation of hairs from Napoleon (Analytical Applications of Nuclear Techniques 2004; Clemenza et al. 2008; Lin et al. 2004).

Fig. 10.2 Shredded plastic for recycling



The circumstances of Napoleon's demise on 5 May 1821 have been shrouded by suspicion. The generally held belief was that he has fell victim to carcinoma of the stomach—the supposed cause of his father's death in 1785. But an analysis of five samples of Napoleon's hair taken after his death showed a largely enhanced level of arsenic. There was a hypothesis that he was poisoned. Therefore several hair samples taken from Napoleon at different stages of his life as well as from other persons living at this period (The King of Rome, Empress Josephine) were investigated by NAA method for determination of the Arsenic contamination with high precision. The Napoleonic hairs came from when he was a boy in Corsica, during his exile on the Island of Elba, on the day of his death (May 5, 1821) on Saint Helena and on the day after his death.

Samples taken from Napoleon's son in 1812, 1816, 1821 and 1826 as well as samples from the Empress Josephine, collected upon her death in 1814, also were analyzed.

The hair samples were provided by the Glauco-Lombardi Museum in Parma (Italy), the Malmaison Museum in Paris and the Napoleonic Museum in Rome.

The samples were placed in capsules near the core of the reactor at the University of Pavia, Italy for neutron activation. The Arsenic concentration was determined from the 559 and 563 keV γ activity from the activation product ^{76}As (Fig. 10.3).

The first result from the investigation was that the average Arsenic level was high but comparable with the typical level at that time. Modern persons show lower levels of Arsenic contamination. The level of arsenic in the hair samples from 200 years ago was found to be 100 times greater than the average level detected in samples from persons living today. In fact, the Emperor's hair had an average arsenic level of around ten parts per one million, whereas the arsenic level in the hair samples from currently living persons was around one-tenth of a part per one million. In other words, at the beginning of the 19th century, people evidently ingested arsenic that was present in the environment in quantities that are currently considered dangerous (Fig. 10.4).

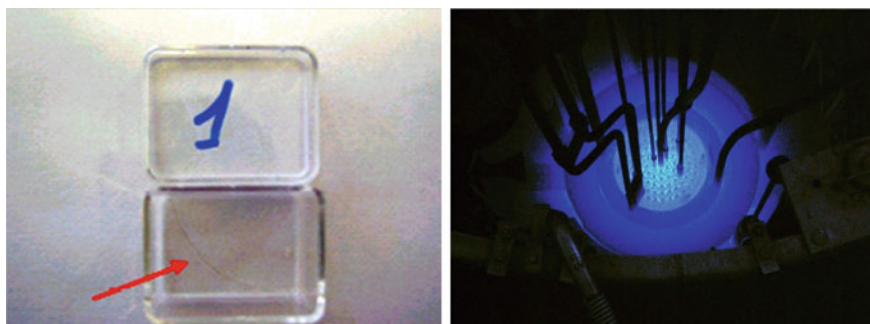


Fig. 10.3 Single hair from Napoleon marked by arrow (*on the left*). Top view of the reactor core of the research reactor at the University of Pavia, Italy (*on the right*)

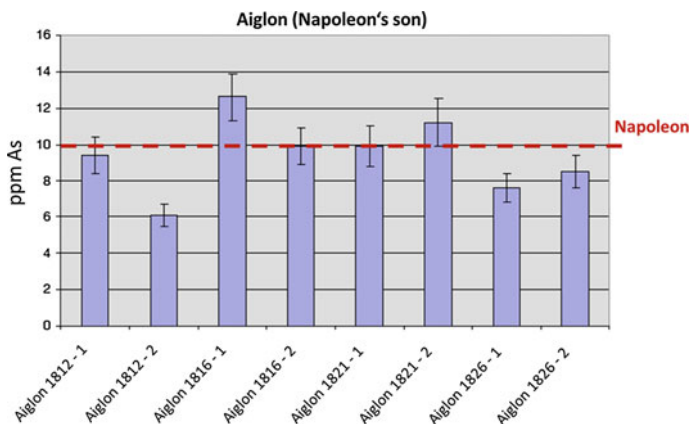


Fig. 10.4 Comparison of the arsenic levels measured in hairs of Aiglon (Napoleon's son) with the arsenic concentration (in parts per one million or ppm) in hairs of Napoleon, measured by NNA method (Analytical Applications of Nuclear Techniques 2004; Clemenza et al. 2008)

The second result was that there were no significant differences in arsenic levels between when Napoleon was a boy and during his final days in Saint Helena. According to the researchers, including toxicologists who participated in the study, it is evident that this was not a case of poisoning but instead the result of the constant absorption of arsenic.

10.6 Facilities

About 100–150 neutron activation analysis facilities exist worldwide, the majority directly affiliated within institutes of organizations governing a nuclear research reactor, such as national nuclear research establishments and/or universities. Other facilities have the irradiations carried out remotely in such a reactor and the neutron-activated samples transferred back for gamma-ray spectrometry and analysis at their premises.

The facilities differ mainly in analytical capabilities due to

- Neutron flux available. This varies between $10^{12} \text{ cm}^{-2} \text{ s}^{-1}$ for the miniature research reactors to $10^{14} \text{ cm}^{-2} \text{ s}^{-1}$ for the high flux reactors.
- Reactor operation schedule. Some research reactors operate for 100 h or more continuously ('around the clock'); others have shorter operation schedules, in some cases only a few hours daily. Reactor schedule affects, to some degree, the analytical capacity (number of samples to be irradiated).
- Availability of irradiation systems for analysis using very short half-life radionuclides (half-lives varying from 10 s to 10 min), essential for measuring elements like Al, Mg, Ti, V, Ca.

- The type and number of gamma-ray spectrometers available for measurement of the induced activity. The gamma-ray spectrometers are equipped with semiconductor detectors. Well-type semiconductors offer the highest counting efficiency but are not available in all facilities.
- Degree of automation. Automation in neutron activation analyses, especially in measurement of the activity, requires self-made sample changers and related software for automated data processing. Facilities are increasingly implementing this, but it is not universal available yet. The higher the degree of automation, the higher the throughput, analysis capacity and the shorter the reporting time.
- Calibration methodology. Many facilities apply the ‘relative’ or ‘comparator’ method in which an unknown is analysed simultaneously with a sample of similar but known composition, like a certified reference material. This limits the number of elements that can be reported, Increasingly, facilities are implemented other calibration methods that allow for reporting of mass fractions and detection limits of over 50 elements, without the need for analysis of a reference material.
- Degree of quality management implementation and laboratory accreditation (compliance with ISO/IEC17025:2005). Many NAA laboratories aim at such an accreditation, amongst others, to satisfy end-users. Accredited NAA laboratories are currently (2016) be found in The Netherlands, Belgium, Hungary, Romania, Slovenia, South Korea, Malaysia, Indonesia, Syria, Pakistan, Chile, Argentina, South Africa. This number of countries is increasing.

In the practice, there are only small differences (max. a factor of 5–10) in detection limits in different facilities. The differences in analysis throughput (number of samples to be analysed in a given period) are larger, depending on the number of spectrometers available, the degree of automation and sometimes the operation schedule of the reactor.

The IAEA Research Reactor Data Base specifies, for each research reactor, if NAA facilities are available and operational. An overview of countries with NAA facilities may be found in given in Table 10.1, without claiming completeness.

Table 10.1 Countries with facilities for research reactor based neutron activation analysis

Region	Countries
Europe	Netherlands, Belgium, France, Portugal, Germany, Poland, Czech Republic, Hungary, Romania, Bulgaria, Italy, Slovenia, Greece, Turkey, Russian Federation, Ukraine
Africa	Morocco, Algeria, Libya, Egypt, Ghana, Nigeria, South Africa
West and Central Asia	Syria, Iran, Israel, Kazakhstan, Uzbekistan, Pakistan, India, Bangladesh
East Asia	China, South Korea, Japan, Thailand, Vietnam, Malaysia, Indonesia
Australia	Australia
North and Central America	Canada, USA, Mexico, Jamaica
South America	Colombia, Peru, Chile, Brazil, Argentina

There are also countries without research reactors in which NAA is carried out using accelerator (neutron generator) based neutrons, or using isotopic neutron sources. These are not listed here.

References

- Analytical Applications of Nuclear Techniques (2004) IAEA STI/PUB/1181, IAEA, Vienna. ISBN 92-0-114703-1, <http://www-pub.iaea.org/books/IAEABooks/6878/Analytical-Applications-of-Nuclear-Techniques>. Last visited 19 Feb 2016
- Clemenza M et al (2008) Misure con attivazione neutronica sulla presenza di Arsenico nei capelli di Napoleone Bonaparte e di suoi famigliari. *Il Nuovo Saggiatore* 24:19–30
- Greenberg RR, Bode P, De Nadai Fernandes EA (2011) Neutron activation analysis: a primary method of measurement. *Spectrochim Acta B* 66:193–241
- Hevesy G, Levi H (1936) The action of neutrons on the rare earth elements. *Det Kgl Danske Vidensk Selsk Mat-Fys Medd XIV*, 5:3–34
- IAEA Research Reactor Data Base. <https://nucleus.iaea.org/RRDB/RR/ReactorSearch.aspx>. Last visited 19 Feb 2016
- IAEA Technical Document (TECDOC) 1215 (2001) Use of research reactors for neutron activation analysis, IAEA, Vienna, Austria. <http://www-pub.iaea.org/books/IAEABooks/6171/Use-of-Research-Reactors-for-Neutron-Activation-Analysis>. Last visited 19 Feb 2016
- Lin X, Alber D, Henkelmann R (2004) Elemental contents in Napoleon's hair cut before and after his death: did Napoleon die of arsenic poisoning? *Anal Bioanal Chem* 379:218–220

Chapter 11

Prompt Gamma Activation Analysis (PGAA)

T. Belgya and Zs. Révay

Abstract Prompt gamma activation analysis is a non-destructive nuclear analytical method offering panoramic analysis for major and minor components, and several trace elements. It has been successfully used for the assay of light elements for decades, it is unique for the determination of H and B, and is used in all areas of science where non-destructive analysis and fast analytical results are important, however, it is still not known well enough to all scientific communities. This chapter summarizes the most important properties of the technique which are useful for archaeologists.

11.1 Introduction

Prompt gamma activation analysis (PGAA) utilizes the characteristic gamma radiation released in the radiative neutron capture reaction to determine the elemental or isotopic composition of samples. It is not as widespread as the instrumental neutron activation analysis (INAA) due to the much more complex gamma-ray spectra. The lack of a suitable analytical database also delayed the propagation of the method (Molnár et al. 2002a, b; Révay et al. 2000). The first complete spectroscopy library was published in 2004 by the Budapest group and it was completely based on their measurements (Molnár et al. 2004).

PGAA is a non-destructive nuclear analytical method which offers panoramic analysis even during the measurement. The method is suitable for bulk analysis of major and minor components, but a few elements with large cross sections can be determined at trace levels, even below ppm, too (Révay et al. 2004a). It is unique in

T. Belgya (✉)
Institute for Energy Security and Environmental Safety,
Centre for Energy Research, Hungarian Academy of Sciences,
Budapest, Hungary
e-mail: belgya.tamas@energia.mta.hu

Zs. Révay
Heinz Maier-Leibniz Zentrum, Technische Universität München, Munich, Germany

the analysis of hydrogen either in bound or unbound chemical states and is very sensitive to boron, an important trace element in geology (Gméling et al. 2005). Its non-destructive character makes it an ideal tool for studying the elemental composition of archaeological objects helping archaeologists to identify the origin or the trading routes of artefacts, or to tell whether an object is fake or not. A combination of neutron imaging and PGAA offers a unique technique PGAI described in Chap. 14).

PGAA facilities with the best performance are located at research reactors or at intense pulsed neutron sources. Here, we will focus on the description of PGAA using reactor neutron sources, while possibilities with pulsed neutron sources can be found in (Burca et al. 2011; Schillebeeckx et al. 2012). The goal of this section is to introduce the PGAA method to non-specialists working in the field of archaeometry.

11.2 Fundamentals of Prompt Gamma Activation Analysis

PGAA is based on the nuclear process of radiative neutron capture: when a sample is irradiated with a beam of low-energy neutrons, then the atomic nuclei in it capture a fraction of them and release prompt gamma rays which can be detected using suitable detectors (see Fig. 11.1).

Both the neutrons and the high-energy gamma rays have a large penetration power, and practically the whole irradiated volume contributes the analytical result, thus providing bulk information on the sample composition. From this point of view, PGAA differs considerably from X-Ray Fluorescence Spectrometry (XRFS), as this latter one can provide analytical information only from a thin surface layer of the sample. Typical penetration depth of the low-energy neutrons is about 1–2 cm

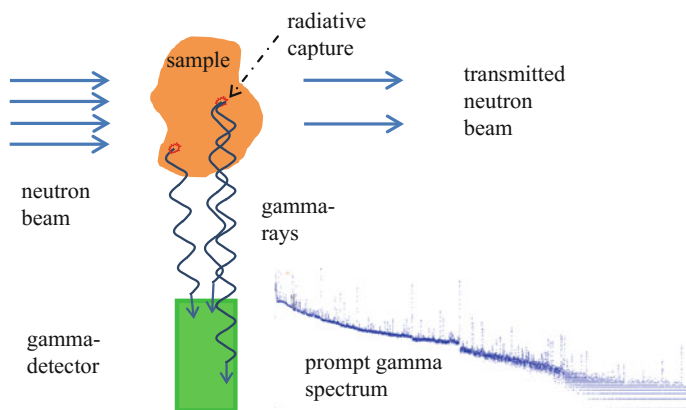


Fig. 11.1 The processes taking place during PGAA. Gamma rays not hitting the detector are not shown

for ceramics or rocks, a few mm in metallic (e.g. bronze) objects or in organic materials (like wood). The penetration depth depends on the so-called neutron capture and scattering cross sections of the elements composing the object. The neutron capture cross section varies widely from elements to elements in contrast to the XRF, where the photon absorption cross section monotonously increases with the atomic number. For these reasons, the two methods are complementary to each other.

The chemical analysis can be performed based on the energy and intensity values of prompt gamma rays which are measured with high-purity germanium (HPGe) detectors and a sophisticated electronics that collect the detected events in so-called gamma-ray spectra. These detectors have a very good energy resolution (i.e. a capability to produce narrow peaks at a specific energy) and a fair detection efficiency to absorb the full energy of the gamma rays. Energies of the emitted gamma rays are characteristic for the elements and their intensities are proportional to their amounts in the sample. These characteristic gamma rays show up as spectrum peaks, and their areas can be expressed as follows:

$$A_\gamma = \frac{m}{M} N_A \sigma_\gamma \Phi \varepsilon t \quad (11.1)$$

where A_γ is the measured peak area, m is the mass of the element in question in the illuminated volume and which is divided by its molar mass M , and multiplied by the Avogadro constant N_A . This expression is equal to the number of atoms. The symbol σ_γ represents the so-called partial gamma-ray production cross section which gives the probability of emitting a given-energy gamma ray by an atom in unit flux during a unit time. Φ is the neutron flux, ε is the detection efficiency, and t is the measurement time.

The σ_γ quantities were measured at the Budapest Research Reactor PGAA facility and published in (Révay et al. 2004b) and in (Choi et al. 2007). The derivation of the above equations can be found in (Révay 2009; Belgya 2010).

Equation (11.1) can also be used for the determination of other quantities. Using a standard with known mass and cross section, the flux can be determined, if the flux is known, we can check the efficiency. The counting efficiency for a given sample can be different from that for the detector as determined by using calibrated sources. The reason for that is the self-attenuation of gamma rays inside large samples.

In most cases, an even simpler equation can be used:

$$\frac{A_1 \varepsilon_2}{A_2 \varepsilon_1} = \frac{n_1 \sigma_{\gamma,1}}{n_2 \sigma_{\gamma,2}} \quad (11.2)$$

where A is the peak area, ε is the efficiency, n is the number of moles for the given element, and σ_γ is the partial cross section, while the indices refer to two chemical elements in the sample. This equation can be obtained from Eq. 11.1 written for the components 1 and 2 and forming their ratio. It can be seen that quantities being

equal in the two equations cancel, like the Avogadro constant, the flux and the time. The mass ratio weighted by the molar mass ratio yields the molar ratio, or the ratio of the stoichiometric coefficients.

Using this equation, one can determine not just the molar ratio, but also the partial cross section, or the efficiency at a given energy, if all other quantities are known.

The concentration of an element (Z) can be calculated using the summed mass of the components, if all major and minor elements are observed:

$$c_Z = \frac{m_Z}{\sum_i m_i}. \quad (11.3)$$

To detect all important elements is sometimes difficult with PGAA. It would require very long measurements which is not always feasible. Then, one can determine the detection limits for the invisible components. It has to be mentioned that unobserved trace elements do not change the sum significantly in Eq. (11.3) thus the calculated compositions of visible elements will not be influenced.

A few important elements have small cross sections; the most abundant one is oxygen. In many cases, like for ceramics or rocks, one can assume that all possible elements are fully oxidized, thus the composition can be determined more precisely based on stoichiometry than based on the low-precision oxygen analysis. In other cases, certain elements can be excluded based on our knowledge on the chemistry of the sample, like say beryllium as a major component.

If no such assumption can be made, or if important elements remain undetected, mass ratios of the components help in the characterization of the samples. In the case of complex samples, hidden internal parts can also be interesting, for which neutron imaging combined with PGAA can offer more information (see Chap. 14 for details).

11.3 Existing Experimental Systems

There are about two dozen operational or planned PGAA facilities in the world (Révay et al. 2015). Only a few of them are really active in PGAA-related research according to their reports for the cited database. Currently the most active facilities are in Japan, USA, Germany, and Hungary. Here, we will focus on the description of the two European facilities.

The construction of the PGAA facility at the Budapest Research Reactor started in 1993 with the support of the International Atomic Energy Agency. Since the beginning of its operation in 1996, several major upgrades were accomplished in order to improve its performance and productivity (Belgya et al. 1997; Révay et al. 2004c; Szentmiklósi et al. 2010a, b). Currently, two experimental stations are operational, they use spatially separated beams at the end of a 30-m long, curved supermirror neutron guide. On the upper beam, the PGAA station is installed close

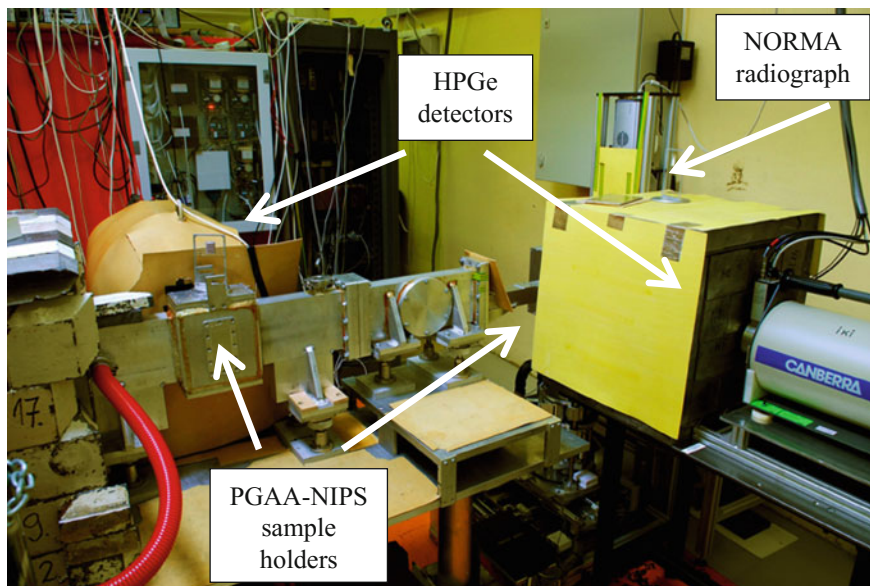


Fig. 11.2 View of a PGAA-NIPS facilities with the modular aluminium neutron flight tube

to the end of the guide and the Neutron Induced Prompt-gamma Spectroscopy (NIPS) station is situated about 1 m downstream on the lower beam. The experimental station can be seen in Fig. 11.2. The modular neutron flight tube enables to construct various experimental arrangements. Both stations are equipped with HPGe detectors surrounded by BGO annuli in a thick lead shielding. The NIPS facility has been equipped with a neutron imaging apparatus called NORMA (see Chap. 14) and a well shielded, Compton suppressed HPGe detector.

The PGAA method (Belgya et al. 1997, 2003, 2008a, b, 2011; Fazekas et al. 1997; Molnár et al. 1997; Révay and Belgya 2004, 2005, 2008; Szentmiklósi et al. 2005a, b; Kis et al. 2015) together with the spectroscopy library (Szentmiklósi et al. 2006, 2010a, b, Révay et al. 2003, 2010) have significantly improved at the Budapest laboratory during the past 20 years.

The high-flux PGAA facility at Heinz Maier-Leibnitz Zentrum in Garching is located at the end of a curved supermirror neutron guide with a length of 55 m. The last 7 m is elliptically tapered, and the final guide element with the length of 110 cm can be removed from the beam, and replaced with a series of collimators (see Fig. 11.3).

The focused beam has a thermal equivalent neutron flux of $6 \times 10^{10} \text{ cm}^{-2} \text{ s}^{-1}$ in the focal point which is the highest beam flux reported. The flux in the collimated beam is $2 \times 10^9 \text{ cm}^{-2} \text{ s}^{-1}$. The beam profile is of course inhomogeneous in the first case, while it is highly uniform in the second. The sample chamber can be evacuated, and contains an automatic sample changer accommodating six samples. The 60 % HPGe detector is surrounded by a BGO Compton suppressor and 15–20 cm of lead (see Fig. 11.4).

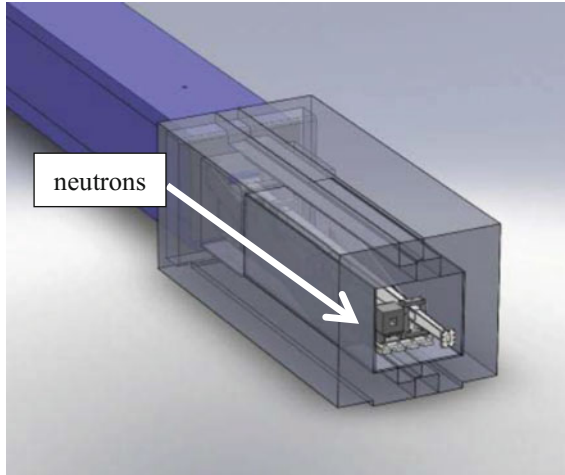


Fig. 11.3 The last section of the neutron guide at the Garching PGAA facility with the interchangeable elliptical guide-collimator system

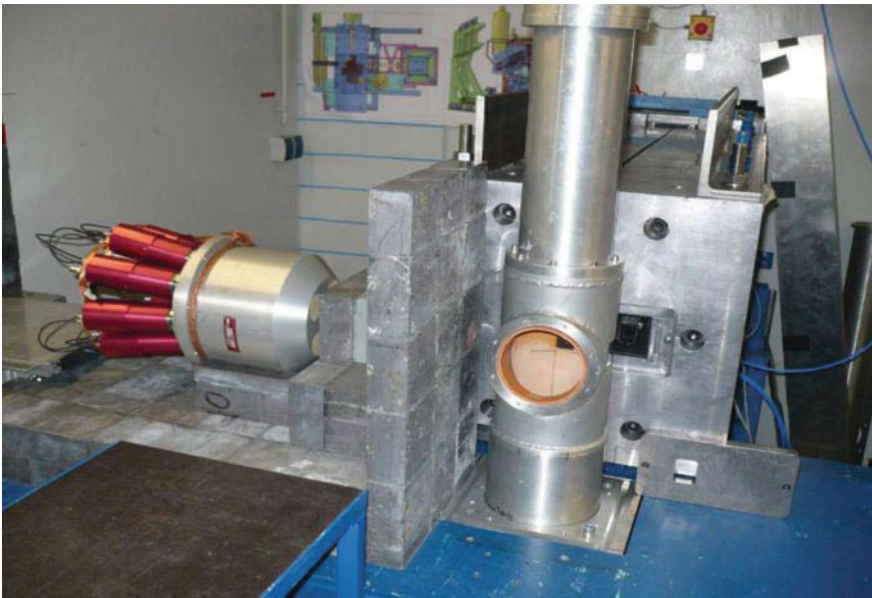


Fig. 11.4 The PGAA facility at garching without the lead shielding. To the *left*: the BGO with the gamma collimator and the frontal lead shielding, in the *middle*: the sample chamber (lined with ${}^6\text{Li}$ -containing polymer), behind it the end of the neutron guide in its lead shielding. The focusing neutron focus is now off-beam, and can be seen to the *right* of the sample chamber

The room background produces 4 counts per second in the full spectrum. The beam backgrounds are 20 cps and 400 cps for the collimated and for the high-flux beam, respectively. A series of beam attenuators help to adjust the neutron flux to control the optimum count rate in the spectrometer. Together with the collimator/focusing guide change, they allow for irradiations in a flux range of over more than three orders of magnitude. Using the highest flux, it is possible to analyse samples with masses of less than a milligram.

11.3.1 PGAA Investigation of Samples

The measurement in PGAA is simple. The sample can be in solid, liquid or gaseous form. Powders are usually sealed in Teflon bags. Smaller self-holding objects or the packed samples are placed in a frame, between Teflon strings. (Fluorine and carbon have very low neutron capture cross sections, for this reason fluorinated polymers are used.) The sample frame is then inserted into the target chamber where it is irradiated in the neutron beam. The gamma rays emitted by the activated sample are detected with a Compton-suppressed HPGe detector, as was discussed in earlier sections. The detector signals are electronically processed, and then their heights are digitized and recorded in a PC-driven multi-channel analyzer (MCA). When detecting a photon, a count is added to a channel of the spectrum. The channel number corresponds to the height of the signal which is proportional to the gamma-ray energy of the photon. The recorded histogram of counts in the MCA is called the gamma spectrum. The detected photons with discrete energies appear as peaks in the spectrum. A typical PGAA spectrum of an archaeological ceramic is shown in Fig. 11.5, it contains about 900 peaks.

The acquired spectra are then evaluated with a peak-fitting program. It provides a peak list with their positions and areas. At Garching and Budapest we use Hypermet-PC (Kis et al. 2015; Szentmiklósi et al. 2006, 2010a, b), which is freely available for download. The peak positions and energies are then transformed into energy and activity values with the help of energy and efficiency calibrations, respectively. For calibration, standard radioactive sources and simple chemical compounds (containing nitrogen or chlorine) are measured regularly (Kis et al. 1998; Molnár et al. 2002a, b, 2003; Belgya et al. 2008c; Fazekas et al. 1998, 1999).

The chemical analysis uses the calibrated peak data to determine the masses of elements according to Eq. (11.1). This is performed with a homemade EXCEL software (Révay et al. 2004a; Gmeling et al. 2007a, b) called ProSpeRo (prompt gamma spectrum rover) also at both labs. It compares the peak list with the partial gamma-ray production cross sections (σ_γ) in the spectroscopy database (Révay et al. 2004b; Choi et al. 2007).

The simplified flow diagram of the software (Révay 2009) is shown in Fig. 11.6. The algorithm uses the most intense (maximum 25) gamma-ray peaks of the elements for calculating their masses. The masses of the components are determined from the weighted average of the mass values from individual peaks. A longer version of the spectroscopy library is used for the identification of spectral

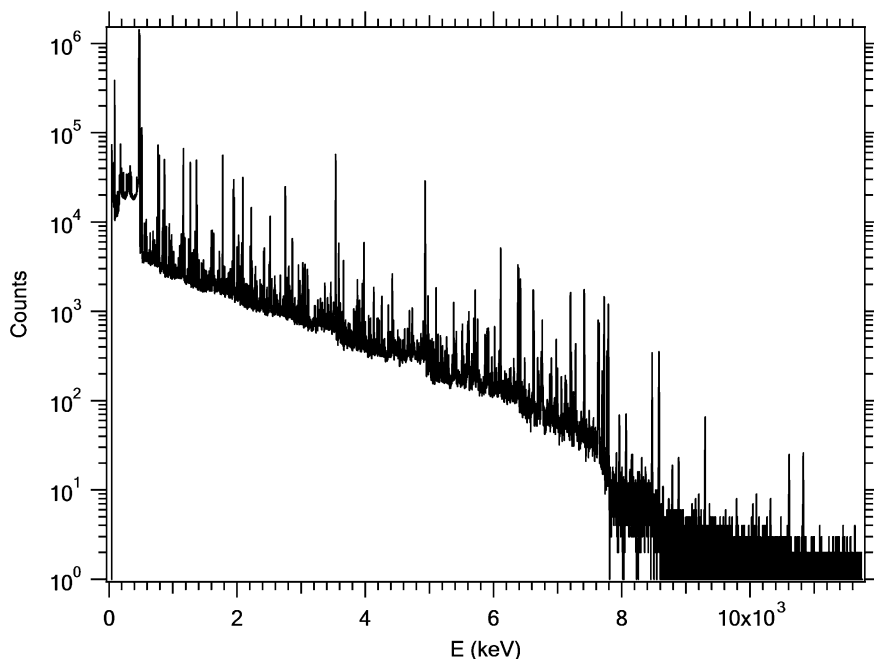


Fig. 11.5 PGAA spectrum of archaeological ceramic

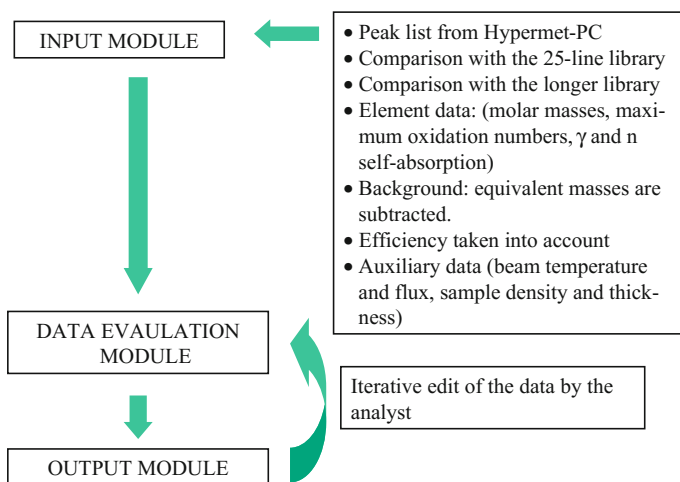


Fig. 11.6 Simplified flow diagram of the PGAA analysis software

Z	El	M	m meas	unc %	m Bkg	unc %	m net	ox. st.	m ox	unc %	c% atom	unc %	c% el/el	unc %	c% el/ox	unc %	c% ox/ox	unc %
1	H	1.008	2.24E-4	0.2	1.92E-5	7.5	2.05E-4	1	1.83E-3	0.3	2.67	1.3	0.0984	1.3	0.0506	0.7	0.452	1.4
5	B	10.81	1.70E-4	0.3	3.10E-8	2.3	1.70E-4	3	5.47E-4	0.3	0.206	1.3	0.0815	1.3	419 ppm	0.7	0.1349	1.4
11	Na	22.99	2.03E-2	1.6		0.0	2.03E-2	1	2.73E-2	1.6	11.6	1.9	9.7	1.9	5.0	1.7	6.7	2.1
12	Mg	24.31	6.53E-3	5		0.0	6.53E-3	2	1.08E-2	5	3.5	5	3.1	5	1.6	5	2.7	5
13	Al	26.98	2.71E-2	1.4	1.08E-3	4	2.60E-2	3	4.91E-2	1.4	12.6	1.8	12.5	1.8	6.4	1.5	12.1	1.9
14	Si	28.09	0.133	2.0		0.0	0.13	4	0.28	2.0	62	0.8	64	0.8	33	1.3	70	0.6
16	S	32.07	1.08E-3	2.8		0.0	1.08E-3	6	2.69E-3	2.8	0.44	3.1	0.52	3.1	0.27	2.9	0.66	3.1
17	Cl	35.45	7.33E-4	0.8	7.40E-7	5	7.32E-4	-1	7.32E-4	0.8	0.271	1.5	0.351	1.5	0.181	1.1	0.181	1.6
19	K	39.1	5.77E-3	1.3		0.0	5.77E-3	1	6.95E-3	1.3	1.94	1.8	2.77	1.8	1.42	1.5	1.71	1.9
20	Ca	40.08	1.13E-2	2.1		0.0	1.13E-2	2	1.58E-2	2.1	3.7	2.4	5.4	2.4	2.8	2.2	3.9	2.5
22	Ti	47.87	4.03E-4	2.3		0.0	4.03E-4	4	6.72E-4	2.3	0.110	2.6	0.193	2.6	0.099	2.4	0.166	2.7
23	V	50.94	1.92E-5	10		0.0	1.92E-5	5	3.44E-5	10	50 ppm	10	90 ppm	10	47 ppm	10	80 ppm	10
25	Mn	54.94	1.13E-4	2.6	7.83E-6	4	1.05E-4	3	1.51E-4	2.8	250 ppm	3.1	0.050	3.1	260 ppm	2.9	370 ppm	3.2
26	Fe	55.85	2.95E-3	2.2	3.01E-4	4	2.65E-3	3	3.79E-3	2.5	0.62	2.8	1.27	2.8	0.65	2.6	0.93	2.8
27	Co	58.93	1.04E-4	1.6		0.0	1.04E-4	2	1.32E-4	1.6	231 ppm	2.0	500 ppm	2.0	256 ppm	1.7	330 ppm	2.1
60	Nd	144.2	8.00E-6	7		0.0	8.00E-6	3	9.33E-6	7	7.3 ppm	7	38 ppm	7	20 ppm	7	23 ppm	7
62	Sm	150.4	6.28E-7	4		0.0	6.28E-7	3	7.28E-7	4	0.55 ppm	5	3.0 ppm	5	1.5 ppm	4	1.8 ppm	5
64	Gd	157.3	7.16E-7	5		0.0	7.16E-7	3	8.25E-7	5	0.60 ppm	5	3.4 ppm	5	1.8 ppm	5	2.0 ppm	5

Fig. 11.7 Analytical result for the archaeological ceramic. Masses are in gram unit. Major and minor elements are given in percents, while trace elements in parts per million (ppm)

interferences with weaker lines. Individual peaks can be left out of the calculation by the analyst, but the method proved to be independent of the analyst’s person, once following the same routine.

The output for the archaeological ceramic is shown in Fig. 11.7. It contains the most important input parameters of the analysis and the results. The c% columns contain different concentration values (molar percents, weight percents of elements when oxygen content is not taken into account, the same when the sample assumed to be an oxide, and finally the oxide composition).

The result shows the bulk composition, which helps the scientists conclude about the origin of their samples, or the conditions of their manufacturing etc. In case of a large number of samples, statistical methods can be used to sort the results. In archaeometry, this can be used in provenance studies or investigating trading routes. Non-destructive chemical analysis also supports identifying manufacturing techniques or helps the work of conservators.

11.3.2 Applications of PGAA

Beside the development of the method, the operators of both facilities constantly try to expand its analytical applications in various research fields such as geology (Gmeling et al. 2007a, b, 2014; Kodolanyi et al. 2012), in-beam catalysis (Révay et al. 2008; Teschner et al. 2008, 2012; Armbruster et al. 2012; Szentmiklósi et al. 2010a, b; Belgya et al. 1997; Fazekas et al. 1997; Molnár et al. 1997), material sciences (Révay and Belgya 2004; Révay et al. 2005; Szentmiklósi et al. 2005a, b; Belgya et al. 2008a) and even in such a complex interdisciplinary research like the investigation of megafauna extinctions in North America during Younger Dryas cooling about 12,900 years ago (Belgya et al. 2008b). Detailed descriptions of some successful archaeological applications can be found in the Chap. 6 (Kasztovszky).

In case of complex samples, the distribution of elemental masses depends on the positions in the sample. Well-collimated neutron beam and gamma detection can be used to study the internal elemental distribution (Belgya et al. 2008a, b) in a complex sample as is presented in Chap. 14 (Zoltan Kis).

It is an important question samples of what size can be measured and how they can be placed in the sample chamber or positioned in the neutron beam. In the following, we show a few examples. Figure 11.8 presents a montage of photographs taken from various objects measured at the Budapest PGAA facilities.

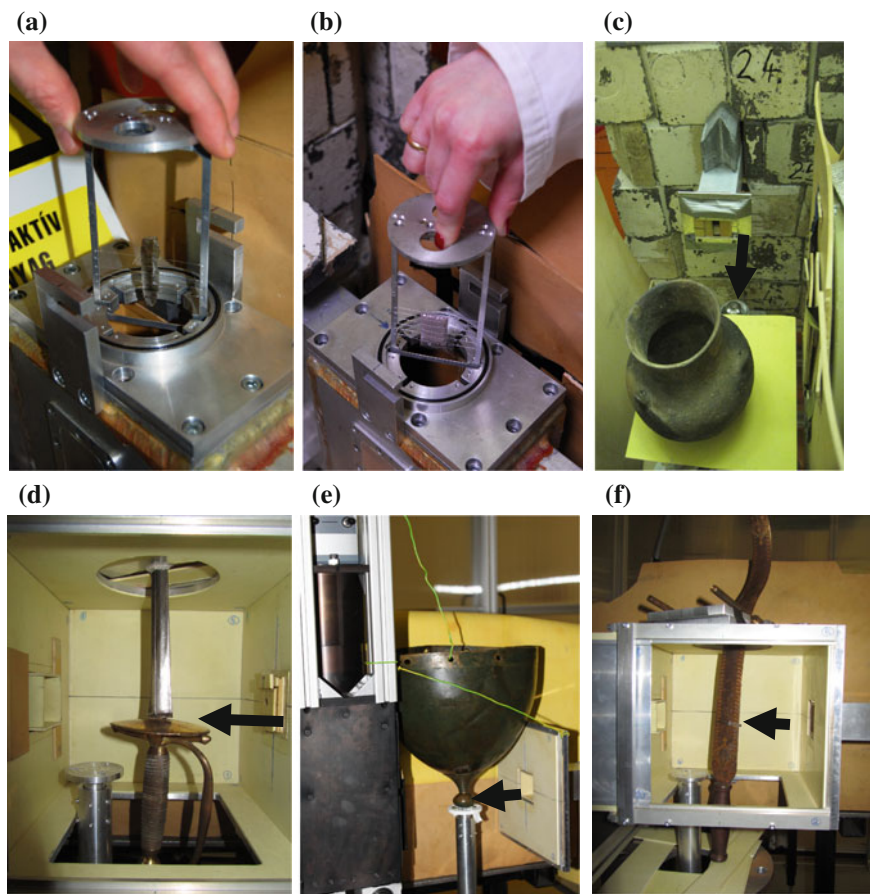


Fig. 11.8 Archaeological objects and their positioning in the neutron beam. The *black arrows* shows the direction of the neutron beam. **a** Obsidian blade (late palaeolithic obsidian blade from Rudna, Poland. Property of the Archaeological Museum in Poznan). **b** Soil sample, no historical value. **c** *Middle* neolithic (Zselic culture) ceramic vessel from Nagytétény, Hungary. From the collection of the Hungarian National Museum. **d, f** 17th–18th century oriental swords from the Wallace Collection, UK. **e** Late Bronze Age helmet found in Mezőkövesd, Hungary. From the collection of the Hungarian National Museum

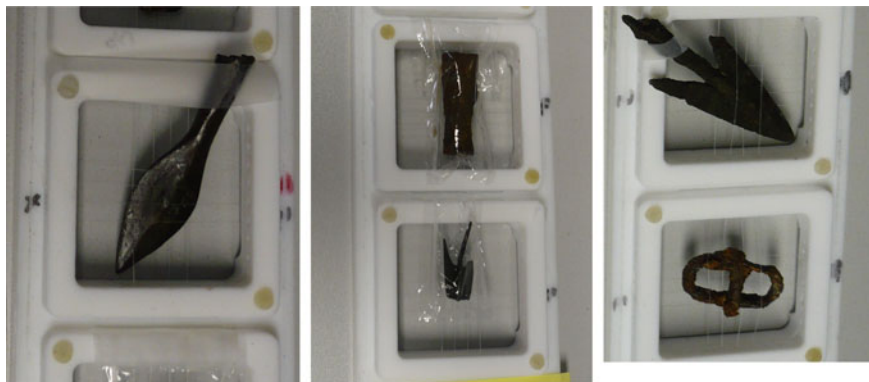


Fig. 11.9 Sample positioning in the teflon frames of small objects. The width and height of the sample holder is 6 cm (the objects belong to the Archäologische Staatssammlung München)

The upper right photographs show small, flat object that can be placed in the PGAA target chamber. The others show swords, a bronze vase, and a bronze helmet. The swords and the helmet were placed in the target chamber of the NIPS-NORMA station. This chamber has a cubic shape with the sides of 10 cm, while in the case of the helmet the side walls of the chamber had to be removed to accommodate the object. The vase was measured at the PGAA station and its modular sample chamber was removed to give sufficient place for the vase with dimensions of 15 cm diameter and 20 cm height.

The tube shaped target chamber (see Fig. 11.4) at Garching can also be removed when larger objects are to be measured. In the target chamber a ladder moves vertically, and six smaller objects can be placed on it between Teflon strings. Examples are shown in Fig. 11.9.

Acknowledgments One of the authors acknowledges the Infrastructure Support of the Hungarian Academy of Sciences.

References

- Armbruster M, Kovnir K, Friedrich M, Teschner D, Wowsnick G, Hahne M, Gille P, Szentmiklosi L, Feuerbacher M, Heggen M, Girgsdies F, Rosenthal D, Schlogl R, Grin Y (2012) Al_3Fe_4 as a low-cost alternative for palladium in heterogeneous hydrogenation. *Nat Mater* 11:690–693
- Belgya T (2010) Target preparation for in-beam thermal neutron capture experiments. EUR—Scientific and technical research series, pp 21–26. ISSN 1018-5593
- Belgya T, Szentmiklosi L, Kis Z (2011) Cold neutron source spectra at the Budapest PGAA-NIPS facilities. (INDC(NDS)–0590). International Atomic Energy Agency (IAEA)
- Belgya T, Révay Z, Fazekas B, Héjja I, Dabolczi L, Molnár GL, Kis Z, Östör J, Kaszás G (1997) The new budapest capture gamma-ray facility. In: Molnár G, Belgya T, Révay Z (eds) 9th

- international symposium on capture gamma-ray spectroscopy and related topics. Springer, Budapest, p 826
- Belgya T, Révay Z, Ember PP, Weil J, Molnár GL, Qaim SM (2003) In: Kvasil J, Cejnar P, Krticka M (eds) The cold neutron PGAA-NIPS facility at the Budapest Research Reactor. 11th international symposium on capture gamma-ray spectroscopy and related topics. World Scientific, New Jersey, London, Singapore, Hong Kong, Pruhonice near Prague, Czech republic, pp 562–568
- Belgya T, Kis Z, Szentmiklósi L, Kasztovszky Z, Festa G, Andreanelli L, De Pascale MP, Pietropaolo A, Kudejova P, Schulze R, Materna T (2008a) A new PGAI-NT setup at the NIPS facility of the Budapest Research Reactor. *J Nucl Radioanal Chem* 278:713–718
- Belgya T, Kis Z, Szentmiklósi L, Kasztovszky Z, Kudejova P, Schulze R, Materna T, Festa G, Caroppi PA (2008b) First elemental imaging experiments on a combined PGAI and NT setup at the Budapest Research Reactor. *J Nucl Radioanal Chem* 278:751–754
- Belgya T et al (2008c) New gamma-ray intensities for the N-14(n,gamma)N-15 high energy standard and its influence on PGAA and on nuclear quantities. *J Radioanal Nucl Chem* 276:609–614
- Burca G, James JA, Kockelmann W, Fitzpatrick ME, Zhang SY, Hovind J, Van Langh R (2011) A new bridge technique for neutron tomography and diffraction measurements. *Nuclear instruments and methods in physics research. Sec A Accel Spectrom Dect Assoc Equip* 651:229–235
- Choi HD, Firestone RB, Lindstrom RM, Molnár GL, Mughabghab SF, Paviotti-Corcuera R, Révay Z, Trkov A, Zerkin V, Zhou C (2007) Database of prompt gamma rays from slow neutron capture for elemental analysis. International Atomic Energy Agency, Vienna, ISBN 92-0-101306-X
- Fazekas B, Molnár G, Belgya T, Dabolczi L, Simonits A (1997) Introducing HYPERMET-PC for automatic analysis of complex gamma-ray spectra. *J Radioanal Nucl Chem* 215:271–277
- Fazekas B, Östör J, Kiss Z, Simonits A, Molnár GL (1998) Quality assurance features of “HYPERMET-PC”. *J Radioanal Nucl Chem* 233:101–103
- Fazekas B, Révay Z, Östör J, Belgya T, Molnár G, Simonits A (1999) A new method for determination of gamma-ray spectrometer nonlinearity. *Nucl Instrum Methods Phys Res Sect A Accel Spectrom Dect Assoc Equip* 422:469–473
- Gmélíng K, Harangi Sz, Kasztovszky Zs (2005) Boron and Chlorine concentration of volcanic rocks: An application of prompt gamma activation analysis. *J Radioanal Nucl Chem* 265:201–212
- Gmélíng K, Nemeth K, Martin U, Eby N, Varga Z (2007a) Boron concentrations of volcanic fields in different geotectonic settings. *J Volcanol Geoth Res* 159:70–84
- Gmélíng K, Kasztovszky Z, Szentmiklósi L, Révay Z, Harangi S (2007b) Boron concentration measurements by prompt gamma activation analysis: Application on miocene-quaternary volcanics of the Carpathian-Pannonian Region. *J Radioanal Nucl Chem* 271:397–403
- Gmélíng K, Simonits A, Sziklai LI, Parkanyi D (2014) Comparative PGAA and NAA results of geological samples and standards. *J Radioanal Nucl Chem* 300:507–516
- Kis Z, Fazekas B, Östör J, Révay Z, Belgya T, Molnár GL, Koltay L (1998) Comparison of efficiency functions for Ge gamma-ray detectors in a wide energy range. *Nucl Instrum Methods Phys Res Sect A Accel Spectrom Dect Assoc Equip* 418:374–386
- Kis Z, Szentmiklósi L, Belgya T (2015) NIPS-NORMA station-A combined facility for neutron-based nondestructive element analysis and imaging at the Budapest Neutron Centre. *Nucl Instrum Methods Phys Res Sect A Accel Spectrom Dect Assoc Equip* 779:116–123
- Kodolanyi J, Pettke T, Spandler C, Kamber BS, Gmélíng K (2012) Geochemistry of Ocean Floor and Fore-arc Serpentinites: Constraints on the Ultramafic Input to Subduction Zones. *J Petrol* 53:235–270
- Molnár GL (2004) Handbook of prompt gamma activation analysis with neutron beams. Kluwer Academic Publisher Dordrecht, Boston, London, Budapest

- Molnár GL, Belgya T, Dabolcsi L, Fazekas B, Révay Z, Veres Á, Bikit I, Kiss Z, Östör J (1997) The new prompt gamma-activation analysis facility at Budapest. *J Radioanal Nucl Chem* 215:111–115
- Molnár GL, Révay Z, Belgya T, Firestone RB (2002a) New catalog of Neutron Capture g-rays for Prompt Gamma Activation Analysis. *J Nucl Sci Technol Supplement* 2:1338–1343
- Molnár GL, Révay Z, Belgya T (2002b) Precise determination of gamma-ray intensities for high-energy calibration standards, summary report of the third research co-ordination meeting on update of X- and gamma-ray decay data standards for detector calibration and other applications. IAEA, INDC(NDS)-437
- Molnár GL, Révay Z, Belgya T (2003) New intensities of high energy gamma-ray standards. In Kvasil J, Cejnar P, Krťicka M (eds) 11th international symposium on capture gamma-ray spectroscopy and related topics. World Scientific, New Jersey, London, Singapore, Hong Kong, Pruhonice near Prague, Czech republic, pp 522–530
- Révay Z (2009) Determining Elemental Composition Using Prompt gamma Activation Analysis. *Anal Chem* 81:6851–6859
- Révay Z, Belgya T (2004) Principles of the PGAA method. In: Molnár GL (ed) Handbook of prompt gamma activation analysis with neutron beams. Kluwer Academic Publishers, Dordrecht, Boston, London, pp 1–30
- Révay Z, Ridikas D (2015) Database of PGNAA facilities prompt gamma neutron activation analysis. IAEA
- Revay Z, Belgya T, Szentmiklosi L, Kis Z, Woosch A, Teschner D, Swoboda M, Schlogl R, Borsodi J, Zepernick R (2008) In situ determination of hydrogen inside a catalytic reactor using prompt gamma activation analysis. *Anal Chem* 80:6066–6071
- Revay Z, Szentmiklosi L, Kis Z (2010) Determination of new $k(0)$ values for prompt gamma activation analysis at Budapest. *Nucl Instrum Methods Phys Res Sect A Accel Spectrom Dect Assoc Equip* 622:464–467
- Révay Z, Molnár GL, Belgya T, Kasztovszky Z, Firestone RB (2000) A new gamma-ray spectrum catalog for PGAA. *J Radioanal Nucl Chem* 244:383–389
- Révay Z, Molnár GL, Belgya T, Kasztovszky Z (2003) In-beam determination of $k(0)$ factors for short-lived nuclides. *J Radioanal Nucl Chem* 257:561–564
- Révay Z, Firestone RB, Belgya T, Molnár GL (2004a) Prompt Gamma-Ray Spectrum Catalog. In: Molnár GL (ed) Handbook of prompt gamma activation analysis with neutron beams. Kluwer Academic Publishers, Dordrecht, Boston, London, pp 173–366
- Révay Z, Belgya T, Kasztovszky Z, Weil JL, Molnár GL (2004b) Cold neutron PGAA facility at Budapest. *Nucl Instrum Methods Phys Res Sect B Beam Interact Mater Atoms* 213:385–388
- Révay Z, Belgya T, Kasztovszky Z, Szentmiklosi L, Molnár GL (2004c) Recent Developments in Prompt Gamma Activation Analysis. In: Qaim SM (ed) Advances in nuclear and radiochemistry 6 (NRC-6). Forschungszentrum Jülich GmbH. Aachen, Németország, 29 Aug–3 Sept, pp 163–165
- Révay Z, Belgya T, Szentmiklősi L, Molnár GL (2005) Prompt gamma activation analysis using a chopped neutron beam. *J Rad Nucl Chem* 264:277–281
- Schillebeeckx P, Borella A, Emiliani F, Gorini G, Kockelmann W, Kopecky S, Lampoudis C, Moxon M, Perelli Cippo E, Postma H, Rhodes NJ, Schooneveld EM, Van Beveren C (2012) Neutron resonance spectroscopy for the characterization of materials and objects. *JINST* 7: C03009
- Szentmiklősi L, Belgya T, Révay Z, Molnár GL (2005a) Digital signal processing in prompt-gamma activation analysis. *J Rad Nucl Chem* 264:229–234
- Szentmiklősi L, Révay Z, Molnár GL (2005b) Three-dimensional data processing for time resolved gamma-ray spectrometry. *J Radioanal Nucl Chem* 265:213–219
- Szentmiklősi L, Révay Z, Belgya T (2006) Measurement of partial gamma-ray production cross-sections and $k0$ factors for radionuclides with chopped-beam PGAA. *Nucl Instr Methods A* 564:655–661

- Szentmiklósi L, Belgya T, Révay Z, Kis Z (2010a) Upgrade of the Prompt-Gamma Activation Analysis (PGAA) and the Neutron Induced Prompt-gamma Spectroscopy (NIPS) facilities at the Budapest Research Reactor. *J Radioanal Nucl Chem* 286:501–505
- Szentmiklósi L, Révay Z, Belgya T (2010b) Measurement of partial gamma-ray production cross-sections and $k(0)$ -factors for radionuclides with chopped-beam PGAA-Part II. *Nucl Instrum Methods Phys Res Sect A Accel Spectrom Dect Assoc Equip* 622:468–472
- Teschner D, Borsodi J, Wootsch A, Révay Z, Havecker M, Knop-Gericke A, Jackson SD, Schlogl R (2008) The roles of subsurface carbon and hydrogen in palladium-catalyzed alkyne hydrogenation. *Science* 320:86–89
- Teschner D, Novell-Leruth G, Farra R, Knop-Gericke A, Schlogl R, Szentmiklosi L, Hevia MG, Soerijanto H, Schomacker R, Perez-Ramirez J, Lopez N (2012) In situ surface coverage analysis of RuO₂-catalysed HCl oxidation reveals the entropic origin of compensation in heterogeneous catalysis. *Nat Chem* 4:739–745

Chapter 12

Neutron Resonance Analysis

H. Postma and P. Schillebeeckx

Abstract The presence of resonance structures in neutron induced reaction cross sections is the basis of Neutron Resonance Transmission Analysis (NRTA) and Neutron Resonance Capture Analysis (NRCA). NRTA and NRCA are powerful non-destructive methods for determining the elemental and isotopic composition of materials and objects. Both methods are non-invasive and do not require any sample preparation. They mostly result in a negligible induced radioactivity of the objects. This is due to the relatively high detection efficiency and the neutron energy spectrum that is needed. The energy positions of the resonance profiles provide qualitative information about the composition, while the contents of the observed resonance peaks in a capture spectrum or the dips in a neutron transmission spectrum give quantitative information about the bulk composition. In this contribution the basic principles of NRTA and NRCA are discussed and a review of applications is given, with an emphasis on studies of archaeological objects and artefacts by NRCA at the time-of-flight facility GELINA.

12.1 Introduction

The energy dependence of the probability that neutrons interact with nuclei shows sharp peaks. This is illustrated in Fig. 12.1 where the total cross section for neutron induced reactions in several nuclides is compared. The peaks, known as resonances, appear at energies that are specific for each nuclide. Hence, resonances are fingerprints of nuclides and can be used to determine the elemental and isotopic composition of materials (Postma and Schillebeeckx 2009). The resonance

H. Postma (✉)

Reactor Institute Delft, Mekelweg 15, 2629, JB Delft, The Netherlands

e-mail: postma-bosch@dataweb.nl

P. Schillebeeckx

European Commission, Joint Research Centre, Retieseweg 111, B-2440 Geel, Belgium

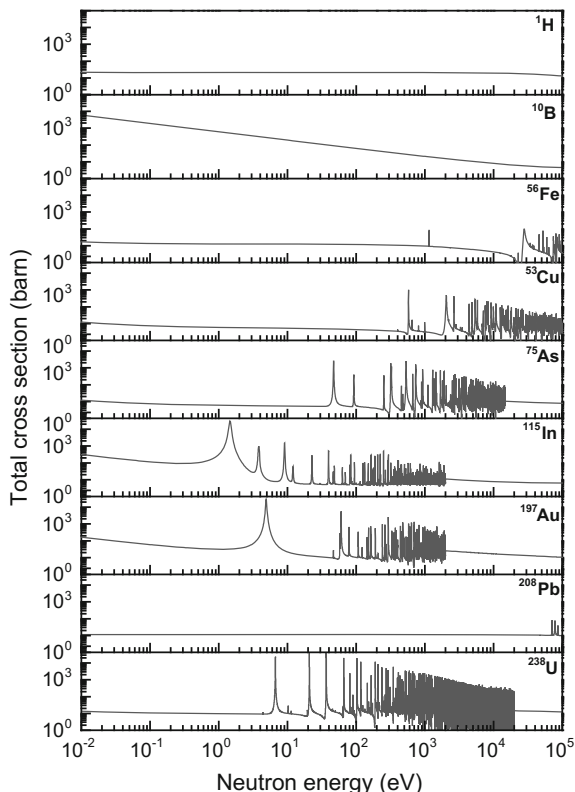
e-mail: peter.schillebeeckx@ec.europa.eu

© Springer International Publishing Switzerland 2017

N. Kardjilov and G. Festa (eds.), *Neutron Methods for Archaeology and Cultural Heritage*, Neutron Scattering Applications and Techniques,
DOI 10.1007/978-3-319-33163-8_12

235

Fig. 12.1 Total cross section as a function of neutron energy for neutron induced reactions in ^1H , ^{10}B , ^{56}Fe , ^{63}Cu , ^{75}As , ^{115}In , ^{197}Au , ^{208}Pb and ^{238}U . The cross sections are taken from the JEFF-3.2 data base



structures in neutron induced reaction cross sections are the basis of two neutron resonance analysis (NRA) methods, i.e. neutron resonance transmission (NRTA) and neutron resonance capture analysis (NRCA). NRCA relies on the analysis of resonance capture spectra, which are obtained by detecting prompt γ -rays emitted after a neutron capture reaction in the sample. For NRTA the transmission of neutrons through a sample is measured with a neutron detector placed at a distance behind the sample. Both NRA methods rely on time-of-flight (TOF) measurements at a pulsed neutron source, which is a well-known technique for neutron resonance spectroscopy (Schillebeeckx et al. 2012b).

The use of NRTA as a non-destructive analysis method has already been demonstrated by Priesmeyer and Harz (1975). They derived the ^{235}U content in fresh and spent nuclear fuel pins from transmission measurements using a fast-chopper TOF-spectrometer installed at a research reactor. Resonance structures resulting from the detection of prompt γ -rays have been used by Moxon et al. (1974) to determine impurities in reference samples.

The breakthrough of NRCA, in particular for archaeological applications, came after test experiments with small samples at the TOF-facility GELINA of the EC-JRC in Geel (BE) in 2000 by Hans Postma of the Delft University of Technology (NL) and

Franco Corvi of the EC-JRC (Postma et al. 2001). After these feasibility studies a 12.5 m measurement station of GELINA was made available on a regular basis for a joint project of EC-JRC and the Delft University of Technology (NL) to study archaeological objects by NRCA. More extensive projects under improved experimental conditions, using a second beam with a longer flight path, were performed in collaboration with several museums and archaeological institutes providing interesting artefacts. These projects concerned mainly the study of objects made from copper alloys. In addition, applications in other fields were explored, e.g. the characterization of reference materials for cross section measurements (Schillebeeckx et al. 2010) and of special nuclear materials (Schillebeeckx et al. 2014, 2015), and support was given to the development of imaging techniques combined with neutron resonance spectroscopy as part of the Ancient Charm project (Gorini et al. 2007).

In the following sections the basic theory of neutron resonances will be discussed together with important aspects that influence the shape of observed resonance profiles. The principles of NRTA and NRCA together with experimental details are described. In the last section, applications are presented with an emphasis on NRCA studies of cultural heritage objects and artefacts at GELINA.

12.2 Theory of Neutron Induced Reaction Cross Sections

12.2.1 Single Level Breit-Wigner Formalism

Resonance structured cross sections can be parameterized by the R-matrix nuclear reaction formalism (Lane and Thomas 1958). In case of an isolated, single-state resonance the Single-Level-Breit-Wigner (SLBW) expressions (Breit and Wigner 1936) can be used. For a single s-wave resonance, with an orbital momentum of the neutron-nuclear system $\ell = 0$, the total cross section as a function of energy $\sigma_{\text{tot}}(E)$ for a target nucleus at rest is:

$$\sigma_{\text{tot}}(E) = \pi \lambda^2 g_J \frac{\Gamma_n \Gamma}{(E - E_\mu)^2 + (\Gamma/2)^2} + 4\pi \lambda^2 g_J \frac{\Gamma_n (E - E_\mu) R'}{(E - E_\mu)^2 + (\Gamma/2)^2} + 4\pi R'^2, \quad (12.1)$$

where $\lambda = \lambda/2\pi$ is the reduced neutron wavelength, g_J a factor depending on the combination of the spins of the neutron and target nucleus and the orbital moment, E_μ is the resonance energy, Γ is the total width of the resonance, Γ_n is the neutron width, and R' is the effective scattering radius. The total width is the sum of the partial widths of all open reaction channels. A partial width expresses the

probability that a specific reaction occurs. In case only neutron capture and elastic scattering are possible, the total width is $\Gamma = \Gamma_n + \Gamma_\gamma$, with Γ_γ the radiation width.

The capture cross section $\sigma_\gamma(E)$ as a function of neutron energy in SLBW-approximation is:

$$\sigma_\gamma(E) = \pi \lambda^2 g_J \frac{\Gamma_n \Gamma_\gamma}{(E - E_\mu)^2 + (\Gamma/2)^2}. \quad (12.2)$$

The radiation width Γ_γ is the sum of the partial widths related to all primary γ -rays emitted from the capture state. The maximum capture cross section σ_γ^0 :

$$\sigma_\gamma^0 = 4\pi \lambda^2 g_J \frac{\Gamma_n \Gamma_\gamma}{\Gamma^2}, \quad (12.3)$$

is reached at the resonance centre E_μ .

The total cross section in Eq. (12.1) is a sum of a resonance term, a potential scattering term and an asymmetric term resulting from the interference between potential and resonance elastic scattering. The capture cross section contains only a resonance term.

For an s-wave resonance the energy dependence of the neutron width is:

$$\Gamma_n(E) = \Gamma_n^0 \sqrt{E/E_0}, \quad (12.4)$$

with $E_0 = 1$ eV and Γ_n^0 denotes the energy-independent reduced neutron width. In the region of the resonance, the energy dependence of the neutron width can be neglected, such that the capture cross section and the resonance term in Eq. (12.1) have a symmetric Lorentzian shape $1/(1 + x^2)$, with $x = 2(E - E_\mu)/\Gamma$. For $E \ll E_\mu$ and $E \ll \Gamma$, i.e. in the low energy region far from the resonance, the capture cross section varies with $E^{1/2}$. This leads to a cross section that is inversely proportional to the neutron velocity v . The contribution of this $1/v$ component is visible in the total cross section for e.g. ^{115}In and ^{197}Au in Fig. 12.1.

The area under the resonance term of the total cross section in Eq. (12.1) is:

$$A_{\text{tot}} = 2\pi \lambda^2 g_J \Gamma_n, \quad (12.5)$$

and the resonance area of the capture cross section in Eq. (12.2) is:

$$A_\gamma = 2\pi \lambda^2 K_\gamma, \quad (12.6)$$

with the capture kernel K_γ defined by:

$$K_\gamma = g_J \frac{\Gamma_n \Gamma_\gamma}{\Gamma}. \quad (12.7)$$

Not all resonances can be fully characterised and for certain resonances only the capture kernel is reported. A more detailed discussion on resonance structured neutron induced reaction cross section can be found in Fröhner (2000).

12.2.2 Doppler Broadening

Thermal motion of atomic nuclei causes a shift of the relative kinetic energy in the neutron-nucleus system. Since thermal motion is a statistical process, the observed resonance profile will be broadened, this is known as Doppler broadening. A Doppler broadened cross section, denoted by $\bar{\sigma}$, can be obtained by convoluting the cross section σ for a target nucleus at rest, with an energy transfer function $S(E, E')$. Within the free gas model (FGM) and for energies much larger than the Doppler width, i.e. $E \gg \Delta_D$, a Doppler broadened cross section $\bar{\sigma}(E)$ can be approximated by a Gaussian broadening of the reaction rate, that is, by a convolution of $\sqrt{E'}\sigma(E')$ with a Gaussian distribution (Bethe and Placzek 1937; Fröhner 2000):

$$\bar{\sigma}(E) \cong \frac{1}{\Delta_D \sqrt{\pi}} \int_{-\infty}^{\infty} dE' e^{-\left(\frac{E'-E}{\Delta_D}\right)^2} \sqrt{\frac{E'}{E}} \sigma(E'), \quad (12.8)$$

with the Doppler width Δ_D given by:

$$\Delta_D = \sqrt{\frac{4Ek_B T}{M/m}}, \quad (12.9)$$

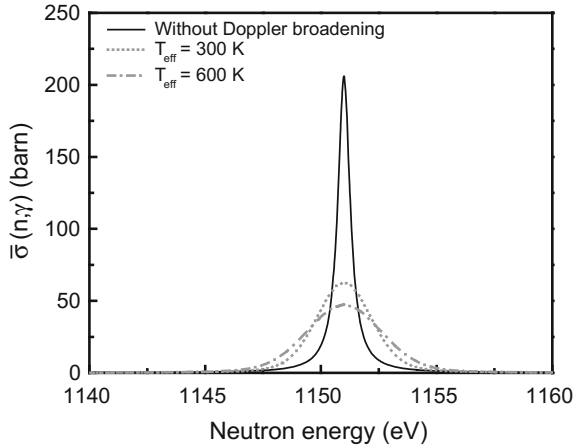
where the rest mass of the target nucleus and neutron are denoted by M and m , respectively, the Boltzmann constant by k_B and T is the sample temperature. The FGM approximation can also be applied for a crystalline solid by replacing the sample temperature in Eq. (12.9) by an effective temperature T_{eff} (Lamb 1939), which can be related to the Debye temperature θ_D by:

$$T_{\text{eff}} \cong \frac{3}{8} \theta_D \coth\left(\frac{3}{8} \frac{\theta_D}{T}\right). \quad (12.10)$$

For most elements the effective temperature for a sample at room temperature $T = 300$ K is only a few per cent larger than $T = 300$ K. For iron ($\theta_D = 470$ K), copper ($\theta_D = 315$ K), zinc ($\theta_D = 234$ K) and lead ($\theta_D = 100$ K) the effective temperatures for $T = 300$ K are $T_{\text{eff}} = 334, 315, 309$ and 301.6 K, respectively.

For elements dissolved in another element or as a compound, the Debye temperatures will be different. In the case of a solid solution of an element in a bronze object, a modified “Debye temperature” based on a simple interpolation model can be introduced to estimate the effective temperature with Eq. 12.10. Some elements,

Fig. 12.2 Capture cross section around the 1.15 keV resonance of ^{56}Fe . The cross section without Doppler broadening is compared with the Doppler broadened cross section for a T_{eff} of 300 K and 600 K



e.g. lead, occur as clusters in bronze and thus their elemental Debye temperature can be used. With artefacts at room temperature the effective temperatures will in most cases be slightly larger than 300 K.

The Doppler broadened capture cross section around a single resonance can be approximated by:

$$\bar{\sigma}_{\gamma}(E) \cong \sigma_{\gamma}^0 \Psi(\beta, x), \quad (12.11)$$

with:

$$\Psi(\beta, x) = \frac{1}{\beta\sqrt{\pi}} \int_{-\infty}^{\infty} dy \frac{1}{1+y^2} e^{-\frac{(x-y)^2}{\beta^2}}, \quad (12.12)$$

where $\beta = 2\Delta_D/\Gamma$, $x = 2(E - E_{\mu})/\Gamma$ and $y = 2(E' - E_{\mu})/\Gamma$. Equation (12.12) is known as the Voigt function. It has a Gaussian shape around the central energy E_{μ} and a Lorentzian shape in the wings of the broadened resonance. The convolution lowers and broadens the resonance curve, but its area remains the same. The maximum of the resonance peak is reduced by a factor:

$$\Psi(\beta, 0) = \frac{\sqrt{\pi}}{\beta} e^{\frac{1}{\beta^2}} \operatorname{erfc}\left(\frac{1}{\beta}\right) \quad (12.13)$$

in which erfc is the complementary error function. The broadening and lowering of the resonance peak due to the Doppler effect is shown in Fig. 12.2 for the 1.15 keV resonance of ^{56}Fe . Numerical values of the parameters, Γ , Δ_D , β and $\Psi(\beta, 0)$, for resonances of interest for archaeological NRA applications are given in Table 12.1.

Table 12.1 Resonance energy E_{μ} , total width Γ , Doppler width Δ_D , parameter β and peak reduction factor $\Psi(\beta,0)$ for resonances of interest for objects at room temperature

Nuclide	E_{μ} (eV)	Γ (eV)	Δ_D (eV)	β	$\Psi(\beta,0)$
⁵⁶ Fe	1152	0.636	1.511	4.76	0.299
⁵⁹ Co	132	3.043	0.4957	0.326	0.954
⁶³ Cu	579	0.780	0.9935	2.55	0.469
	650	0.358	1.0526	5.87	0.252
⁶⁵ Cu	230	0.254	0.6166	4.86	0.293
⁶⁴ Zn	281.8	0.297	0.6802	4.58	0.307
⁶⁶ Zn	323.5	0.192	0.7179	7.48	0.205
⁷⁵ As	47.0	0.274	0.2586	1.89	0.564
	92.4	0.265	0.3626	2.74	0.448
¹⁰⁷ Ag	16.3	0.141	0.1267	1.80	0.579
¹⁰⁹ Ag	5.2	0.142	0.0708	0.995	0.759
	30.4	0.1337	0.1714	2.56	0.468
¹¹⁵ In	1.5	0.0735	0.03613	0.983	0.763
¹¹⁶ Sn	111.2	0.0860	0.3195	7.43	0.206
¹¹⁷ Sn	38.8	0.1021	0.1879	3.68	0.363
¹²¹ Sb	6.24	0.0889	0.0736	1.66	0.605
	15.5	0.0961	0.1160	2.41	0.487
	29.65	0.0871	0.1605	3.68	0.363
¹²³ Sb	21.4	0.1133	0.1352	2.39	0.489
¹⁹⁷ Au	4.9	0.1316	0.0511	0.776	0.822
²⁰⁶ Pb	3357.0	0.3220	1.30	8.07	0.192

12.3 Neutron Time-of-Flight Measurements

12.3.1 Pulsed White Neutron Source Facilities

NRTA and NRCA rely on neutron resonance spectroscopic measurements at a white neutron source applying the TOF-technique. This can be realized at a continuous neutron source using a chopper or at an accelerator-driven neutron source operated in pulse mode. Measurements using a chopper are limited to study elements with resonances in the low-energy region, below about 100 eV. To cover a wide range of elements a white neutron source based on a pulsed electron or proton beam is best suited.

In electron-based accelerators, a pulsed high-energy electron beam is stopped in a target that is made out of a material with a high mass number (e.g. Ta, Hg or U). The resulting Bremsstrahlung radiation generates neutrons via photonuclear and photofission reactions in the target. High-energy proton accelerators produce neutrons by the spallation process in a target made out of a high mass number material (e.g. W, Hg, Pb, Bi). Neutrons produced by photonuclear reactions or spallation

Table 12.2 Characteristics of accelerator driven neutron TOF-facilities, which could be used for NRTA and/or NRCA applications

Facility	Ref.	Charged particle beam		Target	Pulse width (ns)	Frequency (Hz)	Flight path length (m)
		Type	Energy (MeV)				
GELINA	1	e ⁻	80–140	U	1	40–800	10–400
KURRI (short pulse)	2	e ⁻	20–46	Ta	2, 5, 10, 22, 33, 47, 68, 100	1–300	10, 13, 24
KURRI (long pulse)	2	e ⁻	7–32	Ta	100–4000	1–100	10, 13, 24
ORELA	3	e ⁻	140	Ta	2–30	1–1000	10–200
POHANG	4	e ⁻	75	Ta	2000	12	11
RPI	5	e ⁻	60	Ta	7–5000	500	10–250
J-PARC/MLF	6	p	3000	Hg	100 ^a	25	21, 28
n_TOF	7	p	20,000	Pb	6	0.4	20, 185
ISIS (target 1)	8	p	800	W ^c	65 ^b	50	15–25
ISIS (target 2)	8	p	800	W ^c	65 ^b	10	15–60

Similar comparisons of some of these facilities can be found in Koehler (2001, 2007; Schillebeeckx et al. 2012b)

1 Mondelaers and Schillebeeckx (2006)

2 Kobayashi et al. (2004)

3 Böckhoff et al. (1990)

4 Wang et al. (2008)

5 Overberg et al. (1999)

6 Kino et al. (2011)

7 Chiaveri et al. (2014)

8 ISIS, private communication

^aDouble pulse: two pulses of 100 ns FWHM separated by 600 ns

^bDouble pulse: two pulses of 65 ns FWHM separated by 320 ns

^cClad with Ta

have an energy spectrum with a maximum in the energy region above 1 MeV. Such a spectrum is not directly useful for NRTA and NRCA applications. To increase the amount of low-energy neutrons and produce a spectrum covering the resonance region, a moderator consisting of hydrogen rich material is used.

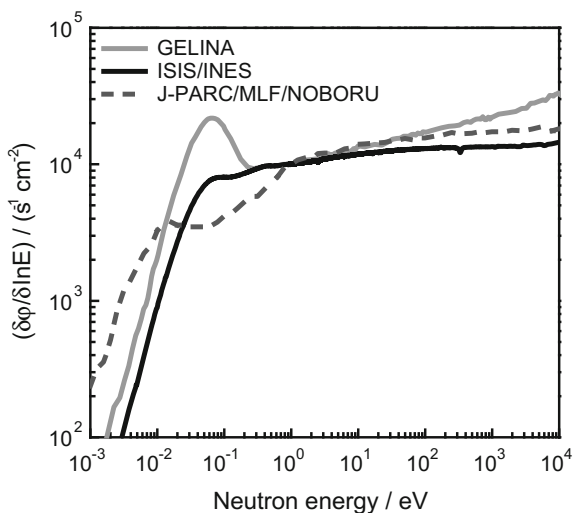
In Table 12.2 characteristics of accelerator driven neutron TOF-facilities are listed. Up to now most of the NRA applications, have been carried out at the GELINA facility of the EC-JRC in Geel (BE). This facility was especially designed and constructed to study resonance structured cross sections of neutron induced reactions (Mondelaers and Schillebeeckx 2006). It is a multi-user TOF-facility, providing a white neutron source with a neutron energy range from 10 meV to 20 MeV. Up to ten experiments can be performed in parallel, at measurement

stations located between 10 and 400 m from the neutron production target. The linear accelerator produces a pulsed electron beam with a maximum energy of 150 MeV and a repetition rate ranging from 50 to 800 Hz. A compression magnet reduces the width of the electron pulses to about 1 ns (Tronc et al. 1985). The electron beam hits a mercury cooled uranium target producing Bremsstrahlung and subsequently neutrons via photonuclear reactions (Salomé and Cools 1981). Two water-filled beryllium containers mounted above and below the neutron production target are used to moderate the neutrons.

Within the ANCIENT CHARM project (Gorini et al. 2007) feasibility studies for imaging applications have been carried out at the INES station of the ISIS facility. ISIS is a pulsed spallation neutron source at the Rutherford Appleton Laboratory providing beams of neutrons and muons to probe microscopic structure and dynamics of matter. Extensive studies to develop NRTA combined with imaging are carried out at the NOBORU facility (NeutOn Beam-line for Observation and Research Use) at J-PARC/MLF/ (Hasemi et al. 2015). The J-PARC facility is a multi-purpose and multidisciplinary facility producing neutron, pion, kaon and muon beams (Ikeda 2009). The applications include fundamental nuclear and particle physics, materials and life science, and nuclear technology. The Materials and Life Science Experimental Facility (MLF) aims at promoting materials science and life science using intense pulsed neutron and muon beams which are produced using a 3 GeV proton beam with a current of about 300 μA and a repetition rate of 25 Hz.

The neutron spectrum of GELINA is compared in Fig. 12.3 with the one at the INES station of ISIS and the NOBORU facility of J-PARC/MLF/. The spectra in Fig. 12.3 are normalized to a fluence rate of $10^4 \text{ s}^{-1} \text{ eV}^{-1} \text{ cm}^{-2}$ at 1 eV, which corresponds to a nominal neutron output at GELINA for measurements at 10 m distance with the accelerator operated at 800 Hz and an average current of 70 μA .

Fig. 12.3 Comparison of the neutron spectra for beam lines at GELINA, ISIS/INES and J-PARC/MLF/NOBORU. The spectra are normalized to a fluence rate of $10^4 \text{ s}^{-1} \text{ eV}^{-1} \text{ cm}^{-2}$ at 1 eV



For a similar distance and a 50 Hz operating frequency at ISIS and 25 Hz frequency at J-PARC, which are their normal operational conditions, the neutron intensity at these facilities is about 2 orders of magnitude larger.

Below 1 MeV, the spectra can be approximated by a Maxwellian distribution in the thermal energy region and a $1/E^\alpha$ dependence in the epi-thermal region, with $\alpha \sim 0.85$ for GELINA, $\alpha \sim 0.95$ for ISIS/INES and $\alpha \sim 0.95$ for J-PARC/MLF/NOBORU. The spectrum shape strongly depends on the moderator conditions. The spectrum at GELINA is for a beam-line viewing two water-filled beryllium containers placed above and below the neutron producing uranium target. The neutron beam at the INES station results from a decoupled water moderator that is poisoned with Gd and the one at J-PARC/MLF/NOBORU from a coupled water moderated neutron beam. More details on the neutron spectra at the J-PARC/MLF/ facility can be found in Harada et al. (2007), Maekawa et al. (2010) and Kino et al. (2011).

12.3.2 Time-of-Flight Technique

The energy of a neutron can be derived from the time t a neutron needs to travel a given distance L (see Fig. 12.4). For low-energies, the non-relativistic expression suffices to relate the energy E and velocity v of the neutron to the time t and distance L by:

$$E = \frac{1}{2}mv^2 = \frac{1}{2}m\left(\frac{L}{t}\right)^2. \quad (12.14)$$

For practical applications it reads:

$$E = \left(72.298\frac{L}{t}\right)^2, \quad (12.15)$$

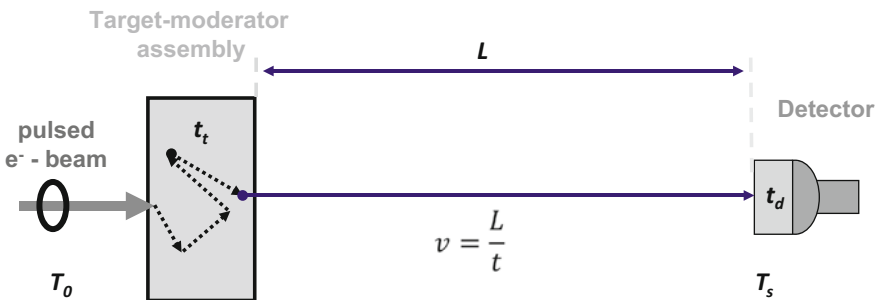


Fig. 12.4 Schematic representation of the TOF-technique in case of a transmission measurement. The symbols are clarified in the text

with the energy E expressed in eV, the distance L in m and the time t in μs . Experimentally a time-of-flight t_m is derived from the difference between a stop signal T_s obtained from the detection system and a start signal T_0 delivered by the accelerator or chopper. The observed time-of-flight t_m is the sum of three contributions (Schillebeeckx et al. 2012b):

$$t_m = t + t_t + t_d \quad (12.16)$$

where

- t_t is the time difference between the moment the neutron leaves the target-moderator assembly and its time of creation,
- t is the time that a neutron, leaving the target-moderator assembly with a velocity v , needs to travel the distance L , and
- t_d is the time difference between the time of detection and the moment the neutron enters the detection system or the sample.

12.3.3 Response Function

Since the neutron transport in the target-moderator assembly and in the detection system (or sample) is a stochastic process, the times t_t and t_d will be statistically distributed. Consequently, the experimentally observed resonance profiles will be broadened. To describe the broadened profiles the response function of the TOF-spectrometer is required. Such a response function $R(t_m, E)$, expressing the probability that a neutron with energy E produces a TOF-signal t_m , depends on the distributions of the times (T_s , T_0 , t_t and t_d) and the distance L .

The distance L can be determined accurately by metric measurements and its contribution to the broadened profile can be neglected. The contribution due to the difference ($T_s - T_0$) is influenced by the characteristics of the pulsed charged particle beam. At GELINA the contribution due to the start pulse T_0 is approximated by a normal distribution with a width that is reduced to 1 ns at FWHM (Full Width Half Maximum) due to the use of a compression magnet (Tronc et al. 1985). At ISIS this contribution creates a double structure, that can be represented by a sum of two normal distributions, which are separated by 320 ns and each distribution has a FWHM of 65 ns, as shown in Fig. 12.5. The profile in Fig. 12.5 results from a measurement of the γ -ray flash with a scintillator. At J-PARC/MLF a similar double-pulsed structure, with a separation of 600 ns between the two pulses and for each peak a FWHM of 100 ns, has to be taken into account.

For TOF-measurements at a moderated neutron beam an important broadening component results from the neutron transport in the target-moderator assembly, i.e. the broadening due to the time t_t . The probability distribution due to this component strongly depends on the neutron energy. For practical reasons response functions due to the neutron transport are better represented by introducing an equivalent

Fig. 12.5 Contribution of the pulsed proton beam to the response function for TOF-measurements at ISIS. The experimental data, which were obtained from measurements with a scintillator, are parameterized by a sum of two normal distributions

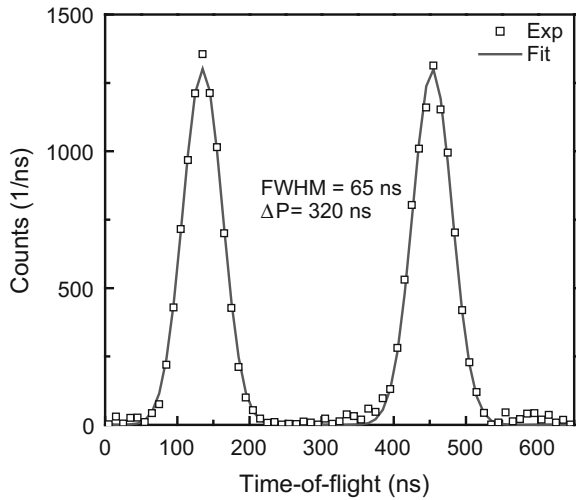
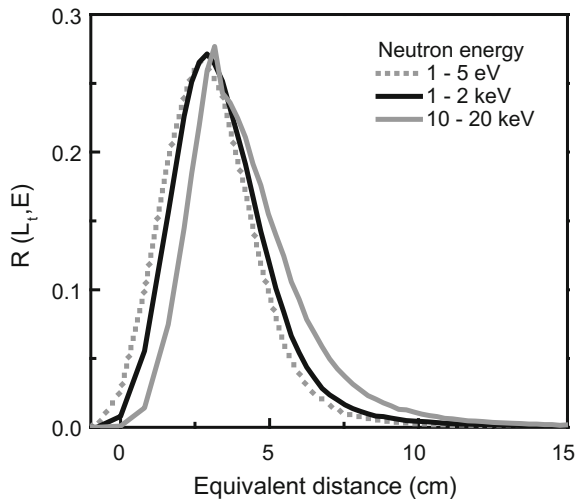


Fig. 12.6 Probability distribution of the equivalent distance L_t for a beam line at GELINA forming an angle of 18° with the normal to the face of the moderator viewing the flight path. The data result from Monte Carlo simulation of Ene et al. (2010)



distance, which is defined by $L_t = v t_t$. Such a transformation of variables results in distributions that are less dependent on the neutron energy (Schillebeeckx et al. 2012b). Examples of such distributions are shown in Fig. 12.6. These distributions result from Monte Carlo simulations for a moderated neutron beam at GELINA and a flight path that forms an angle of 18° with the normal to the exit face of the moderator (Ene et al. 2010). They have two common components, an exponential decay due to the primary neutron production in the uranium target and a χ^2 -distribution due to the moderation process. The latter, first introduced by Groenewold and Groendijk (1947), dominates the response.

For the GELINA facility these distributions depend on the angle of the flight path with respect to the moderator. They have a full width at half maximum (FWHM) of about 2.5 and 3.5 cm for a flight path forming an angle of 9° and 18°, respectively, with the normal to the exit face of the moderator. A comparison of response functions for different pulsed neutron source facilities reveals that the resolution for TOF-measurements at a pulsed white neutron source resulting from photonuclear reactions is significantly better compared to the resolution at a spallation source (Schillebeecx et al. 2012b, 2014, 2015). Response functions for the ISIS and J-PARC/MLF/ spallation sources strongly depend on the moderation conditions. The best resolution is obtained at a de-coupled moderator loaded with strong neutron absorbing material.

The total energy resolution can be approximated by:

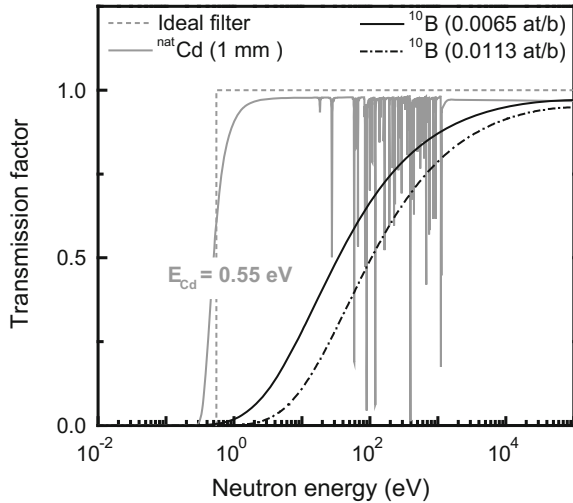
$$\frac{\Delta E}{E} = 2 \frac{\Delta v}{v} = \frac{2}{L} \sqrt{(v\Delta T_0)^2 + (v\Delta T_s)^2 + \Delta L_t^2 + \Delta L_d^2}, \quad (12.17)$$

where it is supposed that the different components follow a Gaussian distribution and that they are not correlated. The components (ΔT_0 , ΔT_s , ΔL_t , ΔL_d) are in first approximation independent of the neutron energy. Therefore, the energy resolution for a fixed energy improves with increasing distance. Since the neutron intensity decreases with the inverse of the square distance a compromise has to be made between resolution and intensity. In defining an optimum distance one also has to consider that at low energies the Doppler broadening dominates (Schillebeecx et al. 2014, 2015).

12.3.4 *Overlap and Background Filters*

For measurements at a relatively short flight path and an accelerator operating at a high frequency the detection of slow neutrons produced by a previous accelerator pulse, referred to as overlap neutrons, will contribute to the background. To reduce this background component a ^{10}B or Cd overlap filter can be placed in the beam. The transmission through a 1 mm thick $^{\text{nat}}\text{Cd}$ filter as a function of neutron energy is shown in Fig. 12.7. The transmission is compared with an ideal rectangular transmission with cut-off energy at 0.55 eV. The transmission through a $^{\text{nat}}\text{Cd}$ creates a structured neutron flux. The structures can overlap with resonances of the elements of interest. This can be avoided by using a ^{10}B filter, which has a smooth total cross section that in first approximation is inversely proportional to the velocity of the neutron. The transmissions through ^{10}B filters with areal densities of 0.013 at/b and 0.0065 at/b are also shown in Fig. 12.7. The disadvantage of a ^{10}B filter is that it attenuates the neutron beam in a broad energy region. This can be a problem when elements with resonances in the low energy region have to be quantified. The optimum type and thickness of an overlap filter depends on the

Fig. 12.7 Transmission through a 1 mm thick metal disc of ^{nat}Cd is compared with an ideal rectangular filter with cut-off energy of 0.55 eV and with the transmission through a filter consisting of ^{10}B with an areal density of 0.0065 and 0.0113 at/b. The cross sections were taken from the JEFF-3.2 library



various experimental parameters, i.e. energy region of interest, flight path length and operating frequency.

To reduce the background due to the γ -ray flash and 2.2 MeV γ -rays resulting from neutron capture in hydrogen present in the moderator, a Pb or Bi-filter can be placed in the beam. When an accurate determination of the background is required the use of fixed black resonance filters is recommended (Schillebeeckx et al. 2012b). A 10 cm thick S-filter removes more than 99 % of the neutrons in a wide region around the resonance at 102 keV and acts in addition as a shield against γ -rays. Again the optimum γ -ray and background filters depend on the applications.

12.3.5 Activation of Objects

A neutron-capture reaction results in a nucleus of the same element with one more bound neutron. After the emission of prompt γ -rays, this nucleus is either stable or radioactive. Hence, not all capture events lead to radioactivity. In addition, some of the produced nuclei may have a short half-life, such that most of the activity is already decayed directly after the NRTA and NRCA experiments. When radionuclides with longer half-lives are produced, the amount of radioactivity should be considered carefully.

The radioactivity depends on the production rate and decay constant λ . The production rate is the product of the cross section, $\sigma(E)$, and flux, $\phi(E)$, integrated over the neutron energy. In practice the activation of an object can be split into a part related to the thermal energy region and a part related to the epi-thermal energy region of the neutron spectrum (Postma and Schillebeeckx 2009). For a thin sample the activity A for a measurement time τ is:

$$A = \lambda n \tau \left(\int_0^{E_c} \sigma_\gamma(E) \varphi(E) dE + \int_{E_c}^{\infty} \sigma_\gamma(E) \varphi(E) dE \right), \quad (12.18)$$

neglecting the decay during the measurement time. In this expression E_c is a suitably chosen upper energy of the thermal region and n is the areal number density of the target nucleus. In the energy below E_c the capture cross section is often inversely proportional to the neutron velocity. The activity produced by neutrons in the thermal energy region can be reduced considerably by placing a ^{nat}Cd or ^{10}B filter in the beam. As mentioned above, such filters are very useful for reducing the background contribution due to overlap neutrons. The activation due to the second term of Eq. (12.18) can be estimated on the basis of the resonance areas (Eq. 12.6).

In all NRCA experiments at GELINA with bronze artefacts activation has been very low. The objects could always be returned to the owners after a short waiting time, usually on the same day or the day after the measurement was carried out. For example, the activation of a bronze arrowhead of 6.4 g, used in one of the early NRCA measurements (Postma et al. 2001) at a 12.5 m station of GELINA with a Cd filter in the beam, was estimated in Postma and Schillebeeckx (2009). Most of the activation is due to capture in ^{63}Cu leading to the production of ^{64}Cu with a half-life $T_{1/2} = 12.7$ h. After an irradiation time of 1 h this activity is about 3 Bq, leading to a specific activity of 0.5 Bq/g, which is well below the official limit of 100 Bq/g for free release of the object. Additional radioactivity due to the production of ^{66}Cu ($T_{1/2} = 5.1$ min) and the tin isotopes ^{113}Sn ($T_{1/2} = 115$ d), ^{121}Sn ($T_{1/2} = 27$ h), ^{123}Sn ($T_{1/2} = 129$ d) and ^{125}Sn ($T_{1/2} = 9.6$ d) are very low. The same is valid for trace elements present in the arrowhead.

12.4 Theoretical Observables

The quantity of interest for NRTA applications is the transmission T , which is the fraction of the neutron beam that traverses the sample without any interaction. For a parallel neutron beam, which is perpendicular to a slab of material, this fraction is given by:

$$T(E) = e^{-\sum_k n_k \bar{\sigma}_{\text{tot},k}(E)}, \quad (12.19)$$

where $\bar{\sigma}_{\text{tot},k}$ is the Doppler broadened total cross section and n_k is the areal number density (or number of atoms per unit area) of nuclide k in the sample. The transmission is directly related to the total cross section and the areal density. Assuming that the total cross sections of the nuclides present in the sample are known, a measurement of the transmission can be used for elemental and isotopic analysis.

In a capture experiment the total number of capture events per incident neutrons is assessed. This number, which is also referred to as capture yield and denoted by Y_γ , can be expressed as a sum of primary events $Y_{0,k}$ and multiple interaction events $Y_{m,k}$ for each nuclide present in the sample:

$$Y_\gamma(E) = \sum_k (Y_{0,k}(E) + Y_{m,k}(E)). \quad (12.20)$$

Multiple interaction events $Y_{m,k}$ result from a neutron capture by nuclide k after at least one neutron scattering in the sample. For a parallel neutron beam and a homogeneous slab of material perpendicular to the beam, the primary yield can be written as:

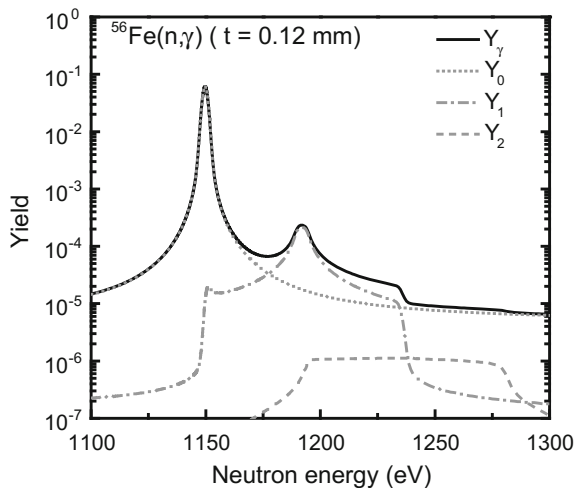
$$Y_{0,k}(E) = F(E)n_k\bar{\sigma}_{\gamma,k}, \quad (12.21)$$

where $\bar{\sigma}_{\gamma,k}$ is the Doppler broadened capture cross section and $F(E)$ is the self-shielding correction due to the reduction of the neutron beam in the sample. This correction is given by:

$$F(E) = \frac{(1 - e^{-\sum_j n_j \bar{\sigma}_{\text{tot},j}})}{\sum_j n_j \bar{\sigma}_{\text{tot},j}}. \quad (12.22)$$

Multiple interaction events produce an additional structure on the high-energy side of a resonance profile obtained from TOF-measurements. This is illustrated in Fig. 12.8, which shows the theoretical capture yield for a 0.12 mm thick ^{56}Fe sample in the region of the 1.15 keV resonance of ^{56}Fe as a function of neutron energy. In case of elastic scattering prior to capture the neutron loses part of its

Fig. 12.8 Theoretical capture yield for a 0.12 mm thick metal disc of pure ^{56}Fe as a function of energy as calculated for a TOF-experiment. The yield is given around the 1.15 keV resonance of ^{56}Fe . The contribution of primary events Y_0 , capture after one scattering Y_1 and capture after at least two scattering interactions Y_2 are shown



energy. This energy is transferred to the target nucleus without changing the time information. Consequently, the TOF created by such an event does not correspond to the energy of the neutron creating the capture reaction but to the energy of the neutron entering the sample prior to the elastic scattering. The energy E' of a neutron after an elastic collision with a target nucleus is:

$$E' = E \left(\frac{m}{M+m} \right)^2 \left(\cos \vartheta + \sqrt{(M/m)^2 - \sin^2 \vartheta} \right)^2 \tag{12.23}$$

with E the neutron energy before the collision and ϑ the angle of the scattered neutron in the laboratory system. The loss in neutron energy is transferred into the energy of the recoil nucleus. The energy lost by the neutron runs from zero for a forward scattering to a maximum for fully backward scattering. For fully backward scattering the energy of the scattered neutron is:

$$E'(\vartheta = 180^\circ) = E \left(\frac{M-m}{M+m} \right)^2 . \tag{12.24}$$

Hence, the contribution of single-scattering events followed by capture ranges from the resonance energy E_μ up to an energy:

$$E_\mu \left(\frac{M+m}{M-m} \right)^2 . \tag{12.25}$$

The contribution of multiple-interaction events is illustrated in Fig. 12.8 for the 1.15 keV in ^{56}Fe . The events due to single scattering followed by capture contribute to the yield in the energy region from 1.150 to 1.235 keV. A pronounced structure occurs when a thin disc or foil is placed perpendicular in the neutron beam. This

Fig. 12.9 Theoretical capture yields for 0.12, 1.2 and 12.0 mm thick metal discs of pure ^{56}Fe as a function of energy calculated for a TOF-experiment. The yields are given around the 1.15 keV resonance of ^{56}Fe

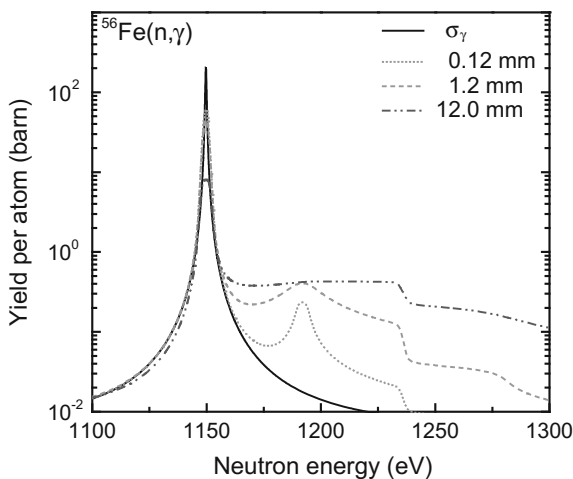
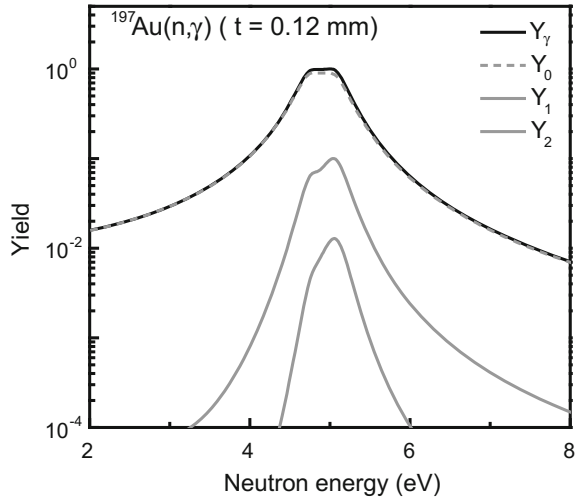


Fig. 12.10 Theoretical capture yield for a 0.1 mm thick metal disc of pure ^{197}Au as a function of energy in a TOF-experiment. The yield is given around the 4.9 eV resonance of ^{197}Au . The contribution of primary events Y_0 , capture after one scattering Y_1 and capture after at least two scattering interactions Y_2 are shown



structure is due to the higher probability of events resulting from incoming neutrons with an initial energy of 1.192 keV which are captured after a single elastic scattering with $\vartheta = 90^\circ$. As illustrated in Fig. 12.9 this structure disappears with increasing sample thickness.

The separation between multiple interaction events and the primary yield is present at high energies and for samples consisting of light elements. With decreasing energy and for heavier elements, the contribution of the primary yield and multiple interaction events overlap. This is illustrated in Fig. 12.10, which shows the capture yield around the 4.9 eV resonance of ^{197}Au for a 0.1 mm thick gold disc.

A correct calculation of the capture yield, in particular the contribution of multiple interaction events, is rather complex. For a parallel neutron beam and samples with a simple geometry and composition, the yield can be approximated by analytical expressions that have been developed by Moxon and Brisland and implemented in the REFIT code (Moxon and Brisland 1991). However, for complex geometries, relatively thick samples and/or strong scattering resonances, Monte Carlo simulations are required to correctly describe the capture yield (Schillebeeckx et al. 2014).

Equations (12.20)–(12.22) show that the capture yield can be used to derive the areal density of the nuclides present in the sample. Unfortunately, only in case of thin samples and/or small total cross sections there is a direct proportionality between the capture yield and the areal number density. For relatively thick samples the contribution due to self-shielding and multiple interactions complicates this relationship.

12.5 Neutron Resonance Transmission Analysis

12.5.1 Experimental Conditions

NRTA is based on an analysis of resonance dips present in an experimental transmission through the sample of interest. The methodologies to measure the attenuation of a neutron beam through a sample are well established and have been recently reviewed (Schillebeeckx et al. 2012b). The experimental transmission T_{exp} is derived from the ratio of a TOF-spectrum of a sample-in (C_{in}) measurement and a sample-out (C_{out}) measurement after subtraction of their background contributions B_{in} and B_{out} , respectively:

$$T_{\text{exp}} = \frac{C_{\text{in}} - B_{\text{in}}}{C_{\text{out}} - B_{\text{out}}}. \quad (12.26)$$

The spectra in Eq. (12.26) are corrected for losses due to the dead time of the detection system. They are normalized to the same intensity of the neutron beam and have the same TOF-bin structure. The background contributions B_{in} and B_{out} are a sum of a time independent and time dependent component. The latter is due to the detection of Schillebeeckx et al. (2012b):

- γ -rays produced in the neutron producing target-moderator assembly,
- neutrons scattered inside the detector station, and
- overlap neutrons.

Each of these components can be approximated by an analytical expression. The free parameters in the expressions are derived from a least squares fit to saturated resonance dips observed in a TOF-spectrum taken with black resonance filters in the beam. These are samples of elements with strong absorption (scattering, capture) resonances. The thickness of the filters is chosen such that the transmission at the resonance energy is less than 10^{-4} . When thick samples are measured, their presence will alter the background. To account for the impact of the sample on the background level, measurements with at least one fixed background filter are recommended (Schillebeeckx et al. 2012b). In case the sample contains an element with strong resonances, which black out, the corresponding transmission dips in the sample-in spectrum can be considered as self-indicating black resonance dips.

An example of a sample-in and sample-out TOF-spectrum together with the corresponding background contributions and their components are shown in Figs. 12.11 and 12.12. These TOF-measurements were carried out at a 50 m transmission station of GELINA using a fixed Na and Co black resonance filter. The sample was a 10 mm thick metal disc of natural copper. In the sample-in spectrum the black resonance dips due to strong resonances in Cu are used to derive the background with an accuracy of better than 3 % (Schillebeeckx et al. 2014, 2015).

By alternating sequences of sample-in and sample-out measurements the uncertainty on the normalization due to slow variations in time of both the beam

Fig. 12.11 Sample-out TOF-spectrum resulting from measurements at a 50 m station of GELINA with the accelerator operating at 800 Hz. The background spectrum is plotted together with the contribution due to the time independent background b_0 and due to the detection of γ -rays $b_1 \exp(-\lambda_1 t)$, scattered neutrons $b_2 \exp(-\lambda_2 t)$ and overlap neutrons $b_3 \exp(-\lambda_3(t+t_0))$

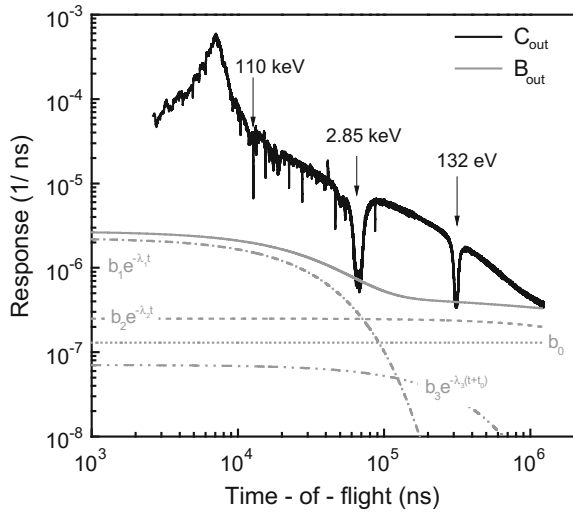
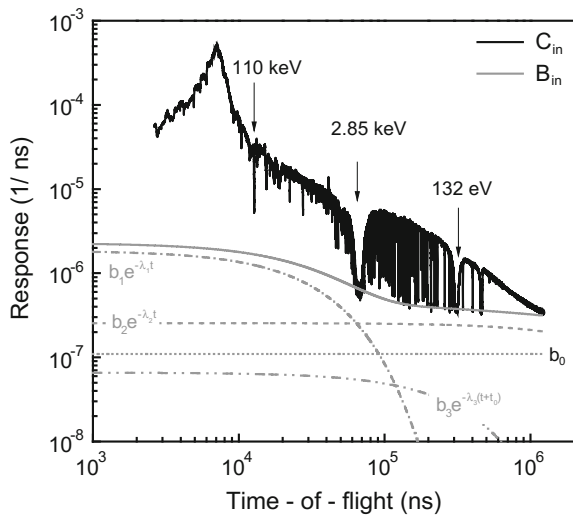


Fig. 12.12 Sample-in TOF-spectrum resulting from measurements at a 50 m station of GELINA with the accelerator operating at 800 Hz. The background spectrum is plotted together with the contribution due to the time independent background b_0 and due to the detection of γ -rays $b_1 \exp(-\lambda_1 t)$, scattered neutrons $b_2 \exp(-\lambda_2 t)$ and overlap neutrons $b_3 \exp(-\lambda_3 t)$



intensity and detection efficiency are reduced to less than 0.25 % (Schillebeeckx et al. 2012b).

To derive the experimental transmission from the TOF-spectra and produce covariance data the AGS (Analysis of Geel Spectra) code has been developed at the EC-JRC (Becker et al. 2012). The code, which is available from the OECD/NEA data bank, is based on a compact formalism that propagates both the correlated and uncorrelated uncertainties.

Since the experimental transmission is derived from a ratio of TOF-spectra measured with the same detector, it is independent of the detector efficiency and

neutron flux. Hence, the determination of T_{exp} does not require any additional calibration measurement using calibration samples which are representative for the sample under investigation. In addition, when the measurements are performed in good transmission geometry, the experimental transmission T_{exp} is a direct measure of the theoretical transmission T of Eq. (12.19). A good transmission is realized when:

- the sample is placed perpendicular with respect to a parallel incoming neutron beam,
- all detected neutrons have passed through the sample, and
- neutrons scattered by the sample and collimators are not detected.

These conditions can be realised by a proper collimation. An experimental set-up in good transmission geometry is shown in Fig. 12.13. It is a schematic representation of a 50 m transmission station at GELINA. This flight path forms an angle of 9° with the normal of the moderator surface viewing the flight path. In case these conditions are not fulfilled, e.g. in case of imaging applications using a position sensitive detector (see Chap. 16) special procedures are required to account for the background due to the detection of neutrons which are scattered by the sample (Perelli Cippo et al. 2011).

For low energy neutrons, with energies below 1 MeV, Li-glass scintillators enriched in ^6Li are mostly used as neutron detectors. The neutron transport in the scintillator will contribute to the final resolution. This contribution is also best expressed in terms of an equivalent distance L_d (Schillebeeckx et al. 2014, 2015). An example of such equivalent distance distributions is shown in Fig. 12.14 for the detection of neutrons with energies of 10 and 100 eV in a 6.35 mm thick scintillator. Evidently such distributions depend on the scintillator size. The size has to be optimised and a compromise has to be made between resolution and efficiency.

Unfortunately, the responses of a ^6Li -glass scintillator to a 2.2 MeV γ -ray and a low energy neutron are very similar and pulse shape discrimination between events

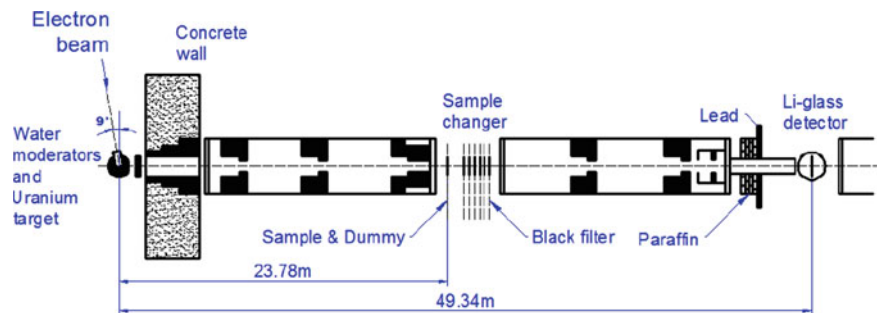
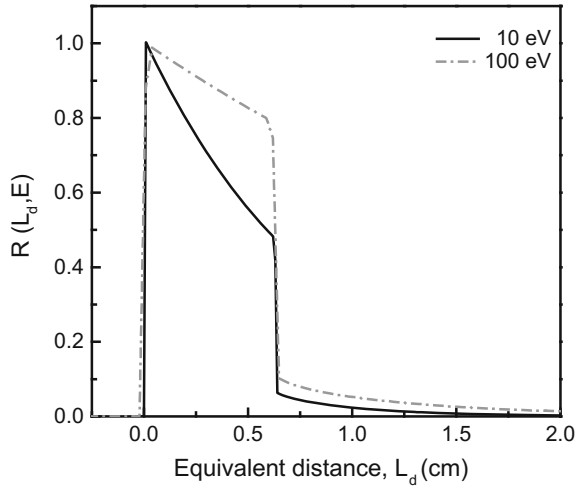


Fig. 12.13 A schematic drawing of a set-up for transmission measurements in good transmission geometry. The drawing is based on a 50 m transmission station of GELINA (Sirakov et al. 2013)

Fig. 12.14 Equivalent distance distributions for the detection of neutrons of 10 and 100 eV in a 6.35 mm thick scintillator. The results are obtained from the analytical expressions implemented in the REFIT code (Moxon and Brisland 1991)



resulting from the detection of γ -rays and neutrons is not evident. Therefore, γ -rays resulting from the neutron capture in the moderator will have a significant contribution to the background in the TOF-region corresponding to the moderation process. This contribution is shown in Figs. 12.11 and 12.12.

12.5.2 Analysis Procedures

When measurements are performed in an ideal transmission geometry and corrections for dead time losses and background are applied, the composition of the sample can be derived from a least-squares adjustment to the experimental transmission. The areal density of the nuclides present in the sample is determined by minimizing the expression:

$$\chi^2(n_{1,\dots,p}) = (T_{\text{exp}}(t_m) - T_M(t_m))^T V_{T_{\text{exp}}}^{-1} (T_{\text{exp}}(t_m) - T_M(t_m)), \quad (12.27)$$

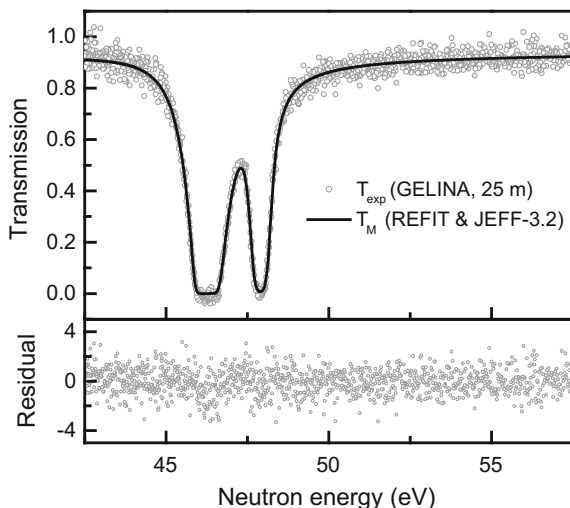
with the theoretical estimate $T_M(t_m)$ defined by:

$$T_M(t_m) = \frac{\int dE R(t_m, E) e^{-\sum_{k=1}^p n_k \bar{\sigma}_{\text{tot},k}(E)}}{\int dE R(t_m, E)}. \quad (12.28)$$

It should be noted that this equation is only valid for homogeneous samples with a regular shape.

The least-squares adjustment can be performed by a resonance shape analysis (RSA) code, which takes into account experimental effects such as the Doppler

Fig. 12.15 Transmission through a 1 mm thick metal disc of natural W. The full line reflects the result of a least squares adjustment using REFIT with only the areal density as free parameter (Becker et al. 2015)



broadening, sample properties, detector characteristics and response function of the TOF-spectrometer. REFIT (Moxon and Brisland 1991) and SAMMY (Larson 2008) are codes that can be used for such an analysis. NRTA applications at GELINA using the REFIT code have been reported by Noguere et al. (2007) and Schillebeeckx et al. (2014). The performance to characterize samples from transmission profiles measured at the J-PARC/MLF/NOBORU facility with REFIT are discussed in Hasemi et al. (2015).

An example of a resonance shape analysis is shown in Fig. 12.15. The data result from transmission measurements through a 1 mm thick metal disc of natural tungsten at a 50 m station of GELINA (Becker et al. 2015). In the fit only the areal density was considered as an adjustable parameter and the resonance parameters were fixed. The result of a least-squares adjustment using the resonance parameters recommended in JEFF-3.2 is shown in Fig. 12.15. Using these parameters the areal density derived from the experimental transmission approaches within less than

Table 12.3 The areal number density n_{fit} of a metal disc of $^{\text{nat}}\text{W}$ derived by NRTA

Library	n_{fit} (at/b)	$100 \times n_{\text{fit}}/n_{\text{ref}}$
JEFF—3.2	$(6.402 \pm 0.032) \times 10^{-3}$	100.2 ± 0.5
ENDGF/B-VI.8	$(7.009 \pm 0.032) \times 10^{-3}$	109.7 ± 0.5
JENDL—3.3	$(7.111 \pm 0.032) \times 10^{-3}$	111.3 ± 0.5
ENDF/B-VII.1	$(7.111 \pm 0.070) \times 10^{-3}$	111.3 ± 1.1
Lynn et al. (2002)	$(6.280 \pm 0.064) \times 10^{-3}$	98.3 ± 1.0

The ratio with the reference is also given. Results are given using the parameters recommended in the JEFF-3.2, ENDF/B-VI.8, JENDL 3.3 and ENDF/B-VII.1 libraries and for the parameters reported in Lynn et al. (2002). Only for the value derived with the resonance parameters in ENDF/B-VII.1 and (Lynn et al. 2002) their uncertainties were propagated

0.2 % the reference value $n_{\text{ref}} = (6.389 \pm 0.001) \times 10^{-4}$ at/b. This value was derived from the mass and area.

Evidently the accuracy of the areal density derived from such a fit depends on the quality of the nuclear data. This is illustrated in Table 12.3, which reports the areal density that is derived from a fit to the experimental transmission using different data libraries. Using the parameters recommended in the latest ENDF/B-VII.1 file, which includes covariances of the resonance parameters, the areal density is overestimated by more than 10 %. This bias is not covered by the uncertainties of the resonance parameter. More extensive studies of bias effects due to nuclear data are reported by Tsuchiya et al. (2014) and Schillebeeckx et al. (2014, 2015). For the analysis of bronze objects the use of Cu resonance parameters determined by Tsuchiya et al. (2014) are recommended.

All samples analysed in the above mentioned references were homogeneous samples with a regular shape such that Eq. (12.28) is valid. Analytical expressions for homogeneous samples with irregular shapes have been reported by Harada et al. (2014). The analysis of inhomogeneous samples is far more complex (Schillebeeckx et al. 2013). Algorithms, that can be applied to characterize heterogeneous samples, have been extensively studied by Becker et al. (2013a, 2014) as part of a project to apply NRTA for the characterization of melted fuel that originates from severe nuclear accidents. For these studies the models proposed by Kopecky et al. (2007) and the LP-model of Levermore et al. (1986) were implemented in the REFIT code (Becker et al. 2013b). To validate the models transmission experiments on mixed powder samples were carried out at GELINA. From the results of these measurements one can conclude that the LP-model is very well suited to analyse samples consisting of particles, which vary strongly in shape and size (Becker et al. 2014). Some samples might contain strong neutron absorbing materials, which do not have resonances in the low energy region. To account for the contribution of such elements in the data analysis a method has been proposed and validated in Schillebeeckx et al. (2014, 2015).

12.5.3 Facilities

Measurements in good transmission geometry have been carried out at the 25 and 50 m stations of GELINA. Samples are placed in automatic sample changers, which are positioned approximately halfway between the detector and the neutron-producing target. More details about the 25 and 50 m stations can be found in Lampoudis et al. (2013) and Sirakov et al. (2013), respectively. Recently the 25 m station was replaced by a 10 m station. This station has been constructed for transmission measurements in the low energy region and to demonstrate the potential of NRTA for the characterization of special nuclear material (Schillebeeckx et al. 2014, 2015). Mostly measurements are performed with the accelerator operated at 800 Hz and a ^{10}B overlap filter (0.013 at/b at 50 m and 0.0065 at/b at 10 m). At 10 m also a 4 mm thick $^{\text{nat}}\text{Cd}$ overlap filter is used to study

resonance structures between 1 eV and 60 eV with a 800 Hz operating frequency. This station is equipped with a rectangular Li-glass scintillator with dimensions $76 \times 76 \times 6.4 \text{ mm}^3$. The detector at the 25 m station was a 12.7 mm thick and 110.0 mm diameter NE905 scintillator type. The one installed at the 50 m station is a 6.35 mm thick and 101.6 mm diameter NE912 Li-glass scintillator. These scintillators are enriched to about 95 wt% in ^6Li and coupled to a photomultiplier tube. The time-of-flight of a detected neutron is determined by a multi-hit time-to-digital converter with a 1 ns resolution.

Up to now NRTA at GELINA was primarily applied to characterize reference materials for cross measurements. The potential to determine the elemental composition of bronze objects by a resonance shape analysis of a transmission profile has been demonstrated by transmission measurements at the 25 m station using a set of copper alloy reference samples (Schillebeeckx et al. 2012a). These samples were certified for their Cu content and relative amount of As, Pb, Sn and Zn

Fig. 12.16 Transmission through a bronze reference sample that is certified for the amount of Cu and relative amounts of As, Pb, Sn and Zn. The measurements were performed at a 25 m station of GELINA (Schillebeeckx et al. 2012a)

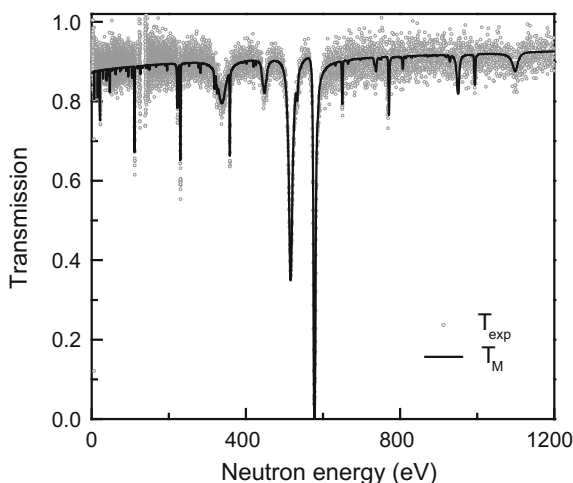


Table 12.4 Elemental composition of a bronze reference sample determined by NRTA is compared with the reference values

Element	Mass fractions	
	NRTA	Reference
Cu	0.8553 ± 0.0043	0.7873 ± 0.0001
Sn	0.0391 ± 0.0004	0.0716 ± 0.0021
Zn	0.0718 ± 0.0010	0.0602 ± 0.0022
As	0.0019 ± 0.0001	0.0019 ± 0.0001
Pb	0.0259 ± 0.0026	0.0790 ± 0.0070
Sb	0.0032 ± 0.0012	
Mn	0.0027 ± 0.0010	

The uncertainties on the NRTA values are only due to counting statistics. Data taken are from (Schillebeeckx et al. 2012a)

(Ingelbrecht et al. 2001). The transmission through one of these reference samples is shown in Fig. 12.16 as a function of neutron energy. The result of a least-squares adjustment with the areal densities of As, Pb, Sn, Zn, Sb and Mn as free parameters is shown by the full line. The resonance parameters were taken from the JEFF-3.1.1 data library. For Cu the parameters reported in Weigmann and Winter (1968) were adopted. In addition, most of the resonance energies had to be adjusted to obtain a good agreement between the experimental and calculated transmission. The mass fractions resulting from a fit to the data are listed in Table 12.4. They are in agreement with the reference values. Results of measurements on a bronze vessel sample are discussed in Sect. 12.5.

NRTA studies have been carried out at the J-PARC/MLF/NOBORU facilities (Tremisn et al. 2014; Hasemi et al. 2015). The studies concentrated on the performance of both the neutron beam and position sensitive neutron detectors for imaging applications, which will be discussed in more detail in Chap. 16.

In the MeV region NRTA is a valuable technique to analyse objects consisting of light elements like H, C, N and O (e.g. Sowerby and Tickner 2007; Mor et al. 2011). Another application is the use of the Doppler broadened resonance profile as a thermometer to study properties of materials (Hecker et al. 1994; Tokuda et al. 2001; Yuan et al. 2005) and statistical properties of phonon spectra (Lynn et al. 2002). An extended overview of such applications of NRTA is given in Schillebeeckx et al. (2014, 2015).

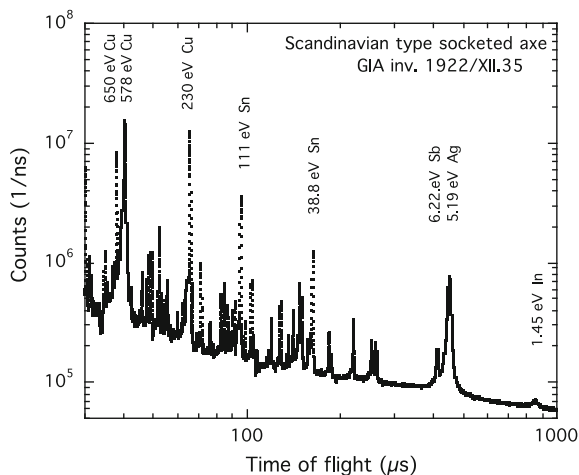
12.6 Neutron Resonance Capture Analysis

12.6.1 *Experimental Conditions*

NRCA relies on the analysis of resonance peaks in a TOF-spectrum that is obtained from the detection of prompt capture γ -rays. In most cases a number of γ -rays is emitted after a neutron is captured. For the majority of nuclides the average γ -ray multiplicity, or total number of γ -rays needed to reach the ground state, varies between 2 and 6. This number and the possibility to use large detectors, which can be placed close to the object, make it possible to obtain a relatively high detection efficiency for capture events.

An ideal detection system for NRCA applications should have a good time resolution and a low sensitivity to neutrons that are scattered from the sample. Since the main parameter of interest is the time at which the capture event is created, a good γ -ray energy resolution is not important. The system should also be flexible to accommodate relatively large samples with irregular shapes. These conditions exclude the use of total absorption detection systems based on BGO or BaF₂ scintillators. A comparison of the performance of different scintillator types for NRCA applications considering the performance of a liquid C₆D₆ scintillator as a reference is reported in Perelli Cippo et al. (2010). C₆D₆ scintillators are considered as one of the best detection systems for capture measurements of non-fissile

Fig. 12.17 Resonance capture spectrum as function of the TOF of the captured neutron. The spectrum results from measurements at a 12.5 m station of GELINA of a small Scandinavian socketed axis on loan from GIA (Postma et al. 2007)



material in a broad energy region (Schillebeeckx et al. 2012b). Measurements were carried out at a 12.5 m station of GELINA using detectors with C_6D_6 , bismuth germanium oxide (BGO), barium fluoride (BaF_2), yttrium aluminium perovskite (YAP), and yttrium silicon oxide (YSO) scintillators (Perelli Cippo et al. 2010). Results of measurements with a 0.4 mm thick Cu sample, containing Sn as an impurity, revealed that the time resolution of BGO, BaF_2 , YSO and YAP detectors is sufficient for NRCA applications below 5 keV. In the energy region below 500 eV BGO and BaF_2 detectors suffer from the impact of their sensitivity to neutrons largely related to resonances of germanium and barium. For neutron energies below 1 keV the performance of the YAP and YSO crystals is comparable to the one of C_6D_6 . Above 1 keV, they suffer from the presence of resonances in yttrium.

An example of a resonance spectrum as a function of TOF is shown in Fig. 12.17 (Postma et al. 2007). It shows the dead time corrected counts per nanosecond. The plot concerns a small, socketed axe of Scandinavian origin on loan from the Groningen Institute of Archaeology (GIA). The plot covers the TOF-range from 30 to 1000 μs . Marked resonances are suitable for analysing copper, tin, antimony, silver and indium (Postma et al. 2007). Due to the relatively high count rate, most of the elements (including impurities) can be recognized on-line, that is, early during the measurement. This offers the possibility to modify, if necessary, the experimental conditions or to adapt the total measurement time. This figure reveals one of the advantages of NRCA compared to other neutron active interrogation techniques such as prompt γ -ray analysis (PGA). In a TOF-spectrum one can select an optimum TOF-region where the contribution due to minor elements is not disturbed by the presence of the main element(s). In a PGA experiment, the γ -ray spectrum is completely dominated by the response resulting from elements with the largest macroscopic cross section.

12.6.2 Analysis

Characterisation of samples resulting from a resonance shape analysis of experimental capture yields has been reported by Schillebeeckx et al. (2010). The objects were reference samples with a regular shape for which the observed capture yields could be approximated by the analytical expressions of Moxon and Brisland (1991). These expressions cannot be used for large objects and objects with irregular shapes. In addition, procedures to derive from a capture TOF-spectrum the capture yield, which is required for such an analysis, are far more complicated as in the case of NRTA. It requires complex detection systems or techniques to obtain a detection efficiency that is independent of the capture event and dedicated measurements and procedures to correct for the background (Schillebeeckx et al. 2012b).

For practical applications, such as cultural heritage objects with an irregular shape, a more empirical approach relying on the use of calibration samples of known composition is preferred. The experimental observable in such an approach is the net area of a resonance peak. This area corrected for the impact of self-shielding is supposed to be directly proportional with the areal density of the corresponding nuclide. In such an approach, the ratio of masses of the nuclides X and Y, denoted by W_X and W_Y , is derived from the ratio of net areas of resonances μ and λ of nuclide X and Y, respectively:

$$\frac{W_X}{W_Y} = K_{\mu,\lambda} \frac{F_\lambda N_\mu}{F_\mu N_\lambda}, \quad (12.29)$$

with N_μ and N_λ the net peak area of resonances μ and λ . The corrections for self-shielding due to the neutron beam attenuation in the sample are F_μ and F_λ . The calibration factor $K_{\mu,\lambda}$ is determined from measurements with calibration samples of known composition and areal densities using the same experimental set-up and beam conditions. This factor, in which measurement time, neutron intensity and solid angle subtended by the sample and detectors cancel out, accounts for nuclear data, isotopic abundances and experimental conditions such as detection efficiency and the energy dependence of the neutron flux. Applying this approach, which is referred to as the double ratio method, little information about the underlying physics and instrumentation is needed. Supposing that all elements have been analysed, these mass ratios can be converted into mass fractions.

The content of an isolated resonance peak can be determined by simply adding the counts under the peak and by subtracting the contributions of the background and multiple interaction events. In case of overlapping resonances or a strong contribution of multiple interaction events, such a simple approach is not possible, and a fitting procedure is needed. A suitable analytical description of the observed resonance profile is a Voigt function for the resonance peak, together with a parametric representation of the multiple interaction events. A polynomial can be added to account for the smooth background component. The Voigt function can be approximated by the pseudo-Voigt function, which is the sum of a Gaussian

distribution $G(E)$ and a Lorentzian function $L(E)$ with weight factors ξ and $1 - \xi$, respectively. The normalized pseudo-Voigt function $V_p(E)$ becomes:

$$V_p(E) = \xi L(E) + (1 - \xi)G(E). \quad (12.30)$$

The widths of the normalised Lorentzian and Gaussian functions together with the net area of the resonance peak are the adjustable parameters. The total width of the Voigt profile accounts for the combined effect of the resolution of the TOF-spectrometer, the Doppler broadening and the total resonance width Γ . The contribution due to multiple interaction events can be parameterized by one or more Gaussians as shown in Fig. 12.18. This figure compares the experimental and analytical response in the region of the 230 eV resonance of Cu resulting from measurements of the Jutphaas dirk, which is a flat and relatively thin object. The number of counts, N , in a resonance can be determined either from the parameters of the fitted resonance curve or by summing the counts from the measured resonance points and subtracting the calculated background and multiple interaction structure in a suitably chosen region as shown in Fig. 12.18.

The correction for neutron self-shielding in Eq. (12.29) for a resonance μ is an average of the energy dependent self-shielding in Eq. (12.22):

$$F_\mu = \frac{\int \sigma_\gamma F(E) dE}{\int \sigma_\gamma dE} \quad (12.31)$$

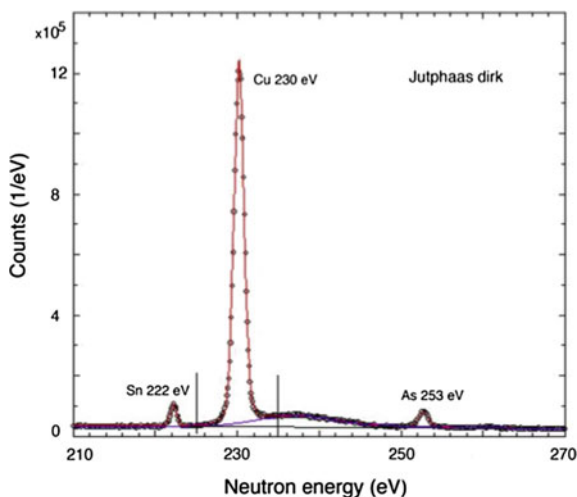


Fig. 12.18 Results of capture measurements of the Jutphaas dirk carried out at a 12.5 m station of GELINA (unpublished data). The observed profile around the 230 eV resonance of copper, i.e. ^{63}Cu , is shown together with the analytical approximation of the structure at the high-energy side of the resonance. The latter is mainly due to single scattering followed by capture. Two weak resonances of Sn and As were fitted together with this Cu resonance

Fig. 12.19 Average self-shielding (Eq. 12.31) as a function of the areal density of Cu for several resonances in Cu

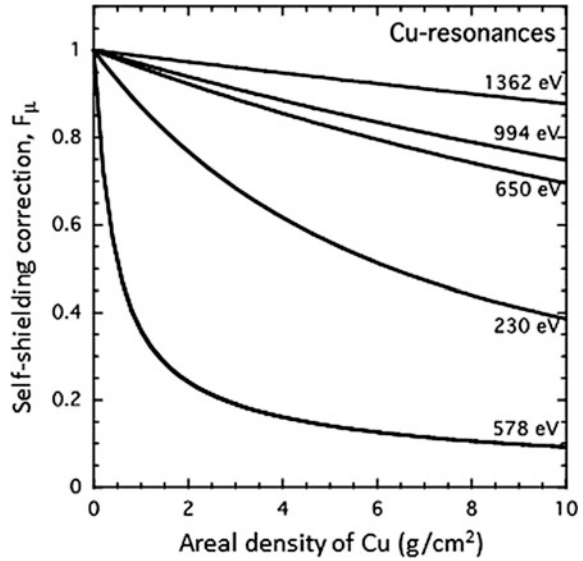
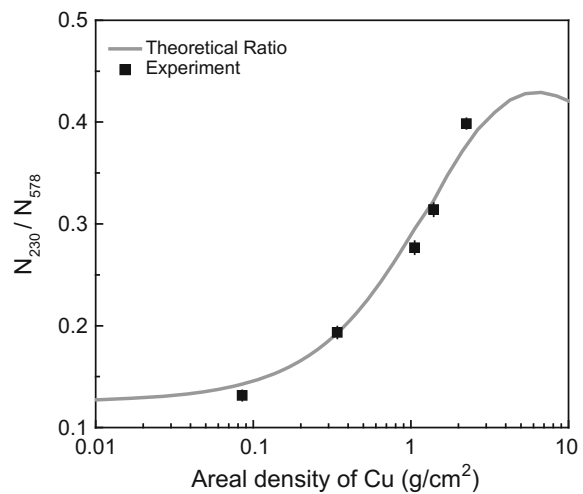


Fig. 12.20 Ratio of the net areas of the 230 and 578 eV resonances as a function of the Cu areal density. The experimental data (*dots*) were obtained from measurements at a 12.5 m station of GELINA. The *full line* is the theoretical ratio after normalization to the experimental data



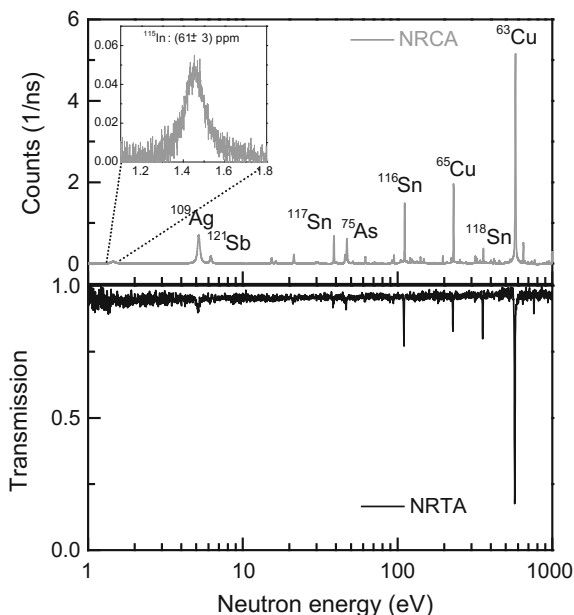
The self-shielding correction for an isolated resonance is mainly due to the resonance part of the total cross section of the resonance. For calibration samples with a regular shape and known composition the correction can be derived from Eqs. (12.22) and (12.31) using total cross sections recommended in evaluated data libraries. Figure 12.19 shows the self-shielding correction as a function of the copper areal density for several Cu resonances. In case of a large areal density of an element it is better to use weak resonances to avoid large self-shielding corrections and problems due to an irregular shape.

For objects with an irregular shape an effective areal density is introduced. The correction for self-shielding as a function of areal density in Fig. 12.19 indicates that the ratio of areas of resonances of the same element, however, with different strengths can be used to derive an effective areal density of Cu. This is shown in Fig. 12.20 where the ratio of the net area of the 230 and 578 eV Cu resonances is plotted as a function of the areal density. The experimental data were derived from measurements with Cu foils of known mass and dimensions. The full line, which is based on Eq. (12.31) and normalized to match the experimental data, can be used to derive an effective areal density of Cu from the observed ratio of resonance areas.

Such an approach is reported in Postma et al. (2003). From the ratio of the resonance area of the 230 and 578 eV resonances derived from the TOF-spectrum obtained with a bronze vessel (*cauldron*) from *Satricum*, an areal density for copper of $0.54 \pm 0.04 \text{ g/cm}^2$ was obtained. This value combined with the 77.8 wt% mass fraction of Cu, which was derived with the double ratio method, results in a total areal density of $0.69 \pm 0.05 \text{ g/cm}^2$. This value is in perfect agreement with the total areal density of 0.68 g/cm^2 derived from a measurement of the mass and area.

The areal density for Cu was confirmed by the areal density $0.55 \pm 0.02 \text{ g/cm}^2$ derived from results of transmission measurements performed at a 10 m station of GELINA on the same object. From these transmission measurements mass ratios $W_{\text{Ag}}/W_{\text{Cu}} = (1.112 \pm 0.010) \times 10^{-3}$ and $W_{\text{Sn}}/W_{\text{Cu}} = 0.243 \pm 0.007$ were derived. These values are in good agreement with those derived from NRCA measurements, which are $(1.14 \pm 0.09) \times 10^{-3}$ and 0.2681 ± 0.0013 , respectively (Postma et al. 2003). The quoted uncertainties are only due to counting statistics.

Fig. 12.21 Capture spectrum as a function of neutron energy resulting from measurements of the *cauldron* sample at a 12.5 m station of GELINA and the experimental transmission through the same object at a 10 m transmission station of GELINA



As already mentioned, the areal density and mass ratios derived from transmission measurements, are obtained in an absolute way without the need of any additional calibration measurements. On the other hand capture spectra have a more favourable detection limit to identify and quantify impurities and trace elements. This is illustrated in Fig. 12.21, which compares the experimental transmission and capture response for the cauldron object. The relative amount of In, 61 ± 3 ppm, was derived from the capture data. Such a quantity is not sufficient to create an observable dip in the transmission. In general, the sensitivity (or detection limit) for transmission is almost an order of magnitude different.

When areas of more than one resonance per element are available for the analysis, several pairs of resonances can be used to estimate the mass ratio. The resulting ratios should be consistent. This is shown in Fig. 12.22, which shows mass ratios obtained for nine combinations of resonances of Sn (38.8, 45.7 and 111.0 eV) and Cu (230, 650 and 994 eV). The resonance areas, derived from capture measurements at the 12.5 m station of GELINA, were used to derive the elemental composition of the “Buggenum” sword (Postma et al. 2010). When self-shielding corrections are neglected, the estimates of the Sn/Cu mass ratio differ significantly. By including a correction for self-shielding, the mass ratios derived from the different pairs of resonance areas agree within the uncertainties due to counting statistics.

The areal density used in the analytical expression for the self-shielding correction was obtained from a least-squares fit to the pairs of corrected resonance areas. This is illustrated in Fig. 12.23, which plots the average mass ratio and variance calculated from the nine mass ratios as a function of the areal density of Cu. The mean and variance are plotted for three values for the areal density of Sn (0.50, 0.55 and 0.60 g/cm²). The variance as a function of areal density reveals a pronounced minimum. The overall minimum occurs at an areal density of Cu and

Fig. 12.22 Mass ratio for tin and copper resulting for nine pairs of resonances. The mass ratio obtained from the ratio of resonance areas without (*black open dots*) and with correction (*red squares*) for self-shielding are given. The data are from measurements of the Buggenum sword at GELINA (Postma et al. 2010)

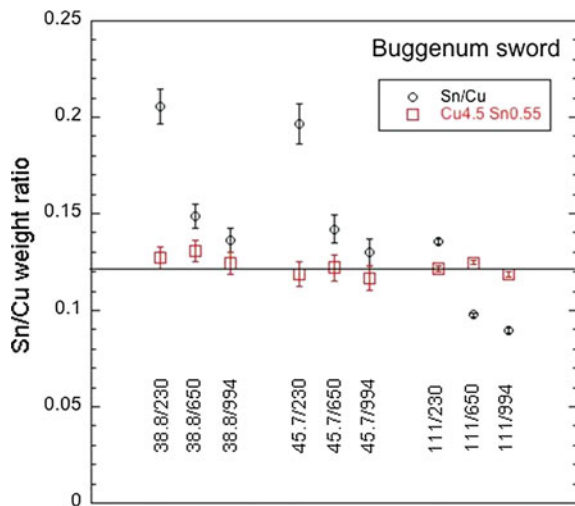
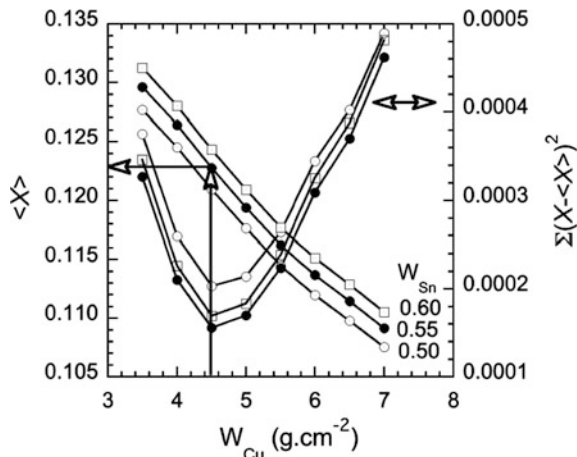


Fig. 12.23 Averaged value $\langle X \rangle$ and variance, resulting from nine estimates of the Sn/Cu mass ratio. The estimates were derived from nine ratios of resonance areas from measurements of the Buggenum sword at GELINA (Postma et al. 2010). The average and variance are given as a function of the Cu areal density for three values of the areal density of Sn. The Sn/Cu mass ratio at the minimum of the variance is taken as the best value



Sn of about 4.5 and 0.55 g/cm², respectively. The resulting average Sn/Cu mass ratio is 0.123. This value is in full agreement with the ratio 0.122 resulting from the areal densities and confirms the consistency of the method. In case of an irregularly shaped sample the resulting areal density represents an effective areal density.

To avoid strong corrections for self-shielding and multiple interaction effects, the use of strong resonances should be avoided. In such cases, it is recommended to use weaker resonances. The presence of resonances with different strengths is a very strong tool of NRCA. Areas of weak resonances can be used to quantify the main elements of an object. The amounts of impurities and trace elements can be quantified from areas of strong resonances. For an object with an irregular shape a multi-pair analysis based on areas of resonances with different strengths provides an effective areal density and related self-shielding corrections.

12.6.3 Facilities

Most of the NRCA applications reported in the literature have been carried out at the GELINA TOF-facility. Three measurement stations at 12.5, 30 and 60 m distance from the neutron target are available for the characterisation of materials by NRCA. Depending on the elements of interest the accelerator is operated at 100, 400 and 800 Hz using a ^{nat}Cd or ¹⁰B overlap filter. The detection systems (i.e. γ -ray detectors, neutron flux detector, electronics and data acquisition system) are similar. Prompt γ -rays are detected by C₆D₆ detectors (12.5 cm in diameter and 7.5 cm

thick). The energy dependent neutron spectrum is measured in parallel with a ^{10}B Frisch-gridded ionization chamber placed at about 80 cm before the sample. At the 12.5 and 30 m station two C_6D_6 detectors are installed. At the 60 m station the sample is surrounded by four detectors.

In the first NRCA experiments at GELINA a system of four Bismuth-Germanate (BGO) detectors (7.5 cm diameter and 7.5 cm thick) was used at the 12.5 m station. Since these detectors are very sensitive to neutrons, each of them had in front an aluminium disk filled with ^6LiF . An additional cylindrical ring containing ^6LiF was inserted in the beam. In later experiments C_6D_6 scintillation detectors, installed for accurate capture cross section measurements, were used. These detectors are much less sensitive to neutrons and do not need shielding against neutrons. In addition, they have very good timing properties.

Figure 12.24 shows a set-up with two C_6D_6 detectors and a bronze sword, known as the Riegseeschwert (invent. no. 16910). The sword belongs to the Museum Joanneum in Graz (Austria) and was on loan to Marianne Mödlingen for experiments at GELINA. The flux monitor mounted at the exit window of the beam tube is also visible. This picture shows the open geometry with little additional structural material that could lead to a background contribution from ambient and in-beam neutrons, which are scattered in the sample and produce a γ -ray background due to neutron capture in the surrounding materials. Due to the open construction, large objects can be accommodated. The collimation at the 12.5 m station is very flexible. In case spatial distribution of sample properties are required, scanning measurements can be performed with a beam diameter of 19 mm at



Fig. 12.24 Capture set-up at a 12.5 m measurement station of GELINA. The set-up consists of two C_6D_6 detectors and a ^{10}B loaded ionisation chamber. The sample is a sword with its hilt located in the centre of the beam

FWHM. To enhance the efficiency more, larger C_6D_6 detectors can be installed. An example of such measurements (Postma et al. 2010) concerns experiments with the Buggenum sword discussed in Sect. 12.7. More details about the 12.5 m station can be found in Borella et al. (2006).

Calibration factors $K_{\mu,\lambda}$ for several combinations of resonances have been determined for the 12.5 and 30 m station of GELINA. Calibration samples were made from melts of known quantities of different elements or by stacking sets of thin foils of the components. Since most of the applications so far focussed on bronze artefacts, the ratios were derived relative to Cu resonances. Elements for which calibration factors have been obtained are Ag, As, Co, In, Fe, Ni, Pb, Sb and Sn. A first analysis is based on measurements at the 12.5 m station. In case elements with relative high-energy resonances, such as Ni and Pb, have to be quantified, measurements at a station with a longer flight path distance are required. Schut et al. (2008) determined the relative amount of lead in copper-alloy artefacts from the area of the 3063 and 3357 eV resonances in Pb from measurements at the 30 m station. The resonance areas were compared with the areas of a cluster of weak copper resonances near 3 keV as is shown in Fig. 12.25. The insert in Fig. 12.25 shows the relation between the ratio of areas of a Pb resonance and a Cu resonance versus the Pb/Cu mass ratio determined from measurements with three calibration samples. In this example there are no serious complications with self-shielding and scattering before capture.

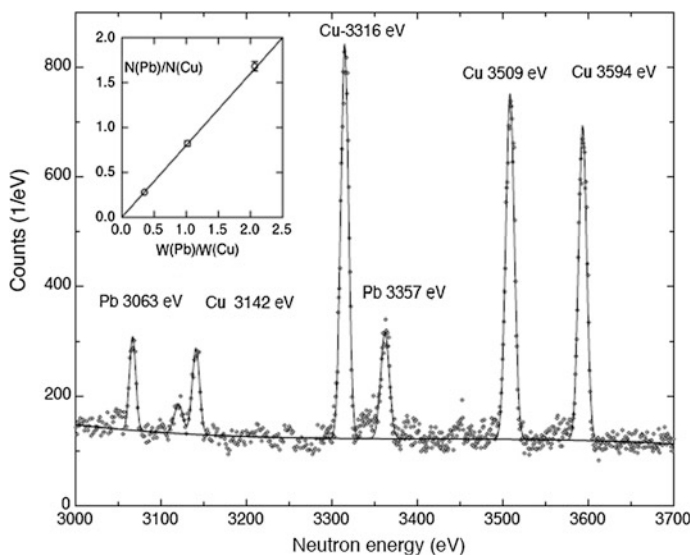
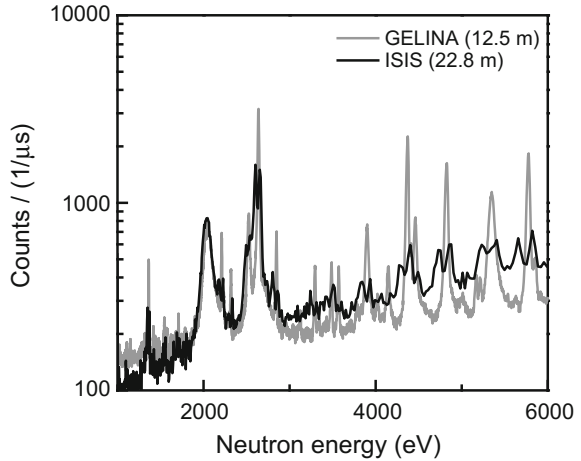


Fig. 12.25 Capture spectrum with two lead resonances (3063 and 3357 eV) and a cluster of copper resonances in the region between 3 and 3.65 keV. The spectrum is obtained from measurements at a 30 m capture station of GELINA (Schut et al. 2008)

Fig. 12.26 TOF-spectra resulting from measurements of the same bronze sample at a 12.5 m station of GELINA and a 22.8 m station of ISIS (Pirelli Cippo et al. 2010)



Due to the low capture cross section of lead, it is not possible to identify and quantify lead by NRCA when it is present as an impurity or trace element. However, often a considerable quantity of lead is added in copper alloys to influence the material properties or to make a cheaper material. In such cases NRCA is a valuable technique to analyse the amount of lead.

An analysis relying on resonance areas requires a good TOF-resolution such that the resonances are well separated. A good resolution is in particular required for an analysis in the keV region as illustrated in Fig. 12.25. Due to the characteristics of the pulsed charged particle beams at J-PARC and at ISIS, it will be very difficult, if not impossible, to determine lead quantities from an area analysis of TOF-spectra determined at these facilities. This is demonstrated in Fig. 12.26, which compares the results of capture measurements of a bronze sample carried out at a 12.5 m station of GELINA and at the 22.8 m INES station of ISIS (Pirelli Cippo et al. 2010). To analysis the spectrum at ISIS a resonance spectrum analysis (RSA) is required. A similar conclusion can be drawn based on results of measurements obtained at the NOBURU station of J-PARC/MLF/(Tremisn et al. 2014).

At present calibration factors were obtained from resonance areas derived from the observed dead time corrected TOF-spectra, without correction for background and without dividing by the neutron flux. More general factors can be derived from an analysis of a quantity Y'_{exp} :

$$Y'_{\text{exp}} = \frac{C - B}{\phi'}, \quad (12.32)$$

where C is the observed TOF-spectrum, B is the TOF-spectrum for measurements without a sample in the beam and ϕ' is the relative energy dependence of the neutron flux. Both the spectra C and B are corrected for count losses due to dead time effects. The energy dependence of the neutron flux can be measured with e.g. a

^{10}B ionisation chamber (Schillebeeckx et al. 2012b). The background B accounts for the time dependent but sample independent background in the capture detection system. This is mostly the dominating background component at the capture stations of GELINA (Schillebeeckx et al. 2014, 2015). Hence, an analysis of the observable Y'_{exp} , which is a first approximation of the capture yield, will be simpler compared to the analysis of a not corrected TOF-spectrum. In addition the resulting calibration constants will only depend on the detection system and do not depend on the neutron flux and presence of filters.

12.7 Advantages, Limitations, Comparison with Other Methods

Important advantages of NRCA and NRTA are that:

- they are non-invasive and determine the bulk composition of artefacts. Hence, they do not require to take or prepare samples as in other methods like neutron activation analysis (NAA), or atomic spectroscopy methods,
- the induced radioactivity is low and mostly well below the limit for free release after a short waiting period, and
- large objects can be tested due to the detection geometry.

For NRA no surface treatment, like polishing of the surface, is required. Hence, the composition of the effective surface, including patina and possibly corrosion, is included. In most cases this concerns only a thin layer compared to the bulk mass of the object and thus this has little influence on the determination of the bulk composition. Methods like X-ray fluorescence (XRF) or proton induced X-ray analysis (PIXE) are limited to the determination of the composition of the surface layer, which may not be representative for the bulk composition. Comparison with results from NRA might be interesting. Surface compositions may be different due to diffusion or reactions of elements at the surface, or by plating the surface with for instance silver. Similarly, NRA and time-of-flight neutron diffraction (TOF-ND) are very complementary. They can be combined to study alloys in terms of both the elemental and phase compositions (Schut et al. 2008; Postma et al. 2010).

A limitation of NRA concerns the number of elements that can be determined. For the majority of elements NRCA has a more favourable detection limit compared to NRTA. The difference is roughly a factor ten. A suitable parameter to study the sensitivity for detection of elements by NRCA is the product of the isotopic abundance and the resonance area $A_{\gamma,\mu}$ divided by the flux (Postma and Schillebeeckx 2005):

$$S_{\mu} = a \frac{A_{\gamma,\mu}}{E_{\mu}^{\alpha}}, \quad (12.33)$$

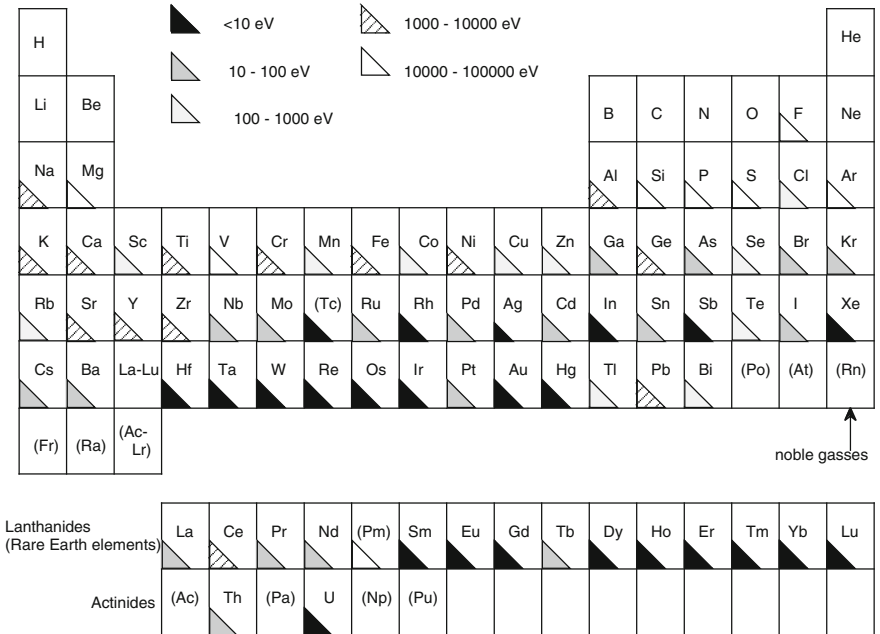


Fig. 12.27 Periodic table in which regions of resonances suitable for NRCA are indicated: *black* for elements with resonances below 10 eV, *grey* for elements with resonances between 10 and 100 eV etc

where the abundance is denoted by a and the energy dependence of the neutron flux is approximated by $1/E^\alpha$. Based on this parameter, together with experience from NRCA applications presented in the next session, one concludes that for elements with resonances between 1 and 10 eV the detection limit is in the range of parts per million (ppm). When the resonances have energies between 10 and 500 eV the lowest detectable mass fraction is between 10^{-3} and 10^{-5} . Detection limits for resonances in the keV region are not better than one per cent. Figure 12.27 indicates for each element the energy region of resonances that are suitable for NRCA. This schematic representation together with the corresponding detection limits reveals that NRCA is not very suitable to detect small quantities of light elements and of elements like lead with neutron and/or proton numbers close to a magic shell. For such elements prompt γ -ray analysis (PGA) is a better alternative. In general PGA and NRCA are very complementary (Postma and Schillebeeckx 2005).

12.8 Archaeological and Cultural Heritage Applications

Bronze is the general name for a large number of metal alloys with copper as main component. Most bronze objects contain tin in amounts of a few to about 20 wt%. Lead can be added to tin-bronze to about 30 wt% to make a cheaper material. Copper with zinc added is known as brass. Ancient bronzes may contain a large number of impurities, like arsenic, antimony, cobalt and nickel, sometimes in considerable amounts. Bronze artefacts are interesting objects to be studied with NRCA. In some cases NRCA is combined with TOF-ND experiments. Such studies are helpful to answer questions concerning archaeology, material culture in past periods or about the cultural heritage. Hereafter, some examples of NRCA studies at GELINA are given.

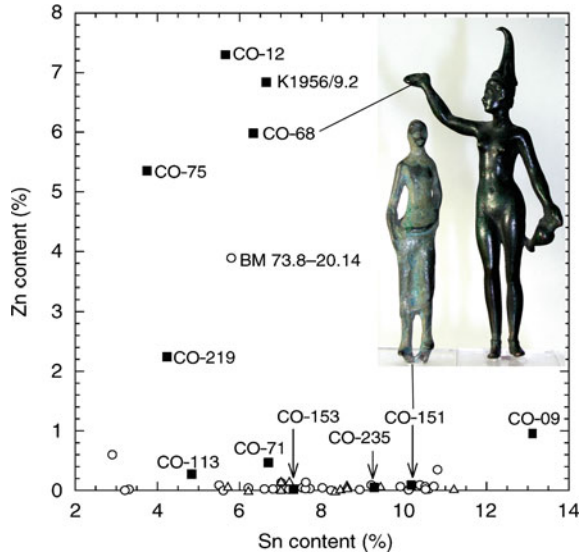
12.8.1 *Etruscan Statuettes*

The first extensive study of bronze artefacts by NRCA was carried out in collaboration with R.B. Halbertsma from the National Museum of Antiquities (NMA) in Leiden (NL). It concerned ten bronze statuettes as part of a collection bought by the Dutch government in 1826 as Etruscan artefacts from count Corazzi of Cortona (Italy). Another Etruscan statuette, an elongated figure obtained by NMA in 1956, and a statuette, offered to NMA by a private person, were included in this study (Postma et al. 2004). There were some questions about the claimed Etruscan origin of these objects. Determination of their compositions can be helpful to settle these questions. The owners of these artefacts preferred the non-invasive method NRCA.

NRCA measurements showed that all of these objects contain about 4–10 wt% of tin except the statuette from the private owner with only 1 wt% of tin. Five of these objects contain between 7 and 24 wt% lead and thus are leaded tin-bronzes. All objects contain small amounts of arsenic, antimony, silver, iron and cobalt. A remarkable observation concerns the amounts of zinc in some of these objects. Five of the objects contain 2–7 wt% of zinc and the object of the private owner has even 26 wt% of zinc. The other objects have only trace amounts of zinc.

Zinc occurs in bronze artefacts from the Etruscan and neighbouring regions only in very small amounts, mostly considerably less than 1 wt%, as is shown in extensive studies by Craddock (1985, 1986). Eight of the 333 objects in his study contain considerable amounts of zinc. However, these objects were later considered to be fakes, imitations or repairs from later periods. Also mirrors of Etruscan origin are made from copper with at most very small amounts of zinc. Figure 12.28 shows the relative zinc content of the NMA artefacts plotted against the relative tin content. The black squares concern the ten artefacts from the NMA. The open circles and triangles concern Etruscan statuettes from the 4th to 2nd century BC, respectively from the 7th to 6th century BC (Craddock 1985, 1986), all of them with small amounts of zinc, except the one marked as BM 73.8-20.14. In a private discussion with Dr. J. Swadding from the British Museum this statuette was rejected as Etruscan (Postma et al. 2004).

Fig. 12.28 The relative zinc content of the statuettes (*black squares*) on loan from the NMA in Leiden is plotted as function of the relative tin content. The *open circles* concern Etruscan objects from a study by Craddock, all having at most very small amounts of zinc except one (BM 73.8-20.14), which was later rejected as an Etruscan object. The *insert* shows two statuettes of female priests, a genuine and an imitation (Postma et al. 2004)



The technique of alloying copper and zinc, known as the cementation process¹, was mastered by the Romans in the first century BC (Craddock 1977). Before that time it was not known in the Italian region. Hence, this method of making brass was learned well after the bronze production by the Etruscans, which ceased after the Romans had completely conquered, destroyed and colonized the cities and land of the Etruscans in the second century BC. Consequently the five objects (NMA catalogue numbers CO12, CO68, CO75, CO219 and K1956/9.2) shown in Fig. 12.28 with zinc well above 1 wt% cannot be of Etruscan origin. They must have been made in later times as reproductions, imitations or fakes, possibly during the Renaissance. The object CO-09 with 1 wt% is dubious. The insert of Fig. 12.28 shows two female priests. The artefact at right (CO-68) has about 6 wt% zinc and must have been made in later times. The other one (CO-151) at left has only 0.1 wt% zinc and is a genuine Etruscan statuette. The object, offered to NMA by a private person, with about 26 wt% zinc cannot be Etruscan and is likely made in Roman or later times.

¹To make copper alloys with large amounts of zinc (brass) requires special techniques. The problem is that zinc with a boiling temperature of 907 °C evaporates and disappears from the furnace before copper melts. In the cementation method copper fragments mixed with zinc oxide (or carbonate) and charcoal are heated in a closed crucible to a high temperature, but such that copper does not melt. In this process zinc oxide is reduced, it is vaporized and thereafter slowly absorbed by the solid copper in the closed crucible. The largest amount of zinc in copper in this process that could be obtained in the process by the Romans and during most of the Middle Ages was about 28 wt%.

Fig. 12.29 Three socketed axes from GIA. The two at the left are Geistingen-type socketed axes. The other axe, added for comparison of the size, is a functional axe



This study showed the value for Museums to determine compositions of objects including minor elements. It may prevent them from accepting fake artefacts or imitations without carrying out material studies.

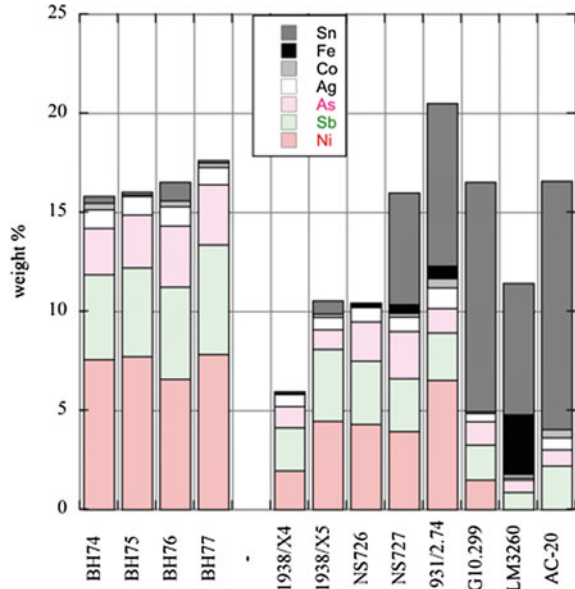
12.8.2 Enigmatic Socketed Axes of the Geistingen Type

In 1935 a hoard of 26 (or 28) socketed axes was discovered in the Belgian village Geistingen on the board of the river Meuse (Butler and Steegstra 2001/2002). These axes were distributed among private persons. Only a small number found their way to museums, four are in the Gallo-Roman Museum (GRM) in Tongeren (BE).

Socketed axes are the latest development of axes in the Bronze Age. Geistingen axes are a remarkable kind of socketed axes as can be learned from the catalogue by Butler and Steegstra (2001/2002). They are long (15–16 cm) and narrow, have thin walls (1–2 mm) and have a rather straight and sharpened cutting edge. Because of their low weight and since they could not have been hafted, they are clearly not functional axes (Fontijn 2003). They may have been votive, ceremonial or valuable exchange objects. Similar axes have been found in nearby locations along the river Meuse and lower Rhine (Butler and Steegstra 2001/2002; Postma et al. 2011). Figure 12.29 shows two Geistingen axes found at the Caberg near Maastricht. They are compared with a more standard and functional socketed axe that is shown at right.

In total twelve axes of the Geistingen type were analysed with NRCA (Postma et al. 2011). Four obtained from the Gallo Roman Museum (GRM) are from the Geistingen hoard, two from the Groningen Institute of Archaeology (GIA) were found at the Caberg, three from NMA were found near Kleve and Nijmegen, two

Fig. 12.30 Bar plot showing the elements alloyed together with copper of some Geistingen type socketed axes

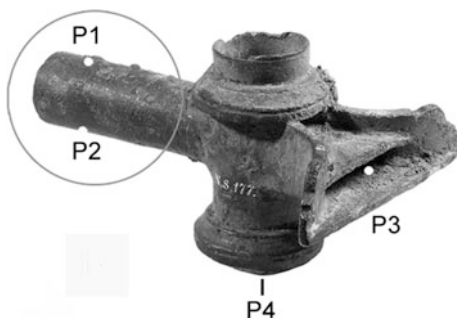


from the Limburg Museum (LM) were discovered in Herten/Roermond and one from the Museum het Valkhof (MhV) was found in Ubbergen. The metal compositions of these Geistingen axes are remarkable. Instead of tin-bronze, they are copper alloys with considerable amounts of other elements as is shown in the bar plot of Fig. 12.30. The four axes from the Geistingen hoard shown on the left side of the bar plot have very similar compositions: nickel (7.4 ± 0.5) wt%, antimony (4.7 ± 0.6) wt%, arsenic (2.8 ± 0.3) wt%, and silver (0.93 ± 0.03) wt%. They have only small amounts of tin and trace amounts of cobalt. The other eight Geistingen axes shown in the bar plot of Fig. 12.30 have much more varying compositions. Considering the four Geistingen axes from GRM as a random selection from the hoard, it can be concluded that the compositions of a large number of axes of the hoard must have been very similar and that they are likely from the same melt and thus made by one smith.

It has been argued (Nienhuis et al. 2013; Postma et al. 2011) that the Geistingen axes are made from imported ingots, which were produced by smelting weathered Fahlore ($\text{Cu}_{12}\text{X}_4\text{S}_{13}$ with X being As and Sb) and nickel bearing minerals. The varying amounts of tin are assumed to come from bronze scrap added to the melts.

Remarkably the metal compositions of the Geistingen type axes resemble bronzes made in the Early Bronze Age. An example is the Singen culture from the Early Bronze Age with artefacts that have comparable compositions (Krause 1989). During most of the Bronze Age minerals of copper oxides have been used. There might have been a reappearance of the use of Fahlore minerals at the end of the Bronze Age. Socketed axes were produced at the end of the Late Bronze Age. The Geistingen axes may be even from the early Iron Age (Fontijn 2003).

Fig. 12.31 Photo showing the outside housing of the Nijmegen water tap. Photo T. Penders, RACM, permission P.A.C. Schut. The circle shows the part that has been studied by NRCA. TOF-ND has been applied at the locations P1 to P4



12.8.3 Roman Water Taps from the Netherlands

Four parts of Roman water taps were found in the Netherlands in the Rhine-Meuse region: two inner cylindrical parts of very similar construction and two outside housings. They were studied by NRCA at GELINA and by TOF-ND at ISIS (Schut et al. 2008).

The results obtained with the “Nijmegen” outside housing, shown in Fig. 12.31, are presented as an example. This tap may have been used to regulate the water inflow for a Roman bath. The cylindrical tube of this object was positioned in the neutron beam. The multi-pair resonance method was applied to obtain the tin-to-copper weight ratio. The following resonances were used: for copper the resonances at 230, 650, 994 and 1362 eV and for tin those at 33.8, 45.7 and 111 eV. For the tube of the Nijmegen valve this resulted in a mass ratio $W_{\text{Sn}}/W_{\text{Cu}} = (0.1114 \pm 0.0038)$ and an effective areal density for Cu of 7.2 g/cm^2 . For a cylinder, with diameter D and wall thickness d , the relation between the mean areal density ρ_a and the volume density ρ_v is $\rho_a = \pi d \rho_v (1 - d/D)$. Using this relation and an areal density of 9.8 g/cm^2 derived for the cylindrical pipe and volume density $\rho_v \approx 0.9 \text{ g/cm}^3$ for leaded tin-bronze, the wall thickness becomes $d = 3.9 \pm 0.5 \text{ mm}$. This value is in good agreement with the measured wall thickness, which is between 4.0 and 4.5 mm.

Table 12.5 Elemental mass ratios relative to Cu and mass fractions of the Nijmegen tap

Element/Cu	Mass ratio	Element	Mass fraction $\times 100$
		Cu	73.56 ± 1.72
Sn/Cu	0.1114 ± 0.0038	Sn	8.19 ± 0.32
Sb/Cu	0.00159 ± 0.00005	Sb	0.117 ± 0.005
As/Cu	0.00075 ± 0.00003	As	0.055 ± 0.003
Ag/Cu	0.00072 ± 0.00003	Ag	0.053 ± 0.003
Zn/Cu	0.0120 ± 0.0005	Zn	0.883 ± 0.042
Fe/Cu	0.021 ± 0.006	Fe	1.54 ± 0.44
Pb/Cu	0.212 ± 0.031	Pb	15.6 ± 1.9

In Table 12.5 the mass ratios of the observed elements relative to Cu and the deduced mass fractions for the Nijmegen tap are given. The mass fractions are derived under the assumption that all main constituents were analysed. Evidently, some trace elements might not have been detected, but this will not influence the given fractions considerably. Corrections related to the copper thickness were applied to all elements given in this table except for lead. The Pb/Cu ratio was obtained from a direct comparison of lead and copper resonances in the 3-keV region where self-shielding effects can be neglected (see Fig. 12.25).

TOF-ND measurements were carried out at ISIS at the positions of the Nijmegen tap that are indicated in Fig. 12.31. The main interest of TOF-ND experiments is to obtain information about the microstructure and to get a better understanding about the production and mechanical work carried out on the object. From these measurements also the Sn/Cu and Pb/Cu mass ratios were derived. With TOF-ND it is possible to determine the expansion of the Cu-lattice due to the additional elements into the copper lattice. If it is assumed that the expansion is due to tin as the main additional element, the Sn/Cu mass ratio determined for positions P1 and P2 of the Nijmegen valve is 0.120, to be compared with 0.1114 ± 0.0038 obtained by NRCA. However, the elements As, Sb and Ag given in Table 12.5 also change the lattice. Correcting for these elements the Sn/Cu ratio determined from TOF-ND becomes 0.1115 in good agreement with the NRCA result (Schut et al. 2008). TOF-ND also provides information about the lead content. Averaging over the two positions P1 and P2 gives a Pb/Cu mass ratio of 0.227, in good agreement with 0.212 ± 0.031 obtained with NRCA. The agreement between the NRCA and TOF-ND results validates these methods and underlying models.

To conclude, the four parts of water taps excavated in the Netherlands are made of leaded tin-bronze. The amounts of tin of the two housings, Hoogeloon and Nijmegen, are 8 wt%, while the two inner parts, Wychem-1 and -2, contain less (4–6 wt%). The amount of lead ranges from 15 to 23 wt%. Hence, the Romans may have used leaded tin-bronze for technical applications like water systems.

12.8.4 *Buggenum Sword*

This sword, from the National Museum of Antiquities (NMA) in Leiden (NL), is well preserved and richly decorated at the hilt and pommel. It is considered to be from the Upper-Danube and its tributaries and dated to the Halstatt A1 period of the



Fig. 12.32 Picture of the Buggenum sword with 13 measurement locations with a beam of 19 mm diameter FWHM. Two series of runs, A and B, at respectively 8 and 4 positions and a run, C, at a fixed position were carried out. The sword is 68 cm long

Bronze Age or slightly later, early in the Late Bronze Age (Fontijn 2003). There is interest in knowing details about its construction, and therefore it was decided to carry out neutron-based measurements such as NRCA and TOF-ND in the frame of the ANCIENT-CHARM collaboration (Gorini et al. 2007), which do not require sample taking. Among other aspects it was questioned whether this sword was made out of one piece of metal. The determination of the metal composition by NRCA at various locations of the sword could answer this question.

NRCA measurements were carried out with a neutron beam that was collimated down to a diameter of 19 mm at FWHM (Postma et al. 2010). The sword was moved with a dedicated sample changer such that different locations of the sword could be studied. This was done in two series of measurements, A and B, (see Fig. 12.32). These measurements were subdivided into short runs at consecutive positions of the sword in both directions in order to average out small variations in beam intensity during the data taking. A long run was carried out at position C where the hilt is connected to the blade.

The resulting tin mass fraction of the blade derived from the data taken at the eight positions of series A and two positions of series B is 11.06 ± 0.14 wt%, with a small change (at most 2 %) between the tip and end of the blade. The tin mass fraction of the hilt is 13.05 ± 0.15 wt%. This shows that the sword is made of two pieces of slightly different tin-bronze. In addition Co, Zn, As, Ag, In and Sb were detected in small amounts (Postma et al. 2010).

References

- Becker B, Bastian C, Emiliani F, Gunsing F, Heyse J, Kauwenberghs K, Kopecky S, Lampoudis C, Massimi C, Otuk N, Schillebeeckx P, Sirakov I (2012) Data reduction and uncertainty propagation of time-of-flight spectra with AGS. *J Instrum* 7:P11002–P11021
- Becker B, Harada H, Kauwenberghs K, Kitatani F, Koizumi M, Kopecky S, Moens A, Schillebeeckx P, Sibbens G, Tsuchiya H (2013a) Particle size inhomogeneity effect on neutron resonance densitometry. *ESARDA Bulletin* 50:2–8
- Becker B, Kauwenberghs K, Kopecky S, Harada H, Moxon M, Schillebeeckx P (2013b) Implementation of an analytical model accounting for sample inhomogeneities in REFIT. *JRC Scientific and Policy Reports*, JRC 86936, ISBN 978-92-79-35095-5
- Becker B, Kopecky S, Harada H, Schillebeeckx P (2014) Measurement of the direct particle transport through stochastic media using neutron resonance transmission analysis. *Eur Phys J Plus* 129:58–59
- Becker B, Kopecky S, Schillebeeckx P (2015) On the methodology to calculate the covariance of estimated resonance parameters. *Nucl Data Sheets* 123:171–177
- Bethe HA, Placzek G (1937) Resonance effects in nuclear processes. *Phys Rev* 51:450–484
- Böckhoff KH, Carlson AD, Wasson OA, Harvey JA, Larson DC (1990) Electron linear accelerators for fast neutron data measurements in support of fusion energy applications. *Nucl Sci Eng* 192–207
- Borella A, Volev K, Brusegan A, Schillebeeckx P, Corvi F, Koyumdjieva N, Janeva N, Lukyanov AA (2006) Determination of the Th-232(n, gamma) cross section from 4 to 140 keV at GELINA. *Nucl Sci Eng* 152(1):1–14
- Breit G, Wigner EP (1936) Capture of Slow Neutrons. *Phys Rev* 49:519–531

- Butler JJ, Steegstra H (2002) Bronze age metal and amber in the Netherlands (III:2). Catalogue of the socketed axes, Part B. *Palaeohistoria* 43/44:263–319
- Chiaveri E et al (2014) The CERN n_TOF facility: neutron beams performances for cross section measurements. *Nucl Data Sheets* 119:1–4
- Craddock PT (1977) The composition of the copper alloys used by the Greek, Etruscan and Roman civilizations. *J Archaeol Sci* 5:1–16
- Craddock PT (1985) The metallurgy of Italic and Sardinian bronzes. In: J Swaddling (ed) *Italian iron age artefacts in the British museum*. British Museum, London, pp 143–150
- Craddock PT (1986) The metallurgy and composition of Etruscan bronze. *Studi Etruschi* 52:211–271
- Ene D, Borcea C, Flaska M, Kopecky S, Negret A, Mondelaers W, Plompen AJM (2010) Global characterisation of the GELINA facility for high-resolution neutron time-of-flight measurements by Monte Carlo simulations. *Nucl Instr Meth Phys Res A* 618:54–68
- Fontijn DR (2003) *Sacrificed landscapes, cultural biographies of persons, objects and natural places in the Bronze Age of the southern Netherlands, c. 2300-600 BC*. Ph.D thesis. University of Leiden
- Fröhner FH (2000) Evaluation and analysis of nuclear resonance data, JEFF report 18, Nuclear Energy Agency, (OECD)
- Gorini G, Ancient Charm collaboration (2007) Ancient charm: a research project for neutron-based investigation of cultural-heritage objects. *Il Nuovo Cimento C* 30, 47 – 58
- Groenewold HJ, Groendijk H (1947) Non-thermal neutron cascade. *Physica XIII*:141–152
- Harada M, Watanabe N, Teshigawara M, Kai T, Kato T, Ikeda Y (2007) Neutronics of a poisoned para-hydrogen moderator for a pulsed spallation neutron source. *Nucl Instr Meth Phys Res A* 574:407–419
- Harada H, Kimura A, Kitatani F, Koizumi M, Tsuchiya H, Becker B, Kopecky S, Schillebeeckx P (2014) Generalized analysis method for neutron resonance transmission analysis. *J Nucl Sci Technol*. doi:[10.1080/00223131.2014.982738](https://doi.org/10.1080/00223131.2014.982738)
- Hasemi H, Harada M, Kai T, Shinohara T, Ooi M, Sato H, Kino K, Segawa M, Kamiyama T, Kiyonagi Y (2015) Evaluation of nuclide density by neutron transmission at the NOBORU instrument in J-PARC/MLF. *Nucl Instr Meth Phys Res A* 773:137–149
- Hecker NE, Mook HA, Harvey JA, Hill NW, Moxon M, Golovchenko JA (1994) Absence of anomalous vibrations in $\text{YBa}_2\text{Cu}_3\text{O}_{7-\delta}$. *Phys Rev B* 50:16129–16132
- Ikeda Y (2009) J-PARC status update. *Nucl Instr Meth Phys Res A* 600:1–4
- Ingelbrecht C, Adriaens A, Maier EA (2001) The certification of arsenic, lead, tin and zinc (mass fractions) in five copper alloys—BCR-91. European Commission, Report EUR 19778/1 EN
- Kino K, Furusaka M, Hiraga F, Kamiyama T, Kiyonagi Y, Furutaka K, Goko S, Harada H, Harada M, Kai T, Kimura A, Kin T, Kitatani F, Koizumi M, Maekawa F, Meigo S, Nakamura S, Ooi M, Ohta M, Oshima M, Toh Y, Igashira M, Katabuchi T, Mizumoto M (2011) Measurement of energy spectra and spatial distributions of neutron beams provided by the ANNRI beam line for capture cross-section measurements at the J-PARC/MLF. *Nucl Instr Meth Phys Res A* 626–627:58–66
- Klug J, Altstadt E, Beckert C, Beyer R, Freiesleben D, Galindo V, Grosse E, Junghans AR, Legrady D, Naumann B, Noack K, Rusev G, Schilling KD, Schlenk R, Schneider R, Wagner A, Weiss F-P (2007) Development of a neutron time-of-flight source at the ELBE accelerator. *Nucl Inst Meth Phys Res A* 577:641–653
- Kobayashi K, Lee S, Yamamoto S, Kawano T (2004) Neutron capture cross-section measurement of ^{99}Tc by linac time-of-flight and the resonance analysis. *Nucl Sci Eng* 146:209–220
- Koehler PE (2001) Comparison of white neutron sources for nuclear astrophysics experiments using very small sample. *Nucl Inst Meth Phys Res A* 460:352–361
- Kopecky S, Siegler P, Moens A (2007) Low energy transmission measurements of $^{240,242}\text{Pu}$ at GELINA and their impact on the capture width. In: *Proceedings of International Conference on Nuclear Data for Science and Technology, Nice, France*, pp 623–626
- Krause R (1989) Early tin and copper metallurgy in south-western Germany at the beginning of the Early Bronze Age. In: Hauptmann A, Pernicka E, Wagner GA (eds) *Old world archaeometallurgy*. pp 25–32

- Lamb WE (1939) Capture of neutrons by atoms in a crystal. *Phys Rev* 55:190–197
- Lampoudis C, Kopecky S, Bouland O, Günsing F, Noguere G, Plompen AJM, Sage C, Schillebeeckx P, Wynants R (2013) Neutron transmission and capture cross section measurements for ^{241}Am at the GELINA facility. *Eur Phys J Plus* 128:86–105
- Lane AM, Thomas RG (1958) R-matrix theory of nuclear reactions. *Rev Mod Phys* 30:257–353
- Larson NM (2008) Updated users guide for SAMMY: Multilevel R-matrix fits to neutron data using Bayes' equations, Report ORNL/TM-9179/R8 and ENDF-364/R2. Oak Ridge national laboratory, USA
- Levermore CD, Pomraning GC, Sanzo DL, Wong J (1986) Linear transport theory in a random medium. *J Math Phys* 27:2526–2536
- Lynn JE, Trela WJ, Meggers K (2002) Neutron Doppler broadening studies of tantalum and tungsten metal. *Nucl Instr Meth Phys Res B* 192:318–330
- Maekawa F, Harada M, Oikawa K, Teshigawara M, Kai T, Meigo S, Ooi M, Sakamoto S, Takada H, Futakawa M, Kato T, Ikeda Y, Watanabe N, Kamiyama T, Torii S (2010) First neutron production utilizing J-PARC pulsed spallation neutron source JSNS and neutronic demonstrated. *Nucl Instr Meth Phys Res A* 620:159–165
- Mondelaers W, Schillebeeckx P (2006) GELINA, a neutron time-of-flight facility for high-resolution neutron data measurements. *Notiziario Neutroni e Luce di Sincrotrone* 11(2):19–25
- Mor I, Vartsky D, Feldman G, Dangendorf V, Bar D, Goldberg MB, Tittelmeier K, Broomberger B, Weierganz W, Brandis M (2011) Parameters affecting image quality with Time-Resolved Optical Integrative (TRION) detectors. *Nucl Instr Meth Phys Res A* 640:192–199
- Moxon MC, Brisland JB (1991) GEEL REFIT, a least squares fitting program for resonance analysis of neutron transmission and capture data computer code, AEA-InTec-0630, AEA Technology
- Moxon MC, Endacott DAJ, Haste TJ, Jolly JE, Lynn JE, Sowerby MG (1974) Differential neutron cross-sections of natural hafnium and its isotopes for neutron energies up to 30 eV, AERE—R 7864
- Nienhuis J, Postma H, Creemers G (2013) Four remarkable socketed axes from the Geisingen hoard. In: Creemers G (ed) *Archaeological contributions to materials and immateriality*, vol 4. Gallo-Roman Museum (Tongeren, BE), ATUATUCA, pp 8–21
- Noguere G, Cserpak F, Ingelbrecht C, Plompen AJM, Quétel CR, Schillebeeckx P (2007) Non-destructive analysis of materials by neutron resonance transmission. *Nucl Instr Meth Phys Res A* 575:476–488
- Overberg ME, Moretti BE, Slovacek RE, Block RC (1999) Photoneutron target development for the RPI linear accelerator. *Nucl Instr Meth A* 438:253–264
- Perelli Cippo E, Borella A, Gorini G, Kockelmann W, Pietropaolo A, Postma H, Rhodes NJ, Schillebeeckx P, Schooneveld EM, Tardocchi M, Wynants R (2010) A detector system for neutron resonance capture imaging. *Nucl Instr Meth Phys Res A* 623:693–698
- Perelli Cippo E, Borella A, Gorini G, Kockelmann W, Moxon M, Postma H, Rhodes NJ, Schillebeeckx P, Schooneveld EM, Tardocchi M, Dusz K, Hajnal Z, Biro K, Porcinai S, Andreani C, Festa G (2011) Imaging of cultural heritage objects using neutron resonances. *J Anal At Spectrom* 26:992–999
- Postma H, Schillebeeckx P (2005) Non-destructive analysis of objects using neutron resonance capture. *J Radioanal Nucl Chem* 265(2):297–302
- Postma H, Schillebeeckx P (2009) Neutron resonance capture and transmission analysis, encyclopedia of analytical chemistry. In: Meyers RA (ed) John Wiley & Sons Ltd. (chapter a9070)
- Postma H, Blaauw M, Bode P, Mutti P, Corvi F, Siegler P (2001) Neutron resonance capture analysis of materials. *J Radioanal Nucl Chem* 248:113–120
- Postma H, Blaauw M, Schillebeeckx P, Lobo G, Halbertsma RB, Nijboer AJ (2003) Non-destructive elemental analysis of copper-alloy artefacts with epithermal neutron-resonance capture. *Czech J Phys* 53:A233–A240
- Postma H, Schillebeeckx P, Halbertsma RB (2004) Neutron resonance capture analysis of some genuine and fake Etruscan copper alloy statuettes. *Archaeometry* 46:635–646

- Postma H, Butler JJ, Schillebeeckx P, van Eijk CWE (2007) Neutron resonance capture applied to some prehistoric bronze axes. *Il Nuovo Cimento C* 30:105–112
- Postma H, Amkreutz L, Borella A, Clarijs M, Kamermans H, Kockelmann W, Paradowska A, Schillebeeckx P, Visser D (2010) Non-destructive bulk analysis of the Buggenum sword by neutron resonance capture analysis and neutron diffraction. *J Radioanal Nucl Chem* 283:641–652
- Postma H, Schillebeeckx P, Kockelmann W (2011) The metal compositions of a series of Geistingen-type socketed axes. *J Archaeol Sci* 38:1810–1817
- Priesmeyer HG, Harz U (1975) Isotope content determination in irradiated fuel by neutron transmission analysis. *Atomenergy* 25:109–113
- Salomé JM, Cools R (1981) Neutron producing target at GELINA. *Nucl Instr Meth* 179:13–19
- Schillebeeckx P, Borella A, Drohe JC, Eykens R, Kopecky S, Massimi C, Mihailescu LC, Moens A, Moxon M, Siegler P, Wynants R (2010) Target requirements for neutron induced cross-section measurements in the resonance region. *Nucl Instr Meth Phys Res A* 613:378–385
- Schillebeeckx P, Borella A, Emiliani F, Gorini G, Kockelmann W, Kopecky S, Lampoudis C, Moxon M, Perelli Cippo E, Postma H, Rhodes NJ, Schooneveld EM, Van Beveren C (2012a) Neutron resonance spectroscopy for the characterization of materials and objects. *JINST* 7: C03009
- Schillebeeckx P, Becker B, Danon Y, Guber K, Harada H, Heyse J, Junghans AR, Kopecky S, Massimi C, Moxon MC, Otuka N, Sirakov I, Volev K (2012b) Determination of Resonance Parameters and their Covariances from Neutron Induced Reaction Cross Section Data. *Nucl Data Sheets* 113:3054–3100
- Schillebeeckx P, Abousahl S, Becker B, Borella A, Harada H, Kauwenberghs K, Kitatani F, Koizumi M, Kopecky S, Moens A, Sibbens G, Tsuchiya H (2013) Development of Neutron Resonance Densitometry at the GELINA TOF Facility. *ESARDA Bulletin* 50:9–17
- Schillebeeckx P, Becker B, Harada H, Kopecky S (2014) Neutron resonance Spectroscopy for the characterisation of materials and objects. *JRC Science and Policy Reports*. European Commission, Joint Research Centre, Report EUR 26848-EN
- Schillebeeckx P, Becker B, Harada H, Kopecky S (2015) Neutron resonance spectroscopy for the characterization of materials and objects, Subchap. of Chap. I, Introduction: Recent State of Art in Neutron Resonance Spectroscopy, *Landolt-Börnstein: Numerical Data and Functional Relationships in Science and Technology—New Series, Subvolume I/26A, Subseries: Elementary Particles, Nuclei and Atoms, Supplement to Subvolume B*, Springer, Berlin, Heidelberg, New York
- Schut PAC, Kockelmann W, Postma H, Visser D, Schillebeeckx P, Wynants R (2008) Neutron resonance capture and neutron diffraction analysis of Roman bronze water taps. *J Radioanal Nucl Chem* 278:151–164
- Sirakov I, Becker B, Capote R, Dupont E, Kopecky S, Massimi C, Schillebeeckx P (2013) Results of total cross section measurements for ^{197}Au in the neutron energy region from 4 to 108 keV at GELINA. *Eur Phys J A* 49:144–153
- Sowerby BD, Tickner JR (2007) Recent advances in fast neutron radiography for cargo inspection. *Nucl Instr Meth Phys Res A* 580:799–802
- Tokuda K, Kamiyama T, Kiyanagi Y, Moreh R, Ikeda S (2001) Direct observation of Effective Temperature of Ta Atom in Layer Compound TaS_2 by Neutron Resonance Absorption Spectromoter. *Jpn J Appl Phys* 40:1504–1507
- Tremsin AS, Shinohara T, Kai T, Ooi M, Kamiyama T, Kiyanagi Y, Shiota Y, McPhate JB, Vallerga JV, Siegmund OHW, Feller WB (2014) Neutron resonance transmission spectroscopy with high spatial and energy resolution at the J-PARC pulsed neutron source. *Nucl Instr Meth Phys Res A* 746:47–58
- Tronc D, Salomé JM, Böckhoff K (1985) A new pulse compression system for intense relativistic electron beams. *Nucl Instr Meth* 228:217–227
- Tsuchiya H, Harada H, Koizumi M, Kitatani F, Takamine J, Kureta M, Iimura H, Kimura A, Becker B, Kopecky S, Kauwenberghs K, Mondelaers W, Schillebeeckx P (2014) Impact of systematic effects on results of neutron transmission analysis. *Nucl Instr Meth Phys Res A* 767:364–371

- Wang TF, Meaze AKMMH, Khandaker MU, Rahman MS, Kim GN, Zhu LP, Xia HH, Zhou ZY, Oh YD, Kang H, Cho MH, Ko IS, Namkung W (2008) Measurement of the total neutron cross-section and resonance parameters of molybdenum using pulsed neutrons generated by an electron linac. *Nucl Instr Meth Phys Res. B* 266:561–569
- Weigmann H, Winter J (1968) Neutron radiative capture in Cu, *Zeits. für Physik* 213:411–419
- Yuan VW, Bowman JD, Funk DJ, Morgan GL, Rabic RL, Ragan CE, Quintana JP, Stacy HL (2005) Shock Temperature Measurement Using Neutron Resonance Spectroscopy. *Phys Rev Lett* 94:125504

Chapter 13

Neutron Resonance Imaging

G. Gorini, E. Schooneveld, E. Perelli Cippo and D. Di Martino

Abstract Neutron Imaging using epithermal neutron beams is a technique that is not yet widely exploited. However, it offers an interesting potential allowing for joining the advantages of imaging (i.e. space-resolved information) along with element sensitivity (at least for most medium-weight elements). In the following pages, the development of Neutron Resonance Transmission Imaging (NRTI) is presented. In recent years it has been developed by two separated groups making use of the characteristics of pulsed sources optimized for Time-of-Flight measurements. An application to a cultural heritage object at the ISIS facility is presented as an example in this chapter.

13.1 Neutron Resonance Transmission Imaging

13.1.1 History

Since *Neutron Resonance Capture Analysis* (NRCA) and *Neutron Resonance Transmission Analysis* (NRTA) techniques are well established (see Chap. 12), it seems natural to extend them into imaging, i.e. space-resolved techniques. Such an extension would have a significant interest especially in the Cultural Heritage field of application, due to the possibility not only to identify, but also to localize specific elements (and isotopes) inside an artefact with no need of sampling. This is especially important in the case of archaeological samples or museum objects, where

G. Gorini · D. Di Martino
Dipartimento di Fisica “G. Occhialini”, Università degli Studi di Milano-Bicocca,
Milan, Italy

E. Schooneveld
STFC, Rutherford-Appleton Laboratory, ISIS Facility, Chilton, UK

E. Perelli Cippo (✉)
Istituto di Fisica del Plasma “P. Caldirola”, Consiglio Nazionale delle Ricerche,
Milan, Italy
e-mail: perelli@ifp.cnr.it

non-invasivity is paramount for every analysis technique to be applied. In this respect, neutrons techniques proved to be suitable from the beginning even for large cultural heritage objects. In fact neutrons penetrate through samples with minimal attenuation, a property that makes them an ideal probe for non-destructive testing. Neutron diffraction, for instance, has been widely used as an analysis technique for cultural heritage samples, not to mention neutron radiography and tomography.

Examination of samples through observation of neutron resonances in transmission geometry has been proposed for nuclear fuel analysis applications (Priesmeyer and Harz 1975). Soon thereafter, Schrack et al. (1983) described an apparatus to obtain “images with isotopic and chemical element discrimination”. The limits of the technique at that time resided in the fact that space sensitivity was only possible through mechanical scanning of the sample in the beam and the use of a position-sensitive ^3He proportional counter. The measurements, although promising, resulted to be, in the words of the authors, “quite inefficient”. Despite that, other authors proposed a similar approach for the non-destructive inspection of air luggage or cargo containers (see for instance Chen and Lanza 2002; Sowerby and Tickner 2007; Brandis et al. 2012; Mor et al. 2013).

In recent years, a European Union (EU) project involving an international team had been launched to develop the already established NRTA into an imaging technique (Gorini et al. 2007); the “*Ancient Charm*” project made use of an especially developed *Position Sensitive Neutron Detector* (PSND) optimized for epithermal ($1 \text{ eV} < E_n < 1000 \text{ eV}$) neutrons to test neutron transmission imaging possibilities in a suitable resonances range for applications to Cultural Heritage samples (museum artefacts, archaeological findings etc).

A separated line of research on the subject was started a few years later by a European-American group, with a different approach: starting from a promising position-sensitive detector for thermal ($E_n \sim 25 \text{ meV}$) neutrons, based on the *Micro-channel Plates* (MCP) technology, they are extending its imaging performances to an energy range in which neutron resonances lie (Tremsin et al. 2012).

While dedicated beamlines for imaging in the thermal range are already available in different facilities worldwide, some beamlines (typically diffractometers or spectrometers) are being tested for the application of imaging in the epithermal range, in which a suitable flux of epithermal neutrons is available.

13.1.2 Theory

Neutron scattering and neutron absorption processes can occur when neutrons interact with matter (Lovesey 1987; Furrer et al. 2009). The probability that neutrons interact with nuclei as a function of neutron energy may show sharp peaks. These peaks known as *resonances*, appear at energies specific for each nuclide (Mughabghab 2006). They can be used to identify elements of the object traversed by a neutron beam (see Chap. 12 for more details about the theory for neutron resonances).

The neutron energy can be easily determined by measuring the time it needs to travel a known distance. With a pulsed neutron source the *time-of-flight* (TOF) can be determined from the *start* pulse of the source and a *stop* signal generated by detection. For relatively low neutron energies, the neutron energy E is given by the expression:

$$E = \frac{1}{2}m \frac{L^2}{t^2} \quad (13.1)$$

where m is the mass of the neutron, t is the TOF and L is the path length.

In a transmission measurement we record the fraction of the neutron beam crossing the sample without any interaction. This fraction (or transmission T), for homogeneous samples and a parallel neutron beam perpendicular to the sample, is given by:

$$T = e^{-\sum_k \bar{\sigma}_{tot,k} n_k} \quad (13.2)$$

where $\bar{\sigma}_{tot,k}$ is the (Doppler-broadened) total cross section and n_k is the number of atoms per unit area referred to the nuclide k . Hence, the transmission T is directly related to the total cross section and the area density of the elements within the sample. Therefore, the attenuation measurement of the incident neutron beam crossing the sample can be used for elemental analysis (see Chap. 12).

Experimentally, the transmission T_{exp} can be derived from the calculation:

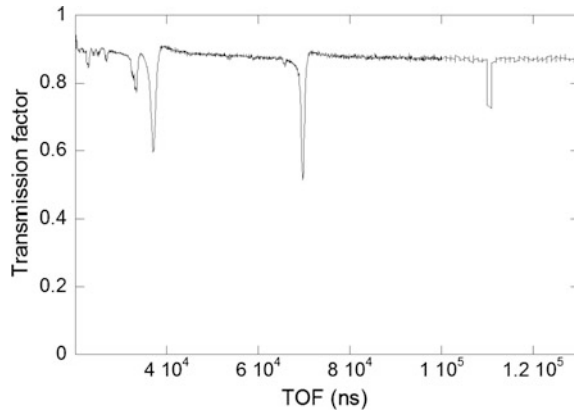
$$T_{exp} = \frac{C_{in} - B_{in}}{C_{out} - B_{out}} \quad (13.3)$$

where C_{in} are the counts of a sample-in measurement and C_{out} for a sample-out measurement, and B_{in} and B_{out} are the corresponding background contributions, respectively. It is assumed that all the spectra are properly normalized to the neutron beam intensity and have the same time structure. From this calculation we derive that the experimental transmission is independent of both the detector efficiency and incoming neutron flux.

NRTA exploits the fact that, when represented as a function of TOF, the transmission shows the presence of dips due to the resonant removal of neutrons by selected nuclides into the sample (see Fig. 13.1). Such dips uniquely identify the resonant nuclei. Moreover, with good approximation, the cross section in proximity of a resonance is dominated by the resonance itself, and the removal effect by off-resonance scattering or absorption is usually negligible in such a time interval.

Obtaining the experimental transmission requires special procedures to correct for dead time effects and the background contributions. Details on the data reduction procedures required to derive T_{exp} from the observed TOF-spectra are described in detail elsewhere in this book and also in the available literature (see for instance Syme 1982; Kopecky et al. 2009; Schillebeeckx et al. 2012).

Fig. 13.1 An example of the transmission factor recorded from a 2 mm thick copper sample at the ISIS neutron source with the PSND described later in this chapter



When the measurements are performed in an ideal transmission geometry and the background and dead time corrections are properly applied, the elemental composition can be deduced from a least squares adjustment to the experimental transmission (Schillebeeckx et al. 2014). This can be done by a *resonance shape analysis* (RSA) code, such as REFIT (Moxon 1989). This code, which has been developed to parameterize cross-section data in terms of resonance parameters, is based on the Reich-Moore approximation of the R-Matrix formalism (Reich and Moore 1958).

A resonance shape analysis provides an optimal interpretation of the results of a transmission measurement. However, a proper resonance shape analysis requires dedicated data reduction procedures.

In the case of space-resolved transmission measurements a large number of spectra needs to be analysed to obtain *imaging* information. As each *pseudoradiograph* (i.e. space-resolved transmission measurement) is composed of hundreds of spectra (each containing a very large number of resonance dips to be fitted) the whole procedure of data reduction and analysis becomes very time consuming.

Another approach can be used, based on the assumption that the area of a transmission resonance dip is in first approximation proportional to the concentration of the absorbing nuclide. This hypothesis (Perelli Cippo et al. 2011) is valid when the product $\bar{\sigma}_{tot,k} n_k$ is small. For thick samples this means that only weak resonances can be used for the analysis.

In this approximation, single spectra may be analysed just by fitting the relevant dips to obtain the area of the resonance and thus estimating the concentration of the relevant element or isotope. The latter requires a series of calibrations obtained with well-known, thin reference samples. Such an approach is described elsewhere (Perelli Cippo et al. 2011; Festa et al. 2015).

While arranging the concentration values for every pixel in a 2D matrix, the result is a map of the relative concentration of a single atomic species along a chord crossed by the neutron beam (i.e. a *projection* of the concentration).

In order to extend this technique to 3D maps of relative elemental abundance inside the sample a *tomography* approach is necessary. In this respect, techniques (and related software) already available for neutron tomography (NT) may be used. A series of NRT shots must be performed while rotating the sample to different angles; the number of rotation N_{rot} should follow, whenever possible, the *Nyquist criterion* (or sampling theorem, see Shannon 1998), i.e. for practical neutron radiography $N_{\text{rot}} = \pi/2 \times N_{\text{pix}}$ where N_{pix} is the number of pixels in a single detector column. A standard tomographic procedure requires the application of a *Filtered Back-Projection* (FBP) algorithm (Kak and Slaney 1988) to the experimental data (for instance the 2D matrix of the elemental distributions obtained by the previous procedures). The FBP, developed for X-ray tomography and implemented for instance in the IMGREC software (Martz et al. 2009), returns the 3D distribution of relative concentrations of the considered atomic specie, that can be visualized either in terms of *slices* or as a full 3D false-colours *object* with standard visualization codes.

The main difference between such a *resonance tomography* and a more standard, neutron tomography in the thermal energy region is that in the first case the attenuation coefficient is valid for a specific energy range and that it can be positively ascribed to a specific element or isotope. As a consequence, the resulting image or map is element-selective.

13.1.3 Instrumentation

In principle, there are two ways to produce space-resolved neutron transmission spectra, and namely:

- (a) the use of a position sensitive detector coupled with a wide beam
- (b) the use of a well collimated beam and scanning the sample through it.

The “ideal” geometry of the experiment would require a perfectly rectilinear (with the meaning of not-divergent) beam before and after the sample. It is clear that this condition is far from being reached due to (1) the natural divergence of the neutron beam, and (2) the divergence induced in the transmitted beam by scattering inside the sample. Case (b) minimizes the natural divergence of the beam, and the spatial resolution is dominated by the beam collimation itself. With this option, a good-transmission geometry can be reached, and the results can be easily analysed using well-established methods. In this case, the transmission detector is better positioned far from the sample, to lower the detection of scattered neutrons. This option is the one used for instance in NRTA applications and the reader is referred to the relevant chapter in this book for details (Chap. 12). However, this option is time-consuming when space-resolved information of samples is required.

Case (a) is the set-up of choice for present *neutron radiography/tomography* beamlines in the thermal energy region. In this case, wide area beams are used and

the sample has to be put very close to the (position sensitive) detector, in order to minimize the effect of scattering or beam divergence. In this option, resolution is driven by the characteristics of the detector and the scattering in the sample itself.

In the case of imaging with neutrons in the epithermal range, we have to consider that a “typical” design of instrumentation does not exist, although most of the known applications were performed in the “option a” geometry.¹ In fact, the technique was implemented in very limited way, and the detectors used were substantially different one from the other. While in fact many PSNDs exist for applications in the thermal range (and typically neutron radiography/tomography), they cannot usually be used for epithermal neutrons with advantage. The fundamental difference is in fact the requirement for the NRTI detector to measure a broader neutron energy range than thermal, namely from 1 eV up to a few keV. A first example of a detector conceived from the beginning as specialized for NRTI was the one developed by Schooneveld et al. (2009) within the EU project *Ancient Charm* (Gorini et al. 2007). The detector was designed based on the experience of a previous 100-pixels transmission detector optimised for cold neutron *Bragg Edge* transmission on the ENGIN-X diffractometer (Steuwer et al. 2005) at the ISIS neutron source of the *Rutherford-Appleton Laboratory* (UK). The development of the detector went through the construction of a smaller-size prototype. The latter consisted of 100 Li-glass pixels (16 pixels in the prototype) arranged in a 10×10 array (4×4 in the prototype) with a 625 mm^2 active area (see Fig. 13.1); the pitch between adjacent pixels was 2.5 mm. Each pixel ($1.8 \times 1.8 \times 9 \text{ mm}^3$) was made of *GS20* scintillator glass, credited of a 6.6 % total lithium content, of which 95 % ^6Li . Each pixel was embedded in a $25 \times 25 \text{ mm}$ support made of boron nitride plates, and separated by Al foils from neighbouring pixels (Fig. 13.1, right panel). The individual pixels were coupled via a 0.5 mm thick glass disperser (for better optical coupling) to a bundle of four 1 mm diameter acrylic optical fibres, feeding the light signals to a series of seven 16-channel photomultiplier tubes (PMT) (also providing spare channels). This geometry was chosen in order to prevent the PMT from sitting in the direct neutron beam; much care was also taken in gathering and folding the optical fibres in bundles to be positioned outside the neutron beam pipe, to minimize possible distortion effects from scattering of neutrons on the plastic. The whole detector was inserted into an Al-made structure (Fig. 13.2, left panel) and support conceived to be transportable, in order to be used into different beamlines at ISIS.

The design of the detector, with respect to both the geometry and materials, had been optimized with simulations of the neutron transport performed with the GEANT4 code (Perelli Cippo et al. 2008).

The detector is based on neutrons interacting with ^6Li in Li-glass via the reaction:

¹A noteworthy exception is indeed the system used by Schrack et al. with the use of a 1-D position-sensitive He^3 detector coupled with a slit collimator parallel to the Helium tube. With this configuration, space resolution was given by the sensitive detector in one direction and the aperture of the slit in the perpendicular one (Schrack et al. 1983).

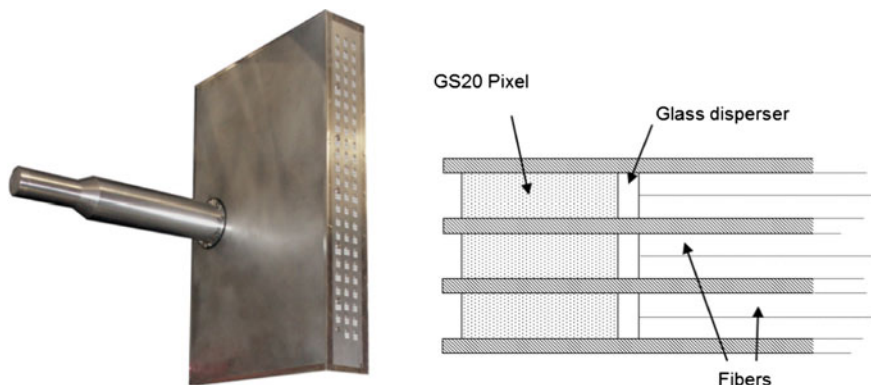
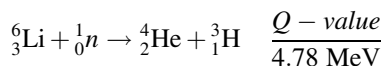


Fig. 13.2 *Left* image of the PSND realized at the ISIS neutron source. *Right* schematic layout of the PSND structure (see text for details)

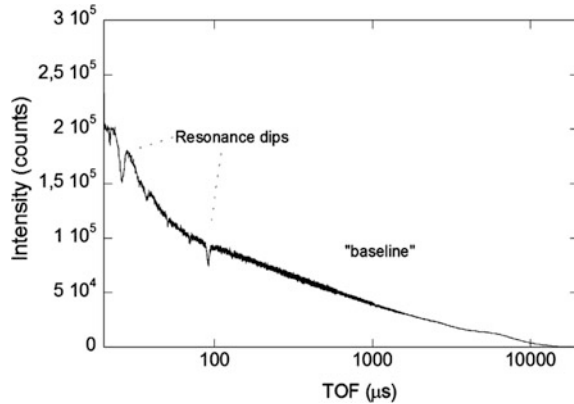


The charged particles deposit their energy in the glass, thus causing scintillation and consequent production of a light signal to be collected by the PMT. The detector contribution to the time resolution is small compared to the pulse width at spallation sources such as ISIS and J-PARC. Simulations conducted with the GEANT4 simulation package have shown that the time resolution due to the neutron transport in the PSND pixels is about 40 ns for 1000 eV neutrons and 250 ns for 10 eV neutrons. Thus only for neutron energies below 10 eV the time resolution of the PSD is comparable with e.g. the 300 ns pulse width at ISIS and significantly contributes to the overall time resolution.

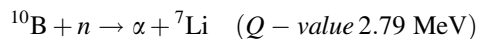
The PSND was used at the INES diffractometer beamline at ISIS. It was connected to the standard ISIS *Data Acquisition Electronics* (DAE) for the registration of TOF spectra. The efficiency of the single pixels (with a lower level discrimination energy of 4 meV) was about 25 % for 10 eV and 4 % for 1000 eV neutrons, respectively. As the INES beamline has a typical neutron flux of $10^6 \text{ n s}^{-1} \text{ cm}^{-2}$, this resulted in an average count rate in the order of 40 kHz per channel on the whole ISIS accelerator duty cycle. However, due to concentration of epithermal neutrons in the very first moments of the neutron pulse, maximum instantaneous count rates of approximately 200–500 kHz per channel were recorded. The dead time resulted to be in the order of 5 %.

Typical TOF spectra were recorded with a variable time binning (*accordion*), with maximum time resolution allowed by the DAE (i.e. $62.5 \text{ ns} = 1/16 \mu\text{s}$) in the region 0–1 ms, where the most important resonances were expected to lie. A typical spectrum recorded by the PSND is shown in Fig. 13.3.

Fig. 13.3 A typical TOF-spectrum recorded at INES by the PSND. The information resides in the dips caused by the resonances of elements; the two strongest are related to copper. Most of the counts form a base-line, i.e. the recorded events from undisturbed flux of transmitted neutrons



A different perspective, though starting from the same physical issue, was used in several works by Tremsin et al. (2012, 2014). They adapted the MCP technology, which was successfully developed for imaging X-ray astronomy and many other photon- or particle-counting applications. MCP detectors (Vallerga et al. 2009) are based on insulator (usually glass) plates with closely packed *channels* of typical diameter in the order of 10 mm, depending on the forming procedure (drawing, etching, or firing in hydrogen). The plate surfaces are layered by a coat of a conductive material (usually nickel-based alloy) to act as input and output electrodes. When a suitable voltage (usually in the range of hundreds of volts) is applied, every channel acts like a *continuous dynode electron multiplier*, as it multiplies electrons through secondary emission from the channel walls. MCPs can be made neutron-sensitive for instance through the addition of ¹⁰B to the glass matrix (Tremsin et al. 2005); the neutrons interact according to the reaction:



The alpha particle or ⁷Li, moving 180° apart to conserve momentum, has a high probability of emerging from the channel wall surfaces into an open channel, thus triggering a secondary electrons cascade, and thus a detectable output pulse. Another approach to make the MCPs neutron-sensitive is by the addition of Gd (Fraser and Pearson 1990).

In order to preserve the spatial resolution allowed by the MCPs (basically the pitch between adjacent channels being 15–20 mm), a reading anode with similar resolution should be used. In the present case, Tremsin et al. made use of a *Timepix* readout device (Llopart et al. 2007). Timepix is an *application specific integrated circuit* (ASIC) based on the CMOS technology, composed of 256 × 256 pixels, each behaving as an amplifier, discriminator and counter.

MCPs based neutron detectors have been used in many applications; limiting to the case of epithermal neutrons, Tremsin et al. (2012) used two different devices: the first one was 14 × 14 mm, with a nominal spatial resolution of 55 μm and time resolution in the sub-nanosecond range. This device was used at the ROTAX

beamline at ISIS to image Au, Gd, In and Ag sample foils, these elements having resonance energies below 100 eV, and returning simple transmission images, though at high spatial resolution (about 150 μm). The TOF technique was exploited at the pulsed neutron source of ISIS. Transmission images were recorded over a limited TOF (and thus energy) range, corresponding to selected resonances. In this way, images were obtained where contrast (i.e. black/white levels) were due to the presence of a selected element (see Figs. 13.4 and 13.5), not just to the amount of

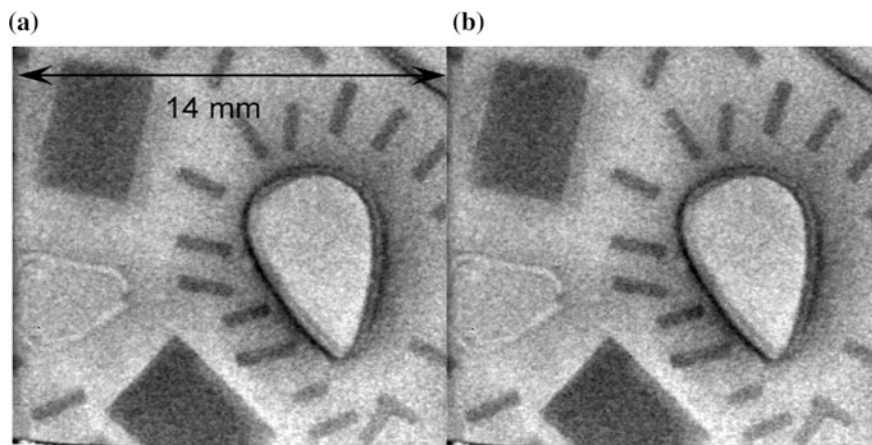


Fig. 13.4 Neutron transmission radiography of a belt mount replica. **a** Full spectrum of the beam containing epithermal, thermal and cold neutrons. **b** Only neutrons in the energy range of 1–100 eV are registered in this image (Tremisn et al. 2012)

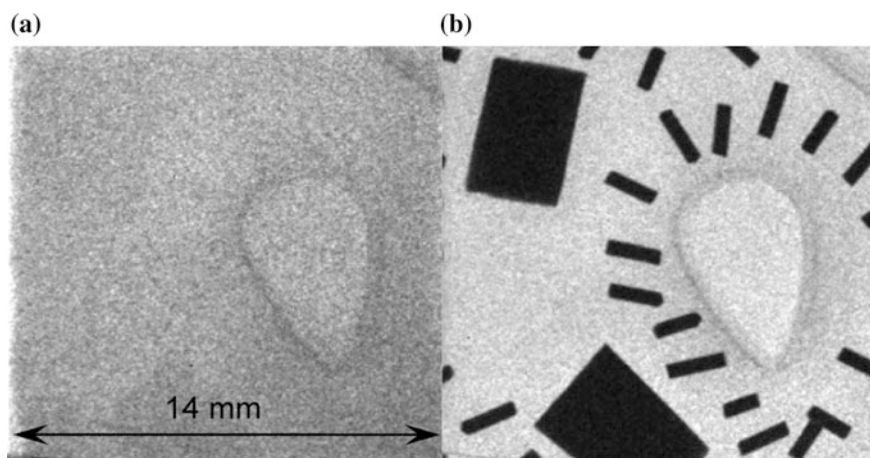


Fig. 13.5 Transmission images of the belt mount taken at the resonance energy of Ag and away from it, same area as in Fig. 13.4. **a** Transmission image obtained with neutrons around 1.63 eV energies. No resonances are present around that energy range. **b** Image obtained at the 5.3 eV silver resonance. Both images are normalized by the open beam and represent the spatial variation of transmission coefficient at the corresponding neutron energy (Tremisn et al. 2012)

matter crossed by the neutron beam (as is usually the case with thermal neutron radiography).

The second device (28 mm diameter) was also used at the NOBORU beamline of J-PARC with samples made of elements also presenting resonances at higher energies (like Cd, Co, Cu and Ta). The estimated efficiency of the detector was estimated in the order of 70 and 50 % for cold and thermal neutrons, respectively, although the authors admit they don't have a precise estimation of the efficiency in the epithermal range (Tremisn et al. 2014). TOF spectra recorded by the detector were compared to calculated spectra in order to assess a quantitative analysis for future studies. In this respect, we have to consider that the dominant effect in time resolution is due not to the detector itself but to the time structure of the neutron pulse, that is about 300 ns for ISIS and about 600 ns for J-PARC.

13.1.4 Facilities

A neutron facility optimized to exploit resonance imaging should have the following proprieties:

- (1) It should provide pulsed neutrons with the shortest possible pulse
- (2) It should provide a reasonable flux of epithermal neutrons at sample position
- (3) The gamma-ray background (typically from the spallation target and moderator) should be as low as possible
- (4) For the sake of imaging, it should have a large beam transversal section
- (5) It should present a very reduced beam divergence

It is evident that requirements 2 and 3 are antithetical. In fact, both the neutron emission from the source and the amount of gamma background varies as the inverse of the square of the source-sample distance. Some thermal neutrons-optimized beamlines (typically diffractometers) with low-angle detectors reduce the gamma background by the use of choppers, whose pulsation is timed with the neutron pulse. Such choppers cut away most of the (instantaneous) *gamma flash* from the spallation target while transmitting the (slower) thermal neutrons. However, this practice is difficult when epithermal (faster) neutrons are necessary; in fact, in most practical situations, epithermal neutrons are fast enough to arrive at the shutter position *along with* the gamma flash that is supposed to be cut.

Requirements 4 and 5 are also somehow antithetical. Some neutron beamlines optimized for NR in the thermal range present transversal beam sections as wide as 200×200 mm with limited divergence. However, detectors for NR are also usually of large dimensions (at least the scintillator converters); to all practical purposes, in the case of NRTI, it is of no use to have a beam wider than the dimension of the transmission detector itself. As an example, in the case of the setup developed at ISIS, the dimensions of the detector were 25×25 mm, and the boron carbide jaws used in the INES beamline for the definition of the beam spot were usually set

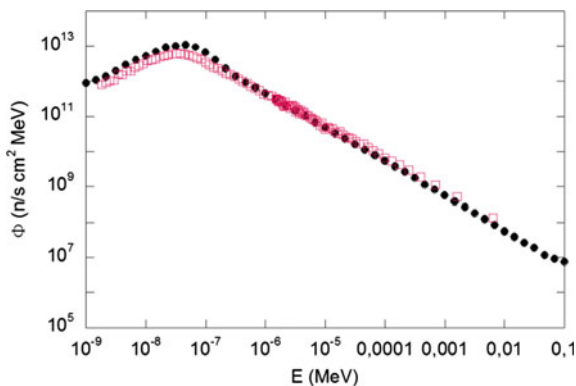
to match such dimensions (the fully open beam at INES is 40×40 mm). In the case of samples larger than these dimensions, a scanning procedure was unavoidable.

The PSND developed at ISIS was used on the INES (Imberti et al. 2008) diffractometer beamline, while the mentioned smaller prototype was also tested at the VESUVIO (Mayers and Reiter 2012) beamline of the same facility and at the GELINA (Mondelaers and Schillebeeckx 2006; Ene et al. 2010) facility of the Joint Research Centre at Geel (B).

INES (an acronym standing for *Italian Neutron Experimental Station*) is a TOF diffractometer optimised for high resolution at low d-spacings. It makes use of thermal neutrons, and thus, as for most beamlines at ISIS, it is subdued to a suitable moderator, in this case made of water at 316 K. The resulting neutron spectrum presents a typical shape made of (1) a Maxwellian peak at about 25 meV (2) a tail of higher-energy neutrons with typical $1/E^{1/2}$ dependence. The resulting flux of neutrons, at the sample position (about 23 m from the neutron source) is in the order of 10^6 n s⁻¹ cm⁻² in the epithermal range. The beam transverse section at sample position is 40×40 mm. INES is positioned on the same line-of-sight of another neutron instrument (and namely the spectrometer TOSCA) and it is equipped with a chopper used to cut away the gamma background (and fast neutrons) from the two instruments; thus, when used for NRTI, the chopper has to be set at fully open position to make use of the epithermal neutrons.

VESUVIO is an *inverted-geometry* neutron TOF spectrometer optimized for epithermal neutrons. Being devoted to the exploitation of neutrons in the eV to hundreds of eV region, it is *undermoderated*, i.e. it is subdued to a room temperature moderator whose thickness (30 mm) is not enough to provide a complete neutron beam thermal equilibrium. This results in a spectrum, which is distinctly not a Maxwell-Boltzmann distribution for energies above 100 meV ($\Phi \approx 1/E$), and an order of magnitude higher flux of epithermal neutrons than well-moderated sources (details on the VESUVIO flux and spectrum can be found in Bedogni et al. 2009). VESUVIO is not equipped with a neutron chopper. The sample position is

Fig. 13.6 The VESUVIO beamline neutron flux. *Black dots* as from MCNPX simulations. *Red squares* experimental data from VESUVIO monitor detector



located 11.055 m away from the source (about one half of the INES flight path), thus resulting in a higher flux (see Fig. 13.6) but also in a lower TOF resolution.

Of the three mentioned facilities, GELINA was especially designed for high resolution neutron-cross-section measurements in the resonance region. The facility is based on a pulsed electron *linac* with a 800 Hz duty cycle and 70 μA average current. Typical pulse length is 10 ns; however, a *pulse compression system* allows for pulse width of about 1 ns at FWHM. The electrons are directed to a U/Mo 90/10 alloy target, where, through Bremsstrahlung and consequent photonuclear reactions, produce neutrons with an average neutron flux of 3.4×10^{13} 1/s. The obtained neutron spectrum is distributed from thermal to about 20 MeV energies; as for VESUVIO and INES, the neutron beams are (under-) moderated in order to obtain a reasonable amount of neutrons in the energy range below, say, 100 keV. The emitted neutrons feed 10 beamlines with a series of experimental stations that are located at different distances from the source (up to about 400 m).

The MCP-based detector was used both at ISIS and at the NOBORU beamline (Maekawa et al. 2009) of the *Japan Proton Accelerator Complex* (J-PARC). The acronym NOBORU stands for *NeutrOn Beamline for Observation & Research Use*; it is a beamline dedicated to testing of neutron devices and detectors. The beamline is credited with a neutron flux in excess of 10^7 n s⁻¹ cm⁻² in the energy region up to 1 MeV, and the beam transverse area is a generous 100×100 mm.

13.1.5 Examples

Several studies in the literature showed two-dimensional elemental mappings from NRT data. Many different materials were tested (not always in the epithermal energy range): from luggage inspection and contraband materials, like drug and explosive simulants (Chen and Lanza 2002; Sowerby and Tickner 2007; Brandis et al. 2012; Mor et al. 2013), to cultural heritage materials (Tremisn et al. 2012; Perelli Cippo et al. 2011).

Actually, only one NRTI application producing 3D contrast figures of some elements was recently published (Festa et al. 2015).

This study was conducted at ISIS, using a dedicated set-up on the INES beamline (see before), and it demonstrates the viability of NRTI technique using an early mediaeval disc fibula, from the Hungarian National Museum in Budapest. The methodology and analysis procedures described in the previous sections were applied. The artefact, is an ancient fibula, see Fig. 13.7, dated to the end of the 6th century AD, and coming from the cemetery site of K lked-Feketekapu, one of the most important in the Carpathian basin, where ancient Germanic population lived. This kind of object was commonly used along the River Rheine (by the Franks) and in southern Germany (by the Alemanni).

Fig. 13.7 Frontal and lateral pictures of the analysed disc fibula from Kölked-Feketekapu (Hungary), dated to the end of 6th century AD. The diameter of the fibula is about 3 cm (Festa et al. 2015)



A set of 16 NRTI radiographs was collected at different angles, using the PSND described before. Since the total lateral dimension of the sample exceeds the active area of the detector, four exposures were recorded for each rotation. The 64 exposures were matched together, and each radiograph contained 256 NRTI spectra (in a 16×16 matrix). Single spectra were analysed by the aid of routines in the OPEN GENIE software, in order to: (i) normalise the spectra and (ii) fitting the relevant dips. As reported before, instead of using REFIT, the areas of the dips were derived in the approximation of a linear background in a limited TOF interval, and a Gaussian function reconstruction. The values of the areas so obtained in this way, were gathered in a two-dimensional 16×16 matrix, the so-called pseudo-radiograph. By choosing a selected number of elements (i.e. Ag, Au, Cu, Fe), a series of pseudo-radiographs was obtained (see Fig. 13.8 for examples).

To derive 3D contrast figures of some elements present in the fibula, an FBP algorithm was applied, returning 3D matrices, then transformed into 8-bit data, a readable format for commercial visualization programs. Each matrix was element selective, since it represents an attenuation pseudo-coefficient due to the presence of a specific resonance. The 3D-visualization is depicted in Fig. 13.9.

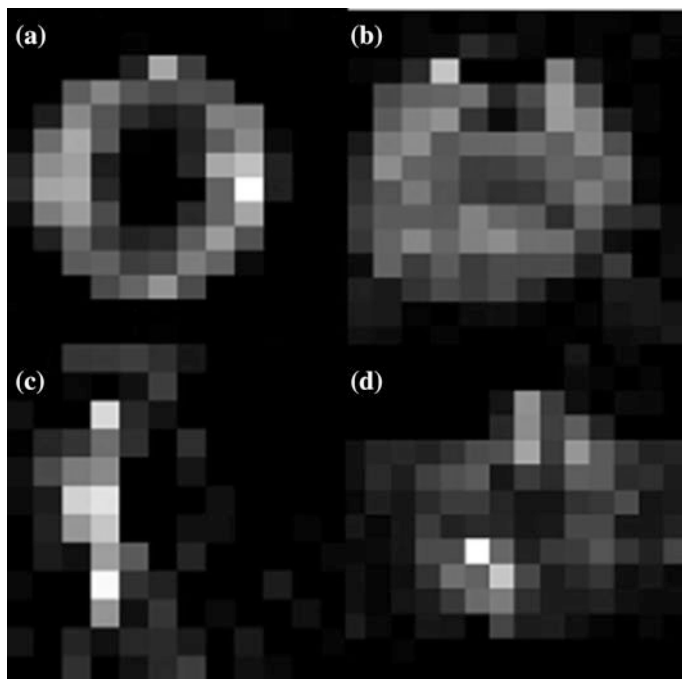


Fig. 13.8 Slice of copper (a), gold (b), silver (c), iron (d) and data sets obtained from the reconstruction process (Festa et al. 2015)

13.1.6 Areas of Application

Among other non-destructive neutron-based imaging techniques, NRTI is a potential technique to study the bulk elemental composition within a sample. As for most neutron-based techniques, no specimen preparation is needed and an entire object (without sampling) can be investigated returning the bulk element concentrations. These advantages make NRTI especially useful whenever non-destructive inspections are needed, like for cultural heritage objects or advanced materials (prototypes and unique samples).

Concerning spatial resolution, other neutron-based imaging techniques have a higher resolution. As a general rule, the overall spatial resolution is strictly related to the detector resolution. However, an intrinsic limit is given by the mean free path of an epithermal neutron in an absorbing material, which can be in the order of a few mm for the upper end of the energy range considered (in the order of 1 keV). In practice, NRTI, from the literature data, was developed at high (150 μm ; Tremsin et al. 2012) and low resolution (2.5 mm; Festa et al. 2015, but also Tomita et al. 2012). The study based on the higher resolution detector has the drawback of the limited element quantification (only 2D and not 3D output was shown).

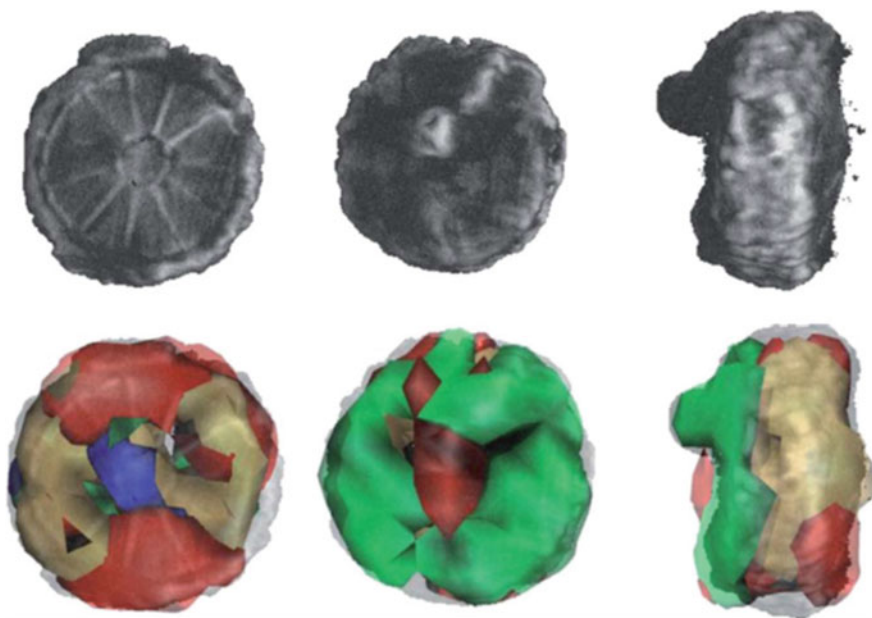


Fig. 13.9 *Top part* Neutron tomography (previous result, Schulze et al. 2013). *Bottom part* 3D visualization of the elements in the fibula (isosurfacescolor map: Cu = green, Fe = red, Au = yellow, Ag = blue; Festa et al. 2015)

On the other side, neutron tomography can reach for example 15 μm resolution, but has no elemental sensitivity.

Prompt Gamma Activation Imaging (PGAI) and NRTI have been applied to the same specimen namely a disk-fibula from Kőlked-Feketekapu (Hungary), making it possible to compare features of both methods (Perelli Cippo et al. 2011; Schulze et al. 2013).

Comparing the two techniques, we could observe that:

- Currently (Schulze et al. 2013) PGAI has a spatial resolution of about 2.5 mm. For NRTI, as we already described, the spatial resolution can be improved by improving the resolution of the detector, whereas, for PGAI, the spatial resolution can only be improved by reducing the size of the neutron beam (hardly to obtain).
- NRTI requires lower acquisition times with respect to PGAI. Indeed, PGAI measurements performed on the ancient *fibula* (Schulze et al. 2013), required a 10 days period of neutron irradiation for the analysis of a quadrant of the artefact, while one day of measurements was sufficient for NRTI of the whole object (Festa et al. 2015). Almost an order of magnitude in time requirements could be very important for a twofold reason: (a) costs of neutron measurements require to reduce beam time as much as possible, and (b) cultural heritage

objects could be forbidden for too long irradiation times at least in the case when for museum objects lending time and insurance costs are considered.

- NRTI can map a lower number of elements than PGAI,

A limitation is that elements must have resonances in the epithermal region. This is true for many elements, but not for the lightest elements and for some heavy nuclei with magic proton and neutron numbers.

Currently only fairly small objects can be studied mainly because of the detector active area, but also due to the sample holder and beamline instrumentation. Samples larger than the active detector area may still be measured, just merging several radiographs, though requiring longer irradiation times. Beam sizes are fixed, though at the moment future beamlines are being designed for hosting very large samples (as for instance the future IMAT beamline at ISIS).

References

- Bedogni R et al (2009) Characterization of the neutron field at the ISIS-VESUVIO facility by means of a bonner sphere spectrometer. *Nucl Instr Meth A* 612:143
- Brandis M et al (2012) Neutron measurements with Time-Resolved Event-Counting Optical Radiation (TRECOR) detector. *J Instrum* 7:C04003
- Chen G, Lanza RC (2002) Fast neutron resonance radiography for elemental imaging: theory and applications. *IEEE Trans Nucl Sci* 49:1919
- Ene D et al (2010) Global characterisation of the GELINA facility for high-resolution neutron time-of-flight measurements by Monte Carlo simulations. *Nucl Instr Meth A* 618:54
- Festa G et al (2015) Nuclear resonance transmission imaging for 3D elemental mapping at the ISIS spallation neutron source. *J Anal At Spectrom* 30:745
- Fraser GW, Pearson JF (1990) The direct detection of thermal-neutrons by imaging microchannel-plate detectors. *Nucl Instr Meth A* 293:569
- Furrer A, Mesot J, Straessle T (2009) Neutron scattering in condensed matter physics. World Scientific, London
- Gorini G et al (2007) Ancient charm: a research project for neutron-based investigation of cultural-heritage objects. *Il Nuovo Cimento C* 47(30). See also <http://ancient-charm.neutron-eu.net>
- Imberti S, Kockelmann W, Celli M et al (2008) Neutron diffractometer INES for quantitative phase analysis of archaeological objects. *Meas Sci Technol* 19:034003
- Kak AC, Slaney M (1988) Principles of computerized tomographic imaging. IEEE Press, Piscataway, USA
- Kopecky S et al (2009) The total cross section and resonance parameters for the 0.178 eV resonance of Cd-113. *Nucl Instrum Meth B* 267:2345
- Llopart X, Ballabriga R, Campbell M, Tlustos L, Wong W (2007) Timepix, a 65k programmable pixel readout chip for arrival time, energy and/or photon counting measurements. *Nucl Instrum Meth A* 581:485 details of the Timepix device can be found in webpage: <http://medipix.web.cern.ch/medipix/pages/medipix2/timepix.php>
- Lovesey SW (1987) Theory of neutron scattering from condensed matter. Clarendon Press, Oxford
- Maekawa F et al (2009) NOBORU: J-PARC BL10 for facility diagnostics and its possible extension to innovative instruments. *Nucl Instr Meth A* 600:335
- Martz HE et al (2009) X-ray Imaging. CRC Press Inc, Bosa Roca
- Mayers J, Reiter G (2012) The VESUVIO electron volt neutron spectrometer. *Meas Sci Technol* 23:045902

- Mondelaers W, Schillebeeckx P (2006) GELINA, a neutron time-of-flight facility for high-resolution neutron data measurements, *Notiziario Neutroni e Luce di Sincrotrone* 11:19
- Mor I et al (2013) Parameters affecting temporal resolution of Time Resolved Integrative Optical Neutron Detector (TRION). *J Instrum* 8:P11012
- Moxon M (1989) REFIT2: a least squares fitting program for resonance analysis in neutron transmission and capture data, NEA—0914/02
- Mughabghab S (2006) Atlas of neutron resonances. Elsevier, Netherlands
- Perelli Cippo E et al (2008) Simulations and design of detectors for imaging with epithermal neutrons, *Meas Sci Technol* 19:034027
- Perelli Cippo E et al (2011) Imaging of cultural heritage objects using neutron resonances. *J Anal At Spectrom* 26:992
- Priesmeyer HG, Harz U (1975) Isotopic content determination in irradiated fuel by neutron transmission analysis. *Atomkernenergie* 25:109
- Reich CW, Moore MS (1958) Multilevel formula for the fission process. *Phys Rev* 111:929
- Schillebeeckx P et al (2012) Determination of Resonance Parameters and their Covariances from Neutron Induced Reaction Cross Section Data. *Nucl Data Sheets* 113:3054
- Schillebeeckx P et al (2014) Neutron resonance Spectroscopy for the characterisation of materials and objects. JRC Science and Policy Reports. European Commission, Joint Research Centre Institute for Reference Materials and Methods, Report EUR 26848-EN
- Schooneveld EM et al (2009) A new position-sensitive transmission detector for epithermal neutron imaging. *J Phys D Appl Phys* 42:152003
- Schrack RH et al (1983) Neutron radiography In Burton JP, van der Hardt P (ed) Springer, Netherlands, pp 495–502
- Schulze R et al (2013) The ANCIENT CHARM project at FRM II: three dimensional elemental mapping by prompt gamma activation imaging and neutron tomography. *J Anal At Spectrom* 28:1508
- Shannon C (1998) Proceedings of the IRE 37:10–21 (1949). Reprinted in Proceedings of the IEEE 86:447
- Sowerby BD, Tickner JR (2007) Recent advances in fast neutron radiography for cargo inspection. *Nucl Instr Meth A* 580:799
- Steuwer A et al (2005) Using pulsed neutron transmission for crystalline phase imaging and analysis. *J Appl Phys* 97:074903–074911
- Syme DB (1982) The black and white filter method for background determination in neutron time-of-flight spectrometry. *Nucl Instrum Meth* 198:357
- Tomita H et al (2012) Development of epithermal neutron camera based on resonance-energy-filtered imaging with GEM. *J Instrum* 7:C05010
- Tremsin AS, Feller WB, Downing RG (2005) Efficiency optimization of microchannel plate (MCP) neutron imaging detectors. 1. Square channels with B-10 doping. *Nucl Instrum Meth A* 539:278
- Tremsin AS et al (2012) High resolution neutron resonance absorption imaging at a pulsed neutron beamline. *IEEE Trans Nucl Sci* 59:3272
- Tremsin AS et al (2014) Neutron resonance transmission spectroscopy with high spatial and energy resolution at the J-PARC pulsed neutron source. *Nucl Instr Meth A* 746:47
- Vallerga J et al (2009) The current and future capabilities of MCP based UV detectors. *Astrophys Space Sci* 320:247

Chapter 14

Prompt Gamma Activation Imaging (PGAI)

Z. Kis, L. Szentmiklósi, R. Schulze and E. Abraham

Abstract The neutron is an ideal probe for elemental composition and structural analysis of samples due to its deep penetration into materials. This feature makes it especially suitable for the non-invasive investigation of bulky samples from geology, material science, crystallography, and archaeometry. PGAI (Prompt Gamma Activation Imaging)—a novel non-destructive, neutron based, two-dimensional, 3-dimensional (2D/3D) elemental imaging method—was invented as an extension of the well-established PGAA (Prompt Gamma Activation Analysis) bulk elemental analysis method, in combination with NR/NT (Neutron Radiography/Tomography). The spatial resolution obtained so far for the elemental imaging part is on the order of 5 mm. Selected experiments will be discussed to highlight the capabilities of this technique, including the analysis of cultural heritage objects. The results obtained can answer questions of historical interest, like the state of craftsmanship during an era, or the authenticity, and/or provenance of the investigated objects, as well as aspects of restoration and conservation procedures.

14.1 The Motivation

Most methods employed to characterize a variety of chemical, physical and (micro) structural properties of objects are invasive (e.g. Inductively Coupled Plasma Mass Spectrometry, Atomic Absorption Spectroscopy) or have limited penetration depth in solid matter (e.g. methods using X-rays and charged particles). However neutrons, as particles without charge, can penetrate deeply into objects and non-destructively provide information about the structure and composition of the

Z. Kis (✉) · L. Szentmiklósi
MTA Centre for Energy Research, Budapest, Hungary
e-mail: kis.zoltan@energia.mta.hu

R. Schulze
University of Cologne, Cologne, Germany

E. Abraham
University of Bordeaux, Bordeaux, France

whole interior. While the potential of neutron-based element and structure analysis techniques is large, their development has begun only recently. Few attempts have been made till now to use neutrons for qualitative or quantitative position-sensitive elemental analysis, e.g. towards developing the PGAI technique. The motivation to develop such a technique is to benefit from its unique features, i.e. it is non-destructive, can be sensitive to chemical elements, even isotopes and structure, can have a spatial resolution in the order of a few mm, and it is possible to investigate bulky objects that are too thick for e.g. X-rays. In this chapter we present the way the PGAI technique evolved, briefly mentioning other neutron-based position-sensitive elemental analysis methods. After giving some examples, the limitations and peculiarities are mentioned as well.

14.2 The Basic Principles of Neutron-Based Position-Sensitive Elemental Analysis

Two- or three-dimensional element imaging data can be obtained in two basic ways. The neutron-based position-sensitive elemental analysis techniques use either the principles of tomography or the direct method. The first approach applies mathematical algorithms to determine the spatial distribution from the measured integral quantities, while the other, the direct method, uses collimated irradiation and detection to define the source of the measured data. The detected particles could be the neutrons themselves, or the gamma-rays emerging from the radiative neutron capture. The prompt and/or delayed gamma-rays originate from a distributed irradiated region in the sample, since they are produced wherever neutrons interact with the material along the beam path. The energies of the measured gamma-rays determine the elemental composition; while their intensities are a measure of the concentrations inside the irradiated part of the sample.

Adopting the principles of transmission or emission tomography means the use of a mathematical algorithm, such as the filtered back projection, and successive rotations and translations of the object in front of a “camera” to create numerous image projections in the plane of its sensitive screen (Spyrou 1987). In its original implementation (i.e. transmission tomography) the “camera” detects only the attenuation of the beam, i.e. the loss of intensity (Spyrou 1994). The disadvantage of the method is that the attenuation coefficients of the different materials could by chance be very similar making the identification of an element or compound unreliable. In recently established methods (Anderson et al. 2009), such as Neutron Resonance Capture Imaging (NRCI), Neutron Resonance Transmission (NRT) and energy-selective neutron imaging using Bragg-cutoffs, the “camera” could be element- and position-sensitive as is discussed in other chapters of this book.

Another way to have position-sensitive elemental data is to apply the direct method, where a narrow collimation of the neutron beam and of the gamma-detection can reduce the probed volume, so that the origin of the detected

gamma rays is well defined. This provides the basis to obtain the element distribution of the sample by scanning, i.e. measuring a set of gamma spectra at different positions in the sample (Baechler et al. 2001; Belgya et al. 2008b). This technique was named *Prompt Gamma Activation Imaging* (PGAI).

14.3 The Collection of 2D/3D Data

14.3.1 *The Tomographic Reconstruction*

According to the theory of computed tomography (i.e. Fourier slice theorem), a 3D elemental map of the sample can be constructed non-destructively slice by slice (Kak and Slaney 2001). The slices, which are treated independently, give the spatial variation of the measured quantity (e.g. linear attenuation coefficient, energy and intensity of gamma rays) in a horizontal plane through the object. A slice refers to a pixel row in an image; and is composed of the information recovered from the same row in the successive projections. To do this, the collection of spectra of the characteristic prompt (Spyrou Kusminarto and Nicolaou 1987) or delayed (Spyrou et al. 1987) gamma-rays are required at a number of angles distributed over the 360° rotation of the irradiated sample (this method is called emission tomography). It is theoretically equivalent whether the sample or the detector is rotated. The efficiency of the system is reduced because either the neutron beam or the gamma-ray detector must be collimated in order to provide position information for tomography. That is, for delayed gamma-rays the narrow collimation of the gamma-ray detector, while for prompt gamma-rays the narrow collimation of the neutron beam makes it possible to detect gamma-rays emitted in a given plane of the sample, respectively (Spyrou 1987). Both versions enable a non-destructive analysis for the determination of elemental composition of the irradiated part of the samples for major as well as minor components.

The method has been published as neutron-induced gamma-ray emission tomography (NIGET) (Spyrou et al. 1997; Spyrou 1999), or neutron-induced prompt γ -ray analysis with computed tomography (PGA-CT) (Segawa et al. 2009). In this latter case the measurements were carried out mainly using a single, well collimated high-resolution Ge detector and a narrowly collimated neutron beam on a Cd test sample, a three-sided wireframe pyramid of 1 cm side lengths.

The acquisition of gamma-ray spectra in tomographic mode is time consuming because of the low detection efficiency. Using state-of-the-art reconstruction methods such as the maximum likelihood expectation maximization (ML-EM), measurements with even poor statistics can be evaluated (Segawa et al. 2009). There are some restrictions in the case of delayed gamma-ray measurements, because the half-lives of the radionuclides less than some hours (Spyrou 1987) limit the set of elements to be studied effectively during a given scanning time. In prompt gamma-ray measurements this time constraint is avoided.

The reconstruction algorithm of this method makes it mandatory that the integral information recorded with a detector along the beam path must cover the whole sample thickness in a slice. This poses further limitations on the size and neutron attenuation of the sample, and on the activity and spatial distribution of the radionuclides of interest.

14.3.2 *The Direct Method*

This is the most natural transition from a bulk analytical technique to a 3D-capable method, and it is best used in the case of prompt gamma-ray measurements (Kasztovszky and Belgya 2006). It is preferred if the detector used does not provide intrinsic position resolution and if the beam of slow neutrons, can be sharply collimated.

The conventional PGAA method provides the average elemental composition of an illuminated volume (Molnár 2004). With a highly collimated neutron beam and gamma-detection, the probed volume (a volume at the geometrical intersection of the neutron beam path and the gamma collimator's solid angle) is reduced. Such a collimated neutron beam is often called a "pencil beam", and in case of thermal neutrons, its dimension can be reduced down to 2–3 mm. The gamma-ray collimator is usually of similar or slightly larger size. Thus the spatial information of the elemental distribution in the sample can be obtained by scanning, i.e. measuring a set of gamma spectra at different positions in the sample. This technique is named Prompt Gamma Activation Imaging (PGAI). PGAI utilizes low-energy, i.e. thermal or cold neutrons, as the cross-section for neutron capture reactions is increasing for lower neutron energies according to the so-called $1/v$ law. In present-day laboratories, a typical PGAI setup (Fig. 14.1) consists of a sample holder at the end of a neutron beam guide and a shielded Compton-suppressed gamma spectrometer placed perpendicular to the beam (Belgya et al. 2008a; Kudejova et al. 2008; Kis et al. 2015).

Basically two measurement configurations can be applied (Fig. 14.2). In the *chord geometry* only the neutron beam is collimated, so the resolution along the beam direction is lost (Fig. 14.2a). Such data are suitable whenever 2D data are enough for meaningful results, and the gamma collimation can be omitted in favor of a higher event rate (Segawa et al. 2008). One of the first experiments of this kind was performed on a piece of the 2-billion-year-old Oklo natural reactor (Baechler et al. 2001). To obtain spatially resolved data the cold neutron beam was focused, and it was reduced to a 1 mm^2 area at the focal point. Because the object was a thin sample and was placed perpendicular to the beam, the 2D elemental map was representative of the elemental distribution of the whole sample.

If both the neutron beam and the gamma detector are collimated, the intersection of the neutron beam and the solid angle of the collimated gamma-detector define a probing volume, the so-called *isovolume* (Fig. 14.2b). The concept of this isovolume, called earlier "invisible container geometry", was used with success in the past

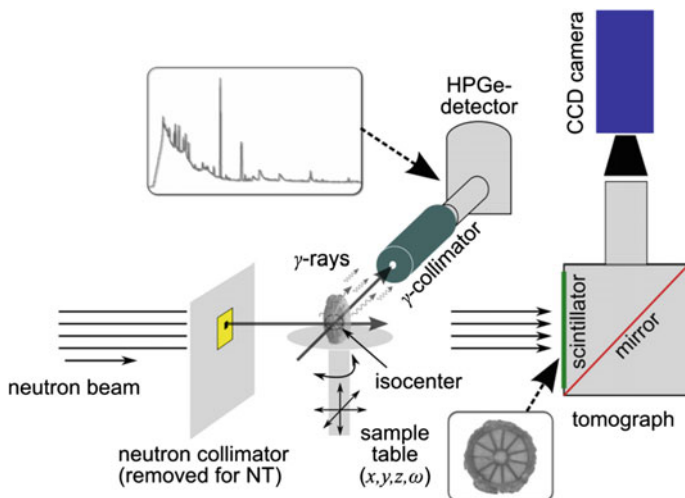


Fig. 14.1 Illustration of a combined PGAI/NT setup. For PGAI measurements the neutron collimator is put into the beam, while for NT an open neutron beam is needed (Schulze et al. 2011)

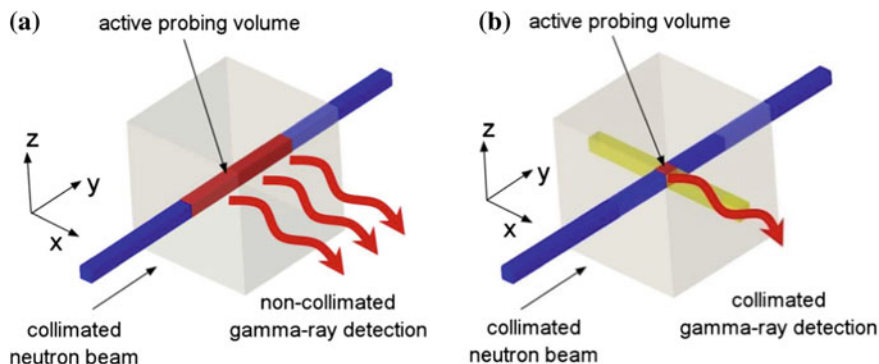


Fig. 14.2 Illustration of the active measurement volume for the scanning based approach. **a** 2D setup without gamma collimator (chord geometry). **b** 3D setup with neutron and gamma collimator (double collimated geometry). The blue line represents the path of the neutron beam. The yellow line shows the collimated view of the gamma detector. The intersection of the two lines gives the currently measured sample volume for **b** while for **a** the whole volume irradiated by the neutron beam is measured

to suppress background from metallic canisters of pressurized gases and lead containers (Révay 2008), and to determine micrograms of hydrogen inside a catalytic reactor assembly (Révay et al. 2008). Ideally it is a small fixed volume in space which is the source of the analytical information. Its middle point is called *isocentre*. Due to count rate considerations the smallest feasible volume was a few tens of mm^3 so far. This approach to delivering 3D information gives a direct image

and does not involve the filtered back-projection principle. The data required to fill up the 3D grid is measured isovolume by isovolume, applying a systematic scanning of the whole sample, which is placed on a motorized sample stage. This scan can either be over the full sample volume or only of a smaller region of interest (Belgya et al. 2008b). A consequence of the better spatial resolution in comparison to PGAA is the reduced count rate, which makes the systematic PGAI scans very time consuming.

The data reduction in this case is straightforward: The measured raw data are plotted against the coordinates of the sample stage, i.e. the positions in the 3D space. However, this raw image is affected by biases from self-shielding of the neutrons and self-absorption of the gammas, and the distortion effects of the gamma-ray collimator's transmission function, which have to be point-wise corrected for. A correction method is under development using random numbers (Monte Carlo method) to yield quantitative results (Kis et al. 2011).

With the isovolume measurements—unlike the tomographic reconstruction techniques—it is not mandatory to measure and reconstruct the whole sample, but one can focus on selected parts of the object which may speed up the measurement. For real samples it is usually safe to assume that they are made of a few homogeneous parts, and useful results can be made even if the full scanning with a given resolution is not feasible. To do this a suitable option is to couple the position sensitive PGAI with faster neutron imaging methods. Radiography, or even a full tomography of a complex sample, can be completed in minutes/hours, and often provides enough information to define regions of interest. If the spatial data from radiography or tomography is linked to the positions of a motorized xyzω sample stage, one can move the selected parts of the sample into the probed volume. If necessary, the accuracy of the positioning could be confirmed by repeated neutron images, or even with a real-time video loop. The detailed elemental analysis by PGAI is then carried out only at these spots, saving a substantial amount of beam time. This makes the technique, called *neutron radiography*, *neutron tomography* (*NR/NT*) driven PGAI, much more feasible and productive than PGAI of the whole sample.

In the framework of the EU FP6 ANCIENT CHARM (*Analysis by Neutron resonant Capture Imaging and other Emerging Neutron Techniques: new Cultural Heritage and Archaeological Research Methods*) project (2006–2009) novel 3D-capable structure, phase and element analysis techniques were worked out as the combination and extension of the conventional Neutron Tomography (NT), Prompt Gamma Activation Analysis (PGAA), Time-of-Flight Neutron Diffraction (TOF-ND), Neutron Resonance Capture Analysis (NRCA) and Neutron Resonance Transmission (NRT). One of the major innovations was PGAI-NT, realized first in Budapest (Belgya et al. 2008a) and later at the FRM II PGAA station, Garching, Germany (Kudejova et al. 2008). It was demonstrated that a complete two or three-dimensional element mapping with adequate resolution is possible, but is presently feasible only for small objects due to constraints of experimental time and neutron flux. Nowadays the only permanent facility for NR/NT-driven PGAI in operation, NIPS-NORMA, can be found at the Budapest Neutron Centre (BNC) as

an advanced version of the one built during the ANCIENT CHARM project. The detailed technical specifications of NIPS-NORMA are available in Szentmiklósi et al. (2010, 2013) and Kis et al. (2015).

14.4 Examples of PGAI-NT Studies

14.4.1 PGAI of a Disc Fibula from the 6th Century

First PGAI-NT pilot studies were accomplished on a fibula found at the Kölked-Feketekapu site, Hungary, dated to the end of 6th century AD, and kept at the Hungarian National Museum. It has a diameter of 31 mm, a thickness of ~ 10 mm, and weighs 20.08 g. It was thought that the fibula contains an outer ring, presumably made of iron, and a main round part consisting of gold cells with garnet (almandine) inlays. A pearl of unknown material is placed in the center of the fibula front. It had earlier been assumed that the back-plate was made out of bronze.

In the course of the PGAI method development, procedures had to be developed for calibration, sample handling and software development. This was carried out at the Institute of Isotopes (presently the Centre for Energy Research, HAS) in Budapest, Hungary, using replica samples of selected archaeological objects. The final measurements were then performed at the Forschungs-Neutronenquelle Heinz Maier-Leibnitz (FRM II) in Garching, Germany which has a hundred times higher neutron flux. This high neutron flux made the measurement of the 3D elemental mapping of real archaeological samples feasible.

For the preparation of the elemental imaging measurements, a short PGAA measurement of the bulk sample was made at the Budapest PGAA setup, which identified the major elements Fe (64.5), S (15.3), Au (7.9), Cu (7.2), H (2.2), Al (1.2), Ag (0.9 %), Mn (0.7 %), and Cl (0.1 %) with relative fractions in weight percent in brackets. From these results the measurement acquisition time for each spot of the following PGAI measurement could be estimated, so as to be long enough to provide enough counts for a reliable elemental identification. Additionally the bulk measurement allowed the estimation of a potentially long lasting sample activation, which could delay the release of the sample due to radiation protection reasons. To reduce this risk the measurement time should be kept as short as possible, when isotopes with a long decay time are produced in larger amounts.

As a PGAI scan of the full sample would be unfeasibly long (in the order of weeks!), the knowledge of the morphological structure can be used to limit the measurement scan to a few small regions typical of given parts of the object. For this fibula the NT confirmed the already expected rotational symmetry. Thus it seemed to be justified to measure only one quadrant of the sample and to extend the measured elemental distribution over all four fibula quadrants by mirroring. To further decrease the measurement time, the scanning grid was limited to three layers

in the fibula, which were assumed to provide representative results for the full fibula (see Fig. 14.3). The first layer was positioned to provide information about the almandine inlays, the second layer was placed to analyze the filling material, and the third layer was selected to measure the composition of the fibula back-plate. In each layer the measurement's grid was further reduced to measure only every second position in the 2×2 mm step-size grid according to a checkerboard pattern (Fig. 14.3). Even with all these limitations the acquisition time for the 77 measured spectra was around 10 full days (Schulze et al. 2013).

The spatial alignment of the datasets (from NT and PGAI) was carried out after the analysis of raw data, and some qualitative results for the significant elements are shown in Fig. 14.4.

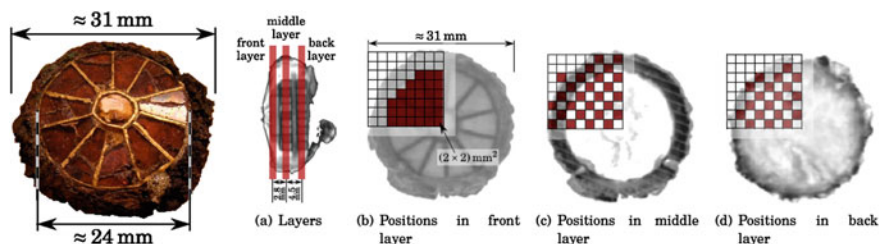
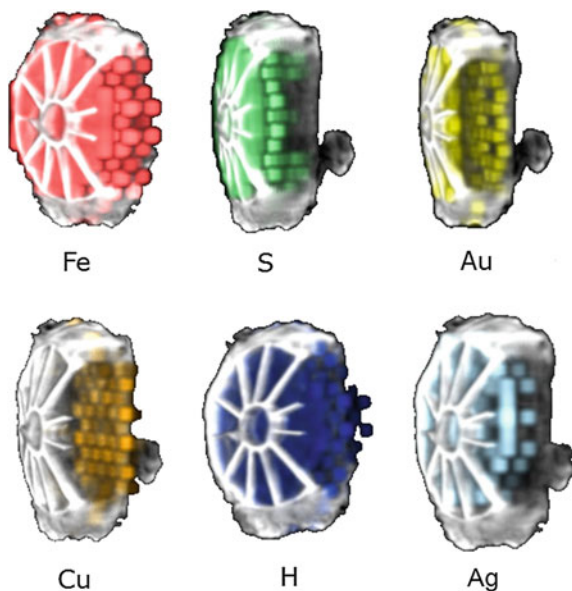


Fig. 14.3 The disc fibula and the defined measurement grid for the PGAI experiment (reproduced from Schulze et al. 2013 with permission of The Royal Society of Chemistry)

Fig. 14.4 Spatial maps of selected elements as registered data-sets from the PGAI and NT imaging modalities. The voxels are single data-points from PGAI measurements. The highlighted voxels represent regions where the given element was detected, whereas other voxels were made transparent. Reproduced from Schulze et al. (2013) with permission of The Royal Society of Chemistry



The PGAI measurement revealed iron in nearly all measured positions, with the highest intensities in the back-plate and outer ring. Sulphur was detected in the inner part of the fibula, so it is likely a component of the filling material. Gold was measured in the front and back layer. The distribution in the front layer confirmed the presence of a golden lining of the almandine inlays. The copper presence in the back layer was a hint to confirm that the back-plate is made of copper-alloy, probably bronze. Unfortunately, tin was not detected because its quantity is likely below detection limit in the copper matrix. The uniform distribution of hydrogen in the front and middle layer indicates that it is another component of the filling material. The measured silver distribution follows the lining of the almandine inlay, so it could be a soldering component. At some discrete points on the back-plate chlorine was measured. The discrete distribution leads to the assumption that it was not an original component of the fibula material, but might be a contamination from either chlorination while buried or restoration or conservation procedures.

These results confirmed some assumptions of the archaeologists, e.g. it had earlier been assumed, that the fibula was repaired with an iron band which should keep the inlays and the back-plate in place. The internal distribution of iron may originate from some washing of iron oxide into the filling material. It was also confirmed that the lining of the front inlays were made out of pure gold.

14.4.2 NT-Driven PGAI of an Eighteenth Dynasty Egyptian Sealed Pottery

An Eighteenth Dynasty Egyptian sealed pottery from the Museum of Aquitaine (Bordeaux, France) has been investigated using computed tomography (CT) of various modalities (terahertz electromagnetic radiation (Jackson et al. 2011), X-rays and neutrons) and NT-driven PGAI in order to analyze the bottle itself and its contents (Abraham et al. 2014). X-ray and neutron imaging are routinely used, but terahertz (THz) imaging is only recently used to analyze museum artefacts non-destructively. This multi-modal study emphasizes the complementarity and specificity of the three imaging methods, together with the position-sensitive elemental mapping technique, all of which are shown to be of a prime importance for historians and museum curators dealing with cultural heritage.

The CT images of the pottery using THz radiation are presented in Fig. 14.5. The internal volume of the bottle has been estimated to be 100 cm^3 with about 25 cm^3 filled by a movable content. At the bottom of the pottery, where THz radiation is strongly absorbed, it was concluded that either the bottle is filled by a fixed content in this part or that the pottery walls are thicker here so that THz radiation is not transmitted.

With X-ray CT, front and axial views clearly confirmed the presence of the movable and deformable content (Fig. 14.6), previously revealed by THz CT. Higher spatial resolution makes it possible to see that the content is inhomogeneous

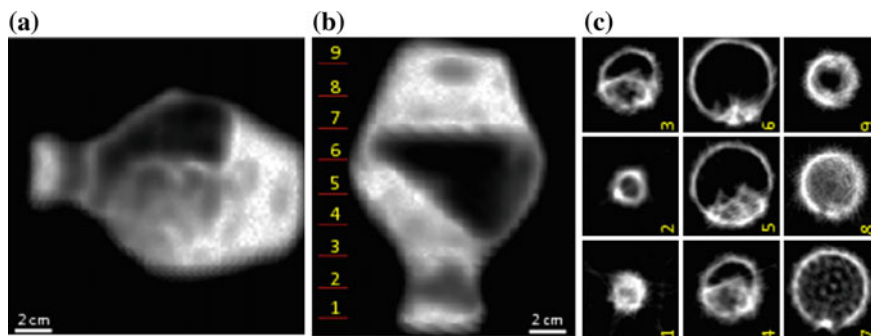


Fig. 14.5 THz CT. **a** Front view, horizontal position. **b** Front view, upside-down vertical position. **c** Axial views at the positions indicated in **b**. (Abraham et al. 2014)

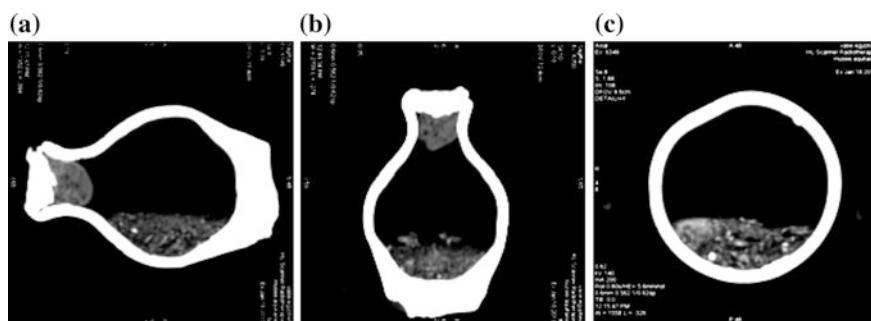


Fig. 14.6 X-ray CT (140 kV–200 mA). **a** Front view 1, **b** Front view 2, **c** Axial view (Abraham et al. 2014)

with small and larger fragments. It is not composed of mineral materials since its density is much lower than the pottery walls made of clay and its X-ray absorption is weak. The front views also reveal that the cork consists of two parts with an external sealing of clay (saturated white color) and an inside one made of an unknown low contrast material (grey color).

Neutron imaging gave information about the way the object has been closed by a double stopper (clay and probably a ball of linen or some other string-like organic material) and provided a more accurate representation of the mobile and heterogeneous content, probably consisting of germinated herbal seeds (Fig. 14.7).

The elemental composition of three different parts of the jar was determined with NT-driven PGAI (Fig. 14.7a). The investigated parts were the following: (1) ‘Full’: irradiation of the inner content and surrounding wall; (2) ‘Void’: irradiation of a void part of the bottle without the filling material (e.g., practically only the wall material); and (3) ‘Plug’: irradiation of the cork region and surrounding walls. Due to the uncertainty in the self-absorption corrections only a semi-quantitative

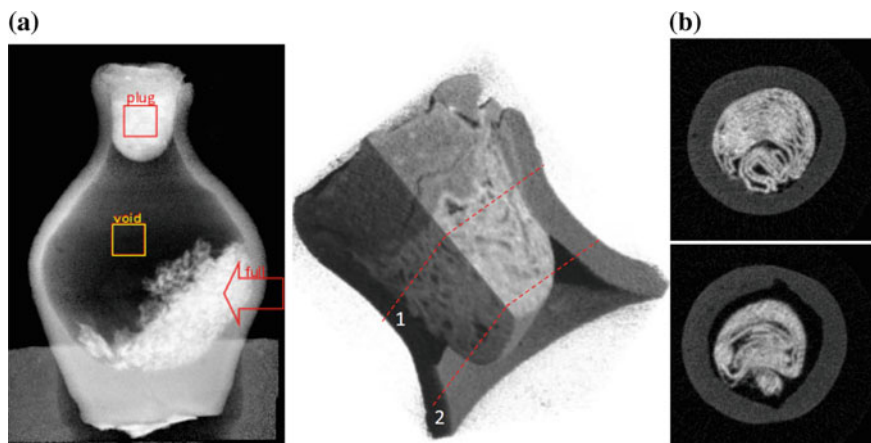


Fig. 14.7 Neutron CT. **a** Global front view. **b** 3D representation of the cork. Axial views of the cork at the position 1 and 2 indicated in **b** (Abraham et al. 2014)

elemental composition for the inner content could be given instead of absolute concentrations of the identified components. The amounts of the characteristic elements for ceramics (Na, Mg, Al, Si, K, Ca, Ti, Mn, and Fe) were roughly the same in both ‘Full’ and ‘Void’ measurements. On the other hand, some elements characteristic of organic material (H, C, N, S, and Cl) show an excess in case of the ‘Full’ measurement, compared with that of the ‘Void’. Furthermore, the composition of the plug also shows an excess of H, C, N, S, and Cl, which confirms the organic nature of the fabric.

As a result, the content could consist of germinated seeds (or any other dried organic material) such as barley that was a staple cereal of ancient Egypt. It is concluded that the internal cork could be made of a ball of linen.

14.5 Method Limitations and Peculiarities

14.5.1 Sample Positioning and Alignment

In addition to the development of various imaging methods, the tasks of spatial registration of the data and object transportation have to be addressed if the study on a sample involves more than one setup. The joint use of different datasets has advantages over their separate evaluations. A marker-based approach was chosen in combination with the development of universal sample holders which aim to solve the problems of safe transportation, reproducible positioning and unique data registration.

14.5.1.1 Requirements

A crucial task is the correct placement of the samples in the desired measurement positions. It is essential that the accuracy of the sample positioning be better than the resolution of the measurement method itself. This means that the alignment has to be accurate to about 1 mm or better.

To define measurement positions which lie on the surface of the sample, a laser beam can be used which is coincident with the path of the neutrons. The sample can easily be positioned by eye in such a way that the laser hits the desired part of the sample. This method fails when it is desirable to investigate internal parts of a sample, e.g. the glue or resin used during the manufacturing process of an object. For this case another method has to be used.

14.5.1.2 Sample Holders and Reference Markers

The construction of universal sample holders for the objects, which protect the valuable objects from any possible damage during transportation from one facility to another, and which ensure the unique and well-defined positioning on the different instruments (Kudejova 2008) is sometimes necessary. Reference markers should be attached to these sample holders at precisely determined positions relative to the sample (see Fig. 14.8a).

These reference markers have to be detectable by all measurement methods and should be small enough to allow accurate determination of their positions. For the unique alignment of these markers in 3D space at least four markers have to be used. For the tomography based methods it is essential that the markers, which have high neutron absorption, never appear in front or behind the samples during the rotation, because then the filtered back-projection algorithm would fail.

For the cold neutron based methods, i.e. PGAI and NT, pin-heads, which were painted with gadolinium-loaded white nail polish, were used to mark the reference positions. Due to the high cross-section of gadolinium for cold neutrons they were easily detectable with these methods. Because of the nearly spherical shape the determination of their position could be performed very accurately by using the centre of the spheres as reference.

14.5.1.3 Positioning with the Help of Reference Markers

By performing a neutron tomography of the sample in the frame with attached reference markers one gets a 3D “map” of the inner and outer parts of the object. The reference markers provide known points in space which can be used to convert from 3D voxels inside this map to millimetre coordinates in the laboratory coordinate frame.

The determination of the reference marker positions in the laboratory coordinate system, which is usually given by motor steps of the xyz ω -tables used for sample

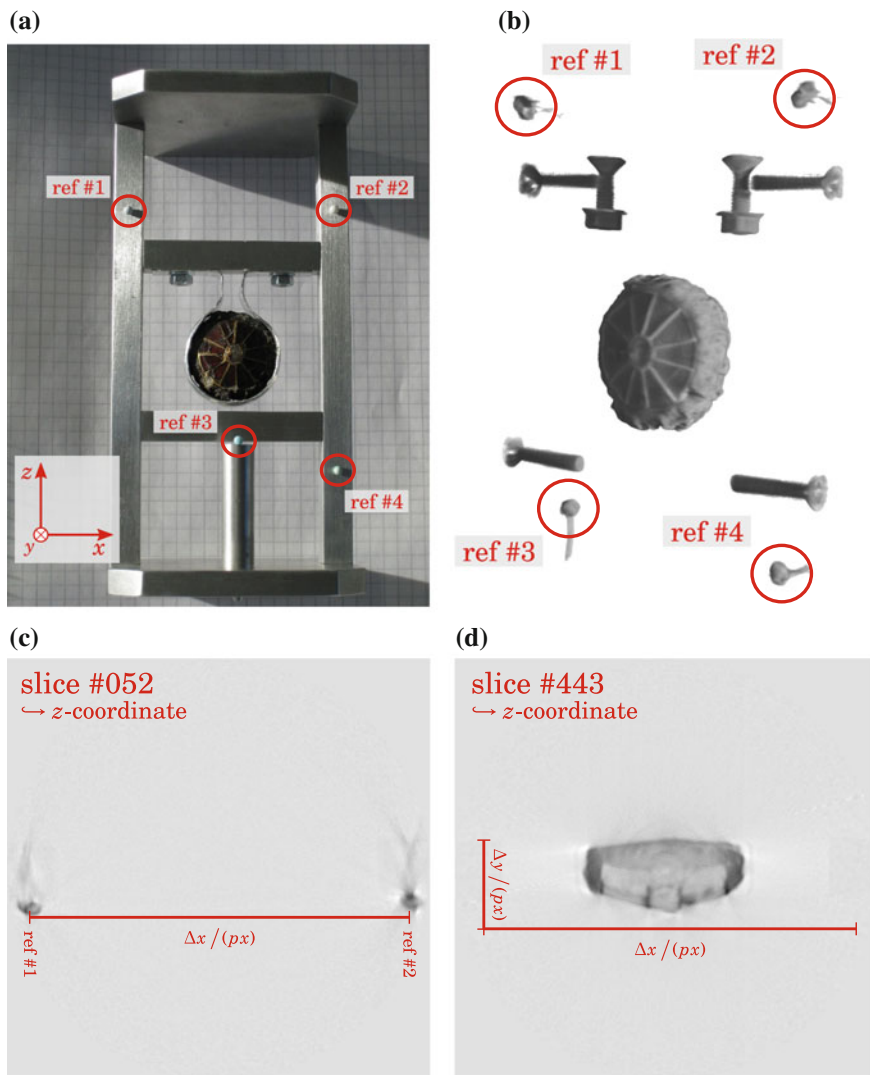


Fig. 14.8 Use of reference markers for sample positioning. **a** Fibula sample in holder with reference markers. **b** NT of fibula. The references markers are clearly visible in the reconstruction. **c** and **d** Slices of the NT reconstruction. The slice number gives the z-coordinate. **c** A slice across the middle of the two upper reference markers gives the x-direction calibration. The known distance in mm of the reference markers and the distance in pixels in the reconstruction slice give the conversion factor for the transfer of positional information from reconstruction to laboratory system. For the y-axis the lower front reference marker can be used. **d**: Slice in the middle of the fibula (Schulze et al. 2011)

positioning, can be achieved by different means, e.g. by measuring the distance from fixed known positions in the laboratory system with a ruler or caliper, utilizing a laser to place the markers to a known position or by doing an in-beam scan. The motor positions obtained from these scans give a correspondence between sample stage and detector, and therefore the detected data.

With the known positions of the reference markers in the laboratory coordinate system, sample positioning is now a task of

- selecting a desired measurement point in the NT data-set,
- determining the offset of this point in NT coordinates, i.e. pixel numbers and slices in the reconstruction, from the positions of the reference markers in the reconstruction (Fig. 14.8c,d),
- and transferring these offsets to the laboratory coordinate system by applying translation vectors, scaling factors and a rotation matrix.

The transferred coordinate offsets are finally added to the known position of one of the reference markers when in the measurement position, which gives the final coordinates for the point and hence the sample stage setting.

14.5.1.4 Combination and Registration

It is important to have the ability to combine the results gained from the different measurement methods. In the end a full 3D representation of the object, containing the morphological structure, the measurement of elemental distributions and the crystallographic properties is desirable. For this task 3D visualisation software could be used, which allows the import and combination of different 3D data-sets and the navigation inside the combined data-sets for easy interpretation of the results.

For the alignment of the different data-sets the reference markers used for the positioning of the samples can be used. The collected data is inserted in a 3D voxel space, where the voxel size is chosen according to the resolution of the measurement method. The position of the single data-points in this “voxel space” is determined relative to the reference markers, which are also included into these 3D data-sets. The final registration is then done by aligning the positions of the reference markers.

14.5.2 Temporary Neutron Activation of the Objects

An a priori calculation of the potential activation due to the neutron irradiation of the museum objects could be of high importance when judging the feasibility of an experiment. Based on the results, an upper limit of irradiation time can be defined which keeps the activity level of the objects below the exemption levels declared by

the law. The exemption levels are different for the different isotopes and, moreover, they might differ from country to country. An example is presented below. The activity values shown can be scaled according to the various irradiation situations.

The activity of an isotope (A_i) during a continuous neutron irradiation follows a saturation curve. If the number of activated atoms is zero at $t = 0$, then:

$$A_i = n_i \cdot \sigma_i \cdot \Phi \cdot (1 - e^{-\lambda_i t})$$

where n_i is the number of atoms of the i th isotope ($n_i = \Theta_i \times n_{\text{elem}}$, where Θ_i is the isotopic abundance of the i th isotope of the element, n_{elem} is the number of the atoms of the chemical element in the path of the neutron beam), σ_i is the neutron absorption cross section of the i th isotope for thermal neutrons ($v = 2200$ m/s), Φ is the time independent thermal equivalent neutron flux of the cold or thermal neutrons assumed to be constant over the volume of the object, λ_i is the decay constant of the i th isotope ($\lambda_i = \ln(2)/T_{1/2}$, where $T_{1/2}$ is the half-life of the isotope). If the irradiation circumstances are steady and the saturation activity is reached, it will be constant until the end of the irradiation due to the dynamical equilibrium between generated and decaying nuclei. After the end of irradiation the activity of the isotope will follow an exponential decay curve.

A silver sphere weighting 0.298 grams was irradiated in a thermal equivalent neutron flux of $1.2 \times 10^8 \text{ cm}^{-2}\text{s}^{-1}$ for 1 h at the PGAA station of the Budapest Research Reactor, Hungary, representing a worst-case scenario, since silver has a high neutron capture cross-section and also a long half-life. A measurement after 1 day cooling time yielded ~ 10 Bq radioactivity for silver (Ag-110m) in the whole sample, which is a very low value compared to its exemption level (10^6 Bq) for activity. This means that a rather large quantity of silver (\sim some grams) in museum objects could be irradiated for longer time in a similar neutron beam without any radiation protection consequences. For other typical components of an artefact with significant activation, such as Cu, Zn, Au, Na, the situation is even safer.

For a more general calculation for these elements, let us consider 10 mmol (6×10^{21} atoms) of the i -th isotope, n_i . Hence, for an isotope of mass number A the weight of the isotope is $A/100$ g: e.g. for Ag-109 $m_A = 1.09$ g. This latter implies that the weight of the elemental silver in the sample is $1.09 \text{ g}/0.48 = 2.27$ g, where 0.48 is the isotopic abundance of Ag-109. Let the thermal equivalent neutron flux be $1 \times 10^8 \text{ cm}^{-2}\text{s}^{-1}$ in the whole volume of the sample (i.e. as a worst case approach we do not consider the self-shielding effect of the sample material). In Fig. 14.9 the activities of the isotopes after 1 h irradiation are presented for different σ_i values. It can be seen that the activities are going to be saturated if the value of $\lambda_i \times t_{\text{irr}}$ is at least 5 or larger. From Fig. 14.9 one can see that e.g. Ag-110m (the metastable product after capture of a neutron by Ag-109) and Zn-65 are far from the saturation, which is due to their rather long half-lives. It can also be seen that Al-28 is already saturated after 1 h irradiation, because its half-life is just 2.24 min.

An irradiated object should no longer be considered as radioactive if its activity or activity concentration is below the exemption levels. If the activity after the

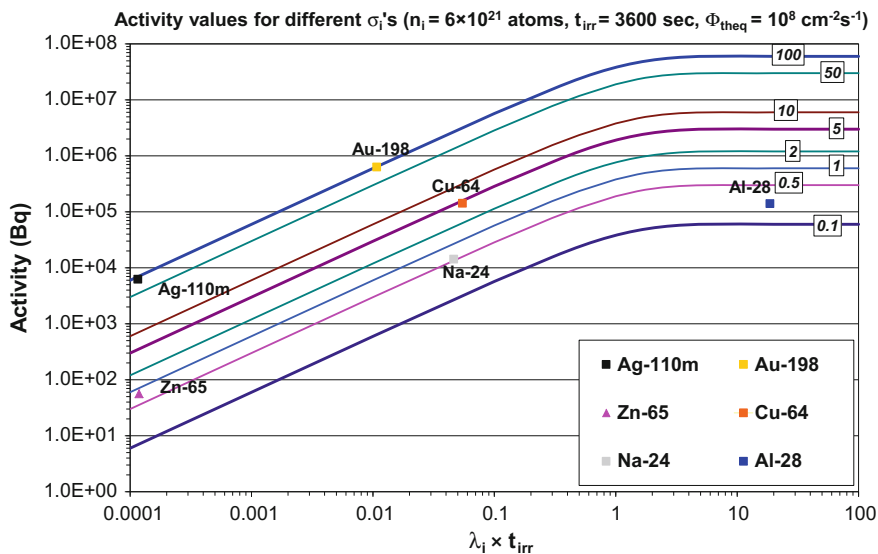


Fig. 14.9 Activity values after 1 h irradiation. The number of atoms of the irradiated isotopes is 10 mmol (6×10^{21} atoms) in a thermal equivalent neutron flux of 10^8 cm $^{-2}$ s $^{-1}$. The curves refer to typical cross section values between 0.1 and 100 barns. For better clarity the activity values for some interesting isotopes are presented as well. (The activity values do not contain the activity produced during measurements due to irradiation with epithermal or higher energy neutrons.)

irradiation would exceed the limit for an isotope then the object should be considered as radioactive material, and should be kept in a locker until its activity has decreased below the exemption level. This could be a problem for materials containing isotopes of rather long half-life (e.g. $T_{1/2}(\text{Ag-110m}) = 249.95$ days). For example, the exemption level for the activity of Ag-110m is 10^6 Bq in Hungary, therefore the irradiations of an object at different facilities should be optimized in a way not to exceed this level. For isotopes of shorter half-life (e.g. $T_{1/2}(\text{Au-198}) = 2.69$ days) exceeding the exemption level is not such a serious problem. One should leave sufficient cooling time between measurements or after the last measurement before the sample is released again. This must be considered already at the planning stage of an experiment, i.e. the owners of the artefacts need exact dates of the loan period well in advance.

14.6 Conclusions

The results of elemental mapping obtained by position-sensitive neutron-based analytical techniques (PGAI, NR/NT-driven PGAI) alone could already answer many relevant questions in the cultural heritage science. The combination of these

results with resonance neutron-based and scattering methods, or even with non-nuclear (e.g. X-ray, THz) imaging, opens the possibility of a comprehensive approach to answer cultural-heritage-specific questions.

References

- Abraham E, Bessou M, Ziéglé A, Hervé M-C, Szentmiklósi L, Kasztovszky Zs, Kis Z, Menu M (2014) Terahertz, X-ray and neutron computed tomography of an eighteenth dynasty Egyptian sealed pottery. *Appl Phys A* 117:963–972
- Anderson IS, McGreevy RL, Bilheux HZ (eds) (2009) Neutron imaging and applications. Springer, New York
- Baechler S, Materna T, Jolie J, Cauwels P, Crittin M, Honkimaki V, Johner H, Masschaele B, Mondelaers W, Kern J, Piboule M (2001) Non-destructive analysis of a bulky sample from a natural fossil reactor. *J Radioanal Nucl Chem* 250:39–45
- Belgya T, Kis Z, Szentmiklósi L, Kasztovszky Zs, Festa G, Andreanelli L, De Pascale MP, Pietropaolo A, Kudejova P, Schulze R, Materna T (2008a) A new PGAI-NT setup at the NIPS facility of the budapest research reactor. *J Radioanal Nucl Chem* 278:713–718
- Belgya T, Kis Z, Szentmiklósi L, Kasztovszky Zs, Kudejova P, Schulze R, Materna T, Festa G, Caroppi PA (2008b) First elemental imaging experiments on a combined PGAI and NT setup at the budapest research reactor. *J Radioanal Nucl Chem* 278:751–754
- Jackson JB, Bowen J, Walker G, Labaune J, Mourou G, Menu M, Fukunaga K (2011) A survey of terahertz applications in cultural heritage conservation science. *IEEE Terahertz Sci Technol Trans* 1:220–231
- Kak AC, Slaney M (2001) Principles of Computerized Tomographic Imaging. *Soc Ind Appl Math*
- Kasztovszky Zs, Belgya T (2006) From PGAA to PGAI: from bulk analysis to elemental mapping. 3:16–21
- Kis Z, Belgya T, Szentmiklósi L (2011) Monte Carlo simulations towards semi-quantitative prompt gamma activation imaging. *Nucl Instrum Methods Phys Res A* 638:143–146
- Kis Z, Szentmiklósi L, Belgya T (2015) NIPS-NORMA station—a combined facility for neutron-based nondestructive elemental analysis and imaging at the Budapest Neutron Centre. *Nucl Instrum Methods Phys Res Sect Accel Spectrometers Detect Assoc Equip* 779:116–123
- Kudejova P (2008) Supports for accurate positioning and alignment of archaeological objects. FRM2, Garching, Germany
- Kudejova P, Meierhofer G, Zeitelhack K, Jolie J, Schulze R, Türler A, Materna T (2008) The new PGAA and PGAI facility at the research reactor FRM II in Garching near Munich. *J Radioanal Nucl Chem* 278:691–695
- Molnár G (2004) Handbook of prompt gamma activation analysis with neutron beams. Kluwer Academic Publishers, Dordrecht
- Révay Z (2008) Prompt gamma activation analysis of samples in thick containers. *J Radioanal Nucl Chem* 276:825–830
- Révay Z, Belgya T, Szentmiklósi L, Kis Z, Woosch A, Teschner D, Swoboda M, Schlögl R, Borsodi J, Zepernick R (2008) In situ determination of hydrogen inside a catalytic reactor using prompt gamma activation analysis. *Anal Chem* 80:6066–6071
- Schulze R, Szentmiklósi L, Kis Z, Collaboration Ancient Charm (2011) The ancient charm project: new neutron based imaging methods for cultural heritage studies. *Archeol E Calcolatori* 21:281–299
- Schulze R, Szentmiklósi L, Kudejova P, Canella L, Kis Z, Belgya T, Jolie J, Ebert M, Materna T, Biro KT, Hajnal Z (2013) The ancient charm project at FRM II: three-dimensional elemental mapping by prompt gamma activation imaging and neutron tomography. *J Anal At Spectrom* 28:1508–1512

- Segawa M, Matsue H, Kureta M (2009) Development of three-dimensional prompt γ -ray analysis system. *Nucl Instrum Methods Phys Res Sect Accel Spectrometers Detect Assoc Equip* 605:54–56
- Segawa M, Matsue H, Sekiya Y, Yamada S, Shinohara T, Oku T, Sasao H, Suzuki J, Shimizu HM (2008) 2D elemental analysis approach in focused neutron beam induced prompt gamma-ray analysis at JAEA. *J Radioanal Nucl Chem* 278:647–651
- Spyrou Kusminarto NM, Nicolaou GE (1987) 2-D reconstruction of elemental distribution within a sample using neutron capture prompt gamma-rays. *J Radioanal Nucl Chem* 112:57–64
- Spyrou NM (1987) Prompt and delayed radiation measurements in the elemental analysis of biological materials: the case for neutron induced gamma-ray emission tomography. *J Radioanal Nucl Chem* 110:641–653
- Spyrou NM (1994) Tomography and elemental analysis using neutrons in transmission. *J Radioanal Nucl Chem* 179:285–294
- Spyrou NM (1999) Neutron activation analysis challenges: problems and applications in biomedical and other areas. *J Radioanal Nucl Chem* 239:59–70
- Spyrou NM, Balogun FA, Davies G (1987) Investigation of elemental distributions within a biological sample using neutron activation tomography. *J Radioanal Nucl Chem* 113:417–421
- Spyrou NM, Sharaf JM, Rajeswaran S, Mesbahi E (1997) Determination of the elemental distribution in a sample using neutron induced gamma-ray emission tomography. *J Radioanal Nucl Chem* 217:237–241
- Szentmiklósi L, Belgya T, Révay Z, Kis Z (2010) Upgrade of the prompt gamma activation analysis and the neutron-induced prompt gamma spectroscopy facilities at the budapest research reactor. *J Radioanal Nucl Chem* 286:501–505
- Szentmiklósi L, Kis Z, Belgya T, Berlizov A (2013) On the design and installation of a compton-suppressed HPGe spectrometer at the budapest neutron-induced prompt gamma spectroscopy (NIPS) facility. *J Radioanal Nucl Chem* 298:1605–1611

Chapter 15

Neutron Activation Autoradiography

A. Denker, N. Kardjilov and B. Schröder-Smeibidl

Abstract Autoradiography uses a photographic film or imaging plate which are placed in direct contact with a painting after irradiation by slow neutrons. The pigments become radioactive after the interaction with the neutron beam and the emitted radiation (gammas, X-rays and electrons, so called beta-rays) is registered in the film or plate. The blackening of the film is mainly due to the beta-rays because the gamma rays are high energetic and hardly interact with the film. In this way the obtained picture can be called beta-radiography, but since the radioactive elements in the painting itself are the source of beta rays, the technique is called “autoradiography.” In addition gamma spectrometry can be applied for detecting the emitted radiation from activated elements and by analysis of the position of the energy peaks and their intensity information about the chemical composition and the amount of the pigments can be obtained. In this way position sensitive elemental analysis is possible.

15.1 History

The neutron activation autoradiography was first developed by Heather N. Lechtman and Edward V. Sayre and used for investigation of nineteenth century American paintings and, later, of various paintings at the Hecksher Museum, Huntington, New York. In addition a group of seventeenth century Dutch and Flemish paintings from the Metropolitan Museum of Art was analyzed and the results have been published in (Ainsworth 1982).

In 1980 Prof. Dr. Bock from the Gemäldegalerie Berlin and Prof. Dr. J. Riederer from the Rathgen research laboratory contacted Prof. Dr. H. Dachs and W. Leuther at the former Hahn-Meitner-Institute Berlin and proposed an instrument for neutron

A. Denker (✉) · N. Kardjilov · B. Schröder-Smeibidl
Helmholtz-Zentrum-Berlin, Hahn-Meitner-Platz 1, 14109 Berlin, Germany
e-mail: denker@helmholtz-berlin.de

N. Kardjilov
e-mail: kardjilov@helmholtz-berlin.de

activation autoradiography at the BER-II research reactor. The effect of this initiative was the installation of irradiation position at the thermal column of the reactor in 1984. In 1992 a dedicated instrument called B8 was installed at the cold neutron source. For the time of operation until nowadays more than 70 paintings are investigated.

15.2 Theory

The neutron activated autoradiography (NAAR) is based on the following principle: The painting is irradiated by intense beam of slow neutrons provided by a nuclear installation (e.g. research reactor). The neutrons interact with nuclei of the atoms of the pigments in the picture and some of the neutrons are captured. At this nuclear reaction the pigments become slightly radioactive. Immediately after the irradiation of several hours the painting is transferred from the irradiation position to a separated post-processing room. Here the residual radioactivity emitted from the interacted pigment atoms (isotopes) is depicted on a film placed on the top of the painting as shown in Fig. 15.1.

The isotopes of certain element possess the same number of protons in the atomic nucleus but the number of neutrons is different. If the isotope is not in a stable state then it emits energy in form of radioactive radiation (X-rays, gammas, electrons, beta-particles etc.) in order to reach its stable configuration. The different isotopes of one element are designated by their atomic mass number which corresponds to the sum of the number of protons and number of neutrons. Manganese atoms, for example, have 25 protons in the atomic nucleus and there is one stable non-radioactive isotope with 30 neutrons, resulting in an atomic mass number of 55. When a neutron is captured, the neutron number and the atomic number increases by one. The atomic number is designated with an index above and to the left of the element symbol:

^{55}Mn and ^{56}Mn (as shown in Fig. 15.1).

Fig. 15.1 Neutron capture in an atomic nucleus

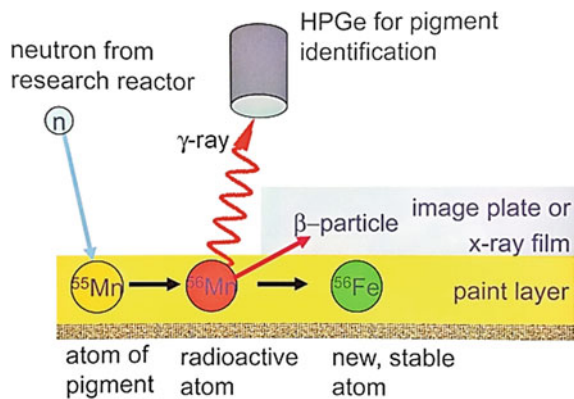


Table 15.1 NAAR-Table of elements

Element	Isotope	Half-life	Pigments
Manganese	⁵⁶ Mn	2.6 h	Umbra, dark ochres
Potassium	⁴² K	12.4 h	Canvas
Copper	⁶⁶ Cu	5.1 min	Azurit, malachite, verdigris
Copper	⁶⁴ Cu	13 h	Azurit, malachite, verdigris
Sodium	²⁴ Na	15 h	Canvas, glue, ultramarine
Arsenic	⁷⁶ As	26.5 h	Realgar, auripigment, smalt
Antimony	¹²² Sb	2.7 days	Naples yellow
Phosphorus	³² P	14 days	Bone black
Mercury	²⁰³ Hg	47 days	Vermilion
Cobalt	⁶⁰ Co	5.3 years	Smalt

The signal detected in the X-ray film is mainly caused by β -radiation (beta) consisting of electrons. The radioactive isotopes emit also γ -radiation (gamma) which is characteristic for each element and thus opens the possibility of identifying the pigments by using of position sensitive gamma spectrometry as shown in Fig. 15.1.

Radioactive materials decay with time and the time needed for half of the material to decay is called half-life. The neutron autoradiography uses the fact that the rate of the decay is different for each isotope. Some atoms such as the copper isotope ⁶⁶Cu decay very fast (minutes) and others such as the radioactive isotopes of mercury decay considerably slower (many days), see Table 15.1. Thus several film layers can be laid onto the painting consecutively and removed after well-defined waiting times. In this way the radiation of only few of the elements can be recorded separately on each of the film layers.

The Table 15.1 lists the typical elements presented in the pigments used by the old painters and the corresponding radioactive isotopes and their half-lives.

15.3 Instrumentation

The irradiation facility for NAAR uses usually a collimated neutron beam which transmits the painting through a small tilt angle, see Fig. 15.2. In this way a horizontal stripe with a length of about one meter on the painting is irradiated where the neutrons undergo nuclear interaction with the pigment layers. By scanning the painting in vertical direction the painting is activated homogenously. After the neutron irradiation which takes typically several hours the painting is transferred to another post-processing laboratory which is located usually outside the reactor hall. There layers of X-ray films or X-ray imaging plates are lain on the top of the painting. The 2D maps of the activated pigments are saved in digital format by direct read out of the imaging plates or scanning of the X-ray films. The different decay times of the various activated elements permits to visualize a certain pigment

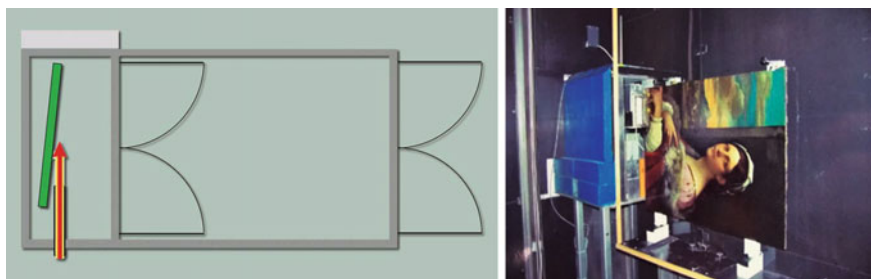


Fig. 15.2 Painting irradiation instrument for autoradiography investigations at the BER-II research reactor in Berlin (*top view*). The painting is fixed on a support in front of a neutron guide end with an open area of $3.5 \times 12.5 \text{ cm}^2$. The surface of the painting is adjusted under a small angle ($<3^\circ$) with respect to the axis of the guide. Thus a 12.5 cm wide strip of the painting is illuminated by the neutrons. The main free path of the neutrons within the paint layer is much longer than in the case of perpendicular transmission. The support is moved up and down with a velocity of a few cm/s in order to achieve a uniform activation of the total area of the panel. The facility is installed in a secure closed container. The basic area of the container is $250 \times 450 \text{ cm}^2$. On a special table in a shielded room in the basement the film exposure and the gamma spectroscopy can be performed for the suitable times (up to more than 4 weeks) depending on the half-lives of the isotopes

by removing of the film and the imaging plate layers at defined time periods, see Table 15.1.

The first film is exposed immediately after the painting irradiation. In this way mainly the radiation of atoms of the manganese isotope ^{56}Mn (half-life = 2.6 h) is recorded as the other elements decay much slower and their radiation is too weak to register on the film during this short period of time. Manganese is contained in brown pigments such as umbra or dark ochre. The image on the first film will show the distribution of these pigments in the painting.

The next film can be exposed for the following 20 min and will record radiation from Sodium and Copper atoms which decay a little slower than the Manganese atoms. The procedure is continued with still more films exposed for longer periods of time so the radiation of the slower decaying atoms can be recorded as well. The whole procedure yields some 5–10 film layers and takes up to 50 days to complete.

15.4 Example

An example of such a post-processing procedure is shown in Fig. 15.3.

A painting from the Gemäldegalerie Berlin similar to one painted by the French Court Painter Georges de la Tour (1593–1652) owned by the Louvre was investigated by NAAR in order to gain more information about its authorship—is it a copy painted by George de la Tour himself or by his son Etienne de la Tour?

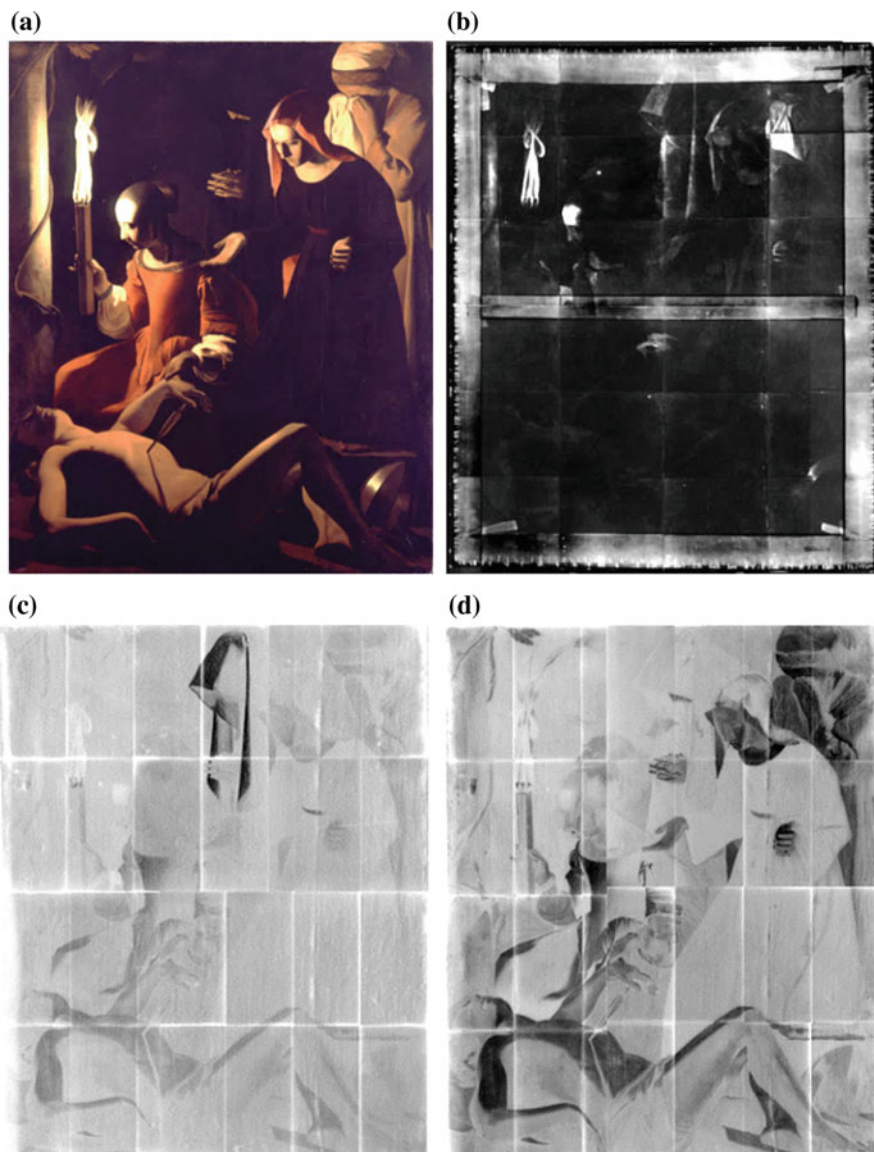


Fig. 15.3 **a** Photo of the painting St. Sebastian ca. 1649, exposed in the Gemäldegalerie Berlin. **b** X-ray radiography. The white pigment is well visible because it contains lead which is strong absorber for X-rays. The other pigments based on less absorbing elements like P or Cu are not visible. **c** Autoradiography image after 1 day: $2\text{CuCO}_3 \cdot \text{Cu}(\text{OH})_2$ (azurite) is mainly visible in mourners veil. **d** Autoradiography image after 5 days: the long-lived activity of ^{203}Hg (vermillion HgS) is clearly recognizable in the red dress and the lighter flesh colors. Also the body contour shows ^{32}P (Phosphorous in bone black)

The painting was irradiated by a neutron flux of 10^9 n/cm² s at the Autoradiography instrument B8 at the BER-II research reactor in Berlin. After the neutron irradiation the induced activity was detected with imaging plates as shown in Fig. 15.2.

Furthermore, the γ activity is recorded in different time steps at different locations on the painting: e.g. after 5 days in order to distinguish between Mercury ²⁰³Hg ($T_{1/2} = 46.6$ d) and Phosphorous ³²P ($T_{1/2} = 14.2$ d)

The autoradiography image (Fig. 15.3 d) shows the advantage of the autoradiography method for visualizing the distribution of pigments containing very light elements like Phosphorus. The visualisation of this element in deeper paint layers is impossible using X-ray based techniques, as the absorption of above lying layers will prohibit its detection.

The analysis gives evidence that painting is original copy by Georges de la Tour himself because the paint stroke is similar to the one used in other paintings. In addition there is clear outline and lack of overlap between painted areas which indicates the use of cartoons by the painter which is also typical for Georges de la Tour.

15.5 Areas of Application

The NAAR method is used for investigation of artistic, technical or geological items (foils, stones etc.) and other materials by qualitative depicting the elemental distribution in the sample using imaging plates or by quantitative analysis based on position sensitive gamma-spectroscopy. The NAAR instruments should be optimized for investigation of large format paintings. The cooperation with national museums and galleries is of vital importance. In case of the B8 instrument at the BER-II research reactor in Berlin two important external cooperation partners for joint research projects are the Painting Gallery of the Berlin State Museum (Staatliche Museen Preussischer Kulturbesitz, Gemäldegalerie zu Berlin) and the Prussian Palaces and Gardens Foundation Berlin-Brandenburg (Stiftung Preussischer Schlösser und Gärten Berlin-Brandenburg) in Potsdam.

15.6 Facilities

At the moment, the instrument B8 at the Berlin research reactor is the only dedicated facility for the neutron autoradiography of paintings.

15.7 Particularities

The autoradiography can be considered as a non-destructive method because 4 from 10^{12} atoms become radioactive on average. In extended studies (Ainsworth 1982) it has been shown, that dose of orders of magnitudes higher than applied today would create changes in the material.

As shown in Table 15.1 there are some elements which produce isotopes with very long half-life times after irradiation with neutrons, e.g. ^{60}Co ($T_{1/2} = 5.3$ years) and if such elements are activated they will need very long time to decay. In order to make sure that no hidden layers with these elements are present, a short test irradiation is performed every time when a new painting is prepared for autoradiography investigation. In this way by using of gamma spectrometry the amount of critical elements is estimated and a very conservative prediction about the expected decay time until the dose rate is below the radiation protection limit is made. Finally, the painting returns to the museum after going through a standard control procedure regulated by law and without any critical activity left, so that the painting does not represent any risk for public health or the health of the conservators.

Reference

Ainsworth MW (1982) Art and autoradiography, metropolitan museum of art. New York

Chapter 16

Neutron Imaging

N. Kardjilov, E. Lehmann, M. Strobl, R. Woracek and I. Manke

Abstract Neutron imaging is a non-destructive experimental method, which allows for revealing of the inner structure of the investigated objects. The high-penetration depth of the neutron beam in metal and rock materials in combination with the high-sensitivity to light-elements like hydrogen, lithium and boron determines the complimentary of the method to the wide spread X-ray and synchrotron imaging. In modern archaeology and paleontology neutron radiography and tomography are mainly applied for investigations of large scale samples, detection of organic materials and inspection of the level of degradation. Beside absorption contrast, other contrast mechanisms can be utilized in neutron imaging. Within the last decade, major technique developments included energy selective (monochromatic) imaging, phase-contrast imaging, dark-field (USANS) imaging, polarized neutron imaging, neutron resonance absorption imaging and diffraction contrast imaging. The latter, often also referred to as Bragg edge imaging, is based on energy selection by a monochromator or by time of flight and can be regarded as a powerful tool for applications in cultural heritage and archaeology.

16.1 Absorption Contrast Based Neutron Imaging

16.1.1 History

The application of the neutron to produce radiographs quickly followed its discovery by Chadwick in 1932. Kallman and Kuhn in Germany in 1935 used neutrons produced by an accelerator to make radiographs but the quality was poor due

N. Kardjilov (✉) · I. Manke
Helmholtz-Zentrum-Berlin, 14109 Berlin, Germany
e-mail: kardjilov@helmholtz-berlin.de

E. Lehmann
Paul-Scherrer- Institute, Villigen, Switzerland

M. Strobl · R. Woracek
ESS Lund, Lund, Sweden

to the weak and ill-defined beam (Kallmann and Kuhn 1940). This coupled with the complexity of the apparatus and the fact that hours of exposure were required did not lead to early exploitation as had happened with X-rays. Nevertheless, the methods and potential of the technique were clearly demonstrated followed by some basic experiments performed by Peter (1946).

The development of nuclear reactors during and after the war increased the intensity of neutron fluxes available for experimental purposes by many orders of magnitude, but further work on neutron radiography was not reported until 1956. The first use of a beam of neutrons from a reactor to produce a radiograph was by Thewlis and Derbyshire (Thewlis 1956). They used a beam from the 6 MW graphite reactor BEPO at Harwell to produce good quality images.

The technique developed slowly for several years until problems associated with the inspection of radioactive materials encouraged its more active revival. Several researchers reported their work in the early 1960s. But it was principally the work of Berger et al. (1964) of Argonne Laboratories in USA, followed by Barton (1965) at Birmingham University that led to its revival.

The history of neutron radiography stretches back 80 years; although, it is only in the last 30 years that it has come to the forefront as an accepted method of nondestructive testing.

16.1.2 Theory

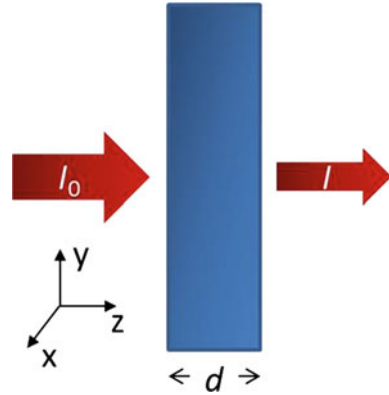
Absorption contrast imaging is based on recording the intensity attenuation for a sample transmitted by a neutron beam. The attenuation properties of materials are dependent on the specific interaction processes with the used radiation like absorption and scattering. In conventional radiography the attenuation of the incident beam by a sample can be described by an exponential function of two parameters—the transmitted thickness d and the linear attenuation coefficient Σ of the sample, Eq. (16.1).

$$I = I_0 \exp(-\Sigma d) \quad (16.1)$$

I_0 and I are the intensities of the incident and transmitted beam through the sample, Fig. 16.1.

For high resolution radiography purposes of bulk samples mainly two kinds of radiation are used: X-rays and neutrons. The charge-free neutron interacts with the nucleus of the atom, while in contrast X-rays interact with the charge distribution of the electron shell. Therefore the X-ray attenuation coefficients increase with the atomic number of the elements, i.e. with the number of electrons. The interaction probability of neutrons with the nucleus depends on the total cross section σ_t . The neutron cross section can be considered as the likelihood of interaction between an incident neutron and a target nucleus. As a consequence, the total cross section can be represented as sum of the scattering and the absorption cross sections $\sigma_t = \sigma_s + \sigma_a$. The standard unit for measuring the cross section is the *barn*, which is

Fig. 16.1 A schematic representation of beam attenuation by a material with thickness d



equal to 10^{-24} cm². The relation between neutron cross section and attenuation coefficient is given by Eq. (16.2).

$$\Sigma = \frac{N_a \rho}{at.wt.} \sigma_t \tag{16.2}$$

where N_a is the Avogadro number, ρ is the density and *at.wt.* is the atomic weight of the correspondent element. For some simplification in case of comparison between different aggregate states the ratio Σ/ρ , called *mass attenuation coefficient*, can be used.

The neutron cross section does not show a systematic dependence on the atomic number of the element. As a consequence, the attenuation properties of the elements for neutrons show a non-systematic dependence on the atomic number as shown in Fig. 16.2.

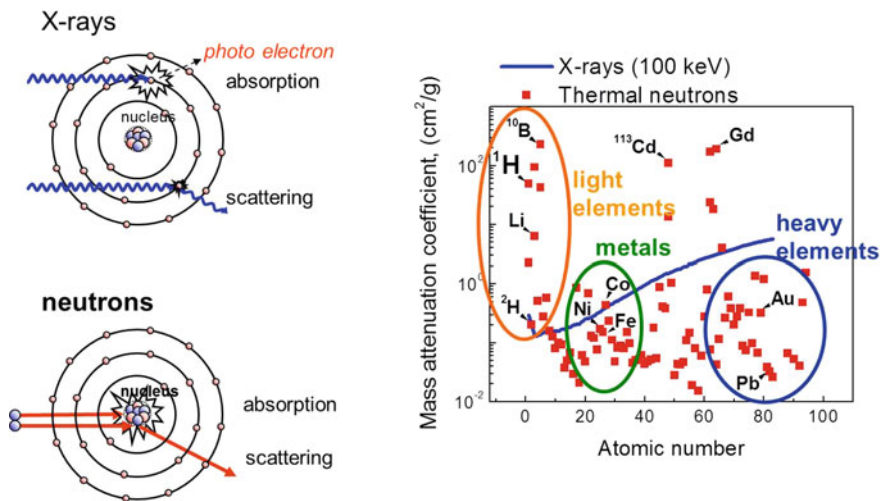


Fig. 16.2 Interaction mechanisms of X-rays and neutrons with matter

Table 16.1 Attenuation coefficients of some metals for thermal neutrons

Material	Au	Ag	Cu	Sn	Bronze	Pb	Zn	Fe
Σ (cm ⁻¹)	6.28	3.99	0.99	0.20	0.87	0.37	0.34	1.20

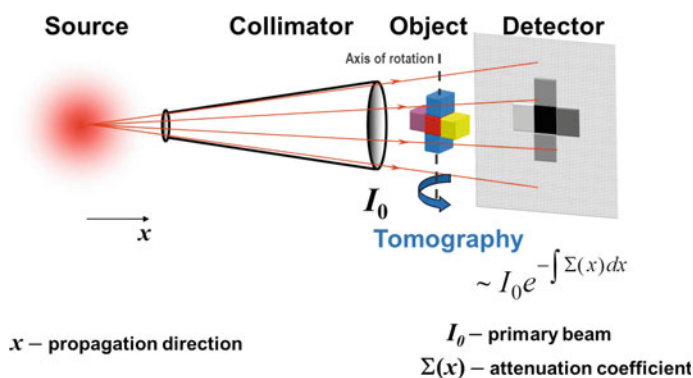
The neutron attenuation is sensitive to the isotope composition of the sample. The comparison of the attenuation coefficients for hydrogen ¹H and its isotope deuterium ²H in Fig. 16.2 shows much higher attenuation properties of hydrogen. For radiography purposes the energy of the neutrons is typically in the order of meV (thermal or cold neutrons). X-ray energies are normally in the order of ten to several hundred keV. Comparing the mass attenuation coefficients for different elements for the case of X-rays and thermal neutrons (see Fig. 16.2) the following main conclusions can be drawn:

- The neutrons are very sensitive to some light elements like H, Li, B, where X-rays do not provide a good contrast (low and similar atomic numbers);
- The distribution of attenuation coefficients for neutrons is independent of the atomic number which helps to achieve contrast even for neighbouring elements, while for X-rays one finds an approximately exponential increase with the atomic number;
- The neutrons easily penetrate thick layers of metals like Pb, Fe and Cu where standard X-ray imaging facilities with energies of several hundred keV fail;
- The neutrons can distinguish between isotopes (for instance ¹H and ²H) which is not the case for X-rays.

The attenuation coefficients of some metals, which are of high relevance for archaeological investigations, are listed in Table 16.1.

More about the interaction mechanism of neutrons with matter is provided in Banhart (2008).

In case of tomography investigation the sample is rotated around a defined axis where 2-dimensional projections are recorded under different rotation angles. The mathematical reconstruction of the matrix of the attenuation coefficients in the sample volume can be done using the collected set of projections as shown in Fig. 16.3.

**Fig. 16.3** A schematic view of a standard tomographic arrangement

Examples of application of neutron radiography and tomography in materials science are presented in Kardjilov et al. (2011a, b) and Strobl et al. (2009).

16.1.3 Instrumentation

A main parameter in neutron imaging experiments is the achieved spatial resolution. For this purpose a well-defined neutron beam from a neutron source is used to illuminate objects and to obtain “shadow images” on a two-dimensional detector screen. A schematic view of a typical tomographic arrangement is shown in Fig. 16.3.

Installations for neutron imaging are located at large-scale facilities where the requirements for high intensity and good beam definition can be fulfilled and are stationary setups surrounded by a corresponding infrastructure. An example of this

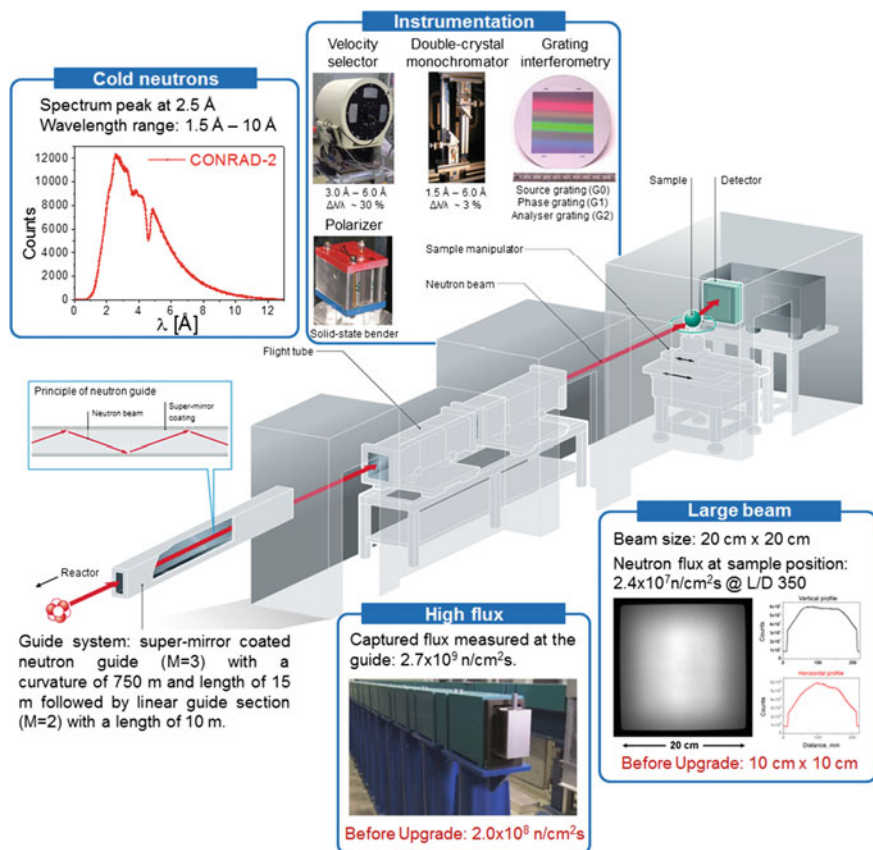


Fig. 16.4 Layout of the neutron imaging instrument CONRAD-2 at Helmholtz-Zentrum-Berlin (Kardjilov et al. 2016)

is shown in Fig. 16.4 where the facility CONRAD-2 at HZB (Kardjilov et al. 2016) is presented.

The large dimensions of the facility are given mainly by the massive shielding required for radiation protection and the space left for the experimental infrastructure.

The single components of neutron imaging instrument are presented in the following sections.

16.1.3.1 Source

Free neutrons can be produced in different ways: in nuclear reactors by fission reactions, in spallation sources by particle (proton) bombardment and the induced spallation process, in neutron generators by fusion reactions or in radioactive sources by photo-neutron emission.

The neutron energy of the primarily obtained neutrons is relatively high (between some tens of keV and hundreds of MeV), depending on the particular reaction. To obtain neutrons with lower energies, a moderation process has to be used, where the velocity of the fast neutrons is reduced by elastic collisions with the nuclei of the moderator material. The most common moderated neutrons suitable for imaging are either thermal (around 25 meV) or cold (around 3 meV) ones. It depends on the individual installation and in particular where the source point of the imaging beam line is located, which part of the spectrum can be used for imaging. A cold neutron spectrum is shown in Fig. 16.4 (top-left).

16.1.3.2 Geometry (Beam Line Design)

The beam of a tomography facility needs a pinhole collimation, expressed by the L/D ratio (L = distance from pinhole to sample, D = pinhole diameter), high enough to satisfy the condition for geometrical blurring (Schillinger 2001), see Fig. 16.5:

$$L/D > \frac{l}{d} \quad (16.3)$$

Here, the distance between the sample and the detector l and the required resolution d are of importance. Because the object is rotated during the inspection, l must be considered conservatively (as the maximum distance of an object point from the detector) because the distances will change.

As a real example, a 10 cm distance between the sample and the detector plane and a resolution better than 0.1 mm would require an L/D ration in the order of 1000, see (16.3). With smaller L/D values, lower spatial resolution in the tomography data will be obtained. Only in recent developments for a micro-setup with

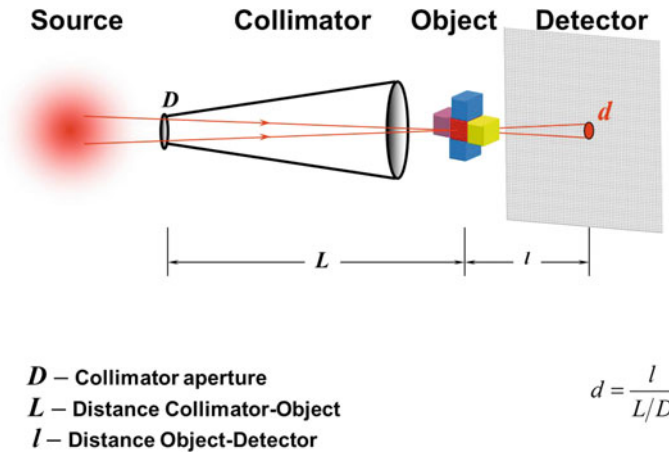


Fig. 16.5 A layout of the geometrical blurring in neutron imaging experiment which is defined by the L/D ratio and the distance to the detector l . (Schillinger 2001)

Field-of-View (FOV) of 10 mm resolutions better than 20 μm were realized (Williams et al. 2012).

For general applications, including those relevant to archaeology and cultural heritage, the best possible experimental conditions that neutron tomography facilities can offer today are based on a well collimated, nearly parallel and extended (up to 30 cm beam size) thermal or cold beam.

16.1.3.3 Detectors

Neutrons are uncharged particles and hence unable to cause direct ionisation. The detection process for neutrons happens via nuclear reactions, based on absorption, scattering or fission. Only the secondary charged reaction products are able to initiate a detection reaction.

The primary detectors in neutron imaging are based on layers of neutron sensitive materials (${}^6\text{Li}$, Gd, ${}^{10}\text{B}$) embedded inside an excitation material. They are placed perpendicular to the neutron beam. A summary of reactions within materials suitable for the neutron detection processes is given in Table 16.2. The secondary

Table 16.2 Capture reactions for thermal and cold neutrons

${}^3\text{He} + {}^1_0\text{n} \Rightarrow {}^3\text{He} + {}^1_1\text{p} + 0.77 \text{ MeV}$
${}^6\text{Li} + {}^1_0\text{n} \Rightarrow {}^3\text{H} + {}^4\text{He} + 4.79 \text{ MeV}$
${}^{10}\text{B} + {}^1_0\text{n} \Rightarrow {}^7\text{Li} + {}^4\text{He} + 2.78 \text{ MeV} (7 \%)$ $\Rightarrow {}^7\text{Li}^* + {}^4\text{He} + 2.30 \text{ MeV} (93 \%)$
${}^{155}\text{Gd} + {}^1_0\text{n} \Rightarrow {}^{156}\text{Gd} + \gamma\text{'s} + \text{CE's} (7.9 \text{ MeV})$
${}^{157}\text{Gd} + {}^1_0\text{n} \Rightarrow {}^{158}\text{Gd} + \gamma\text{'s} + \text{CE's} (8.5 \text{ MeV})$
${}^{235}\text{U}, {}^{239}\text{Pu} + {}^1_0\text{n} \Rightarrow \text{fission products} + 80 \text{ MeV}$

process, which is the actual detection process, can either be scintillation (light emission), charge transfer or stimulated luminescence.

For neutron scintillators, developments over years have shown that ZnS layers doped with colour centres to shift the emission wavelength are most useful in respect to light efficiency. However, they are limited in the spatial resolution due to the dissipation length of the reaction products from the neutron capture (e.g. ^4He and ^3H from ^6Li neutron capture) and due to the diffuse light output, when single grains of the scintillators get excited.

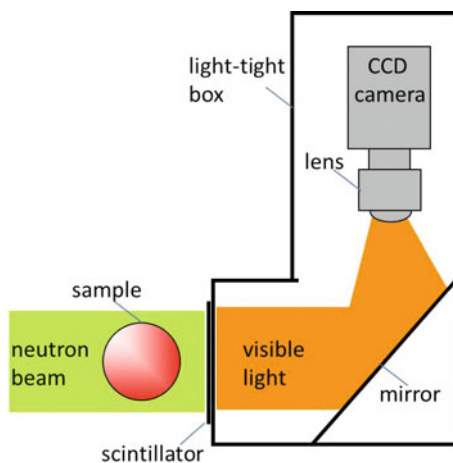
The requirements in neutron imaging for best possible performance are:

- the images must be in a digital format whereas the signal per pixel should be in linear dependence to the applied radiation dose;
- the detector position must be fixed in relation to beam and sample desk;
- the area of interest should be larger than the object size in any projection;
- the dynamic range of the imaging systems should be as large as possible (e.g. 16 bit);
- the sensitivity of the detection system with respect to perturbing beam components (gamma radiation, neutrons with higher energies) must be as low as possible;
- the noise level must be low and constant during all inspection work.

Specialized CCD-camera detectors are commonly in use for neutron tomography as simplified shown in Fig. 16.6 (Kardjilov et al. 2011a, b).

Due to the extremely high light sensitivity of the CCD cameras a light-tight cover is needed around all component of the detector system (scintillator screen, mirror, camera, shielding). The camera is placed outside the beam to prevent radiation damage to the CCD chip. It is optically coupled via a 45° mirror and a lens to the scintillator.

Fig. 16.6 Schematic layout of CCD-camera based detector system. (Kardjilov et al. 2011a, b)



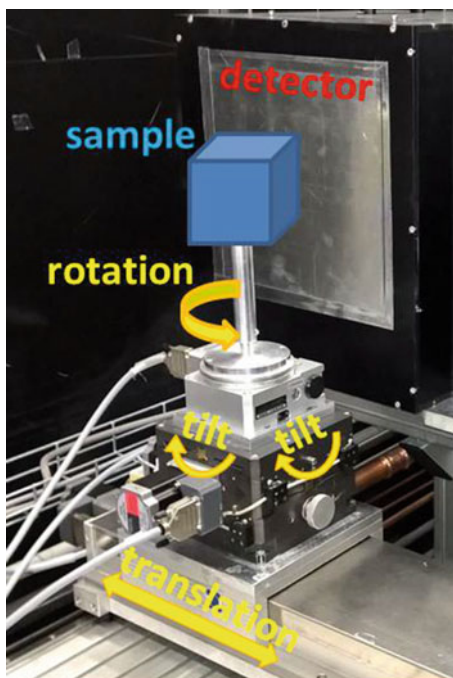
Depending on the neutron intensity, the CCD performance, the camera settings and the readout properties, the exposure time per frame is in the order of few seconds to some minutes. Such relative long exposure is only possible with cooled CCDs using mainly Peltier elements. Typical temperature levels on the chip are in the order of $-50\text{ }^{\circ}\text{C}$. Due to the required number of projections a tomography run typically takes times of the order of one hour or even longer. This is a reasonable timing compared to X-ray machines and sufficient for stationary investigations, where the object or process stays stable over the whole investigation time.

Most of the neutron imaging instruments have CCD cameras in use. Using a back-illuminated chip technology, the light collection efficiency has its maximum for the spectral range of the visible light produced by the ZnS scintillator.

16.1.3.4 Sample Environment

The precise positioning of the sample in tomography configuration is a major condition for a successful experiment. For this purpose the beam lines are equipped with a set of translation and tilt stages which allow for movement of the sample in the through-plane in respect to the beam. A rotation table is used for collection of angular projections from the sample and a translation stage helps for movement of the sample out of the beam area for collecting a set of open beam images. Typical sample environment configuration is shown in Fig. 16.7.

Fig. 16.7 Typical sample environment including detector and sample manipulator (rotary, tilt and translation tables)



16.1.3.5 Shielding

As mentioned above, a strong neutron source is an important prerequisite for high quality neutron imaging. For every radiation source, there are legal requirements regarding the safe operation and radiation protection of the personnel. A neutron imaging facility is therefore located within a measuring room, constructed of thick concrete shielding walls, and accessible only through a labyrinth secured by a safety door.

16.1.4 Examples

The use of Neutron Tomography (NT) for archaeometric investigations is quite recent. The first neutron tomography results for a non-destructive investigation on archaeological samples were reported in 1996 (Schillinger et al. 1996). In the following years a growing number of tomography measurements with neutrons have been performed on such kind of samples. One of the key reasons of this success is the fast development in digital image recording and processing, which enables the computation of tomographic reconstructions from high-resolution images at a reasonable timescale. The development of new detectors with better signal-to-noise characteristics and faster read-out electronics has allowed overcoming some of the spatial and time resolution limitations of conventional neutron radiography and tomography. On the other hand, the property of neutrons to easily transmit through large, dense samples is of great importance in modern archaeology. In fact, the three dimensional visualization of the inner structure of samples of archaeological interest helps to understand the technological process of manufacturing or provides information about the source of materials used in ancient masterpieces, especially noble metals. Therefore, it is not surprising that there is a growing interest of the scientific community towards the use of NT for archaeometric investigations. The neutron probe shows its advantages, as well as complementarities, with respect to classical X-rays investigation techniques, especially when materials containing hydrogen are investigated. Indeed the high sensibility of neutrons for some light elements (for example H, Li, B) solves most of the interpretation problems arising from samples characterized by the presence of polymeric or aqueous components. For this reason another application of NT in modern archaeology is the non-destructive inspection of the quality of specimens for conservation purposes. In such case, due to the high sensitivity of neutrons to hydrogenous materials, neutron tomography allows visualization of the distribution of impregnating solutions, for example, in treated woods and/or in partially corroded metal matrices.

For instance, the Neutron Tomography might be of extreme importance for obtaining the digital 3D reconstruction of recovered underwater items before starting the restoration work. First of all, the restoration and conservation work might be supported by the high resolution of the digital images, avoiding therefore

Late Roman sword (IV-V century A.D.) from ship wrecks near Sicily (Scoglio della Bottazza)



The corrosion process fully removed the metal part leaving only the calcareous matrix around the objects.

Fig. 16.8 Investigation of the handle of a late roman sword (*left*) by NT technique. A two-dimensional transmission image by neutrons is shown in the *middle*. A single slice from the 3D-tomographic volume is shown on the *right*. The *color* scale corresponds to the presented attenuation coefficients for neutrons from *blue* (hollow space) to *red* (iron). The *green* part represents the distribution of dissolved iron (Iron oxide) (Kardjilov et al. 2015)

wrong removal procedures of the calcareous concretion matrix of objects. In addition other precious information might be obtained for evaluating the degree of embedding of the concretion matrix inside and outside the object and the damages caused to the metallic parts, deciding whether or not the restoration work can take place (the metallic parts might collapse after years under water). Figure 16.8 shows the tomographic reconstruction of a portion of a late Roman sword from ship wrecks in an area not far from Sicily southern coast characterized by a dangerous cliff Scoglio della Bottazza (Kardjilov et al. 2015).

Another example of application of NT in this context is shown in Fig. 16.9, where the tomographic volume of the hidden object (a nail) inside a calcareous concretion shell has been extracted. Still there are many other objects that need to be recovered from the sea and the NT technique might help in building a database for identifying the correct historical frame period and also the correct conservation approach.

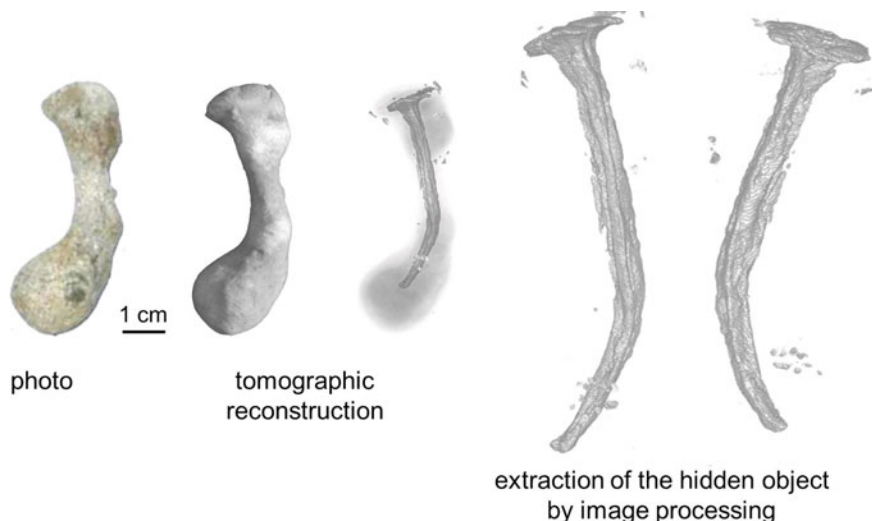


Fig. 16.9 Neutron tomographic investigation of object inside a calcareous concretion shell. The photo of the sample is shown on the *left*. The tomographic volume of the extracted nail is shown in the three images following the tomographic reconstruction of the object (Kardjilov et al. 2011a, b)

16.1.5 Areas of Application

Besides archaeology and cultural heritage, there is a broad spectrum of applications using the absorption contrast imaging techniques including materials research, life sciences, and paleontology. Industrial applications including fuel cell research have also been improved through these new developments (Kardjilov et al. 2011a, b; Strobl et al. 2009).

16.1.6 Facilities

Establishing neutron imaging as a standard tool for non-destructive testing and material research required dedicated access to suitable beam lines at strong neutron sources. In the past years it was possible to establish stations for neutron tomography at leading neutron sources in Europe (as well as outside Europe).

Some more facilities are under preparation and installation. All these facilities differ to some extent concerning some key criteria like flux and spectra. The right choice of beam line for a certain task might be important for the success of a specific investigation. The access to the beam lines and to user support is organised via proposal procedures of the different facilities. European funding supports the scientific use of this research infrastructure. A map of the facilities can be seen in Fig. 16.10.



Fig. 16.10 Map of the neutron imaging facilities worldwide (*red*: user operation; *green*: inhouse research; *yellow*: under construction). Interactive version of the map can be found under: <http://isnr.de/index.php/facilities>

Well established neutron imaging facilities having user operation (dating to the year 2016) can be found in the following countries related to different geographic regions: <http://isnr.de/index.php/facilities/user-facilities>

16.2 Diffraction Contrast Based Neutron Imaging

16.2.1 History

Early experiments to study the nuclear cross-sections of elements, using transmission measurements, have already been reported by Fermi et al. in 1947 (Fermi et al. 1947) and Winsberg et al. in 1949 (Winsberg et al. 1949). The transmission technique was even applied to study the effect of cold rolling on brass, including discussion of grain size effects, by Weiss et al. back in 1952 (Weiss et al. 1952). In

1950, Cassels provided a summary on total neutron scattering cross sections, including Bragg edges. (Cassels 1950) In the mid-1990', a group of the Nuclear Physics Institute (Czech Republic) implemented the Bragg edge transmission method at a neutron diffractometer instrument at a reactor source, aiming to measure (residual) strain (Mikula et al. 1995; Wagner et al. 1997). Those measurements were performed at reactor sources using monochromator crystals, which was time consuming and no spatially resolving detectors were available.

With the advent of neutron spallation sources in the 1970s (Carpenter 1977), the time of flight technique now provided the possibility to record the transmission spectrum much more efficiently. In 1982, Johnson and Bowman used the NBS (now National Institute of Standardization) 100 MeV Electron Linac to record and distinguish Bragg edges for iron (Johnson and Bowman 1982). The next generation of spallation sources installed at Los Alamos National Laboratory (USA; LANSCE) and Rutherford Appleton Laboratory (UK; ISIS), provided unprecedented opportunities. Novel detector technology (Bowman et al. 1990) was used at LANSCE by Meggers and Priesmeyer et al. to study the phase transformation of austenite to bainite in gray iron in real time (Meggers et al. 1994a, b). At ISIS, D. Wang showed in his dissertation in situ (tensile and compressive) loading of steel samples measured by neutron transmission vs. surface strain gauges. (Wang 1996) The Bragg edge transmission technique was further developed at LANSCE, with a focus to investigate kinetics of structural phase transitions, and at ISIS, with a focus on the measurement of d-spacings and strain. Some notable publications as part of these developments at LANSCE and ISIS include the work by Priesmeyer et al. (1999) and Santisteban et al. (2002a, b), as well as the dissertation projects by Vogel at LANSCE (Vogel 2000, 3) and Steuwer at ISIS (Steuwer et al. 2001, 2003). A comparison of Bragg-Edge neutron-transmission spectroscopy at both facilities is given by both groups in Santisteban et al. (2002a, b). The recent implementation of monochromator devices at existing imaging beamlines at reactor sources (Treimer et al. 2006; Lehmann et al. 2009) has opened the possibilities to exploit the same contrast mechanisms while readily providing good spatial resolution and a large field of view. It was shown that in principal even strain radiography is feasible at an imaging beamline (Woracek et al. 2011) and more relevant applications include the quantification of metallic phases by diffraction contrast tomography (Woracek et al. 2014).

16.2.2 Theory

Information related to the crystal structure of crystalline materials (strain, phase, texture) is traditionally obtained using (X-ray or neutron) diffractometers. In a diffractometer where a fixed wavelength is used, the diffraction angle is determined. If a wavelength spectrum is available (typically at neutron spallation sources), a wavelength-dependent intensity spectrum is recorded under some fixed angles to the direction of the incident neutron beam. The detected intensity maxima (so-called Bragg peaks) are accordingly plotted as a function of diffraction angle or wavelength.

Due to the same (Bragg scattering) effect, the same information can (in principle) be obtained by recording the transmitted neutron beam through the sample: Some neutrons travel without interaction through the sample, some are absorbed, while those that are scattered out of the direction of the incident beam (which would be detected in a diffractometer), leave a characteristic pattern of missing neutrons in the transmitted intensity spectrum, so-called Bragg edges. Hence, additional spatial information in two dimensions can be obtained if an imaging detector is used in transmission geometry.

Performing Bragg edge transmission imaging with a detector positioned behind the sample, requires the possibility to record the transmitted neutron intensity as a function of wavelength. For a particular hkl family in a powder-like multi-crystalline sample, the scattering angle increases as the wavelength is increased until the Bragg scattering condition cannot be fulfilled any longer, which occurs for wavelengths larger than $\lambda = 2d_{hkl} \sin 90^\circ = 2d_{hkl}$. At this particular wavelength, the transmitted intensity increases drastically (the so called Bragg edge: see Fig. 16.11). Obviously, any change in d_{hkl} would shift the Bragg edge correspondingly, and consequently, strains along the beam direction ($\theta_{BC} = 90^\circ$) can be resolved, hence the method is sometimes termed “strain radiography”. Analogous to a diffraction pattern, phase and texture differences will also lead to differences in the Bragg edge spectrum.

The Bragg edge transmission technique has recently gained attention again, due to the new generation of spallation sources (SNS, J-PARC, ISIS 2nd target station,

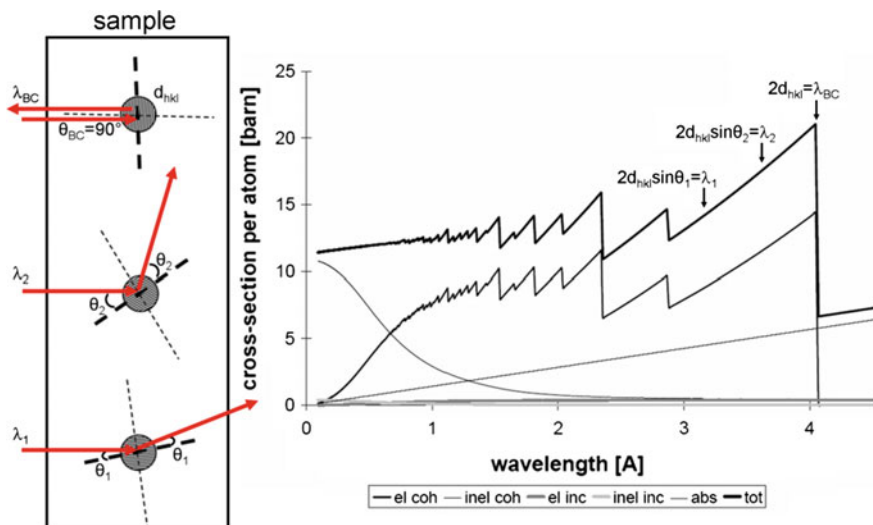


Fig. 16.11 The Bragg scattering process in polycrystalline material is given schematically on the left. An example of the energy dependent attenuation spectrum for iron is given on the right with a bold line. The positions of the wavelengths fulfilling the Bragg law on the left are marked with arrows

ESS) and the fact that many existing neutron imaging facilities now provide the possibility of (tunable) wavelength selection.

16.2.3 Instrumentation

At several neutron imaging beamlines at steady neutron sources, monochromator devices are available or are currently being installed, which allow choosing a certain neutron energy (wavelength). The most common monochromator devices at continuous sources are velocity selectors and double crystal monochromators, which provide an unchanged beam direction and usually can be tuned to different energies. Velocity selectors (also called turbine selectors) typically provide energy resolutions of $\Delta\lambda/\lambda$ of $\approx 10\text{--}15\%$, while a double crystal monochromator (Treimer et al. 2006) provides about 3 % (can be varied between $<1\text{--}10\%$ depending on the type of crystal being used). For pulsed sources (e.g. a spallation source), time resolved data analysis provides the option to record neutrons of particular wavelengths. The same can also be performed at a continuous source if choppers are being used. (Strobl et al. 2010) In all cases, if a better $\Delta\lambda/\lambda$ is desired, a loss of neutron intensity linearly with the resolution improvement is to be expected. Neutron imaging at time-of-flight (spallation based) sources has only recently started and cannot yet be considered an established method. However, it has the advantage that the wavelength spectrum is readily available, but sophisticated time resolving imaging detectors are necessary and only recently have become available (Tremisn et al. 2005, 2008, 2009, 2010a, b; Siegmund et al. 2007), but it is expected that significant advancements will happen within the next few years. A comprehensive overview of energy selective options for neutron imaging is given by Lehmann et al. (2009). The double crystal monochromator at the CONRAD-2 instrument is shown in Fig. 16.12.

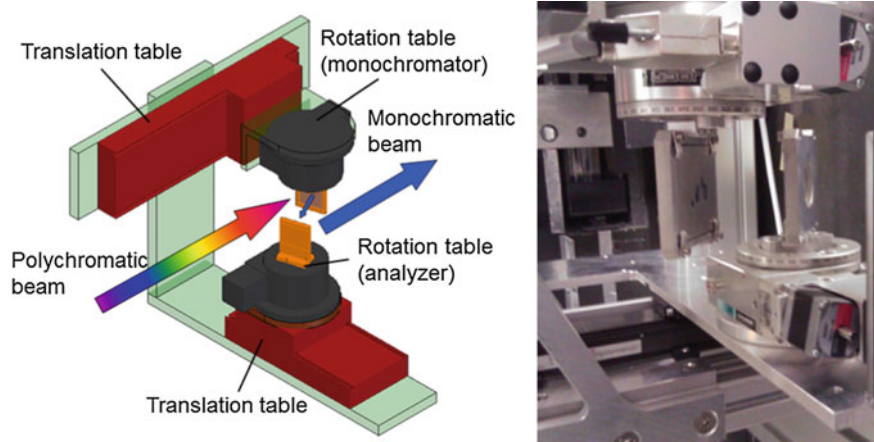


Fig. 16.12 Double crystal monochromator for CONRAD at HZB

New detectors are being developed for time of flight imaging applications. Kiyanagi et al. (2014) report about the developments at J-PARC, that those detectors typically have a high counting rate with a medium to low spatial resolution (about 2–3 mm pixel size) or a medium counting rate with smaller pixel sizes (approx. 1 mm), while the active area is reasonably large (4–100 cm²). The detector technology that was developed by Tremsin and co-workers, is based on (doped with neutron absorbing atoms) microchannel plates (MCPs) and a Medipix/Timepix readout sensor (Tremsin et al. 2005; Siegmund et al. 2007). Tremsin describes the detection principle: “The process of neutron detection by the MCP consists of three stages: absorption of incoming neutron within the MCP glass; escape of the reaction products into adjacent pore; release of charged particles from the pore walls which initiate the electron avalanche in the pore producing the signal detected by the detector readout” (Tremsin et al. 2008).

The latest version of this detector possesses a pixel size of 55 μm, a 512 × 512 pixel field of view, and a temporal resolutions below 1 μs can be achieved. The MCP detector has been used for proof-of-concept studies at ISIS (Tremsin et al. 2009) and SNS (Tremsin et al. 2010a, b), as well as for texture imaging of zirconium at ISIS (Santisteban et al. 2011). The same detector can be used for strain mapping under in situ loading. It was also used for phase mapping in samples that have undergone transformation induced plasticity effect.

On the other hand, several dedicated neutron radiography/tomography instruments at steady state sources can readily provide spatial resolutions on the order of or smaller than 50 μm (Kardjilov et al. 2009) and therefore implementation of energy selective Bragg-edge imaging techniques could open many new applications. In principle there are two possibilities to do such energy dependent measurements at a reactor source (Lehmann et al. 2009): (a) using the time-of-flight information in distance from the source using a specifically designed chopper system or (b) selection (or suppression) of neutrons from specific spectral parts. In the latter case the wavelengths can be selected by a velocity selector or a wavelength tunable device, e.g. a double crystal monochromator. Using different settings or crystals allow selection of a very narrow spectral part, but one should keep in mind that the flux decreases as a narrower wavelength band is selected.

16.2.4 Examples

Proof of principle measurements have been reported by neutron imaging facilities, for the case of microstructural differences in welds (Lehmann et al. 2009; Schulz et al. 2009, 2010, 2011; Kardjilov et al. 2012), for differentiating materials and strain variations in a bend steel plate (Treimer et al. 2006), for texture effects in a processed aluminium foam sandwich (AFS) (Kardjilov et al. 2009), for microstructural differences in ancient swords (Salvemini et al. 2012) and historical copper (Peetermans et al. 2012). In 2008, the group at HZB (N. Kardjilov, I. Manke,

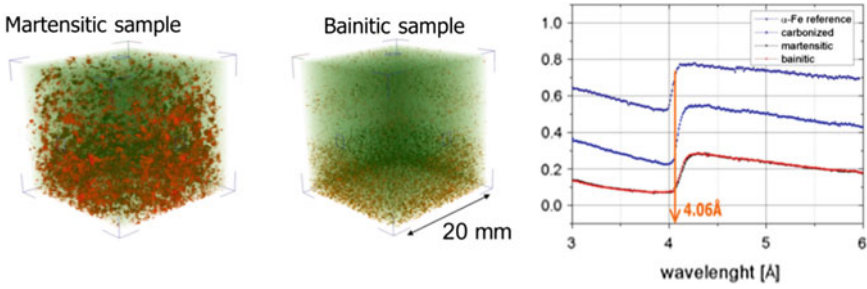


Fig. 16.13 Demonstration of a monochromatic neutron tomography for discrimination of two different crystalline phases. The measurement was taken at 4.06 Å

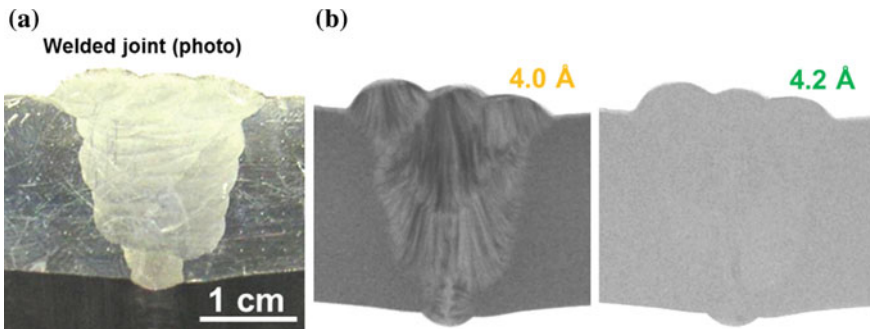


Fig. 16.14 Energy selective neutron images of weld joint between two austenitic steel plates. **a** Photographic image. **b** Radiographic images at two wavelengths around the Bragg edge for iron corresponding to (110) lattice space. Bragg scattering from individual crystallites causes contrast in the radiographs due to preferred crystallographic orientations inside the weld, while no more scattering takes place after the Bragg-cut-off (Kardjilov et al. 2012)

T. Kandemir) demonstrated tomographic reconstructions of metallic samples (Fig. 16.13), which consisted of varying amount of martensite and bainite.

The majority of the published results, which have been obtained at existing neutron imaging facilities using the Bragg edge method, were largely of qualitative—rather than quantitative—nature. Nonetheless, images recorded in this mode can reveal inhomogeneities and features that would remain undetected otherwise. The example radiographs for a steel weld, obtained at wavelengths before and after the Bragg cut off, shown in Fig. 16.14 present such an example. A comparison of transmission measurements of different welds with electron backscatter diffraction (EBSD) have been performed by the group at PSI (Lehmann et al. 2014). A prominent example for quantification of phase fractions in a metastable stainless steel is given by Woracek and co-workers (Woracek et al. 2014) where austenite and martensite was visualized and quantified in radiography and tomography. It should be noted that in this emerging field, ongoing method development is expected to lead to even further improvements in the experimental capabilities.

Table 16.3 List of the countries possessing neutron imaging facilities providing user service (in year 2016)

Europe	Germany, Switzerland, Hungary
Asia and Oceania	South Korea, Japan, Australia
Nord America	USA
South America	Brazil
Africa	South Africa

16.2.5 Facilities

The energy-selective neutron imaging can be established at every imaging instrument using appropriate technique for beam monochromatization. Therefore all facilities mentioned in Table 16.3 and Fig. 16.10 can be used for energy-selective investigations where the spallation sources like J-PARC (Japan) and ISIS (United Kingdom) are preferable for this kind of measurements. In this case the time-of-flight method provides the best conditions for achieving high wavelength resolution. New imaging installations are planned at SNS (USA) and at the future ESS (Sweden) which will extend the capabilities for energy-selective imaging.

References

- Banhart J (2008) Advanced tomographic methods in materials research and engineering. Oxford University Press, New York
- Barton JP (1965) Radiographic examination using cold neutrons. *Br J Appl Phys* 16:1051
- Berger H, Tyłka J, Talbot J (1964) Determination of cadmium burnup in reactor control rods by neutron radiography. *Nucl Sci Eng* 18:236
- Bowman JD, Szymanski JJ, Yuan VW, Bowman CD, Silverman A, Zhu X (1990) Current-mode detector for neutron time-of-flight studies. *Nucl Instrum Methods Phys Res Sect A* 297:183–189 (published online Epub11/15/)
- Carpenter JM (1977) Pulsed spallation neutron sources for slow neutron scattering. *Nucl Instrum Methods* 145:91–113 (published online Epub8/15/)
- Cassels J (1950) The scattering of neutrons by crystals. *Prog Nucl Phys* (editor OR)
- Fermi E, Sturm WJ, Sachs RG (1947) The transmission of slow neutrons through microcrystalline materials. *Phys Rev* 71:589–594 (published online Epub05/01/)
- Johnson R, Bowman C (1982) High resolution powder diffraction by white source transmission measurements. *AIP Conf Proc* 89:53–56 (published online Epub191)
- Josic L, Steuwer A, Lehmann E (2010) Energy selective neutron radiography in material research. *Appl Phys A* 99:515–522 (published online Epub2010/06/01)
- Josic L, Lehmann E, Kaestner A (2011) Energy selective neutron imaging in solid state materials science. *Nucl Instrum Methods Phys Res Sect A* 651:166–170 (published online Epub9/21/)
- Kallmann H, Kuhn E (1940) Vol US Patent No 2186 757
- Kardjilov N, Hilger A, Manke I, Strobl M, Dawson M, Banhart J (2009) New trends in neutron imaging. *Nucl Instrum Methods Phys Res Sect A* 605:13–15
- Kardjilov N, Manke I, Hilger A, Strobl M, Banhart J (2011a) Neutron imaging in materials science. *Mater Today* 14:248
- Kardjilov N, Dawson M, Hilger A, Manke I, Strobl M, Penumadu D, Kim FH, Garcia-Moreno F, Banhart J (2011b) A highly adaptive detector system for high resolution neutron imaging. *Nucl Instrum Methods Phys Res A* 651:95–99

- Kardjilov N, Manke I, Hilger A, Williams S, Strobl M, Woracek R, Boin M, Lehmann E, Penumadu D, Banhart J (2012) Neutron Bragg-edge mapping of weld seams. *Int J Mater Res* 151:154
- Kardjilov N, Hilger A, Manke I, Benfante V, Lo Celso F, Triolo R, Ruffo I, Tusa S (2015) Neutron tomography in archaeology. *Mater Prufung* 57
- Kardjilov N, Hilger A, Manke I, Woracek R, Banhart J (2016) CONRAD-2: the new neutron imaging instrument at the Helmholtz-Zentrum Berlin. *J Appl Crystallography* 49:195–202
- Kiyanagi Y, Kamiyama T, Kino K, Sato H, Sato S, Uno S (2014) Pulsed neutron imaging using 2-dimensional position sensitive detectors. *J Instrum* 9:C07012
- Lehmann EH, Frei G, Vontobel P, Josic L, Kardjilov N, Hilger A, Kockelmann W, Steuwer A (2009) The energy-selective option in neutron imaging. *Nucl Instrum Methods Phys Res Sect A* 603:429–438
- Lehmann E, Peetermans S, Josic L, Leber H, van Swygenhoven H (2014) Energy-selective neutron imaging with high spatial resolution and its impact on the study of crystalline-structured materials. *Nucl Instrum Methods Phys Res Sect A* 735:102–109
- Meggers K, Priesmeyer HG, Trela WJ, Bowman CD, Dahms M (1994a) Real time neutron transmission investigation of the austenite-bainite transformation in grey iron. *Nucl Instrum Methods Phys Res Sect B* 88:423–429 (published online Epub6/2/)
- Meggers K, Priesmeyer HG, Trela WJ, Dahms M (1994b) Investigation of the austenite-bainite transformation in gray iron using real time neutron transmission. *Mater Sci Eng A* 188:301–304 (published online Epub11/30/)
- Mikula P, Vrána M, Lukáš P, Šaroun J, Strunz P, Wagner V, Alefeld B (1995) Bragg optics for strain/stress measurement techniques. *Physica B Condensed Matter* 213–214:845–847 (published online Epub8/1/)
- Peetermans S, van Langh R, Lehmann E, Pappot A (2012) Quantification of the material composition of historical copper alloys by means of neutron transmission measurements. *J Anal At Spectrom* 27:1674–1679
- Peter O (1946) Neutronen-Durchleuchtung. *Zeitschrift Naturforschung Teil A* 1:557
- Priesmeyer HG, Stalder M, Vogel S, Meggers K, Bless R, Trela W (1999) Bragg-Edge Transmission as an Additional Tool for Strain Measurements. *Textures Microstruct* 33:173–185
- Salvemini F, Grazi F, Peetermans S, Civita F, Franci R, Hartmann S, Lehmann E, Zoppi M (2012) Quantitative characterization of Japanese ancient swords through energy-resolved neutron imaging. *J Anal At Spectrom* 27:1494–1501
- Santisteban JR, Edwards L, Fitzpatrick ME, Steuwer A, Withers PJ (2002a) Engineering applications of Bragg-edge neutron transmission. *Appl Phys A Mater Sci Process* 74:s1433–s1436
- Santisteban JR, Edwards L, Priesmeyer HG, Vogel S (2002b) Comparison of Bragg-Edge neutron-transmission spectroscopy at ISIS and LANSCE. *Appl Phys A Mater Sci Process* 74: s1616–s1618
- Santisteban JR, Vicente-Alvarez MA, Vizcaino P, Banchik AD, Vogel SC, Tremsin AS, Vallergera JV, McPhate JB, Lehmann E, Kockelmann W (2011) Texture imaging of zirconium based components by total neutron cross-section experiments. *J Nucl Mater*
- Schillinger B (2001) Improved radiography and 3D tomography due to better beam geometry. *Nondestr Test Eval* 16:277–285
- Schillinger B, Gebhard R, Haas B, Ludwig W, Rausch C, Wagner U (1996) 3D computer tomography in material testing and archaeology. In: Presented at the 5th World Conference on Neutron Radiography. Berlin, Germany, June 17–20
- Schulz M, Böni P, Calzada E, Mühlbauer M, Schillinger B (2009) Energy-dependent neutron imaging with a double crystal monochromator at the ANTARES facility at FRM II. *Nucl Instrum Methods Phys Res Sect A* 605:33–35 (published online Epub6/21/)
- Siegmund OH, Vallergera JV, Tremsin AS, McPhate J, Feller B (2007) High spatial resolution neutron sensing microchannel plate detectors. *Nucl Instrum Methods Phys Res Sect A* 576:178–182

- Steuwer A, Withers PJ, Santisteban JR, Edwards L, Bruno G, Fitzpatrick ME, Daymond MR, Johnson MW, Wang D (2001) Bragg Edge Determination for Accurate Lattice Parameter and Elastic Strain Measurement. *physica status solidi (a)* 185:221–230
- Steuwer A, Santisteban JR, Withers PJ, Edwards L, Fitzpatrick ME (2003) In situ determination of stresses from time-of-flight neutron transmission spectra. *J Appl Crystallogr* 36:1159–1168
- Strobl M, Manke I, Kardjilov N, Hilger A, Dawson M, Banhart J (2009) Advances in neutron radiography and tomography. *J Phys D Appl Phys* 42:243001
- Strobl M, Steitz R, Kreuzer M, Nawara A, Mezei F, Rose M, Amitesh P, Grunze M, Dahint R (2010) BioRef—a time-of-flight neutron reflectometer combined with in-situ infrared spectroscopy at the Helmholtz Centre Berlin. *J Phys Conf Ser* 251:012059
- Thewlis J (1956) Neutron radiography. *Br J Appl Phys* 7:345
- Treimer W, Strobl M, Kardjilov N, Hilger A, Manke I (2006) Wavelength tunable device for neutron radiography and tomography. *Appl Phys Lett* 89:203504
- Tremisn AS, Bruce Feller W, Gregory Downing R (2005) Efficiency optimization of microchannel plate (MCP) neutron imaging detectors. I. Square channels with 10B doping. *Nucl Instrum Methods Phys Res Sect A* 539:278–311
- Tremisn AS, Vallergera JV, McPhate JB, Siegmund OHW, Feller WB, Crow L, Cooper RG (2008) On the possibility to image thermal and cold neutron with sub-15 μm spatial resolution. *Nucl Instrum Methods Phys Res Sect A* 592:374–384
- Tremisn AS, McPhate JB, Kockelmann WA, Vallergera JV, Siegmund OHW, Feller WB (2009) Energy-Resolving Neutron Transmission Radiography at the ISIS Pulsed Spallation Source With a High-Resolution Neutron Counting Detector. *Nucl Sci IEEE Trans* 56:2931–2937
- Tremisn AS, McPhate JB, Vallergera JV, Siegmund OHW, Feller WB, Bilheux HZ, Molaison JJ, Tulk CA, Crow L, Cooper RG, Penumadu D (2010a) Transmission Bragg edge spectroscopy measurements at ORNL Spallation Neutron Source. *J Phys Conf Ser* 251:012069
- Tremisn AS, Muhlbauer MJ, Schillinger B, McPhate JB, Vallergera JV, Siegmund OHW, Feller WB (2010b) High resolution stroboscopic neutron radiography at the FRM-II ANTARES facility. *Nucl Sci IEEE Trans* 57:2955–2962
- Vogel S (2000) A Rietveld-Approach for the Analysis of Neutron Time-of-Flight Transmission Data. Ph.D., Thesis at University of Kiel, Germany (http://macau.uni-kiel.de/receive/dissertation_diss_00000330)
- Wagner V, Kouril Z, Lukas P, Mikula P, Saroun J, Strunz P, Vrana M (1997) Residual strain/stress analysis by means of energy-dispersive neutron transmission diffraction (EDNTD). *Proc. SPIE* 2867, International Conference Neutrons in Research and Industry, pp 168–171, doi:10.1117/12.267893
- Wang DQ (1996) Strain measurement using neutron diffraction. The Open University
- Weiss RJ, Clark JR, Corliss L, Hastings J (1952) Neutron diffraction studies of cold-worked brass. *J Appl Phys* 23:1379–1382
- Williams SH, Hilger A, Kardjilov N, Manke I, Strobl M, Douissard PA, Martin T, Riesemeier H, Banhart J (2012) Detection system for microimaging with neutrons. *J Instrum* 7:P02014
- Winsberg L, Meneghetti D, Sidhu SS (1949) Total neutron cross sections of compounds with different crystalline structures. *Phys Rev* 75:975–979 (published online Epub03/15/)
- Woracek R, Penumadu D, Kardjilov N, Hilger A, Strobl M, Wimpory R C, ... & Banhart J (2011) Neutron Bragg-edge-imaging for strain mapping under in situ tensile loading. *J Appl Phys* 109 (9):093506
- Woracek R, Penumadu D, Kardjilov N, Hilger A, Boin M, Banhart J, Manke I (2014) 3D Mapping of Crystallographic Phase Distribution using Energy—Selective Neutron Tomography. *Adv Mater*, 26(24):4069–4073